Spectroscopic Patterns Encode Unimolecular Dynamics

by

Matthew Paul Jacobson

Submitted to the Department of Chemistry
in partial fulfillment of the requirements for the degree of

Doctor of Philosophy

at the

MASSACHUSETTS INSTITUTE OF TECHNOLOGY

June 1999

Author_____
Department of Chemistry
April 29, 1999

Certified by_____
Robert W. Field
Professor of Chemistry
Thesis Supervisor

Certified by_____
Robert J. Silbey
Professor of Chemistry
Thesis Supervisor

Accepted by_____
Dietmar Seyferth
Chairman, Departmental Committee on Graduate Students

This doctoral thesis has been examined by a Committee of the Department of Chemistry that included

Professor Jianshu Cao _____
(Chairperson)

Professor Andrei Tokmakoff _____

Professor Robert J. Silbey _____
(Thesis Supervisor)

Professor Robert W. Field _____
(Thesis Supervisor)

Spectroscopic Patterns Encode Unimolecular Dynamics

by

Matthew Paul Jacobson

Submitted to the Department of Chemistry
on April 29, 1999, in partial fulfillment of the
requirements for the degree of
Doctor of Philosophy

Abstract

This thesis investigates the unimolecular vibrational dynamics of acetylene with up to 15,000 cm^{-1} of internal energy, as encoded by dispersed fluorescence spectra of the acetylene $S_1 \rightarrow S_0$ system. Above 10,000 cm^{-1} of vibrational energy, these spectra are extremely congested and cannot be analyzed using conventional spectroscopic assignment procedures. Instead, a numerical pattern recognition technique entitled Extended Cross Correlation (XCC) is introduced which utilizes methods of robust estimation to identify *a priori* unknown patterns that are repeated in multiple spectra. In particular, the XCC identifies spectroscopic patterns in the dispersed fluorescence spectra that are associated with approximately conserved polyad quantum numbers.

This pattern recognition analysis makes possible detailed modelling, using an effective Hamiltonian, of the acetylene unimolecular vibrational dynamics up to 15,000 cm^{-1}. Of special interest are the large-amplitude bending motions of acetylene at high energy (22 quanta of bend excitation), which are investigated using techniques of quantum, semiclassical, and nonlinear classical mechanics. At 15,000 cm^{-1}, the classical mechanics associated with the bending system is profoundly different from that at low energy, where normal mode motions (*trans* and *cis* bend) dominate. Specifically, classical chaos coexists with stable classical motions that are unrelated to the normal mode motions. The most stable large amplitude bending motions include "local bend" (one hydrogen bending) and "counter-rotation" (the two hydrogens undergoing circular motion at opposite ends of the molecule) motions. The existence of these stable motions at high energy is a manifestation of a normal-to-local transition in the bend degrees of freedom that is analogous to, but substantially more complicated than, the well-known normal-to-local transitions in the stretch degrees of freedom of ABA molecules.

In addition to the XCC, two additional numerical tools for spectroscopic analysis are discussed: Hybrid Linear Pattern Analysis (HLPA) and Robust Baseline Estimation (RBE). HLPA is a hybrid of conventional least-squares fitting and XCC which is applicable when certain patterns contained in a spectroscopic data set are known *a priori* but others are not. HLPA is applied to investigate the kinetics of inter-

molecular energy transfer in atmospheric simulation experiments involving carbon monoxide. RBE is a technique for baseline removal; that is, it permits the separation of the sharp features in a spectrum from a continuous, slowly varying baseline.

Thesis Supervisor: Robert W. Field
Title: Professor of Chemistry

Thesis Supervisor: Robert J. Silbey
Title: Professor of Chemistry

Acknowledgments

First and foremost, I would like to thank my advisors past and present:

- Bob Field, whose depth of commitment to his graduate students, and insistence that they provide the intellectual direction for his research group, are unparalleled;
- Bob Silbey, whose incisive theoretical insights have amazed and inspired me; and
- Dick Zare, whose infectious enthusiasm convinced me that I wanted to be a physical chemist.

Ramachandra Dasari also acted as an informal advisor during the period in which I built the picosecond laboratory in the Spec Lab and collaborated with Betsy Jamieson (Lippard group, MIT) on single photon counting experiments.

Secondly, I would like to acknowledge the funding agencies that made the work in this thesis possible. During the second, third, and fourth years of my graduate work, I was supported by the Department of the Army under a National Defense Science and Engineering Graduate Fellowship. During my fifth and final year, I was supported by the Fannie and John Hertz foundation. Being supported by external graduate fellowships contributed substantially to my self-confidence as an independent scientist, and I would like to thank both organizations for their support. The research in Part I of this thesis, on spectroscopic pattern recognition, was supported by AFOSR. The research on acetylene unimolecular dynamics, in Part II, was supported by the Department of Energy.

I have been privileged to collaborate with a number of outstanding scientists at MIT and elsewhere, including

- Howard Taylor (USC) and Christof Jung (UNAM), from whom I learned a tremendous amount about semiclassical methods;
- Steve Coy, who introduced me to, and collaborated with me on, spectroscopic pattern recognition;

- Jon O'Brien, my immediate predecessor on the acetylene project;
- Dave Moss (Boston University), who collaborated on SEP studies of acetylene;
- Michelle Silva, who helped to launch a new effort on $^{13}C_2H_2$; and
- Steve Lipson, Jim Dodd, Ron Lockwood, Dave Vititoe, Pete Armstrong, and Bill Blumberg (Air Force Research Lab, Hanscom AFB), with whom I have enjoyed a highly productive collaboration on applications of spectroscopic pattern recognition.

More recently, Richard Duan has begun to take an active role in the research on acetylene unimolecular dynamics. In addition, collaborations have been initiated relatively recently with Andreas Ruckstuhl (Australian National University), on spectroscopic applications of robust estimation; and with Stefano Oss, Alejandro Frank, and Renato Lemus, on vibron models for the acetylene bending degrees of freedom.

I have also benefited from informal collaborations and substantive scientific correspondence with a number of other scientists, including Mike Kellman, Ned Sibert, Ann McCoy, Stavros Farantos, Jim Watson, Soji Tsuchiya, Kaoru Yamanouchi, Steve Leone and Jonathan Reid, Alec Wodtke, Bob Wyatt, John Stanton, Eric Heller and Kazuo Hirai, Kevin Lehmann, Michael Feld and his group, Katharina Kohse-Höinghaus and Wolfgang Kreutner, and Chris Gittins.

For Judy

Contents

Chapter 1

Introduction

This thesis is divided into two major parts. Part I describes newly invented numerical pattern recognition techniques for spectroscopy; Part II investigates the unimolecular dynamics of acetylene at extreme levels of vibrational excitation. As the title of this thesis suggests, these two parts of the thesis are closely related. This Introduction outlines the major scientific questions posed in this thesis and the inter-relationships among them, and foreshadows some of the key results.

1.1 Numerical Spectroscopic Pattern Recognition

Pattern recognition lies at the heart of spectrum interpretation. The patterns that are present in spectra range from simple, textbook examples, such as P, Q, and R rotational branches or Franck-Condon vibrational progressions, to more complex examples such as polyatomic bright state fractionation patterns (considered in Part II of this thesis) that are parameterized in a complicated fashion. The identification of patterns in spectra has most frequently been performed "by eye". Traditional spectroscopic assignment proceeds by visual identification of spectroscopic patterns that permit the assignment of quantum numbers to the upper and lower energy levels involved in each observed transition; the frequencies and intensities of the assigned transitions can then be related to a quantum mechanical Hamiltonian model that allows insight into the system being studied.

In complex or congested spectra, however, the process of manual assignment may be difficult, tedious, or ill-advised. As an example, consider the simulated spectrum in Fig. 1-1, which is a superposition of four copies of a single simple pattern (the construction of the simulated spectrum is shown explicitly in Fig. 1-2). The repeated pattern in the spectrum is not obvious; finite signal-to-noise and resolution, as well as overlap between the patterns, cause the spectrum to appear complicated. In such situations, a *numerical* pattern recognition method of recovering information from spectra may be desirable, in particular to identify diagnostically important but *a priori* unknown patterns that are obscured by the complexity of the nascent spectroscopic data.

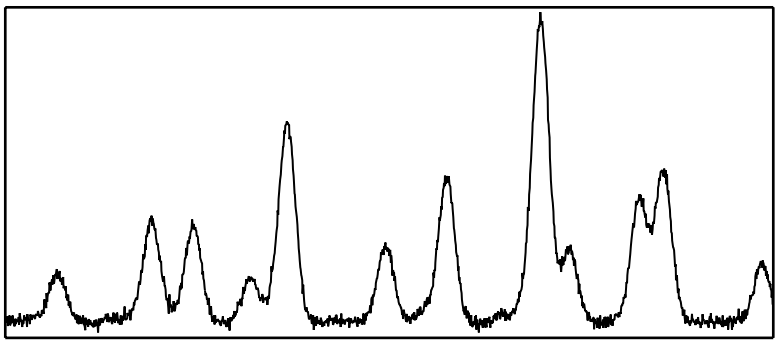

Figure 1-1: This simulated spectrum is composed of a single pattern repeated four times. The underlying simplicity of the spectrum is obscured by finite signal-to-noise and resolution, as well as overlap between the patterns. The patterns present in this spectrum are depicted in Fig. 1-2.

Two specific advantages of numerical, as opposed to visual, techniques for spectroscopic pattern recognition can be advanced:

1. *Numerical pattern recognition is fast.* With modern spectroscopic techniques, huge data sets can be recorded rapidly, and often one has no *a priori* knowledge of the nature and number of the patterns present in the data. Efficient numerical methods of preprocessing such data without human intervention are often desirable.

2. *Numerical pattern recognition is rigorous.* Any application of pattern recognition, whether human- or machine-based, relies on certain assumptions about the data in question. However, in a numerical approach, the assumptions can be made concrete, thus making the process of pattern recognition reproducible and reducing the number of "judgment calls".

Much of the spectroscopic data considered in this thesis is quite complex and thus can be expected to benefit from processing by numerical algorithms. Specific challenges involved in interpreting the complex experimental spectroscopic data discussed in Chapters 2, 3, and 5 motivated the following question, which underlies the work in Part I:

- What numerical techniques can be used to identify *a priori* unknown patterns

in, and extract them from, spectroscopic data sets? A useful numerical technique must be applicable to a wide range of spectroscopic pattern recognition problems and must be tolerant of finite signal-to-noise and spectral congestion.

Few numerical techniques for spectroscopic pattern recognition currently exist, and as discussed in Chapter 2, the realm of applicability of many of these techniques makes them unsuitable for the pattern recognition problems considered in this thesis.

The numerical pattern recognition techniques that I discuss in Part I are based upon techniques of robust estimation [1, 2, 3] and are complementary to previously existing techniques. The pattern recognition problems that are considered in this thesis have in common the goal of identifying *a priori* unknown patterns that are repeated in multiple spectra. The algorithm used to solve these problems is called Extended Cross Correlation (XCC). Among the applications of the XCC considered in this thesis are

1. *Spectra of unknown mixtures* [Chapter 2]. It is difficult to obtain spectra of pure samples of the ammonia mixed isotopomers (ND_2H and NDH_2) because of the strong adsorption of ammonia and water on most cell surfaces, which causes rapid exchange of H and D. An alternate approach is to obtain spectra of mixtures of ammonia isotopomers with varying (but not precisely known) deuterium fractions. The spectrum of each pure isotopomer can be considered a pattern that is repeated in each mixed spectrum with a different amplitude, and the XCC can be used to extract the spectrum of each isotopomer from the spectra of several mixtures.

2. *Kinetic studies* [Chapter 3]. Time-resolved infrared emission spectra of CO have been obtained in atmospheric simulation experiments at the LABCEDE facility (Air Force Research Laboratory, Hanscom Air Force Base) by S. J. Lipson, R. B. Lockwood, P. S. Armstrong, D. L. Vititoe, and W. A. M. Blumberg. These time-resolved spectra are highly congested and consist of poorly resolved ($0.5\ cm^{-1}$), overlapping $\Delta v = 1$ emission bands from $v' = 1$ up to at least $v' = 12$. The analysis of the time-dependence of the emission bands is stymied

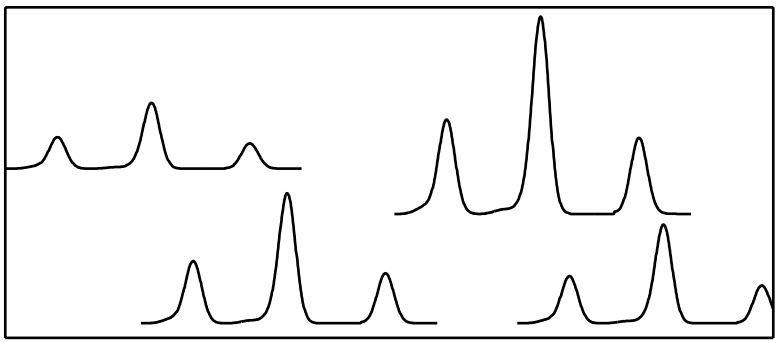

Figure 1-2: The spectrum in Fig. 1-1 is a superposition of four copies of a simple three-line pattern, shown here. The patterns are offset vertically for ease of viewing.

by a severe optical opacity effect in the $v = 1 \rightarrow 0$ emission which is difficult to simulate. Thus, conventional least-squares fitting cannot be employed to determine the time-dependence of this emission band, or that of at least three other emission bands that overlap strongly with it. However, a hybrid least-squares/XCC technique permits the $v = 1 \rightarrow 0$ emission band to be treated as a pattern, while the other bands continue to be analyzed using least-squares fitting. This hybrid approach succeeds in determining the time-dependence of all of the vibrational bands, as well as the frequency dependence of the $v = 1 \rightarrow 0$ emission.

3. *Quantum number assignments* [Chapter 2]. The assignment of rotational quantum numbers to spectral features is often aided by recording spectra at multiple temperatures and noting the changes in intensity of the observed transitions. Spectral features that share the same initial state can be considered patterns in this context, and a variant of the XCC can be used as a preprocessing tool for making rotational assignments in congested spectra. This application of the XCC is illustrated using simulated spectra of OH radical at high temperatures (>1500 K) and relatively low resolution (0.5 Å) that were provided by Dr. W. Kreutner and Prof. K. Kohse-Höinghaus (U. Bielefeld, Germany).

The greatest motivating factor for developing the XCC, however, was to identify patterns in dispersed fluorescence spectra of acetylene that encode the unimolecular

dynamics of the molecule at high vibrational excitation. In fact, as discussed in the next section, the XCC made possible the entirety of Part II of this thesis.

1.2 Acetylene Unimolecular Dynamics

The central scientific questions addressed in Part II of this thesis are the following:

- How are large-amplitude vibrational motions of small polyatomic molecules encoded in their gas phase spectra?
- To what extent can these vibrational dynamics be characterized as "chaotic" or "regular"? [In the former case, statistical models of vibrational energy exchange may be appropriate, whereas in the latter case, approximate constants of motion exist.]

Both of these questions are given concrete answers in Part II of this thesis, with respect to a single small polyatomic molecule—acetylene, which is an important prototype molecule because of its importance in combustion; because as a tetratomic, it is a relatively simple yet highly nontrivial organic molecule; and because it is one of the simplest isomerizing systems.

Figure 1-3 is a schematic representation of the system under study. The most stable configuration of acetylene in its ground electronic state (S_0) is linear, but a diradical called vinylidene exists as a quasi-stable species, whose zero-point level lies $\sim$15,000 cm^{-1} above the linear zero-point [4]. The acetylene ground electronic state has previously been, and continues to be, extensively characterized by absorption spectroscopy, which is sensitive primarily to CH stretch excitation (see Refs. [5] and [6] for a review of available acetylene absorption data). However, as Fig. 1-3 makes clear, the acetylene-vinylidene isomerization motion is more closely related to the bending and CC stretch motions of acetylene than to the CH stretch motions; the isomerization involves bending one of the hydrogens from one side of the CC core to the other, and the conversion of the CC bond from a triple to a double bond.

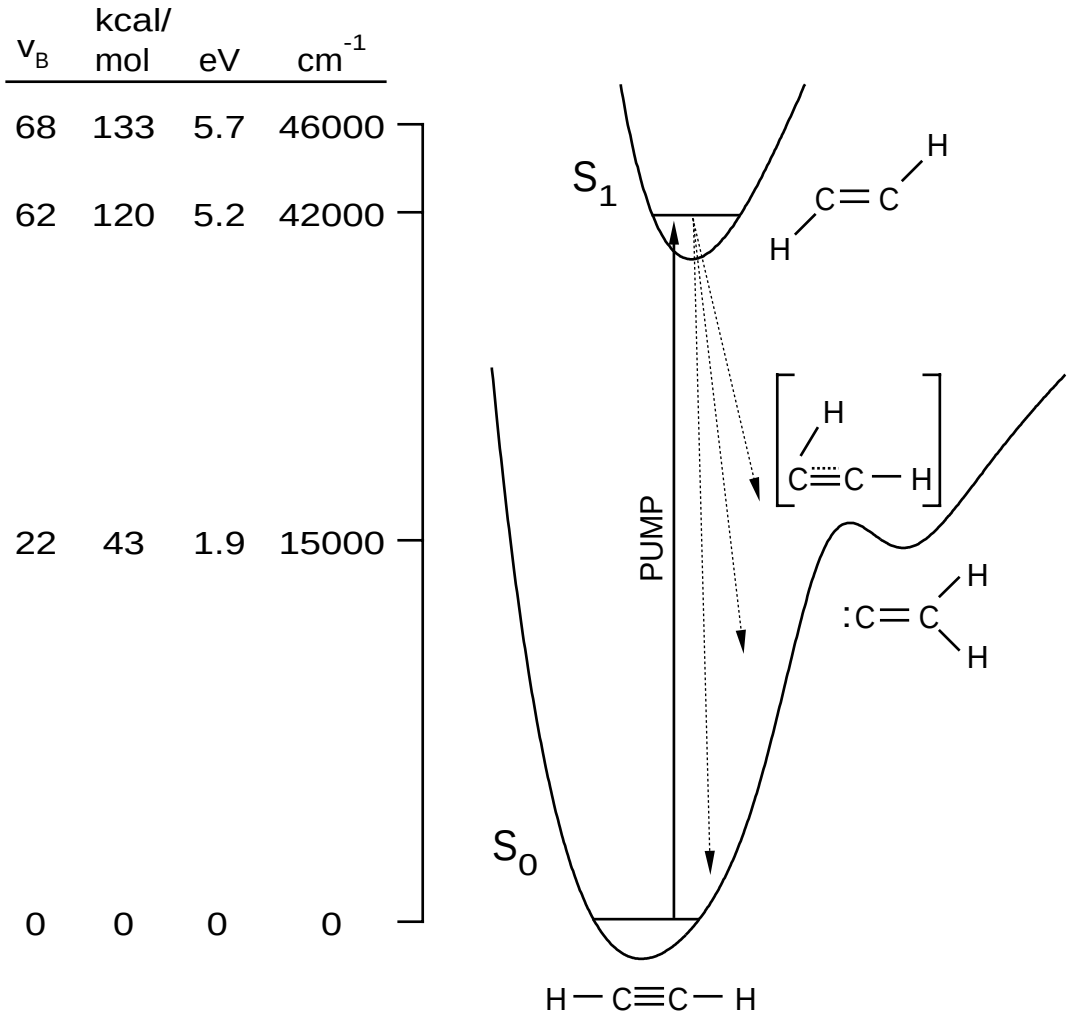

Figure 1-3: Schematic representation of the ground and first excited singlet states of acetylene, with key structures and energies (accurate to two significant figures). The most stable configuration of acetylene in its ground electronic state is linear, but vinylidene exists as a quasi-stable species, whose zero-point level lies ∼15,000 cm^{-1} above the linear zero-point. The transition state for the acetylene-vinylidene isomerization has a half-linear structure. The zero-point level of the *trans*-bent first excited singlet state lies at ∼42,000 cm^{-1}, ∼4000 cm^{-1} below the first dissociation limit [7] of the ground electronic state. The units "v_b" refer to the approximate number of quanta of bend excitation.

In order to obtain spectroscopic data more directly relevant to acetylene-vinylidene isomerization, the Field group has for many years [8, 9, 10, 11, 12] recorded double resonance spectra of acetylene using rovibrational levels of the S_1 state as intermediates. It is not my intention to review all of the Field group's research on acetylene, other than to point out that the majority of the experiments that have been performed have utilized the stimulated emission pumping (SEP) technique [13]. These SEP studies were carried out by using a PUMP laser to populate single rovibrational levels of the acetylene S_1 state, and a DUMP laser to stimulate emission back down to excited rovibrational levels of the S_0 state. The large geometry change between the S_0 and S_1 states allows the DUMP transitions to probe the S_0 surface at rather high internal energies (up to at least 26,000 cm^{-1}). In particular, the Franck-Condon principle suggests that, since the S_1 state has a *trans*-bent geometry with a nominal CC double bond, S_0 vibrational levels with large degrees of excitation in the CC stretch and *trans*-bend modes will be particularly prominent in double resonance spectra that use S_1 rovibrational levels as intermediates.

More recently, the SEP studies of acetylene have been complemented by dispersed fluorescence (DF) spectra. The DF experiments differ from SEP in that a DUMP laser is not used; instead, the intensity of the spontaneous emission is recorded as a function of wavelength using a monochromator and an appropriate detector. The DF spectra that have been recorded from the S_1 state of acetylene have much lower resolution (>4 cm^{-1}) than the SEP spectra, in which the resolution is limited by the DUMP laser bandwidth, which is ~ 0.05 cm^{-1} for typical commercial dye laser systems. The decreased resolution of the DF spectra makes it possible to map out large regions of the S_0 potential surface much more rapidly than is possible with SEP. Recording a 1000 cm^{-1} region of spectrum using SEP requires weeks, if not months, of data collection, whereas the same region can be recorded in minutes using DF. The lower resolution of DF, of course, limits the level of spectroscopic detail. However, from the standpoint of understanding unimolecular dynamics, low resolution corresponds to short-time dynamics, and for polyatomic molecules at high internal energy, the short-time dynamics (a few ps) can provide a wealth of insight into the potential energy

surface under study. As can be seen in Fig. 1-4, high resolution, high sensitivity techniques such as SEP generate enormous amounts of detail that relate to the long-time dynamics of the molecule; the panoramic perspective afforded by DF spectra provides the essential framework for understanding such details.

As can be seen in the top panels of Fig. 1-5 and 1-4, however, the DF spectra of acetylene are by no means simple. These spectra will be analyzed in detail in Chapter 5; here I wish only to point out a few of the key qualitative features. The emission tends to peak between 10,000 and 15,000 cm^{-1}, but transitions to states at least as high as 25,000 cm^{-1} can be recorded with reasonable signal-to-noise. The spectrum becomes increasingly congested and complicated as internal energy increases. This trend is, of course, conventionally considered to be due to increasingly rapid and unrestricted intramolecular vibrational redistribution (IVR). The potential surface near the global minimum can be approximated as a multi-dimensional harmonic oscillator, and the low-lying eigenstates can generally be assigned normal mode quantum numbers. However, at higher internal energy, anharmonicities of the potential energy surface introduce resonant couplings among the normal mode states. In the frequency domain, these couplings are manifested by increasing complexity of the spectra; in the time domain, energy flow among the normal modes is possible. From either perspective, the IVR reflects the nonconservation of the normal mode quantum numbers.

Prior to the work reported in this thesis, the acetylene DF spectra were only partially analyzed up to $\sim$10,000 cm^{-1}. Above this energy, the spectra are simply too complicated to yield to conventional spectroscopic analysis, which emphasizes assignment of individual eigenstates. In this thesis, a detailed and essentially complete analysis of the spectra up to 15,000 cm^{-1} is presented; recent work that is reported in Chapter 10 has extended the analysis to even higher energy (up to $\sim$20,000 cm^{-1}, although this work is ongoing and the analysis is not yet complete).

The analysis of the extremely complicated DF spectra above 10,000 cm^{-1} has been made possible by the use of numerical pattern recognition. Specifically, the bottom panel of Fig. 1-5 depicts spectroscopic patterns that can be extracted from

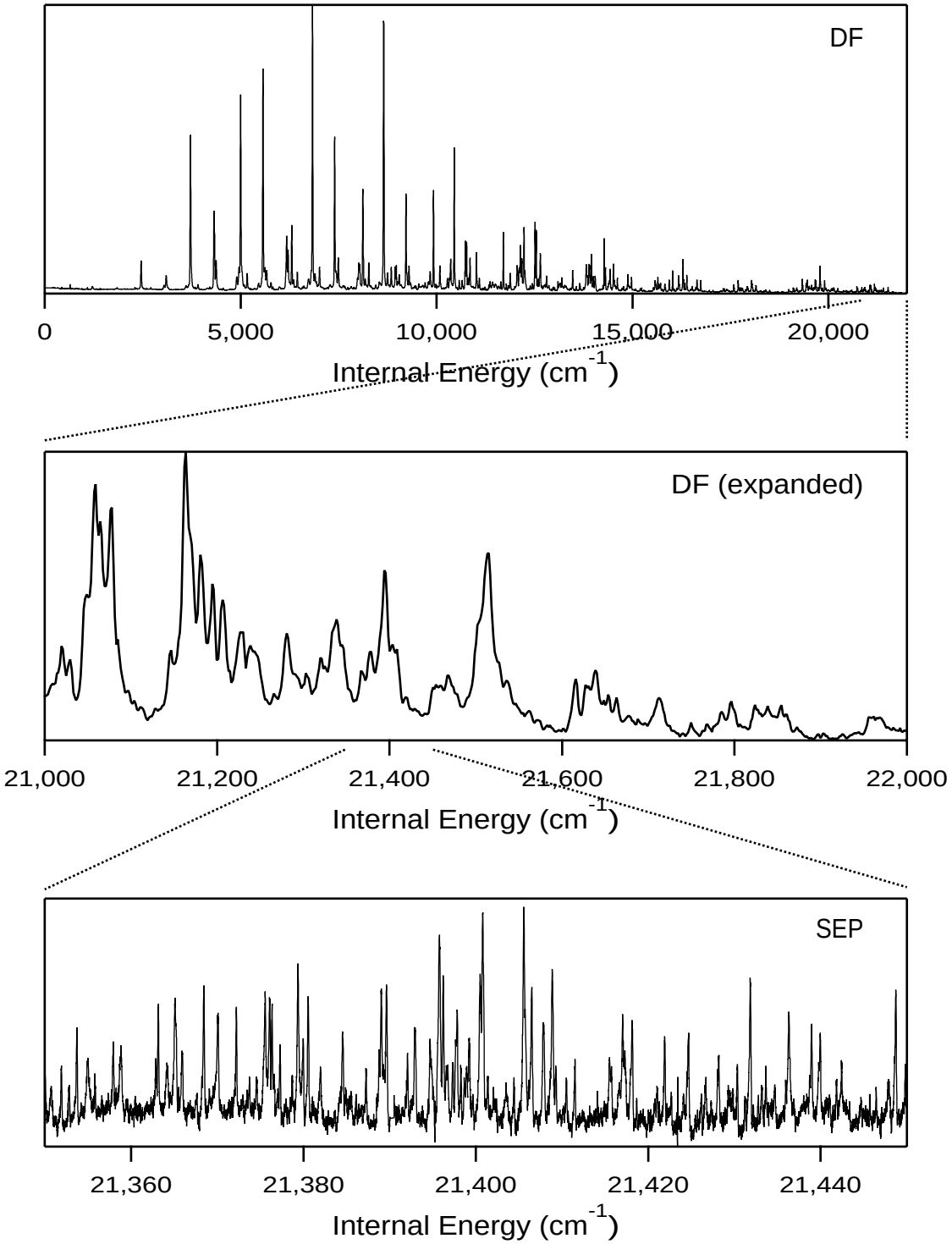

Figure 1-4: Complementary use of DF and SEP spectroscopy to study acetylene dynamics. The spectra in each case are recorded using the $Q(1)$ line of the $V_0^2K_0^1$ band of $^{13}C_2H_2$ (see Chapter 5 for notation). Top and middle: DF spectrum ($\sim$16 cm^{-1} resolution). Bottom: SEP spectrum ($\sim$0.15 cm^{-1} resolution).

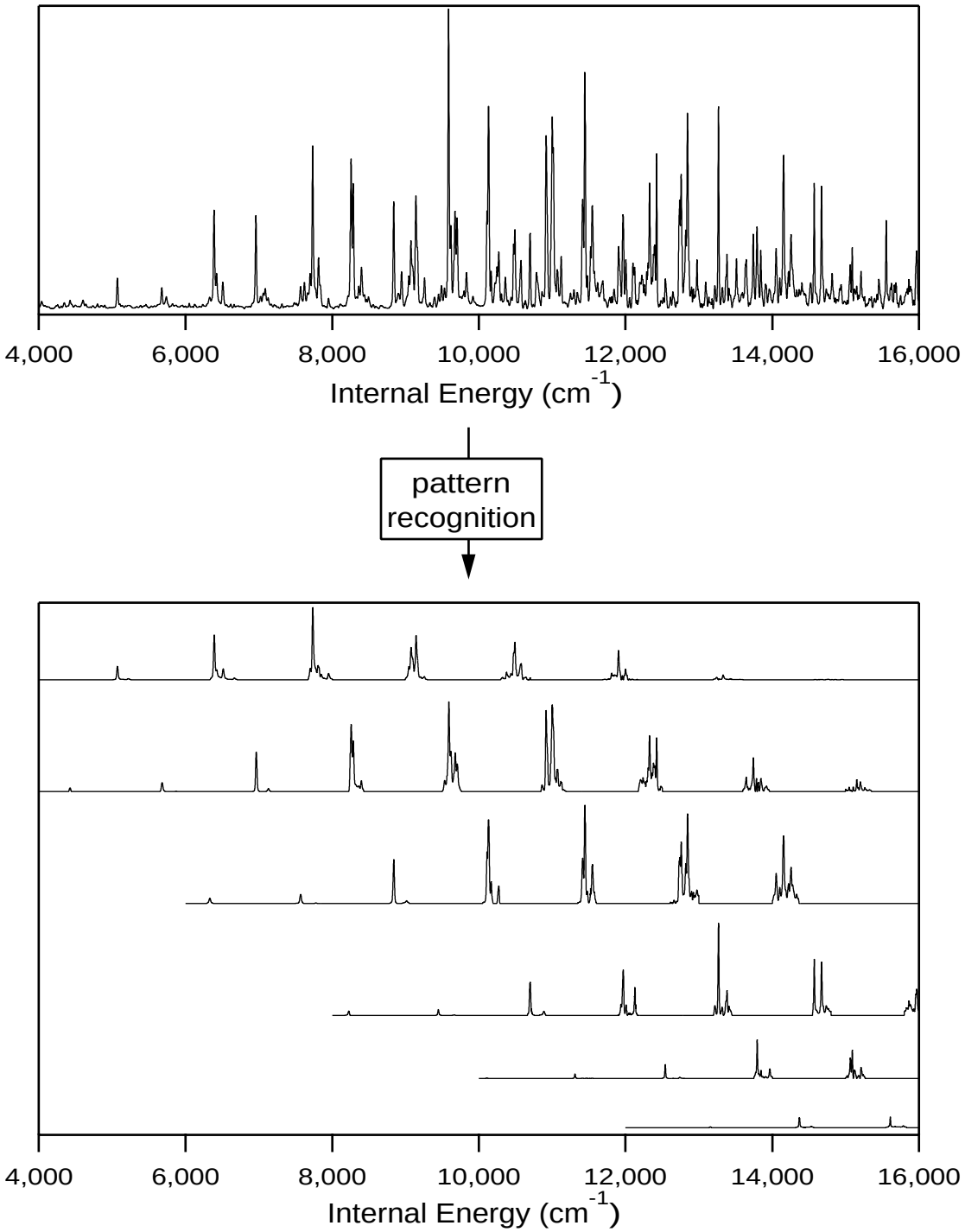

Figure 1-5: Numerical pattern recognition (XCC) can be used to decompose acetylene dispersed fluorescence spectra (top) into several series of patterns (bottom). Most of the patterns consist of only a few intense lines, and clear trends can be observed within and among the pattern progressions. Thus, the complicated appearance of the acetylene DF spectrum obscures the (relative) simplicity of the patterns that can be extracted from it.

the acetylene DF spectra using the XCC technique that is discussed in Section 1.1. The acetylene DF spectra can be seen to be similar to the simulated spectrum in Fig. 1-1, in that the complicated appearance of the acetylene DF spectrum obscures the (relative) simplicity of the patterns that can be extracted from it. The nature of the patterns in the acetylene DF spectra is discussed in some detail in Chapter 5. Here I wish to point out only that the patterns are associated with (approximately) conserved quantum numbers.

The association of spectroscopic patterns with conserved quantities is a general phenomenon. Consider, for example, the infrared absorption spectrum of acetylene or other small molecules. The majority of the absorption bands are characterized by the easily recognizable P and R branch (and in some cases Q branch) pattern of lines. The existence of these regular patterns indicates that there exist approximately conserved vibrational (i.e., normal mode) and rotational quantum numbers for the molecule that can be used to label the transitions. However, for many molecules, some of the absorption bands are perturbed, meaning that the usual spectroscopic pattern is degraded in some way. The partial or localized breakdown of a spectroscopic pattern indicates nonconservation of some nonrigorously conserved quantum number. In acetylene, for example, the antisymmetric stretch fundamental absorption band is strongly perturbed. In that case, the perturbation is due to an anharmonic resonance between the $(0,0,1,0^0,0^0)$ and $(0,1,0,1^{+1},1^{-1})$ vibrational levels, which indicates that the normal mode quantum numbers are at least locally nonconserved. In other cases, the perturbation may be rotationally inhomogeneous (i.e., due to a Coriolis mechanism), indicating that the approximately conserved rotational quantum number (as opposed to the rigorously conserved total angular momentum) is nonconserved. Note that the ability to detect a perturbation of the usual spectroscopic pattern will in general be a function of resolution. That is, from a dynamical standpoint, a perturbation that can be detected at low resolution indicates quantum number nonconservation on a relatively short timescale.

In the case of the patterns in the acetylene DF spectra, the approximately conserved quantum numbers associated with the patterns are referred to as polyad quan-

tum numbers [14, 15, 16, 17], which can be thought of as generalized vibrational quantum numbers that remain conserved even when the usual normal mode quantum numbers are nonconserved, due to IVR. It should be made clear that the existence of (approximately) conserved quantum numbers does not *guarantee* that patterns will appear in the spectra in a form that is easily recognizable either by eye or with a numerical technique. However, it is a necessary prerequisite. The destruction of all nonrigorously conserved quantum numbers is of course associated with classical chaos (and its quantum manifestations) [18]. If a molecule could be studied that approaches this "bag of atoms" limit [19] at sufficiently high internal energy, one would expect to be unable to identify any spectroscopic patterns, and the only insights to be gained would be statistical in nature.

The ability to identify patterns in the acetylene spectra up to 20,000 cm^{-1} is strong evidence that some vibrational quantum numbers remain at least approximately conserved up to that energy. This result is itself interesting since it implies that acetylene-vinylidene isomerization, at least within the first several thousand cm^{-1} above the isomerization barrier, is unlikely to be describable by statistical theories. However, the majority of the work in Part II of this thesis is devoted to the detailed analysis of the vibrational dynamics of acetylene at high internal energy (>10,000 cm^{-1}). As discussed in Chapter 5, many qualitative insights can be gained from merely inspecting the patterns that are extracted from the acetylene DF spectra (bottom panel of Fig. 1-5). One of the most surprising insights is that there exists a series of vibrational levels up to at least 18,000 cm^{-1} that can be labeled with normal mode quantum numbers (see Chapter 9). These account for only a small fraction of the states at high internal energy, but their existence implies that IVR is highly nonuniform, with some states experiencing virtually no IVR (on a timescale of at least several ps) even when acetylene-vinylidene isomerization is energetically feasible.

However, the majority of the insights into acetylene unimolecular dynamics in Part II are gained by developing an explicit numerical model for the acetylene vibrational structure. The separation of the DF spectra into patterns associated with conserved quantum numbers, using numerical pattern recognition tools, makes the

task of developing such a model vastly simpler. In principle, one could determine from the data a potential energy surface for the ground electronic state. That is, one could define an appropriate analytical expression to represent the potential energy surface, and adjust the parameters to achieve maximal agreement between the observed eigenenergies and those calculated using the surface. However, six vibrational degree of freedom systems (at high energy) currently represent the state of the art in fully quantum mechanical, variational calculations. Thus, our results present a challenge for both electronic and vibrational structure calculations (i.e., can a potential energy surface be constructed that reproduces our results, at least qualitatively, to 15,000 cm^{-1}, and can fully 6D variational [20, 21] or wavepacket propagation [22] methods be used efficiently to investigate the spectra and dynamics of acetylene at high internal energy?).

It should be noted that some work has been done to develop potential energy surfaces [23, 24] and force fields [20, 25] for S_0 acetylene and vinylidene, and in some cases these potentials have been refined against (certain) experimental data. However, no representation of the S_0 potential energy surface has yet been demonstrated to reproduce the highly excited bending states near 15,000 cm^{-1} that are a central concern in Part II. In the absence of a potential surface with sufficient accuracy, which becomes increasingly difficult for larger molecules, effective Hamiltonians[1] can provide substantial insights into quantum vibrational dynamics. In fact, even when accurate potential energy surfaces are available, effective Hamiltonian models (which can be derived from the potential by perturbation theory [26, 24]) are still frequently found to provide insights that are complementary to calculations performed directly with a potential surface; see recent work on acetylene [24, 27] and HCP [26, 28] for examples.

In Chapters 9 and 6, an effective Hamiltonian model is developed that reproduces the qualitative fractionation patterns that are observed in the acetylene DF spectra up to 15,000 cm^{-1}. Particularly good agreement is obtained for states with high bending

[1]In this thesis, an effective vibrational Hamiltonian will be defined as a Hamiltonian that can be expressed entirely in terms of (harmonic oscillator) raising and lowering operators for the various vibrational degrees of freedom.

excitation; 83 bending vibrational energy levels of acetylene, with up to 22 quanta of excitation, are reproduced with 1.4 cm^{-1} RMS error, which is approximately equal to the average measurement error for frequencies in the DF spectra. The vibrational dynamics associated with this effective Hamiltonian are then investigated from several different perspectives, which are summarized in Fig. 1-6.

In Chapter 6, the quantum bending dynamics of acetylene are explored. The effective Hamiltonian is defined in a zero-order, normal mode basis set. Any given zero-order state is not an eigenstate of the Hamiltonian, due to the existence of off-diagonal resonant couplings in the model, and is thus nonstationary (i.e., it represents a wavepacket that will evolve with time in the zero-order state space of the effective Hamiltonian). Much of Chapter 6 is devoted to the time-dependent evolution of those zero-order states (with nonzero excitation in the Franck-Condon active CC stretch and *trans* bend modes) that are most directly relevant to the experimentally observed DF spectra. In other words, Chapter 6 provides a time-domain interpretation of the frequency domain experiments, focusing on the evolution of the bending dynamics with increasing energy. One surprising result of this investigation is that the bending dynamics are significantly more complicated at 10,000 cm^{-1} than they are at 15,000 cm^{-1}, as judged by both qualitative and quantitative measures.

Although the exploration of state-space dynamics can provide substantial insight into the bending dynamics of acetylene, one weakness of this approach is that it is basis set dependent. That is, one understands the dynamics in terms of energy flow among the zero-order normal mode states. However, Chapter 6 provides substantial evidence that the normal mode basis set is a poor zero-order representation for the bending states of acetylene above $\sim$10,000 cm^{-1}, which limits the insights that can be gained at high energy using the state-space approach. In Chapters 7 and 8, the vibrational structure of acetylene is investigated using *basis set independent* methods. Specifically, in Chapter 7, the eigen*functions* of the effective Hamiltonian are investigated and revealed to be qualitatively different at low and high internal energy. As expected, at low vibrational energy the eigenfunctions have well-defined nodal coordinates and can be assigned normal mode quantum numbers. More surprising is

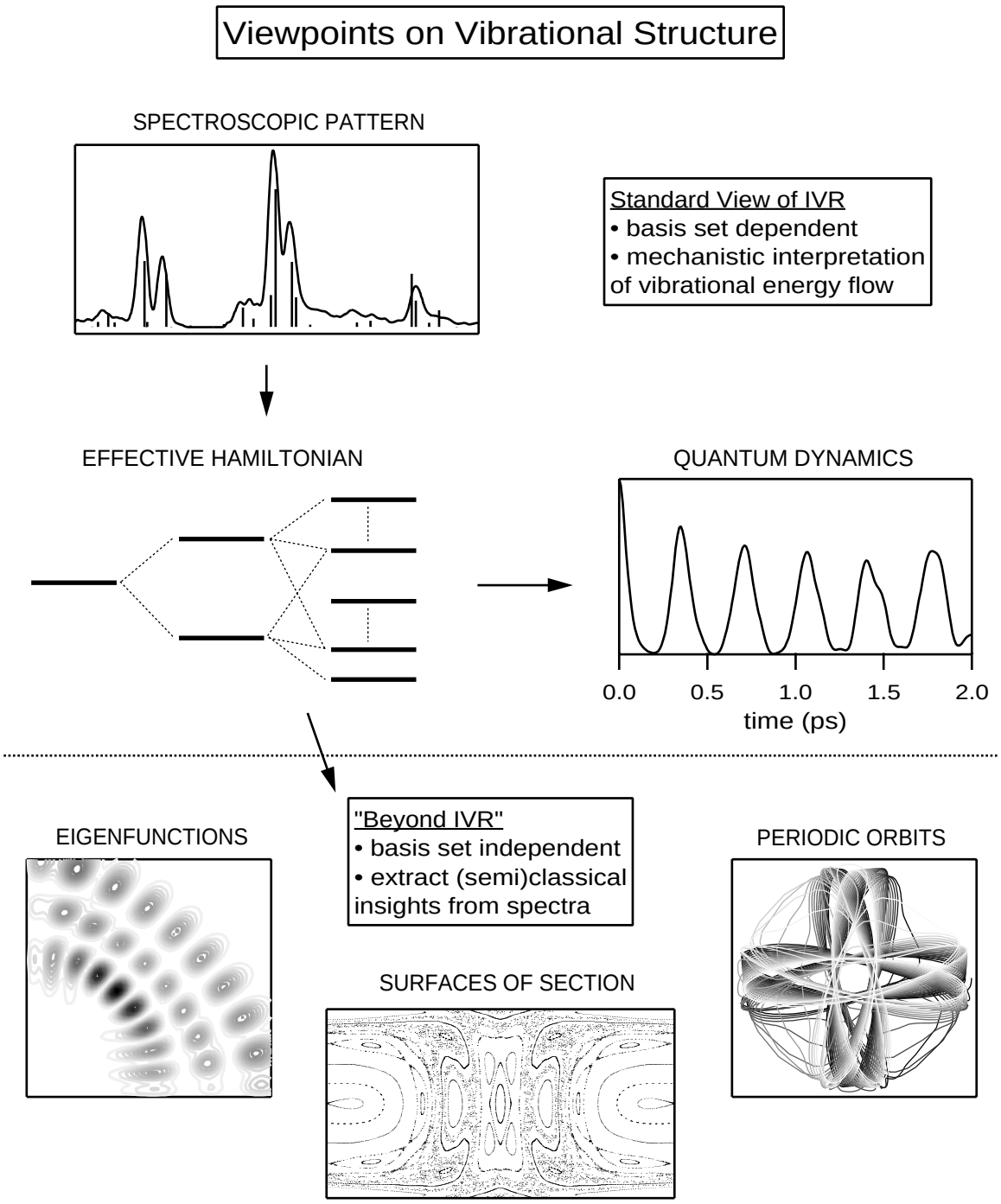

Figure 1-6: Spectroscopic patterns can be fit to an effective Hamiltonian model that provides insights into the unimolecular vibrational dynamics. The zero-order states in the effective Hamiltonian are represented by horizontal lines; the dotted lines represent resonant couplings among the zero-order states. Measures of the quantum dynamics, such as the survival probability, are often used to describe IVR, but semiclassical interpretations may yield greater insights.

that at high internal energy (15,000 cm^{-1}), many of the eigenfunctions also have simple, well-defined nodal coordinates, but these nodal coordinates are entirely distinct from those at low internal energy which are organized by the normal modes. That is, the eigenfunctions show strong evidence for the existence of new types of stable vibrational motions at high internal energy.

Two specific classes of vibrational motion are demonstrated to be particularly important at high internal energy, as depicted in Fig. 1-7. The first is called "local bend", which involves the bending of one hydrogen atom while the other remains colinear with the CC bond. The second is called "counter-rotation", in which the two hydrogen atoms undergo circular motions on opposite ends of the CC bond. Both of these motions are a natural result of a transition from normal to local mode behavior in the bending dynamics of acetylene that occurs near 9,000 cm^{-1}. As reviewed in Chapter 7, local mode behavior has been demonstrated previously for a wide variety of molecules with coupled stretching modes [29, 30, 31, 32, 33]. The typical behavior of a local stretching system is illustrated in the left column of Fig. 1-7. At low internal energy, the normal mode motions dominate (symmetric and antisymmetric stretch), but as vibrational energy increases, new stable motions emerge that involve the stretching of just one bond (local stretch). In this thesis I demonstrate that an analogous effect occurs in acetylene when the *trans* and *cis* bend motions are replaced by local bend and counter-rotation at high internal energy. Not surprisingly, the normal-to-local transition for the acetylene bend modes is substantially more complicated than the analogous effect for stretch modes, since each bend mode is two-dimensional, while stretch modes are one-dimensional. A local mode Hamiltonian is also derived for the acetylene bends in Chapter 7 and is demonstrated to be equivalent to the normal mode Hamiltonian, in the sense that either can be used to describe the dynamics of the molecule at any energy. However, the normal mode model is a better zero-order representation at low energy, while the local mode model is superior at high energy.

All of the insights into the local mode bending behavior of acetylene in this thesis are gained from an effective Hamiltonian model, but the local mode behavior must,

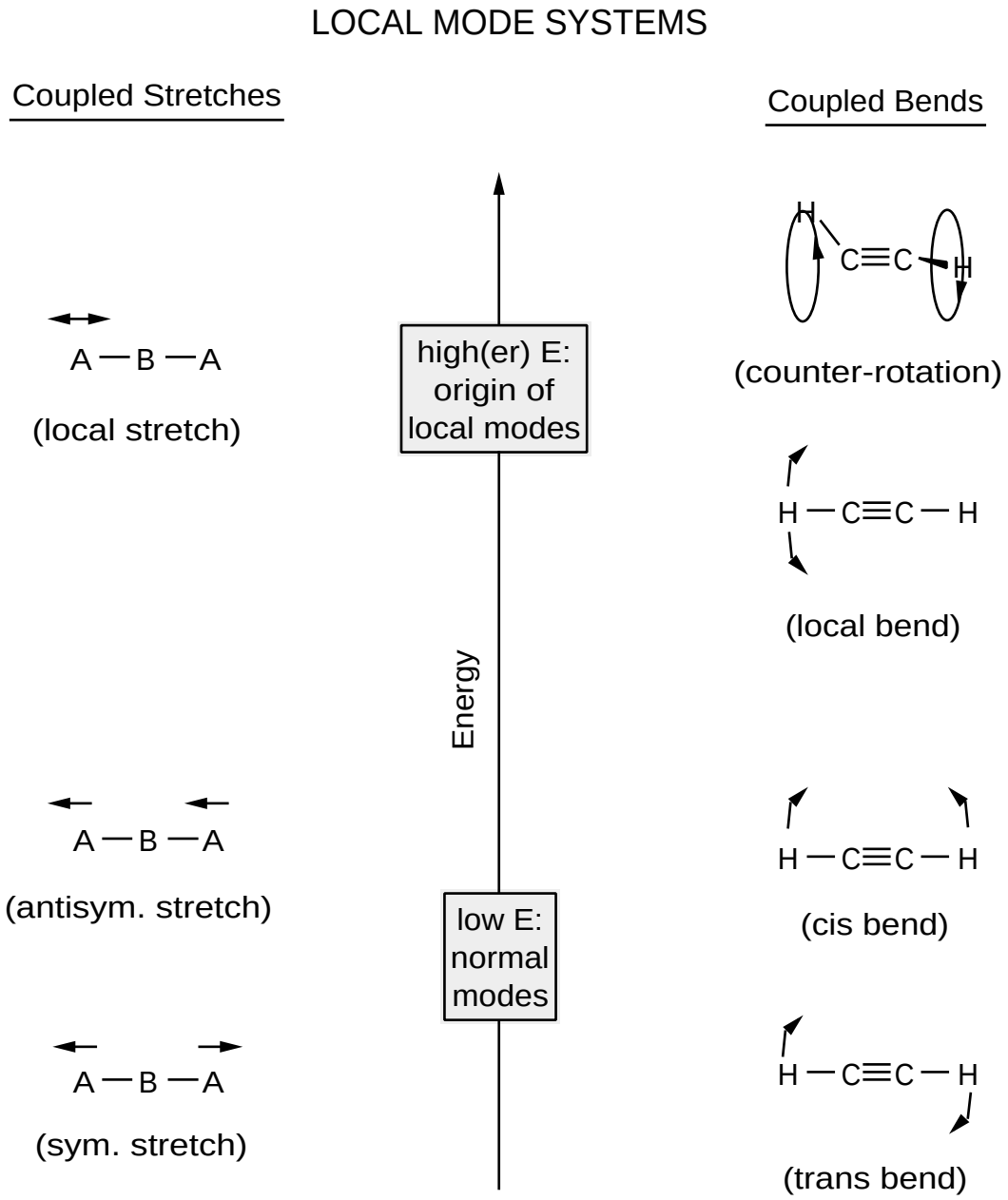

Figure 1-7: In local mode systems, new stable vibrational motions arise at high internal energy that are distinct from the normal mode motions. Local stretch systems have previously been studied extensively [29, 30, 31, 32, 33]; in this thesis it is demonstrated that an analogous, but significantly more complicated, phenomenon can occur for coupled bending modes, such as in acetylene.

of course, be related to the structure of the potential surface. In the absence of a potential surface that can reproduce the experimental results, it is not possible to make any firm conclusions, but qualitative features of the S_0 potential surface certainly suggest that the emergence of the stable local bend motion is closely related to acetylene-vinylidene isomerization. A representation of the S_0 bending potential, based upon the Halonen, Child, and Carter surface [23], is depicted in Fig. 1-8. The two large wells marked by "A" represent the linear configuration, while "C" marks the shallow vinylidene local minimum. The transition state between the two, marked by "B", has a half-linear configuration (as confirmed by numerous high-level *ab initio* calculations [34]), in which one CCH angle is $\sim$60°, while the other is $\sim$180°.

Figure 1-9 provides a closer look at the minimum energy isomerization pathway from acetylene to vinylidene, again as represented by the Halonen, Child, and Carter surface [23]. The left panel depicts the vibrational energy along the minimum energy isomerization path, and the right panel represents the vibrational motion along that path. The motion of each atom is depicted, and the shading of the lines in the right panel matches the shading in the left, such that black represents acetylene and light gray represents vinylidene. Note that hydrogen #2 moves very little at all during the early stages of the isomerization motion, from acetylene to the transition state, while hydrogen #1 bends well past 90°. That is, the early stages of the isomerization motion are well-described as a local bend motion.

The overall picture that emerges from Figs. 1-8 and 1-9 is that, although neither pure *trans* nor pure *cis* bend motions are expected to promote isomerization of acetylene to vinylidene, the local bend motions, which have been demonstrated to be highly stable at $\sim$15,000 cm^{-1}, are closely related to the isomerization. This observation may help to provide an explanation for some intriguing recent experimental results by the group of Z. Vager (Weizmann Institute), who performed Coulomb Explosion Imaging experiments (CEI) on S_0 vinylidene, which was prepared by electron photodetachment [35]. The vinylidene rovibrational states that are prepared in such an experiment are not eigenstates of the full S_0 state Hamiltonian; the vinylidene local minimum is shallow, and tunnelling interactions between acetylene and vinylidene are

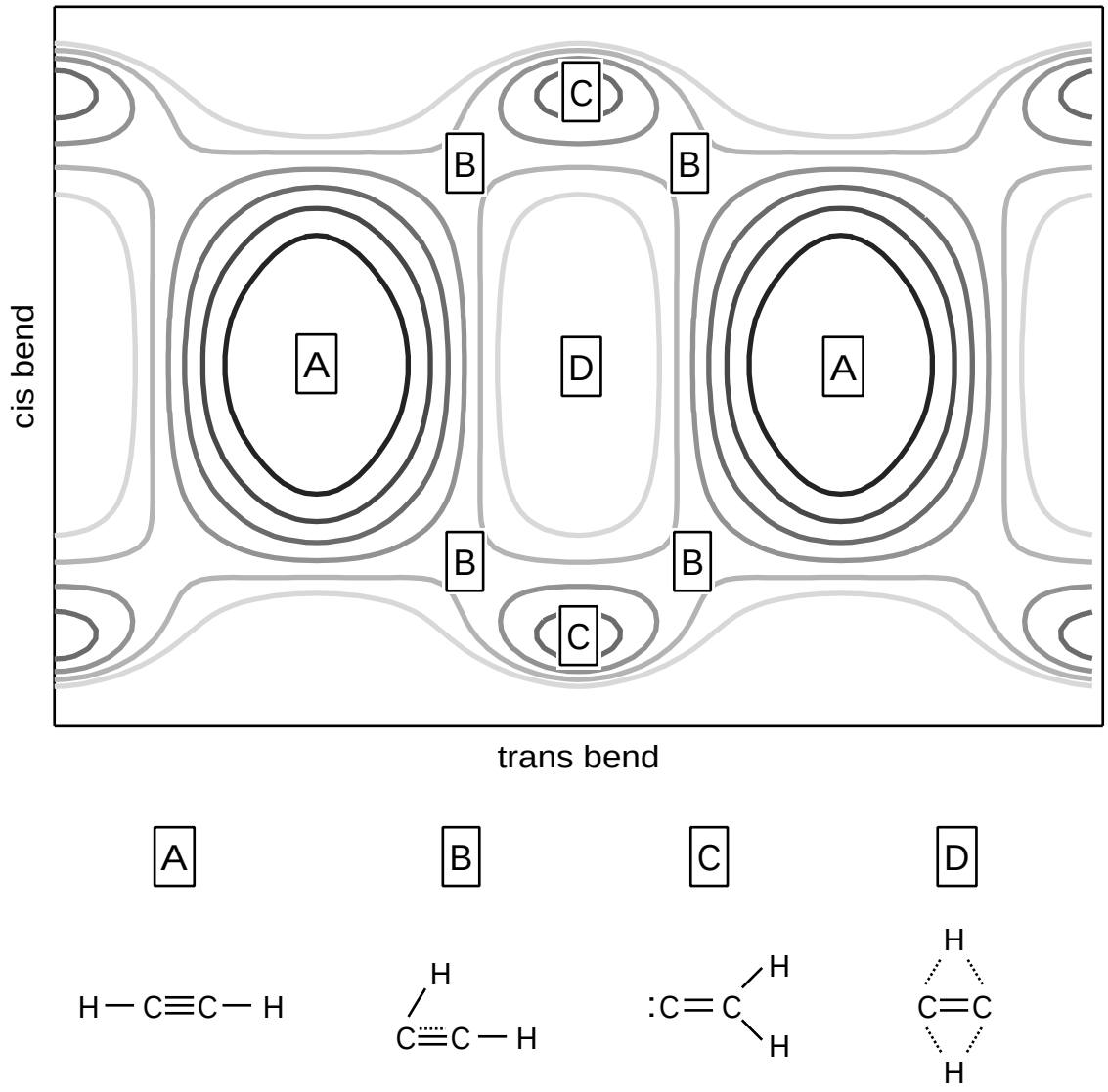

Figure 1-8: The planar bending potential energy surface of acetylene, as represented by the Halonen, Child, and Carter surface [23]. The *trans* and *cis* bend axes represent Jacobi coordinates (the positions of the hydrogens are defined from the center of the CC bond), and the values of the stretching coordinates are optimized for every pair of bending coordinates. Four stationary points of the S_0 surface are depicted. "A" is the linear configuration, which is the most stable. "C" is the quasi-stable vinylidene configuration, and "B" is the transition state for the acetylene-vinylidene isomerization. The bridged structure "D" is highly unfavorable. The contours are plotted every 5000 cm^{-1}.

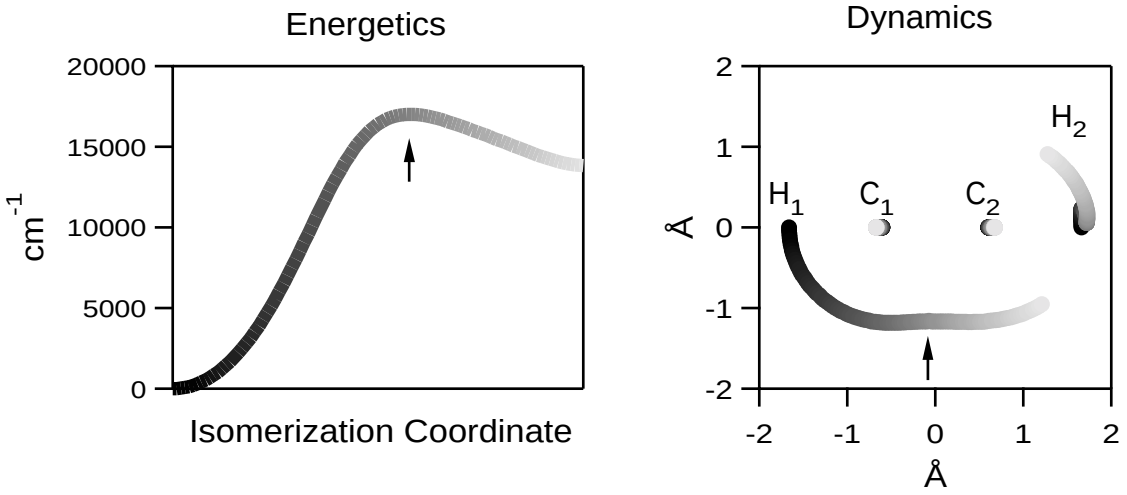

Figure 1-9: Energetics and dynamics of the acetylene-vinylidene isomerization, as represented by the Halonen, Child, and Carter surface [23]. The isomerization coordinate is defined by the path of steepest descent from the transition state, which is marked by an arrow in both panels. The early stages of the isomerization motion, from acetylene to the transition state, are well-described as a local bend motion—one hydrogen bends well past 90°, while the other remains nearly colinear with the CC bond.

expected to be substantial even for the vibrationless level of vinylidene [36, 37]. Thus, the preparation of nominally vinylidene vibrational levels will lead to wavepacket dynamics that sample both the vinylidene and linear acetylene wells. Based upon the much larger density of linear acetylene than vinylidene vibrational levels at the same energy, one might expect the vinylidene character to be highly fractionated among many linear acetylene states (i.e., to fall within the "strong coupling" limit [38]); in the time domain, this would correspond to rapid and irreversible isomerization from vinylidene to acetylene.

In the Vager *et al.* experiments, the molecular structure associated with the evolving wavepacket was probed by CEI 3.5 μs after the photodissociation of the vinylidene anion. If the isomerization from vinylidene to acetylene were in fact rapid and irreversible, very few of the probed molecules would be found in a configuration similar to vinylidene. However, the CEI experiments indicated that $\sim$50% of the molecules could be classified as having structures more similar to vinylidene than to linear acetylene. From this observation, Vager *et al.* conclude that "the observed vinyli-

dene structure corresponds to 2–3 exact states". This conclusion may be reworded somewhat more precisely: The vinylidene character of the zero-order states that are prepared in the electron photodetachment experiment are distributed, on average, over 2–3 eigenstates of the S_0 surface, the remainder of the eigenstate character being accounted for by linear acetylene states.[2]

The Vager *et al.* results are perhaps less surprising given the conclusion of this thesis that the vibrational structure of acetylene near 15,000 cm^{-1} does not approach the statistical/chaotic limit, even for the low frequency bending modes, and that a handful of stable large-amplitude vibrational motions dominate the dynamics. If the conclusion of Vager *et al.* is proven to be correct, then the 2–3 states of linear acetylene into which the vinylidene states are strongly coupled will almost certainly have a large degree of local bending character; the density of such states at high internal energy is of course rather small compared with the total density of vibrational states. Theoretical studies of acetylene-vinylidene isomerization [37, 39, 40] will be critical in establishing more rigorously the connections between the work reported in this thesis and the Vager *et al.* experiments.[3]

The final chapter of this thesis is devoted to recent work on acetylene that I have not yet published. Two major ongoing lines of research discussed in this final chapter are the analysis of the acetylene spectra above 15,000 cm^{-1} (with the goal of identifying spectroscopic signatures of acetylene-vinylidene isomerization), and the investigation of isotopically substituted acetylene species, such as $^{13}C_2H_2$, which are described by the same potential energy surface as $^{12}C_2H_2$ but may undergo substantially different unimolecular dynamics.

[2]Even more precisely, one can state that the average dilution factor (see Section 6.4) of the prepared zero-order vinylidene states is ∼0.5, a point which Vager *et al.* make, although they do not use the term "dilution factor".

[3]I wish to point out that previous semiclassical calculations of Miller *et al.* on vinylidene-acetylene isomerization [37] are not necessarily antithetical to the Vager *et al.* results. The semiclassical calculations investigate the early-time decay of the vinylidene wavepacket, which may be quite fast, even if the vinylidene character is distributed over only 2–3 eigenstates. The fast early-time decay, however, would have to be followed by a series of strong and regular partial recurrences.

Part I

Spectroscopic Pattern Recognition

Chapter 2

Extended Cross Correlation

This chapter describes a spectroscopic pattern recognition technique entitled Extended Cross Correlation (XCC) that was jointly invented by Steve Coy and myself. The majority of this work has been published as two articles [41, 42] in the Journal of Chemical Physics. The work in Section 2.5 has not been published; this work was stimulated by an informal collaboration with the group of Prof. Katharina Kohse-Höinghaus, who have an interest in applications of pattern recognition to combustion spectroscopy.

2.1 Motivation for XCC

Recent improvements in spectrum excitation, recording and processing capabilities have led to an enormous enhancement in the quality and quantity of spectroscopic data sets. These data sets generally contain a prodigious amount of information. The task of extracting this information is made difficult by extrinsic (resolution, signal-to-noise, spectral coverage) and intrinsic (unknown or overlapping patterns) factors.

One traditional approach to understanding the information encoded in spectroscopic data has been first to assign approximate quantum numbers to the upper and lower energy levels involved in each observed transition and then to relate the frequencies and intensities of the assigned transitions to a quantum mechanical Hamiltonian model that allows insight into the system being studied. In complex or congested spectra, however, the process of manual assignment may be difficult, tedious, or ill-advised. In such situations, a pattern-recognition based, rather than model based, method of recovering information from spectra may be desirable, in particular to identify diagnostically important but *a priori* unknown patterns that are obscured by the complexity of the nascent spectroscopic data.

Extended Cross Correlation (XCC) is a pattern recognition technique that is well suited to take advantage of large, high quality data sets. Spectra are used to decode each other without any advance knowledge of or assumptions about the nature and number of patterns that are sought. More specifically, the XCC permits the rapid identification and extraction of patterns that are repeated in multiple spectra.

One of the simplest examples of the application of the XCC, which will be considered in some detail in this chapter, is to identify, in spectra of mixtures of chemical species, which peaks correspond to which chemical species. This application of the XCC is of considerable practical importance. Certain chemical species (e.g. transient molecules, single isotopomers) are difficult to isolate. If it is desired to characterize such a species spectroscopically, then frequently one must be content with obtaining spectra of unspecified mixtures of chemical species, one of which is the species of interest. A number of approaches are possible to determine which features in the spectra of such mixtures correspond to the species of interest. One straightforward method is to obtain spectra of several mixtures, each of which contains the species of interest in a different (but not precisely measured) fractional abundance. Peaks in the spectra that belong to the species of interest will have intensities that vary linearly with its fractional abundance; the relative intensity of a peak in the various spectra can be used to assign it to a chemical species. The process of assigning spectral features to distinct chemical species thus represents a type of pattern recognition: the spectrum of one chemical species is a pattern which is identified in several spectra simultaneously.

This application of the XCC is illustrated in this chapter with both synthetic data and experimental spectra of mixtures of ammonia isotopic species. Other applications of the XCC are reported in subsequent chapters. In Chapter 3, the XCC is applied to atmospheric emission simulation experiments with carbon monoxide. All of Part II of this thesis was also made possible by the XCC, and Chapter 5 in particular reports the application of the XCC to identify fractionated bright states that are repeated in multiple dispersed fluorescence spectra of the acetylene $S_1 \rightarrow S_0$ system. Note that, although all of the applications of the XCC that are discussed in this thesis involve spectroscopic data, the XCC is applicable to other types of data as well, as long as the data fulfill certain criteria that are discussed in Section 2.2.

This chapter proceeds as follows. Section 2.2 describes the motivation for the XCC, and illustrates its use for identifying patterns that are repeated in two synthetic spectra. Section 2.3 discusses the application of the XCC to data sets which

consist of more than two spectra. Section 2.4 illustrates the use of the XCC with real experimental data, namely, spectra of mixtures of deuterated ammonia isotopomers. In Section 2.5, a variant of the XCC entitled "windowed XCC" is introduced and used to identify rotational progressions in congested absorption spectra of OH. Section 2.6 concludes with comments on the complementarity between the XCC and other pattern recognition techniques that have been used in spectroscopic applications.

2.2 XCC in Two Dimensions

The XCC is introduced in this section and applied to a synthetic data set that illustrates one of the simplest applications of the XCC: the partitioning of spectra of mixtures of chemical species into separate spectra of each species. In this application, the patterns to be identified are the spectra of the individual species.

Figure 2-1 depicts two patterns (the spectra of two individual chemical species) and two synthetic spectra that are generated by taking distinct linear superpositions of the patterns. That is,

$$I_1(x) = a_1 I_A(x) + b_1 I_B(x) \tag{2.1}$$

$$I_2(x) = a_2 I_A(x) + b_2 I_B(x) \ . \tag{2.2}$$

Note that numbers are used to label spectra, and letters to label patterns. The parameter "x" in a real experimental spectrum would represent (for example) frequency, wavelength, or internal energy. In this synthetic example, the discrete intervals x_k at which the spectra are sampled will be referred to generically as "spectral elements". The coefficients a_1, a_2, b_1, and b_2 describe the amplitudes of the patterns in each spectrum, and in this particular example have the values of 1.00, 1.11, 1.00, and 0.33 respectively. In addition, to make the spectra resemble real, experimental data sets, Gaussian random noise is superimposed upon each of the synthetic spectra.

Understanding the point of view used in the XCC requires a bit of mental gymnastics to invert the way in which the experimental data is organized. A spectroscopic

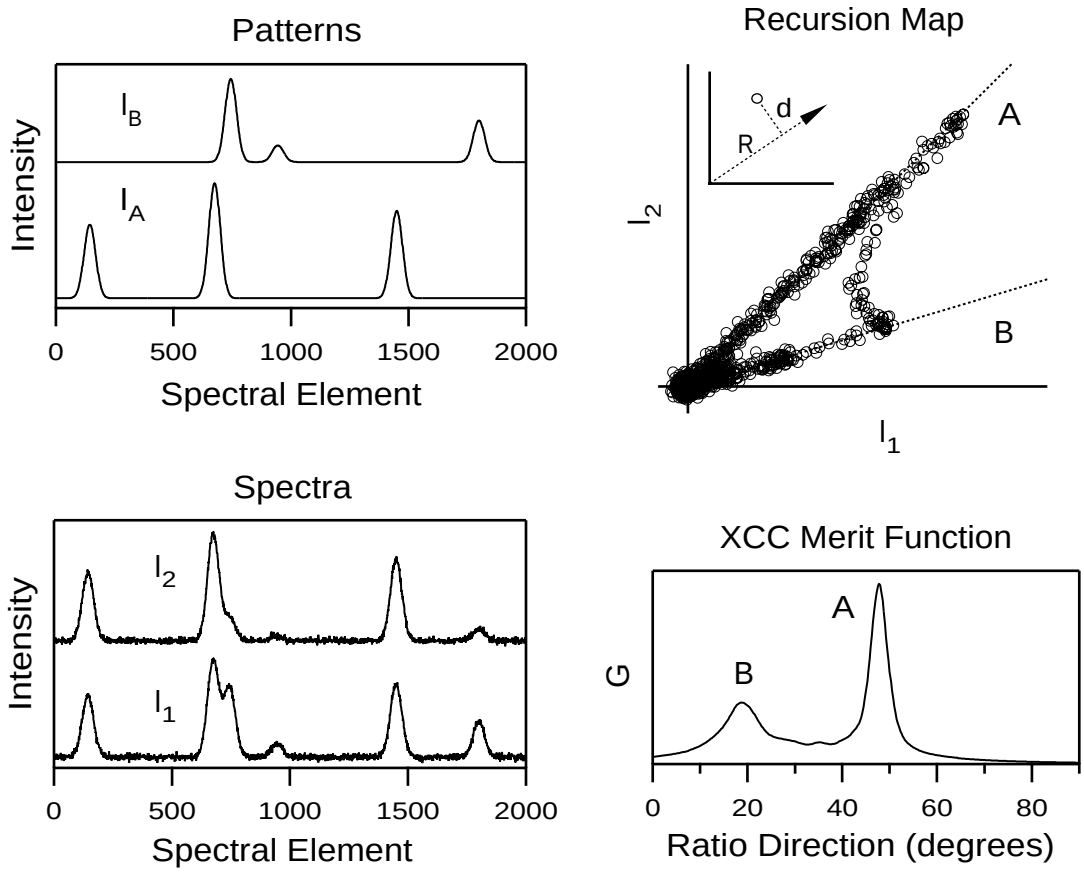

Figure 2-1: The XCC technique is illustrated using synthetic spectra. Top left: Patterns A and B, which contain features with Gaussian line shapes of half-width at half maximum (HWHM) of 30. Bottom left: Synthetic spectra 1 and 2, which are constructed by taking two different linear combinations of the patterns, and adding in Gaussian random noise. Top right: Recursion map of the synthetic spectra. The axes of the recursion map represent intensity values in each of the two spectra. The inset shows the (R,d) coordinates that are used to define the XCC merit function. Ratio directions optimized from the merit function are shown as dotted lines. Bottom right: XCC merit function (Eq. 2.7) computed for the synthetic data set for ratio directions making angles between 0° and 90° with the axis for intensity in spectrum 1. Locating ratio directions in the recursion map is equivalent to finding peaks in the XCC merit function.

data set is conventionally regarded as a group of spectra, each of which consists of a set of (usually discrete) measurements. The XCC regards a spectroscopic data set as groups of measurements, each of which is made in all spectra at a single measurement position (i.e., frequency, wavelength, etc.). To make this idea concrete, a *recursion map*[1] is defined in Fig. 2-1 for the two synthetic spectra. The recursion map in this case is two-dimensional, with the coordinates representing the intensity values in the two spectra. That is, the spectra are represented on the recursion map by plotting each spectral element of the entire data set as a point; the coordinates of the point are the intensities in the two spectra of the given spectral element. No information about spectral elements (frequency, wavelength, etc.) appears on the recursion map.

The points on the recursion map can be categorized as follows:

1. *Points near the origin.* These points correspond to spectral elements that have low intensities in both spectra. Although these points may have some signal content, this signal content is too weak relative to the noise to be useful in identifying patterns. The scatter of these points about the origin is due to the Gaussian random noise that is added to the synthetic spectra.

2. *Points that cluster about "rays" that pass through the origin.* The points that scatter about these rays have signal content that can be associated with one of the two patterns. That is, these points correspond to spectral elements that lie on spectral features which are not overlapped. The scatter of the points about the rays is due to noise. The most distant points from the origin represent the strongest features in a pattern.

3. *Points that cross between, and possibly through, rays.* These points correspond to spectral elements at which two or more patterns overlap.

For the goal of identifying patterns from the synthetic spectra, the points in category 2 are of the greatest interest. The presence of two rays of points in the

[1]The word recursion is used because a connection is made between measurements taken in independent experiments.

recursion map clearly indicates that two patterns are present in the data set. The upper of these rays comprises points that are well-described by

$$I_1 \approx a_1 I_A \tag{2.3}$$

$$I_2 \approx a_2 I_A \tag{2.4}$$

while the lower ray comprises points well-described by

$$I_1 \approx b_1 I_B \tag{2.5}$$

$$I_2 \approx b_2 I_B. \tag{2.6}$$

Note that these rays of points appear in the recursion map only if there exist regions in the spectra which can be accounted for by just one pattern. As will be seen below, the XCC is capable of disentangling overlapped patterns, but well-defined "pattern rays" must exist in the recursion map representation. Thus, one criterion for the success of the XCC is that some part of the line shape of at least some of the features in each pattern must not overlap with features from other patterns. Data in which the patterns are poorly resolved and highly overlapped are generally not ideal for analysis by XCC, and other, complementary pattern recognition techniques (such as those based upon principal component analysis) may provide a more satisfactory solution. As discussed in Ref. [42], however, when the XCC is applicable, it generally provides superior results to pattern recognition techniques based on principal component analysis when the XCC is applicable.

Prior to defining a numerically rigorous technique for identifying the patterns, it is clear that one could crudely identify which features in the spectra correspond to which patterns simply by partitioning the points into those that scatter about one or the other of the two rays of points in the recursion map. The task of the XCC is to provide a numerically rigorous method for this process of pattern identification. Following Eqs. 2.3 and 2.5 above, each pattern is considered to be defined by sets of spectral elements in which the ratio of intensities in the two spectra is nearly constant.

This ratio of intensities is referred to as the *ratio direction*, and each pattern contained in the spectra can be uniquely labeled by a ratio direction. The simplest numerical definition of the ratio direction for a given pattern is the slope of the ray of points that define the pattern. In the case of the synthetic data, the ratio directions are known *a priori*, and can be expressed in terms of the coefficients a_1, a_2, b_1, and b_2 defined in Eq. 2.1. Specifically, pattern A has a ratio direction of $a_2/a_1 = 1.11$ and pattern B a ratio direction of $b_2/b_1 = 0.33$.

In experimental data, however, the ratio directions are not known *a priori* and it is the task of the XCC to determine an unbiased estimate of the ratio direction for each pattern. At first glance, conventional least-squares fitting algorithms might appear to be appropriate, since finding an unbiased estimate of a ratio direction is equivalent to finding the slope of a best-fit line that is constrained to pass through the origin. However, linear least-squares fitting is a global optimization technique in the sense that it determines *one* set of model parameters which best describes all of the data. By contrast, for the synthetic data, unbiased estimates are desired for *two* ratio directions. Linear least-squares fitting with the recursion map data results in a best-fit line with a slope of 0.91, intermediate between the two correct ratio directions. Obviously, since least-squares provides a single best-fit line, the "best-fit slope" does not provide a good estimate for either ratio direction.

From a different perspective, least-squares fitting is undesirable for the purpose of obtaining estimates of the ratio directions because of its well-known sensitivity to "outliers". Least-squares fitting uses the χ^2 statistic as the figure-of-merit function; since χ^2 is defined as the sum of squares of deviations from the model, outliers strongly influence the best-fit parameters. Thus, when attempting to estimate the ratio direction for pattern A in the synthetic data, all of the points which are determined primarily by pattern B would be outliers in the least-squares fit, and *vice versa*.

Least-squares fitting has become firmly entrenched in spectroscopic practice. As a result, alternative merit functions often are not considered. However, other classes of merit functions, which minimize the effects of outliers but still provide an unbiased

estimator of the desired parameters, have been used in optimization on entire data sets [43]. Fitting techniques that are based on merit functions that are influenced by outliers to a lesser degree than χ^2 are often referred to as robust fitting techniques. One common robust technique uses as a merit function the sum of the absolute deviations from the model [44]. A special class of robust estimators is referred to as redescending robust estimates [1, 2, 3]. In contrast to the the chi-squared merit function used in least-squares fitting, the redescending robust merit functions consist of point-by-point sums of weight functions that have small magnitudes for outliers and larger magnitudes for points that are well-described by the model. A redescending robust estimator is desirable for the task of identifying the two model ratio directions in the recursion map precisely because extraction of more than one model estimate is desired.

The XCC is based on a redescending robust estimate, G, which in the case of two data records takes the form

$$G(\alpha) = \sum_k g_k(\alpha) = \sum_k R_k * \exp(-d_k^2/2V_k^{(d)}) \ . \tag{2.7}$$

Since the "fit line" is constrained to pass through the origin, the merit function is taken to be a function of just one parameter, α, which represents the ratio direction. In practice, α may represent either the slope of the fit line, or, equivalently, the angle between the fit line and one of the axes. The sum over k represents a sum over all spectral elements (all points on the recursion map). The g_k are referred to as weight functions; thus, the merit function takes the form of a sum of weight functions which are computed for each point on the recursion map.

The weight function in Eq. 2.7 consists of a product of two terms. The second term takes the form of a Gaussian function of d. As can be seen in the inset in Fig. 2-1, d represents the distance of any point in the recursion map from the fit line, and thus points that are more distant from the fit line are weighted less than those near the fit line. This provides the merit function with the property that it can estimate ratio directions for more than one pattern (i.e., this second term in the weight

function makes the merit function a redescending robust estimate). $V_k^{(d)}$ represents the expected variance of a point k on the recursion map along the d-direction. The next section considers how to calculate this quantity in general; for now, it is noted that if the noise amplitude in the two spectra is identical and independent of intensity, then $V_k^{(d)} = \sigma_0^2$, where σ_0 is the baseline noise amplitude associated with the spectra. By incorporating $V_k^{(d)}$ into the weight function, not only are points that are irrelevant to the fit automatically excluded, but the weights of each point are also determined in a statistically optimal manner, based on knowledge of the noise in the spectra.

The first term in the weight function, R, is simply the projection of the point on the recursion map onto the fit line (see the inset in the recursion map in Fig. 2-1). The justification for the form of this term is less rigorous than that for the second (Gaussian) term, and rests on the assumption that the spectral elements with the strongest intensities are the least likely to be corrupted by overlap with other patterns, or by noise or other experimental artifacts. Some function of R could, in theory, be substituted for R; other options have been discussed previously [45]. However, the use of simply R in the weight function provides accurate estimates of pattern ratio directions in tests on synthetic data with many different characteristics. In addition, the inclusion of R in the weight function makes possible the "weights method" for pattern reconstruction that is described below.

Note that R can have both positive and negative values. The only points that generate negative values of R are those that can be categorized as baseline noise points (i.e., those accounted for purely by random noise). It can be shown that for any ratio direction, one-half of all baseline points will have positive values of R and one-half will have negative values of R, which results in a suppression of the effects of baseline noise points on the merit function.

Figure 2-1 shows the XCC merit function as a function of ratio direction for the simulated spectra, using the known variance of the added noise. Two maxima are observed in the merit function at 20.1° and 47.5°. These values differ only slightly from the values of 18.4° and 48.0° used to construct the synthetic spectra.

With the number of patterns and the ratio directions identified, it is now possible

to assign spectral features to patterns. Several approaches to this task are feasible. Among them are the following two:

1. *XCC Weights Method*. In this method, the value of the weight functions are plotted (for each spectral element) with the value of α set equal to one of the optimized pattern ratio directions. Because the weight functions are largest for those spectral element that are well described by intensity derived from only one pattern, it is simple to identify those features in the spectra that are assignable unambiguously to one pattern.

2. *Inversion Method*. Note that Eq. 2.1 is invertible and that therefore the pattern intensities at any given spectral element can be determined from the spectral intensities if the coefficients a_1, a_2, b_1, and b_2 are known. The coefficients a, b are equivalent to the pattern ratio directions determined by XCC. Although it may appear that we are attempting to use two pattern ratio directions to determine four coefficients, any two of the coefficients (such as a_1 and b_1) can be assigned arbitrary values; this is equivalent to introducing arbitrary scaling factors for the patterns, I_a and I_b.

The results from the weights method are shown in Fig. 2-2. The weights evaluated at the maxima of the XCC function clearly identify features in the original spectra as belonging to one or the other of the patterns. Note that the overlapped spectral feature (near spectral element 750) is correctly separated into two components. The nearly 100/That is, some points will happen to have larger values of d (and thus smaller weights) due purely to random spectral noise. These noise-induced fluctuations in the weights can be reduced by smoothing. In the bottom panel of Fig. 2-2, the weights are convolved with a Gaussian line shape with a width equal to one-half of the width used in constructing the data set; this provides smoothing without significantly broadening the features. The result is "reconstructed patterns"[2] that resemble quite closely the original patterns used to construct the synthetic data,

[2]Note that the ability of the smoothed weight functions to reconstruct the patterns is made possible by the inclusion of R in the definition of the weight functions.

although the shapes and widths of the two lines that were overlapped in the synthetic spectra are only approximately reproduced.

The results of linear inversion are shown in Fig. 2-3. Although the intensities and line shapes of the peaks in the patterns are reproduced excellently, note that the signal-to-noise in the "reconstructed patterns" using the linear inversion technique is lower than that in the synthetic spectra. This "noise amplification" can be understood in terms of the transformation between the spectrum representation of the data and the pattern representation, but first consider two extreme cases:

1. If the ratio directions for the patterns are identical, then the patterns are indistinguishable (in essence, the signal-to-noise of the patterns after linear inversion is zero, and the noise amplification is infinite).

2. If the ratio directions for the patterns are 0° and 90°, then the patterns are already separated in the spectra, and no linear inversion is necessary. The signal-to-noise of the patterns is identical to that of the spectra (the noise amplification is zero).

Thus, it is clear that this noise amplification effect will be greater when the ratio directions for the two patterns are closer together.

To put this discussion on a mathematical foundation, consider the explicit expressions for the patterns in terms of the spectra, which result from the inversion of Eqs. 2.1:

$$I_a = \frac{1}{a_1 b_2 - a_2 b_1}[b_2 I_1 - b_1 I_2] \tag{2.8}$$

$$I_b = \frac{1}{a_1 b_2 - a_2 b_1}[-a_2 I_1 + a_1 I_2]. \tag{2.9}$$

Using these relationships, the noise in the patterns is related to the noise in the spectra according to

$$\sigma(I_a) = \frac{\sqrt{b_1^2 + b_2^2}}{a_1 b_2 - a_2 b_1}\sigma_0 \tag{2.10}$$

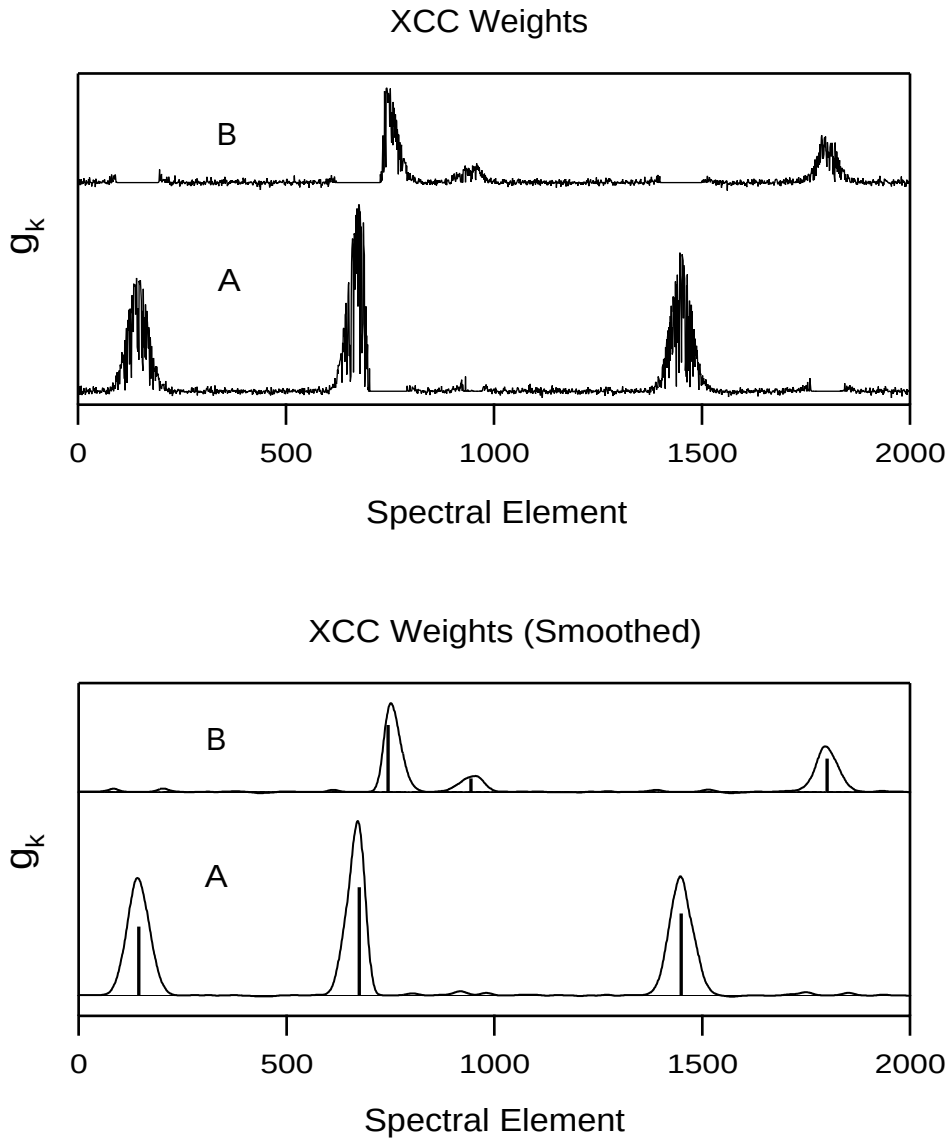

Figure 2-2: Reconstruction of the patterns from the spectral data using the "weights method". Top: XCC weights calculated for the two patterns identified in the synthetic data set. Bottom: XCC weights after convolution with a Gaussian to reduce the noise and replicate approximately the lineshapes in the synthetic spectra in Fig. 2-1. The vertical bars in the bottom panel represent the positions and intensities of the features in the patterns used to create the synthetic spectra.

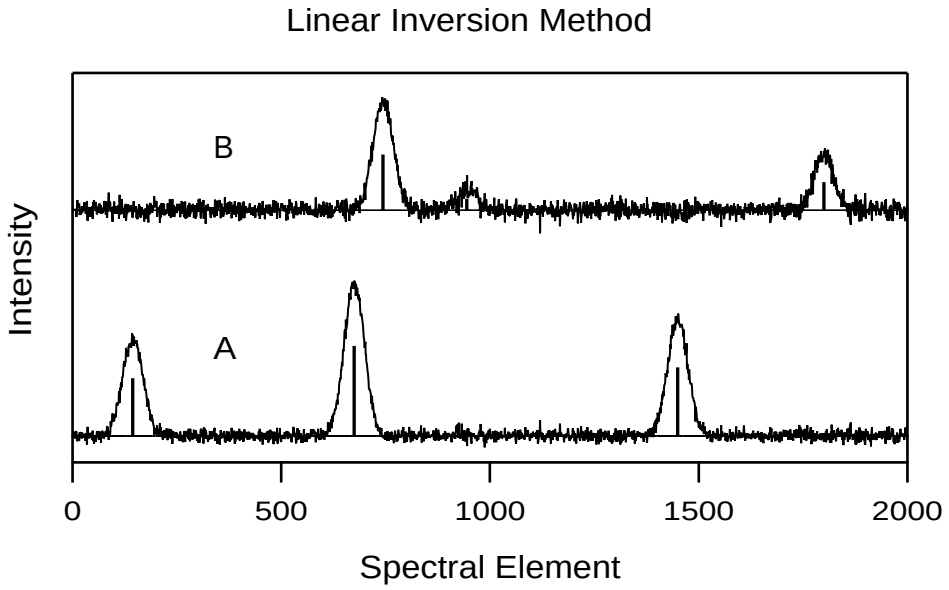

Figure 2-3: Reconstruction of the patterns from the spectral data by the linear inversion method. Linear inversion results in a worse S/N ratio than the weights method (Fig. 2-2), but provides a better line shape for overlapped features. The vertical bars represent the positions and intensities of the features in the patterns used to create the synthetic spectra.

$$\sigma(I_b) \;=\; \frac{\sqrt{a_1^2 + a_2^2}}{a_1 b_2 - a_2 b_1}\sigma_0 \;, \tag{2.11}$$

where σ_0 is the standard deviation of the noise in the spectra. For the specific values of the coefficients a_1, a_2, b_1, and b_2 used in the example here, the explicit noise amplification factors are

$$\sigma(I_a) \;=\; (1.35)\sigma_0 \tag{2.12}$$

$$\sigma(I_b) \;=\; (1.92)\sigma_0 \;. \tag{2.13}$$

The interpretation of these noise amplification factors depends on how the patterns are normalized. In the example here, the amplitude of the extracted patterns was chosen to be equal to the intensity of the patterns in spectrum one, by choosing $a_1 = b_1 = 1$. Thus, a precise interpretation of the noise amplification factor in this case is the ratio of the signal-to-noise of a given peak in the extracted pattern to the

signal-to-noise of the same peak in spectrum 1. Since the absolute intensity of the patterns is arbitrary, one can always make this choice (other possible choices include square normalizing the ratio directions to a value of one; this is the "natural scale" referred to in Ref. [42]). For a more thorough discussion of noise amplification, see Ref. [42], where this treatment is extended to consider arbitrary numbers of spectra, although only cases where the number of patterns equal the number of spectra are considered.

Note that despite the noise amplification of the linear inversion method, it reconstructs the lineshapes, line positions, and intensities of the original patterns much more accurately than the weights method, even with smoothing. Thus, because the XCC determines ratio directions by the least overlapped portions of strong features, linear inversion can determine the correct intensity and line shape of features that are completely obscured by overlap. On the other hand, the weights method can be used without modification when there are more patterns than spectra; the linear inversion technique cannot be employed in a straightforward way in such a case.[3]

2.3 Generalization of XCC to Multiple Dimensions

Although it is simplest to define and visualize the XCC in two dimensions (i.e., two spectra, as considered exclusively in Section 2.2), the technique is readily generalized to any number of spectra. The dimensionality of the recursion map will of course be equal to the number of spectra (N_s); see Ref. [42] for an example of a three-dimensional recursion map. The definition of the XCC merit function G in Eq. 2.7

[3]It is not strictly impossible to use linear inversion when the number of patterns exceeds the number of spectra. One useful approach that will not be discussed here is a "dimensionality reduction approximation". The key idea is that, except in highly congested spectra, the number of patterns that contribute strongly *at any given spectral element* is typically quite small (usually one or two) and thus less than or equal to the number of spectra. The XCC weights method can be used to determine, in an automated fashion, which patterns contribute significantly to any given section of spectrum, and then the linear inversion technique can be used to extract just the strongly contributing patterns. See Chapter 5 for an application of the reduced dimensionality approximation.

can be used for any number of dimensions, although the quantities d, R, and $V^{(d)}$ are somewhat more complicated to compute.

To compute these quantities in arbitrary dimensions, and also to provide a somewhat more rigorous conceptual foundation for the XCC, it is useful to introduce a vector notation in which each point on a multi-dimensional recursion map is represented by a vector $\vec{I}_k$, where the index k refers to the particular spectral element in question. Ratio directions are likewise denoted by a *unit vector* $\vec{\alpha}$. To evaluate g_k for arbitrary N_s, it is necessary first to define a coordinate transformation from the N_s-dimensional recursion map space to a two-dimensional space defined by the coordinates (R, d). These coordinates are illustrated graphically in the inset in the upper right panel of Fig. 2-1 for the 2D case. The first axis (R) coincides with the ratio direction vector $\vec{\alpha}$; the projection of a recursion map point on this axis is

$$R_k = \vec{I}_k \cdot \vec{\alpha}. \tag{2.14}$$

The coordinate d is defined to be orthogonal to R and to point towards the recursion map point. Gram-Schmidt orthogonalization permits the computation of the magnitude d_k and direction (defined by a unit vector $\vec{\beta}_k$) according to

$$d_k \vec{\beta}_k = \vec{I}_k - R_k \cdot \vec{\alpha} \ . \tag{2.15}$$

Note that the unit vector $\vec{\alpha}$ is the same for every recursion map point k for a given ratio direction, but $\vec{\beta}$ is different for each point on the recursion map.

The final quantity needed to compute the XCC in arbitrary dimensions is $V^{(d)}$, the variance associated with the recursion map points in the d direction. That is, the XCC is defined as a function of both the set of recursion map points as well as their variances (i.e., the experimental uncertainties in each measurement). If the variances associated with each point in each spectrum are defined to be $\vec{V}_k$, then the component of the variance along d is

$$V_k^{(d)} = \vec{\beta}_k \cdot \vec{V}_k. \tag{2.16}$$

Note that, using this definition, the XCC can accommodate data in which the measurement error is different in each of the spectra, or even cases in which the measurement error changes from one spectral element to the next. Such a case might occur if the noise level in a spectrum varies as a function of wavelength/frequency, or if the measurement error depends on the intensity in the spectrum, through a relationship such as

$$V(I) = \sigma_0^2 + \sigma_1^2 I^2, \tag{2.17}$$

where σ_1 represents a component of the experimental noise that is (directly) proportional to intensity.

At this point, it should be clear that the XCC can be utilized to identify patterns in any number of spectra. However, working with more than three spectra creates new challenges, and I wish to conclude this section by outlining strategies that I have found useful for working with large numbers of spectra.

With more than three spectra, it becomes impossible to visualize the recursion map or XCC merit function. Visualization of the merit function is convenient because it permits facile determination of the number of patterns and reasonable initial guesses for the ratio directions. One strategy for dealing with more than three spectra is to sample the merit function as evenly as possible over non-negative values of the $N_s - 1$ independent coordinates that describe the ratio directions. Local maxima in the XCC merit function can then be identified and optimized, each of which corresponds to one pattern. This "brute force" technique, however, is computationally tedious and may not be practical for more than a handful of spectra.

In practice, this sort of multidimensional sampling is often unnecessary. Frequently, all of the patterns in a data set can be identified in a small subset of the full N_s-dimensional data set. That is, each of the desired patterns often can be identified as a maximum in the XCC merit function using just two or three of the available spectra. Once the patterns have been identified in a subspace of the full data set, then the rest of the spectra in the data set can be incorporated, one at a time, to refine the patterns. I have found this technique to be effective with very large data

sets (more than 100 spectra). However, this technique could be risky if the number of patterns in the data set is not known *a priori*. In such a case, one cannot be sure that all of the patterns contained in the full data set have been identified in a subspace of the data set, and one could conceivably "miss" a pattern entirely in this way.

Finally, it should also be noted that the linear inversion technique that is described in Section 2.2 can also be used when number of spectra is greater than the number of patterns. In these cases, the term "inversion" of the equations is used in a generalized least-squares sense (the inversion being accomplished by singular value decomposition, for example). Moreover, it should be recognized that the noise amplification associated with linear inversion will be mitigated when the number of spectra exceeds the number of patterns, because of the averaging which occurs when "extra" spectra are included in the inversion.

2.4 Application to Spectra of Deuterated Ammonia Isotopomers

To illustrate the application of the XCC to real experimental data, the technique is used to extract the spectra of pure isotopomers from infrared spectra [46] of mixtures containing ND_3, ND_2H, NDH_2, and NH_3. It is difficult to obtain spectra of pure samples of the ammonia mixed isotopes (ND_2H and NDH_2) because of the strong adsorption of ammonia and water on most cell surfaces, which causes rapid exchange of H and D. The XCC, however, can extract the spectra of ND_2H and NDH_2 as patterns from a data set consisting of mixtures of ammonia isotopomers with varying deuterium ratio. The analysis of the mixed isotopomer spectra would make a considerable contribution to the understanding of the potential energy surface of ammonia, shedding light on the normal-to-local mode transition, stretch-bend interactions, and other vibrational couplings [47, 48].

Figure 2-4 depicts a small section of three spectra obtained by Hernandez, Lehmann and Lafferty [46] of mixtures of the ammonia isotopomers. The lower spectrum was obtained by introducing ND_3 into a cell that was preconditioned with D_2O. In

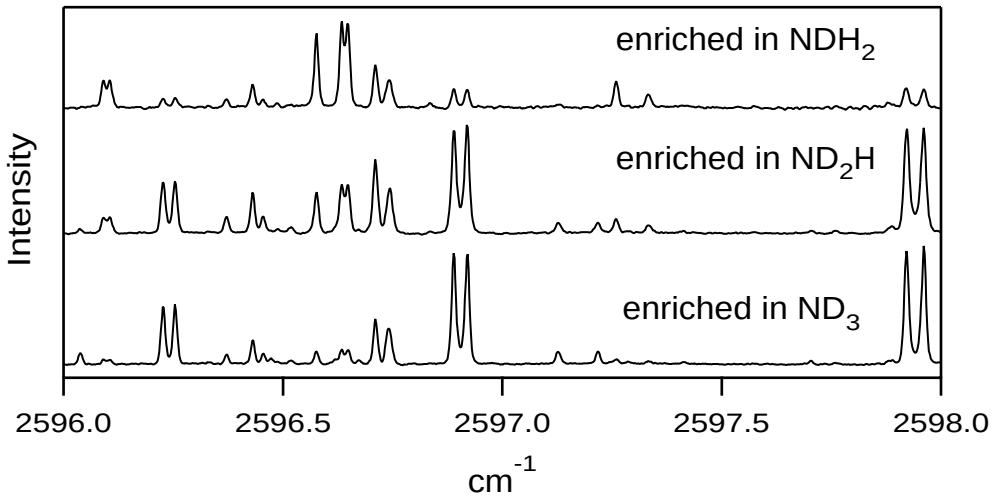

Figure 2-4: Infrared spectra of mixtures of deuterated ammonia isotopomers. The lower spectrum is of a sample of ND_3 in a sample cell pretreated with D_2O, so that ND_3 is expected to be the most abundant species. The other two spectra are mixtures of ND_3 and NH_3 in 1:2 (upper) and 2:1 (middle) ratios in a cell pretreated with D_2O and H_2O in the same ratio.

the absence of contamination, this sample should contain only the ND_3 isotopomer; however, low levels of contamination by H often prove difficult to avoid. The upper two spectra were obtained with samples that consisted of a mixture of ND_3 and NH_3 in ratios of 1:2 (upper) and 2:1 (middle). The cell in these cases was preconditioned with a mixture of D_2O and H_2O in the same ratio, and the relative abundances of each of the ammonia isotopomers can be estimated by the binomial distribution.

The full spectra recorded by Hernandez et al. [46] contain several thousand features and cover the entire ND and NH stretch fundamental regions. For ease of presentation, only a 2.0 cm^{-1} section between 2596 cm^{-1} and 2598 cm^{-1} is considered here. This region contains absorption due to the N-D stretch chromophore; because the N-H stretch does not contribute in this region, the only patterns that are expected are those due to ND_3, ND_2H, and NDH_2. Even in this small section of spectrum, and with only three of the four species contributing, the number of lines is large. Without a technique for labeling the lines according to which species produced them, it would be difficult to apply traditional spectrum assignment techniques such as combination-differences.

In Section 2.3, the XCC was defined for arbitrary dimensions. However, before applying these definitions to the ammonia data considered here, it is instructive first to employ the more intuitively simple tools of Section 2.2, in which the discussion was restricted to pairs of spectra. Figure 2-5 depicts the recursion maps for each possible pair of spectra in Fig. 2-4. Three rays of points are clearly observed in each recursion map, although these rays of points are better separated in some of the recursion maps than others. These rays of points, of course, indicate the presence of three patterns in the spectra, one corresponding to each contributing isotopomer. Since ND_3 is expected to contribute more strongly to the more highly deuterated samples, and NDH_2 to contribute more strongly to the less deuterated samples, one can immediately assign each of the patterns to one of the isotopomers (it is evident that the sample of "pure ND_3" must have been contaminated to some extent by H_2O or NH_3 due to the presence of ND_2H, and NDH_2 in this sample). The noise characteristics of the data can also be estimated by inspecting the recursion maps.

The XCC, of course, is successful in identifying all three patterns in each of the pairs of spectra, and in principle, the weights method could be used with any one of the pairs to identify the three patterns. However, it is to be expected that utilizing *all* of the spectra simultaneously to identify the patterns will yield the best results. The techniques outlined in Section 2.3 can be applied directly to calculate the XCC merit function, as a function of ratio direction, for all three of the spectra in Fig. 2-4. In this case, the ratio direction can be visualized as a vector in a three-dimensional space that originates from the origin. In the case of the two-dimensional XCC discussed in Section 2.2, the angle of the fit line with one of the axes of the recursion map was found to be a convenient coordinate for plotting the XCC. In the case of three spectra, two such angles are needed to uniquely define a ratio direction.

A contour plot[4] of the XCC merit function, as a function of two such coordinates, is depicted in Fig. 2-6. Three maxima are clearly observed in the XCC merit func-

[4]The best way to visualize the XCC merit function in the case of three spectra is as a contour plot on an octant of a sphere, as in Ref. [42]. However, this type of plot requires specialized software. The contour plot represented here can be thought of as the octant of a sphere projected onto a plane, much like the projections used for wall maps of the Earth.

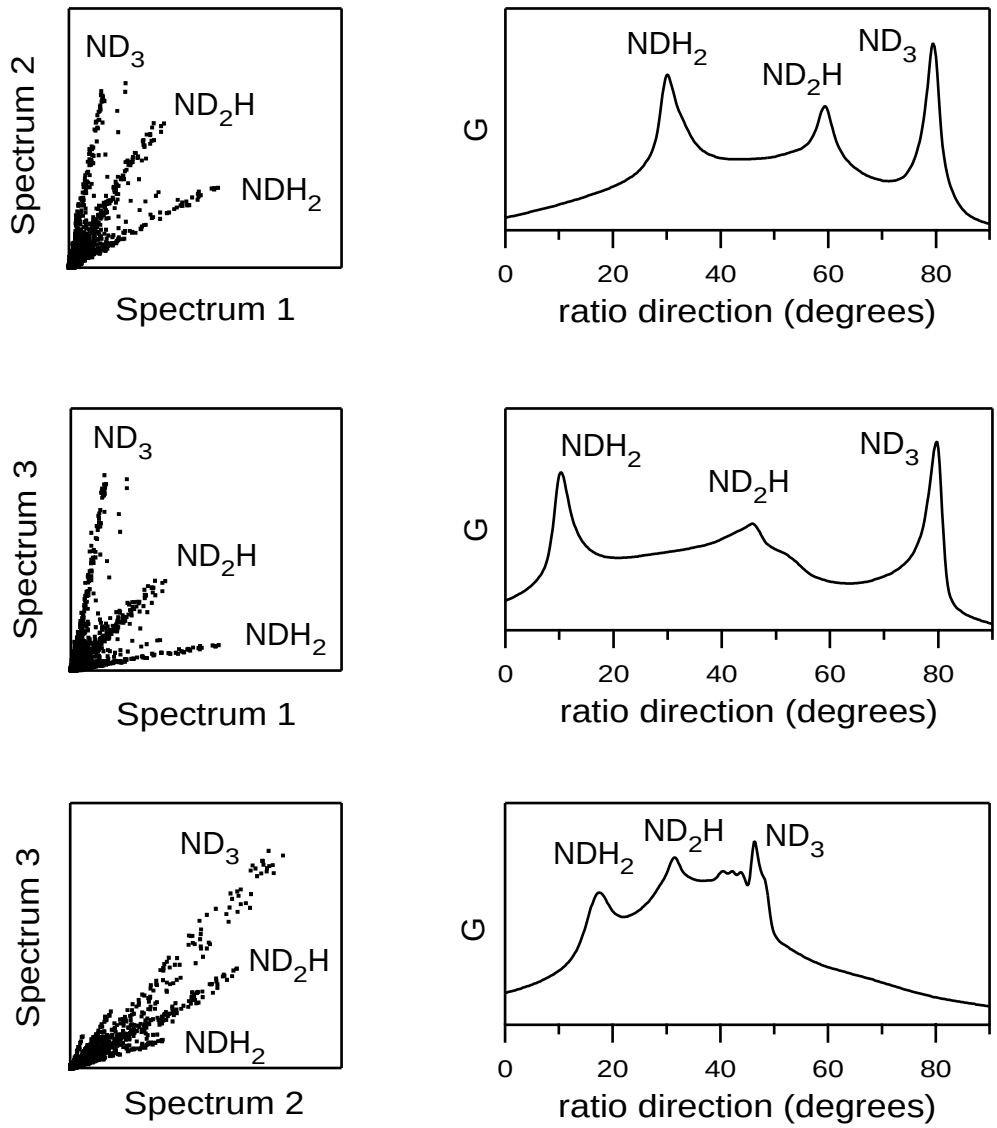

Figure 2-5: Application of the XCC method to all possible pairs of spectra in Fig. 2-4. Left column: Recursion maps, indicating the presence of three patterns, that correspond to the three deuterated ammonia species. Right column: XCC merit function plotted as a function of the ratio direction (angle between the "fit line" and the x-axis). Each ratio direction can be assigned to a specific isotopic species using knowledge of how the samples were prepared.

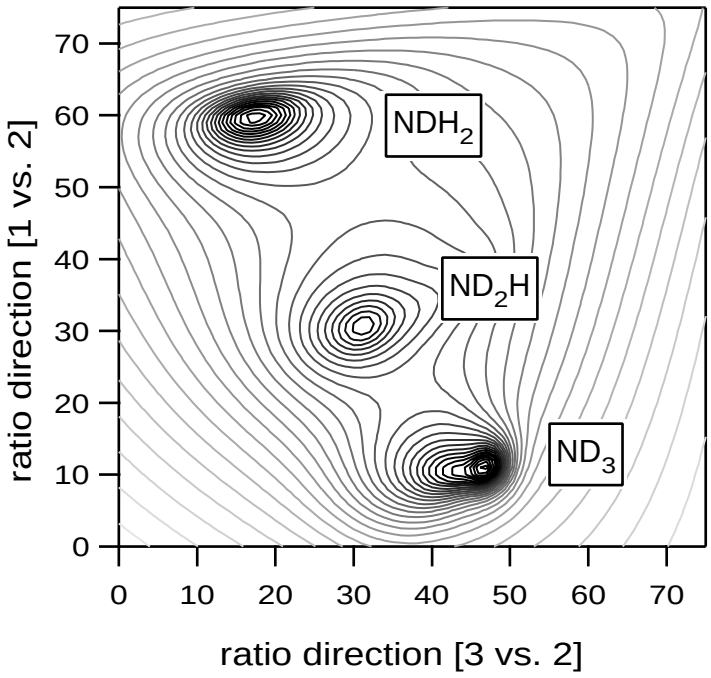

Figure 2-6: Contour plot of the XCC merit function for the ammonia mixed isotope data, labeled with the associated isotopomer pattern.

tion, and it is once again trivial to assign these to deuterated ammonia isotopomers. Optimized ratio directions for each pattern can be obtained by using standard maximization routines [44].

Having identified the maxima in the XCC merit function, the weights method can be used to separate immediately the spectra into three patterns. The weights, after convolution with a Gaussian to replicate approximately the lineshapes observed in the spectra, are depicted in Fig. 2-7. Virtually all of the lines in the spectra can be assigned to one of the isotopomers using these plots. As noted in the previous section, the weight functions will not necessarily accurately represent the intensities of the patterns (in this case, the intensities in the spectra of the individual isotopomers). In this particular case, although the spectra are reasonably congested, there is minimal overlap between peaks and the weights method can be expected to perform reasonably well.

The second technique that was discussed in Section 2.2 for partitioning the spectra into patterns is entitled linear inversion. The strength of the linear inversion tech-

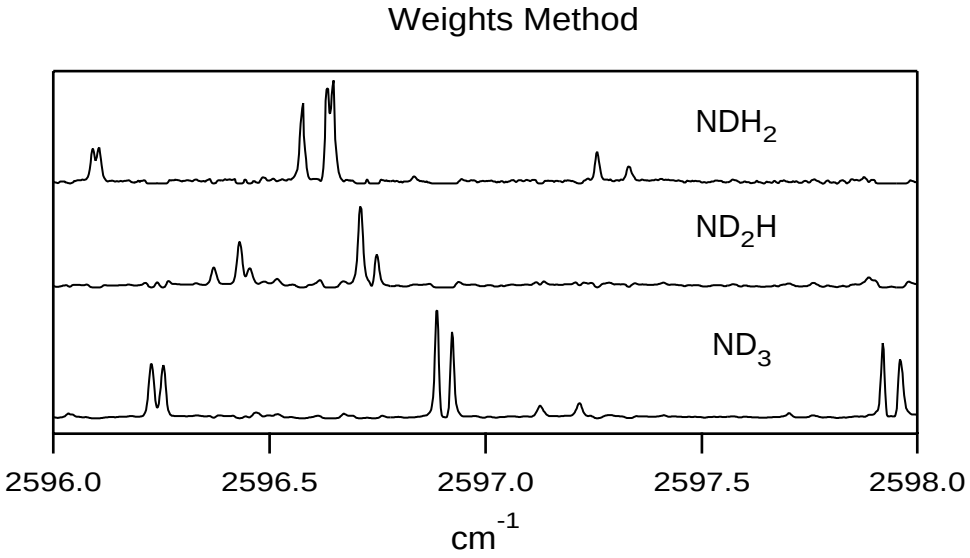

Figure 2-7: Results of the XCC weights method for identifying the patterns present in the ammonia mixed isotope data. Each trace corresponds to one of the pattern ratio directions determined as a local maximum in the merit function in Fig. 2-6. This plot permits assignment of most of the lines in Fig. 2-4 to one of the isotopic species.

nique is its ability to determine accurate intensities and lineshapes for the patterns even when features from more than one pattern overlap. However, the discussion of noise amplification in Section 2.2 indicates that linear inversion is most successful when the ratio directions are widely separated in the recursion map space. Although the three maxima in Fig. 2-6 are well-resolved, they fall close to lying on a line in recursion map space. In this sense the three pattern ratio directions poorly "span" the recursion map space, which suggests that the three mixed ammonia isotope spectra are not ideal for purposes of extracting three patterns by linear inversion. For this reason, the linear inversion method will not be used here. Note that Ref. [42] provides a thorough discussion of noise amplification for ammonia mixed isotope spectra, including a calculation of the optimal deuterium fractions that would result in the best pattern identification by linear inversion. For other examples of linear inversion applied to three or more spectra, see Chapters 3 and 5.

2.5 Windowed XCC

In this section I propose a variant of XCC called "windowed XCC" that may be a useful preprocessing tool for assigning rotational transitions in congested spectra, among other possible applications.

To motivate the windowed XCC, Fig. 2-8 depicts a pair of simulated absorption spectra of OH, at two different temperatures (1500 K and 2000 K, which are typical in combustion experiments), that were provided to me by W. Kreutner and K. Kohse-Höinghaus. The challenge of interpreting these spectra is that, at the high temperatures of the simulation, many rovibrational states of OH are populated, leading to a congested spectrum that is difficult to assign.

From the standpoint of the XCC, the patterns that are repeated in the two spectra are groups of lines that originate from the same rovibrational state; as the temperature is varied, the relative amplitudes of the patterns vary due to different Boltzmann factors. These patterns, however, are not clearly identifiable in the recursion map for the two spectra, and in fact all of the points on the recursion map cluster closely around the line $I_1 = I_2$. The XCC merit function does clearly indicate the presence of the expected patterns, although the ratio directions of these patterns cluster in a narrow range, and several local maxima in the merit function appear to overlap.

Since the number of patterns greatly exceeds the number of spectra, the weights method must be used to identify the patterns. The results are shown in the bottom panel of Fig. 2-8 for several of the pattern ratio directions identified by the XCC. The patterns that are identified consist of a small number of peaks; all of the peaks in each pattern are expected to originate from the same initial state. By stacking these patterns on top of each other in order of descending ratio direction, it is clear that the patterns are closely related and form a (rotational) progression; that is, adjacent patterns likely correspond to levels originating from rotational states differing in J'' by one.

Thus, the XCC technique appears to be of some utility in assigning the initial rotational states of the lines observed in these spectra. However, the large number

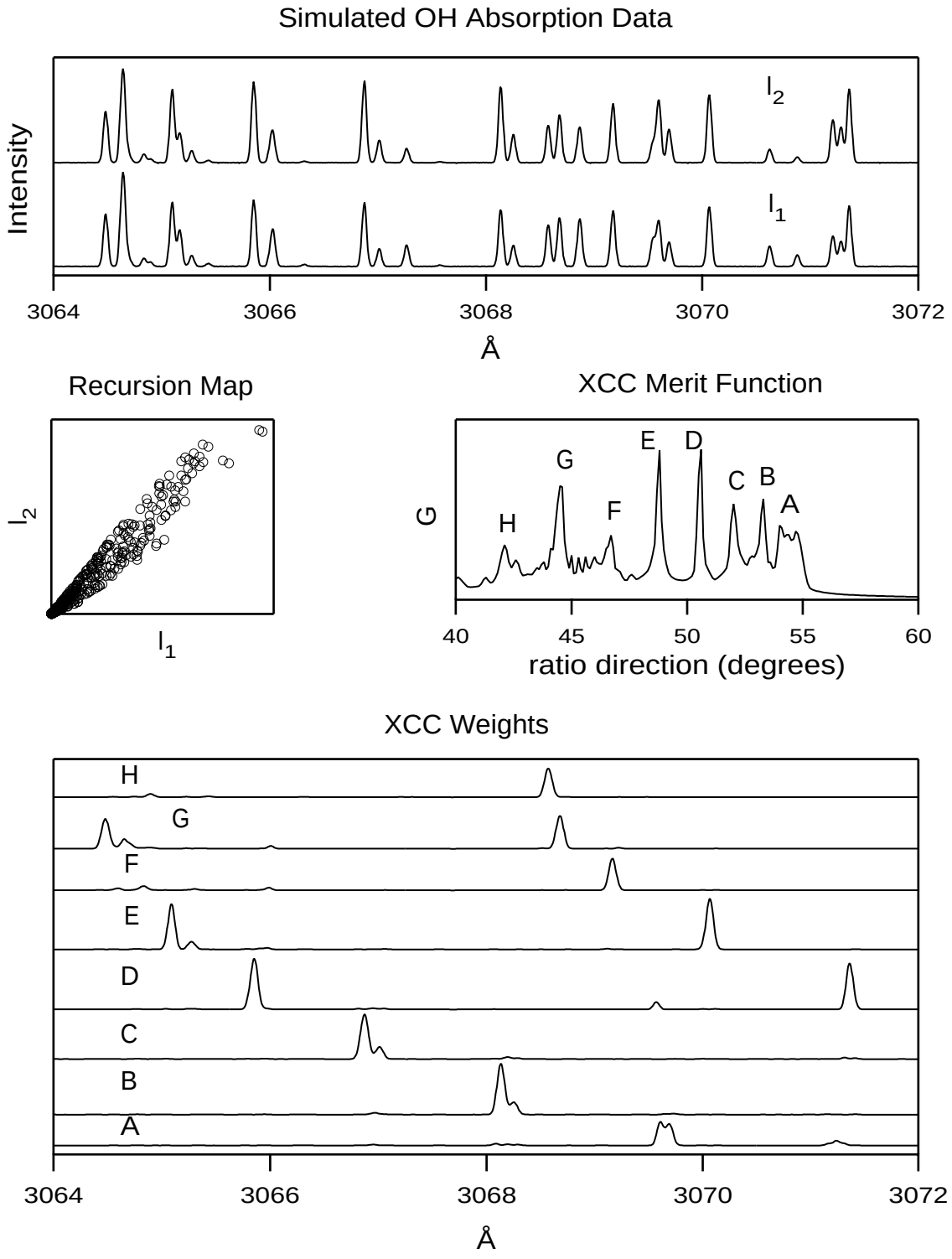

Figure 2-8: Top: Simulated absorption spectra of OH at 2000 K (upper) and 1500 K (lower). Middle left: Recursion map of the two simulated spectra. Middle right: XCC merit function indicating the existence of several patterns with similar ratio directions. Bottom: XCC weights calculated at a few of the local maxima in the XCC merit function.

of patterns identified by the XCC makes using the weights method a bit awkward, and it is difficult to be certain that one has not "missed" a pattern in the congested XCC merit function. Real experimental data are expected to present even greater challenges due to measurement error, other interfering patterns, and experimental artifacts such as baseline drift.

For these reasons, I have pursued a somewhat different approach for this and related problems that I entitle windowed XCC. As the name suggests, the windowed XCC algorithm performs the XCC over a limited range of spectrum, specifically within a window whose width is roughly equal to that of one peak in the spectrum. This may seem counterintuitive, since the XCC is designed to group even widely separated peaks together into patterns. The windowed XCC is not, however, strictly speaking a pattern recognition technique; it is, rather, a preprocessing tool that makes spectroscopic patterns easier to identify.

The windowed XCC algorithm proceeds as follows. At each window position, the XCC merit function is optimized as a function of ratio direction. Because the window generally includes only one or two peaks, it is generally simple to locate the global maximum of the merit function, if in fact there are multiple maxima at all. The window is then shifted slightly, and the optimization is performed again, until the windowed XCC has been performed across the entire spectrum. At each step, three values are recorded: the window position, the optimized ratio direction, and $G_{\max}$, the value of the XCC merit function at the optimum ratio direction.

These results are summarized in Fig. 2-9 for the OH absorption data. Note that the value of $G_{\max}$ achieves a local maximum at every window position which is centered around a peak that appears in both spectra; this is due to the inclusion of R in the definition of the XCC merit function (Eq. 2.7). The value of the optimized ratio direction at one of the local maxima of $G_{\max}$ thus corresponds to the approximate ratio direction for one peak in the pair of spectra. In this sense, the windowed XCC can be thought of as simply an "automated ruler" that can identify the relative intensities of the peaks which appear in a pair (or more) of spectra.

Although this might seem like a fairly trivial use of the XCC, the ability to per-

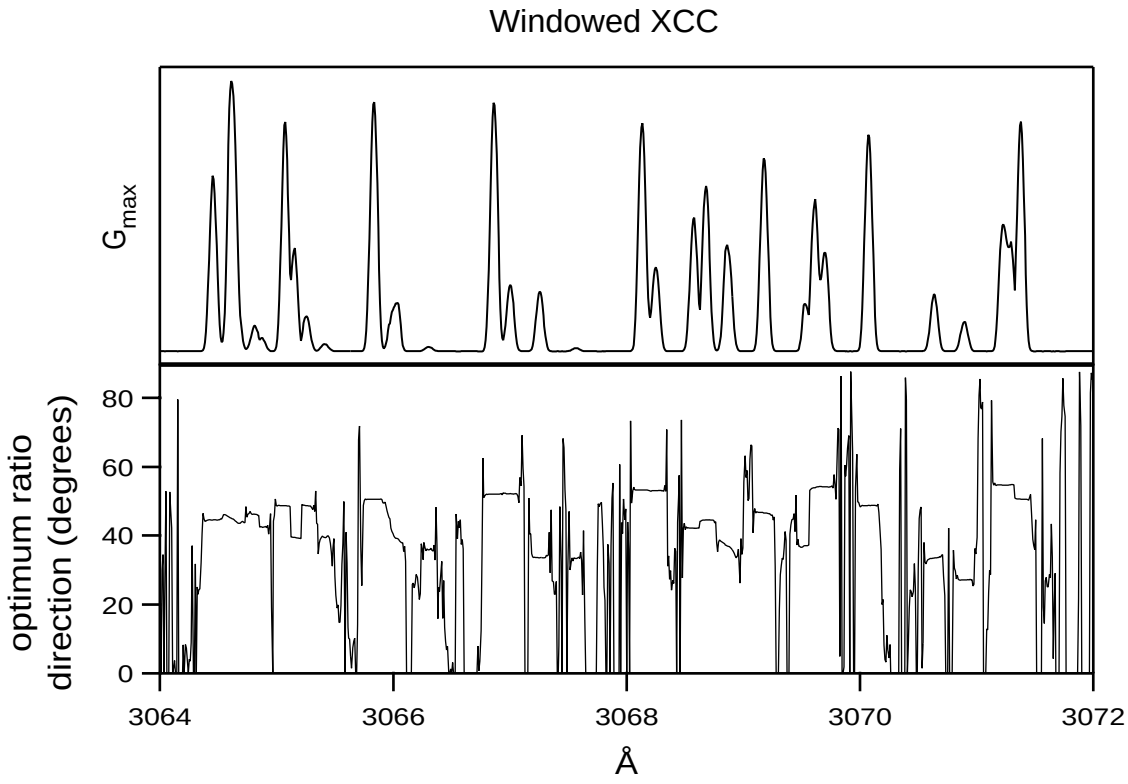

Figure 2-9: Illustration of the windowed XCC algorithm. Maximum value of the XCC merit function (top) and corresponding optimum ratio direction (bottom) at each window position for the simulated OH spectra.

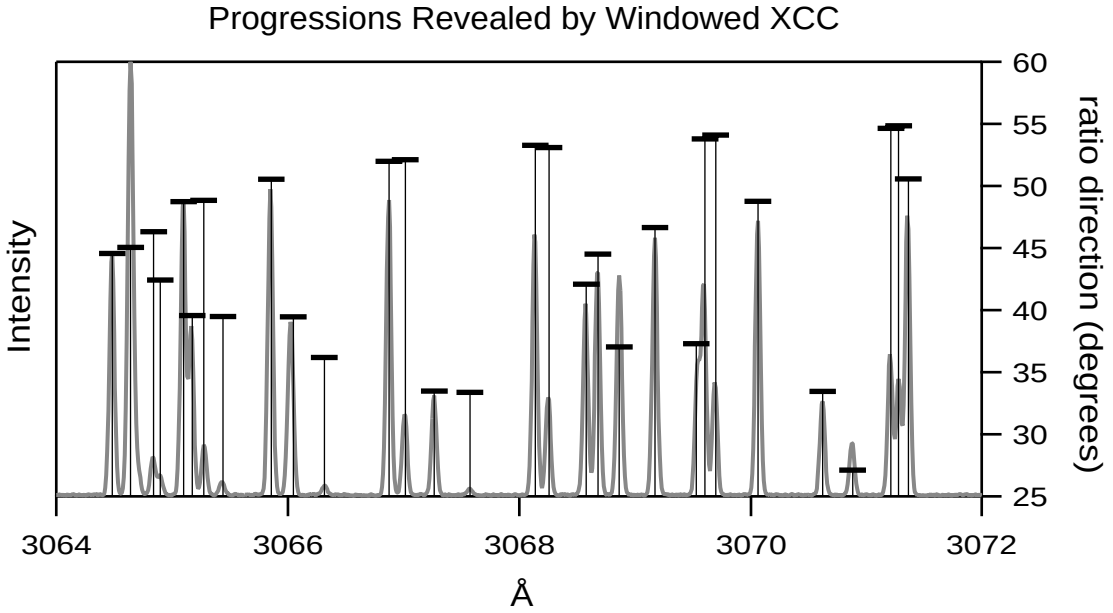

Figure 2-10: Results of the windowed XCC algorithm for the simulated OH data. The gray trace is one of the two spectra. The vertical sticks mark the frequencies at which a local maximum is observed in $G_{\max}$, while the bars on top of the sticks indicate the optimized ratio directions (right axis) at these frequencies. Two progressions of states, which appear to form band heads, are immediately obvious

form such a preprocessing task in an automated and rapid way can be very useful, as revealed in Fig. 2-10. One of the two simulated spectra is shown in gray. The vertical sticks mark the frequencies at which a local maximum is observed in $G_{\max}$. The bars on top of the sticks indicate the optimized ratio directions (right axis) at these frequencies. Two progressions of states, which appear to form band heads, are immediately obvious, even more so than in the application of the weights method depicted in Fig. 2-8. It can be envisioned that the windowed XCC could be coupled with other algorithms to identify automatically combination-differences and thus provide rotational assignments; in this example, the rotational temperatures of the two samples could also be estimated.

Although only considered synthetic data have been considered here, it is hopefully clear that spectroscopic pattern recognition techniques like the XCC and windowed XCC may be useful in the field of combustion spectroscopy. Many different chemical species are present in flames. This chemical complexity, combined with high

temperatures, makes absorption or emission spectra of flames rather congested. Preprocessing such spectra using pattern recognition algorithms may make their analysis much simpler. One can envision using the XCC in particular to decode spectra that are recorded from different spatial positions in a flame, or spectra recorded from flames with different fuel mixtures.

2.6 Conclusion

A spectroscopic pattern recognition technique entitled Extended Cross-Correlation has been introduced in this chapter. The XCC permits the identification of patterns that are repeated in multiple spectra and can be applied in a model-free way, meaning that the forms and number of patterns to be identified can be completely unknown at the outset. The XCC permits the identification of multiple patterns within a set of spectra, including the possibility of identifying larger numbers of patterns than the number of spectra. Finally, the XCC takes into account knowledge about noise in the spectroscopic data in a natural fashion.

The examples of the application of the XCC technique that have been presented in this chapter are simple ones, and it would be possible to identify by eye the patterns that are present in both the synthetic data in Section 2.2 and the deuterated ammonia isotopomer data in Section 2.4. However, the ammonia spectra that were presented in Section 2.4 represent only a small fraction of the total available spectra. The spectra extend over hundreds of cm^{-1}, and the numerical pattern recognition techniques can easily be automated to provide isotopomer assignments for most of the lines in the entire data set. In addition to avoiding tedious analysis of *large* data sets, a numerical pattern recognition technique such as the XCC can also be particularly useful for analyzing *complex* data sets which consist of many spectra and/or contain a high density of overlapping peaks. Finally, even when a pattern recognition task can be accomplished "by eye", the numerical rigor of a technique such as the XCC can reduce human error and the necessity for "judgement calls" in analyzing a spectroscopic data set.

The XCC is similar in spirit to several other pattern recognition techniques that have been reported, particularly those that are based on principal component analysis, such as classification analysis [49] and Iterative Target Transformation Factor Analysis (ITTFA) [50, 51]. These techniques start from the same assumption as the XCC: that a set of spectra can be considered to be linear superpositions of patterns. Another similarity is that principal component analysis can, in principle, be used to determine the number of patterns that are contained in a data set without any *a priori* knowledge. However, the "patterns" that are obtained directly from principal component analysis generally do not have any physical meaning, although techniques have been reported that permit the transformation of the abstract principal components into physically meaningful patterns [50, 51]. In addition, the successful use of PCA-based techniques generally requires the availability of many more spectra than the number of patterns to be identified. In this respect, XCC provides an attractive alternative to pattern recognition techniques based on PCA. In cases in which spectra do not consist primarily of well-resolved features, however, PCA techniques may hold an advantage [42].

A number of other numerical techniques have been employed to identify and extract patterns from spectroscopic data sets; techniques whose goals or procedures are at least tangentially related to the XCC include

- robust estimation (non-least squares estimators) [1, 2, 3],
- covariance mapping [52],
- genetic algorithms [53],
- neural network pattern recognition [54],
- two frequency correlation [55],
- wavelet transformations [56],
- multidimensional scaling [57],
- tree analysis [58].

These methods have in common with this work the desire to extract related patterns from the midst of unrelated structures and to generate compact representations of large quantities of data. Each of these techniques, however, differs significantly from the XCC in capabilities and domains of application. Indeed, in researching these techniques, I was struck by two things: 1) the complementarity between the various pattern recognition techniques available, and 2) the minimal intercommunication among the groups of chemists, physicists, biologists, applied mathematicians, and engineers (among others) who use/invent pattern recognition tools in their research. Certainly much would be gained by increased interdisciplinary discussion of pattern recognition techniques and their applications.

Acknowledgments

This research was supported by AFOSR grants F49620-94-1-0068 and F49620-97-1-0040. My work on this project was supported by the Department of the Army for support under a National Defense Science and Engineering Graduate Fellowship. We are grateful to Prof. Rigoberto Hernandez of U. Penn, Prof. Kevin Lehmann of Princeton, and Dr. Walter Lafferty of National Institute of Standards and Technology (NIST) for use of the ammonia mixed isotopes spectra. We thank Professors David Hercules and Joel Tellinghuisen for introducing us to the ITTFA technique, and Dr. Wolfgang Kreutner and Prof. Katharina Kohse-Höinghaus for the simulated OH spectra. Finally, sincere thanks to Steve Coy for a stimulating and productive collaboration.

Chapter 3

Hybrid Linear Pattern Analysis

This chapter represents the results of a long-term collaboration with a group of researchers at what is now called the Air Force Research Laboratory, Space Vehicles Directorate, at Hanscom Air Force Base. The researchers with whom we (myself, Steve Coy, and Bob Field) collaborated include Steven J. Lipson, Ronald B. Lockwood, David L. Vititoe, Peter R. Armstrong, and William A. M. Blumberg. A slightly modified version of this chapter has been submitted to the Journal of Physical Chemistry for publication.

3.1 Motivation for HLPA

A technique entitled Hybrid Linear Pattern Analysis (HLPA), which represents a combination of model-based and pattern recognition-based approaches to the analysis of spectroscopic data, is introduced in this chapter and applied to analyze the kinetics associated with time-resolved emission spectra of CO.

Consider a spectroscopic data set in which each spectrum is a linear superposition of a finite number of patterns. These patterns might be associated with, for example, different chemical species (Chapter 2), polyad quantum numbers (Chapter 5), or different vibrational bands of a single species (this chapter). A "model-based" analysis of such a data set is possible if the patterns (relative intensity vs. frequency) that are contained in the spectra can be predicted *a priori*. The relative amplitude of each pattern in each spectrum can then be determined by conventional optimization procedures. Least squares fitting algorithms [44] are by far the most commonly used for such optimizations, although robust methods of estimation [1, 2, 3] can reduce the sensitivity of the fit to outliers (which could be due to either experimental artifacts or deficiencies in the model).

If, on the other hand, it is not possible to predict *a priori* the number or appearance of the patterns, then pattern recognition techniques may provide a successful approach to the analysis of the data set. A wide variety of pattern recognition techniques have by now been applied to spectroscopic data. Among the most common are techniques based on principal component analysis (PCA) (see, for example, Refs. [49],

[50], [51], and [59]); other approaches include applications of neural networks [54], genetic algorithms [53], covariance mapping [52], and the Extended Cross Correlation (XCC) technique that was introduced in Chapter 2. These various pattern recognition techniques differ greatly in terms of their assumptions about the data to be analyzed, their realms of applicability, and the numerical algorithms employed. However, the majority of these share the goal of identifying unknown patterns that are repeated either within one spectrum or among multiple spectra.

The case in which some of the patterns contained in a data set can be predicted *a priori*, but others cannot, has received less attention in the literature. One possible approach to this type of problem would be to apply one of the pattern recognition techniques discussed above in an attempt to identify all of the patterns in the data set, including those that are previously known. However, it is of course advantageous to incorporate any *a priori* knowledge of the patterns into the spectral analysis.[1] The HLPA technique makes this possible. It employs techniques of pattern recognition to identify the unknown patterns but explicitly incorporates *a priori* knowledge of the remaining patterns.

The use of this technique is illustrated in Section 3.2 with synthetic data, and in Section 3.3 with time-resolved emission spectra of CO that were recorded in atmospheric emission simulation experiments conducted at the LABCEDE facility at the Air Force Research Laboratory, Hanscom AFB. Details of the experimental setup have been reported previously [61, 62]. In brief, an electron beam is pulsed through a 10 mTorr sample of CO in a cryogenic chamber. Time-resolved infrared emission spectra of CO are recorded both during the 10 ms electron pulse and for 50 ms afterwards. The time-resolved spectra provide information about the nascent populations and collisional deactivation rates of the excited vibrational levels of the ground state of CO. At least twelve excited vibrational levels of the electronic ground state of CO

[1] I wish to point out the existence of a technique called hybrid linear analysis (HLA) [60] that is conceptually similar to HLPA. HLA is not a pattern recognition technique, but rather a technique for linear multivariate calibration (used to determine the concentration of one species in a multicomponent sample, for example) that improves upon standard partial least-squares methods by incorporating the spectrum of the desired species into the calibration procedure.

can be observed to be populated by processes initiated by the electron beam, and at the resolution of the experiment ($\sim$2.5 cm^{-1}), the overlapping emission bands are only partially resolved.

Previously, this data has been partially analyzed using standard least squares procedures. As discussed in Section 3.3, the rotational distribution of the sample can be modeled to a good approximation by a Boltzmann distribution that is independent of time. Thus, vibrational emission band "basis functions" can be constructed (the emission frequencies are well-known from spectroscopic studies of CO), and least squares algorithms can in principle be utilized to fit the relative contribution of each basis function to each spectrum and thereby to recover the intensity of emission from the various vibrational bands as a function of time.

However, this analysis has been stymied by an optical opacity effect in the $v = 1 \rightarrow 0$ emission band. That is, although the rotational distribution of the $v = 1$ vibrational level can be assumed to be described by the same Boltzmann distribution as the higher vibrational levels, the frequency dependence of the emission from this band *as seen at the detector* cannot be easily predicted due to strong self-absorption of the emission by ground vibrational state molecules, which are present at much higher concentration than all excited vibrational levels. The inability to construct a "basis function" for this $v = 1 \rightarrow 0$ emission band prohibits the use of least squares fitting to determine the time-dependence of the emission intensity *as well as that of every vibrational band that overlaps substantially with it*. Thus, prior to this work, only a limited analysis of this data has been possible.

Here, a complete analysis of the CO atmospheric simulation data is reported using the HLPA technique. The optically thick $v = 1 \rightarrow 0$ emission band is considered to be a pattern that is repeated in over 100 time-resolved spectra. As a first step in the HLPA technique, the XCC pattern recognition technique is used to determine the time-dependent intensity of the $v = 1 \rightarrow 0$ emission with no knowledge of its band profile. The HLPA technique also permits a statistically rigorous determination of the time dependences of the remaining (*a priori* known) emission bands, as well as the band profile of the optically thick $v = 1 \rightarrow 0$ emission.

3.2 The HLPA Technique

In the case of the CO atmospheric simulation experiments that are analyzed in Section 3.3, the information to be extracted from the data is kinetic in nature: How do the emission intensities of various vibrational emission bands change with time? To illustrate how pattern recognition (in particular, XCC) and the HLPA technique can assist in this analysis, a simulated data set is defined in Fig. 3-1 that mimics several key properties of the real experimental data. Each synthetic spectrum is a linear superposition of the two "emission bands" in the top left panel of Fig. 3-1. That is, if the spectra are designated by numbers and the individual emission bands by letters, then

$$\begin{aligned} I_1(\omega) &= a_1 I_a(\omega) + b_1 I_b(\omega) \\ I_2(\omega) &= a_2 I_a(\omega) + b_2 I_b(\omega) \\ I_3(\omega) &= a_3 I_a(\omega) + b_3 I_b(\omega) \ , \end{aligned} \tag{3.1}$$

in which ω represents frequency (spectral element) and the coefficients $\{a\}$ and $\{b\}$ represent the relative amplitudes of the emission bands in each spectrum. Gaussian random noise has been superimposed upon each of the spectra such that the signal-to-noise is approximately 100. In addition, in spectrum 1, the intensity of one of the spectral elements (number 75) has been increased by 50%. The purpose of this deliberate corruption of the data is to illustrate the way in which the XCC and HLPA methods deal with deviations from Eq. 3.1 that are neither small nor random; the ability of these techniques to identify patterns even in the presence of such "corruptions" of the data is critical to the successful analysis of the CO data set in Section 3.3.

The simulated spectra can thus be considered to represent three time-resolved emission spectra, and the goal of the analysis is to determine the time dependence of the two emission bands, as represented by the coefficients $\{a\}$ and $\{b\}$. Note that that the intensity vs. frequency profiles of the bands are assumed not change as a

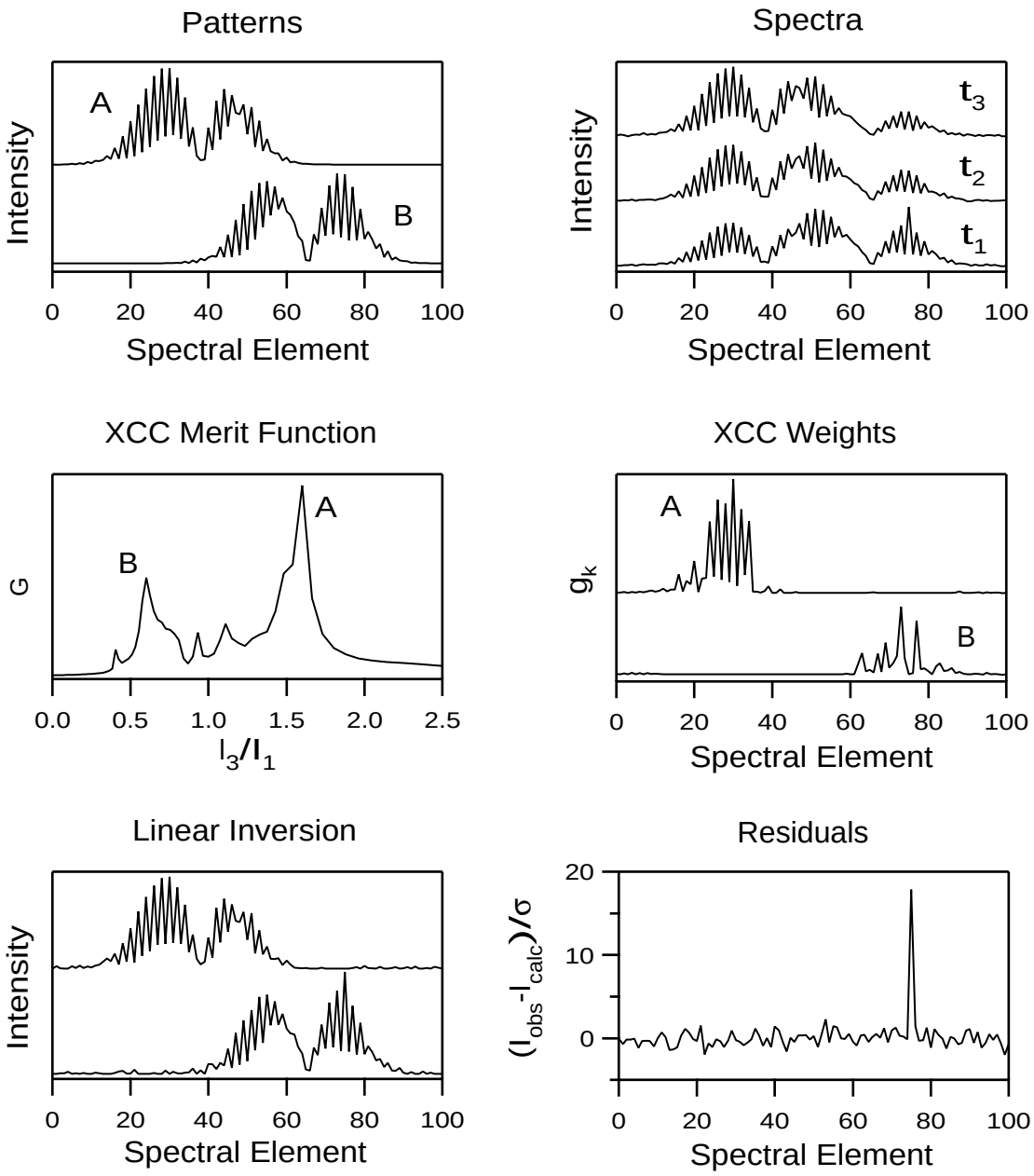

Figure 3-1: Top row: The simulated spectra (right) are each linear superpositions of the two patterns (left), plus noise. Middle left: The XCC merit function G for spectra 1 and 3, as a function of the ratio direction I_3/I_1. Middle right: Weight functions, g_i, computed at the two largest maxima in the XCC and plotted as a function of spectral element. Bottom left: Results of the inversion of the patterns (vibrational emission bands) from the spectra utilizing the coefficients determined by XCC. Bottom right: Weighted residuals of the inversion procedure for spectrum 1.

function of time; a similar assumption will be made in the analysis of the CO data set in Section 3.3. If the intensity profiles of the emission bands were known *a priori*, then the task of obtaining the coefficients would be straightforward using standard linear least squares fitting routines. When at least one of the two emission bands A and B is unknown, then techniques of pattern recognition must be employed. The case in which both patterns are unknown will be considered first; the XCC can be used to determine the coefficients $\{a\}$ and $\{b\}$, as well as the frequency dependence of the emission bands $(I_a(\omega), I_b(\omega))$, if so desired.

From the standpoint of the XCC, the emission bands constitute patterns that are repeated in three different spectra. As described in Chapter 2, the XCC is a model-free pattern recognition technique, and in principle no prior knowledge is necessary of either the form or the number of patterns that are present in the data. However, there is one important condition for the success of the XCC: some portion of the features in each pattern must not be overlapped with any other pattern. In the case of the synthetic data in Fig. 3-1, note that although the two patterns overlap heavily in the central portions of each spectrum, the intensity in the "wings" of the spectrum arises almost entirely from one of the two patterns. For example, consider spectral elements 0 through 30. To a good approximation, the intensity in each of the spectra over this range arises solely from vibrational band A:

$$I_k(\omega) \approx a_k I_a(\omega); (k = 1, 2, 3). \tag{3.2}$$

Conversely, for spectral elements 70-100,

$$I_k(\omega) \approx b_k I_b(\omega); (k = 1, 2, 3). \tag{3.3}$$

Thus, one could imagine determining the $\{a\}$ and $\{b\}$ coefficients by simply integrating the intensities of the spectra over these spectral ranges. However, the patterns are assumed to be unknown *a priori*, which makes it difficult to judge, in the absence of a numerical tool, precisely which regions of the spectra contain contributions from just one pattern (the real experimental data analyzed in the next section are even

more challenging).

The XCC can be used to identify, in a numerically rigorous and automated way, those regions of spectra that can be accounted for by just one pattern. The middle left panel of Fig. 3-1 depicts the use of the XCC merit function G to identify the patterns that are present in spectra 1 and 3 of the synthetic data set. Since only two spectra are used for this illustration, the search for patterns occurs in a one-dimensional space that represents the relative amplitude of each pattern in the two spectra (the ratio I_3/I_1 has been chosen, arbitrarily, to represent the "ratio direction"; see Chapter 2). Two pronounced maxima can be observed in the merit function, which occur at $I_3/I_1 = 1.604$ and 0.604; these correspond to vibrational bands B and A respectively, and compare quite favorably with the values of 1.6 and 0.6 which were used to construct the synthetic spectra. As described in Section 2.3, the XCC can also be used to identify the patterns in all three of the spectra simultaneously; although the resultant contour plot of the XCC merit function is not depicted, the results are similarly excellent, with the relative pattern amplitudes (ratio directions) again determined by XCC to within 1% of the correct values.

The XCC weights functions g_k (Eq. 2.7) make it easy to identify those portions of the spectra which represent fragments of the patterns that are uncorrupted by overlap with other patterns. In the middle right panel of Fig. 3-1 are plotted the weight functions at the ratio directions corresponding to the two largest maxima in the merit function G. Note that neither set of weight functions includes any substantial amplitude over the central spectral elements (40-60) in which the two patterns overlap substantially. Note also that spectral element number 75, which was deliberately corrupted in spectrum 1, has a weight of nearly zero in both traces; the XCC has automatically excluded this point from its determination of the time-dependence of the pattern amplitudes. This insensitivity of the XCC to nonidealities in the data and its ability to identify multiple patterns simultaneously are consequences of its definition as a redescending *robust* estimator [2].

At this point the XCC has been successfully used to determine the time dependence of the emission from the two different vibrational bands with no knowledge of

what the vibrational bands look like. The linear inversion method, described in Section 2.2, can now be used to extract the patterns from the spectra. That is, since the coefficients $\{a\}$ and $\{b\}$ are now known from the application of the XCC, the set of equations labelled as Eq. 3.1 above is overdetermined. At any given value of ω, there exist three equations with only two unknowns ($I_a(\omega)$ and $I_b(\omega)$), and the spectra can be inverted (in a least squares sense) to determine the patterns, one spectral element at a time.

The bottom panels of Fig. 3-1 depict the result of this inversion process. The emission band patterns (bottom left) that are inverted from the spectra are nearly identical to the patterns that were used to construct the synthetic spectra originally. One notable discrepancy is observable at spectral element number 75; the intensity of this spectral element in the reconstructed emission band B differs significantly from its true value. This discrepancy is due, of course, to the deliberate corruption of spectrum 1 at spectral element 75. It was noted previously that the XCC is *insensitive* to this corruption of the data in its determination of the ratio directions (time dependence of the emission bands). It may seem paradoxical that the inversion from spectra to patterns is sensitive to the corruption of the data, but it should be kept in mind that the inversion is mathematically equivalent to a linear least squares fit, which implicitly assumes that any deviations from the model conform to a Gaussian distribution; clearly this is not true for spectral element 75. However, the results of the inversion themselves indicate that spectral element 75 should be treated with suspicion. In the bottom right panel of Fig. 3-1 are plotted the residuals of the inversion for spectrum 1. The residuals are mostly comparable to the noise level in the spectra, except at spectral element 75, indicating that the model (Eq. 3.1) cannot accurately represent the data at this spectral element.

Thus, the pattern recognition approach to the synthetic "time-resolved emission spectra" proceeds by first identifying the number of patterns (vibrational bands) present in the data set along with their time-dependent amplitudes, and then using this time-dependence to extract, if desired, the frequency dependence of the bands (i.e., their shape). This pattern recognition approach is conceptually distinct from

the least squares fitting techniques that are commonly applied to this type of data set. In the standard least squares approach, the intensity profiles of the emission bands A and B must be calculable from a model, and these "basis functions" are fit to each individual spectrum in order to determine the time-dependent emission intensities of the vibrational bands.

A hybrid between the least squares and pattern recognition approaches is possible if a situation arises in which *some*, but not all, of the patterns that are represented in a data set are known *a priori*. It has already been suggested in the introduction to this chapter that such is the case with the CO atmospheric simulation data. Such a hybrid approach would also be applicable to the synthetic example considered in this section if, for example, the frequency dependence of vibrational band A could be predicted *a priori* but that of vibrational band B could not. To motivate the HLPA technique, the emission intensity in the synthetic spectra is expressed as a function of both frequency (spectral element) and time (t):

$$I(\omega, t) = a(t)I_a(\omega) + b(t)I_b(\omega) \tag{3.4}$$

in which a and b refer to the two emission bands as before. Experimentally, the frequency- and time-dependences of the emission are sampled only at discrete intervals. In the case of the synthetic data, there are 3 time intervals, and 101 spectral elements (frequency intervals). Thus, 303 equations of the form

$$I(\omega_j, t_k) = a(t_k)I_a(\omega_j) + b(t_k)I_b(\omega_j) \tag{3.5}$$

are necessary and sufficient to describe the data set. Of the parameters in this set of equations, $b(t_1)$, $b(t_2)$, and $b(t_3)$ can be determined from the application of the XCC, and the full set of $\{I_a(\omega_j)\}$ are assumed to be known *a priori*. The parameters to be determined are $a(t_1)$, $a(t_2)$, and $a(t_3)$, and the set of $\{I_b(\omega_j)\}$: a total of 104 parameters. Thus, the system of equations represented by Eq. 3.5 is overdetermined, and standard least squares algorithms can be used to determine the 104 parameters of interest from the set of 303 equations. This somewhat unconventional application

of linear least squares is referred to as Hybrid Linear Pattern Analysis.

The time-dependent amplitude of vibrational band A is determined by the HLPA approach to be $a(t_1) = 0.992$, $a(t_2) = 1.303$, and $a(t_3) = 1.593$, in close agreement with the values of 1.0, 1.3, and 1.6, respectively, which were used to construct the synthetic spectra. The remaining 101 parameters determined from the fit represent the frequency dependence of vibrational band B, and are not depicted since they are nearly identical to the parameters determined from the purely pattern recognition approach.

3.3 HLPA Analysis of CO Atmospheric Simulation Experiments

Evidence for very high rotational excitation, with over 2 eV of energy in rotation alone, has been observed in infrared spectra of the diatomic molecules NO [63] and OH [64] in the atmosphere. In order to model the rotationally excited populations of such species in the atmosphere, it is necessary to measure the formation and loss rates for the relevant molecular states, and thus it is necessary to produce measurable populations in the laboratory. The experiments on CO considered here represent one approach to the study of these rotationally excited species. CO itself is an important infrared-active species in the upper atmosphere, and significant effects on the infrared spectra of atmospheric CO due to optical opacity, isotopic concentrations, and the temperature structure of the atmosphere have been observed [65, 66].

The experimental apparatus for the CO atmospheric emission simulation experiments (the LABCEDE facility at the Air Force Research Laboratory at Hanscom AFB) has been described previously [61, 62]. In the data to be analyzed here, a 4.0 kV, 10.0 ms electron beam is pulsed through a sample of CO at 10.0 mTorr in the cryogenic chamber. A Michelson interferometer is utilized to obtain time-resolved, infrared emission spectra at 0.25 ms intervals, both during the electron beam excitation pulse, and for ∼50.0 ms after the electron beam pulse is terminated. Two of these spectra are depicted in Fig. 3-2. The time-resolved emission spectra consist

of overlapping $\Delta v = 1$ emission bands from at least 12 excited vibrational states ($v' = 1 - 12$) of the ground electronic state ($X^1\Sigma^+$) of CO. At the $\sim$2.5 cm^{-1} resolution of the spectra, the individual emission bands are not well resolved in the data.

Above 2200 cm^{-1}, several prominent band heads are evident in the emission spectra. The band heads in CO are known to occur at $J \approx 90$ in the R-branch, and thus the rotational distribution of the CO resulting from processes initiated by the electron beam includes very high-J states. On the other hand, the majority of the emission below 2200 cm^{-1} can be accounted for by low-J ($J < 15$) emission. Thus, the rotational distribution of the CO is believed to be bimodal. This behavior is consistent with the expectation that the rates of rotational relaxation of the high- and low-J levels are quite different. For the low-J levels, rotational equilibration occurs quickly (μs) with respect to the timescale of the experiment (ms), and thus the low-J rotational distribution is expected to conform to a Boltzmann distribution. Further, this distribution is, to a good approximation, invariant over the course of the experiment, since only a small fraction of the CO molecules are excited by the electron beam, while the "bath" of molecules that are not excited are rotationally equilibrated to the temperature of the walls of the cryogenic chamber. An effective rotational temperature of 90 K can be empirically determined to reproduce optimally the observed low-J emission (other than the $v = 1 \rightarrow 0$ emission; see below). The high-J molecules experience rotational relaxation at a slower rate than lower-J molecules because the level spacings at high-J are comparable with vibrational spacings. Thus, a small fraction of the excited state population can become "trapped" in the high-J states, although the exact rotational distribution (and its time-dependence) are difficult to predict.

On the other hand, the five "band heads" observed in the data above 2200 cm^{-1} do not overlap each other substantially, and can easily be integrated to determine their time-dependent amplitudes. The band heads are not explicitly analyzed in the analysis presented here, except insofar as they overlap with the low-J bands. A more serious obstacle to the analysis is an optical opacity effect that is associated with the $v = 1 \rightarrow 0$ low-J emission band. Although the $v = 1$ molecules are expected to

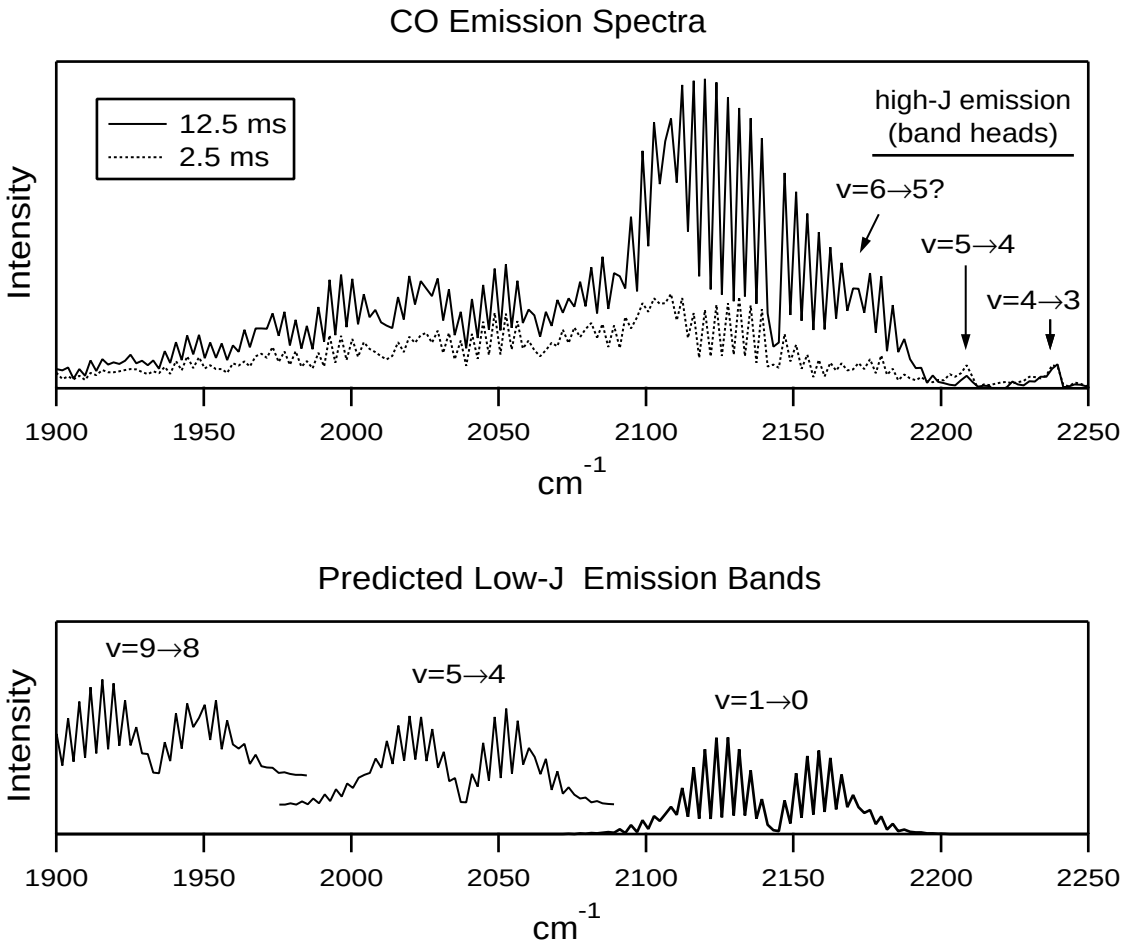

Figure 3-2: Top: Two examples of time-resolved emission spectra shown over a limited frequency range. Three additional band heads can be observed in the complete spectra at higher frequencies than are depicted here ($v = 3 \rightarrow 2$, $v = 2 \rightarrow 1$, $v = 1 \rightarrow 0$). Bottom: Three predicted low-J vibrational emission bands, assuming an effective rotational temperature of 90 K. The predicted emission bands from $v = 2$ and higher are expected to represent the data accurately, but the predicted $v = 1 \rightarrow 0$ emission band does not take into account the effects of optical opacity.

have an effective low-J rotational temperature that is identical to that of the $v \geq 2$ molecules, the large relative concentration of $v = 0$ molecules leads to an optical opacity in the $v = 1 \rightarrow 0$ emission band *as seen at the detector*. This optical opacity is extremely difficult to model under the measurement conditions because, while the density of molecules in the ground vibrational state is essentially uniform throughout the chamber, the spatial distribution of excited state molecules is highly nonuniform and forms an irregular cloud of varying density along the one meter path of the electron beam. This path in turn obliquely intercepts the conical viewing region.

The optical opacity in the $v = 1 \rightarrow 0$ emission is clearly evident in Fig. 3-2. The majority of the emission observed in the time-resolved spectra between 2130 and 2190 cm^{-1} is due to the $v = 1 \rightarrow 0$ emission, but the observed band shape does not even approximately match the band shape predicted by a Boltzmann-distribution assumption, neglecting self-absorption. The inability to predict the frequency dependence of the $v = 1 \rightarrow 0$ emission band implies that the time dependence of this emission cannot be determined in a simple fashion by least squares fitting. In addition, the $v = 1 \rightarrow 0$ emission overlaps substantially with several other emission bands, particularly the $v = 2 \rightarrow 1$, $v = 3 \rightarrow 2$, and $v = 4 \rightarrow 3$ emission bands. For this reason, the time dependence of the emission from these bands is not easily determined using standard least squares techniques, despite the fact that their band profiles are known.

The HLPA technique that was outlined in Section 3.2 provides an alternative data analysis approach, in which the $v = 1 \rightarrow 0$ emission band can be treated as a pattern to be identified by XCC. The remaining low-J vibrational emission bands, however, need not be treated by pattern recognition, since their shapes have been accurately determined by synthetic spectral fitting. Thus, the HLPA technique permits the utilization of the known band shapes, together with the time-dependence of the $v = 1 \rightarrow 0$ band determined by pattern recognition, to determine simultaneously the remaining parameters of interest: the frequency-dependence of the $v = 1 \rightarrow 0$ band, and the time-dependences of the remaining low-J bands.

It should be noted that the pattern recognition approach to the CO data set implicitly assumes that the band shape of the optically thick $v = 1 \rightarrow 0$ emission

does not change as a function of time. The exact band shape is governed by the relative populations of the $v = 1$ and $v = 0$ states, the oscillator strengths of the various $v = 1 \rightarrow 0$ rotational transitions, collisional deactivation rates, transport of molecules out of the field of view, the rotational distribution of the $v = 1$ molecules, and geometrical considerations. Of these parameters, only the population of the $v = 1$ excited state is expected to change with time (as with the other excited vibrational states, the low-J rotational distribution of the $v = 1$ molecules is expected to conform to a time-independent Boltzmann distribution). However, the population of the $v = 1$ excited state remains a small fraction of that of the ground vibrational state, and thus all changes in the band shape are expected to be minor. The results of the HLPA analysis presented below support this argument.

The first step in the HLPA analysis of the CO data set is the pattern recognition determination of the time-dependent amplitude of the optically thick $v = 1 \rightarrow 0$ band. As explained in Section 3.2, the XCC identifies patterns within a data set by searching for fragments of the patterns that are repeated uncorrupted (by overlap with other patterns) in each of the spectra. As is clear in Fig. 3-2, the optically thick $v = 1 \rightarrow 0$ emission band overlaps heavily with other emission bands. At frequencies above $\sim$2165 cm^{-1}, the $v = 1 \rightarrow 0$ emission band should be *relatively* free from overlap, although it almost certainly overlaps with the $v = 5 \rightarrow 4$ band head above 2190 cm^{-1}. In addition, the existence of a $v = 6 \rightarrow 5$ band head around 2180 cm^{-1}, obscured by the much stronger $v = 1 \rightarrow 0$ band, cannot be ruled out. Finally, it is difficult to determine the exact frequency at which the optically thick band can be assumed to be free from overlap with the $v = 2 \rightarrow 1$ emission band.

The XCC can be used to determine the amplitude of the $v = 1 \rightarrow 0$ emission band in over 100 spectra, a result that will be discussed below. First, however, this application of the XCC is illustrated with just two spectra, in particular, the two spectra depicted in the top panel of Fig. 3-2, over the frequency range 2165–2215 cm^{-1} (also depicted in the upper left panel of Fig. 3-3). Two maxima are observed in the XCC merit function (upper right panel of Fig. 3-3), indicating the presence of two "patterns", and in the lower left panel of Fig. 3-3, the weight functions

corresponding to each of these maxima are plotted as a function of frequency. As explained in Section 3.2, the weight functions indicate those portions of patterns that are repeated, uncorrupted by overlap with other patterns, in each of the spectra. Thus, on the basis of these weight functions, the two maxima observed in the merit function are clearly assignable as the $v = 1 \rightarrow 0$ optically thick emission and the $v = 5 \rightarrow 4$ band head emission. The $v = 2 \rightarrow 1$ emission band is not identified as a distinct pattern, because no regions of the spectra exist within which this emission band is uncorrupted by overlap with other vibrational bands. Notice, however, that the weight functions for the $v = 1 \rightarrow 0$ optically thick pattern are very nearly zero at two resolution elements below 2170 cm^{-1}. This observation is consistent with the $v = 1 \rightarrow 0$ optically thick pattern overlapping with the "tail" of the $v = 2 \rightarrow 1$ emission band below this frequency.

In addition, the XCC weights provide evidence for the existence of a $v = 6 \rightarrow 5$ band head near 2180 cm^{-1}. Although the XCC weights for the optically thick pattern are not zero near 2180 cm^{-1}, they are substantially lower than the weights at higher and lower frequencies; this observation is consistent with a slight "corruption" of the pattern by overlap with a weak band head. This evidence is augmented by the application of the linear inversion technique for pattern reconstruction (Section 3.2) to this frequency region. In this case, it is not expected that the two identified patterns will account for 100% of the intensity observed within the frequency interval chosen, but the linear inversion method can be applied naively to this region anyway, and the results are depicted in the bottom panel of Fig. 3-3. As expected, the "tail" of the $v = 5 \rightarrow 4$ band head is observed to extend to below 2190 cm^{-1}. Intriguingly, a small bump is also observed in this "reconstructed pattern" around 2180 cm^{-1}. Although it is possible that this bump might represent an unexpected feature in the $v = 5 \rightarrow 4$ band head, the bump occurs at the frequency at which the maximum of the $v = 6 \rightarrow 5$ band head is predicted to be located. Thus, a reasonable inference is that the $v = 6 \rightarrow 5$ band head is present, although the emission is weak, and that it has a time dependence that is approximately the same as that of the $v = 5 \rightarrow 4$ band head. As far as either the XCC or the linear inversion methods are concerned, patterns with

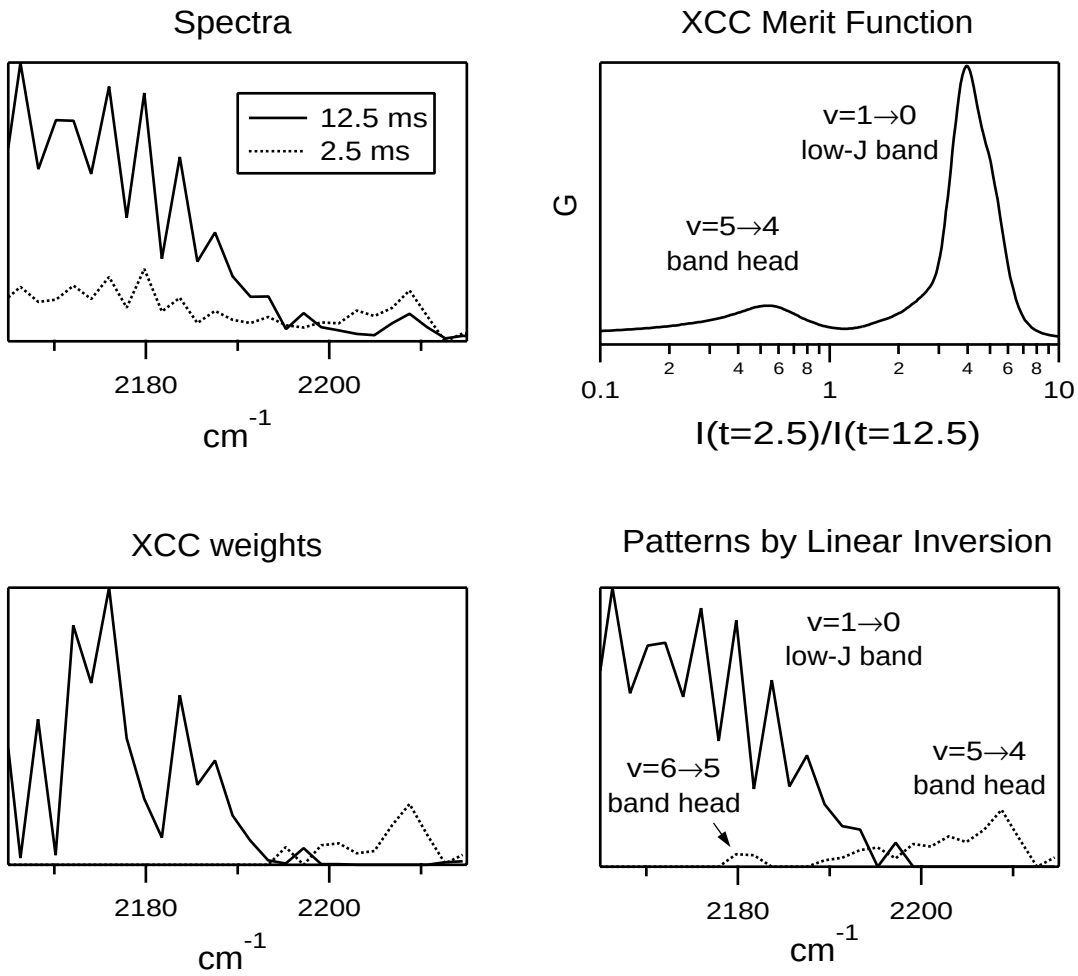

Figure 3-3: Upper left: Two of the time-resolved CO emission spectra over the frequency interval 2165–2215 cm^{-1}. Upper right: XCC merit function G as a function of ratio direction for these two spectra. The two maxima correspond to the $v = 5 \rightarrow 4$ band head emission, and the optically thick $v = 1 \rightarrow 0$ low-J emission. Lower left: XCC weight functions plotted as a function of frequency at ratio directions corresponding to the two maxima in the XCC merit function. Lower right: Results of the linear inversion method.

identical time-dependent amplitudes (ratio directions) are indistinguishable, and thus the $v = 6 \rightarrow 5$ and $v = 5 \rightarrow 4$ band heads may be lumped together into one pattern.

The ability of the XCC to isolate those portions of the emission spectra that are due only to optically thick $v = 1 \rightarrow 0$ pattern makes in possible to determine the time-dependent amplitude of this band. The top left panel of Fig. 3-4 depicts the time-dependence of the $v = 1 \rightarrow 0$ emission intensity that is determined by applying the XCC to 100 spectra simultaneously. Thus, by adopting a pattern recognition analysis of the data set, the time-dependence of the $v = 1 \rightarrow 0$ emission intensity has been determined without any knowledge of the band profile. At this point, it remains to determine the time-dependent amplitudes of the $v = 2 \rightarrow 1$, $v = 3 \rightarrow 2$, and $v = 4 \rightarrow 3$ emission bands, which also could not be determined by standard least squares techniques due to their overlap with the optically thick band.

The HLPA approach outlined in Section 3.2 provides a conceptually straightforward way to determine these time-dependences. Numerically, the HLPA technique relies on the fact that the data set can be described by a set of equations of the form in Eq. 3.5, except that in the present application, there are many more than two patterns. If all 100 of the spectra were included in the HLPA analysis, the total number of equations would be ∼20,000, with ∼1400 unknown parameters. Obviously, the problem is highly overdetermined, but in practice such a large fit is computationally tedious, and unnecessary. The time-resolved spectra change slowly from one time-interval to the next, and it is sufficient to choose a small subset of the data that evenly spans the time interval in which the kinetics of interest is played out. The calculations reported here utilize ten of the time-resolved spectra, which were chosen at 2.0 ms intervals, from 2.0 to 20.0 ms (after the electron beam is turned on). Figure 3-5 depicts one of these time-resolved spectra decomposed into its constituent patterns by HLPA.

The bottom left panel of Fig. 3-4 examines in greater detail the frequency dependence of the optically thick $v = 1 \rightarrow 0$ band determined by the HLPA method, by juxtaposing it with the band shape that is predicted by neglecting the effects of optical opacity. This comparison underscores the enormity of the optical opac-

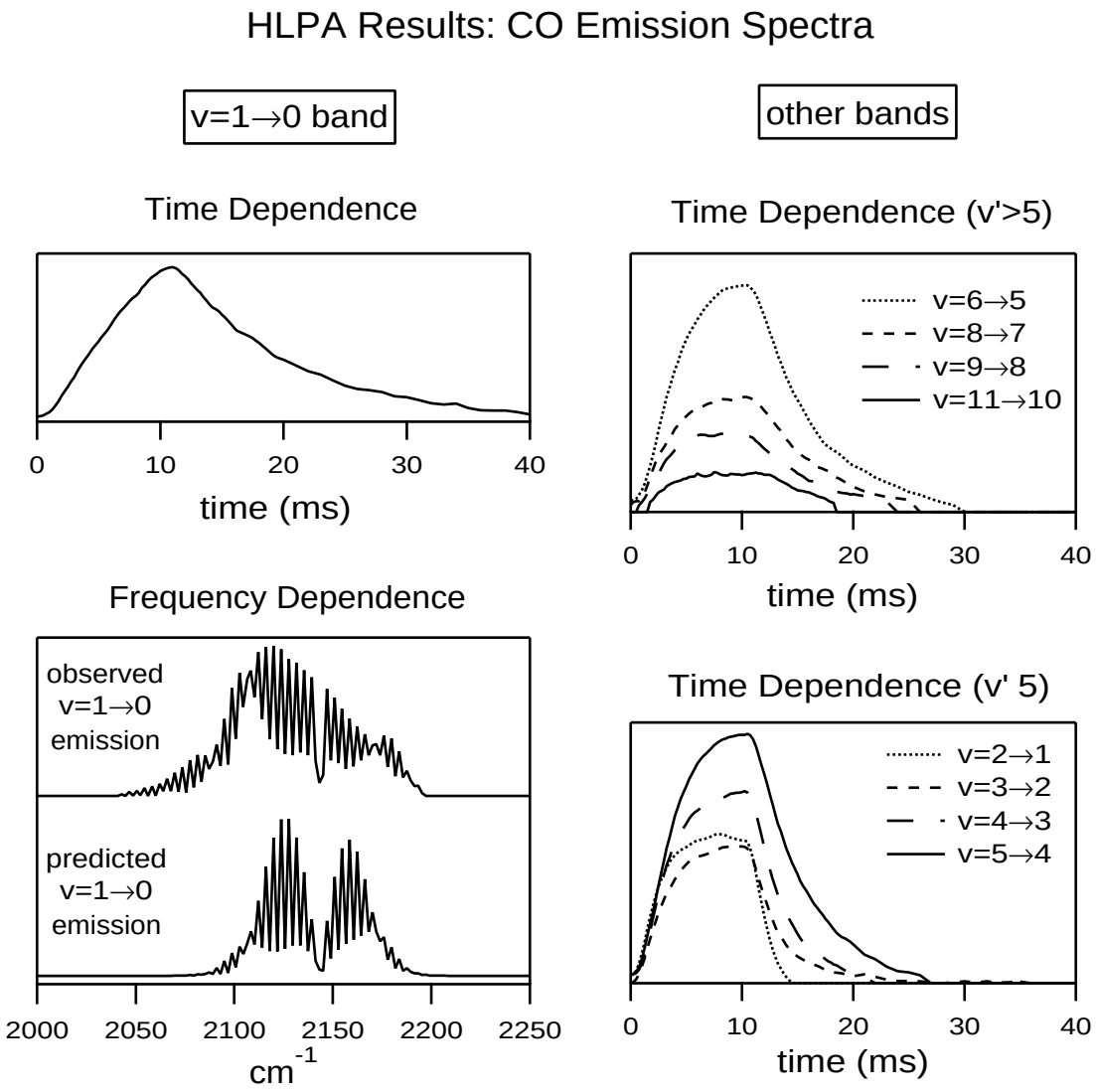

Figure 3-4: Left panels: Time (upper) and frequency (lower) dependences of the optically thick $v = 1 \rightarrow 0$ emission band. The band profile of the optically thick band, as determined by the HLPA technique, is compared with the band shape predicted by neglecting the effects of optical opacity. Right panels: Time dependence of the emission intensity from selected low-J vibrational bands as determined by the HLPA technique.

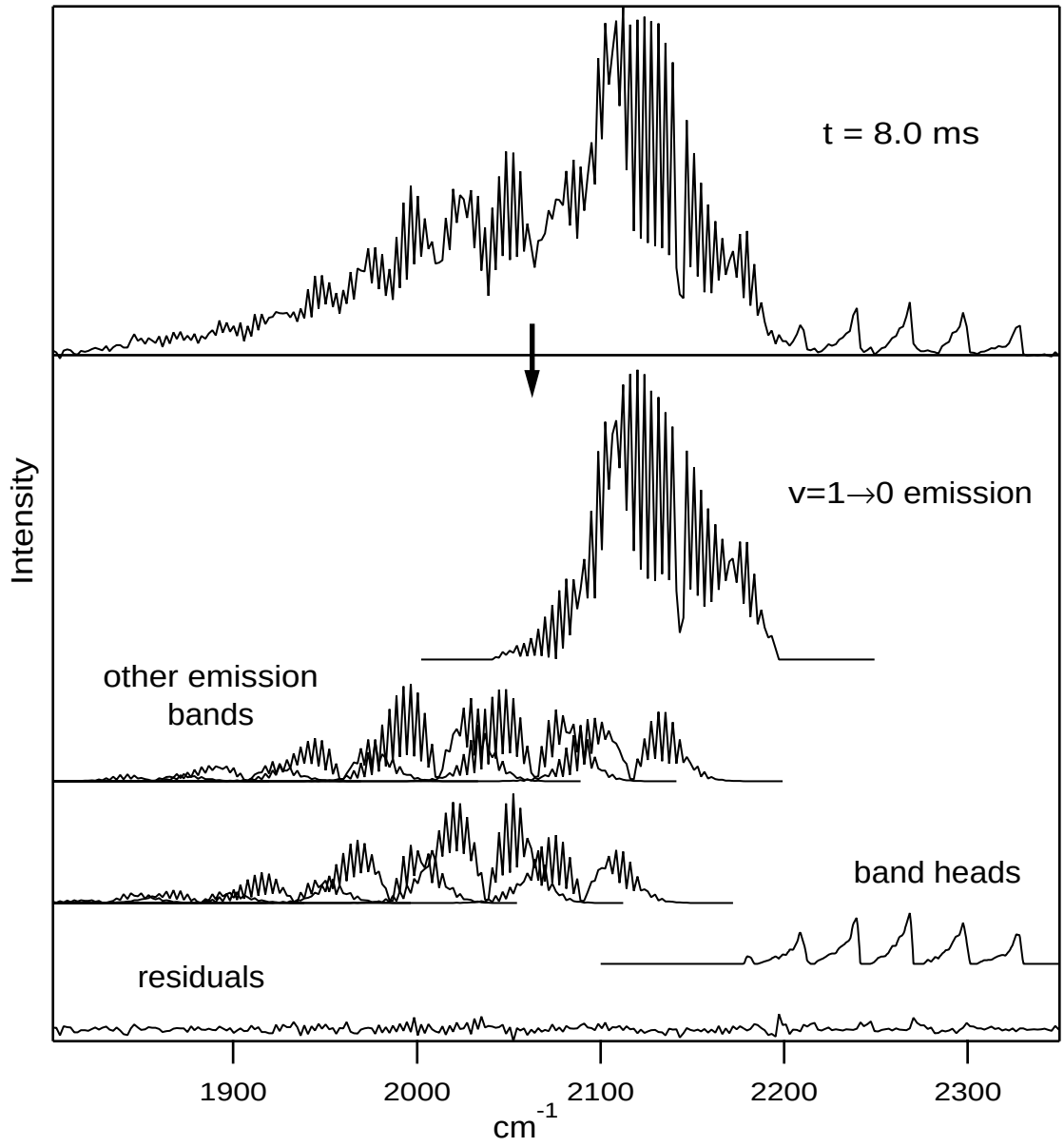

Figure 3-5: One of the time-resolved emission spectra of CO decomposed into its constituent patterns by HLPA.

ity, and may aid in the modeling of the self-absorption, transport, and deactivation effects that lead to the optical opacity. The right column of Fig. 3-4 depicts the time-dependent emission intensity from selected low-J vibrational bands, as determined by the HLPA technique. As mentioned previously, only ten time-intervals were included in the HLPA calculations, but the intensities of the various vibrational bands at all other times can be determined in a straightforward manner by least squares fitting (since the frequency dependence of the optically thick $v = 1 \rightarrow 0$ band has been determined). The smoothness of the curves in Fig. 3-4 constitutes evidence that the HLPA technique provided a physically reasonable solution. The kinetics of the system will be analyzed in a future publication by the Hanscom group.

Finally, in the left panel Fig. 3-6 are depicted the residuals of the HLPA calculation for three of the ten time-resolved spectra that were included in the analysis, along with a spectrum taken *before* the electron beam was turned on, for comparison. The residuals of the fit are similar in amplitude to the "background" spectrum at most time intervals. However, at early and late times, the residuals above 2075 cm^{-1} are significantly larger than the background noise. Intriguingly, the structure in the residuals appears to invert from 4.0 ms to 20.0 ms, and the two prominent "lobes" in this structure line up in frequency with the P- and R-branches of the $v = 1$ low-J emission band, which likely implies that the optically thick $v = 1 \rightarrow 0$ band profile changes slightly with time. It should be emphasized that the structures observed in the residuals are small relative to the integrated intensity of the $v = 1 \rightarrow 0$ band, and the corresponding changes in the shape of the optically thick band are subtle. The right panel of Fig. 3-6 depicts the change in band shape of the $v = 1 \rightarrow 0$ emission between 4.0 ms and 20.0 ms, assuming that the structure in the residuals is due entirely to the breakdown of the assumption of constant band shape. That is, the band shapes that are depicted in the right panel of Fig. 3-6 were generated by adding the residuals (above 2075 cm^{-1}) to the $v = 1 \rightarrow 0$ band shape that was determined by the HLPA technique (in Fig. 3-4). The difference in band shape between 4.0 ms and 20.0 ms is subtle but noticeable; the band shapes at intermediate times vary smoothly between these extremes.

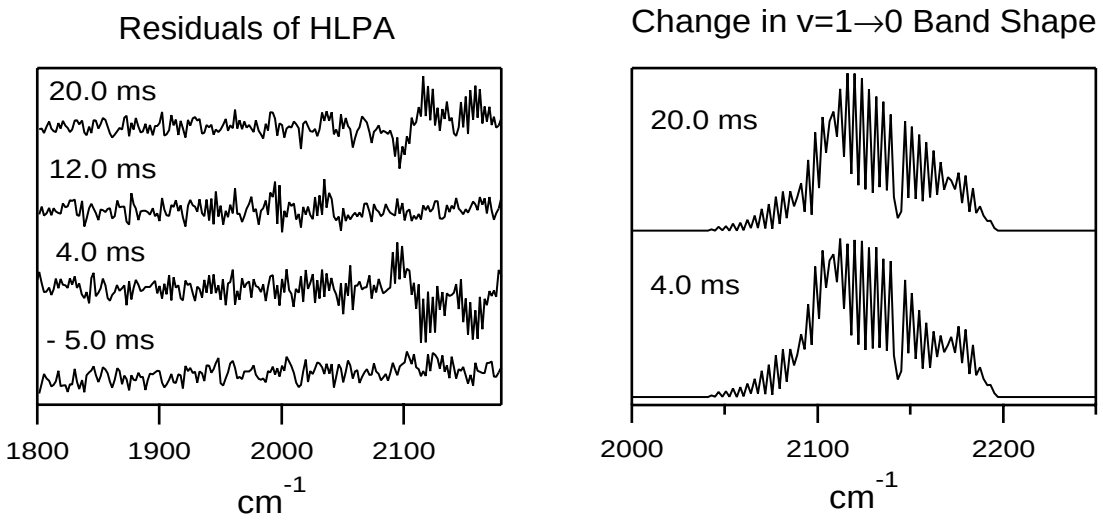

Figure 3-6: Left panel: Residuals (observed minus calculated) of the HLPA calculation for three of the ten time-resolved spectra included in the fit. The bottom trace, for comparison, is a spectrum taken 5.0 ms before the electron beam is turned on, which provides a measure of the experimental noise. Right panel: The change in the shape of the optically thick $v = 1 \rightarrow 0$ band as a function of time, assuming that the structure in the residuals is due entirely to the breakdown of the assumption of constant band shape. That is, the band shapes depicted here were generated by adding the residuals (above 2075 cm^{-1}) to the $v = 1 \rightarrow 0$ band shape that was determined by the HLPA technique (lower left panel in Fig. 3-4).

3.4 Conclusion

Numerical pattern recognition algorithms (and in particular the Hybrid Linear Pattern Analysis (HLPA) technique that is introduced here) have played a critical role in the successful analysis of CO atmospheric emission simulation experiments. Similar techniques may also be useful for analyzing "field data", such as the infrared emission spectra of the Earth's atmosphere that were recently obtained from the CIRRIS 1A instrument aboard the Space Shuttle [65]. Analysis of such data is complex, due to the large number of emitting species, each of which may have substantial populations in highly excited rovibrational states. Spectroscopic pattern recognition techniques such as the Extended Cross Correlation (XCC) and HLPA may be valuable in extracting from such data sets the relative contributions from individual chemical species, as in Chapter 2, and the various vibrational bands belonging to a single species, as done here. Other potential applications of these techniques include spectra that are obtained for purposes of surveillance or in atmospheric remote sensing experiments. The spectra that are obtained in both cases frequently contain features which result from unknown species, as well as optical opacity effects. As a result, such spectra often cannot be analyzed with standard least-squares techniques, and the ability of the XCC and HLPA to identify and extract unknown patterns may prove useful in these cases [67].

Acknowledgements

This research has been supported by AFOSR under Grant No. F49620-97-1-0040 and LRIR 92VSO4COR. My work on this project was supported by the Department of the Army under a National Defense Science and Engineering Graduate Fellowship, and by the Fannie and John Hertz Foundation.

Chapter 4

Robust Baseline Estimation

The work in this chapter has not been published and should be considered a work in progress. However, the technique introduced here, Robust Baseline Estimation, has already been used by a number of scientists, and for this reason I wish to document the technique as it currently stands. This chapter represents the starting point for a collaboration with Dr. Andreas Ruckstuhl (Australian National University), concerning applications of robust estimation to spectroscopic problems, but this collaboration is still in a nascent stage.

4.1 Motivation for RBE

The Robust Baseline Estimation (RBE) technique that is presented in this chapter is not, strictly speaking, a pattern recognition technique. RBE is a technique for baseline removal; that is, in spectra that consist of sharp features superimposed upon a continuous, slowly varying baseline, it is designed to permit the separation of the two components, spectrum and baseline. There exist, of course, numerous techniques for baseline removal from spectra, because the problem is ubiquitous within spectroscopy. In many cases, baselines are simply removed "by eye". There is nothing inherently wrong with this approach, but I believe that, even for a "mundane" task such as baseline removal, it is beneficial to use numerical tools which minimize the need for judgement calls and permit reproduction of the results by others. Among the most common numerical techniques for baseline removal are those based upon digital filtering; a "high pass" filter can be successful in suppressing a relatively slowly varying baseline, although often at a cost of distorting the remaining "sharp" components of the spectrum. Many other numerical techniques have been used for baseline subtraction, too numerous to mention here.

The technique presented here for baseline removal, RBE, is based upon principles of robust estimation, as the acronym suggests. These principles of robust estimation also underlie the Extended Cross Correlation (XCC) technique that was discussed in Chapters 2 and 3, and in fact, the RBE technique was inspired by the XCC; it is for this reason that the RBE technique is presented here. No specific claims are made

that the RBE technique is better or faster or more accurate than other techniques for baseline removal, but the RBE does appear to be an attractive alternative to other techniques with which I am familiar, particularly when accurate baseline removal is critical to the interpretation of spectroscopic results. Among the attributes of the RBE technique are that it

1. uses techniques of robust estimation to provide, insofar as possible, an unbiased estimate of the baseline;

2. takes into account the measurement error in the data in a natural way;

3. can be applied to a wide variety of baseline subtraction problems; and

4. requires minimal human intervention.

In Section 4.2, the RBE technique is introduced and its properties established using synthetic spectra; in Section 4.3, RBE is applied to real experimental data.

4.2 The RBE Technique

It is important to realize from the outset that the question "what is the baseline in my spectrum" is, in the absence of further information, an ill-defined question—in general, there exist an infinity of possible models for the baseline that are consistent with the data. A more well-defined question is, given a model for the baseline function, what is the probability that the observed spectroscopic data could have occurred? However, the presence of peaks superimposed upon the baseline makes answering even this question difficult. In essence, only *some* of the data is useful for determining the baseline function; data points on top of peaks are generally useless for determining the baseline.[1] If it is possible to estimate the baseline function at all, then the baseline must be assumed, at the very least, to be smooth and to vary slowly. In this way,

[1] A possible exception would occur if the line shapes and, perhaps, relative intensities of the peaks were known *a priori*. In this chapter, I will make no assumptions about the peaks observed in the spectra, other than that they must be sufficiently narrow that the baseline changes minimally across the width of the peak

the baseline can be safely interpolated across the width of a peak. The baseline also cannot in general be estimated if the peaks which are superimposed upon the baseline are so congested that there are few regions in the spectrum that represent the contribution of *only* the baseline.

Given these caveats, I believe that techniques of robust estimation may be quite useful for estimating the baselines present in spectra in a great many cases. Robust estimation is something of a catch-all term which, in the simplest sense, refers to techniques of estimation that are less sensitive to outliers than the conventional least-squares approach. From the standpoint of estimating the baseline in a spectrum, the points in the spectrum that lie on top of peaks can be considered outliers, and thus one can imagine using a robust estimator to determine a baseline function by more-or-less ignoring those points that lie on peaks.

There are several nontrivial issues which face implementation of this simple idea. The first is to choose a functional form for the baseline to fit to the spectrum. In practice, this is generally not an insurmountable problem; it is usually possible to determine a fairly good functional form, such as a low order polynomial, by inspecting the data, and the results of using several functional forms can be compared. In the case of an irregularly oscillating baseline, the baseline can usually be estimated *locally* by a low order polynomial; see Section 4.3. A more difficult problem is, having chosen a functional form for the baseline estimation, the choice of initial parameters for the fit. Robust estimators in general have multiple local minima as a function of the model parameters; the global minimum is the solution that is desired. Sophisticated minimization techniques such as simulated annealing [44] can generally be counted on to determine the global minimum of a hypersurface in finite time, although they are not guaranteed to do so and are computationally intensive. Thus, a more productive strategy might be to attempt to obtain initial estimates for the model parameters for the baseline that are as close as possible to the global minimum; standard optimization routines can then be used to determine precisely the global minimum.

To illustrate how such a strategy can be achieved, two synthetic spectra are analyzed in Figs. 4-1 and 4-2. Figure 4-1 is the simpler of the two examples. A synthetic

spectrum, shown in gray, is superimposed upon a broad baseline generated by a third order polynomial. The solid black line is the baseline determined by robust estimation. The robust estimator used to determine the baseline was

$$\Gamma = \sum_i \rho(\delta_i) = \sum_i [1 - \exp(-\delta_i^2/2)] \tag{4.1}$$

where

$$\delta = \frac{I_{\text{obs}} - I_{\text{calc}}}{\sigma}; \tag{4.2}$$

σ is the estimated measurement error, and thus δ is a unitless, noise-weighted deviation from the model. The figure-of-merit function is thus chosen to be a sum of Gaussian functions of δ; note the resemblance to the XCC merit function (Eq. 2.7). The Gaussian function is "inverted", by subtracting it from one, in order to make the estimator compatible with most optimization routines, which are designed to *minimize* functions; the inversion of the Gaussian is otherwise irrelevant to the performance of the estimator. This merit function can be classified as a *redescending* robust estimator. The hallmark of a redescending robust estimator is that measurements far from the model prediction are weighted minimally (in this case the peaks in the spectrum), while those close to the model prediction are weighted strongly (hopefully, the baseline points). For a more thorough discussion of robust estimators and their application to spectroscopic problems, see Refs. [1], [2], and [3].

In the case of the synthetic data in Fig. 4-1, the baseline can be fit to a third-order polynomial, by construction. The starting values of the baseline parameters for the robust fit were those determined by a least-squares fit to the baseline, shown as a dotted line in Fig. 4-1. The least-squares fit, of course, does a poor job of reproducing the baseline, because of the sensitivity of least-squares to outliers (peaks). However, the least-squares result does appear to be adequate in this case as starting parameters for the fit, and the final solution is quite satisfactory.

Figure 4-2 provides an example of when this simple procedure (using the least-squares fit as starting parameters for a robust fit) fails. The spectrum in Fig. 4-2 is an extremely congested synthetic spectrum, superimposed upon a third-order polynomial

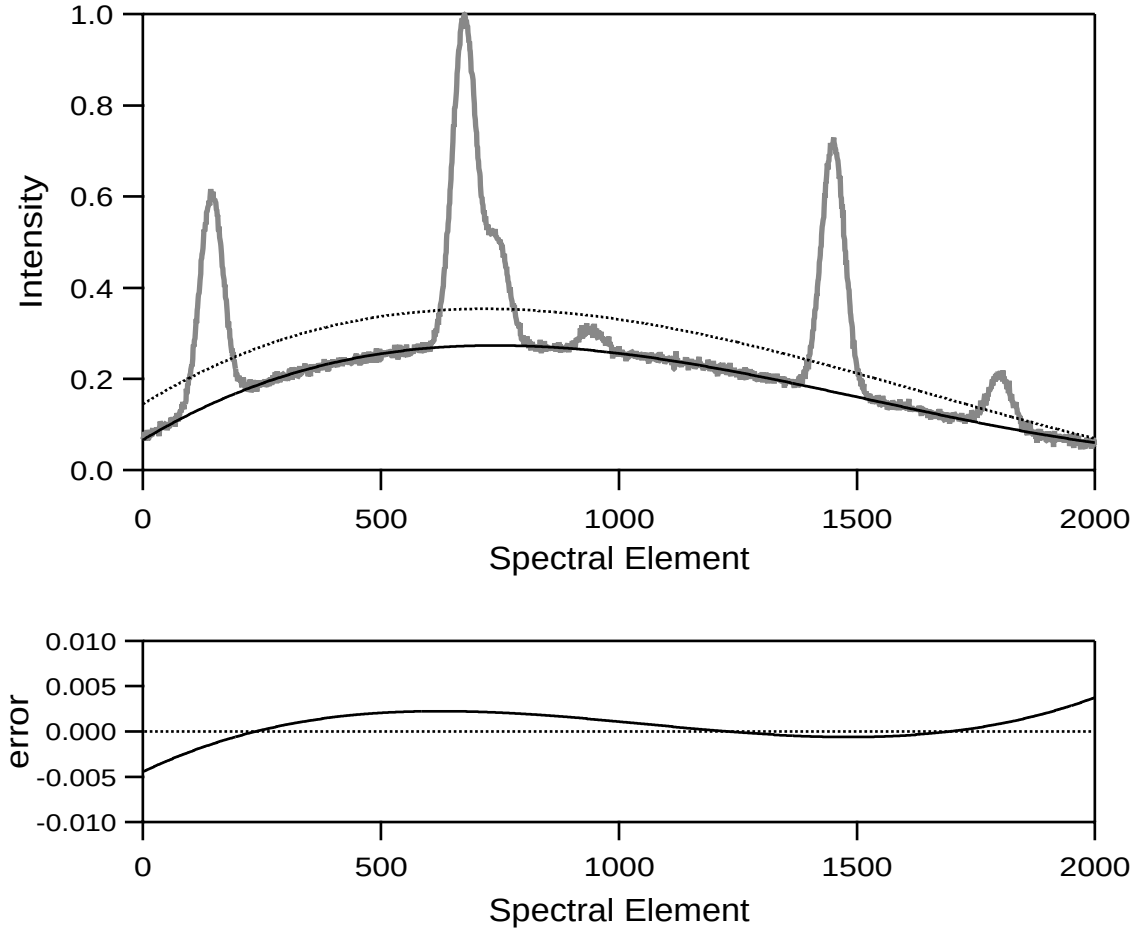

Figure 4-1: Simple example of RBE. Top: A synthetic spectrum (gray) that is superimposed upon a broad baseline generated by a third order polynomial. The dotted line is the baseline determined by least-squares fitting; although this solution is clearly incorrect, it is an adequate starting point for a robust fit, which generates the solution indicated by the solid black line. Bottom: the error in the robust baseline estimation; note the expanded y-scale.

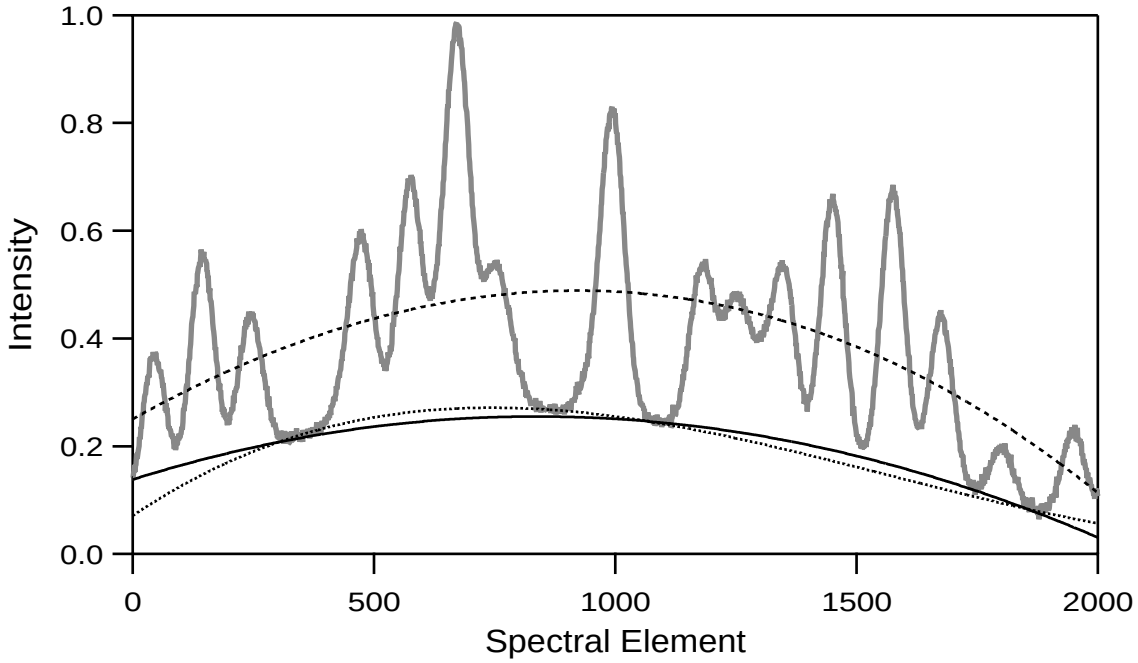

Figure 4-2: Difficult application of RBE. In gray is a very congested synthetic spectrum that is superimposed upon a broad baseline generated by a third order polynomial (dotted line). The dashed line is the baseline determined by RBE, using as initial parameters for the robust fit the results from a least-squares fit; obviously, the robust fit became trapped in a local minimum, and the results are inadequate. The solid line represents a more satisfactory solution, obtained by an iterative series of fits using asymmetrically weighted merit functions.

baseline. The dashed line shows the result of using RBE (with least-squares initial values) for this spectrum. Obviously, the robust fit became "trapped" in a local minimum that is nowhere close to the optimal solution, and the least-squares results are inadequate starting values in this case.

Two modifications of the RBE technique help it to avoid local minima during the robust fit. The first is to define a family of robust estimators with varying behavior depending on the value of a single parameter. Again, the merit function is defined to be a sum of "ρ-functions", $\Gamma = \sum_i \rho(\delta_i)$, but in this case the family of ρ-functions is defined as

$$\rho_\alpha(\delta) = \delta^\alpha[1 - \exp(-\delta^2/2)]. \tag{4.3}$$

The parameter α is limited to $0 \leq \alpha \leq 2$. Note that when $\alpha = 0$, then the ρ-function becomes the simple inverted Gaussian of Eq. 4.1. Less obvious is that when $\alpha = 2$,

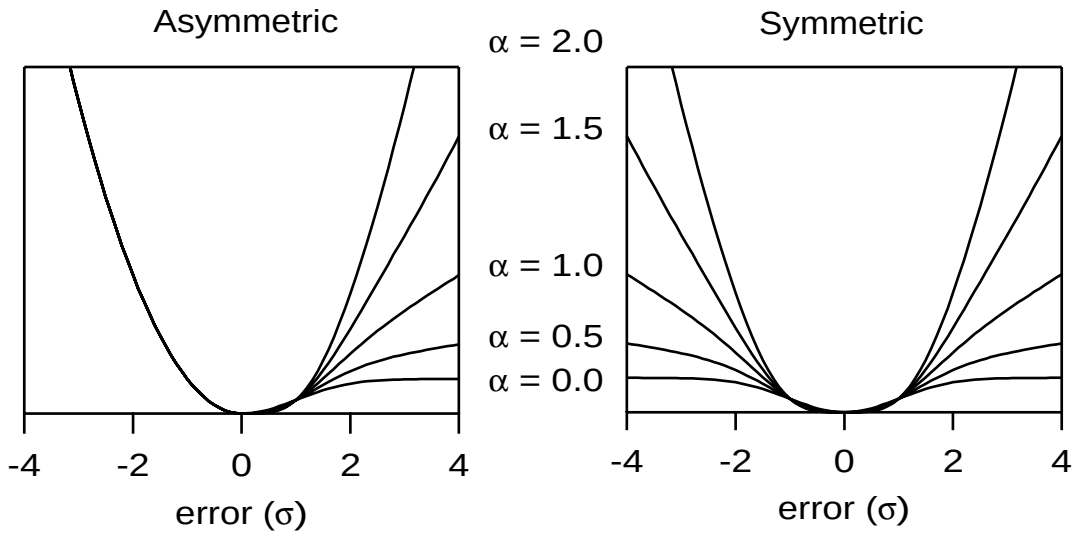

Figure 4-3: Right: The family of symmetric functions ρ_α for several values of α. Note that for $\alpha = 0$, the merit function is an inverted Gaussian. For $\alpha = 2$, the merit function is quite close to the χ^2 function in least-squares. Left: Asymmetric family of ρ-functions.

the merit function behaves very similarly to the the χ^2 function used in least-squares fitting, particularly for large δ:

$$\rho(\delta; 2) = \delta^2[1 - \exp(-\delta^2/2)] \approx \delta^2 \quad (\delta \gg 1). \tag{4.4}$$

This family of ρ-functions, for various values of α, is depicted in the right panel of Fig. 4-3.

This family of merit functions provides a more sophisticated solution to the problem of starting parameter values for the robust fit. Instead of simply using least-squares results as the starting point, one can use an iterative procedure in which α is varied in steps from 2.0 (essentially least-squares) to 0.0 (inverted Gaussian robust estimator), using the results of the previous step as the initial parameters for the next step. The number of steps usually does not need to be large; ten is almost always more than sufficient. The fit at each step generally converges rapidly, since the merit function changes in minor ways from one value of α to the next (outliers are weighted slightly less in each step).

One additional modification to the RBE technique that is extremely useful for accelerating convergence is to utilize asymmetric merit functions—i.e., the functions $\rho(\delta)$ are defined such that they weight a positive deviation from the model differently than a negative deviation. One possible family of asymmetric ρ-functions are those depicted in the left panel of Fig. 4-3, which are described by

$$\rho_\alpha(\delta) = \delta^\alpha[1 - \exp(-\delta^2/2)] \quad (\delta \geq 0) \tag{4.5}$$

$$\rho_\alpha(\delta) = \delta^2 \quad (\delta < 0). \tag{4.6}$$

In other words, they are identical to the symmetric family of ρ-functions (right panel of Fig. 4-3) for positive deviations from the model; for negative deviations, ρ is simply the square of the error, as in least-squares fitting. The rationale for the asymmetric merit functions is simple—in the vast majority of spectra, signal is represented by peaks that point in one direction, usually the positive direction. Thus, in order to determine the baseline accurately, the RBE technique need only be unidirectionally robust; that is, the RBE need only ignore "outliers" in the positive direction, because only these could be due to peaks in the spectrum. Any outliers that lie below the fit line (negative δ) cannot be due to peaks in the spectrum and indicate that the fitted baseline is too high. The asymmetric merit function ensures that any such negative outliers have a strong influence on the fit at all stages, and in general the use of the asymmetric merit function ensures rapid convergence towards a reasonable solution.

One serious concern about the use of asymmetric merit functions is that, by treating positive and negative outliers differently, they might bias the final fitted solution. One can, of course, use the family of asymmetric merit functions to obtain an initial estimate of the baseline, and then use the symmetric merit functions in a final fit to obtain a less biased solution. In practice, however, this may be unnecessary. It is important to keep in mind that the data itself imposes a bias on the baseline fit, since all of the peaks point in one direction. Using a robust estimator helps to minimize that bias, but it is generally impossible to completely eliminate it. The bias introduced by the asymmetric merit function partially counteracts the bias of the

data itself, and the asymmetric merit functions performs better than the symmetric merit functions in many tests on simulated spectra.

The solid line in Fig. 4-2 depicts the results of the modified RBE technique (using the asymmetric merit functions and iteratively reducing α to 0) for a very difficult synthetic test case. Overall, the RBE solution appears to be quite acceptable, although it does diverge from the "true baseline" (dotted line) below spectral element 300. The RBE fitted baseline passes through the spectrum at spectral element 0, whereas the baseline upon which the peaks were superimposed lies substantially lower at this spectral element. However, in the absence of any additional knowledge other than the observed spectrum (in gray), the RBE solution is completely reasonable. The synthetic spectrum considered here is an extreme case; it is so congested that only $\sim$10% of the spectral elements are of any use in determining the baseline. In addition, end points of a spectrum present a special challenge for baseline estimation; a spectral element can generally only be determined to be "baseline" or "peak" in relation to other points around it.

4.3 Applications of the RBE Technique

We consider in this section a few applications of the RBE technique to real spectroscopic data. Since the "true baseline" is unknown for any real spectrum, it is impossible to judge in a quantitative way the performance of the RBE technique, although it is clear that the RBE solutions are reasonable. The emphasis here is on the wide range of problems to which RBE can be applied, with minimal human intervention and minimal assumptions about the spectra. In all cases, the asymmetric merit functions are utilized and α is iteratively reduced from 2.0 to 0.0 in ten increments.

Fig. 4-4 depicts a Raman spectrum of human breast tissue that was provided by the group of Prof. M. S. Feld (MIT Department of Physics and George R. Harrison Spectroscopy Laboratory). The baseline upon which the sharp features are superimposed is an unavoidable result of performing spectroscopy on a condensed phase substance of such complex composition as human tissue. The sharp features are due

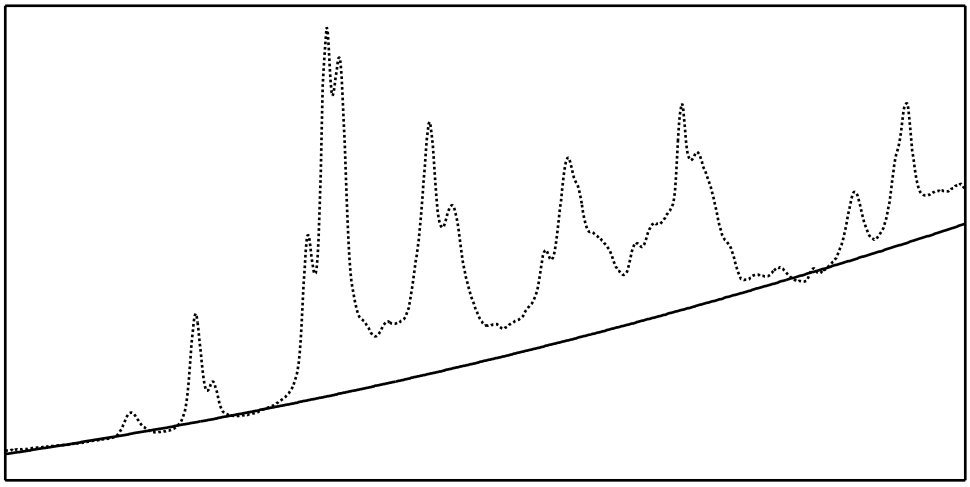

Figure 4-4: Application of the RBE technique to estimate a baseline function for a Raman spectrum of human breast tissue (dotted line), which was provided by the group of Prof. M. S. Feld, MIT Department of Physics and George R. Harrison Spectroscopy Laboratory. The black line is the baseline determined by RBE (asymmetric family of merit functions), assuming that the baseline can be represented by a second order polynomial.

to specific chemical constituents of the tissue, the relative abundances of which are expected to be related to the health of the tissue (i.e., malignancy is associated with distinct spectroscopic signatures). In order to analyze spectra such as this one, it is highly desirable to isolate the sharp features from the continuous baseline.

This Raman spectrum is reminiscent of the synthetic spectrum in Fig. 4-2, in that it is very congested and few spectral elements can be considered useful for determining the baseline. Without any knowledge of an appropriate functional form for the baseline, any estimate of the baseline should be approached with caution. Nonetheless, the baseline appears to be rather smooth and a second order polynomial likely provides a reasonable functional form. The baseline determined using RBE is represented by the solid line in Fig. 4-4. Clearly, the RBE has found a *reasonable* solution, although it is impossible to determine whether it is *correct*.

Figure 4-5 provides another example of an experimental spectrum in which sharp features are superimposed upon a smooth baseline that appears to be representable by a low order polynomial. The spectrum in this case is the dispersed fluorescence

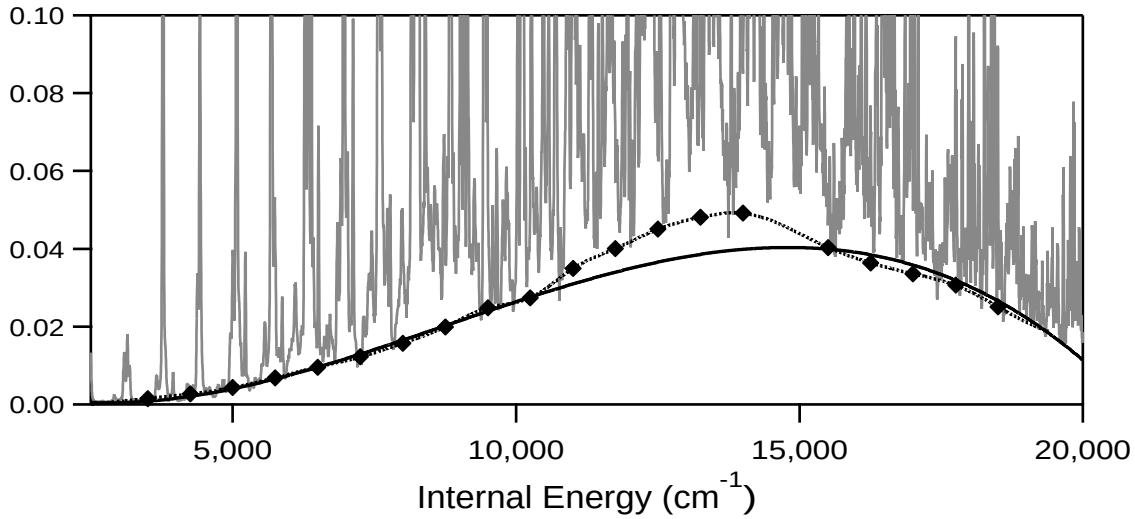

Figure 4-5: Application of the RBE technique to remove the quasi-continuous baseline from the acetylene dispersed fluorescence spectra. In gray is the DF spectrum, which is the same as the one shown in Fig. 5-2. The spectrum is scaled such that the tallest peak has intensity 1.0. In black is the result of the RBE technique, assuming that the baseline can be represented by a third-order polynomial. The diamonds mark the estimated baseline at discrete positions using a localized version of the RBE (assuming that the baseline is quasi-linear over a range of $\sim$3000 cm^{-1}). The dotted line is a cubic spline interpolation between the diamonds. In all applications of RBE, the asymmetric family of merit functions was employed.

spectrum from the $V_0^2K_0^1$ band of acetylene, which is also depicted in Fig. 5-2. As explained in Section 5.3, the quasi-continuous baseline is believed to be unrelated to the emission of the isolated molecule in which we are interested and should be removed. A second order polynomial is clearly not adequate to model the baseline, but a third order polynomial may be reasonable. The baseline estimate from RBE is represented as the solid line, and appears to be an adequate solution, except possibly near 13,000 cm^{-1}, where it lies significantly below the lowest points in the spectrum.

One could, of course, try higher order polynomials for the fit, but a more generally useful strategy is to estimate the baseline *locally*. That is, over a relatively small region of the spectrum, the baseline can be assumed to be quasi-linear. The strategy employed here is to perform a linear RBE fit within a sufficiently narrow window, and then use the amplitude of the baseline at the center of the window as the local estimate of the baseline (by only using the baseline estimate at the center of the

window, edge effects are minimized). The window can then be translated across the spectrum in small steps, and a baseline function can be built up one point at a time. When there are a sufficient number of baseline points, they can be interpolated, using a cubic spline for example, to create a continuous baseline function.

The results of this local RBE fit algorithm are also depicted in Fig. 4-5. The diamond-shaped markers indicate the local estimates of the baseline that were determined by performing linear RBE fits within 3000 cm^{-1} windows. The dotted line is a cubic spline interpolation through these points. This local RBE solution is quite similar to the third-order polynomial solution, except in the ~12,000–14,000 cm^{-1} region. Although the local RBE solution appears to be more reasonable (due to the increased flexibility of not having to choose a functional form for the baseline), it is once again important to emphasize that it is an ill-defined question to ask which solution is better. Each solution is optimal (hopefully) given the assumptions made about the data. In the case of the global fit, the assumption is that the baseline conforms to a third order polynomial. In the case of the local fit, the assumption is that the baseline can be considered linear over 3000 cm^{-1} regions. Both solutions will depend on the estimate of the measurement error (a value of 0.002 was used in these calculations), as well as the implicit assumption that the spectrum is not so congested that it is impossible to determine a reasonable baseline function.

Figure 4-6 presents a final example of the application of the RBE technique to real experimental data. This experiment, which was carried out by J. A. Dodd, R. B. Lockwood, and co-workers (Air Force Research Laboratory, Space Vehicles Directorate, Hanscom Air Force Base), detected OH arising from the reaction $H + O_3 \rightarrow OH + O_2$ by laser induced fluorescence. The goal of the experiment is to quantitate the populations of OH radical in various X-state rovibrational levels. The accuracy of the derived populations depends on an accurate measurement of the intensities of the peaks in the spectrum, which in turn relies on determining an accurate baseline function.

This data is particularly intriguing from the standpoint of numerical baseline estimation because the measurement error varies across the spectrum. This is deliberate;

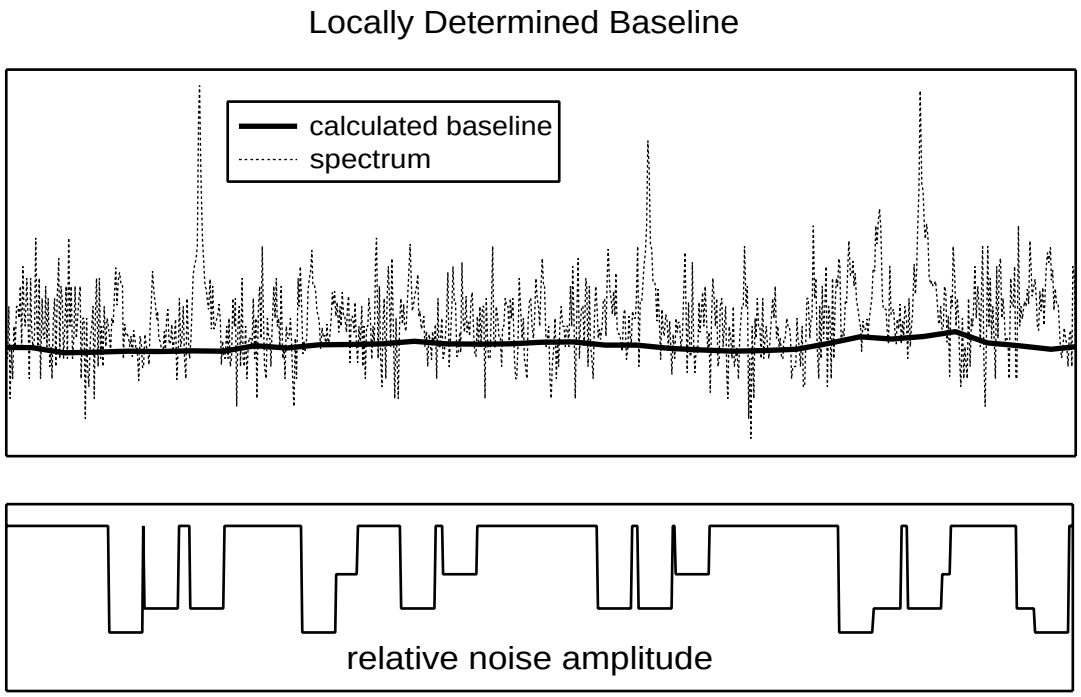

Figure 4-6: Application of the RBE technique to data in which the noise amplitude varies from one spectral element to the next. This data was provided to me by J. A. Dodd, R. B. Lockwood, and co-workers at the Air Force Research Laboratory, Space Vehicles Directorate, at Hanscom Air Force Base. Top: Spectroscopic data (dotted line) and fitted baseline (solid line), using local RBE. Bottom: Relative noise amplitude in the spectroscopic data.

the data collection routine slows down the scan rate near the peaks of interest to improve the signal to noise. It is undesirable to scan at a slow rate across the entire spectrum because to do so would take a prohibitively long time.

The RBE technique has no difficulty in treating data in which the measurement error varies from one spectral element to the next. In Eq. 4.2, the measurement error σ is simply taken to be a function of spectral element. The relative measurement errors can be estimated from the scan rate, which is recorded along with the spectrum. The absolute measurement error is unknown but can be estimated from the data. Clearly, the baseline cannot be represented by a low order polynomial; it oscillates in a seemingly random way. Thus, the baseline is fitted locally using RBE. The resultant fitted baseline is shown as a solid line. In the regions of highest signal-to-noise, the fitted baseline appears to be quite reasonable, cutting just beneath the bases of the peaks. In regions where the noise level is higher it is more difficult to assess the quality of the fitted baseline. The nature of the noise-weighted fit, however, is that the regions with highest signal-to-noise influence the baseline estimate the most, and that is precisely what is desired in this case.

Part II

Acetylene Unimolecular Dynamics

Chapter 5

XCC Analysis of Acetylene DF Spectra

The work in this chapter resulted from a collaborative effort between myself and Jonathan P. O'Brien. The majority of this work has been published in the Journal of Chemical Physics (Ref. [68]).

5.1 Introduction

This chapter is concerned with the identification of spectroscopic patterns in dispersed fluorescence spectra recorded from rovibrational states of *trans*-bent S_1 acetylene. These patterns are associated with approximately conserved vibrational quantum numbers called polyad numbers. The concept of polyads is, by now, well-established [14, 15, 16, 17]. At low internal energy, molecular eigenstates are generally well-described as harmonic oscillator normal mode product states, but as internal energy increases, anharmonicities in the potential energy surface introduce resonant couplings among the zero-order states; when the strength of these couplings increase to the point that they can no longer be treated within the nondegenerate perturbative limit (i.e., $|H_{12}/E_1^\circ - E_2^\circ| > 1$), then the normal mode quantum numbers can no longer be considered to be even approximately good. However, Fried and Ezra [14], and Kellman [15, 16, 17], have demonstrated that, given a set of dynamically important anharmonic resonances, certain generalized vibrational quantum numbers, called polyad numbers, may remain conserved.

Consider as a simple example a hypothetical molecule with two vibrational modes (one stretch mode, v_s, and one bend mode, v_b, for concreteness) that are coupled by a Fermi 2:1 resonance. That is, $\omega_s \approx 2\omega_b$, and anharmonic terms in the potential energy surface couple states with $2\Delta v_s = -\Delta v_b = 2$, which are nearly degenerate. Figure 5-1 depicts the matrix form of an effective Hamiltonian for this hypothetical molecule, assuming that the 2:1 resonance is the only important resonance. The (v_s, v_b) quantum numbers of the zero-order states in the model Hamiltonian are depicted along the diagonal, and the off-diagonal matrix elements, due to the Fermi 2:1 resonance, are represented generically by $H_{s,bb}$ (the numerical values of the off-diagonal matrix elements would be determined by harmonic oscillator scaling rules). The effective

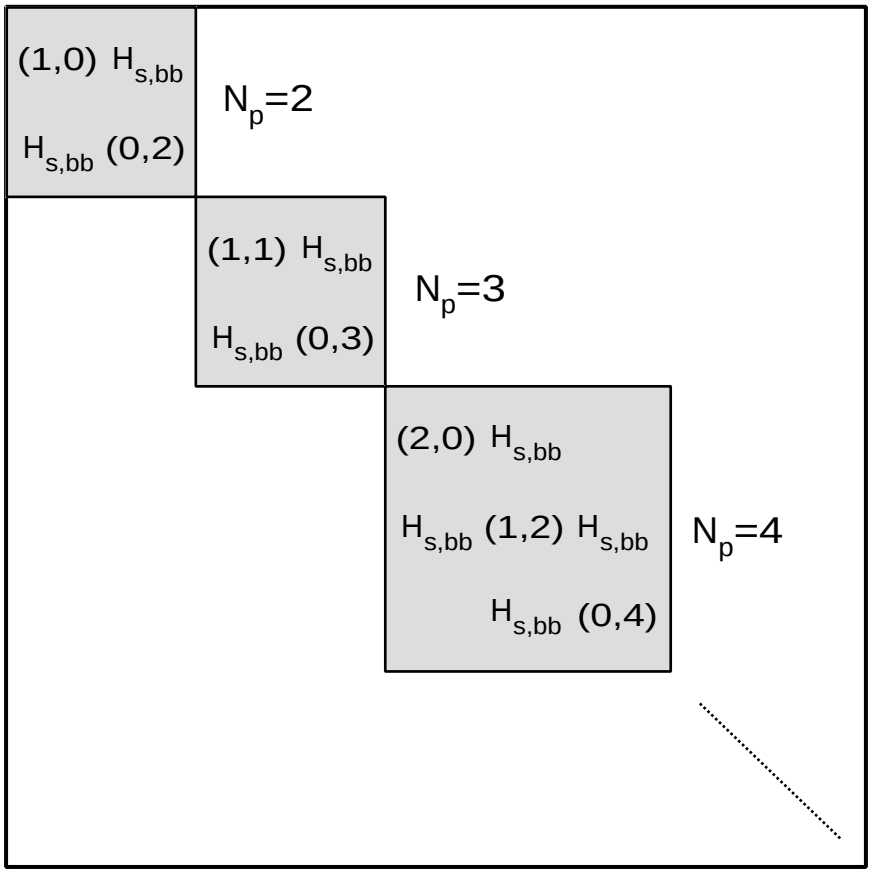

Figure 5-1: Matrix representation for the effective Hamiltonian of a hypothetical molecule with two modes, one bend and one stretch mode, in a Fermi 2:1 resonance. The effective Hamiltonian is block diagonal, and the states in each block can be labelled with the same polyad number, $N_p = 2v_s + v_b$.

Hamiltonian is block diagonal, and all states within one block can be labelled with the same value of $N_p = 2v_s + v_b$, which is the polyad number for this hypothetical system. Thus, the existence of polyad numbers places constraints on the vibrational dynamics of the molecule, since only relatively small groups of states interact with each other; from a semiclassical perspective, the polyad numbers are constants of the motion (see Chapter 8). The block diagonalization of the effective Hamiltonian is also of course convenient from the standpoint of numerical computation since each finite block of the Hamiltonian can be diagonalized exactly; when polyad numbers do not exist, then one must in principle truncate an infinitely large matrix.

The case of acetylene is significantly more complicated than the hypothetical two-mode molecule. Acetylene has seven normal modes, which are conventionally labeled

Mode	Motion
ν_1	symmetric CH stretch
ν_2	CC stretch
ν_3	antisymmetric CH stretch
ν_4	*trans* bend
ν_5	*cis* bend
ℓ_4/ℓ_5	vibrational angular momentum

Table 5.1: Normal mode notation for the acetylene S_0 state.

$(v_1, v_2, v_3, v_4^{\ell_4}, v_5^{\ell_5})$ (see Table 5.1), and 11 anharmonic resonances [69, 5, 70] have been identified through S_0 state absorption and Raman spectroscopy. Nonetheless, it can be demonstrated [15, 16, 17] that this set of resonances does not destroy all of the vibrational quantum numbers, and three conserved polyad numbers survive:

$$N_{\rm res} = 5v_1 + 3v_2 + 5v_3 + v_4 + v_5 \tag{5.1}$$

$$N_s = v_1 + v_2 + v_3 \tag{5.2}$$

$$\ell = \ell_4 + \ell_5. \tag{5.3}$$

The physical meanings of the N_s and ℓ quantum numbers are simple; they represent the total number of quanta of stretching excitation and the total vibrational angular momentum, respectively. The N_{res} quantum number has a slightly more subtle meaning; it reflects the approximate ratios among the normal mode frequencies, and thus represents a restriction under which only states with approximately the same zero-order energy may interact.

It should be emphasized that polyad quantum numbers are approximately but not rigorously conserved, and the conservation or nonconservation of the polyad numbers is a function of both internal energy and spectroscopic resolution (or, equivalently, timescale of the dynamics being probed). That is, the early-time dynamics of the molecule could be adequately described within the framework of the polyad model, whereas an understanding of the longer time dynamics might require the incorporation of inter-polyad couplings into the model. A number of mechanisms could lead to

breakdowns in the goodness of the polyad quantum numbers. As has been discussed previously [5, 71], various Coriolis interactions, in addition to rotational ℓ-resonance, can lead to rotationally induced breakdowns of the polyad quantum numbers. The DF spectra analyzed here sample low rotational quantum numbers ($J = 1,2$), so that rotationally induced polyad breakdown is not expected to be significant. However, purely vibrational breakdown of the polyad quantum numbers is also possible. The polyad model incorporates only the strong anharmonic resonances that have been definitively demonstrated to exist by studies at relatively low internal energy (<10,000 cm^{-1}). Certain higher order anharmonic resonances, that are currently uncharacterized and not incorporated in the polyad model, are likely not to conserve the polyad quantum numbers. If these unaccounted-for resonances are relatively weak, then their existence will be manifested primarily through *local* perturbations at low internal energy, but due to their quantum number scaling, could lead to a *global* breakdown of the polyad numbers at higher internal energy.

Prior to this work, substantial experimental evidence had been presented that the polyad numbers remain approximately conserved to at least 10,000 cm^{-1} [69, 5, 70]. In particular, a preliminary analysis of acetylene DF spectra in the Field group [69] resulted in the assignment of polyad numbers to 75 spectral features below 10,000 cm^{-1}. In this chapter, polyad assignments are provided for hundreds of spectral features up to 15,000 cm^{-1}, and no evidence is found for the destruction of the polyad numbers, on a timescale of $\sim$1 ps, up to at least 15,000 cm^{-1}. In Chapter 10, the analysis of the DF spectra is continued above 15,000 cm^{-1}, where the energetic feasibility of acetylene-vinylidene isomerization [72, 37, 34] might be expected to destroy some or all of the polyad quantum numbers (the destroyed polyad numbers might also be replaced with new approximately conserved quantities). However, no evidence of *global* breakdown of the polyad quantum numbers is observed to at least 20,000 cm^{-1}.

The ability to probe the polyad structure of acetylene at such high internal energy is made possible by the use of *numerical* pattern recognition algorithms, based upon the XCC (Chapter 2). The rationale for using pattern recognition to apportion the

DF spectra into polyad patterns is discussed in Section 5.4; see also Refs. [69], [9], and [8]. Prior studies of the acetylene DF spectra utilized *visual* pattern recognition to assign polyad number to observed spectral features. There are several advantages to using numerical, as opposed to visual, pattern recognition in this context. The XCC performs the identification and extraction of patterns in an automated and numerically rigorous fashion and thus minimizes the number of "judgment calls". The XCC requires no *a priori* knowledge of either the number or nature of the patterns, and, as described in Section 5.5, is capable of identifying and extracting an arbitrary number of patterns from the DF spectra. In addition, the technique is capable of extracting multiple overlapped patterns, which would be difficult to recognize by eye; this advantage of the XCC becomes especially important at high internal energy (i.e., above 10,000 cm^{-1}). Finally, the XCC can accommodate any number of spectra, whereas visual pattern recognition becomes increasingly difficult as the number of spectra increases.

However, the XCC technique does require that the spectral data be well-calibrated. In particular, the XCC algorithm requires that the spectra to be analyzed are frequency calibrated to within the spectral resolution. In addition, as described in Section 5.5, the XCC identifies patterns using the intensity information in the spectra, and thus accurate relative intensities are also essential. For these reasons, a new DF data set for the acetylene $S_1 \rightarrow S_0$ system has been recorded for the express purpose of analysis by numerical pattern recognition algorithms (Section 5.2). DF spectra have the distinct advantage that *both* frequencies and relative intensities can be accurately measured. In terms of frequency calibration, the advent of sensitive array detectors, such as diode arrays and charge coupled devices (CCDs), has obviated the stick-slip problems that hampered the frequency calibration of DF spectra that were recorded with many scanning monochromators. As for intensity calibration, although many spectroscopic techniques can boast sensitivity and/or dynamic range vastly superior to that of DF spectroscopy, the relative intensities of different transitions in the majority of these techniques are inherently either nonlinear or non-reproducible, making it difficult or impossible to calibrate the intensities in such a spectrum. By

contrast, the intensities in DF spectra are linear and can be calibrated by taking into account instrumental effects such as the wavelength dependences of the grating and detector.

One of the primary limitations of DF spectroscopy is resolution, which is determined by the dispersion of the grating used, the path length of the monochromator, and, in the case of array detectors, the pixel size of the array. However, from the standpoint of understanding dynamics, low resolution corresponds to short-time dynamics. For polyatomic molecules at high internal energy, the short-time dynamics (a few ps) can provide a wealth of insight into the potential energy surface under study, as will hopefully be clear in the chapters that follow. High resolution, high sensitivity techniques often generate enormous amounts of detail that relate to the long-time dynamics. The panoramic perspective afforded by DF spectra provides a necessary framework for understanding the details provided by higher resolution and higher sensitivity techniques.

5.2 Acetylene DF Spectra

A new DF data set for acetylene $S_1 \rightarrow S_0$ emission has been recorded. This data set consists of DF spectra excited via $Q(1)$ ($J'_{K_a,K_c} = 1_{1,0}$) lines of the $V_0^0K_0^1$ (origin band), $V_0^1K_0^1$, $2_0^1V_0^1K_0^1$, $V_0^2K_0^1$, and $2_0^1V_0^2K_0^1$ vibrational bands (V represents the *trans* bending mode, v'_3 in the S_1 state and v''_4 in the S_0 state, "2" represents the CC stretch, and K has its conventional meaning as the unsigned, body-fixed projection of the total angular momentum). Selection rules for electronic transitions specify that all eigenstates observed in the DF data set possess g symmetry with respect to the center of inversion. The values of the angular momentum quantum numbers, J and ℓ, are also determined by selection rules. The emission from the selected S_1 state ($J' = 1$, $K' = 1$, f parity) rotational levels consists of two rotational components, ($J'' = 1$, $\ell'' = 0$, e parity), and ($J'' = 2$, $\ell'' = 2$, f parity). As discussed previously [69], the signs and magnitudes of the g_{44} and x_{44} parameters in the standard Dunham

expansion for the S_0 state of acetylene create a tendency[1] for these two lines to collapse into a single feature at the resolution of the DF spectra.

The DF spectrum from each of these five vibrational levels was recorded at two resolutions: $\sim$7 cm^{-1} and $\sim$18 cm^{-1} (as measured at 350 nm). Thus, the complete data set consists of a total of 10 DF spectra. The higher resolution spectra are particularly valuable for extracting highly fractionated and partially overlapping patterns above 10,000 cm^{-1}. The experimental conditions for the origin band spectra have been reported previously [69]; the experimental conditions for the DF spectra recorded from the other four vibrational levels of the S_1 state are briefly reviewed here.

A XeCl excimer laser (Lambda-Physik LPX-210icc), running at 65-85 Hz, was used to pump a grating-tuned dye laser (Lambda-Physik FL2002) containing either Coumarin 440 or 450 dye. The dye laser beam was frequency doubled in BBO to produce $\sim$1 mJ of tunable, 215-230 nm, radiation with a spectral width of $\leq$0.05 cm^{-1}. The frequency doubled laser light was spatially separated from the residual fundamental by two 60° prisms. The residual fundamental laser beam was passed through a frequency-calibration cell containing $^{130}Te_2$, and the dye laser was scanned and locked onto the $^{12}C_2H_2$ $S_1 \leftarrow S_0$ rovibronic transition of interest.

The frequency doubled dye laser output was passed through a static gas cell charged with 5.0 Torr of acetylene, which was obtained from 99.8% pure acetylene-h_2 (Matheson), which had been purified by at least five freeze-pump-thaw cycles. The emission from the static gas cell was imaged onto a monochromator entrance slit. In the case of the lower resolution ($\sim$18 cm^{-1}) spectra, the emission was imaged by $f/5.8$ fused silica optics onto the entrance slit of a Jobin-Yvon HR 640 mm monochromator equipped with a ruled grating (1200 gr/mm, blazed for 500 nm); the entrance slit width was set to $\sim$100 μm and the grating was used in first order. For the higher resolution ($\sim$7 cm^{-1}) DF spectra, the total spontaneous emission was imaged by $f/10$ fused silica optics onto the entrance slit of a Spex 1802 1000 mm monochromator

[1]Exceptions to this trend, particularly at high (>10,000 cm^{-1}) internal energy, are noted in Chapter 6.

equipped with an identical grating; the entrance slit width was set to ∼100 μm and the grating was used in second order.

The dispersed emission in either case was recorded on a Princeton Instruments intensified charge coupled device (ICCD), Model 1024-M059413, which has 256×700 active pixels. The number of laser shots recorded on the ICCD for each DF segment was varied to obtain similar signal-to-noise for each of the spectra, but was on the order of 10^4-10^5. The DF spectra were recorded in overlapping segments, such that adjacent segments overlap by at least 20 Å. In order to permit the identification and subtraction of spurious noise spikes caused by cosmic rays, the dispersed emission at each grating position (each segment) was recorded twice. All intense but narrow features that appeared in only one of the two segment spectra were assumed to be due to a cosmic ray and removed.

Frequency calibration was achieved by recording for each segment (grating position) the emission from a series of wavelength calibration lamps (Fe, Ne, Hg, Kr, Ar, Xe) *immediately after recording the acetylene emission and without moving the grating*. The calibration methodology utilized has been described previously [69, 73, 8] and permits compensation for systematic errors in the calibration, as well as the nonlinearity that is inherent in the dispersion of the grating. The frequency calibration errors were estimated to be ∼2 cm^{-1} (2σ) for the higher resolution series and ∼5 cm^{-1} for the lower resolution series.

Intensity calibration was achieved by recording for each segment the emission from an Optronic Laboratories standard of spectral irradiance lamp, Model (OL-220M-M877). The emission recorded from this lamp is compared to its calculated emission intensity to determine an instrument response function, which reflects the wavelength dependence of the ICCD response and the grating throughput. In addition, in order to correct for fluctuations in the power of the excitation laser, the total spontaneous emission from the acetylene static gas cell was collected by $f/1.7$ fused silica optics and imaged through a Schott glass filter (UG11) onto a solar blind photomultiplier tube (Hamamatsu R166UH). The PMT signal was averaged on an oscilloscope during the period of signal integration of each DF segment to provide an intensity normalization

factor.

The accuracy of the intensity calibration is a function of the wavelengths of the transitions being referred to, in the sense that transitions observed at similar wavelengths have more accurate relative intensities than transitions at very different wavelengths. As a conservative upper bound, it can be estimated [8] that the intensity ratio of *any* pair of peaks within one DF spectrum (i.e., peaks separated by up to 20,000 cm^{-1}) will *always* be accurate to within 20%. This number is a conservative upper bound and refers to pairs of peaks that are separated by ∼20,000 cm^{-1}. The intensity ratios for pairs of peaks that lie within 1000 cm^{-1} of each other are accurate to within ∼2%. [Even more accurate intensity calibration is possible using the methods described in Section 10.2.]

It should be noted that the complete intensity calibration procedure may only be properly applied to spectra recorded in first order on the grating. That is, since the intensity calibration lamp has continuous emission over 2000–9000 Å, the recorded intensity response at the grating positions used for the second-order (higher resolution) series of DF spectra would include contributions from both first and second order. Therefore, only the lower resolution series of DF spectra have the property that peaks separated by several thousand cm^{-1} have accurate relative intensities. Note, however, that the XCC can still be used to analyze the higher resolution spectra, despite their poorer intensity calibration, because each fractionated bright state pattern typically extends over a range of internal energy of <1000 cm^{-1}.

5.3 Quasi-Continuous Baseline

Figure 5-2 depicts the calibrated, concatenated DF spectrum that was obtained at 18 cm^{-1} resolution (first order) from the $V_0^2 K_0^1$ band. Note that the intensities depicted here have been corrected for both the instrument response function and the ω^3 factor in the Einstein A-coefficient. Thus, the y-axis represents the relative Franck-Condon factors for the observed transitions (assuming constant electronic transition moment). One notable feature is what appears to be a quasi-continuous baseline (QCB) that

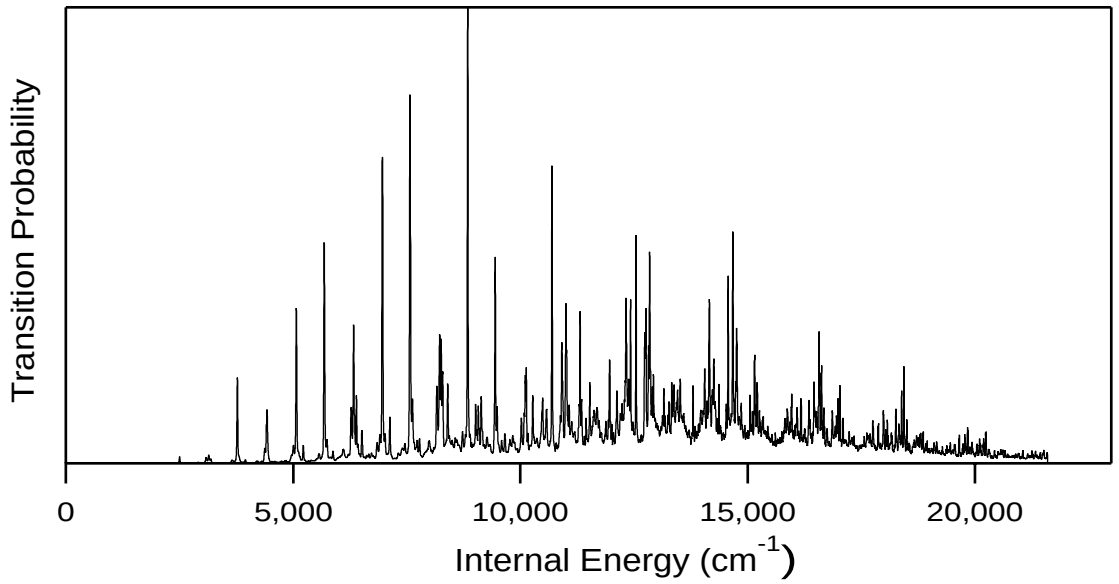

Figure 5-2: Dispersed fluorescence spectrum excited via the $Q(1)$ line of the $V_0^2K_0^1$ band in the $S_1 \rightarrow S_0$ transition. Notice the quasi-continuous baseline above 6,000 cm^{-1}.

commences at approximately 6,000 cm^{-1}. That is, the emission intensity never reaches zero at internal energies greater than 6,000 cm^{-1}.

Several experiments have been performed to help elucidate the origin of the QCB. These experiments were performed using the $Q(n)_e$ line[2] of the $V_0^3K_0^1$ band, which is *not* one of the transitions used to record the DF spectra in the data set discussed in this chapter. However, the DF spectrum recorded using this absorption transition displays a very large QCB (see Fig. 7.2 of Ref. [8]), roughly 5 times more intense (relative to the intensities of the sharp features) than the QCB in Fig. 5-2.

The amplitude of the QCB in the $Q(n)_e$, $V_0^3K_0^1$ DF spectrum was found to be independent of laser power, and thus the QCB is unlikely to represent emission from a species created through multiphoton excitation. On the other hand, as can be seen in Fig. 5-3, the intensity of the QCB does vary as a function of pressure and as a function of the time window (relative to the laser pulse passing through the sample cell) used to record the spectra. That is, the QCB has a larger amplitude relative

[2]The "e" refers to an extra line, which is presumably due to an anharmonic perturbation of the $3v_3'$ vibrational level, and the "n" refers to the fact that the $Q(1)_e$ and $Q(2)_e$ lines are not resolvable at the $\sim$0.05 cm^{-1} resolution of the laser.

to the sharp features at high pressures, and the intensity of the QCB emission varies with time differently than the emission to the sharp features, with the QCB emission dominating at later times.

Both of these results are consistent with the hypothesis that the QCB is associated with intermolecular energy transfer. As mentioned in Section 5.2, the spectral width of the laser is sufficiently narrow to permit the excitation of single rotational transitions in the vibrational bands selected. However, at ∼1 Torr of pressure, each excited state molecule is expected to undergo several, $O(10^1)$, collisions during the several hundred nanosecond lifetimes of the excited rovibrational levels accessed. These collisions may result in a change in rotational and vibrational states, and emission from a *distribution* of rovibrational states could result in a QCB composed of a conglomeration of poorly resolved transitions. However, rotational energy transfer alone cannot account for the QCB; rather, the emission from a distribution of J' levels (in the same vibrational state) would result primarily in a broadening of the observed transitions, and not a QCB.[3] Collisional energy transfer resulting in changes in K' is discussed in Section 10.1 and also cannot be responsible for the QCB.

Thus, the QCB emission is likely related to collisions that change the vibrational and/or electronic states of the excited molecules. Triplet states are may play a key role in this energy exchange. The vibrational density of triplet states (from the T_1, T_2, and T_3 surfaces) that are isoenergetic with the singlet vibrational levels used to record the DF spectra is ∼10 per cm^{-1} [74]. Substantial intersystem crossing has also been observed [74, 75, 76], which implies that the molecular eigenstates are mixtures of singlet and triplet (due to spin-orbit coupling). Thus, all states populated by the laser in $S_0 \rightarrow S_1$ transitions are believed to have substantial triplet character, and the high density of triplet states may promote relatively rapid vibrational energy transfer into a distribution of singlet/triplet mixed states. The resultant emission from this distribution could result in a QCB.

The QCB is a subject of ongoing investigation. Of particular interest is the widely

[3]This prediction can be easily verified by recording the dispersed fluorescence from different rotational lines of a single vibrational band and averaging the spectra. Several such experiments have been performed; see, for example, Fig. 10-23.

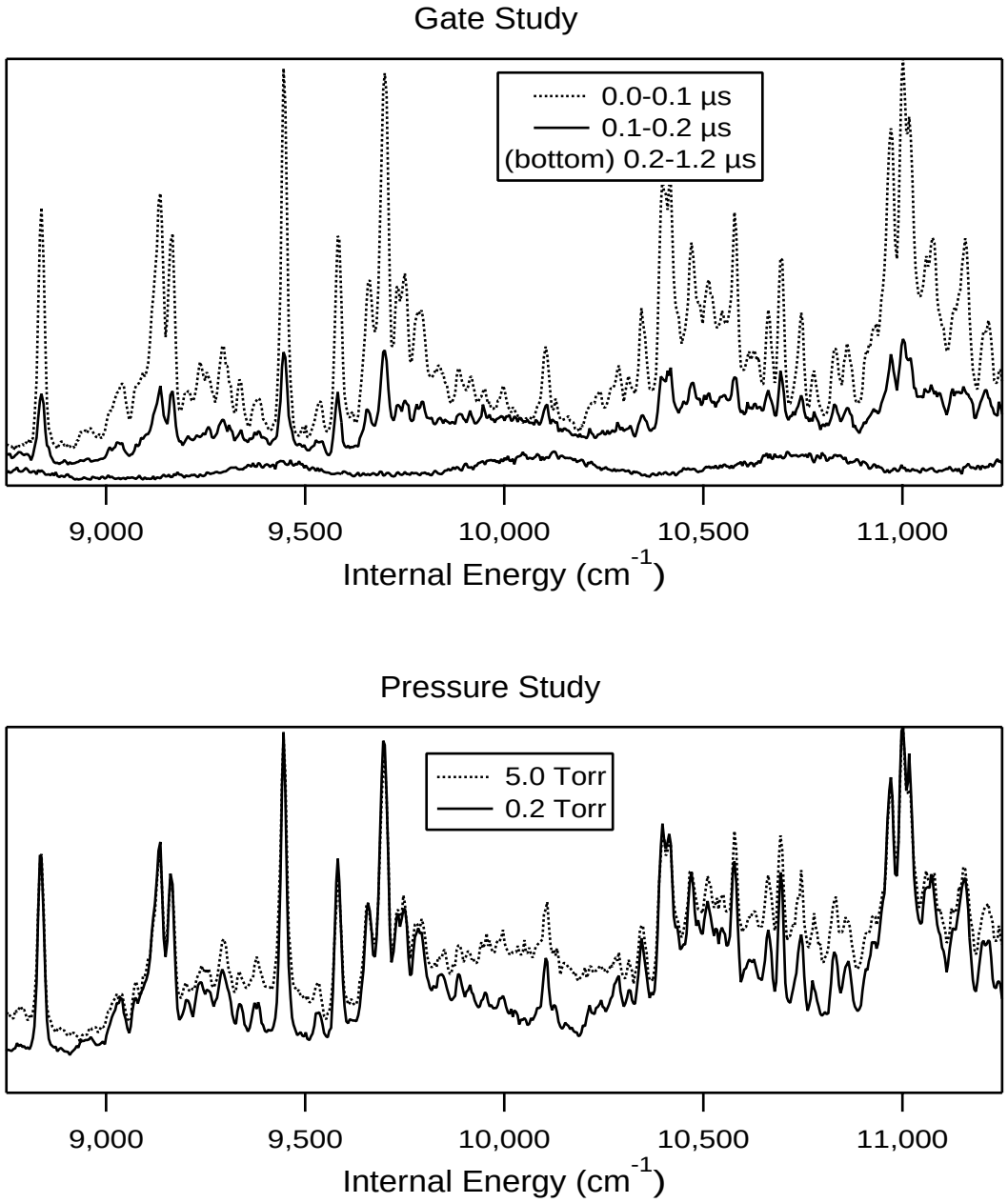

Figure 5-3: Dispersed fluorescence spectra excited via the $Q(n)_e$ line of the $V_0^3 K_0^1$ band in the $S_1 \rightarrow S_0$ transition. Top: The amplitude of the QCB relative to the sharp features varies as a function of the time window (relative to the laser pulse passing through the sample cell) used to record the spectra. Bottom: The QCB has a larger relative amplitude at higher pressures. The pressure study spectra are normalized such that the tallest peak in each has unity intensity.

varying amplitudes of the QCB observed in the DF spectra recorded using different vibrational bands. For the purposes of this study, the baseline was removed from the spectra by subtracting out a baseline function, which was determined using the Robust Baseline Estimation algorithm described in Chapter 4. The baseline-corrected version of the spectrum in Fig. 5-2 is depicted in Fig. 5-4, along with the baseline-corrected DF spectra obtained from the $2_0^1V_0^1K_0^1$ and $2_0^1V_0^2K_0^1$ vibrational bands. The origin band spectrum has been reported previously [69] and is not depicted here. Additionally, the $V_0^1K_0^1$ spectrum is not shown because this spectrum could not be recorded with signal-to-noise comparable to the other spectra. However, the $V_0^1K_0^1$ spectrum is still valuable from the standpoint of identifying fractionated bright states by numerical pattern recognition, because the XCC algorithm takes into account the noise characteristics of each of the spectra and extracts patterns from them in a statistically rigorous manner.

5.4 Theoretical Basis for Pattern Recognition

The DF spectra are ideal for gaining a broad perspective on the polyad structure in the S_0 state, since they span a large range of internal energy (see Figs. 5-2 and 5-4), from below 3,000 cm^{-1} to above 20,000 cm^{-1}. However, a glance at the spectra makes it clear that assigning polyad quantum numbers to observed transitions, and attempting to detect breakdowns of the polyad structure, is not an easy task. There are hundreds of observed transitions, and the features associated with several different polyads often overlap in the DF spectra.

The ability to assign observed spectral features to polyads is made possible by the fact that the zero-order states that are bright in our DF spectra (involving CC stretch and *trans* bend) are distributed such that there exists at most one bright state in each polyad [69]. To a good approximation, the Franck-Condon active modes in acetylene $S_1 \rightarrow S_0$ emission are CC-stretch and *trans* bend (i.e., acetylene in the S_1 state is *trans*-bent with a nominal CC double bond). Thus, the set of zero-order bright states can be written as $(0, v_2, 0, {v_4}^{0/2}, 0^0)$. Note that the restriction that $\ell_4 = 0$ or 2, due to

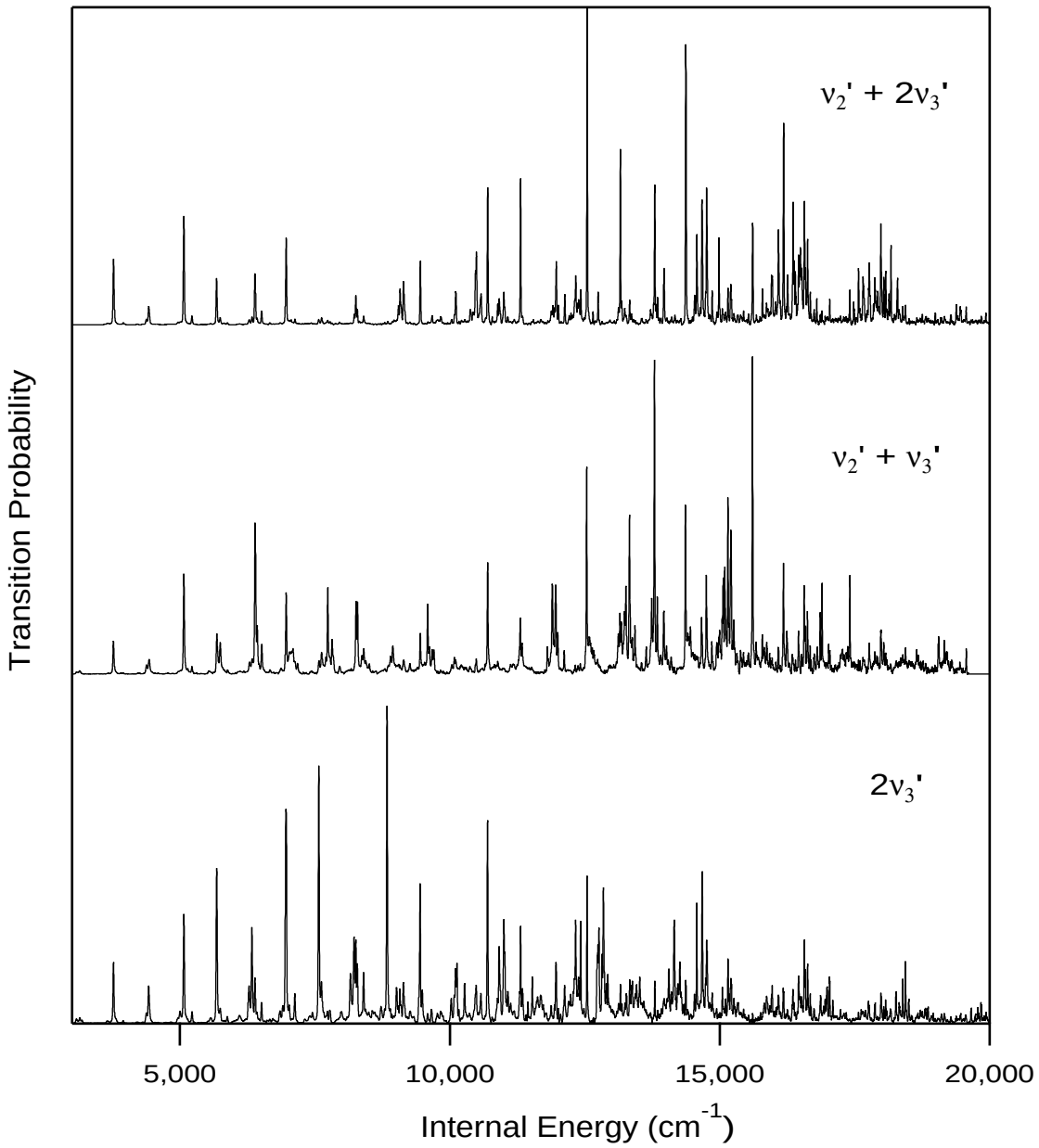

Figure 5-4: Dispersed fluorescence spectra excited via the $Q(1)$ rotational line of the $V_0^2K_0^1$, $2_0^1V_0^1K_0^1$, and $2_0^1V_0^2K_0^1$ bands. The quasi-continuous baseline has been removed using the Robust Baseline Estimation algorithms described in Chapter 4.

rotational selection rules, implies that v_4 must be even. It can be demonstrated that any given polyad contains at most one such zero-order bright state, which implies that no interference effects will be observed between different bright states. That is, each bright state fractionates into a unique set of dark states; conversely, each eigenstate gains intensity from only one zero-order bright state.

It should be noted that the symmetric CH stretching mode is also, in principle, Franck-Condon active in the acetylene $S_1 - S_0$ system, although to a much lesser degree than the CC-stretch or *trans* bend modes. If bright states of the form $(v_1, v_2, 0, {v_4}^{0/2}, 0^0)$ were to have Franck-Condon factors comparable to those of the $(0, v_2, 0, {v_4}^{0/2}, 0^0)$ bright states, then the assumption of one bright state per polyad would be incorrect. However, elementary Franck-Condon calculations [10] indicate that bright states with the symmetric CH stretch excited should have substantially smaller FC factors than bright states with zero quanta of symmetric CH stretch. Specifically, the ratio of the Franck-Condon factors for any pair of states of the form $(0, v_2, 0, {v_4}^{0/2}, 0^0)$ and $(1, v_2, 0, {v_4}^{0/2}, 0^0)$ (with the same v_2, v_4, and ℓ_4) is predicted [10] to be ∼60:1.

However, pairs of states of the form $(0, v_2, 0, {v_4}^{0/2}, 0^0)$ and $(1, v_2, 0, {v_4}^{0/2}, 0^0)$ do not belong to the same polyads. Rather, in every polyad with $N_s \neq 0$ there exists a pair of states of the form $(0, v_2, 0, {v_4}^{0/2}, 0^0)$ and $(1, v_2 - 1, 0, (v_4 - 2)^{0/2}, 0^0)$, and the ratio of the Franck-Condon factors for this pair of states will vary from polyad to polyad, and according to the S_1 state vibrational intermediate used. In certain specific cases, it is even possible that this ratio of Franck-Condon intensities could approach 1:1. That is, for the DF spectra recorded from any of the vibrational bands *other than the origin band*, the excited state vibrational wavefunction has at least one node along the *trans*-bend coordinate. According to simple Franck-Condon arguments, the existence of this node implies that in any of these DF spectra, certain states of the form $(0, v_2, 0, {v_4}^{0/2}, 0^0)$ will have Franck-Condon factors that approach zero. On the other hand, the $(1, v_2 - 1, 0, (v_4 - 2)^{0/2}, 0^0)$ zero-order states within the same polyads *could* have among the largest Franck-Condon factors in the $v_1 = 1$ progression. In such a situation, one would have an optimal opportunity to observe a member of

the rather weak $v = 1$ progression of states. However, the DF spectra have been systematically searched for these types of effects,[4] and there is no definitive evidence of *detectable* Franck-Condon intensity for any states of the form $(1, v_2, 0, {v_4}^{0/2}, 0^0)$. This observation certainly does not rule out the possibility of minor interference effects in the $N_s \neq 0$ polyads, but the weak Franck-Condon activity of the symmetric CH stretching mode does not appear to affect in any substantial way the ability of the numerical pattern recognition techniques to extract the fractionated $(0, v_2, 0, {v_4}^{0/2}, 0^0)$ bright states.

As depicted schematically in Fig. 5-5, the emission spectrum from each of the Franck-Condon active vibrational cold bands of the $S_1 \leftarrow S_0$ absorption spectrum accesses the same optically bright states, and the absence of interference effects between the bright states implies that *each bright state must display the same fractionation pattern in each of the spectra*! Within any spectrum, the absolute intensity of a fractionation pattern, born from a single bright state, arises from a unique Franck-Condon factor (namely that connecting the selected upper level to the single bright state). That is, each DF spectrum contains the same fractionated bright state patterns but with different absolute intensities, and the fractionated bright state patterns can be identified through cross-comparisons of the relative intensities in multiple DF spectra.

One caveat is that pairs of fractionated bright states that differ only in ℓ_4 and J [i.e., $(0, v_2, 0, {v_4}^0, 0^0)$, $J = 1$ and $(0, v_2, 0, {v_4}^2, 0^0)$, $J = 2$] are extracted as a single pattern. The relative intensities of these pairs of bright states are determined by rotational line strength factors, and this ratio is invariant among the DF spectra; thus, the numerical pattern recognition algorithms do not distinguish between these pairs of bright states. Note, however, that this property of the pattern recognition analysis does not imply any constructive/destructive interference between the $\ell = 0$ and 2 bright states. In addition, the fractionation patterns for the $\ell = 0, 2$ pairs of bright states tend to be very similar, and, as mentioned previously, each observed spectral feature tends to be composed of a nearly degenerate $\ell = 0, 2$ pair, at least

[4]This search was informed by the Franck-Condon trends that were elucidated in this work, see Section 5.7.

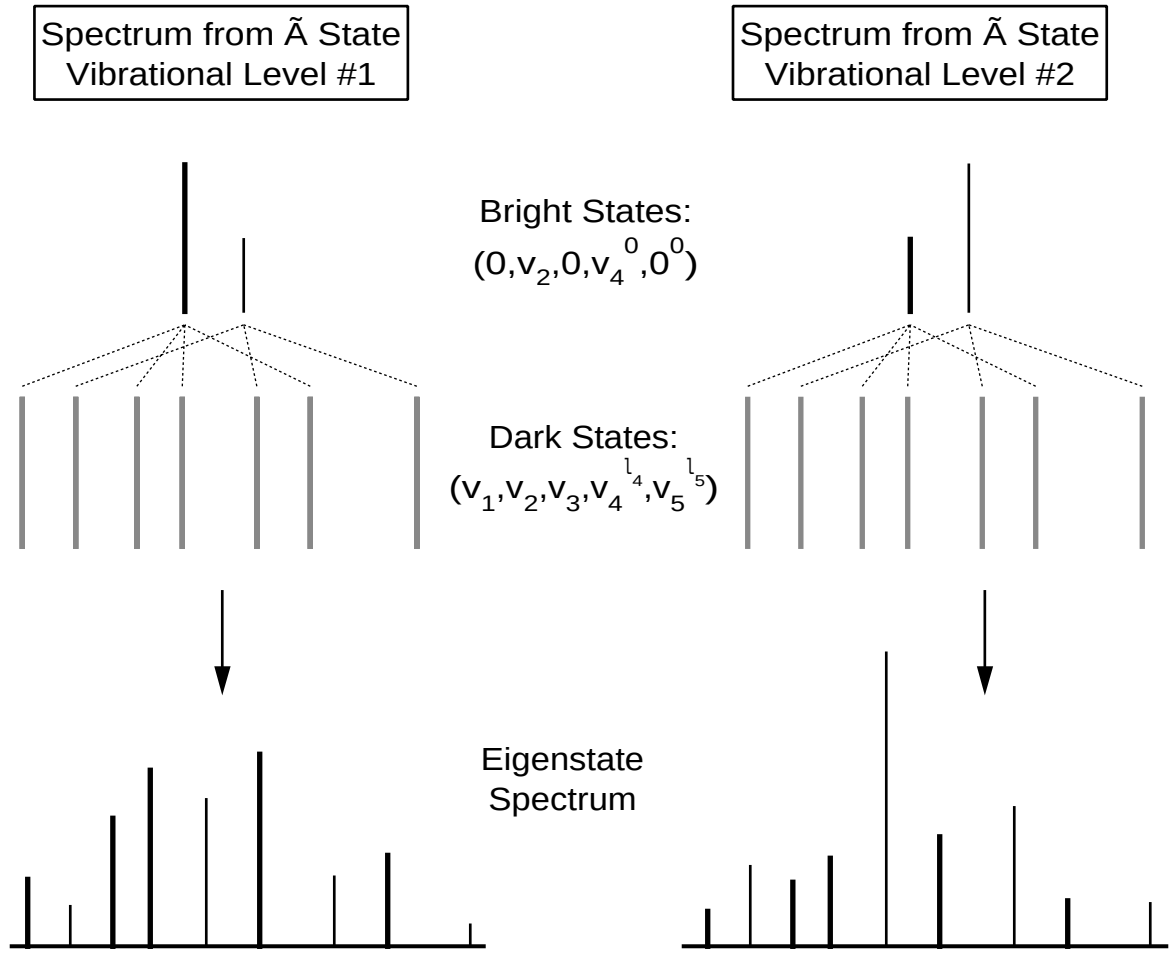

Figure 5-5: Theoretical basis for pattern recognition analysis of the DF spectra. Each zero-order state that is bright in emission from the acetylene S_1 state fractionates into a unique set of dark states; conversely, each eigenstate gains intensity from only one bright state. The bright states have different Franck-Condon factors in the DF spectra recorded from different vibrational levels of the S_1 state, and groups of transitions that have the same *relative* intensities in multiple DF spectra can be identified as arising from a single fractionated bright state. From the standpoint of pattern recognition, the fractionated bright states are patterns that are repeated in multiple spectra and can be extracted using the XCC.

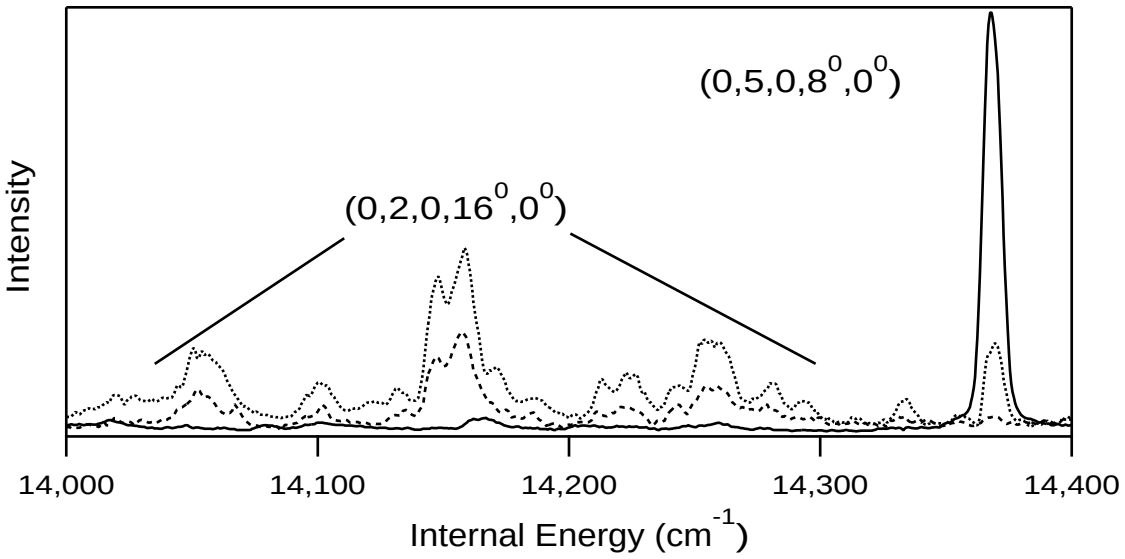

Figure 5-6: At $E_{\rm vib} \approx$ 14,200 cm^{-1}, two fractionated bright states, $(0,2,0,16^{0/2},0^0)$ and $(0,5,0,8^{0/2},0^0)$ can be visually identified in three dispersed fluorescence spectra, $V_0^0K_0^1$ (dashed line), $V_0^2K_0^1$ (dotted line), and $2_0^1V_0^2K_0^1$ (thin line).

at relatively low internal energy (<10,000 cm^{-1}). At higher internal energy, the ambiguity can be resolved using an effective Hamiltonian, as discussed in Chapter 6.

Figure 5-6 displays a 400 cm^{-1} region of three of the higher resolution DF spectra. In this region two fractionated bright states are clearly identifiable. The first zero-order bright state, $(0,2,0,16^{0/2},0^0)$, has significant Franck-Condon factors in the emission from the $V_0^2K_0^1$ (dotted line) and origin (thick line) bands, and is fractionated over at least 300 cm^{-1}. That is, this fractionated bright state can be identified because the emission patterns from the $V_0^2K_0^1$ and origin bands appear to be nearly identical (other than a constant multiplicative factor) from 14,000 cm^{-1} to 14,300 cm^{-1}. The sharp peak at the high internal energy end of this plot obviously belongs to a different fractionated bright state because its ratio of intensities among the three spectra is strikingly different from that of the peaks in the 14,000–14,300 cm^{-1} region. The zero-order bright state that illuminates this peak has a relatively large Franck-Condon factor in the $V_0^2K_0^1$ and $2_0^1V_0^2K_0^1$ band spectra, and can be assigned to be $(0,5,0,8^{0/2},0^0)$ based on its approximate zero-order energy.

One striking feature of this plot is that the $(0,2,0,16^{0/2},0^0)$ bright state appears

to display substantial fractionation (fast IVR), while the $(0,5,0,8^{0/2},0^0)$ bright state, at slightly *higher* internal energy, appears to exhibit little or no fractionation (slow IVR). The fractionation pattern for the $(0,5,0,8^{0/2},0^0)$ bright state does not, in fact, display substantial intensity above 14,400 cm^{-1}, and thus is well-described as a single peak. The existence of a bright state with such minimal fractionation at 14,400 cm^{-1} is surprising, and this and other instances of "anomalously simple IVR" are considered in Chapter 9. The point here is simply that in certain regions of the DF spectrum, the bright state fractionation patterns can be identified by eye. This type of visual identification of fractionated bright states was the basis for the analysis of the origin band DF spectrum published previously by the Field group [69].

At other ranges of internal energy, however, fractionated bright states cannot be visually identified in as trivial a fashion. Figure 5-7 depicts the same three DF spectra as in Fig. 5-6, but at slightly higher internal energy. In this region, it appears to be difficult to determine visually even how many fractionated bright states are present. The answer turns out to be two (as will be demonstrated below), but the source of the difficulty in identifying them visually is that they overlap substantially, particularly just below 14,700 cm^{-1}. Overlap between bright state fractionation patterns is the rule, rather than the exception, at high internal energy, making visual identification of the fractionation patterns tentative. To avoid judgment calls, a *numerical* pattern recognition approach has been developed to identify and disentangle from one another the fractionated bright states in the DF spectra.

5.5 Application of Numerical Pattern Recognition

The numerical pattern recognition approach to identifying fractionated bright states in the DF spectra is based on the Extended Cross Correlation (XCC), which is documented in Chapter 2. The XCC permits model-free identification and extraction of patterns that are repeated in multiple data records when two conditions are fulfilled:

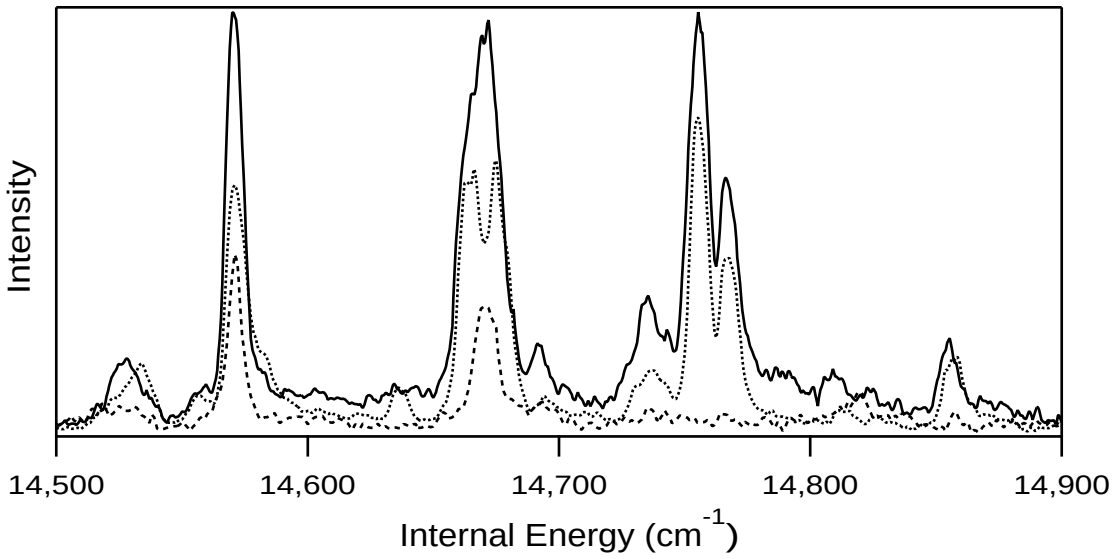

Figure 5-7: At $E_{\text{vib}} \approx 14{,}700$ cm^{-1}, it is difficult to separate the DF spectra into individual fractionated bright state patterns by eye. The DF spectra shown originate from the same upper levels as those in Fig. 5-6.

1. The data records (spectra) can be considered to be linear superpositions of patterns (plus noise).

2. Some portion of the features (peaks) in each pattern must not be overlapped with any other pattern.

In the context of the work discussed here, the patterns to be identified are the fractionated bright states. As discussed in the preceding section, condition 1 will be fulfilled if the acetylene S_0 state polyad numbers are conserved and there is only one bright state per polyad. Condition 2 can be fulfilled by recording DF spectra of sufficient resolution that a substantial portion of the intensity in each of the DF spectra resides in well-resolved peaks.

The central conceptual underpinning of the XCC is the recursion map. In the simplest case of two DF spectra, a recursion map can be constructed by plotting as the x- and y-values of the recursion map the intensities in the two spectra that are observed *at the same energy*. From a practical standpoint, the construction of

a recursion map necessitates the interpolation[5] of the DF spectra so that they are gridded identically (i.e., identical number and placement of resolution elements). For concreteness, the left panel of Fig. 5-8 displays a recursion map that is generated from the $2_0^1V_0^2K_0^1$ and $V_0^2K_0^1$ spectra displayed in Fig. 5-6. These spectra have been interpolated so that there are 800 resolution elements in each spectrum, one every 0.5 cm^{-1}; thus, 800 points appear on the recursion map.

The clustering of the points on the recursion map into two rays that emanate from the origin indicates the presence of two patterns (two fractionated bright states). That is, this clustering occurs because ranges of energy can be identified in which the intensity patterns are nearly identical in each of the spectra, except for a scaling factor. The clustering is imperfect in the sense that the points do not all lie directly along some straight line that passes through the origin. The scatter of the points about these imaginary lines (the dashed lines in the left panel of Fig. 5-8) may be caused by experimental noise, overlap with small peaks from other fractionated bright states (which reside primarily at higher or lower internal energy than that depicted in the Fig. 5-6), or, perhaps, minor breakdowns of the polyad model or the assumption of one bright state per polyad. The right panel of Fig. 5-8 depicts the XCC merit function as a function of θ, the angle between the fit line and the x-axis. Two maxima are observed, each one corresponding to a particular fractionated bright state pattern. The dashed lines in the left panel of Fig. 5-8 represent the "best-fit lines" for each pattern, and it is clear that the XCC has performed well in distinguishing between the two patterns.

In Chapter 2, two methods were presented for reconstructing the patterns from the spectral data: the weights method and the linear inversion method. The weights method applies primarily to cases in which most spectral features are well-resolved; it performs poorly when substantial fractions of a given pattern are overlapped with other patterns. At low internal energy, the weights method might be applicable, but for the purpose of identifying fractionated bright state patterns up to as high an

[5] A four-point interpolation routine was utilized here; the choice of interpolation procedure is not critical.

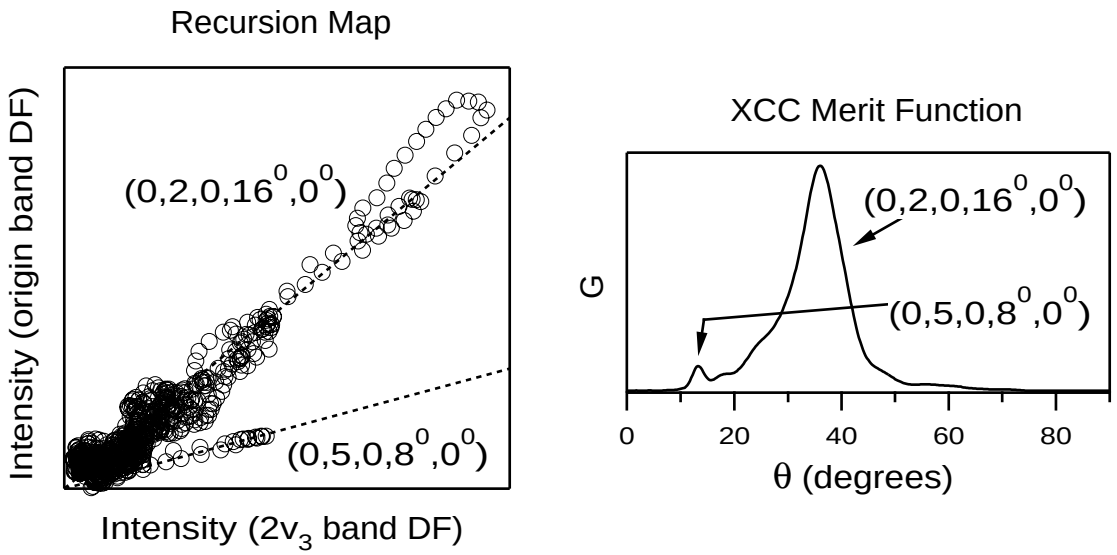

Figure 5-8: Left: A two-dimensional recursion map that utilizes the intensity information from the $V_0^0K_0^1$ (y axis) and $V_0^2K_0^1$ (x axis) DF spectra. The two rays of points that intersect the origin indicate the presence of two fractionated patterns that correspond to the $(0, 2, 0, 16^{0/2}, 0^0)$ and $(0, 5, 0, 8^{0/2}, 0^0)$ bright states. The dotted lines represent the pattern ratio directions as determined from the XCC algorithm. Right: Results of the XCC algorithm applied to this data. The two maxima in the XCC merit function, at $\sim$30° and $\sim$12°, correspond to the $(0, 2, 0, 16^{0/2}, 0^0)$ and $(0, 5, 0, 8^{0/2}, 0^0)$ fractionated bright state patterns, respectively.

internal energy as possible, it is preferable to use the linear inversion method, which permits the disentanglement of heavily overlapped patterns.

One requirement of the linear inversion method is that the number of available spectra be greater than or equal to the number of patterns which are desired to be disentangled. The total number of bright state fractionation patterns below 15,000 cm^{-1} is $\sim$50. The problem of disentangling 50 fractionated bright states from 5 DF spectra would appear to be vastly *under*determined. However, each fractionated bright state extends over a rather limited range of internal energy, such that at any given internal energy, only a few bright states contribute significantly to the spectral intensity. In principle, the range of internal energy over which each bright state fractionates is unknown. However, a previously published [70] acetylene S_0 state effective Hamiltonian provides a suitable initial guess for the approximate zero-order energy and extent of fractionation of any given bright state. To be conservative, the range of internal energy over which each bright state was fractionated was initially assumed to be $\sim$100 cm^{-1} greater than that predicted by the unrefined effective Hamiltonian. Even with a conservative initial guess, the number of patterns (fractionated bright states) that contribute significantly at any given energy is seldom greater than three.

The use of the linear inversion technique to determine a set of patterns from an equal number of spectra was discussed in detail previously in Chapter 2. However, the overdetermined case (more spectra than patterns) was not discussed thoroughly, and I wish to mention two points of practical importance. First, the linear inversion in the overdetermined case is equivalent to a linear least-squares problem, and the covariance matrix that can be obtained from the "fit" contains information that is useful in judging how well each pattern is determined by the data. Second, in each overdetermined linear inversion problem, the values of the pattern intensities were constrained to be positive (constrained least-squares). This assumption, of course, is perfectly physically reasonable, and in certain cases helps to stabilize the fit.[6]

[6]The "noise amplification" effects for the linear inversion method are thus mitigated in the present work both by *always* having more spectra than patterns and by constraining the values of the patterns, for all spectral elements, to be positive.

Efforts were made to automate the pattern recognition process as much as possible. This automation is important not only as a time-saving measure but also as an attempt to make the pattern recognition as free from judgment calls as possible. Specifically, the covariance matrix from the linear inversion was utilized in an automated fashion to determine from the experimental data the extent of fractionation of a given bright state. As mentioned previously, the unrefined effective Hamiltonian can provide a useful initial guess for the extent of fractionation for the purpose of applying the XCC to the data. However, it is desirable to determine from the data itself the energy range over which each bright state fractionates. This was accomplished by determining the point at which the amplitude of a given pattern (fractionated bright state) falls below its estimated error (1σ), as obtained from the covariance matrix. All portions of a fractionated bright state pattern that were not well-determined by the data were constrained to zero.

Figure 5-9 illustrates the application of the numerical pattern recognition algorithms to the DF data shown in Fig. 5-7 (although Fig. 5-7 depicts only three of the DF spectra, the pattern recognition algorithms were applied to the full data set of four spectra). The traces in Fig. 5-9 represent the individual bright state fractionation patterns that have been disentangled from one another, utilizing first the XCC merit function to identify the two patterns, and then the linear inversion method to disentangle them. With this result, the complex appearance of the raw data in Fig. 5-7 can be understood. The sharp peak just below 14,600 cm^{-1} arises from the $(0, 3, 0, 14^{0/2}, 0^0)$ bright state, and the pair of peaks below 14,800 cm^{-1} from the $(0, 0, 0, 22^{0/2}, 0^0)$ bright state. The set of peaks below 14,700 cm^{-1} have an unusual appearance because a pair of peaks from the $(0, 0, 0, 22^{0/2}, 0^0)$ bright state overlap with a single peak from the $(0, 3, 0, 14^{0/2}, 0^0)$ bright state.

5.6 Spectral Features Not Assignable to Polyads

The top panel of Fig. 5-10 displays three of the lower resolution ($\sim$18 cm^{-1}) DF spectra, just below 8,000 cm^{-1} of internal energy. In the bottom panel of Fig. 5-10

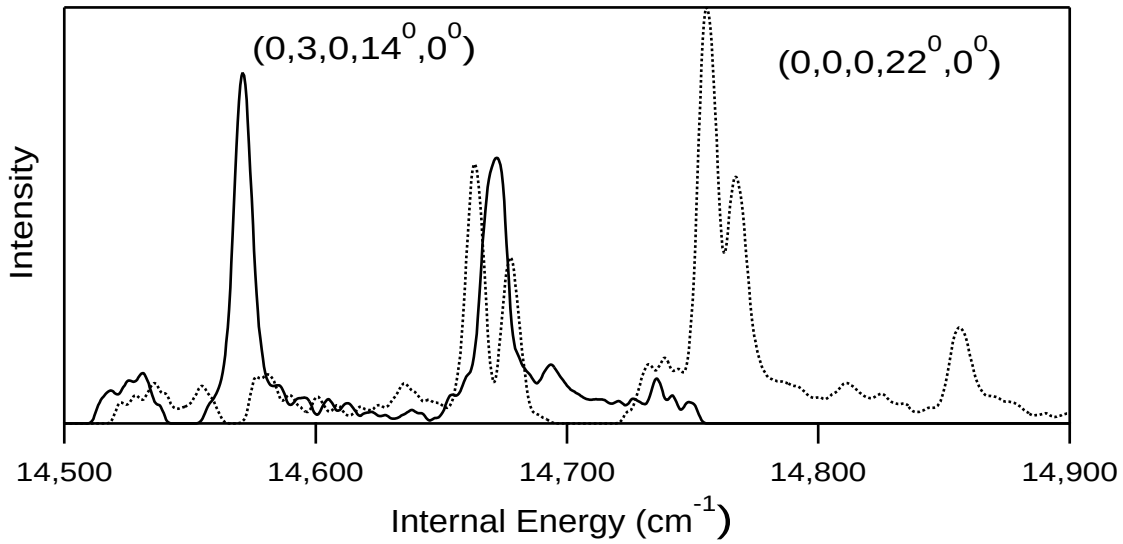

Figure 5-9: Disentangled fractionated bright state patterns, $(0, 3, 0, 14^{0/2}, 0^0)$ and $(0, 0, 0, 22^{0/2}, 0^0)$, as determined by the XCC linear inversion method. Note that the substantial overlap between the two fractionated patterns just below 14,700 cm^{-1} inhibits visual pattern recognition.

are displayed the results of the application of the pattern recognition algorithms to this energy region. Four patterns are identified, despite the fact that only two bright state fractionation patterns are predicted to be present by any reasonable effective Hamiltonian model! The patterns marked by the thick and thin smooth lines match well with the zero-order energies and fractionation patterns predicted by the effective Hamiltonian for the $(0, 2, 0, 6^{0/2}, 0^0)$ and $(0, 0, 0, 12^{0/2}, 0^0)$ bright states respectively, but the other two patterns were completely unexpected.

These features had been observed in previous DF spectra but had not been identified as unusual. The ability to single out these features for further study rests on having obtained an extensive, rigorously calibrated DF data set and having analyzed it using numerical pattern recognition algorithms. In the previous analysis of the origin band spectrum, which utilized visual (as opposed to numerical) pattern recognition and a less-extensive and less rigorously calibrated data set, these "extra" patterns were incorrectly assigned as part of the fractionation pattern of one of the expected bright state patterns [69, 70].

Other "extra" patterns were also identified that did not correspond to any pre-

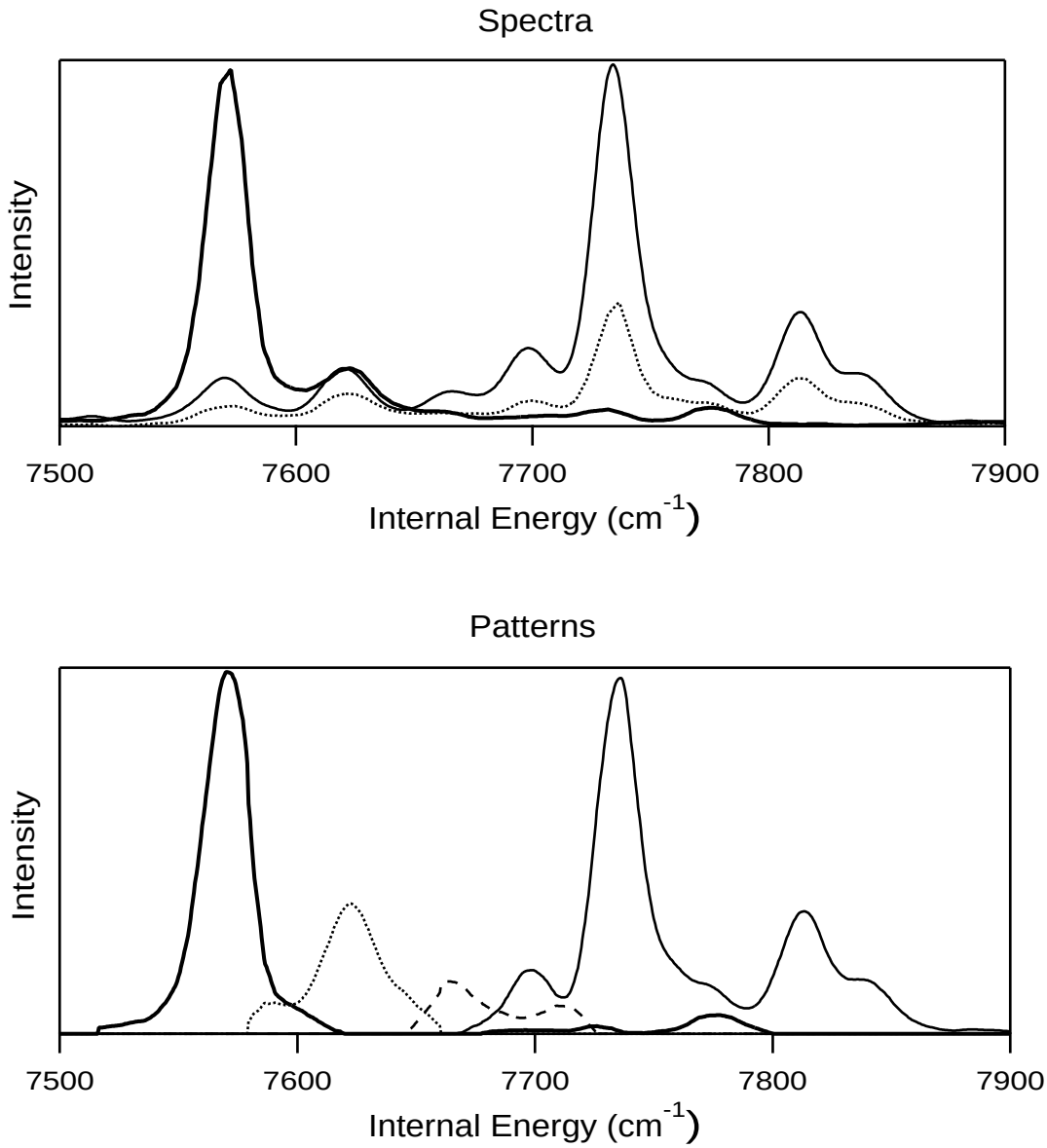

Figure 5-10: Top: The 7,500–7,900 cm^{-1} energy region of three dispersed fluorescence spectra, $V_0^0 K_0^1$ (thin line), $V_0^2 K_0^1$ (thick line), and $2_0^1 V_0^1 K_0^1$ (dotted line). Bottom: The results of the application of the numerical pattern recognition algorithms to this data. Four patterns were extracted from the data using the XCC/linear inversion method. Previous visual pattern recognition identified only two fractionated bright states in this energy region, $(0, 2, 0, 6^{0/2}, 0^0)$ and $(0, 0, 0, 12^{0/2}, 0^0)$. The two "extra" fractionated patterns were originally (incorrectly) assigned to these patterns.

dicted bright state [8]. These unexpected patterns tend to be found close in internal energy to the expected fractionated bright states. However, there is no simple trend that describes the relative intensities of any single one of these unexpected patterns among the different DF spectra, although certain spectra demonstrate a greater propensity for having intense extra patterns. These differences among the spectra can be quantified by I_e/I_{tot}, in which I_e is the total integrated intensity of all of the extra patterns extracted from a given spectrum and I_{tot} is the integrated intensity of the spectrum. This quantity can thus be described as the fraction of the spectral intensity that is accounted for by the extra patterns. Over the energy range 6,000–15,000 cm^{-1}, this fraction is calculated to be 9.5%, 20.8%, 21.4%, and 12.8% for the $2_0^1V_0^2K_0^1$, $2_0^1V_0^1K_0^1$, $V_0^2K_0^1$, and origin band DF spectra respectively (low resolution series).

At the time that the work in this chapter was completed, the identity of the extra patterns was unknown. Since that time, new experimental evidence has permitted them to be identified; this evidence and its interpretation are outlined in Chapter 10 (the extra patterns arise from collisional energy transfer that changes the K_a' quantum number). Here, I will only briefly review the evidence that was available at the time.

- The relative amplitudes of the extra patterns in the DF spectra do not depend on laser power. Varying the average power by a factor of 8 results in no perceptible change in the relative intensities of the lines observed in emission. This result rules out, as an explanation for the extra patterns, emission from some species (C_2H or C_2, for example) created through a multi-photon absorption process.

- The relative amplitude of the extra patterns is insensitive to the intermediate rotational state chosen. It is thus unlikely that the extra patterns represent unexpected rotational transitions in emission due to either S_1 state Coriolis perturbations or $S_1 \leftrightarrow S_0$ axis-switching transitions [77, 78, 79]. If either of these mechanisms were responsible for the extra patterns, their intensity would scale as $\sim J^2$; this prediction is inconsistent with the results of rotational studies, which showed no increase in the amplitude of the extra features from $J' = 1$ to

$J' = 9$.

- The amplitude of the extra patterns does not change as a function of how long the sample of acetylene has been irradiated by the laser. Therefore, it is unlikely that the extra patterns are due to emission from a stable molecule that is formed photochemically upon irradiating acetylene at ∼225 nm.

- The extra features are not observed in SEP spectra. Prof. David Moss (Boston U.) carried out SEP experiments in our laboratory that probed the acetylene S_0 state from 7,000 to 10,000 cm^{-1} [80]. In these studies, no SEP transitions were observed that corresponded to the extra features in the DF spectra, despite the greater dynamic range of SEP than DF. This SEP study confirms that the extra features do not arise from emission from the single rovibrational levels in the S_1 state that are populated by the laser in the DF studies.

Pressure studies were also performed, and the amplitude of the extra features was found to decrease by only ∼10% when the pressure was decreased from 9.0 Torr to 1.0 Torr. In addition, the extra patterns have nonzero amplitude in the origin band DF spectrum, which was recorded in a molecular beam [69]. These observations caused us to reject the possibility of the extra patterns arising from simple intermolecular rotational energy transfer. The new experimental results in Chapter 10 reveal that this conclusion was premature. In terms of the work reported in this chapter, however, the extra features were not a hindrance because they could be treated as patterns and disentangled from the fractionated bright state patterns of interest.

5.7 Polyad Number Assignments

Using the numerical pattern recognition algorithms described in Section 5.5, the fractionation patterns for 38 $(0, v_2, 0, {v_4}^{0/2}, 0^0)$ bright states have been extracted from the DF data set below 15,000 cm^{-1}. Figure 5-11 illustrates the success of the numerical pattern recognition approach in separating the $2_0^1 V_0^2 K_0^1$ DF spectrum into individual fractionated bright states. The top trace of Fig. 5-11 is the DF spectrum as seen in

Fig. 5-4. All of the extracted patterns that could be assigned as fractionated bright states of the form $(0, v_2, 0, {v_4}^{0/2}, 0^0)$ are arranged into progressions below this trace. Each horizontal progression includes all of the bright states with the same number of quanta of CC stretch, v_2, but different number of quanta of *trans* bend, v_4 (which is labeled to the right of each pattern). Note that the ability to extract fractionated bright state patterns in this way up to 15,000 cm^{-1} is strong evidence that breakdown of the polyad quantum numbers is minimal on the timescale ($\sim$1 ps) corresponding to the spectral resolution.

All of the "extra" patterns that were identified, which are not assignable as expected acetylene $S_1 \rightarrow S_0$ emission features, have been lumped together into the "residuals" trace at the bottom of this plot. This residuals trace, in fact, contains all of the intensity in the DF spectrum that is not accounted for by the fractionated bright state patterns; the sum of the $v_2 = 0, 1, 2, 3, 4, 5$ progressions plus the residuals reproduces exactly the DF spectrum at the top of the figure.

By design, each of the DF spectra can be decomposed into the same set of fractionated bright states, albeit with different relative amplitudes. The amplitude of a given pattern in one of the intensity calibrated (low resolution) DF spectra is directly proportional to the Franck-Condon factor for the corresponding bright state. Thus, it is possible to obtain the relative Franck-Condon factors for all of the bright states in one DF spectrum by integrating the intensities of the extracted bright state fractionation patterns. It is clear from Fig. 5-11 that the qualitative trends in the Franck-Condon factors that are observed for the $2_0^1 V_0^1 K_0^1$ DF spectrum are consistent with elementary Franck-Condon arguments. Specifically, the excited state vibrational wavefunction in this case has one node along each of the CC stretch (Q_2) and *trans* bend (Q_4) coordinates. These nodes are expected to be projected onto the observed Franck-Condon factors, and one can, in fact, observe a clear dip in the Franck-Condon factors in each of these two coordinates in Fig. 5-11, at $v_4 = 14 - 16$ and $v_2 = 2$.

Selected Franck-Condon factors for this DF spectrum and others are also plotted in Fig. 5-12 as a function of v_2 and v_4. The consistency of the observed trends in intensity with Franck-Condon arguments provides additional confidence that the extracted

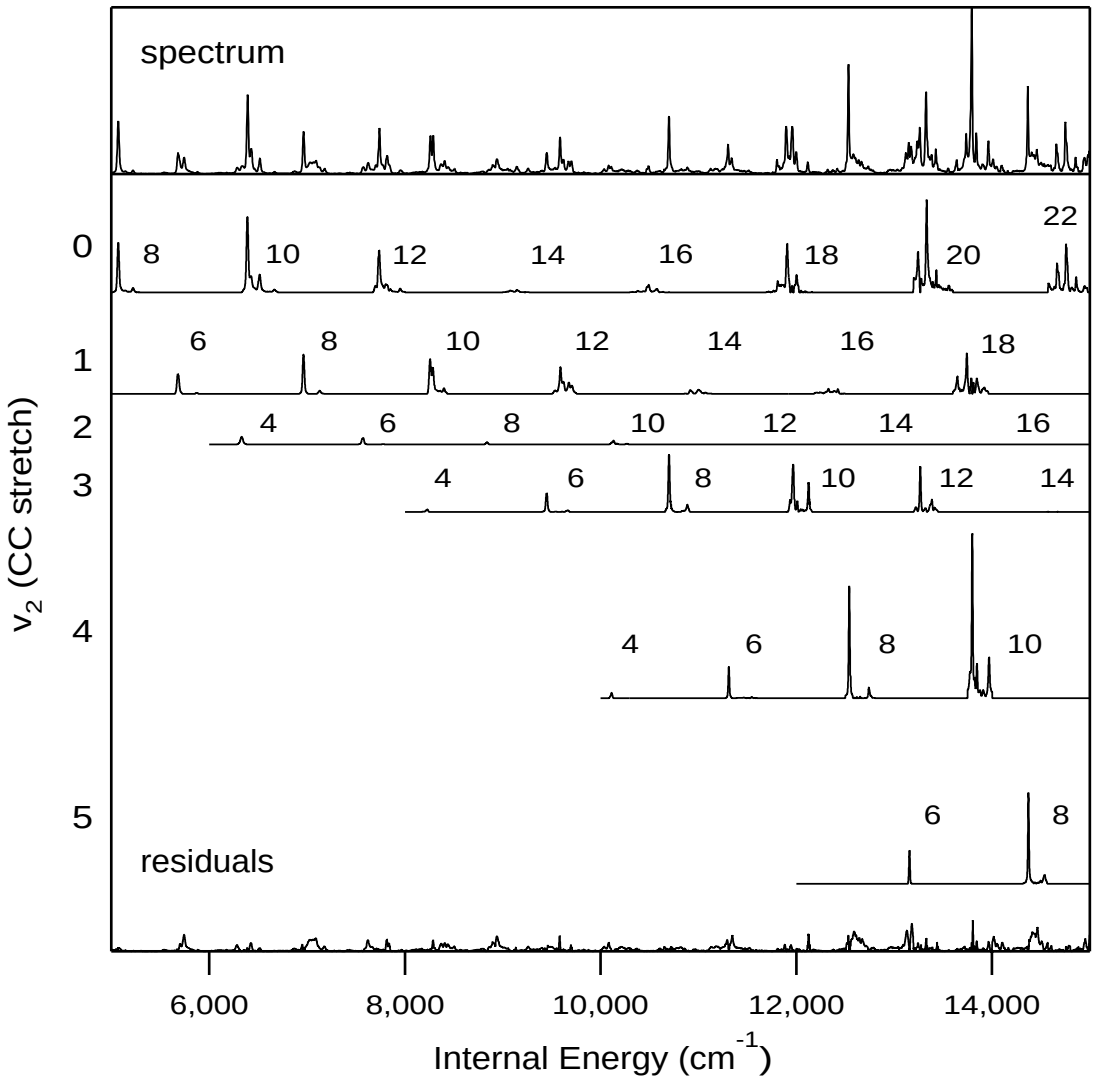

Figure 5-11: The top trace is the 5,000–15,000 cm^{-1} energy region of the $2_0^1 V_0^1 K_0^1$ dispersed fluorescence spectrum recorded via $Q(1)$. The fractionated bright state patterns, which were disentangled from the spectra using numerical pattern recognition, are arranged into progressions below the DF spectrum. Each row contains fractionated bright states with the same number of quanta of CC stretch (v_2) but different number of quanta of *trans* bend (v_4). The bottom trace contains all contributions to the spectral intensity that are not accounted for by the fractionated bright state patterns. The features observed in this residual trace were referred to as "extra features", because they could not be identified as belonging to any of the expected fractionated bright state patterns.

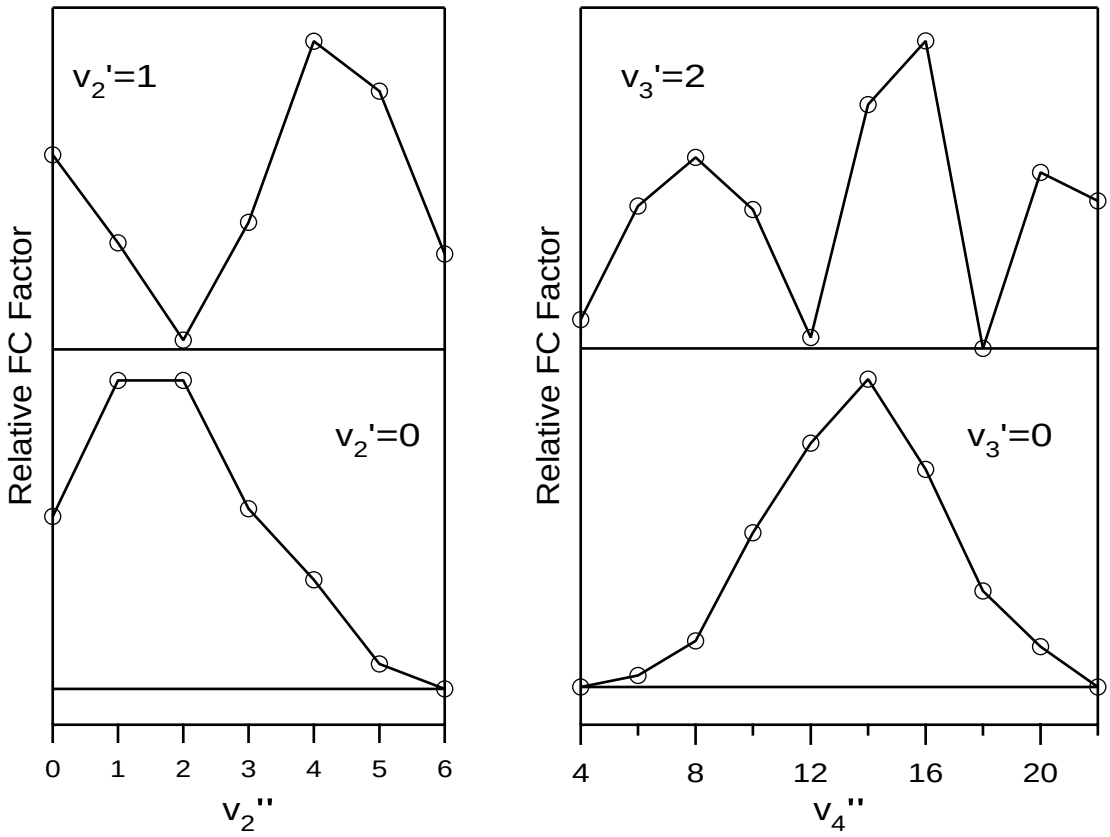

Figure 5-12: Observed Franck-Condon trends. Left: Experimentally determined Franck-Condon factors for the $(0, v_2, 0, 10^{0/2}, 0^0)$ bright states in the $2_0^1 V_0^1 K_0^1$ (top) and origin band (bottom) DF spectra. Right: Experimentally determined Franck-Condon factors for the $(0, 1, 0, v_4^{0/2}, 0^0)$ bright states in the $V_0^2 K_0^1$ (top) and origin band (bottom) DF spectra.

patterns have been assigned correctly. The deperturbed experimental Franck-Condon factors for highly vibrationally excited CC stretch and *trans* bend overtone and combination levels also provides a challenge for theory. J. K. G. Watson has performed harmonic and anharmonic Franck-Condon calculations for the acetylene $S_1 \rightarrow S_0$ system.[81], with good agreement with experiment for the anharmonic calculations.[7] Two groups of theoreticians [82, 83] also plan to perform anharmonic Franck-Condon calculations for acetylene using vibron models.

The polyad quantum number assignments for 134 spectral features below 15,000

[7]Watson points out that the intensities he calculates are not, strictly speaking, Franck-Condon factors because the transition moment must be taken to be dependent on the *trans* bend angle in order to achieve reasonable results.

cm^{-1} are compiled in Tables 5.2 and 5.3. The internal energies in this table were obtained from the fractionated bright state patterns extracted from the higher resolution ($\sim$7 cm^{-1}) set of DF spectra, due to the superior frequency calibration ($\sim$2 cm^{-1}) of these spectra. The relative intensities of the peaks within the polyads, on the other hand, were determined from the lower resolution spectra, which have superior intensity calibration. Both the energies and intensities were determined by fitting Gaussians to individual transitions in the extracted fractionated bright state patterns. A few words of caution regarding this list are in order. First, even in the higher resolution spectra, certain transitions within many of the fractionated bright state patterns were too poorly resolved to be amenable to peakpicking, and thus this list should not be considered to be complete. Second, the relative intensities that are quoted do not necessarily directly reflect the percent of bright state character in each eigenstate. As mentioned previously, for each pair of $N_{\rm res}$ and N_s quantum numbers, *two* polyads are observed, one with ($J = 1$, $\ell = 0$, e parity), and one with ($J = 2$, $\ell = 2$, f parity). At low internal energy, it can be demonstrated that nearly every observed transition in a DF spectrum corresponds to a nearly degenerate pair of these two rotational lines [69]. However, at higher internal energy (i.e., >10,000 cm^{-1}), there is no guarantee that this will be the case, and observed DF transitions could correspond to a single rovibrational line or a conglomeration of several lines. This ambiguity can be resolved by fitting the observed data to an effective Hamiltonian model [70, 84].

Despite these cautions, I believe that Tables 5.2 and 5.3 provide a useful summary of the large quantity of information generated by the application of numerical pattern recognition to the DF data set. The internal energies and relative intensities that are listed for each polyad represent the key features of the observed fractionation patterns. Notice also the sensitivity of the numerical pattern recognition technique. Several spectral features are listed with "relative intensities" of 0.05 or less, meaning that these peaks are observed with intensities of only a few percent of the most intense peak within the polyad. It should be noted that a similar list has been published previously with polyad assignments of spectral features up to 10,000 cm^{-1}

of internal energy, based on the application of *visual* pattern recognition to an earlier DF data set (Table 4 of Ref. [69]). The Table presented here should be considered to supersede this previous list, because certain polyad assignments made previously were incorrect (one of these misassignments has been alluded to previously [70]). The ability to correct these misassignments rests on both having obtained a new extensive, rigorously calibrated DF data set and having used of *numerical*, as opposed to *visual*, pattern recognition.

Figure 5-13 summarizes the results in a somewhat different manner. The fractionated bright states are arranged graphically according to the number of quanta of CC stretch and *trans* bend. This arrangement of the fractionated bright states is particularly convenient from the standpoint of studying trends in IVR, and is referred to within the Field group as an IVR map. Although it is possible to make some qualitative conclusions about trends in IVR from inspecting Fig. 5-13, I have found that quantitative modelling of the trends unearths quite a few insights that are not obvious by eye. In Chapters 9 and 6, the previously published acetylene effective Hamiltonian [5, 70] is refined against all of the progressions of fractionated bright states enclosed in the dotted and dashed boxes in Fig. 5-13, *including states with up to 15,000 cm^{-1} of internal energy*.

The dotted box encloses fractionated bright states with zero quanta of CC stretch, which belong to polyads with $N_s = 0$ (the so-called pure bending polyads). The previously published acetylene effective Hamiltonian reproduced this series of states up to ∼10,000 cm^{-1} ($v_4 = 14$) [70]. The refined effective Hamiltonian described in Chapter 6 extends this agreement (1.4 cm^{-1} RMS error) to 15,000 cm^{-1} ($v_4 = 22$). Among the surprising conclusions of this work is that within the sequence of pure bending bright states, $(0, 0, 0, v_4, 0)$, IVR does *not* increase monotonically with internal energy. Rather, the IVR appears to be the most "complicated", as judged from both frequency and time domain perspectives, at $v_4 = 16$, whereas the dynamics of the bright state with $v_4 = 22$, at nearly 15,000 cm^{-1}, displays a striking regularity over the first few ps.

The sequence of fractionated bright states enclosed in the dashed box, with $v_4 =$

Table 5.2: Polyad quantum number assignments for eigenstates ($N_{\text{res}} < 18$). The ℓ quantum number is not specified because, for each pair of N_{res} and N_s quantum numbers, a pair of polyads are observed: ($J = 1$, $\ell = 0$, e parity) and ($J = 2$, $\ell = 2$, f parity). The observed internal energies (E_{obs}) are listed in units of cm^{-1}. "Rel. Intens." refers to the intensities of the observed lines within a fractionated bright state pattern, relative to the most intense peak within the pattern.

N_{res}	N_s	E_{obs}	Rel. Intens.	N_{res}	N_s	E_{obs}	Rel. Intens.
5	1	3182.3	1.00	14	0	9090.3	0.42
6	0	3770.3	1.00			9102.6	0.34
		3945.6	0.03			9136.2	1.00
7	1	4418.2	1.00			9143.5	0.84
		4430.3	0.50			9162.5	0.45
8	0	5068.8	1.00			9238.0	0.10
		5219.3	0.07			9258.0	0.18
9	1	5676.3	1.00			9266.1	0.17
		5873.6	0.04	15	3	9449.4	1.00
10	2	6329.4	1.00			9665.8	0.07
10	0	6386.1	1.00	15	1	9527.5	0.07
		6423.0	0.22			9586.2	1.00
		6511.0	0.24			9619.3	0.33
		6662.1	0.19			9673.8	0.32
11	1	6960.0	1.00			9700.0	0.35
		7122.6	0.04	16	4	10107.5	1.00
12	2	7570.5	1.00	16	2	10111.5	0.54
		7773.0	0.05			10132.7	1.00
12	0	7698.2	0.15			10167.4	0.19
		7733.6	1.00			10271.6	0.29
		7753.9	0.14	16	0	10374.0	0.16
		7773.3	0.10			10474.8	0.70
		7808.5	0.51			10492.7	1.00
		7836.0	0.19			10549.1	0.17
		7951.5	0.06			10565.0	0.36
13	3	8225.5	1.00			10577.9	0.48
13	1	8255.2	1.00	17	3	10698.1	1.00
		8284.4	0.73			10886.4	0.10
		8397.9	0.20	17	1	10914.8	0.77
14	2	8836.3	1.00			10998.9	1.00
		9012.6	0.07			11015.9	0.68
14	0	9041.0	0.31			11070.7	0.18
		9046.0	0.33			11122.8	0.17
		9073.4	0.93				

Table 5.3: Continuation of Table 5.2, for $N_{\rm res} \geq 18$.

$N_{\rm res}$	N_s	$E_{\rm obs}$	Rel. Intens.	$N_{\rm res}$	N_s	$E_{\rm obs}$	Rel. Intens.
18	4	11309.0	1.00	21	3	13384.4	0.25
		11543.4	0.04			13409.5	0.08
18	2	11414.4	0.35	20	0	13224.7	0.15
		11445.6	1.00			13238.9	0.44
		11478.4	0.14			13327.3	1.00
		11524.1	0.19			13356.5	0.13
		11545.4	0.40			13341.4	0.36
18	0	11812.0	0.23			13428.7	0.25
		11904.0	1.00			13552.9	0.04
		11955.4	0.14	21	1	13641.2	0.40
		12000.8	0.37			13737.9	1.00
19	3	11969.0	1.00			13790.4	0.81
		12010.0	0.24			13840.2	0.55
19	1	12289.6	0.27	22	4	13795.4	1.00
		12306.5	0.37			13845.1	0.18
		12327.2	1.00			13965.1	0.30
		12340.7	0.35	22	2	14053.5	0.37
		12361.0	0.28			14101.2	0.25
		12381.9	0.48			14147.1	0.80
		12397.1	0.36			14157.3	1.00
		12423.4	0.88			14222.8	0.28
20	4	12541.2	1.00			14256.6	0.48
		12649.2	0.03			14279.3	0.25
		12742.5	0.07			14332.5	0.15
20	2	12729.9	0.46	23	5	14368.3	1.00
		12740.0	0.48	23	3	14571.1	1.00
		12760.7	0.59			14671.1	0.81
		12820.0	0.36	22	0	14663.4	0.63
		12843.6	1.00			14677.5	0.39
21	5	13154.6	1.00			14736.0	0.24
21	3	13218.0	0.10			14755.8	1.00
		13266.4	1.00			14767.5	0.59
		13315.2	0.10			14856.2	0.22
				24	6	14983.5	1.00

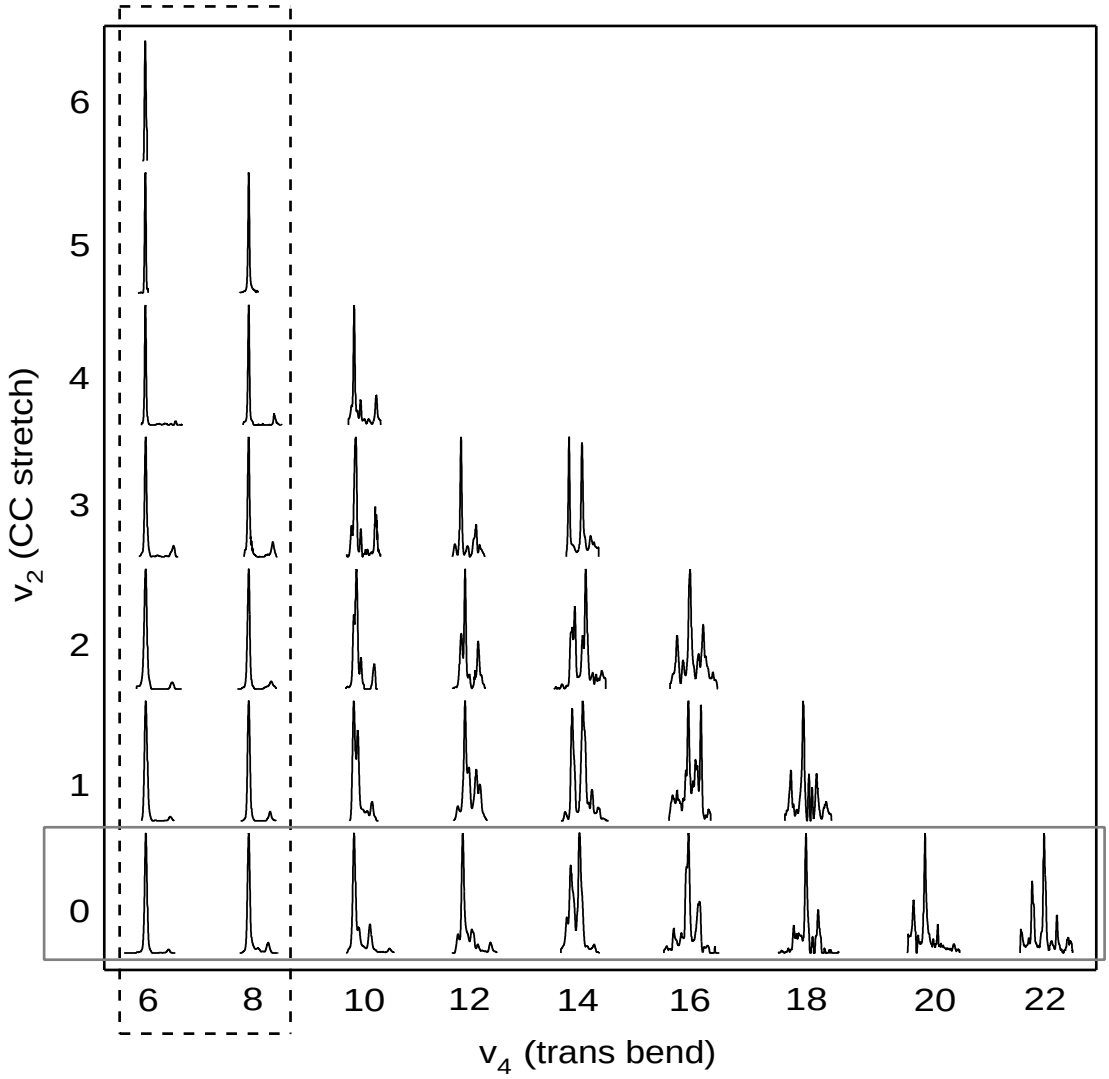

Figure 5-13: IVR map. The fractionated bright state patterns that were extracted by numerical pattern recognition below 15,000 cm^{-1} are arranged according to the corresponding number of quanta of CC stretch and *trans* bend. The dotted box encloses the fractionated bright states with zero quanta of CC stretch, which belong to polyads with $N_s = 0$, the so-called pure bending polyads. The sequence of fractionated bright states enclosed in the dashed box, with $v_4 = 6$ or 8 and $v_2 = 0$–6, is intriguing because increasing quanta of CC stretch appears to result in no notable increase in fractionation.

6 or 8 and v_2 = 0–6, is intriguing because increasing quanta of CC stretch appears to result in no notable increase in fractionation (IVR); if anything, IVR appears to decrease *slightly* with increasing quanta of CC stretch. This trend in the fractionation patterns has been noted previously [69, 85, 86], but a further refinement of the effective Hamiltonian, which is reported in Chapter 9, permits a quantitative explanation for why the effects of stretch-bend resonances appear to be absent for this series of states.

5.8 Conclusion

A new dispersed fluorescence data set for acetylene $S_1 \rightarrow S_0$ emission has been recorded. This data set includes the previously reported origin band spectrum [69] and new DF spectra recorded from four different vibrational levels of the S_1 state of acetylene. The transitions observed in each of these spectra terminate on the same set of S_0 state vibrational levels, leading to a high level of redundancy in the data set. This redundancy is exploited by a numerical pattern recognition approach to the analysis of the spectra, which utilizes the Extended Cross Correlation algorithm (Chapter 2) to associate groups of observed vibrational levels with sets of polyad quantum numbers, even when the spectra are congested and individual transitions overlap with each other.

This pattern recognition approach requires no *a priori* knowledge of the structure of the molecular Hamiltonian. In fact, the technique unexpectedly identified a set of observed transitions as belonging to patterns that are not associated with any set of polyad quantum numbers accessible via the propensity rules for $S_1 \rightarrow S_0$ transitions. The identity of these unexpected transitions is revealed in Chapter 10. The states upon which the remaining observed transitions terminate have been assigned polyad quantum numbers. The success of the numerical pattern recognition approach in making these assignments is strong evidence that no catastrophic breakdown of the polyad quantum numbers occurs by 15,000 cm^{-1}, at least on a time scale faster than $\sim$1 ps (corresponding to the $\sim$7 cm^{-1} resolution of the DF spectra). Preliminary studies of the polyad structure above 15,000 cm^{-1} are discussed in Chapter 10.

The ability to assign polyad quantum numbers to observed transitions using pattern recognition is not simply an academic exercise. Rather, it is an essential first step toward a comprehensive understanding of the dynamics of acetylene in its ground electronic state. Having utilized pattern recognition to apportion the observed transitions among 38 different polyads, the dynamics within each polyad can be studied in detail, as is done in Chapters 9 and 6. Taken together, the dynamics that is encoded in each of these polyad patterns provides a panoramic perspective on the trends in the short-time ($\sim$1 ps) dynamics of the molecule, over a range of internal energy extending to 15,000 cm^{-1} above the zero-point energy.

Acknowledgments

This research has been supported by Dept. of Energy Grant No. DE-FG0287ER13671. My work on this chapter was supported by the Department of the Army under a National Defense Science and Engineering Graduate Fellowship.

Chapter 6

Pure Bending Dynamics

This Chapter, other than the Appendix, has been published in the Journal of Chemical Physics (Ref. [84]).

6.1 Introduction

This chapter is intended as a contribution to the understanding of intramolecular vibrational energy exchange, when it is poorly described by either purely statistical models (i.e., RRKM) or purely separable models (i.e., harmonic oscillator/normal mode descriptions). The system described here is the bending dynamics of acetylene in its electronic ground state. Specifically, I present and analyze a model for the pure bending dynamics of acetylene that reproduces (with 1.4 cm^{-1} RMS error) all available and relevant experimental eigenenergies up to 15,000 cm^{-1} in internal energy (22 quanta of bending excitation). I hope that this system will be of general interest to experimentalists and theoreticians interested in unimolecular dynamics because very large amplitude motions of the molecule, at chemically significant internal energy, are accurately represented by the model presented.

The experimental data on which this model of acetylene bending dynamics is based consist primarily of the dispersed fluorescence (DF) spectra that are described in Chapter 5 (see also Refs. [69] and [68]). The approach to extracting the bending dynamics of acetylene from these spectra consists of two steps: assignment of the spectra, followed by a fit of the assigned transitions to an effective Hamiltonian model. As explained in Chapter 5, the assignments made in the first step of this process are not normal mode quantum numbers, which extensive IVR renders meaningless for most vibrational energy levels at high internal energy, but rather *polyad* quantum numbers [15, 16, 17, 14], which represent approximately conserved vibrational quantities. Polyad numbers have been assigned to hundreds of observed spectral features up to 15,000 cm^{-1}. One subset of these spectral features are those that involve no excitation in the stretch degrees of freedom of the molecule; these states encode the short-time ($\sim$1 ps) pure bending dynamics of acetylene (with up to 22 quanta of bending excitation).

In this chapter an effective Hamiltonian is reported that reproduces all of the observed pure bending levels, including those observed at lower internal energy by absorption spectroscopy. This H^{eff} is similar in structure to previously reported effective Hamiltonians [70, 87], but matches the available data to substantially higher internal energy ($\leq$ 15,000 cm^{-1}). Challenges that are inherent to fitting experimental data at such high internal energy necessitated new methodologies for performing the fit, which are described in Section 6.2. The remainder of the chapter is devoted to analyzing the pure bending dynamics of acetylene, as represented by the H^{eff}, from multiple perspectives. Time-dependent viewpoints on the dynamics are examined first, in Section 6.3, followed in Section 6.4 by a discussion of dilution factors, which are frequently used to quantify the extent of IVR. A framework for understanding the unexpectedly complicated and counterintuitive trends that are outlined in these two sections is presented in Section 6.5, which analyzes the structures of the pure bending polyads.

6.2 Refinement of the Pure Bending H^{eff}

The pure bending dynamics of acetylene are encoded by those fractionated bright states in the bottom row of Fig. 5-13, the "IVR map" that summarizes the results of the pattern recognition analysis of the DF data set. The fractionated bright states in this bottom row are progressions in the *trans* bend mode, $(0, 0, 0, v_4, 0)$, with zero quanta of excitation in all other modes. These bright states are not eigenstates of the molecular Hamiltonian (although at very low internal energy they approximate eigenstates), and the fractionation patterns represent the distribution of bright state character among the eigenstates.

Since the $(0, 0, 0, v_4, 0)$ bright states have zero quanta of excitation in all of the stretching modes, they all belong to polyads with $N_s = 0$ (see Section 5.1), which are referred to as pure bending polyads. For this set of polyads, the N_{res} quantum number simplifies to

$$N_{\text{res}} = v_4 + v_5 = N_b,$$

in which N_b, the number of quanta of bending excitation, is introduced as a shorthand notation for the $N_{\rm res}$ and N_s polyad numbers for the pure bending polyads. It should also be noted that g/u symmetry with respect to the center of inversion is conserved by all resonances in a $D_{\infty h}$ molecule, and thus can also be used to label eigenstates, as well as the rigorously conserved total angular momentum quantum number, J, and parity, which can be labeled using either the $+/-$ or e/f conventions. Thus, to identify a pure bending polyad uniquely, a total of 5 labels need to be specified: N_b, ℓ, J, g/u, and parity. The discussion below will consider only $J = 0$ states, and pure bending polyads will be labeled using the shorthand notation $[N_b, \ell]^{g+}$.

One of the earliest effective Hamiltonians for the pure bending levels of acetylene was defined by Josef Plíva [87]. This $H^{\rm eff}$ included 40 molecular constants that were fit to ∼1200 rovibrational levels of the S_0 state that had been observed by infrared absorption spectroscopy, with a standard deviation of 0.006 $\rm cm^{-1}$. All of the rovibrational levels included in Plíva's fit lay below 3000 $\rm cm^{-1}$ of internal energy, and thus the parameters from that work cannot be expected to represent accurately the highly excited bending levels that are the subject of the present study.

More recently, an effective Hamiltonian has been reported by Abbouti Temsamani, Herman, Solina, O'Brien and Field [70] (hereafter referred to as THSOF) that reproduces the energies of 41 bending vibrational levels of acetylene (up to 8000 $\rm cm^{-1}$) to ± 0.35 $\rm cm^{-1}$ (1σ) accuracy. The THSOF $H^{\rm eff}$ resulted from minor modifications of an $H^{\rm eff}$ previously described by Abbouti Temsamani and Herman [5], which was fit to 122 vibrational levels with $E_{\rm vib} < 12{,}000$ $\rm cm^{-1}$, primarily with $N_s \neq 0$. It is worth noting that the terms included in the THSOF bending $H^{\rm eff}$ are nearly identical to those included by Plíva.

The THSOF $H^{\rm eff}$ has been demonstrated to have substantial predictive power at energies higher than the levels included in the fit. Specifically, as can be seen in Fig. 6-1(a), the THSOF $H^{\rm eff}$ reproduces the key qualitative features of the $(0, 0, 0, 14^{0/2}, 0^0)$ fractionated bright state. There is a one-to-one correspondence between the intense transitions predicted by the $H^{\rm eff}$ (sticks) and the observed transitions (solid line). The predicted and observed eigenenergies differ by up to 15 $\rm cm^{-1}$, but the pattern

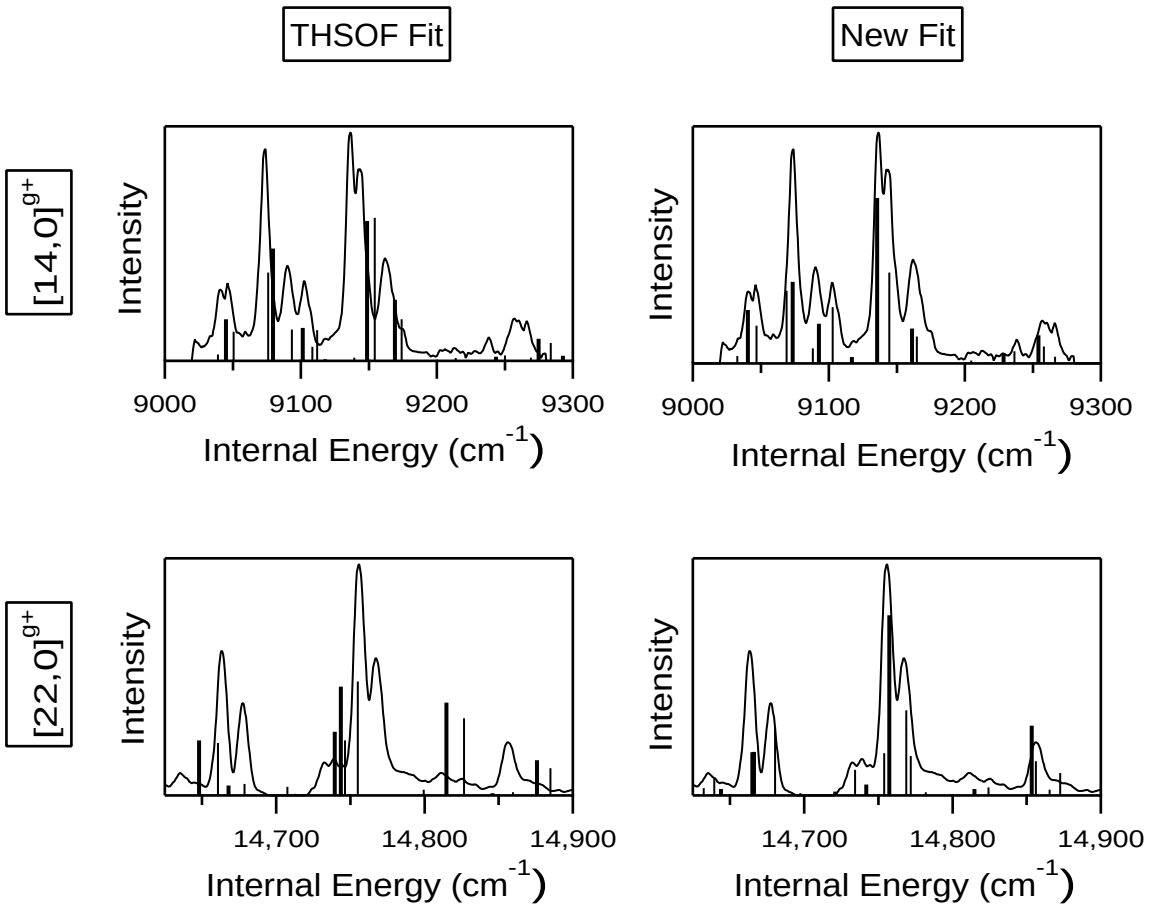

Figure 6-1: Comparison of predictions of the H^{eff} (vertical lines) with the experimentally observed bright state fractionation patterns (solid line). The thick vertical lines correspond to ($J = 1$, $\ell = 0$, e parity); the thin vertical lines represent ($J = 2$, $\ell = 2$, f parity). The left column depicts the predictions of the THSOF H^{eff} model, while the right column depicts the predictions of the refined H^{eff} reported here.

of relative intensities predicted by the H^{eff} bears a strong qualitative resemblance to the DF data.

It should be noted that a discrepancy between the THSOF H^{eff} model and the experimental data for this polyad, which was discussed in Ref. [70], has now been resolved. The peak at 8945 cm^{-1} in Fig. 2 of Ref. [70], which deviated substantially from the predictions of the H^{eff} was, in fact, misassigned previously. The pattern recognition analysis in Chapter 5, which is the basis for the results presented in this chapter, proved that this peak is not assignable to *any* of the expected polyads at this internal energy, and thus this peak has been classified as an "extra pattern".

Note that this peak therefore does not belong to the ($N_s = 4, N_{\rm res} = 14$) polyad, as speculated previously [70].

Above 10,000 cm^{-1}, the agreement between the THSOF $H^{\rm eff}$ and the experimental data degrades substantially. Fig. 6-1 depicts the agreement for the $(0, 0, 0, 22^{0/2}, 0^0)$ fractionated bright state. The THSOF $H^{\rm eff}$ predicts a pattern of eight intense peaks, whereas only five intense peaks are observed experimentally. Of course, it is not reasonable to expect an $H^{\rm eff}$ that has been fit to data only up to 8,000 cm^{-1} to have substantial predictive power at 15,000 cm^{-1}. For this reason, I have performed a refinement of the THSOF $H^{\rm eff}$, which utilizes all of the experimental data that were previously included in the THSOF fit, plus 42 new pure bending vibrational levels, with up to 15,000 cm^{-1} of internal energy, which were identified in the DF data set as described in Chapter 5. Thus, the fit reported here utilizes double the number of vibrational levels as the THSOF fit, and extends to nearly twice as high of an internal energy.

The data included in the fit are listed in Tables 6.1 and 6.2. The column marked ℓ in this table requires explanation. All data that were included in the THSOF fit were $J = 0$ internal energies. For the DF data, which do not access $J = 0$ rotational levels, these rotationless vibrational energies were *inferred* from the experimental data, by subtracting out the "$2B$ rotational contribution . . . prior to the fit" [70]. This approach implicitly assumes that the fractionation pattern for a ($J = 0$, $\ell = 0$) polyad, which is not observed experimentally in the DF spectra, will be identical to that of the corresponding ($J = 1$, $\ell = 0$) polyad that is observed experimentally, other than a constant shift of $2B$. This assumption would be rigorously correct in the absence of vibration-rotation coupling; in practice, deviations from this assumption are negligible compared with the uncertainties in the observed transition frequencies, even at 15,000 cm^{-1}.

However, the ($J = 1$,$\ell = 0$) lines are only one of two sets of rotational lines that are observed in the DF spectra, the other set being ($J = 2$,$\ell = 2$). Unfortunately, it *cannot* be assumed that the fractionation patterns for the ($J = 2$,$\ell = 2$) polyads are the same, except for a constant shift, as the unobserved ($J = 0$,$\ell = 0$) polyads,

because the $\ell = 2$ polyads do not contain the same number of states as the corresponding $\ell = 0$ polyads. In the THSOF fit, the ($J = 2$,$\ell = 2$) lines could be safely ignored, because it can be demonstrated that, at low internal energy, these lines tend to be nearly perfectly blended with corresponding ($J = 1$,$\ell = 0$) lines due to a coincidence arising from the signs and magnitudes of the g_{44} and B parameters [69]. At higher internal energy, the situation is rather different. Although some pairs of ($J = 1$,$\ell = 0$) and ($J = 2$,$\ell = 2$) levels can be observed, see Fig. 6-1, they tend to be resolvable at the experimental resolution. Throwing out the observed ($J = 2$,$\ell = 2$) lines at high internal energy would result in a loss of information that is valuable from the standpoint of fitting the desired parameters.

Rather than attempt to infer the energies of the rotationless vibrational levels from the data, the fit reported here utilizes the *ro*vibrational energies that can be determined directly from the data. In a technical sense, this implies that for each pure bending polyad observed experimentally, two matrices were diagonalized in the fit, one for ($J = 2$, $\ell = 2$) and one for ($J = 1$, $\ell = 0$). The rotational energies of the zero-order states were calculated using

$$E_{\text{rot}} = B_v J(J+1) \tag{6.1}$$

$$B_v = B_0 - \sum_{k=1}^{5} \alpha_k v_k \ , \tag{6.2}$$

and the values of the rotational parameters were constrained to those listed in Table V of Ref. [70]. For those observed transitions that did correspond to an unresolvable pair of ($J = 2$, $\ell = 2$) and ($J = 1$, $\ell = 0$) levels, marked "$0^+/2$" in Table 6.1, the two corresponding calculated eigenenergies were averaged to estimate the approximate location of the maximum of the peak that would be observed experimentally.

The new fit also differs from the previous fit in several other technical details. First, two new parameters were included: y_{445} and y_{555} (the previous fit had included only y_{444} and y_{455}). The effective Hamiltonian used here therefore includes the diag-

Table 6.1: The 51 pure bending vibrational levels, observed by DF spectroscopy (Chapter 5), that are included in the effective Hamiltonian fit. The columns N_b, ℓ, and g/u specify the polyad assignments of the vibrational levels included in the fit. For the $\ell = 0$ polyads, the parity of the vibrational wavefunctions is specified as a superscript; that is, "+" specifies a vibrational wavefunction of $\Sigma^+_{g/u}$ symmetry species, and "−" specifies $\Sigma^-_{g/u}$. All energies are in units of cm^{-1}.

N_b	ℓ	g/u	E_{obs}	E_{calc}	N_b	ℓ	g/u	E_{obs}	E_{calc}
6	$0^+/2$	g	3770.3	3770.1	16	0^+	g	10374.0	10376.4
6	0^+	g	3942.5	3942.6	16	$0^+/2$	g	10474.8	10471.9
6	2	g	3949.5	3949.5	16	$0^+/2$	g	10492.7	10489.5
8	$0^+/2$	g	5068.8	5070.5	16	2	g	10549.1	10548.5
8	0^+	g	5216.0	5217.6	16	$0^+/2$	g	10565.0	10564.1
8	2	g	5221.0	5223.9	16	$0^+/2$	g	10577.9	10575.6
10	$0^+/2$	g	6386.1	6386.4	18	$0^+/2$	g	11812.0	11812.8
10	$0^+/2$	g	6423.0	6424.3	18	$0^+/2$	g	11904.0	11900.8
10	2	g	6462.1	6462.4	20	0^+	g	13238.9	13238.5
10	2	g	6511.0	6513.7	20	$0^+/2$	g	13327.3	13326.7
10	0^+	g	6658.5	6660.2	20	2	g	13341.4	13340.9
10	2	g	6664.5	6667.6	20	2	g	13356.5	13359.4
12	$0^+/2$	g	7733.6	7731.6	20	$0^+/2$	g	13552.9	13551.1
12	2	g	7753.9	7753.8	20	$0^+/2$	g	13428.7	13426.4
12	$0^+/2$	g	7773.3	7772.9	20	2	g	13224.7	13228.1
12	0^+	g	7808.5	7806.4	20	2	g	13443.4	13441.8
12	2	g	7814.0	7813.0	22	0^+	g	14663.4	14665.0
12	0^+	g	7836.0	7834.4	22	2	g	14677.5	14680.2
12	2	g	7843.0	7841.0	22	$0^+/2$	g	14736.0	14736.5
12	$0^+/2$	g	7951.5	7949.0	22	0^+	g	14755.8	14757.4
14	0^+	g	9041.0	9040.6	22	2	g	14767.5	14768.8
14	2	g	9046.0	9046.8	22	$0^+/2$	g	14856.2	14854.2
14	$0^+/2$	g	9073.4	9071.1					
14	$0^+/2$	g	9090.3	9091.4					
14	2	g	9102.6	9102.8					
14	0^+	g	9136.2	9135.6					
14	2	g	9143.5	9144.5					
14	$0^+/2$	g	9162.5	9162.6					
14	2	g	9238.0	9236.2					

Table 6.2: Continuation of Table 6.1. The 32 pure bending vibrational levels, observed through absorption spectroscopy, that were previously included in the THSOF fit and are also included in the fit reported here.

N_b	ℓ	g/u	E_{obs}	E_{calc}
1	1	g	612.9	612.8
1	1	u	730.3	730.3
2	0^+	g	1230.4	1230.7
2	0^+	g	1449.1	1449.1
2	2	g	1233.5	1233.7
2	2	g	1463.0	1463.0
2	0^+	u	1328.1	1328.0
2	0^-	u	1340.5	1340.4
2	2	u	1347.5	1347.5
3	1	g	1855.7	1856.4
3	1	g	2049.1	2049.0
3	1	g	2067.0	2066.9
3	3	g	1861.9	1862.4
3	3	g	2084.8	2084.8
3	1	u	1941.2	1941.3
3	1	u	1960.9	1961.1
3	1	u	2170.3	2170.5
3	3	u	1972.6	1972.8
3	3	u	2198.1	2198.2
4	0^+	g	2648.0	2648.1
4	0^+	g	2880.2	2880.5
4	0^-	g	2661.2	2661.2
4	2	g	2666.1	2666.3
4	2	g	2894.1	2894.4
4	0^+	u	2560.6	2561.1
4	0^+	u	2757.8	2757.8
4	0^-	u	2583.8	2584.3
4	0^-	u	2783.6	2783.7
4	2	u	2561.5	2561.9
4	2	u	2589.7	2590.2
4	2	u	2773.2	2773.1
4	2	u	2795.5	2795.5

onal elements

$$\begin{aligned}\langle v_4^{\ell_4}, v_5^{\ell_5}|H^{\rm eff}|v_4^{\ell_4}, v_5^{\ell_5}\rangle &= \omega_4 v_4 + \omega_5 v_5 + \\ & x_{44}v_4^2 + x_{45}v_4v_5 + x_{55}v_5^2 + \\ & y_{444}v_4^3 + y_{445}v_4^2v_5 + y_{455}v_4v_5^2 + y_{555}v_5^3 + \\ & g_{44}\ell_4^2 + g_{45}\ell_4\ell_5 + g_{55}\ell_5^2 \end{aligned} \tag{6.3}$$

and the following off-diagonal elements (and their Hermitian conjugates):
(a) Darling-Dennison Bend I

$$\begin{aligned}&\langle v_4^{\ell_4}, v_5^{\ell_5}|H^{\rm eff}|(v_4-2)^{\ell_4}, (v_5+2)^{\ell_5}\rangle = \\ &\quad \frac{s_{45}}{4}[(v_4^2-\ell_4^2)(v_5+\ell_5+2)(v_5-\ell_5+2)]^{1/2} \ , \end{aligned} \tag{6.4}$$

(b) Darling-Dennison Bend II

$$\begin{aligned}&\langle v_4^{\ell_4}, v_5^{\ell_5}|H^{\rm eff}|(v_4-2)^{\ell_4\mp 2}, (v_5+2)^{\ell_5\pm 2}\rangle = \\ &\quad \frac{r_{45}+2g_{45}}{16}[(v_4\pm\ell_4)(v_4\pm\ell_4-2)(v_5\pm\ell_5+2)(v_5\pm\ell_5+4)]^{1/2} \ , \end{aligned} \tag{6.5}$$

(c) vibrational ℓ-doubling

$$\begin{aligned}&\langle v_4^{\ell_4}, v_5^{\ell_5}|H^{\rm eff}|v_4^{\ell_4\pm 2}, v_5^{\ell_5\mp 2}\rangle = \\ &\quad \frac{r_{45}}{4}[(v_4\mp\ell_4)(v_4\pm\ell_4+2)(v_5\pm\ell_5)(v_5\mp\ell_5+2)]^{1/2} \ , \end{aligned} \tag{6.6}$$

in which

$$r_{45} = r_{45}^{\circ} + r_{445}(v_4-1) + r_{455}(v_5-1) \ . \tag{6.7}$$

A second technical detail concerning the fit is that the infrared absorption data were weighted more strongly than the DF data (25:1 ratio), because the absorption data are calibrated to higher accuracy than the DF data (<0.01 $\rm cm^{-1}$ vs. $\sim$2 $\rm cm^{-1}$). Note that the weighting ratio differs considerably from the ratio of the reciprocal squared uncertainties associated with the data. The use of the reciprocal squared

uncertainties as weights would be most appropriate if random measurement error were the only source of discrepancies between the fitted model and the experimental observations. However, there is no reason to believe that the H^{eff} model would perfectly fit the data in the absence of measurement error; the truncation of the Dunham expansion for the diagonal elements and the possible omission of weak or localized perturbations from the model can both introduce small, seemingly random deviations from the experimental data. Other ratios of weights were tested but resulted in little change in the fitted parameters.

The methodology of the fit also had to be modified in order to meet certain challenges that are inherent in fitting data at internal energy as high as 15,000 cm^{-1}. First, at the outset of the fit, at high internal energy (e.g. $N_b = 22$) it was not obvious which calculated eigenstates corresponded to which observed transitions (see Fig. 6-1(b)). For this reason, the fit had to be performed in a bootstrapping fashion, by first refining the quality of the fit below 10,000 cm^{-1}, and then gradually adding in eigenenergies above 10,000 cm^{-1}, until the correspondence between the observed and calculated eigenenergies became obvious up to 15,000 cm^{-1}. At this point, all intense, sharp peaks in the DF spectra were included in the fit.

Even when the correspondence between observed transitions and calculated eigenstates is obvious by eye, it is not always trivial to establish this correspondence numerically. Generally, only a small fraction of the eigenstates within a given polyad are observable within the signal-to-noise of the experiment, and the fitting routine must decide in an automated fashion which calculated eigenstate corresponds to which observed transition in order to calculate the (χ^2) merit function. When the correspondence is obvious visually, it is usually because *both* the frequency *and* the intensity of the calculated transition match well with those of the observed line, and this criterion can be encoded numerically by defining a metric, $M_{c,o}$, which quantifies how well a calculated eigenstate c and an observed transition o match each other:

$$M_{c,o} = M^E_{c,o} M^I_{c,o} \tag{6.8}$$

$$M^E_{c,o} = \exp\left\{-\frac{(E_c - E_o)^2}{2(\Delta E)^2}\right\} \tag{6.9}$$

$$M^I_{c,o} \;=\; \exp\left\{-\frac{[(I_c - I_o)/(I_c + I_o)]^2}{2(\Delta I)^2}\right\}. \tag{6.10}$$

This metric is defined to be the product of two factors, $M^E_{c,o}$ and $M^I_{c,o}$, which quantify the frequency and intensity match, respectively. Each of these factors is defined as a Gaussian function of the discrepancy between the observed and calculated quantities, such that the metric $M_{c,o}$ can attain a value near 1.0 only if *both* the frequencies *and* intensities match well. The quantities ΔE and ΔI define what is meant by "a good match" for the frequencies and intensities, respectively. For the fits reported here, $\Delta E = 5$ cm^{-1} and $\Delta I = 0.2$. Each time that the merit function was calculated during the fit (which utilized a modified version of the Numerical Recipes [44] Levenberg-Marquardt algorithm), the value of the metric $M_{c,o}$ was calculated for each observed transition that was included in the fit, o, with every calculated eigenstate, c. The calculated eigenstate with the largest value of the metric $M_{c,o}$ with a given observed transition was assumed to be the correct match, and was used to calculate the merit function.

The final parameters that were obtained from this fit are listed in Table 6.3, along with estimated uncertainties in the parameters that were determined from the covariance matrix. This set of parameters reproduces the 83 eigenenergies included in the fit to ± 1.4 cm^{-1} (1σ). All of the parameters have been determined to greater precision than in the THSOF fit, but most of the parameters have not changed by much more than the 2σ error that was reported in the THSOF fit. The exceptions are x_{44}, y_{455}, r°_{45}, and r_{545}, which were previously reported as 3.600, 0.093, -5.942, and -0.167 cm^{-1} respectively (the new values are 3.483, 0.0242, -6.193, and 0.0110). The likely reason that the first two of these parameters changed by substantial amounts is that the THSOF fit imposed the constraint that $y_{445} = y_{555} = 0.0$. The r°_{45} and r_{545} parameters are much better determined in the current fit due to the inclusion of states at high internal energy ($\sim$15,000 cm^{-1}) which are coupled very strongly by the Darling-Dennison resonances that are parameterized by the r°_{45} and r_{545} constants. However, despite the fact that most of the parameters have not changed by large amounts relative to the THSOF fit, the improvement in the qualitative agreement

Table 6.3: Parameters determined from least-squares fit of the pure bending effective Hamiltonian to the data set described in the text. Numbers in parentheses are 2σ uncertainties in the last digit. All parameters are in units of cm^{-1}.

ω_4	608.657 (34)	y_{444}	-0.03060 (72)
ω_5	729.137 (38)	y_{445}	0.0242 (48)
x_{44}	3.483 (13)	y_{455}	0.0072 (52)
x_{45}	-2.256 (28)	y_{555}	0.00955 (84)
x_{55}	-2.389 (14)	r°_{45}	-6.193 (32)
g_{44}	0.677 (22)	r_{445}	0.0304 (48)
g_{45}	6.670 (30)	r_{545}	0.0110 (64)
g_{55}	3.535 (20)	s_{45}	-8.574 (52)

between the calculated and observed spectrum in Fig. 6-1 is quite dramatic at 15,000 cm^{-1}, and even at 9,000 cm^{-1}.

It is worth reiterating that the development of an H^{eff} with predictive power up to 15,000 cm^{-1} is only possible because single fractionated bright states can be extracted from the DF data set using numerical pattern recognition, despite severe, systematic overlap between many fractionated bright state patterns. This numerical procedure would have been infeasible if the polyad quantum numbers were not at least approximately conserved. In addition, the polyad numbers are rigorously conserved by the H^{eff} model, and the ability of this model to predict quantitatively the bright state fractionation patterns provides additional evidence for the conservation of the polyad numbers on a time scale of $\sim$1 ps. Further, for the pure bending polyads, only a small number of resonances (Darling-Dennison and vibrational ℓ-resonance) are necessary in order to accurately describe the short-time dynamics. The remainder of this chapter is devoted to exploring the insights into the short-time bending dynamics of acetylene that this H^{eff} permits.

6.3 Time Domain Dynamics

The bright states that are accessed experimentally are not eigenstates of the H^{eff}. In the frequency domain, this fact is manifested by a fractionation of the bright state. In

the time domain, the bright state is not stationary, and its time-evolution is governed by

$$\Psi(t) = \sum_{j=1}^{N} c_j \psi_j e^{-i\omega_j t} \ , \tag{6.11}$$

in which ψ_j are the eigenstates, ω_j are the corresponding frequencies ($E_j/\hbar$), $\Psi(0)$ is the bright state, $c_j = \langle \Psi(0) | \psi_j \rangle$, and N is the number of states within the relevant polyad. The coefficients c_j are known from the unitary transformation that diagonalizes the H^{eff}, and thus the time-evolution of the initially prepared bright state is completely determined from information obtainable from the frequency domain spectrum.

The survival probability of the initially prepared state, $|\langle \Psi(0) | \Psi(t) \rangle|^2$, is frequently used to represent this dynamics, and in the second column (dotted lines) of Fig. 6-2 are presented the survival probabilities for the $(0,0,0,10^0,0^0)$, $(0,0,0,16^0,0^0)$, and $(0,0,0,22^0,0^0)$ bright states. For comparison, the fractionation patterns of the bright states (as predicted by the H^{eff}) are also depicted in the first column of Fig. 6-2 (note that the linewidth has been added only for ease of viewing). These two representations of the dynamics, of course, have the same information content; however, they can be considered to be complementary in terms of *conceptualization* of the dynamics.

The survival probability does not, however, provide a complete picture of the dynamics, in the sense that when the survival probability is low, the overlap of the wavepacket with other zero-order states must be relatively large . . . but which zero-order states? One could, of course, calculate the overlap of the time-evolving wavepacket with any of the zero-order states in the relevant polyad, but for the $[22,0]^{g+}$ polyad, for example, the total number of zero-order states is 42, and it is not practical to plot the overlap of the wavepacket with *each* of these states. For this reason, only one such trace is plotted in the second column, which is the overlap squared of the time-evolving wavepacket with the zero-order state $(0,0,0,(N_b-2)^0,2^0)$ (solid line). This zero-order state is chosen because it is one of only two states within any pure bending polyad that is coupled directly with the bright state $(0,0,0,N_b^0,0^0)$ by the known anharmonic resonances. In particular, this state couples to the bright

states *via* the Darling-Dennison I resonance; the other state that couples directly to the bright state is $(0,0,0,(N_b-2)^{+2},2^{-2})$, *via* the Darling-Dennison II resonance. These two states are referred to as *gateway* states because, in order for the vibrational excitation to flow from the bright state into the remainder of the polyad, it must first flow through the $(0,0,0,(N_b-2)^{0},2^{0})$ and $(0,0,0,(N_b-2)^{+2},2^{-2})$ states.

To complement the time-dependent overlap of the wavepacket with the bright state and one of the two gateway states, two other time-domain representations of the dynamics are also presented in Fig. 6-3: the time evolutions of the expectation values of the number operators, $\hat{v}_4$, $\hat{v}_5$, $\hat{\ell}_4$, and $\hat{\ell}_5$:

$$\langle v_b(t)\rangle = \langle\Psi(t)|\hat{v}_b|\Psi(t)\rangle \ , \tag{6.12}$$

$$\langle \ell_b(t)\rangle = \langle\Psi(t)|\hat{\ell}_b|\Psi(t)\rangle, \ b=4,5. \tag{6.13}$$

In colloquial terms, $\langle v_4(t)\rangle$ and $\langle v_5(t)\rangle$ represent the time-dependent average number of quanta in the *trans* and *cis* bending modes, respectively, and $\langle \ell_4(t)\rangle$ and $\langle \ell_5(t)\rangle$ are the time-dependent average number of quanta of vibrational angular momentum. Thus, in the absence of plots of the overlap of the wavepacket with every one of the relevant zero-order states, these time-dependent expectation values provide some insight into the dynamics of the wavepacket within the interior of the polyad, which is comprised of zero-order states that are not directly coupled to the bright state. Note that $\langle v_4(0)\rangle = N_b$, $\langle v_5(0)\rangle = \langle \ell_4(0)\rangle = \langle \ell_5(0)\rangle = 0$, and that $\langle v_4(t)\rangle + \langle v_5(t)\rangle = N_b$ and $\langle \ell_4(t)\rangle + \langle \ell_5(t)\rangle = \ell$ at all times. The signs of $\langle \ell_4(t)\rangle$ and $\langle \ell_5(t)\rangle$ are arbitrary.

Consider first the insights that Figs. 6-2 and 6-3 provide into the dynamics associated with the $(0,0,0,10^{0},0^{0})$ bright state. Both the frequency and time domain representations of the IVR associated with this bright state emphasize the relative simplicity of the dynamics at low internal energy ($\sim$6,000 cm^{-1}). The fractionation pattern contains predominantly one main peak and two smaller peaks at higher internal energy which might be described as perturbers of the bright state (note that one of these two smaller peaks is blended and represents two eigenstate transitions). Together, these four eigenstates account for nearly 99% of the bright state charac-

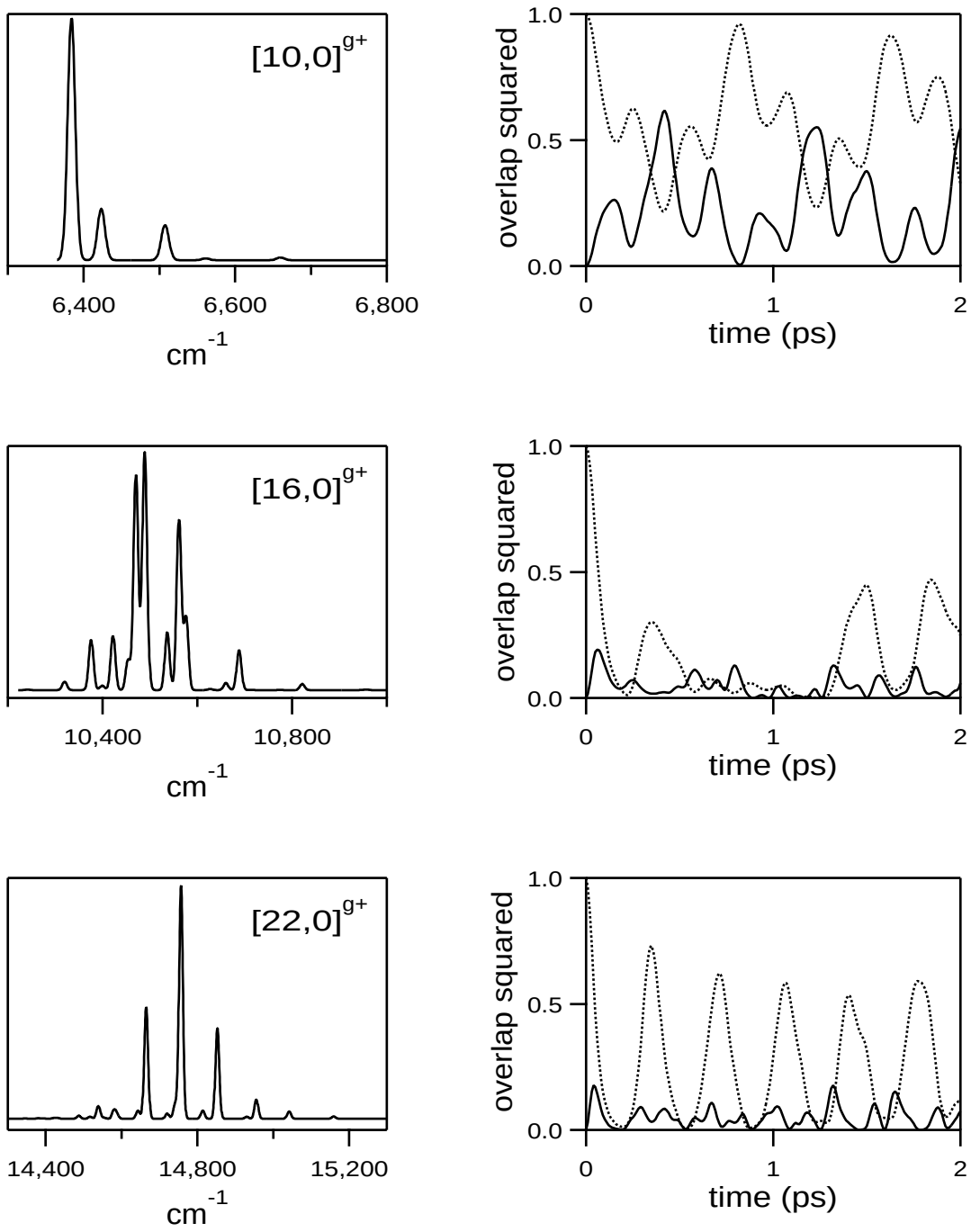

Figure 6-2: Predictions of the H^{eff} for three pure bending polyads, $[10,0]^{g+}$, $[16,0]^{g+}$, and $[22,0]^{g+}$. Left column: fractionation patterns of the bright state, $(0,0,0,{v_4}^0,0^0)$ in each polyad. Right column: survival probability for the bright state, over the first 2.0 ps (dotted line) and time-dependent projection squared of the wavepacket onto one of the two gateway states, $(0,0,0,(v_4-2)^0,2^0)$ (solid line).

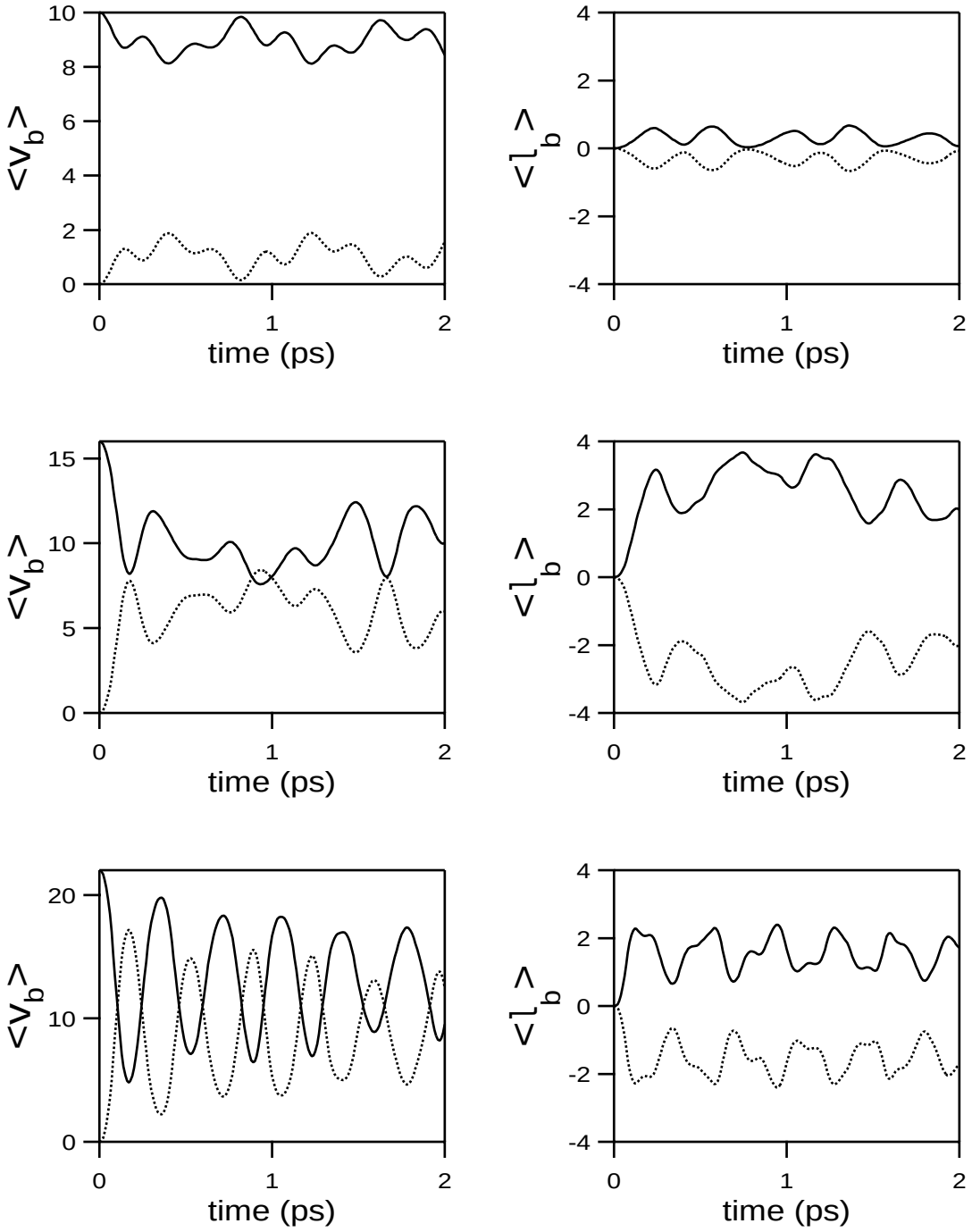

Figure 6-3: Continuation of Fig. 6-2. Left column: average number of quanta (v_4, v_5) in the *trans* (solid line) and *cis* bend (dotted line) modes as a function of time. Right column: average number of quanta of vibrational angular momentum (ℓ_4, ℓ_5) in the two bending modes as a function of time.

ter (the most intense peak accounts for 72.7%). In the time domain, the survival probability of the bright state displays a multiple quantum beating pattern, which also underscores the small number of levels involved in the dynamics. The survival probability never falls below 20%, at least not during the first 2.0 ps. The overlap of the wavepacket with the gateway state $(0,0,0,8^0,2^0)$ nearly mirrors the survival probability, indicating that much of the dynamics of the wavepacket is accounted for by transfer of the vibrational excitation between the bright state and the gateway states. The wavepacket never substantially populates the interior of the polyad, as seen in the plots of $\langle v_b(t)\rangle$ and $\langle \ell_b(t)\rangle$; during the first 2.0 ps of the dynamics, only about two quanta of the *trans* bend excitation are exchanged for *cis* bending excitation, which also indicates that the wavepacket evolution tends not to proceed beyond the gateway states.

In $[16,0]^{g+}$, the dynamics is strikingly different. The fractionation pattern for the $(0,0,0,16^0,0^0)$ bright state is very complicated; the eigenstate with maximal intensity accounts for only 24.6% of the bright state character. In the time domain, the survival probability of the bright state displays a fast early-time decay followed by a series of irregular partial recurrences. The $1/e$ time (τ) for the initial decay is $\sim$80 fs, and by 220 fs, the survival probability reaches a minimum value of less than 0.02. The overlap of the wavepacket with the gateway state in this case does not even approximately mirror the survival probability, which indicates that the wavepacket passes through the gateway state and into the interior of the polyad. As a result, the *trans* and *cis* bend degrees of freedom exchange substantial vibrational excitation as well as angular momentum, as seen in the plots of $\langle v_b(t)\rangle$ and $\langle \ell_b(t)\rangle$. Thus, both the time and frequency domain indicate a drastic change in the nature and extent of the IVR from 6,000 cm^{-1} to 10,000 cm^{-1}. Of course, the two intervening pure bending polyads ($[12,0]^{g+}$, $[14,0]^{g+}$) have been omitted from Figs. 6-2 and 6-3, and the change in the qualitative behavior is gradual from $[10,0]^{g+}$ to $[16,0]^{g+}$.

This qualitative change in behavior would *seem* to be accounted for trivially in terms of the increase in the number of states in each polyad and the strength of the matrix elements that couple them. However, the dynamics associated with the

$(0,0,0,22^0,0^0)$ bright state indicate that such an argument is overly simplistic. From $[16,0]^{g+}$ to $[22,0]^{g+}$, the size of the polyads continues to grow as well as the magnitudes of the off-diagonal matrix elements, but the fractionation pattern and survival probability for the $(0,0,0,22^0,0^0)$ bright state actually appear to be *less* complicated than those for the $(0,0,0,16^0,0^0)$ bright state. A total of only three eigenstates account for 72.0% of the bright state character; the most intense peak accounts for 43.3%. Although the early-time decay in the survival probability for $(0,0,0,22^0,0^0)$ is somewhat faster ($\tau \approx 60$ ps) than that for the $(0,0,0,16^0,0^0)$ ($\tau \approx 80$ ps), the $(0,0,0,22^0,0^0)$ survival probability displays a series of strikingly regular, and strong (>50%), partial recurrences. On the other hand, the overlap of the wavepacket with the gateway state, $(0,0,0,20^0,2^0)$, appears to be at least as complicated as the corresponding trace for $N_b = 16$. The regular series of recurrences in the survival probability is not, therefore, due to simple quantum beating between the bright state and the gateway states. Rather, the recurrences are mirrored in the strong oscillations of $\langle v_b(t)\rangle$, and to a lesser extent, $\langle \ell_b(t)\rangle$, indicating that some regularity is preserved in the dynamics despite the fact that the wavepacket penetrates deeply into the interior of the polyad.

Taken together, the plots in Figs. 6-2 and 6-3 indicate that the extent and complexity of IVR for the *trans* bending bright states in the pure bending polyads is not a simple function of internal energy. Without a conceptual framework for understanding the unexpectedly complicated trends in the IVR, the dynamics in the $[22,0]^{g+}$ polyad seems mysterious, being both extensive (deep penetration into the interior of the polyad) and simple (strong, regular recurrences; simple fractionation pattern). In Section 6.5, a conceptual framework will be presented which explains most of the qualitative trends observed here. First, however, a quantitative measure of the extent of IVR, the dilution factor, is used to provide further insights into the trends in IVR as a function of internal energy.

6.4 Dilution Factors

The dilution factor, or inverse participation ratio [88], is frequently employed as a numerical measure of the fractionation of a zero-order state [89, 90]. Dilution factors are usually reported for the experimentally accessible bright states, but if an adequate model is available to predict the fractionation patterns of zero-order states that have not been observed experimentally, then dilution factors can be calculated for these "hypothetical bright states" as well [91, 92, 93]. In the context of the acetylene pure bending H^{eff}, the dilution factor y is defined as

$$y_k = \sum_{j=1}^{N} |c_{jk}|^4 \ , \tag{6.14}$$

in which k represents a particular zero-order state, j is an index over eigenstates, N is the number of eigenstates within the polyad that contains the zero-order state, and c_{jk} is the projection of the eigenstate onto the zero-order state (one element of the eigenvector matrix). Note that $1 \geq y \geq 1/N$; bright states that display little fractionation have dilution factors near unity, whereas bright states that display extensive fractionation may have dilution factors that approach $1/N$.

It should be noted that generalizations of the dilution factor have been introduced in the literature, the most prominent of which is the $P(a|b)$ statistic, which was introduced by Nordholm and Rice [94] and has been used in many theoretical treatments by Heller [95, 96, 97]. This statistic is defined as

$$P(a|b) = \sum_{j=1}^{N} |c_{ja}|^2 |c_{jb}|^2 \ . \tag{6.15}$$

Note that for $a = b$, the definition reduces to that for the dilution factor; thus, the dilution factor can be considered a special case of the $P(a|b)$ statistic. For $a \neq b$, the statistic describes energy flow between pairs of zero-order states. An analog of the dilution factor that is eigenstate specific, as opposed to zero order state specific, has also been reported [97]; this statistic provides a measure of the inverse of the number of zero-order states with which a particular eigenstate has substantial overlap. These

Table 6.4: Dilution factors (y) calculated for several classes of bright states. Note that $\ell = 0$ refers to the ($J = 1$, $\ell = 0$, e parity) lines observed experimentally, and $\ell = 2$ refers to ($J = 2$, $\ell = 2$, f parity). The columns labeled N list the total number of states within the relevant polyads, for reference.

N_b	y ($\ell = 0$)	N ($\ell = 0$)	y ($\ell = 2$)	N ($\ell = 2$)
4	0.98	4	0.99	4
6	0.95	6	0.95	8
8	0.85	9	0.86	12
10	0.56	12	0.58	18
12	0.36	16	0.31	24
14	0.22	20	0.13	32
16	0.16	25	0.10	40
18	0.22	30	0.17	50
20	0.30	36	0.11	60
22	0.24	42	0.11	72

generalizations of the dilution factor, although extremely useful in general, will not be considered further in this work because they are not as directly relevant to an explanation of the unusual dynamics described in Section 6.3.

Table 6.4 lists the dilution factors for the pure bending bright states that are observed experimentally. Note that the dilution factors for $\ell = 0$ and $\ell = 2$ are nearly identical up to $N_b = 10$, but that at higher internal energy the dilution factors for the $\ell = 2$ bright states are substantially smaller (indicating greater fractionation) than those for the corresponding $\ell = 0$ bright states. This is another manifestation of the observation made in Section 6.2 that, above $\sim$8000 cm^{-1}, ($J = 1$, $\ell = 0$) and ($J = 2$, $\ell = 2$) rotational lines show a diminished tendency to occur in nearly degenerate pairs. The fundamental reason for the dissimilarity of the $\ell = 0$ and $\ell = 2$ dilution factors is that the $\ell = 2$ polyads contain more states than the corresponding $\ell = 0$ polyads. At low internal energy, where the dynamics is restricted and tends not to sample the interior of the polyad, the total number of states in the polyad is largely irrelevant. However, at higher internal energy, where the dynamics samples many of the states in the polyad, the larger $\ell = 2$ polyads display more complicated dynamics than those with $\ell = 0$.

The other striking aspect of this table is that the dilution factors for both the $\ell = 0$ and $\ell = 2$ bright states do not decrease monotonically with increasing internal energy. Rather, in both cases, the absolute minimum in the dilution factors occurs at $N_b = 16$, which lies at only $\sim$10,500 cm^{-1}. Note that this counterintuitive trend, in which the dilution factors decrease monotonically up to $N_b = 16$, then increase somewhat before decreasing again, is not obvious simply by inspecting the fractionated bright state patterns in Fig. 5-13. Direct interpretation of the fractionation patterns is complicated by the presence of two rotational lines, ($J = 1$, $\ell = 0$) and ($J = 2$, $\ell = 2$), in the spectra, which do not appear in nearly degenerate pairs at higher internal energy. The splitting of these pairs of rotational states gives the *appearance* of more substantial fractionation at higher internal energy, and in the absence of an accurate H^{eff}, one might conclude, incorrectly, that fractionation increases more or less monotonically with internal energy.

These trends in the dilution factors, of course, confirm the qualitative observations that were made on the time-domain dynamics in Section 6.3, namely, that the dynamics of the $(0, 0, 0, 22^0, 0^0)$ bright state seemed simpler in certain senses than that of $(0, 0, 0, 16^0, 0^0)$, which lies >4000 cm^{-1} lower in internal energy. One might wonder whether this unusual trend in the dynamics is unique to the set of bright states that are accessible experimentally from the S_1 state of acetylene, or whether the overall structure of the polyads changes in an unusual fashion, which might imply that the dynamics for other classes of bright states would change in an unusual manner as well. In other words, how typical are the dynamics of the pure *trans* bending bright states relative to other bright states that one can *imagine* accessing (even if such access might be difficult experimentally)?

Figure 6-4 addresses this question by plotting the distribution of dilution factors for all of the zero-order states in the $[10, 0]^{g+}$, $[16, 0]^{g+}$, and $[22, 0]^{g+}$ polyads. The $[10, 0]^{g+}$ polyad, for example, encompasses a total of 12 zero-order states. The experimentally accessible bright state in this polyad, $(0, 0, 0, 10^0, 0^0)$, has the second highest dilution factor among all of the zero-order states. The only zero-order state with a larger dilution factor is $(0, 0, 0, 0^0, 10^0)$. In other words, if it were possible to excite

pure *cis* bending, as opposed to pure *trans* bending, bright states experimentally, then the fractionation pattern that would be observed for the $[10,0]^{g+}$ polyad would be slightly simpler. Excitation of any other class of zero-order states, which would necessarily involve both *trans* and *cis* bending, would result in a more complicated fractionation pattern. In this sense, then, the dynamics of the bright state that is accessed experimentally cannot be considered to be typical of the dynamics that would be observed for most other conceivable classes of bright states.

The observation that $(0,0,0,0^0,10^0)$ and $(0,0,0,10^0,0^0)$ possess the largest dilution factors in the $[10,0]^{g+}$ polyad is consistent with studies of many molecular systems which have found that zero-order states with all of the vibrational excitation residing in just one of the modes tend to have atypically simple fractionation patterns [98, 99]. These experimental observations have been explained using the theoretical constructs of "exterior" and "interior" states, and the rather similar concept of "extreme motion states" [100, 101]. The concept of exterior states is associated with a phenomenological argument that states with excitation localized primarily in one mode (or, in the case of larger molecules, in a small number of modes) of the molecule tend be coupled to fewer other zero-order states *via* the important anharmonic resonances than do states with vibrational excitation which is spread more evenly among the modes. It was noted in Section 6.3, for instance, that the bright states $(0,0,0,{v_4}^0,0^0)$ are coupled to only two gateway states, $(0,0,0,(v_4-2)^{+2},2^{-2})$ and $(0,0,0,(v_4-2)^0,2^0)$. The concept of extreme motion states provides a theoretical foundation for these arguments, the central tenet of which is an adiabatic decoupling of the extreme motion (exterior) states from other states. It should be noted that certain limitations of the concept of extreme motion states have been pointed out by Lehmann, Scoles and coworkers, on the basis of their work on propyne [102]. Namely, they note that if the vibrational energy of a molecule is delocalized over modes that interact only weakly with each other, then the excitation in each mode can be expected to relax independently; in other words, an increase in the delocalization of vibrational excitation can, in certain cases, result in a *decrease* in the rate of IVR. However, these criticisms of the concept of extreme motion states are relevant primarily to molecules much larger

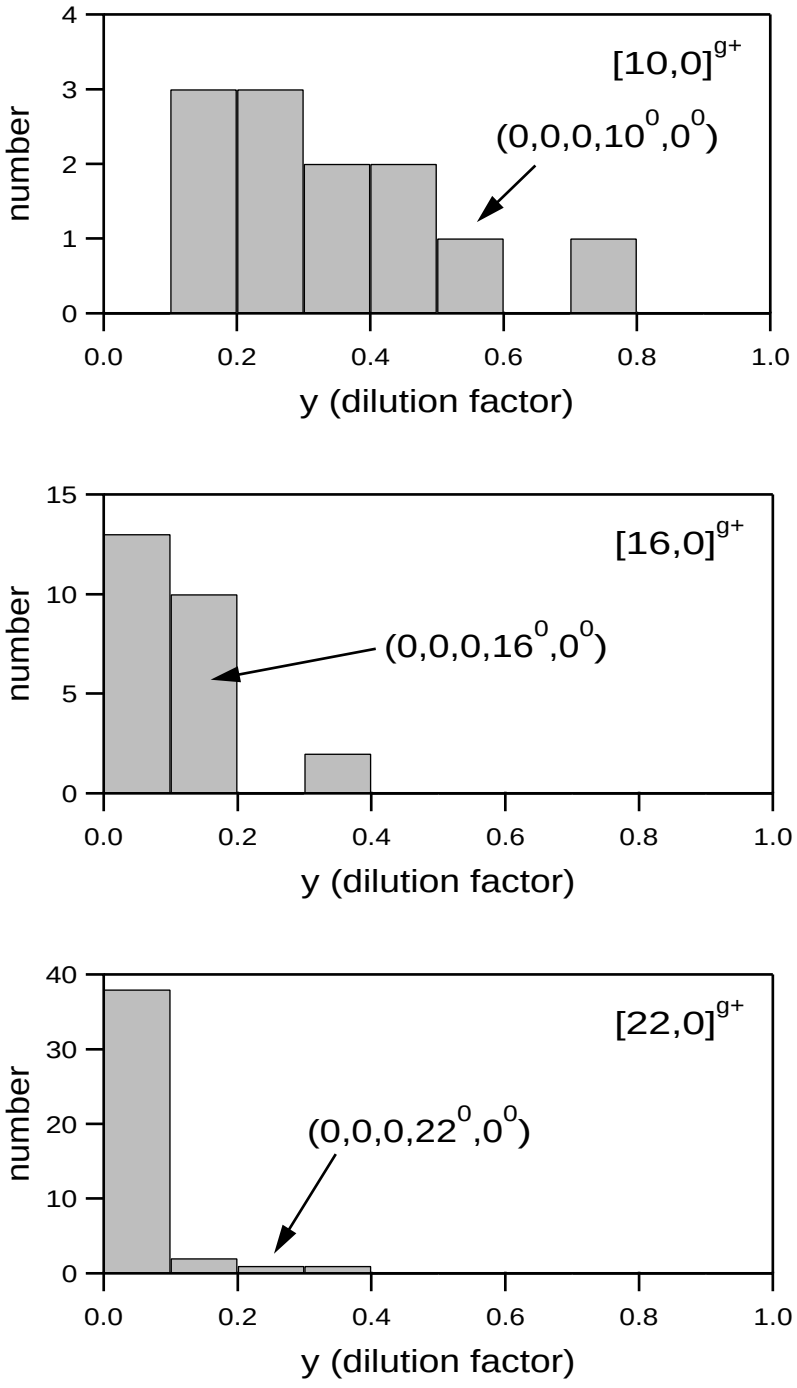

Figure 6-4: Histograms representing the distribution of dilution factors for all zero-order states that compose a polyad. The bright states accessed experimentally generally have dilution factors that are among the highest (least fractionated) within the polyad.

than acetylene.

On the whole, the concept of extreme motion (exterior) states appears to be profitable for the pure bending polyads of acetylene. The states with all of the vibrational excitation localized in the *cis* bending mode *always* have the largest dilution factor in a given pure bending polyad (at least up to $N_b = 22$). In the $[10, 0]^{g+}$ and $[22, 0]^{g+}$ polyads, which are illustrated in Fig. 6-4, the experimentally observed bright state, which has all of the vibrational excitation in *trans* bend, has the second highest dilution factor. In $[16, 0]^{g+}$, however, the *trans* bend bright state has only the fourth highest dilution factor, and nine other zero-order states have dilution factors that also range between 0.1 and 0.2. In other words, in $[16, 0]^{g+}$, the bright state does not behave like an exterior state, in the sense that its IVR seems to be somewhat more typical of the totality of zero-order states within the polyad. From this perspective, then, the unusual trends in IVR that were examined in Section 6.3 reflect the way in which the bright state behaves like an exterior (extreme motion) state at low ($N_b = 10$) and high ($N_b = 22$) internal energy, but not at intermediate ($N_b = 16$) energy. A framework for understanding this behavior of the bright state is presented in Section 6.5.

6.5 Zero-Order Energies as a Framework for Understanding Trends in Dynamics

The unexpectedly complicated trends in IVR above 10,000 cm^{-1} that were noted in Sections 6.3 and 6.4 can be understood by investigation of the structure of the blocks of the H^{eff} matrix that correspond to each of the relevant polyads. It should be noted at the outset that the structure of the polyad blocks of the H^{eff} at high internal energy is rather complicated, in the sense that any given zero-order state typically interacts with several other states *via* the known anharmonic resonances. In addition, many off-diagonal matrix elements have magnitudes that are substantially larger than the energy differences between the zero-order states that they couple.

However, an investigation of the zero-order energies of the states within a polyad

provides a compact framework for understanding certain key elements of the dynamics. The zero-order energies are the diagonal elements of the H^{eff}; they can be considered to represent the energies of the states within a polyad if one could turn off the resonances. Thus, without considering the details of the resonances that couple the zero-order states, the zero-order energies allow one to identify pairs or groups of zero-order states that have small energy differences, and thus might be expected to interact strongly due to small energy denominators.

Rather than simply list the zero-order energies for states within a polyad, however, one can gain greater insight into the structure of the H^{eff} by plotting the zero-order energies in a manner related to the resonance structure that couples the zero-order states. Figure 6-5 illustrates one such way of organizing the zero-order energies, according to the quantum numbers of the corresponding zero-order states, $(v_4, \ell_4, v_5, \ell_5)$. For each polyad, $N_b = v_4 + v_5$, so either v_4 or v_5 needs to be specified, but not both. In addition, only $\ell = 0$ polyads will be considered, such that $\ell_4 = -\ell_5$. Therefore, a pair of quantum numbers, such as $(v_4, |\ell_4|)$, is sufficient to label each zero-order state. In Figs. 6-5 and 6-6, the v_4 quantum number is labeled along the x-axis of the zero-order energy plots, and in each stack of zero-order states at the same value of v_4, the highest energy state corresponds to $|\ell_4| = 0$, and each successively lower state has a value of $|\ell_4|$ that is two greater than that of the preceding state. The stacks contain the largest number of states at intermediate values of v_4 due to the constraint that $|\ell_4| \leq \min(v_4, v_5)$.

This organization of the zero-order energies is convenient, because the anharmonic resonances in the H^{eff} can be illustrated graphically in a simple fashion. For example, the ℓ-doubling resonance, which exchanges two quanta of ℓ_4 for two quanta of ℓ_5 without changing v_4 or v_5, couples only zero-order states that are in the same v_4 stack on the diagram. More specifically, a chain of these resonances couples each zero-order state within a stack to the state directly above it and the state directly below it. The two Darling-Dennison resonances, which interchange two quanta between v_4 and v_5, couple states in adjacent v_4 stacks. The Darling-Dennison I resonance, which preserves the values of ℓ_4 and ℓ_5, couples pairs of states in adjacent stacks with the

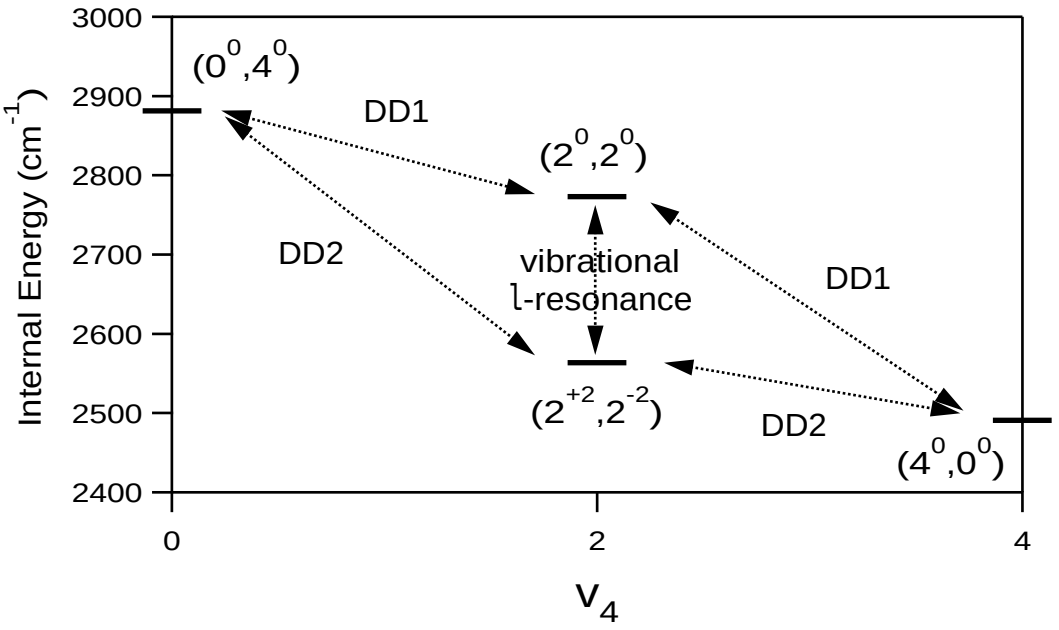

Figure 6-5: Graphical depiction of the zero-order energies within a pure bending polyad ($[4,0]^{g+}$) which elucidates the resonance structure. The zero-order states are arranged in stacks according to v_4, with the top state in each stack having $\ell_4 = 0$, and each successively lower state having ℓ_4 increased by 2. Note that the energy separation between the $(2^0, 2^0)$ and $(2^{+2}, 2^{-2})$ states has been exaggerated for purposes of illustration.

same rank; i.e., the top states in adjacent stacks, or a pair of states which are each third from the top in adjacent stacks. The Darling-Dennison II resonance, which interchanges two quanta between ℓ_4 and ℓ_5, couples states in adjacent stacks with rank differing by one.

In Fig. 6-6, it can be seen that for $[10,0]^{g+}$ (and all lower pure bending polyads) the pure *trans* bending zero-order state (the bright state) has the lowest zero-order energy of all of the states within the polyad. The pure *cis* bending state has the highest zero-order energy, and the states with intermediate values of v_4 and v_5 vary monotonically between these two extremes. This simple structure of the zero-order energies in the low-lying pure bending polyads arises simply from the fact that $\omega_4 < \omega_5$. The resonances that couple the zero-order states at $\sim$6500 cm^{-1} are relatively weak, and the fractionation pattern observed in the eigenstate spectrum (top right panel) is correspondingly simple. The intense peak below 6400 cm^{-1} can be labeled as the perturbed bright state (its overlap squared with the zero-order bright state is 0.728), and the two moderately intense peaks at slightly higher internal energy can be identified as the (Darling-Dennison) perturbers.

The zero-order energy diagram for $[16,0]^{g+}$ differs from that of $[10,0]^{g+}$ in subtle but important ways. First, the bright state is now *nearly*, but not quite, the lowest energy zero-order state within the polyad (the pure *cis* bending state remains at the top). The lowest energy zero-order state is, in fact, $(0,0,0,8^8,8^{-8})$, and a total of 12 zero-order states lie within $\pm$100 cm^{-1} of the bright state. This proliferation of near-degeneracies among the zero-order states near the bottom of the polyad, coupled with the increase in the magnitude of the matrix elements from $N_b = 10$ to $N_b = 16$, can be considered to be responsible for the complicated IVR associated with this polyad that is described in Sections 6.3 and 6.4. The bright state lies right in the middle of a conglomeration of nearly degenerate, strongly coupled states, leading to a complicated fractionation pattern and time-domain dynamics that are atypical for an exterior state.

The underlying reason for the change in structure in the zero-order energy diagram from $[10,0]^{g+}$ to $[16,0]^{g+}$ can be better understood by examination of the

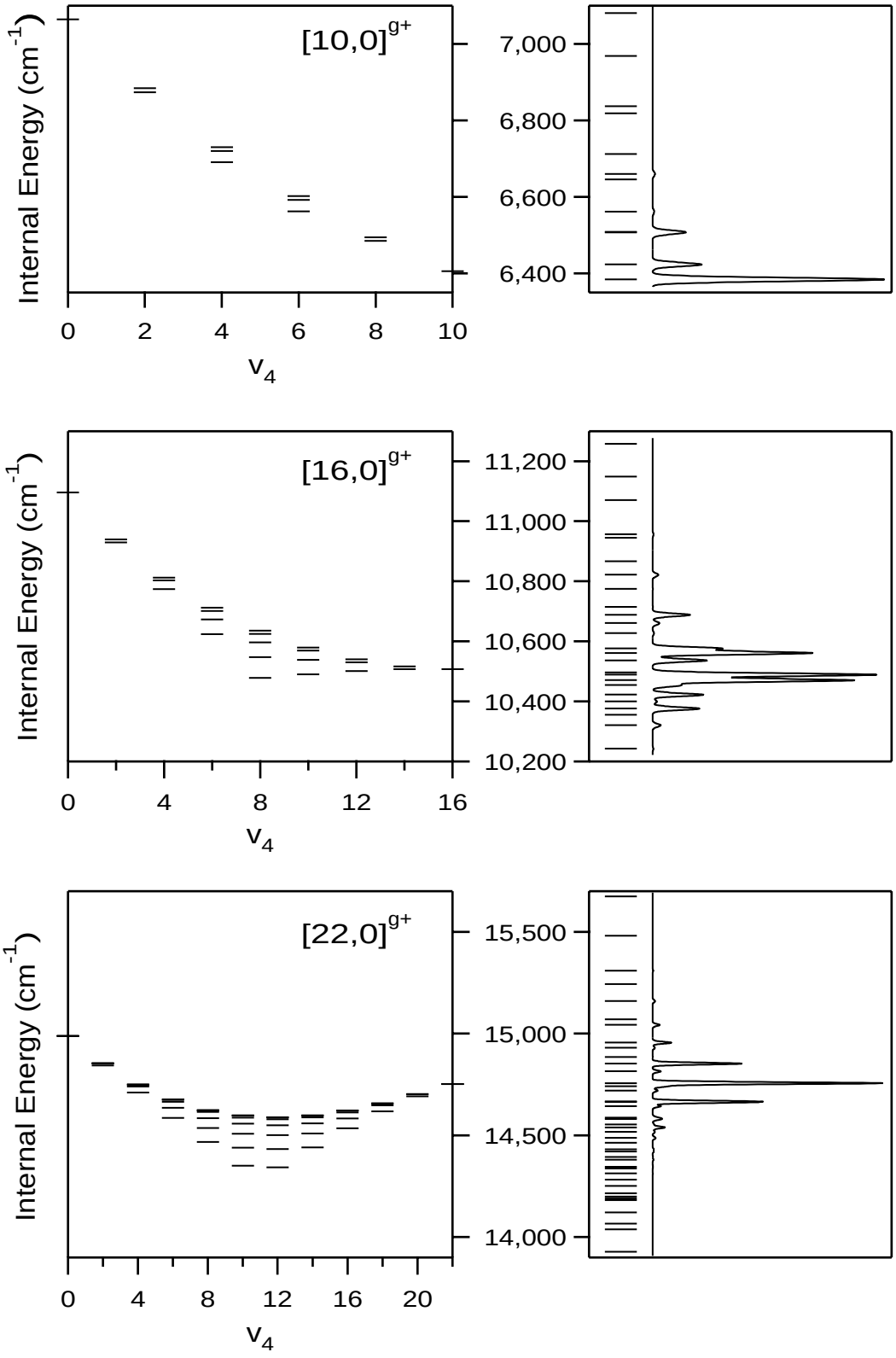

Figure 6-6: Left: Zero-order energies within the $[10,0]^{g+}$, $[16,0]^{g+}$, and $[22,0]^{g+}$ polyads (see Fig. 6-5). Right: Eigenenergies (horizontal lines) and simulated spectrum (solid line).

zero-order energy diagram for $[22,0]^{g+}$. The bright state in this case is no longer at the bottom of the polyad; in fact, it has the fourth highest zero-order energy, and lies less than 250 cm^{-1} lower in energy than the pure *cis* bending zero-order state. This fundamental change in the structure of the polyad is due to the fact that the x_{44} and x_{55} anharmonicity constants have opposite signs. In colloquial terms, the opposing anharmonicities give the *trans* bend end of the polyad a chance to catch up to the *cis* bend end at high internal energy. The states in the interior of the polyad, which have $v_4 \approx v_5$, sag down because the cross-anharmonicity between the two modes, x_{45}, is negative.

The zero-order energy diagram for $[22,0]^{g+}$ helps to explain why the fractionation pattern of $(0,0,0,22^0,0^0)$ appeared to be somewhat less complicated than that of $(0,0,0,16^0,0^0)$. Although the off-diagonal matrix elements, of course, increase substantially from $N_b = 16$ to $N_b = 22$, the bright state is no longer nearly degenerate with as many states. The states in the interior of the $[22,0]^{g+}$ polyad, with $v_4 \approx v_5$, are coupled very strongly with each other, both due to large matrix elements and small zero-order energy differences, but the bright state is coupled less strongly into this bath of states by virtue of its zero-order energy.

This diagram also provides insight into the strong, quasiperiodic exchange of energy between the *cis* and *trans* bending modes that was observed in the plot of $\langle v_b(t) \rangle$ for this polyad (Fig. 6-3). The bright state, $(0,0,0,22^0,0^0)$, can be observed to be nearly degenerate with $(0,0,0,4^0,18^0)$, $(0,0,0,4^{+2},18^{-2})$, and $(0,0,0,4^{+4},18^{-4})$. Although the bright state is not coupled directly to these states *via* the known anharmonic resonances, vibrational excitation can be expected to flow indirectly but strongly from the *trans* bend end of the polyad to the *cis* bend end *via* a chain of Darling-Dennison resonances through the states with $v_4 \approx v_5$. Figure 6-7 underscores this point by plotting the survival probability of the bright state (dotted line) along with the time-dependent squared projection of the wavepacket onto the $(0,0,0,0^0,22^0)$ zero-order state (solid line). During the first 1 ps of the dynamics, nearly 20% of the vibrational excitation is transferred to the pure *cis* bending zero-order state, at the troughs of the survival probability of the pure *trans* bending bright

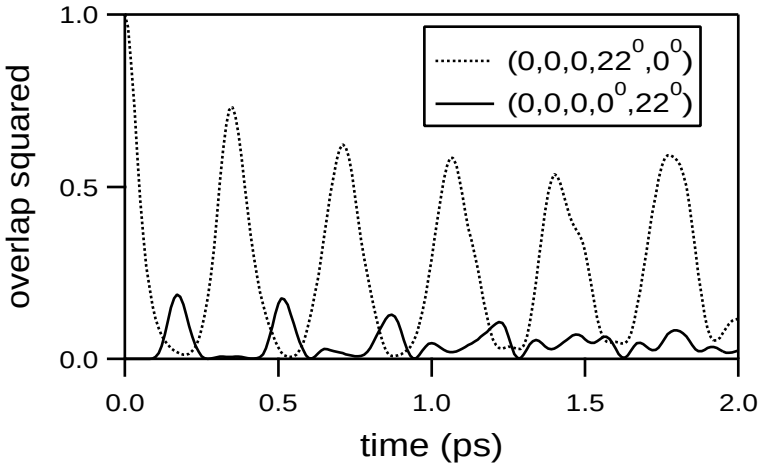

Figure 6-7: Time-dependent overlap squared of the $(0,0,0,22^0,0^0)$ bright state wavepacket with the pure *trans* bend (dashed line) and pure *cis* bend (solid line) ends of the polyad.

state.

This strong transfer of vibrational excitation from one end of the polyad to the other is remarkable because the $(0,0,0,22^0,0^0)$ and $(0,0,0,0^0,22^0)$ zero-order states are coupled only very indirectly to each other, by a minimum of 11 quartic anharmonic resonances ($\Delta v = 44$!) through other zero-order states. At a qualitative level, the magnitude of the anharmonic resonances at $\sim$15,000 cm^{-1} is responsible for the strength of the transfer of energy, and the approximate symmetry of the zero-order states, such that

$$E_{(0,0,0,v_4{}^{\ell_4},v_5{}^{-\ell_4})} \approx E_{(0,0,0,v_5{}^{\ell_4},v_4{}^{-\ell_4})} \ , \tag{6.16}$$

is largely responsible for the regular, quasiperiodic nature of this exchange during the first 1–2 ps. This strong exchange of energy between the *trans* and *cis* normal modes will be explored at a deeper level in Chapters 7 and 8, in which it is demonstrated that a local mode model of the pure bending dynamics of acetylene is appropriate at high internal energy. The $[22,0]^{g+}$ polyad is particularly well-described by a local mode model, and it can be demonstrated that exchange of energy between *trans* and *cis* can approach 100% as the molecule approaches the pure local bending limit.

6.6 Conclusion

The existence of the $N_s = v_1 + v_2 + v_3$ polyad quantum number in the acetylene S_0 state implies the existence of a class of eigenstates (those with $N_s = 0$) that to a good approximation involve no excitation in the stretching modes of the molecule. A great deal of information about the pure bending dynamics of acetylene is encoded in the pattern of frequencies and intensities of the transitions to the pure bending eigenstates that are observed experimentally. The observed pure bending transitions have been modelled using an effective Hamiltonian, described in Section 6.2, which incorporates all of the anharmonic resonances that are known to couple the bending states of acetylene. This effective Hamiltonian is based closely on previously reported work [70], but the agreement between model and experiment has been extended to much higher internal energy, such that *all* known pure bending levels of acetylene up to 15,000 $cm^{-1}$are fit to ± 1.4 cm^{-1} (1σ), including states with up to 22 quanta of bending excitation.

The ability to model the pure bending vibrational levels to such high internal energy affords an opportunity to gain detailed insight into the short-time dynamics of a tetra-atomic molecule with extreme levels of bending excitation. The effective Hamiltonian was investigated using both time-domain (Figs. 6-2, 6-3, and 6-7) and frequency domain (Table 6.4 and Fig. 6-4) formalisms, which together provided a rich, and somewhat surprising, composite picture of the large-amplitude bending dynamics. One major surprise was that the IVR of the bright state with 22 quanta of *trans* bend excitation, at 15,000 cm^{-1} of internal energy, demonstrated a regularity that was absent for the bright state with 16 quanta of *trans* bend excitation, at 10,000 cm^{-1} of internal energy; in other words, from 10,000 cm^{-1} to 15,000 cm^{-1} the IVR seemed in some sense to become *simpler*. This observation was explained in terms of the structures of the polyads (Fig. 6-6).

The eigen*functions* of the H^{eff} developed here are examined in Chapters 7 and 8, where it is demonstrated that many of the eigenfunctions at high internal energy (>10,000 cm^{-1}) are quite regular, in the sense that they have clearly identifiable

nodal coordinates. However, these nodal coordinates do not correspond to the normal mode coordinates, as they do at lower internal energy. Rather, the eigenfunctions at high internal energy are classifiable as "local bending" or "counter-rotating" states. These qualitative observations imply that a different basis set may provide a more compact representation of the pure bending dynamics at high internal energy, and the H^{eff} reported here can be transformed to local mode (as opposed to normal mode) coordinates.

The development of an analytical potential surface for the bending dynamics of acetylene that can also reproduce the available data up to 15,000 cm^{-1} would be highly desirable. Normally, the refinement of a potential surface for a polyatomic molecule against experimental data to such high internal energy would be a very difficult task, but the relatively low dimensionality of the acetylene bending system, combined with the existence of an extensive, rigorously calibrated data set, may make such a task feasible. Recently, McCoy and Sibert have reported the development of a new adiabatic bending potential surface for acetylene, which has shown promise for matching experimental results below $\sim$10,000 cm^{-1} [24, 27], and I hope that the work in this thesis will spur further efforts to develop potential surfaces for acetylene with spectroscopic accuracy at high internal energy.

Acknowledgments

This research was supported by DOE Grant No. DE-FG0287ER13671. My work on this chapter was supported by the Department of the Army under a National Defense Science and Engineering Graduate Fellowship.

6.7 Appendix: Expectation Values of Resonance Operators

In Section 6.3, the pure bending dynamics of acetylene were investigated using time-dependent quantities such as the survival probability, $|\langle\Psi(0)|\Psi(t)\rangle|^2$, and expecta-

tion values of number operators, $\langle v_b(t)\rangle = \langle\Psi(t)|\hat{v}_b|\Psi(t)\rangle$. In this short Appendix, I propose another class of time-dependent quantities—expectation values of resonance operators.

Let $\hat{O}$ be a Hermitian operator that represents a particular resonance that couples the zero-order states in some basis. For example, $\hat{O}$ defined as

$$\hat{a}^\dagger_{4d}\hat{a}^\dagger_{4g}\hat{a}_{5d}\hat{a}_{5g} + \hat{a}_{4d}\hat{a}_{4g}\hat{a}^\dagger_{5d}\hat{a}^\dagger_{5g} \tag{6.17}$$

would represent the Darling-Dennison I resonance; see Section 7.2 for notation. One can then define the expectation value of the resonance operator for a time-evolving wavepacket $|\Psi(t)\rangle$ as

$$\begin{aligned}\langle\hat{O}\rangle(t) &= \langle\Psi(t)|\hat{O}|\Psi(t)\rangle &(6.18)\\ &= \sum_i\sum_j c_i^*(t)c_j(t)\langle\phi_i|\hat{O}|\phi_j\rangle &(6.19)\end{aligned}$$

in which

$$c(t) = \langle\phi|\Psi(t)\rangle\ , \tag{6.20}$$

and $\{|\phi\rangle\}$ is the zero-order basis set in which the resonance is defined. [In a density matrix formalism, the expectation value of the resonance operator can be computed as

$$\langle\hat{O}\rangle(t) = \mathrm{Tr}[\boldsymbol{\rho}(t)\boldsymbol{O}]\ , \tag{6.21}$$

where $\boldsymbol{\rho}(t)$ is the time-evolving density matrix, and $\boldsymbol{O}$ is the matrix representation of the resonance operator; see Ref. [103], p. 298.]

I have found the expectation values of resonance operators to be particularly useful for elucidating dynamics in polyads that involve stretch excitation. In the pure bending polyads, only three resonances exist, and the survival probabilities and expectation values of number operators provided quite a bit of insight into the dynamics associated with the $(0,0,0,v_4^0,0^0)$ bright states. However, in non-pure bending polyads, the dynamics can be quite a bit more complicated because 7 vibrational degrees of freedom are involved, and there are a total of 9 known anharmonic reso-

nances (see Ref. [5], for example) that couple the normal mode zero-order states. The expectation values of resonance operators can help to identify those resonances that are the most important in directing the dynamics.

As an example, Fig. 6-8 depicts the expectation values of two resonance operators, which represent the Darling-Dennison I and (3,245) resonances, and the survival probability for the time-evolving wavepacket that would be associated with preparing the $(0, 1, 0, 10^0, 0^0)$ bright state at $t = 0$. The model used is the effective Hamiltonian that is defined in Section 6.2 and Chapter 9. The survival probability is intriguing because it displays oscillations with two distinct periods. That is, there are a series of nearly complete recurrences of the wavepacket at time intervals of $\sim$1.35 ps, but these broad oscillations are modulated by oscillations with a period of $\sim$0.25 ps. The expectation values of the resonance operators provide an immediate interpretation for these two timescales in the wavepacket dynamics. The expectation value of the Darling-Dennison I operator displays oscillations that match the faster period oscillations in the survival probability, while that for the (3,245) resonance matches the slower oscillations. Thus, redistribution of the energy between the *trans* and *cis* bend modes occurs on a faster timescale than redistribution of the energy between the bend and stretch modes, but both processes are reversible in the sense that nearly 100% recurrences are observed within a few picoseconds.

It should be noted that the expectation values of resonance operators can also be used in a time-independent sense, if the wavepacket $|\Psi(t)\rangle$ is replaced by eigenstates $|\psi\rangle$.

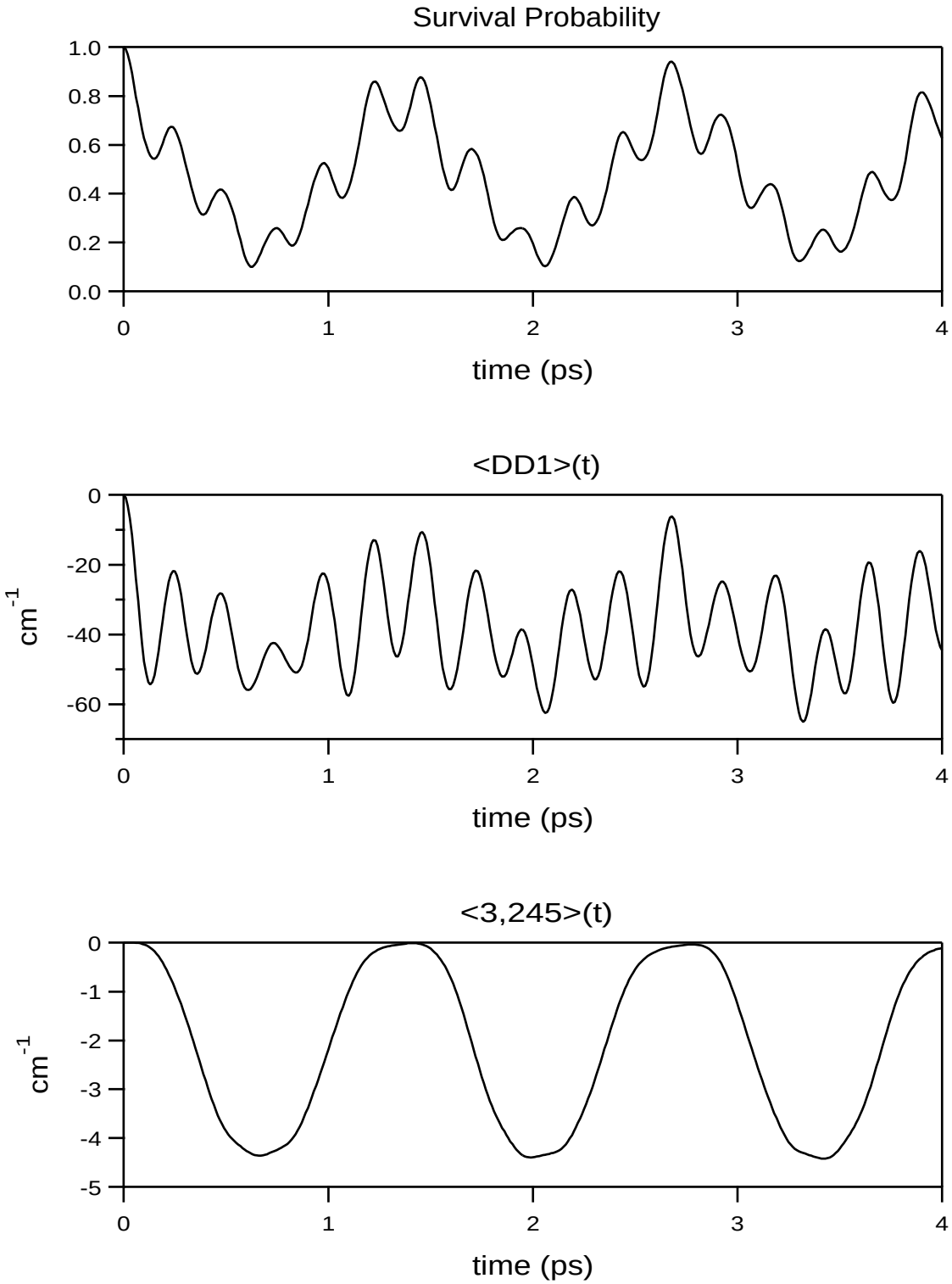

Figure 6-8: Top: Survival probability associated with the $(0, 1, 0, 10^0, 0^0)$ bright state. Middle and Bottom: Time-dependent expectation values of resonance operators that represent the Darling-Dennison I and (3,245) resonances, respectively, for the same wavepacket as in the top panel.

Chapter 7

Local Mode Bending Behavior

The majority of this chapter, other than the two Appendices, has been published in the Journal of Chemical Physics as Ref. [104].

7.1 Introduction

The quantum vibrational eigenfunctions of polyatomic molecules at chemically significant energies are a subject of substantial recent interest, particularly insofar as they may provide mechanistic insights into unimolecular dissociation and isomerization. It is well established, at this point, that traditional spectroscopic analyses, which emphasize assignments based on normal modes, are rarely useful for describing large amplitude vibrational motions of polyatomic molecules. The nonlinearity and nonintegrability that are inherent to these large amplitude vibrations often lead to the observation of stable motions qualitatively distinct from the normal modes, as well as to classical chaos (and, possibly, observable quantum manifestations of the chaos). Some recent contributions to the understanding of the vibrational eigenfunctions of highly excited polyatomics have included

- the fitting and analysis of effective Hamiltonian models that represent large amplitude motions [84, 105, 106, 107, 108];
- classical and semiclassical analysis of molecular quantum Hamiltonians [109, 110, 111, 112, 14, 113, 114];
- theoretical studies of vibrational eigenfunctions at high energy using potential surfaces generated by *ab initio* methods [115, 116];
- algebraic approaches to molecular vibrations [117, 118, 119, 120];
- the polyad formalism for identifying approximately conserved vibrational quantum numbers [15, 16, 17, 14];
- quantum, semiclassical, and classical studies of model systems that mimic important properties of polyatomic systems [121, 122, 123];

- detailed analysis of the equivalence [105, 32, 124, 33, 125, 126, 127, 128] between the traditional normal mode models of vibrational motion and the local mode models pioneered by Mecke, Siebrand, Williams, Henry, Lawton, Child, and others [29, 30, 129, 31, 130, 131];

as well as a wide variety of experimental studies, which are far too numerous to be referenced here.

I present here, as a contribution to this body of literature, a thorough analysis of the bending eigenfunctions of the acetylene S_0 state, as represented by the bending effective Hamiltonian model, introduced in Chapter 6, that reproduces the energies of all pure bending eigenstates up to 15,000 cm^{-1} with 1.4 cm^{-1} RMS error. The eigenfunctions at such high internal energy necessarily represent rather large amplitude bending motions; 15,000 cm^{-1} corresponds to approximately 22 quanta of bending excitation, and is also believed to be within $\sim$500 cm^{-1} of the energy at which acetylene is energetically capable of isomerizing to vinylidene (zero-point dressed barrier height) [72, 37, 34, 132, 36, 4]. Although these high energy eigenfunctions may provide insights into quantum manifestations of classical chaos, this direction is not pursued here. Instead, this chapter focuses on the appearance of qualitatively new, stable bending motions at high internal energy. [Chapter 8 presents a classical and semiclassical study of the acetylene bending system that addresses the correspondence between the quantum wavefunctions and classical periodic orbits and chaos.]

The new bending motions that are observed in highly vibrationally excited acetylene can be referred to as "local bend" and "counter-rotation" motions. Local bend motions have been reported previously in classical, semiclassical, and quantum studies of acetylene [109, 133, 27, 134]. I am unaware of any previous characterization of the counter-rotating motion. The primary goal of this chapter, however, is to demonstrate that the appearance of *both* the local bend *and* the counter-rotating motions can be considered a manifestation of a transition from normal to local mode behavior in the bending dynamics. That is, while a normal mode basis set is appropriate at low energies (below $\sim$8,000 cm^{-1}), a local mode basis becomes a superior zero-order representation at higher energies (above $\sim$10,000 cm^{-1}). The local mode behavior

that is reported here for the bending degrees of freedom of acetylene has obvious parallels with the local mode behavior that has been extremely well-characterized for the stretching dynamics of a wide variety of ABA molecules (as well as some larger systems) [105, 32, 33, 30, 135, 136, 137]. However, the local mode behavior in the acetylene bend degrees of freedom, because it involves two *two*-dimensional rather than two *one*-dimensional vibrational modes, encompasses a richer range of motions for which the conventional language of local stretching systems is not entirely appropriate.

7.2 Determining Eigenfunctions From Spectra

The approach utilized in this chapter to determine the eigenfunctions of acetylene from experimental spectra consists of several steps:

1. Dispersed fluorescence (DF) spectra are recorded from several vibrational levels of the S_1 state of acetylene and subjected to frequency and intensity calibration [Chapter 5].

2. Numerical pattern recognition algorithms are used to extract from the DF data set the fractionation patterns for single bright states [Chapter 5].

3. An effective Hamiltonian (H^{eff}) model is fit to the set of extracted fractionated bright states [Chapter 6].

4. The eigenfunctions of the H^{eff} model are examined graphically in an appropriate coordinate system [this chapter].

It should be noted that this approach is similar in spirit to that of a few other studies, including the Sako and Yamanouchi study of SO_2 [117] and the Ishikawa *et al.* study of HCP [106], but the tetratomic system under study here has required a more elaborate analysis. Steps 1, 2, and 3 of this procedure are documented in preceding chapters; the remainder of this section is devoted to explaining step 4.

The acetylene pure bending effective Hamiltonian will be designated as $H^{\text{eff}}_{\mathcal{N}}$, in which the $\mathcal{N}$ subscript indicates that the effective Hamiltonian is represented in a

normal mode basis, to distinguish it from an equivalent local mode version of the Hamiltonian ($H^{\rm eff}_{\mathcal{L}}$) to be defined in Section 7.6 below. The matrix elements of $H^{\rm eff}_{\mathcal{N}}$ are listed in Chapter 6. Here, to anticipate algebraic manipulation of $H^{\rm eff}_{\mathcal{N}}$ in later sections, the Hamiltonian is expressed in terms of raising and lowering operators for the two dimensional, isotropic harmonic oscillator. These operators are labeled d (right) and g (left), using the notation of Cohen-Tannoudji *et al.* [103], and are defined as

$$\hat{a}_d = \frac{1}{\sqrt{2}}(\hat{a}_x - i\hat{a}_y) \tag{7.1}$$

$$\hat{a}_g = \frac{1}{\sqrt{2}}(\hat{a}_x + i\hat{a}_y), \tag{7.2}$$

where x/y represent the two equivalent rectilinear coordinates for the 2D oscillator. The d/g operators have the convenient property that the number operators corresponding to the conventional quantum number labels for the 2D oscillator can be expressed as

$$\hat{v} = \hat{v}_d + \hat{v}_g = \hat{a}^\dagger_d\hat{a}_d + \hat{a}^\dagger_g\hat{a}_g \tag{7.3}$$

$$\hat{\ell} = \hat{v}_d - \hat{v}_g = \hat{a}^\dagger_d\hat{a}_d - \hat{a}^\dagger_g\hat{a}_g. \tag{7.4}$$

Note that, based upon these definitions, both $\hat{a}_d$ and $\hat{a}_g$ destroy one quantum of vibration (v), but $\hat{a}_d$ decreases the angular momentum (ℓ) by one, while $\hat{a}_g$ increases it by one.

Using the conventional "4" and "5" labels for *trans* and *cis* respectively,

$$\begin{aligned}
\hat{H}^{\rm eff}_{\mathcal{N}} &= \omega_4\hat{v}_4 + \omega_5\hat{v}_5 \\
&+ x_{44}\hat{v}_4\hat{v}_4 + x_{45}\hat{v}_4\hat{v}_5 + x_{55}\hat{v}_5\hat{v}_5 \\
&+ y_{444}\hat{v}_4\hat{v}_4\hat{v}_4 + y_{445}\hat{v}_4\hat{v}_4\hat{v}_5 + y_{455}\hat{v}_4\hat{v}_5\hat{v}_5 + y_{555}\hat{v}_5\hat{v}_5\hat{v}_5 \\
&+ g_{44}\hat{\ell}_4\hat{\ell}_4 + g_{45}\hat{\ell}_4\hat{\ell}_5 + g_{55}\hat{\ell}_5\hat{\ell}_5 \\
&+ s_{45}(\hat{a}^\dagger_{4d}\hat{a}^\dagger_{4g}\hat{a}_{5d}\hat{a}_{5g} + \hat{a}_{4d}\hat{a}_{4g}\hat{a}^\dagger_{5d}\hat{a}^\dagger_{5g}) \\
&+ [r^\circ_{45} + r_{445}(\hat{v}_4 - 1) + r_{545}(\hat{v}_5 - 1)](\hat{a}_{4d}\hat{a}^\dagger_{4g}\hat{a}^\dagger_{5d}\hat{a}_{5g} + \hat{a}^\dagger_{4d}\hat{a}_{4g}\hat{a}_{5d}\hat{a}^\dagger_{5g}) \\
&+ \frac{1}{4}[r^\circ_{45} + r_{445}(\hat{v}_4 - 1) + r_{545}(\hat{v}_5 - 1) + 2g_{45}] *
\end{aligned}$$

$$(\hat{a}^\dagger_{4d}\hat{a}^\dagger_{4d}\hat{a}_{5d}\hat{a}_{5d} + \hat{a}^\dagger_{4g}\hat{a}^\dagger_{4g}\hat{a}_{5g}\hat{a}_{5g} + \hat{a}_{4d}\hat{a}_{4d}\hat{a}^\dagger_{5d}\hat{a}^\dagger_{5d} + \hat{a}_{4g}\hat{a}_{4g}\hat{a}^\dagger_{5g}\hat{a}^\dagger_{5g}). \qquad (7.5)$$

The values of the various parameters in this model[1] are listed in Table 6.3.

The $H^{\rm eff}_{\mathcal{N}}$ is evaluated, of course, in a product basis set of two 2D harmonic oscillators, which represent the *trans* and *cis* bend degrees of freedom. The existence of the polyad quantum numbers (Section 5.1) implies that the matrix representation of $H^{\rm eff}_{\mathcal{N}}$ is block diagonal. Upon diagonalization of any polyad block, the eigenvector matrix permits any eigenfunction in the polyad to be expressed as a linear superposition of the zero-order basis states, and the probability density for any given eigenfunction can be calculated in an appropriate set of coordinates. The most natural coordinates for the 2D isotropic harmonic oscillator are the radial and angular coordinates (ρ, ϕ), in which the wavefunctions for the oscillator take the form

$$\Psi_{v,\ell}(\rho,\phi) = \chi_v^{|\ell|}(\rho)e^{i\ell\phi} \qquad (7.6)$$

$$\chi_v^{|\ell|}(\rho) = N_{v,|\ell|}e^{-\rho^2/2}\rho^{|\ell|}L^{|\ell|}_{(v+\ell)/2}(\rho^2); \qquad (7.7)$$

L represents the associated Laguerre polynomials, and N is a normalization constant. Note that the volume of integration in these coordinates is $\rho\, d\rho\, d\phi$.

A natural set of coordinates for the eigenstates of $H^{\rm eff}_{\mathcal{N}}$ is therefore $(\rho_4, \phi_4, \rho_5, \phi_5)$. Only eigenstates with $\ell = 0$ will be considered, in which case $\ell_4 = -\ell_5$, and the basis set consists of

$$\Psi^0_{v_4,v_5}(\rho_4,\rho_5) = \chi^0_{v_4}(\rho_4)\chi^0_{v_5}(\rho_5) \quad [\ell_4 = \ell_5 = 0] \qquad (7.8)$$

$$\Psi^{\ell_4}_{v_4,v_5}(\rho_4,\rho_5,\Phi_{45}) = \chi^{|\ell_4|}_{v_4}(\rho_4)\chi^{|\ell_4|}_{v_5}(\rho_5)e^{i\ell_4\Phi_{45}} \quad [\ell_4 \neq 0], \qquad (7.9)$$

[1]Note that the diagonal elements of $H^{\rm eff}_{\mathcal{N}}$ differ from a standard Dunham expansion in the treatment of zero-point energy. That is, the zero of energy of $H^{\rm eff}_{\mathcal{N}}$ is defined to be the zero-point level of the molecule, and the ω, x, y, etc. parameters are not the standard Dunham parameters. This nonstandard notation has been adopted for consistency with previous work (Ref. [70]).

in which $\Phi_{45} = \phi_4 - \phi_5$. Note, however, that the latter set of basis functions do not possess well-defined parity; symmetrized basis functions can be defined as

$$\Psi^{|\ell_4|+}_{v_4,v_5}(\rho_4,\rho_5,\Phi_{45}) = \sqrt{2}\chi^{|\ell_4|}_{v_4}(\rho_4)\chi^{|\ell_4|}_{v_5}(\rho_5)\cos(\ell_4\Phi_{45}) \quad (7.10)$$

$$\Psi^{|\ell_4|-}_{v_4,v_5}(\rho_4,\rho_5,\Phi_{45}) = \sqrt{2}\chi^{|\ell_4|}_{v_4}(\rho_4)\chi^{|\ell_4|}_{v_5}(\rho_5)\sin(\ell_4\Phi_{45}). \quad (7.11)$$

Note that the conservation of vibrational angular momentum permits a reduction in the number of coordinates needed to plot the eigenstates from 4 to 3. Also note that the g/u symmetry of the basis functions is determined by v_5 (v_5=odd implies u symmetry; v_5=even implies g symmetry). The shorthand notation $|v_4^{\ell_4}, v_5^{\ell_5}\rangle^{g+}_{\mathcal{N}}$ will be used to indicate the symmetrized basis functions; the superscript, of course, indicates the symmetry, while the subscript $\mathcal{N}$ again indicates the normal mode basis set, to distinguish it from the local mode basis set to be defined in Section 7.4.

7.3 Eigenfunctions in Normal Mode Coordinates

Figures 7-1 and 7-2 depict several eigenfunctions in the $[4,0]^{g+}$ and $[22,0]^{g+}$ polyads, respectively. The $[4,0]^{g+}$ polyad is representative of the low energy polyads ($N_b \leq 8$), in which the eigenfunctions can be rationalized simply in terms of perturbations/mixings among a small number of normal mode zero-order states. The $[22,0]^{g+}$ polyad is the highest energy pure bending polyad that had been characterized experimentally when this work was completed. The eigenstates of this polyad have energies near 15,000 cm^{-1} and are representative of the high energy polyads ($18 \leq N_b \leq 22$), in which few, if any, states are describable in terms of the normal mode basis, but many are describable instead in terms of qualitatively new types of motions, called local bend and counter-rotation. Discussion of the eigenfunctions at intermediate energy ($10 \leq N_b \leq 16$), which are transitional between the low and high energy extremes, will be deferred to Section 7.5.

The $[4,0]^{g+}$ polyad encompasses a total of four eigenstates, which are represented in Fig. 7-1 in the coordinates defined in the preceding section. The four zero-order

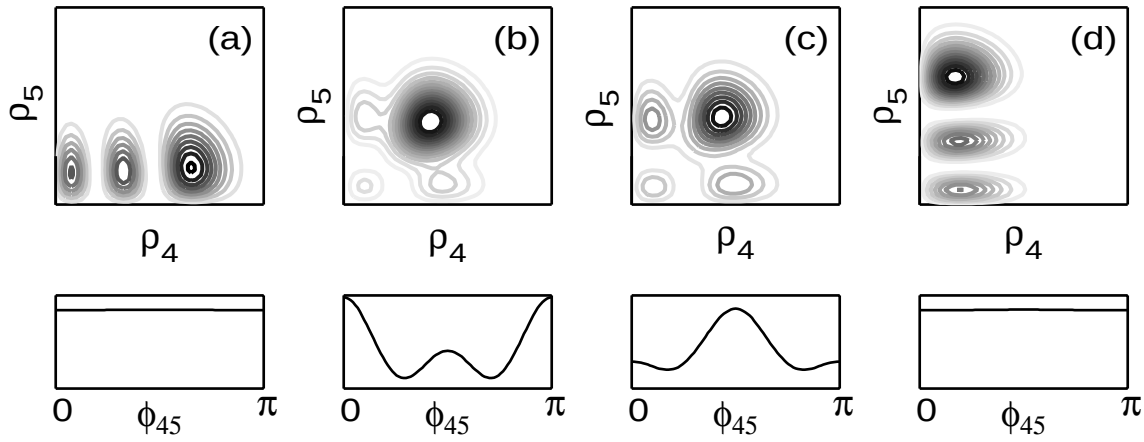

Figure 7-1: Probability densities of the four eigenstates of the $[4,0]^{g+}$ polyad plotted as projections onto the normal mode radial (ρ_4, ρ_5) and torsional (Φ_{45}) coordinates. The lowest energy eigenstate is a minimally perturbed *trans* bend state ($|4^0, 0^0\rangle_{\mathcal{N}}^{g+}$), and the highest a minimally perturbed *cis* bend state ($|0^0, 4^0\rangle_{\mathcal{N}}^{g+}$). The two eigenstates which are intermediate in energy are mixed, due to vibrational ℓ-resonance between $|2^{+2}, 2^{-2}\rangle_{\mathcal{N}}^{g+}$ and $|2^0, 2^0\rangle_{\mathcal{N}}^{g+}$.

states that comprise the polyad are $|4^0, 0^0\rangle_{\mathcal{N}}^{g+}$, $|2^0, 2^0\rangle_{\mathcal{N}}^{g+}$, $|2^{+2}, 2^{-2}\rangle_{\mathcal{N}}^{g+}$, and $|0^0, 4^0\rangle_{\mathcal{N}}^{g+}$, and the projections of the eigenstates onto the basis set can be obtained from the eigenvector matrix that results from the diagonalization of $H_{\mathcal{N}}^{\text{eff}}$. Eigenfunction (a) is the minimally perturbed pure *trans* bend zero-order state, $|4^0, 0^0\rangle_{\mathcal{N}}^{g+}$. That is, this lowest energy eigenstate within the polyad has 99.1% character of $|4^0, 0^0\rangle_{\mathcal{N}}^{g+}$ (the term "character" is used to mean overlap squared between an eigenstate and a given zero-order function). The purity of this state is reflected in the eigenfunction plot; there is a clear nodal coordinate[2] running nearly parallel to the ρ_4 axis, and a nearly flat Φ_{45} probability distribution, which is indicative of $\ell_4 = \ell_5 = 0$. The assignment for eigenstate (d), the highest energy state within the polyad, is equally clear [99.2% $|0^0, 4^0\rangle_{\mathcal{N}}^{g+}$ character].

The two eigenstates in the "middle" of the polyad, by process of elimination, must correspond in some way to the $|2^0, 2^0\rangle_{\mathcal{N}}^{g+}$ and $|2^{+2}, 2^{-2}\rangle_{\mathcal{N}}^{g+}$ zero-order states. Note that the $|2^0, 2^0\rangle_{\mathcal{N}}^{g+}$ zero-order state should have a flat Φ_{45} probability distribu-

[2]In terms of counting nodes in the (ρ_4, ρ_5) plane, it is important to keep in mind that the radial coordinates are defined only for $\rho \geq 0$.

tion, while $|2^{+2},2^{-2}\rangle_{\mathcal{N}}^{g+}$ should have a $\cos^2(2\Phi_{45})$ distribution. Since neither of the eigenstates displays either of these behaviors, they must represent some mixture of the two zero-order states (i.e., the zero-order states perturb each other significantly). The eigenvector matrix confirms this conclusion. Eigenstate (b) can be approximated as

$$|b\rangle \approx 0.80|2^{+2},2^{-2}\rangle_{\mathcal{N}}^{g+} + 0.60|2^{0},2^{0}\rangle_{\mathcal{N}}^{g+}, \tag{7.12}$$

while for eigenstate (c),

$$|c\rangle \approx 0.60|2^{+2},2^{-2}\rangle_{\mathcal{N}}^{g+} - 0.79|2^{0},2^{0}\rangle_{\mathcal{N}}^{g+}. \tag{7.13}$$

The mechanism for the mixing between the two zero-order states is vibrational ℓ-resonance, which couples states with the same v_4 and v_5, but with $\Delta\ell_4 = -\Delta\ell_5 = 2$.

Thus, the overall structure of the pure bending polyads at low internal energy is fairly simple. The *trans* bend mode has a smaller harmonic frequency than the *cis* bend mode ($\omega_4 < \omega_5$), and as a result, the states within the polyad are ordered with the pure *trans* bend state at the bottom, the pure *cis* bend state at the top, and states with a mixture of *trans* and *cis* in the middle. Groups of zero-order states with the same v_4 and v_5 tend to cluster closely in energy, due to the rather weak dependence of the zero-order energies on ℓ_4 and ℓ_5, and perturb each other strongly through vibrational ℓ-resonance. By contrast, the other important anharmonic bending resonances, Darling-Dennison I and II, which couple states with $\Delta v_4 = -\Delta v_5 = 2$, result in relatively minor perturbations, due to the fairly large difference in the frequencies of the two bending modes.

The situation in the $[22,0]^{g+}$ polyad is drastically different. At $\sim$15,000 cm^{-1} of internal energy, this polyad not only encompasses many more zero-order states (42) than the low energy polyads, but these zero-order states are also coupled by off-diagonal matrix elements which are much larger due to their (harmonic oscillator) scaling properties. In addition, as demonstrated in Chapter 6, the energies of the zero-order states do not cluster in a simple fashion, as they do at low energy. Although the pure *cis* bend state, $|0^{0},22^{0}\rangle_{\mathcal{N}}^{g+}$, remains the highest energy zero-order state within

the polyad, the pure *trans* bend state, $|22^0, 0^0\rangle_{\mathcal{N}}^{g+}$, no longer has the lowest energy in the polyad, as it does for the low energy polyads. In fact, the $|22^0, 0^0\rangle_{\mathcal{N}}^{g+}$ state has the fourth highest zero-order energy within the polyad, and the pure *trans* and *cis* bend states are thus nearly isoenergetic at high N_b. The underlying reason for this behavior is that the *trans* and *cis* bend modes have anharmonicities with opposite signs. The *trans* bend mode, which has a lower harmonic frequency, has a *positive* anharmonicity, which causes the effective frequency for this mode at high energy to approach that of the *cis* bend mode, which has a higher harmonic frequency but a negative anharmonicity.

Based on the preceding observations, it is not surprising that the eigenvector matrix for this polyad reveals that the vast majority of eigenstates can be described only in terms of a complicated superposition of many normal mode states (see for example the histogram plot of dilution factors for this polyad in Fig. 6-4). On this basis, one might reasonably expect that the majority of the eigenfunctions of the $[22, 0]^{g+}$ polyad would look very complicated in a graphical representation, with poorly defined nodal patterns. However, as Fig. 7-2 makes clear, many of the eigenfunctions of the $[22, 0]^{g+}$ polyad demonstrate simple, well-defined nodal coordinates. Plots (a), (b), (e), and (f) are representative of the eigenstates at the low and high energy extremes of the polyad, the majority of which have clearly defined nodal coordinates.[3] Although many of the eigenstates in the middle of the polyad, like eigenstate (c), do have complicated structures, others like eigenstate (d) have well-defined nodal coordinates (although somewhat more complicated than at the energy extremes).

It should be emphasized that the eigenfunctions that have a simple appearance are also highly mixed, in the sense that their projection onto the normal mode basis set involves a complicated superposition of all of the zero-order states within the polyad. That is, their simple nodal coordinates are very different than those observed at low internal energy, where the eigenstates can be identified as perturbed/mixed normal mode zero-order states, with the nodal coordinates aligned approximately parallel to

[3]In many local stretching systems, the bottom of a polyad is dominated by local stretch character, whereas the top may remain describable in terms of the normal mode motions. Here, normal mode motions are not in evidence either at the top or the bottom of the polyad.

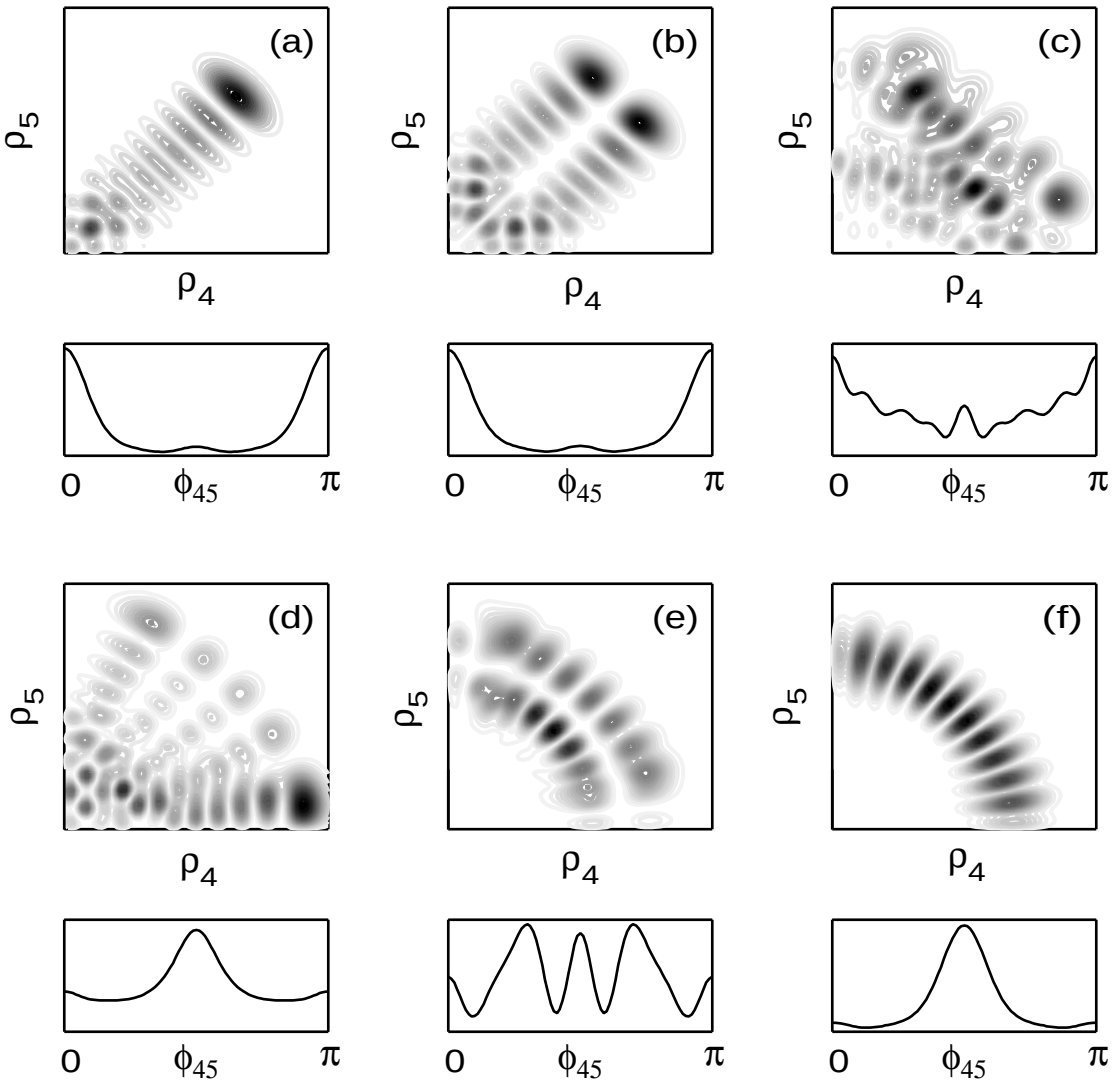

Figure 7-2: Probability densities of six eigenstates in the $[22,0]^{g+}$ polyad plotted as projections onto the normal mode radial (ρ_4, ρ_5) and torsional (Φ_{45}) coordinates. The eigenstate in (a) has the lowest eigenenergy within the polyad (13925.4 cm^{-1}) and eigenstate (b) has the third lowest (14064.32 cm^{-1}). Together, (a) and (b) are representative of the eigenfunctions at the bottom of the polyad, which tend to have probability localized near $\rho_4 = \rho_5$. The eigenfunction in (c) has an energy of 14641.4 cm^{-1} and is representative of a number of eigenstates within the middle of the polyad that appear to have no well-defined nodal coordinates. Eigenstate (d) is depicted because it has the greatest overlap with the bright state (i.e., the greatest intensity in the experimental spectrum); its energy is 14755.0 cm^{-1}. Eigenstates (e) and (f) are representative of many states at the top of the polyad, which tend to have nodal coordinates along lines of constant $(\rho_4^2 + \rho_5^2)$. Eigenstate (e) has an energy of 15067.6 cm^{-1} and (f) has an energy of 15,671.4 cm^{-1}, the highest eigenenergy within the polyad.

the ρ_4 and ρ_5 axes. Put differently, the simple eigenfunctions that predominate at the extremes of the $[22,0]^{g+}$ polyad represent qualitatively new motions which are not present at low internal energy.

It is clear that the eigenfunctions at the high and low energy extremes of the polyad represent two different types of motion. The motion associated with eigenstate (a), the lowest energy eigenstate within the polyad, is somewhat easier to interpret. This eigenfunction has its probability density localized around $\Phi_{45} = 0$, which corresponds to in-plane motion. The nodal coordinate in the (ρ_4, ρ_5) plane is aligned along $\rho_4 = \rho_5$. Classically, the simultaneous excitation of the *cis* and *trans* bending motions with the same amplitude, in-phase and in-plane, corresponds to a "local bending" motion, in which only *one* hydrogen executes a bending motion. From a quantum mechanical perspective, the bending motions of the two equivalent hydrogens are indistinguishable, and one would expect to observe a nearly degenerate *pair* of local bend states which correspond to positive and negative superpositions of the two equivalent local bend motions. In fact, eigenstate (a), which has a computed energy of 13925.94176036 cm^{-1} and $g+$ symmetry, is very nearly degenerate with an eigenstate of the $[22,0]^{u+}$ block of $H_{\mathcal{N}}^{\text{eff}}$, with a computed energy of 13925.94176029 cm^{-1} (splitting of $7 \cdot 10^{-7}$ cm^{-1}). The probability density plots of these two eigenfunctions are also nearly identical. Thus, in close analogy to local stretch states, the local bend states appear in nearly degenerate g/u pairs.

Many of the eigenstates at the low energy end of the polyad can be classified as local benders, such as eigenstate (b), which differs from (a) in that it also involves excitation along a coordinate orthogonal to the local bending coordinate. As expected, this $g+$ symmetry eigenstate, which has an energy of 14064.3221615 cm^{-1}, has a nearly degenerate $u+$ symmetry partner, only $3 \cdot 10^{-6}$ cm^{-1} higher in energy. Several other g/u local bend pairs can be identified at the low energy end of the polyad, including pairs with $-$ parity. All of these states share a nodal coordinate aligned approximately along $\rho_4 = \rho_5$, but many of these, such as (b), also have excitation along an orthogonal coordinate or have probability distributions that are not localized around $\Phi_{45} = 0$. Further discussion of these other local bend states will

be deferred to the next section, in which a different coordinate representation of the eigenfunctions is introduced which makes their assignments more readily apparent.

The motion associated with eigenstate (f), the highest energy eigenstate within the polyad, is somewhat more difficult to interpret. The nodes of this eigenfunction align along a coordinate defined by $\sqrt{\rho_4^2 + \rho_5^2} \approx C$, where C is a constant, and the probability density peaks at $\Phi_{45} = \pi/2$. The absence of substantial probability near $(\rho_4 = 0, \rho_5 = 0)$ implies that the vibrational motion never passes through the linear configuration. On the other hand, the motion must pass through the *trans* and *cis* planar configurations, due to the lobes of probability located near $\rho_4 = 0$ (with nonzero displacement in ρ_5) and $\rho_5 = 0$ (with nonzero displacement in ρ_4). The point $\rho_4 = \rho_5$, with $\Phi_{45} = \pi/2$, corresponds to a configuration of the molecule in which the two hydrogens are located at the same angle with respect to the CC axis, and have a torsional angle between them of 90° [note that Φ_{45} is *not*, however, the torsional angle between the hydrogens, but the torsional angle between the *cis* and *trans* oscillators, as discussed in the next section]. In this way, it becomes clear that a trajectory along the coordinate $\sqrt{\rho_4^2 + \rho_5^2} = C$, with $\Phi_{45} = \pi/2$, corresponds to a molecular motion in which the two hydrogens maintain a given angle with respect to the CC axis, but execute an internal rotation which changes the torsional angle between them. Since total vibrational angular momentum must be conserved, the two hydrogens execute rotations in the opposite sense, and thus eigenstate (f) is identified with a "counter-rotating" motion.

In contrast to the local bend states, counter-rotating states do not appear in g/u pairs with the same parity. However, eigenstate (f), which has $g+$ parity and an energy of 15671.432833 cm^{-1}, is very nearly degenerate with an eigenstate of the $u-$ symmetry block of $H_{\mathcal{N}}^{\text{eff}}$, which has an energy of 15671.432824 cm^{-1} (splitting of $1.2 \cdot 10^{-5}$ cm^{-1}). A number of the other states at the high energy end of the polyad which have nodal coordinates along $\sqrt{\rho_4^2 + \rho_5^2} = C$, such as eigenstate (e), also appear in pairs of either $g+$ with $u-$, or $g-$ with $u+$. That is, the counter-rotation states occur in pairs with opposite g/u symmetry *and* opposite parity. This behavior can be rationalized as follows. Classically, there are two equivalent counter-rotations,

which differ in the direction of rotations of the hydrogens (i.e., clockwise or counter-clockwise). Quantum mechanically, these classical counter-rotations, like the classical local bends, are indistinguishable, and the nearly perfect quantum counter-rotation states such as eigenstate (f) must represent some superposition of the two equivalent motions.

The two equivalent classical counter-rotations can be designated as $(\mathcal{R}, \mathcal{L})$ and $(\mathcal{L}, \mathcal{R})$, where $\mathcal{R}$ and $\mathcal{L}$ represent clockwise and counter-clockwise rotation of one hydrogen. The application of the molecular inversion operator ($\hat{\imath}$) to either classical counter-rotation state generates the other, i.e.,

$$\hat{\imath}(\mathcal{R}, \mathcal{L}) \rightarrow (\mathcal{L}, \mathcal{R}).$$

The application of the parity operator, which for a symmetric top is equivalent to $\hat{\sigma}_v$ (see, for example, Refs. [138] and [10]), has an identical effect:

$$\hat{\sigma}_v(\mathcal{R}, \mathcal{L}) \rightarrow (\mathcal{L}, \mathcal{R}).$$

Thus, upon symmetrizing the equivalent counter-rotation states,

$$\frac{1}{\sqrt{2}} \left[(\mathcal{R}, \mathcal{L}) \pm (\mathcal{L}, \mathcal{R}) \right],$$

it becomes clear that the positive superposition corresponds to $g+$ symmetry, while the negative superposition corresponds to $u-$ symmetry. Thus, while local bend states appear in pairs with opposite g/u symmetry, because $\hat{\imath}$ interchanges the two equivalent local bends ($\hat{\sigma}_v$ is inoperative), counter-rotation states appear in pairs with opposite g/u symmetry *and* opposite parity, because *both* $\hat{\imath}$ and $\hat{\sigma}_v$ interchange the two equivalent counter-rotations.

At this point, eigenfunctions (c) and (d) have not been discussed in detail. There is little to say about eigenstate (c), except that no simple nodal coordinates can be identified, despite a significant degree of localization of probability density around $\Phi_{45} = 0$. The existence of an eigenfunction with such a complicated appearance

raises suspicions that chaos exists in the underlying classical dynamics, at least in the middle of the polyad. This is, in fact, the case, and the intricate coexistence of regular and chaotic regions of phase space for the acetylene bending system at high internal energy is examined in Chapter 8. Eigenstate (d), on the other hand, is representative of a number of eigenstates in the middle of the polyad that have a fairly regular structure (some degree of counter-rotating character is evident). It also has the special significance of being the eigenstate on which the strongest transition to the $[22,0]^{g+}$ polyad terminates in the DF spectra. The substantial overlap of this eigenstate with the pure *trans* bend bright state is evident in the accumulation of probability density near $\rho_5 = 0$.

7.4 Eigenfunctions in Local Mode Coordinates

On the basis of the preceding arguments, it is clear that many of the eigenfunctions at the low and high energy ends of the $[22,0]^{g+}$ polyad should be assignable in terms of quantum numbers representing excitation along local bend and counter-rotation coordinates. In this section, a coordinate transformation is defined from the $(\rho_4, \rho_5, \Phi_{45})$ normal mode coordinates, which were utilized to represent the eigenfunctions in the preceding section, to a new set of coordinates, $(\rho_A, \rho_B, \Phi_{AB})$, which facilitate the assignment of many of the high energy eigenstates in terms of "local mode" quantum numbers. This coordinate transformation, and the assignments that it permits, also provide insight into the relationship that exists between the local bend and counter-rotating motions, as well as the significance of the "imperfect" local bend and counter-rotation states, such as eigenstates (b) and (e).

Although the wavefunctions are plotted in radial coordinates, the coordinate transformation is defined in terms of dimensionless rectilinear coordinates:

$$q_{Ax} = \frac{1}{\sqrt{2}}(q_{4x} + q_{5x}) \tag{7.14}$$

$$q_{Ay} = \frac{1}{\sqrt{2}}(q_{4y} + q_{5y}) \tag{7.15}$$

$$q_{Bx} = \frac{1}{\sqrt{2}}(-q_{4x} + q_{5x}) \tag{7.16}$$

$$q_{By} = \frac{1}{\sqrt{2}}(-q_{4y} + q_{5y}). \tag{7.17}$$

The coordinates A and B are thus defined to be symmetric and anti-symmetric combinations of the *trans* and *cis* bend coordinates, and these new coordinates will be referred to as "local mode" bending coordinates, in the expectation that they represent, to a good approximation, bending coordinates for the two individual hydrogens (the correspondence between the normal and local mode representations of the bend eigenfunctions is established more rigorously in Section 7.6). Upon transforming to radial coordinates, the local and normal mode coordinates are related according to

$$\rho_A^2 = \frac{1}{2}\left[\rho_4^2 + \rho_5^2 + 2\rho_4\rho_5\cos(\Phi_{45})\right] \tag{7.18}$$

$$\rho_B^2 = \frac{1}{2}\left[\rho_4^2 + \rho_5^2 - 2\rho_4\rho_5\cos(\Phi_{45})\right] \tag{7.19}$$

$$\Phi_{AB} = \arctan\left[\frac{2\rho_4\rho_5\sin(\Phi_{45})}{\rho_5^2 - \rho_4^2}\right]. \tag{7.20}$$

These expressions are invertible. Note that Φ_{AB} is easier to interpret than Φ_{45}; Φ_{AB} is simply the torsional angle between the two hydrogens.

The application of this coordinate transformation to the eigenfunctions of Fig. 7-2 is depicted in Fig. 7-3. In order to provide assignments for the eigenfunctions in the local mode coordinate system, a local mode zero-order basis set can be defined in terms of two 2D harmonic oscillators, in a manner analogous to the normal mode basis set defined in Eqs. 7.8–7.11 above:

$$\Psi^0_{v_A,v_B}(\rho_A,\rho_B) = \chi^0_{v_A}(\rho_A)\chi^0_{v_B}(\rho_B) \tag{7.21}$$

for $\ell_A = \ell_B = 0$, and

$$\Psi^{|\ell_A|+}_{v_A,v_B}(\rho_A,\rho_B,\Phi_{AB}) = \sqrt{2}\chi^{|\ell_A|}_{v_A}(\rho_A)\chi^{|\ell_A|}_{v_B}(\rho_B)\cos(\ell_A\Phi_{AB}) \tag{7.22}$$

$$\Psi^{|\ell_A|-}_{v_A,v_B}(\rho_A,\rho_B,\Phi_{AB}) = \sqrt{2}\chi^{|\ell_A|}_{v_A}(\rho_A)\chi^{|\ell_A|}_{v_B}(\rho_B)\sin(\ell_A\Phi_{AB}) \tag{7.23}$$

as the positive and negative parity pairs for $\ell_A \neq 0$. One important distinction from the normal mode basis set is that the local mode basis, as defined above, does not have well-defined g/u symmetry. This can be remedied by taking positive and negative superpositions of $\Psi^{|\ell_A|}_{v_A,v_B}$ and $\Psi^{|\ell_A|}_{v_B,v_A}$ ($v_A \neq v_B$). The set of local mode basis functions with $g+$ symmetry, for example, is then defined as

$$\Psi^{|\ell_A|g+}_{v_A,v_B}(\rho_A,\rho_B,\Phi_{AB}) = \left[\chi^{|\ell_A|}_{v_A}(\rho_A)\chi^{|\ell_A|}_{v_B}(\rho_B) + \chi^{|\ell_A|}_{v_B}(\rho_A)\chi^{|\ell_A|}_{v_A}(\rho_B)\right]\cos(\ell_A\Phi_{AB}). \tag{7.24}$$

The shorthand notation $|v_A^{\ell_A}, v_B^{\ell_B}\rangle^{g+}_{\mathcal{L}}$ will be used for the fully symmetrized local mode basis functions.

Plotted in Fig. 7-4 are four of these basis functions; their correspondence with the eigenstates (a), (b), (e), and (f) in Fig. 7-3 is clear. Eigenstate (a) can be identified as $|22^0, 0^0\rangle^{g+}_{\mathcal{L}}$; it has probability localized along *both* $\rho_A = 0$ and $\rho_B = 0$, the two equivalent local bending coordinates, because of the indistinguishability of the two hydrogens in quantum mechanics. Eigenstate (b) can be identified as $|21^{+1}, 1^{-1}\rangle^{g+}_{\mathcal{L}}$. Note that the single, nearly sinusoidal oscillation of the probability density from 0 to π along Φ_{AB} is indicative of a single quantum of angular momentum in the local bending modes (i.e., $\ell_A = -\ell_B = 1$). The assignment of eigenstate (e) as $|14^{+8}, 8^{-8}\rangle^{g+}_{\mathcal{L}}$ is somewhat more approximate, but the number of oscillations in the Φ_{AB} coordinate matches exactly ($\ell_A = -\ell_B = 8$), and the number and location of the nodes in the radial coordinates are quite similar.

Finally, the highest energy eigenstate within the polyad, eigenstate (f), can be assigned as $|11^{+11}, 11^{-11}\rangle^{g+}_{\mathcal{L}}$. That is, the counter-rotating states correspond to local mode basis functions with maximal or nearly maximal angular momentum associated with each of the individual bond oscillators. The counter-rotational character of this eigenstate is much clearer in the local mode than in the normal mode coordinates. The projection of the probability density in the (ρ_A, ρ_B) plane has no nodes and localizes about a single point ($\rho_A \approx \rho_B$), which indicates that both hydrogens remain at the same (nonzero) angle with respect to the CC axis. All of the nodes of the

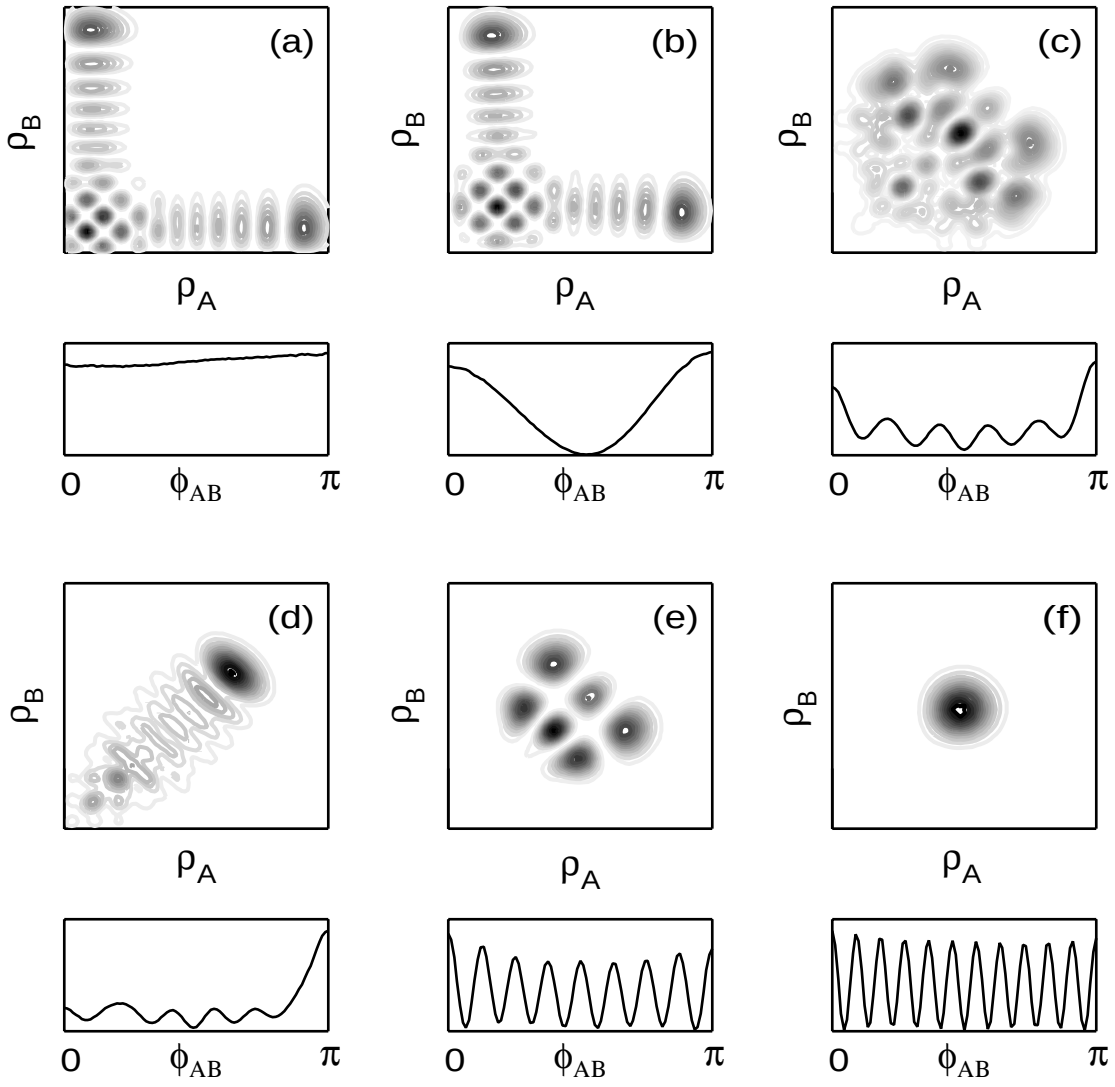

Figure 7-3: The same eigenfunctions as in Fig. 7-2, but plotted using local mode coordinates. ρ_A and ρ_B are the two equivalent single hydrogen bending coordinates, and Φ_{AB} is the torsional angle between the hydrogens.

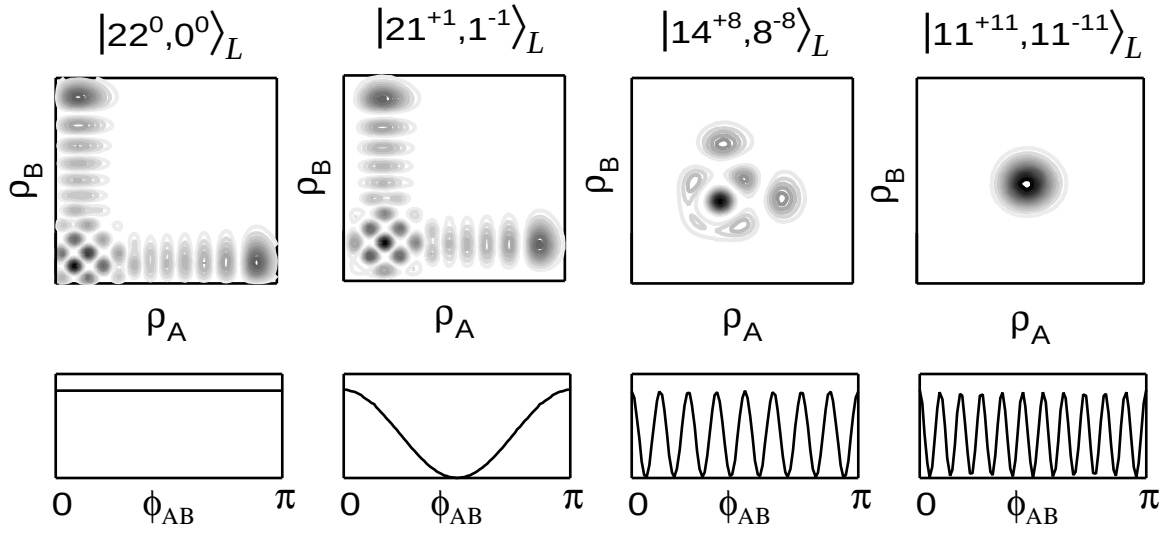

Figure 7-4: Probability densities of 4 symmetrized local mode basis functions, $|v_A^{\ell_A}, v_B^{\ell_B}\rangle_{\mathcal{L}}^{g+}$. Note the similarity between these zero-order states and eigenfunctions (a), (b), (e), and (f) in Fig. 7-3.

wavefunction occur along the Φ_{AB} coordinate, indicating that the motion associated with this eigenstate involves changing the torsional angle between the two hydrogens. The counter-rotational character of the eigenstate is even clearer in Fig. 7-5, which is a projection of the eigenstate onto coordinates (q_{Ax}, q_{Ay}), which are defined by

$$q_{Ax} = \rho_A \cos(\Phi_{AB}) \tag{7.25}$$

$$q_{Ay} = \rho_A \sin(\Phi_{AB}) \ , \tag{7.26}$$

and which represent the motion of a single hydrogen. Twenty-two nodes can be counted in a nearly perfect circle.

Thus, the local mode basis set defined in this section appears to be extremely useful for assigning acetylene bending vibrational levels at high internal energy, because *both* local bend *and* counter-rotation states can be labeled with the same set of quantum numbers. More precisely, the local mode basis set represents a continuum of vibrational character, ranging from pure local bend, $|N_b^0, 0^0\rangle_{\mathcal{L}}$, to pure counter-rotation, $|N_b/2^{(N_b/2)}, N_b/2^{(-N_b/2)}\rangle_{\mathcal{L}}$. Most of the states near the bottom of the polyad, with $v_A \gg v_B$, lie close to the local bend limit, whereas the assignable states near

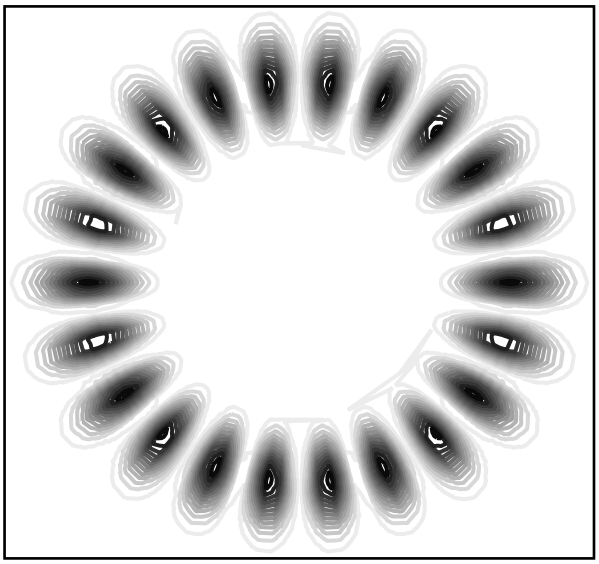

Figure 7-5: Projection of the probability density of eigenfunction (f) (in Fig. 7-3) onto (q_{Ax}, q_{Ay}) coordinates.

the top of the polyad, with $v_A \approx v_B \approx |\ell_A|$, lie close to the counter-rotation limit. As will be seen in Section 7.6, nearly half of the eigenstates of the $[22, 0]$ polyad (of all symmetries) can be assigned using the local mode basis set (using the Hose-Taylor criterion [139]), especially those states at the high and low energy ends of the polyad, but a few in the middle as well. Many other eigenstates can be rationalized in terms of mixings among a few zero-order local mode states.

7.5 Transition from Normal to Local Mode Behavior

It should be clear at this point that the bending eigenfunctions of acetylene in the limits of low ($N_b = 4$) and high ($N_b = 22$) excitation are strikingly different. At low energy, the eigenfunctions can be assigned in terms of perturbed or mixed normal mode states. At high energy, a few eigenfunctions have very complicated nodal patterns (in any coordinates) and do not yield to assignment, but many others have well-defined, simple nodal coordinates corresponding to a continuum of new types of

vibrational motions, ranging from local bend to counter-rotation. In this section, the transition between the low energy, normal mode regime, and the high energy, local mode regime is examined.

To focus this discussion, only the lowest and highest energy eigenstates in each pure bending polyad will be considered. As discussed in Section 7.3, at low N_b, the lowest energy eigenstates in the pure bending polyads can be labeled as minimally perturbed *trans* bend states, while the highest eigenstates are nearly pure *cis* bend states. At high N_b, the lowest energy eigenstate is a local bender, while the highest is a counter-rotator. Thus, one can expect the change from normal to local mode behavior to be manifested in a dual transition, from *trans* bend to local bend behavior at the bottom of the pure bending polyads, and from *cis* bend to counter-rotation at the top (although it is unclear at this point whether these two transitions will necessarily occur at the same energy).

The symmetry properties of the local bend and counter-rotation states provide one method of identifying the energies at which these two transitions occur. That is, as detailed in Section 7.3, pure local bend states are expected to appear in nearly degenerate ($g/+$,$u/+$) pairs, while pure counter-rotation states should occur in ($g/+$,$u/-$) pairs; no such symmetry arguments can be made for purely normal mode states. The second column in Table 7.1 is the difference in energy between the lowest energy eigenstates in corresponding $g/+$ and $u/+$ polyads. For $[6,0]^{g+}$, $[8,0]^{g+}$, and $[10,0]^{g+}$, in which the lowest energy eigenstate can be described as a perturbed *trans* bend state, the g/u energy splitting is >10 cm^{-1}. For $N_b > 12$, however, the energy splitting is less than 1 cm^{-1}, and by $N_b = 22$, the energy splittings become exceedingly small, indicating nearly perfect local bend character.[4] The third column of Table 7.1 is the energy difference between the highest energy eigenstates in corresponding $g/+$ and $u/-$ polyads. The transition from *cis* bend to counter-rotating behavior appears to occur somewhere around $N_b = 16$.

Thus, the bottom of the pure bending polyads seems to demonstrate local mode

[4]Note that these near degeneracies of the local bend eigenstates are predicted by $H_{\mathcal{N}}^{\text{eff}}$ despite the fact that the corresponding g and u symmetry polyads do not even contain the same number of states. For example, the $[22,0]^{g+}$ polyad contains 42 states, while $[22,0]^{u+}$ contains only 36.

Table 7.1: Energy splittings between symmetry pairs reveal the transition from normal to local mode behavior. First column: the polyad quantum number, N_b. In all cases, $\ell = 0$. Second column: energy difference, in cm^{-1}, between the lowest energy eigenstates in pairs of corresponding $g/+$ and $u/+$ symmetry polyads. Small splittings indicate that the states are assignable as local bends. Third column: energy difference between the highest energy eigenstates in pairs of corresponding $g/+$ and $u/-$ symmetry polyads. Small splittings indicate that the states are assignable as counter-rotators.

N_b	$E_{g+} - E_{u+}$	$E_{g+} - E_{u-}$
6	-52.2	83.2
8	-30.8	67.3
10	-10.3	48.1
12	-0.22	25.1
14	-1.7 x 10^{-4}	5.5
16	4.4 x 10^{-6}	0.39
18	6.5 x 10^{-7}	1.5 x 10^{-2}
20	1.2 x 10^{-7}	4.1 x 10^{-4}
22	6.4 x 10^{-8}	9.3 x 10^{-6}

behavior at slightly lower energy than the top. Despite this fairly minor difference, it seems reasonable to conclude that the transition from normal to local mode behavior occurs within the range $N_b = 12$–16 (8,000–10,000 cm^{-1}). This transition is examined in greater detail in Figs. 7-6 and 7-7, which depict the lowest and highest energy eigenstates of the pure bending polyads in the critical energy range. Specifically, Fig. 7-6 depicts the lowest energy eigenstates in the $[10,0]^{g+}$, $[12,0]^{g+}$, and $[14,0]^{g+}$ polyads in both the normal and local mode coordinates that were defined previously. The lowest energy eigenstate in the $[10,0]^{g+}$ polyad can be identified as a somewhat perturbed *trans* bend state in either of the coordinate sets. In the normal mode coordinates, the assignment of the eigenstate as $|10^0,0^0\rangle_{\mathcal{N}}^{g+}$ is indicated by the nodal coordinate in the (ρ_4,ρ_5) plane being nearly parallel to the ρ_4 axis, and by the nearly isotropic distribution of probability density along the Φ_{45} coordinate. In the local mode coordinates, the accumulation of probability along $\rho_A = \rho_B$ indicates that both hydrogens execute equal amplitude motions, and the probability maximum at $\Phi_{AB} = \pi$ indicates that the two hydrogens bend in opposite directions (i.e., *trans* as opposed to *cis*).

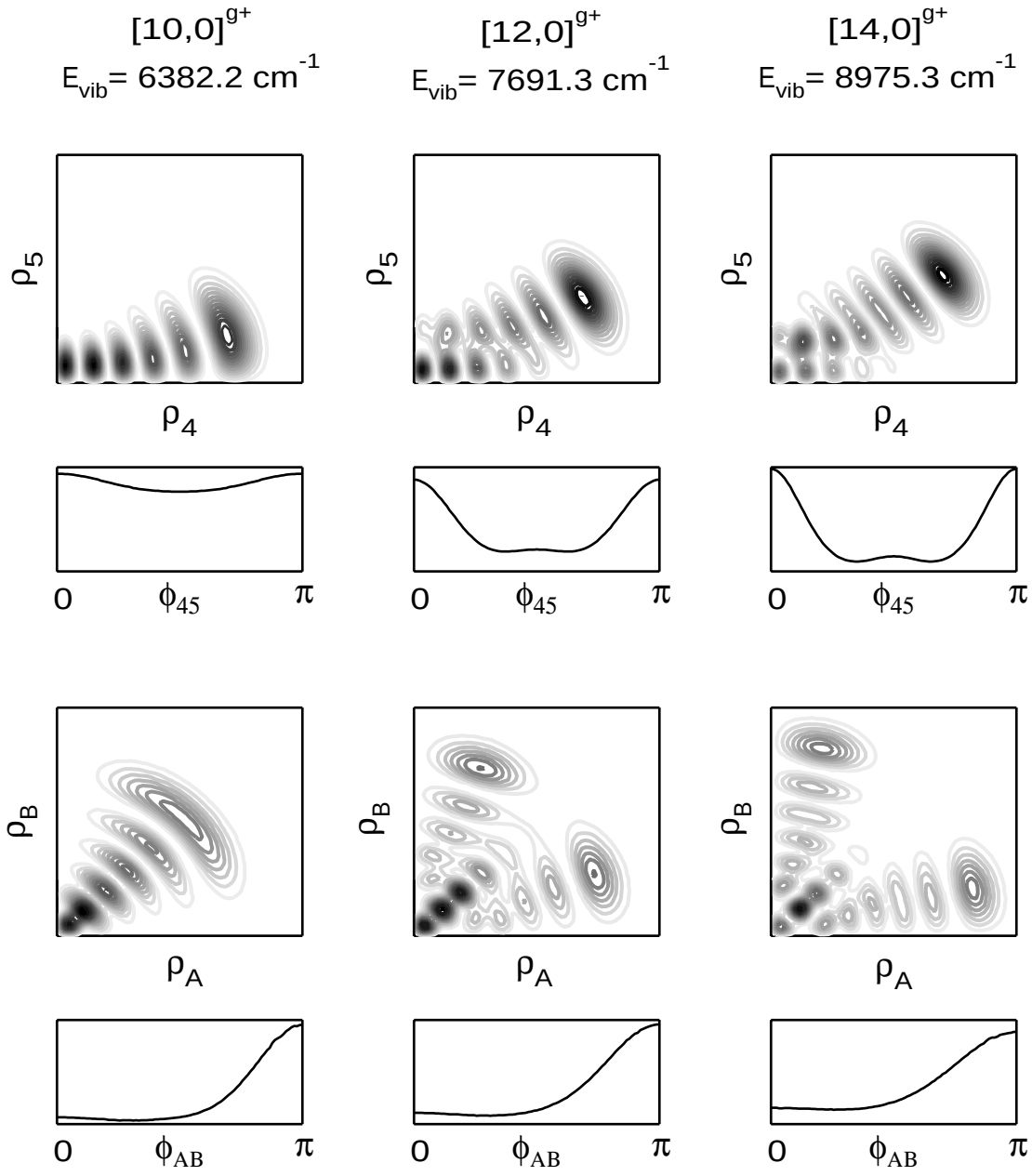

Figure 7-6: The lowest energy eigenstates in the $[10,0]^{g+}$, $[12,0]^{g+}$, and $[14,0]^{g+}$ polyads, in normal and local mode bending coordinates. The qualitative change in eigenstate character from *trans* bend to local bend is clear at $N_b = 12$. In the normal mode coordinates, the nodal coordinate in the (ρ_4, ρ_5) plane pulls away from the ρ_4 axis, and the torsional probability distribution begins to show pronounced peaks at $\Phi_{45} = 0, \pi, \cdots$. In the local mode coordinates, the transition to local bend behavior is marked by the splitting of the probability in the (ρ_A, ρ_B) plane into two lobes.

The lowest energy eigenstate in the $[12,0]^{g+}$ polyad, on the other hand, displays several features which indicate a qualitatively new type of motion, and it cannot be considered to represent merely a perturbed *trans* bend state. First, in the normal mode coordinates, the nodal coordinate in the (ρ_4, ρ_5) plane is no longer even approximately parallel to the ρ_4 axis. The probability density along the Φ_{45} coordinate for the $[12,0]^{g+}$ eigenfunction also displays pronounced maxima at 0 and π which are nearly absent in the $[10,0]^{g+}$ eigenfunction. The transition to a qualitatively new type of motion (which will eventually come to represent the local bend motion) is perhaps the clearest in the local bend coordinates. Specifically, the single nodal coordinate in the $[10,0]^{g+}$ eigenstate appears to have bifurcated in the $[12,0]^{g+}$ eigenstate to form a *pair* of nodal coordinates located symmetrically about $\rho_A = \rho_B$.

The lowest energy eigenstate in the $[14,0]^{g+}$ polyad displays no qualitative features that are not already present in the $[12,0]^{g+}$ lowest energy eigenstate. In fact, from $N_b = 12$ to $N_b = 22$, the change in the nature of the lowest energy eigenfunctions represents a gradual evolution toward the nearly perfect local bending motion associated with the lowest energy eigenstate in the $[22,0]^{g+}$ polyad. In the (ρ_4, ρ_5) plane, the nodal coordinate gradually increases its slope until it reaches nearly unity, and the probability maxima at $\Phi_{45} = 0, \pi, ...$ become more pronounced. In the local mode coordinates, the two symmetrically related lobes of probability gradually move "outward" until they are approximately orthogonal and run parallel to the ρ_A and ρ_B axes. This is perhaps the clearest indicator of the increasing "purity" of the local bend motion. The $\rho_A = \rho_B$ direction represents equal amplitude motions of the two hydrogens, while the ρ_A and ρ_B axes represent the motion of just one hydrogen, with the other hydrogen held stationary at zero degrees. Thus, the migration of probability away from $\rho_A = \rho_B$, and towards $\rho_A = 0$ and $\rho_B = 0$, is a clear indication of the change in behavior from *trans* bend to local bend.

Having characterized the transition from *trans* bend to local bend character at the bottom of the pure bending polyads, we now turn to the corresponding transition at the top of the polyads, from *cis* bend to counter-rotating. Figure 7-7 depicts the highest energy eigenfunctions in the $[12,0]^{g+}$, $[14,0]^{g+}$, and $[16,0]^{g+}$ polyads. The

highest energy eigenfunction in the $[12,0]^{g+}$ polyad appears to be describable as a *cis* bend state. In the normal mode coordinates, most of the probability in the (ρ_4, ρ_5) plane remains localized near the ρ_5 axis, and the probability distribution over the torsional coordinate Φ_{45} is fairly uniform, despite a slight bulge at $\Phi_{45} = \pi/2$. In the $[14,0]^{g+}$ polyad, however, the probability distribution of the lowest energy eigenstate in the (ρ_4, ρ_5) plane has "pulled away" from the ρ_5 axis, and the torsional probability distribution has become much more strongly peaked at $\Phi_{45} = \pi/2$. In the local mode coordinates, the most significant change in the probability distribution between $N_b = 12$ and 14 is that in the $[14,0]^{g+}$ eigenstate, there is little probability density in the vicinity of $(\rho_A = 0, \rho_B = 0)$, indicating that the eigenstate is associated with a motion that never passes through the linear configuration.

Thus, the lowest energy eigenstate in $[14,0]^{g+}$ can be identified as the first that clearly demonstrates a motion qualitatively different from *cis* bending and demonstrates the first signatures of counter-rotating character. In $[16,0]^{g+}$, the counter-rotating character becomes more clear, with the nodal coordinate in the (ρ_4, ρ_5) plane approaching a semi-circle (as it is for the nearly perfect counter-rotating states in $[22,0]^{g+}$). Further, the probability density in the (ρ_A, ρ_B) plane begins to resemble a minimum uncertainty Gaussian, indicating that the hydrogens are becoming locked into a given angle with respect to the CC axis. Finally, the probability distribution along the Φ_{AB} torsional coordinate develops well-defined oscillations (in this case, a total of 8), which indicate the number of quanta of angular momenta associated with each hydrogen.

One of the most interesting conclusions that arises from the preceding analysis is that the transition from *trans* to local bend character at the bottom of the polyad, and from *cis* to counter-rotating at the top, is *abrupt*, in the sense that a single eigenstate can be identified in which the first features of a qualitatively new motion are observed. Figure 7-8 provides an additional perspective on this phenomenon. Plotted in the figure is the energy difference between the lowest (circles) and highest (crosses) energy eigenstates in adjacent ($\Delta N_b = 2$) pure bending polyads. For $N_b \leq 10$, the highest energy eigenstates in each polyad are well approximated as pure *cis* bending

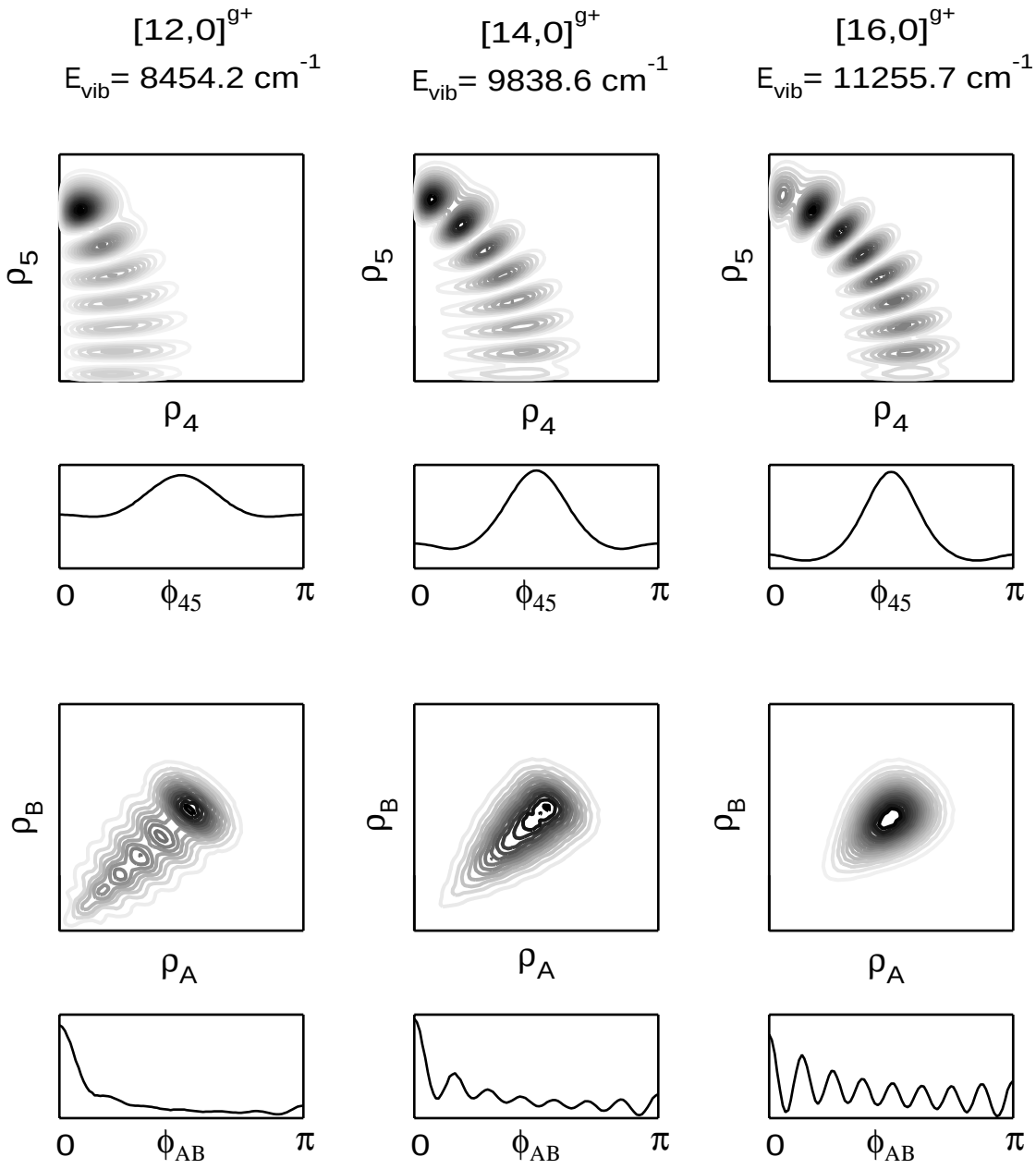

Figure 7-7: The highest energy eigenstates in the $[12,0]^{g+}$, $[14,0]^{g+}$, and $[16,0]^{g+}$ polyads, in normal and local mode bending coordinates. The qualitative change in eigenstate character from *cis* bend to counter-rotating is clear at $N_b = 14$. In the normal mode coordinates, the nodal coordinate in the (ρ_4, ρ_5) plane pulls away from the ρ_5 axis, and the torsional probability distribution begins to show a pronounced peak at $\Phi_{45} = \pi/2$. In the local mode coordinates, the transition to counter-rotating behavior is marked by the disappearance of the probability near $(\rho_A = 0, \rho_B = 0)$, and the development of well-defined oscillations in probability along the Φ_{AB} coordinate.

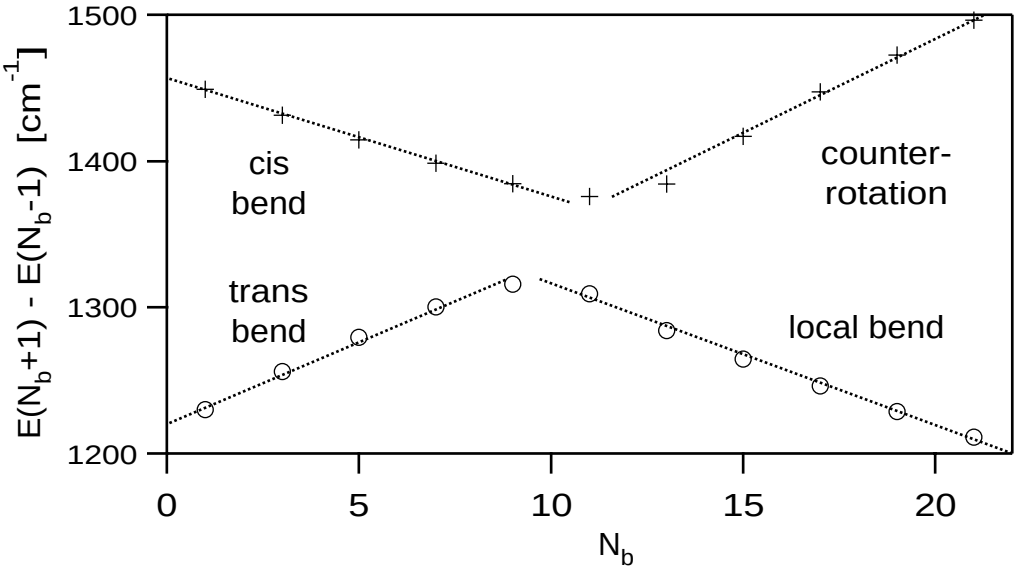

Figure 7-8: Energy differences between the highest (crosses) and lowest (circles) energy eigenstates in adjacent ($\Delta N_b = 2$) pure bending polyads ($\ell = 0$). The dotted lines are drawn for emphasis. The highest energy eigenstates within the polyads change character from *cis* bend to counter-rotation at $N_b \approx 14$, and the lowest energy eigenstates change character from *trans* bend to local bend at $N_b \approx 12$.

states, and the lowest energy eigenfunctions as pure *trans* bending. Thus, the slopes of the two progressions of states can be explained trivially in terms of the opposite anharmonicities of the two normal modes. Above $N_b = 10$ for the lower progression, and $N_b = 12$ for the upper progression, the slopes suddenly reverse. That is, the local bend and counter-rotating progressions of eigenfunctions appear rather suddenly, and can be characterized by negative and positive anharmonicities, respectively.

It should be noted that certain aspects of the analysis presented above have been noted previously in acetylene model systems as well as other Darling-Dennison systems. Sibert and McCoy reported [27, 24] the existence of the local bending class of states in their adiabatic bending Hamiltonian, with properties similar to those reported here (although their calculations extended only to $\sim$10,000 cm^{-1}). [Local bend states were also reported in the earlier work of Sibert and Mayrhofer [133].] Sibert and McCoy do not, however, seem to have noted the existence of the counter-rotating states, perhaps because the counter-rotating states first appear at slightly higher internal energy than the local bend states.

In addition, Rose and Kellman [109] analyzed an earlier version of the acetylene H^{eff} and noted the existence of local bending eigenstates, as well as a set of eigenstates that they classified as "precessional". It should be emphasized that the precessional states described by these authors do not, in fact, accurately represent any acetylene vibrational eigenstates. The precessional eigenstates differ from the counter-rotating states reported here in that they are implied to correspond to an in-plane motion, whereas the counter-rotating states only pass through planar configurations in a transitory way. The origin of this discrepancy is almost certainly due to the simplifying assumptions that Rose and Kellman invoked in order to facilitate the construction of a "catastrophe map", namely their neglect of all of the resonances except Darling-Dennison Bend I. Ignoring this discrepancy, however, the catastrophe maps constructed by these authors do predict several of the qualitative trends observed here, such as the appearance of local benders at the bottom of the polyad, and precessional (counter-rotating) states at the top, as well as the initial appearance of local benders at a lower internal energy than the precessional (counter-rotating) states.

7.6 Local Mode Bending H^{eff}

In the preceding sections, it has been demonstrated that, above E_{vib} ≈10,000 cm^{-1}, many acetylene bending vibrational levels can be assigned using local bend quantum numbers. This analysis has been made possible by the $H^{\text{eff}}_{\mathcal{N}}$, which reproduces all of the relevant experimental data up to 15,000 cm^{-1}. Thus, a *normal* mode Hamiltonian has been used to investigate *local* mode behavior. There is nothing fundamentally wrong with such an approach; in a similar way, a model of Darling-Dennison coupled symmetric and anti-symmetric stretches can be used to predict local stretching behavior [32]. However, the normal mode model provides little insight into the underlying physics of the local mode molecular vibrations. In this section, a local mode effective Hamiltonian, $H^{\text{eff}}_{\mathcal{L}}$, is introduced which is related to $H^{\text{eff}}_{\mathcal{N}}$ by a unitary transformation, but which provides greater insight into the bending dynamics above $E_{\text{vib}} \approx$ 10,000

cm^{-1}

There are a number of possible approaches to converting the bending effective Hamiltonian defined in Equation 7.5 from the normal mode basis set to a local mode basis set. One of the most straightforward is a "shift operator" approach, which has been employed by Baggott [105], Della Valle [128], Lehmann [127], and others in studies of the equivalence of local and normal mode models for stretching systems. Briefly, raising and lowering operators can be defined for the local bend degrees of freedom in the same manner as for the normal modes. By applying the chain rule to the coordinate transformation defined in Equations 7.14–7.17, the normal and local mode raising/lowering operators are related to each other according to

$$\hat{a}_{Ad} = \frac{1}{\sqrt{2}}(\hat{a}_{4d} + \hat{a}_{5d}) \tag{7.27}$$

$$\hat{a}_{Ag} = \frac{1}{\sqrt{2}}(\hat{a}_{4g} + \hat{a}_{5g}) \tag{7.28}$$

$$\hat{a}_{Bd} = \frac{1}{\sqrt{2}}(\hat{a}_{4d} - \hat{a}_{5d}) \tag{7.29}$$

$$\hat{a}_{Bg} = \frac{1}{\sqrt{2}}(\hat{a}_{4g} - \hat{a}_{5g}). \tag{7.30}$$

Using these relationships, the normal mode effective Hamiltonian, $H_{\mathcal{N}}^{\text{eff}}$, can be transformed to an effective Hamiltonian in local mode coordinates, $H_{\mathcal{L}}^{\text{eff}}$, using straightforward operator algebra.

Such a transformation is carried out in an Appendix (Section 7.8). However, the mathematics is tedious, and the resultant local mode effective Hamiltonian, in and of itself, provides little additional insight into the underlying physics of the local mode behavior. A more didactic approach is followed here, using earlier results of Lehmann [140], who considered a simple local mode model Hamiltonian for the acetylene bend modes. In close analogy to the Child and Lawton [30] treatment of ABA local stretching systems, Lehmann defined a system of two identical, harmonically coupled two-dimensional oscillators, which can be represented by the following *local*

mode effective Hamiltonian:

$$\begin{aligned}\hat{H}_{\mathcal{L}}^{\text{model}} &= \omega(\hat{v}_A+1)+\omega(\hat{v}_B+1)+x(\hat{v}_A+1)^2+x(\hat{v}_B+1)^2+g\hat{\ell}_A^2+g\hat{\ell}_B^2 \\ &+ \lambda\left[\hat{a}_{Ad}\hat{a}_{Bd}^\dagger+\hat{a}_{Ad}^\dagger\hat{a}_{Bd}+\hat{a}_{Ag}\hat{a}_{Bg}^\dagger+\hat{a}_{Ag}^\dagger\hat{a}_{Bg}\right] \end{aligned} \tag{7.31}$$

(for acetylene, it can be demonstrated [140] that $x \approx -3g$). This simple model Hamiltonian is capable of representing both local and normal mode behavior, as well as intermediate cases. The local mode limit is achieved trivially when $\lambda = 0$ (i.e., when there is no coupling between the oscillators), or more generally when the anharmonicity of individual bend modes "quenches" the inter-bend coupling. The normal mode limit is achieved if the anharmonicity of the individual oscillators is neglected.

Despite being a useful conceptual tool for understanding normal and local bend behavior in acetylene, $H_{\mathcal{L}}^{\text{model}}$ is much too simple to provide a quantitatively accurate representation of the experimental data. Lehmann examined the limitations of $H_{\mathcal{L}}^{\text{model}}$ by transforming it to a normal mode effective Hamiltonian, $H_{\mathcal{N}}^{\text{model}}$, by applying the relationships in equations 7.27–7.30):

$$\begin{aligned}\hat{H}_{\mathcal{N}}^{\text{model}} &= (\omega-\lambda)(\hat{v}_4+1)+(\omega+\lambda)(\hat{v}_5+1) \\ &+ \frac{x}{2}(\hat{v}_4+1)(\hat{v}_4+1)+\frac{3x+g}{2}(\hat{v}_4+1)(\hat{v}_5+1)+\frac{x}{2}(\hat{v}_5+1)(\hat{v}_5+1) \\ &+ \frac{g}{2}\hat{\ell}_4\hat{\ell}_4+\frac{3g+x}{2}\hat{\ell}_4\hat{\ell}_5+\frac{g}{2}\hat{\ell}_5\hat{\ell}_5 \\ &+ \frac{x-g}{4}(\hat{a}_{4d}^\dagger\hat{a}_{4g}^\dagger\hat{a}_{5d}\hat{a}_{5g}+\hat{a}_{4d}\hat{a}_{4g}\hat{a}_{5d}^\dagger\hat{a}_{5g}^\dagger) \\ &+ \frac{x-g}{4}(\hat{a}_{4d}\hat{a}_{4g}^\dagger\hat{a}_{5d}^\dagger\hat{a}_{5g}+\hat{a}_{4d}^\dagger\hat{a}_{4g}\hat{a}_{5d}\hat{a}_{5g}^\dagger) \\ &+ \frac{x+g}{8}(\hat{a}_{4d}^\dagger\hat{a}_{4d}^\dagger\hat{a}_{5d}\hat{a}_{5d}+\hat{a}_{4g}^\dagger\hat{a}_{4g}^\dagger\hat{a}_{5g}\hat{a}_{5g} \\ &\quad +\hat{a}_{4d}\hat{a}_{4d}\hat{a}_{5d}^\dagger\hat{a}_{5d}^\dagger+\hat{a}_{4g}\hat{a}_{4g}\hat{a}_{5g}^\dagger\hat{a}_{5g}^\dagger). \end{aligned} \tag{7.32}$$

This normal mode representation of the model Hamiltonian ($H_{\mathcal{N}}^{\text{model}}$) can be seen to be similar in structure to the effective Hamiltonian used to fit the experimental data that is defined in Eq. 7.5 ($H_{\mathcal{N}}^{\text{eff}}$). All of the diagonal elements of $H_{\mathcal{N}}^{\text{model}}$ also appear

in $H_{\mathcal{N}}^{\text{eff}}$ (although the treatment of zero-point energy is different)[5]. In addition, there are precisely three anharmonic resonances that generate off-diagonal matrix elements in each Hamiltonian: Darling-Dennison Bend I and II, and vibrational ℓ-resonance.

Thus, $H_{\mathcal{N}}^{\text{model}}$ can be considered to be a special case of $H_{\mathcal{N}}^{\text{eff}}$, in which certain high order terms (y_{444}, y_{445}, y_{455}, y_{555}, r_{445}, r_{545}) are omitted, and the constants for the remaining terms are constrained in certain internal relationships (analogous to the x-K relationships [105, 125, 126, 127, 128] that have been derived for many types of local stretch systems). Lehmann provides a complete list of these x-K relationships (Table I of Ref. [140]). Some of these relationships are approximately obeyed by the parameters in the fitted effective Hamiltonian ($H_{\mathcal{N}}^{\text{eff}}$); for example, the fitted values of r_{45} and s_{45} are -6.193 and -8.572, which agree modestly with the constraint implied by $H_{\mathcal{N}}^{\text{model}}$ that $r_{45} = s_{45}$. On the other hand, as Lehmann emphasizes, $H_{\mathcal{N}}^{\text{model}}$ also implies that $x_{44} = x_{55}$; the fitted constants (x_{44}=3.483 and x_{55}=-2.389) do not even have the correct relative signs.

The serious discrepancies between Lehmann's simple model Hamiltonian ($H_{\mathcal{N}}^{\text{model}}$) and the fitted spectroscopic Hamiltonian ($H_{\mathcal{N}}^{\text{eff}}$) imply that a more sophisticated local mode Hamiltonian (which will be designated $H_{\mathcal{L}}^{\text{eff}}$) is necessary to represent accurately the bending system of acetylene (i.e., $H_{\mathcal{L}}^{\text{eff}}$ will include higher order diagonal and off-diagonal terms that are neglected in $H_{\mathcal{L}}^{\text{model}}$). One straightforward and exact way of developing such a model is to partition the fitted spectroscopic Hamiltonian according to

$$H_{\mathcal{N}}^{\text{eff}} = H_{\mathcal{N}}^{\text{model}} + H', \tag{7.33}$$

in which the H' term represents all of the deviations of the full molecular bending effective Hamiltonian ($H_{\mathcal{N}}^{\text{eff}}$) from the model Hamiltonian ($H_{\mathcal{N}}^{\text{model}}$). The matrix representations of $H_{\mathcal{N}}^{\text{model}}$ and $H_{\mathcal{L}}^{\text{model}}$ are related by a unitary transformation, which can be obtained by diagonalizing $H_{\mathcal{N}}^{\text{model}}$ with $\lambda = 0$. This unitary transformation can

[5]Note that the diagonal elements of $H_{\mathcal{N}}^{\text{eff}}$ differ from a standard Dunham expansion in the treatment of zero-point energy; that is, the zero of energy of $H_{\mathcal{N}}^{\text{eff}}$ is defined to be the zero-point level of the molecule, and the ω, x, y, etc. parameters are not the standard Dunham parameters. This nonstandard notation has been adopted for consistency with previous work (Refs. [84] and [5]).

then be applied to H' to obtain the matrix representation of $H_{\mathcal{L}}^{\text{eff}}$.[6]

The eigenvalues and eigenfunctions of $H_{\mathcal{N}}^{\text{eff}}$ and $H_{\mathcal{L}}^{\text{eff}}$ are, of course, identical. Since these two representations of the effective Hamiltonian are equivalent, either can be used to describe the bending system of acetylene. However, the dynamics and eigenfunctions will generally be more easily understood in the representation in which the basis set functions more closely approximate the eigenfunctions. The preceding sections have already provided a wealth of anecdotal evidence that the eigenfunctions of $H_{\mathcal{N}}^{\text{eff}}$ in $[22,0]^{g+}$ are more readily assignable in a local mode coordinate set, and in fact several eigenstates at the low and high energy extremes of the polyad have been assigned, at least approximately. The development of the local mode representation $H_{\mathcal{L}}^{\text{eff}}$ allows these assignments to be made more rigorously. The eigenvector matrix resulting from the diagonalization of $H_{\mathcal{L}}^{\text{eff}}$ allows one to determine the assignability of all states within the polyad in the local representation using some suitable criterion.

One such criterion has been proposed by Hose and Taylor [139], which specifies that an eigenfunction is *assignable* if at least 50% of its character is attributable to a single basis function. Using this criterion, 65 eigenstates can be assigned in the $[22,0]$ polyad, out of a total of 144 (including all four possible symmetries). A subset of these assignments is listed in Table 7.2. By comparison, only 2 eigenstates in the $N_b = 22$ polyad can be assigned *normal mode* quantum numbers using the Hose-Taylor criterion.[7]

The ability to assign nearly 50% of the eigenfunctions in the $[22,0]$ polyad in the local mode basis set strongly suggests that it provides a superior representation of the bending dynamics of acetylene at high internal energy, as opposed to the traditional normal mode basis set. The suitability of the local mode basis at high internal energy can also be illustrated graphically using a correlation diagram [30, 141] like

[6] This numerical method is analogous to a commonly used procedure for transforming among the various Hund's cases; see R. W. Field and H. Lefebvre-Brion, *Perturbations in the Spectra of Diatomic Molecules* (Academic Press, Orlando, 1986), pp. 50-51.

[7] These two eigenstates have symmetries of $u/+$ and $u/-$, and both have an energy of 14274.8 cm^{-1}. They also each have 81.4% character of $|11^{+11}, 11^{-11}\rangle_{\mathcal{N}}$. Thus, the normal mode states with maximal angular momentum in the *trans* and *cis* oscillators remain decoupled from the rest of the states; they can be considered "extreme motion states" in the normal mode basis.

Table 7.2: Selected assignments of eigenstates in the local mode basis set, $|v_A^{\ell_A}, v_B^{\ell_B}\rangle_{\mathcal{L}}$. All energies are in units of cm^{-1}, and "Character" refers to the projection squared of the eigenfunction onto the relevant local mode basis function. "Perturbed" indicates that no eigenstate can be assigned as a particular local mode function using the Hose-Taylor criterion, because the basis function is substantially perturbed. "Does not exist" indicates that the local mode basis function with the given symmetry does not exist.

	$g+$ symmetry		$u+$ symmetry	
Assignment	Energy	Character	Energy	Character
$\|22^0, 0^0\rangle_{\mathcal{L}}$	13925.9	99.1%	13925.9	99.1%
$\|21^{+1}, 1^{-1}\rangle_{\mathcal{L}}$	14064.3	96.8%	14064.3	96.8%
$\|20^0, 2^0\rangle_{\mathcal{L}}$	14035.6	62.2%	14035.6	62.2%
$\|20^{+2}, 2^{-2}\rangle_{\mathcal{L}}$	perturbed		perturbed	
$\|18^0, 4^0\rangle_{\mathcal{L}}$	14119.8	50.8%	14119.8	50.8%
$\|16^{+6}, 6^{-6}\rangle_{\mathcal{L}}$	14718.4	68.0%	14724.4	54.7%
$\|15^{+7}, 7^{-7}\rangle_{\mathcal{L}}$	14882.6	54.0%	perturbed	
$\|14^{+8}, 8^{-8}\rangle_{\mathcal{L}}$	15067.6	75.5%	15053.4	50.1%
$\|13^{+9}, 9^{-9}\rangle_{\mathcal{L}}$	15240.2	60.6%	15263.5	91.8%
$\|12^{+10}, 10^{-10}\rangle_{\mathcal{L}}$	15478.2	92.2%	15445.8	97.5%
$\|11^{+9}, 11^{-9}\rangle_{\mathcal{L}}$	15306.7	51.3%	does not exist	
$\|11^{+11}, 11^{-11}\rangle_{\mathcal{L}}$	15671.4	97.8%	does not exist	

	$g-$ symmetry		$u-$ symmetry	
Assignment	Energy	Character	Energy	Character
$\|22^0, 0^0\rangle_{\mathcal{L}}$	does not exist		does not exist	
$\|21^{+1}, 1^{-1}\rangle_{\mathcal{L}}$	13984.6	98.9%	13984.6	98.9%
$\|20^0, 2^0\rangle_{\mathcal{L}}$	does not exist		does not exist	
$\|20^{+2}, 2^{-2}\rangle_{\mathcal{L}}$	14136.0	97.6%	14136.0	97.6%
$\|18^0, 4^0\rangle_{\mathcal{L}}$	does not exist		does not exist	
$\|16^{+6}, 6^{-6}\rangle_{\mathcal{L}}$	14722.2	63.8%	14724.6	59.1%
$\|15^{+7}, 7^{-7}\rangle_{\mathcal{L}}$	14888.5	66.6%	14882.3	55.7%
$\|14^{+8}, 8^{-8}\rangle_{\mathcal{L}}$	15053.3	50.3%	15067.4	77.8%
$\|13^{+9}, 9^{-9}\rangle_{\mathcal{L}}$	15263.5	91.8%	15240.2	60.6%
$\|12^{+10}, 10^{-10}\rangle_{\mathcal{L}}$	15445.8	97.5%	15478.2	92.2%
$\|11^{+9}, 11^{-9}\rangle_{\mathcal{L}}$	does not exist		15306.6	51.4%
$\|11^{+11}, 11^{-11}\rangle_{\mathcal{L}}$	does not exist		15671.4	97.8%

the one in Fig. 7-9. The lines in the diagram represent the state energies in the polyad in different limits. In the middle of the diagram are the eigenenergies, and at the far left and right are the zero-order energies of the normal and local mode basis sets, respectively. At positions intermediate between the eigenstate and basis state extremes, the energies are calculated by diagonalizing $H_{\mathcal{N}}^{\text{eff}}$ (left) or $H_{\mathcal{L}}^{\text{eff}}$ (right) with the off-diagonal elements multiplied by a scaling factor between 0 (the unperturbed basis set limit) and 1 (the eigenstate limit). The assignability of the eigenstates in a given basis set can be judged by the ease with which the curves can be followed across avoided crossings from the eigenbasis to the zero-order basis.

This correlation diagram provides substantial evidence for the superiority of the local mode representation in the $[22,0]^{g+}$ polyad. Several of the energy curves correlate directly between the eigenbasis and the local mode zero-order basis without undergoing any anticrossings; the assignments of these eigenstates are trivial. Many other curves on the local mode side of the diagram can also be followed easily through a series of weakly avoided crossings. In contrast, on the normal mode side of the diagram, the energy dispersion of the zero-order basis set is much smaller than that of the eigenbasis, and thus the majority of the energy curves display strong curvature, which can be ascribed to multiple, long-range, avoided crossings. Put in a slightly different way, the local mode basis set provides a superior zero-order representation for the $[22,0]^{g+}$ polyad because the local mode anharmonic resonances are weaker, in the sense that they mix the zero-order basis less strongly. In marked contrast, Fig. 7-9 also makes it clear that in the $[8,0]^{g+}$ polyad, the normal mode basis provides a better zero-order representation of the eigenfunctions, since the energy curves correlate much more simply with the normal mode than the local mode basis set.

Figure 7-10 illustrates how the local and normal mode representations of the effective Hamiltonian provide complementary insights into acetylene bending *dynamics*. Consider first the right-hand column, which depicts the survival probabilities for the series of pure local bend zero-order states, $|N_b^0, 0^0\rangle_{\mathcal{L}}^{g+}$, in the $[6,0]^{g+}$, $[14,0]^{g+}$, and $[22,0]^{g+}$ polyads. The $|22^0, 0^0\rangle_{\mathcal{L}}^{g+}$ zero-order state lies in the high energy, local mode regime, and is very nearly an eigenstate of the effective Hamiltonian. Thus, little

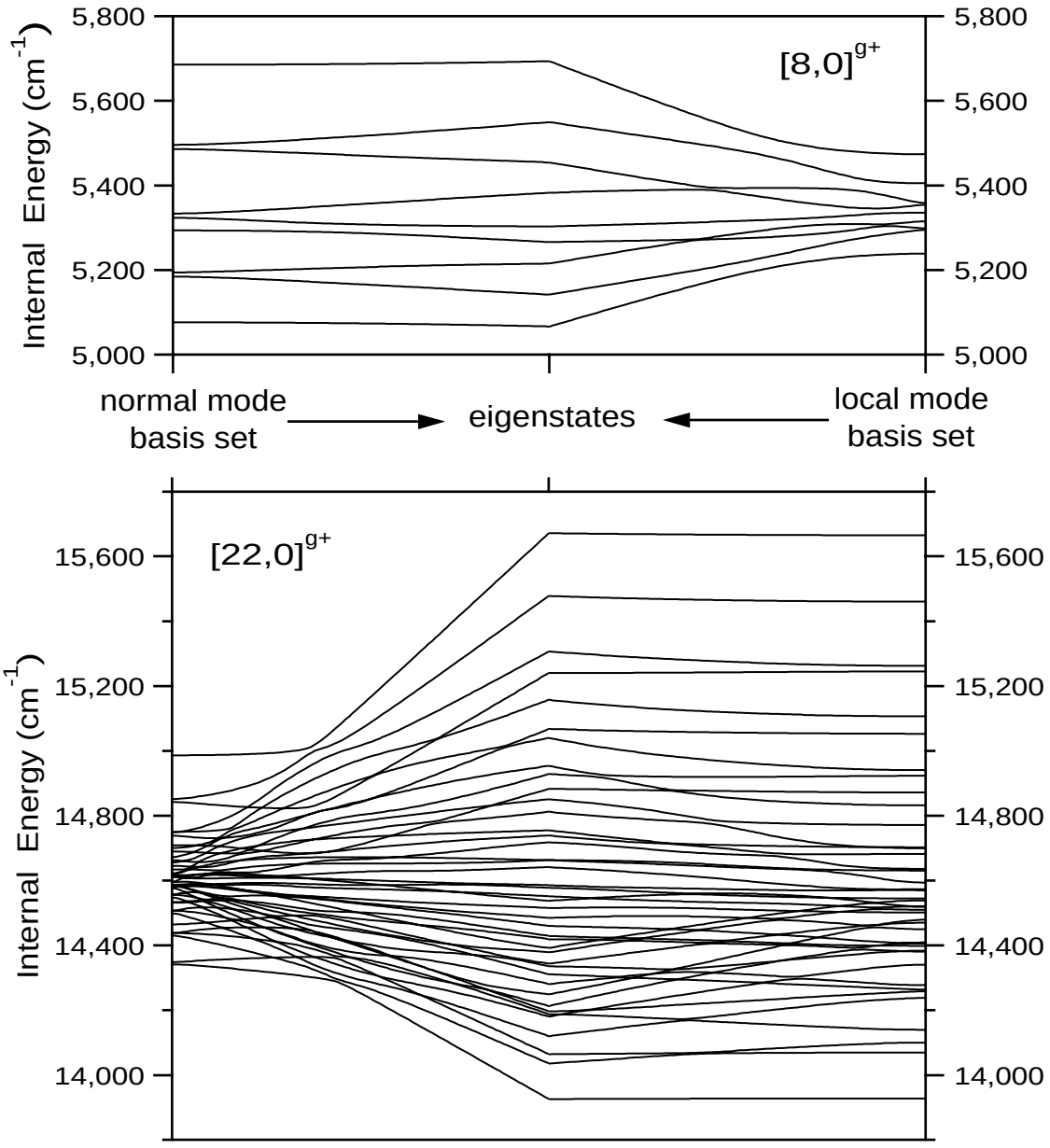

Figure 7-9: Correlation diagrams for the normal and local mode basis sets for the $[8,0]^{g+}$ (top) and $[22,0]^{g+}$ (bottom) polyads. The lines in the diagram represent the state energies in the polyad in different limits. In the middle of the diagram are the eigenenergies, and at the far left and right are the zero-order energies of the normal mode and local mode basis sets, respectively. It is clear from this diagram that many more eigenstates in the $[22,0]^{g+}$ polyad are assignable in the local mode basis set than in the traditional normal mode basis set, but that the normal mode basis set provides a better zero-order description of the eigenstates in the $[8,0]^{g+}$ polyad.

energy flows from this state into any of the other states within the polyad. The behavior of the $|6^0, 0^0\rangle_{\mathcal{L}}^{g+}$ zero-order state contrasts sharply. The rapid early-time decay of the survival probability is followed by a series of regular, strong recurrences. This is the expected behavior for a local mode excitation in the normal mode (low energy) regime. One can imagine a classical analog of this behavior in which one "bends back" one of the two hydrogens of the molecule; for a relatively small amplitude "pluck", the bend excitation would oscillate back and forth between the two equivalent oscillators, since these oscillators exhibit strong coupling in the low energy limit.

Although the survival probabilities of the local bend zero-order states are useful for conceptualizing the bending dynamics in the low and high energy regimes, the bright states that are actually observed in the experimental spectra are pure *trans* bend zero-order states, $|N_b^0, 0^0\rangle_{\mathcal{N}}^{g+}$, as discussed in Chapter 6. The survival probabilities for these bright states are plotted in the left hand column of Fig. 7-10, and the behavior of these states as a function of energy is essentially the opposite of that of the local bend states. In the low energy, normal mode regime ($|6^0, 0^0\rangle_{\mathcal{N}}^{g+}$), little energy exchange occurs, whereas the high energy, local mode regime ($|22^0, 0^0\rangle_{\mathcal{N}}^{g+}$) is characterized by strong, quasi-periodic oscillations in the survival probability. In the intermediate energy regime (i.e., $[14, 0]^{g+}$), in which the transition from normal to local mode behavior occurs, the survival probabilities of *both* the *trans* bend, $|14^0, 0^0\rangle_{\mathcal{N}}^{g+}$, and local bend, $|14^0, 0^0\rangle_{\mathcal{L}}^{g+}$, zero-order states evolve in a rather complicated manner, with fast initial decays ($\sim$100 fs) followed by a series of irregular partial recurrences. Thus, neither the local mode nor the normal mode paradigms provide simple insights into the dynamics in the complicated transitional regime. [In Chapter 8 it will be revealed that classical chaos plays a particularly important role at intermediate energies.]

As an aside, I wish to point out that the vastly different IVR associated with *trans*-bend and local bend bright states could be used to elucidate vibrational dynamics in the S_1 state of acetylene. The S_1 state of acetylene is predicted by *ab initio* theory [142] to support 3 local minima that correspond to *trans*-bent, *cis*-bent, and vinylidene structures. Only the *trans*-bent structure has been definitively observed. The vinylidene structure, although it corresponds to the global minimum of the S_1

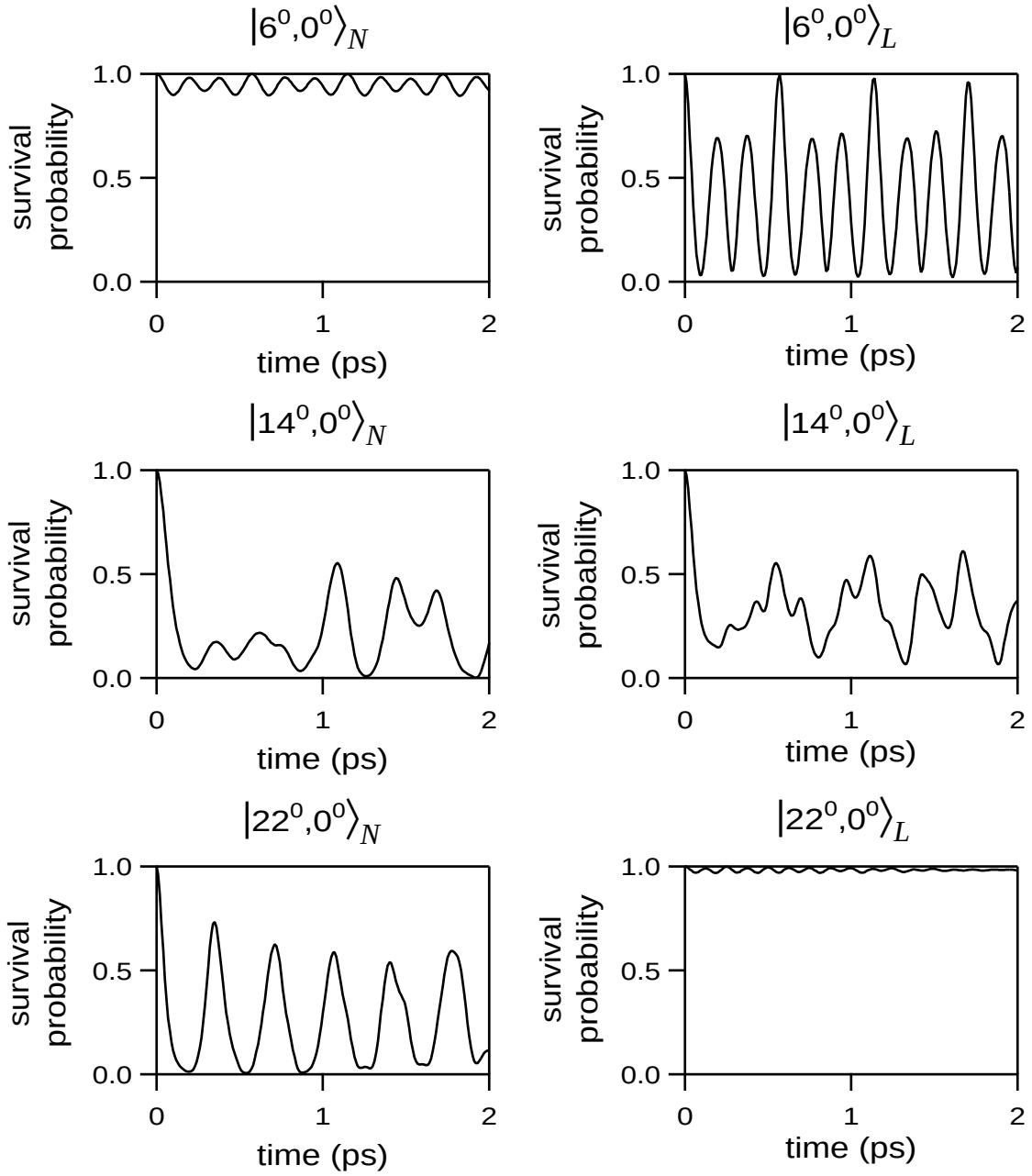

Figure 7-10: Survival probabilities for selected zero-order states in the $[6,0]^{g+}$, $[14,0]^{g+}$, and $[22,0]^{g+}$ polyads. The left column contains the survival probabilities for pure *trans* bend zero-order states ($|N_b^0,0^0\rangle_{\mathcal{N}}^{g+}$), while the right column contains the survival probabilities for pure local bend zero-order states ($|N_b^0,0^0\rangle_{\mathcal{L}}^{g+}$). Exciting a local mode state in the normal mode (low energy) regime, or a normal mode state in the local mode (high energy) regime, results in strong, quasi-periodic oscillations in the survival probability. In the intermediate energy regime ($[14,0]^{g+}$), neither the local nor normal mode representations provide a simple way of conceptualizing the dynamics.

state surface, cannot easily be observed by optical spectroscopy from the linear ground state due to extremely small Franck-Condon factors. However, the zero-point level of the *cis*-bent well is predicted to lie only ∼3000 cm^{-1} above the zero-point level of the *trans*-bent well. The transition state between the *trans*-bent and *cis*-bent structures, which lies ∼4000 cm^{-1} above the *trans*-bent zero-point level, is planar and local bent (half linear); that is, one of the CCH bend angles is ∼178°, while the other is ∼120°.

Thus, although I have glossed over a number of subtleties, there are 3 classes of bright states that one could expect to observe in emission from S_1 state vibrational levels that can be populated in a single resonance experiment (at sufficiently high internal energy above the *trans*-bent zero-point level): *trans*-bend, *cis*-bend, and local bend bright states. At this point, only *trans*-bend bright states have been definitively observed, although Prof. Soji Tsuchiya (Japan Women's University) has recorded spectra from previously unassigned levels in the S_1 state that do not match the usual pattern for *trans*-bend bright states [143]. The fractionation patterns (IVR) associated with the three possible classes of bright states evolve very differently as a function of internal energy, as can be seen in Fig. 7-11. The trends in IVR for the *trans*-bent bright states have been discussed in some detail in Chapter 6. The top panels of Fig. 7-11 depict the fractionation patterns for the $|10^0, 0^0\rangle_{\mathcal{N}}^{g+}$ and $|24^0, 0^0\rangle_{\mathcal{N}}^{g+}$ bright states, according to the effective Hamiltonian model. The $|10^0, 0^0\rangle_{\mathcal{N}}^{g+}$ bright state lies at the bottom of the $[10, 0]^{g+}$ polyad, and fractionation is minimal; the $|24^0, 0^0\rangle_{\mathcal{N}}^{g+}$ displays more extensive fractionation. The *cis*-bent bright states follow a similar pattern, except that the $|0^0, 10^0\rangle_{\mathcal{N}}^{g+}$ bright state lies at the *top* of the $[10, 0]^{g+}$ polyad. The local bend bright states, on the other hand, are *more* highly fractionated at *lower* internal energy! This trend in the frequency domain fractionation patterns is of course equivalent to the trends in the survival probabilities shown in Fig. 7-10. The point here is simply that the vibrational character of an unassigned S_1 state can be definitively identified by the fractionation patterns observed in DF spectra recorded from that state.

To conclude this section, I wish to comment briefly on a weakness of the local mode effective Hamiltonian (and effective Hamiltonians in general), which is that it

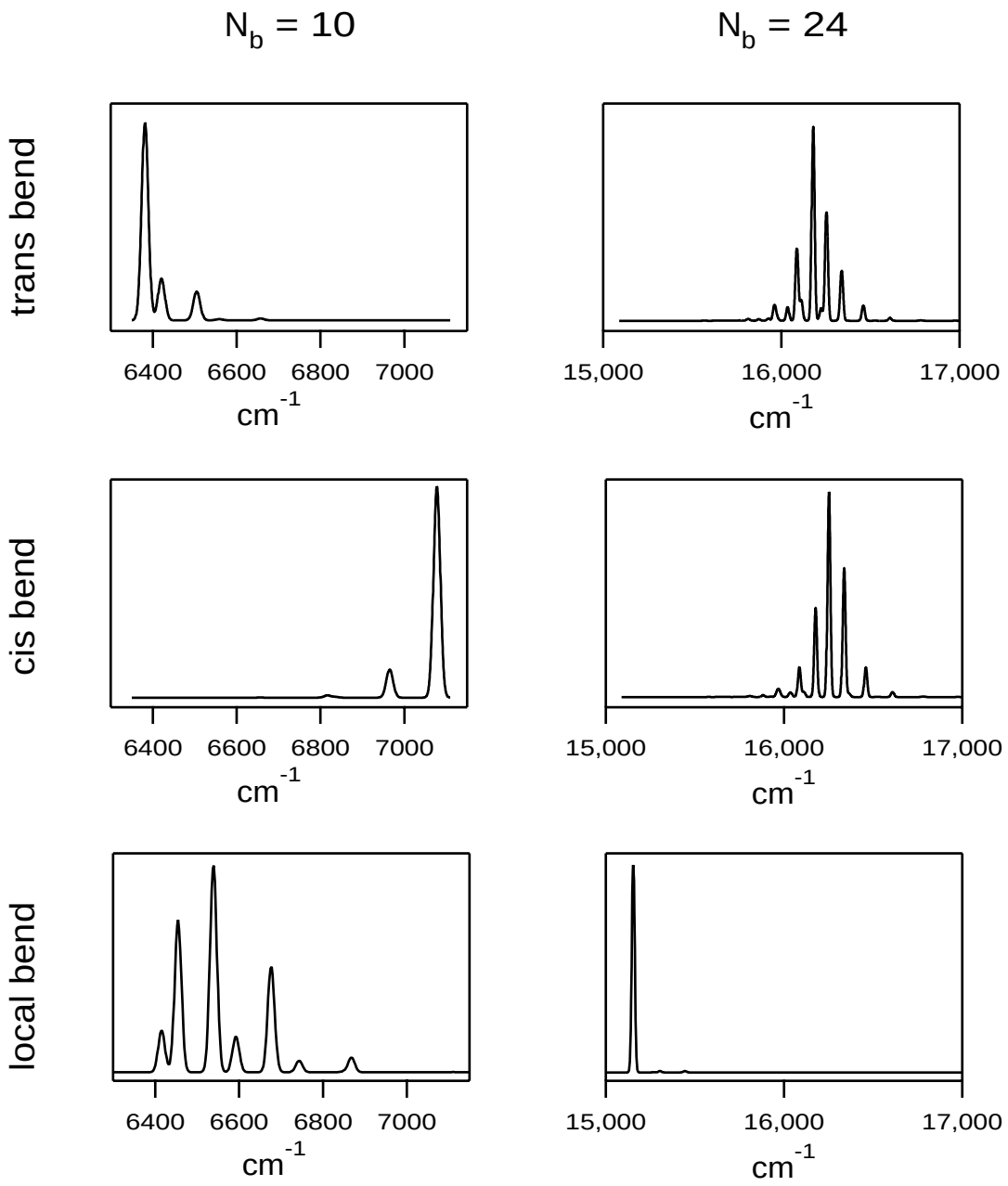

Figure 7-11: Predicted fractionation patterns for *trans*, *cis*, and local bend bright states with 10 and 24 quanta of excitation.

is difficult to relate the coordinate system that is implicit in the H^{eff} to a physical coordinate system of the molecule. As a consequence, it is not possible to *rigorously* determine, for example, the maximum bend angle that is achieved in one of the local bend states

However, a reasonable estimate of the maximum bend angle is possible with a few assumptions. For concreteness, consider the eigenstate depicted in Fig. 7-3(a), which can be assigned, to a very good approximation (see Table 7.2) as $|22^0, 0^0\rangle_{\mathcal{L}}^{g+}$. A reasonable assumption is that the bending coordinate ρ_A (or equivalently ρ_B) is equivalent to the CCH bend angle (θ) of the molecule, i.e., that the local bend motion occurs with no change in the CH bond length. The force field of Bramley, Carter, Handy, and Mills [20] provides an excellent representation of the acetylene potential energy surface near equilibrium, and specifies the dependence of the potential energy on the bend angle as

$$V(\theta) = 6323 \cdot \theta^2 + 1110 \cdot \theta^4$$

with V in units of cm^{-1}. Extrapolating this energy dependence to 19675.9 cm^{-1} (the zero-point referenced eigenstate energy of 13925.9 cm^{-1} plus an estimated 5750 cm^{-1} of zero-point energy), the classical turning point of the $|22^0, 0^0\rangle_{\mathcal{L}}^{g+}$ state is 1.49 rad (85.7°). Although this estimate of the classical turning point certainly cannot be considered quantitatively accurate, it is clear that the high-energy local bend states considered in this chapter involve very large amplitude motions.

7.7 Conclusion

Using graphical and numerical evidence, I have argued for the appropriateness of a local mode representation of the bending system of acetylene at high vibrational energy ($E_{\text{vib}} > 10{,}000$ cm^{-1}), in particular to describe the emergence of prominent local bend and counter-rotation states. On the other hand, it has also been demonstrated that the conventional normal mode representation provides an adequate zero-order representation at low internal energy ($E_{\text{vib}} < 8{,}000$ cm^{-1}). Thus, considerable insight is gained by describing the acetylene bending system with two formally equivalent

but complementary representations, normal and local mode.

However, one can make the argument that the local mode model of acetylene bending dynamics is *globally* superior, in the sense that it provides greater insight into the underlying physics, in terms of simple, intuitive concepts such as momentum and potential coupling between bonds. Local mode formalisms, whether applied to stretches, as in many previous studies, or to bends, as has been done here, also have the advantage of permitting greater insight into trends among a series of molecules with similar structure or functionality. That is, normal mode models tend to be molecule specific, since every molecule has different normal modes, while local mode models are grounded in a valence bond mindset, which lies at the heart of qualitative chemical description.

There may also be a specific advantage to fitting acetylene ground state spectra using a local mode model (most previous fits [5, 70, 87] have used the traditional normal mode model). The coupling terms in a local mode model (off-diagonal elements) will be well-determined by data at low energy (i.e., normal mode behavior dominates in the limit of strong coupling), while the bond anharmonicities (diagonal elements) will be well-determined by data at high energy (i.e., local mode behavior dominates in the limit of strong bond anharmonicity). By contrast, in the normal mode model, high order terms both on- and off-diagonal are determined primarily by data at high energy (only the strongest anharmonic contributions are well-determined at low internal energy). In addition, acetylene has long been known to display local stretch behavior (see, for example, Ref. [30]), and a fitting model that is local both in the stretches and bends may provide an optimal description of the molecule, especially at high energy.

Algebraic approaches to quantum structure, which have been developed by Iachello, Levine and others [118, 120], may provide insights that complement the work reported here. In particular, algebraic theory may provide a deeper understanding of the equivalence of the normal and local perspectives presented in this work, as well as a more powerful way of treating mode anharmonicity.

Finally, as discussed in Chapter 7.1, the transition state for isomerization between

acetylene and vinylidene is predicted by *ab initio* theory [72, 37, 34] to have a structure in which one of the two hydrogens is bent nearly 130° from linearity, while the other hydrogen is bent by less than 2°. For this reason, eigenstates with local bend character can be expected to play a special role in promoting acetylene-vinylidene isomerization.

Acknowledgments

This research has been supported by DOE Grant No. DE-FG0287ER13671. My work on this chapter was supported by the Department of the Army under a National Defense Science and Engineering Graduate Fellowship, and by the Fannie and John Hertz Foundation.

7.8 Appendix: Explicit x-K Relationships

In this Appendix, I consider the exact transformation between the normal and local mode representations of the acetylene pure bending effective Hamiltonian, using the relationships in Eqs. 7.27–7.30. To avoid exceptionally tedious algebra, I omit from this treatment all terms in the Hamiltonians that are sextic in the shift operators; that is, in Eq. 7.5 the y_{444}, y_{445}, y_{455}, y_{555}, r_{445}, and r_{545} terms are omitted. To be explicit, the problem considered here is the transformation of the following Hamiltonian to local mode coordinates, and the derivation of so-called x-K relationships among the normal and local mode parameters:

$$\begin{aligned}
\hat{H}^{\text{eff}}_{\mathcal{N}} &= \omega_4\hat{v}_4 + \omega_5\hat{v}_5 \\
&+ x_{44}\hat{v}_4\hat{v}_4 + x_{45}\hat{v}_4\hat{v}_5 + x_{55}\hat{v}_5\hat{v}_5 \\
&+ g_{44}\hat{\ell}_4\hat{\ell}_4 + g_{45}\hat{\ell}_4\hat{\ell}_5 + g_{55}\hat{\ell}_5\hat{\ell}_5 \\
&+ s_{45}(\hat{a}^\dagger_{4d}\hat{a}^\dagger_{4g}\hat{a}_{5d}\hat{a}_{5g} + \hat{a}_{4d}\hat{a}_{4g}\hat{a}^\dagger_{5d}\hat{a}^\dagger_{5g}) \\
&+ r^\circ_{45}(\hat{a}_{4d}\hat{a}^\dagger_{4g}\hat{a}^\dagger_{5d}\hat{a}_{5g} + \hat{a}^\dagger_{4d}\hat{a}_{4g}\hat{a}_{5d}\hat{a}^\dagger_{5g}) \\
&+ \frac{1}{4}(r^\circ_{45} + 2g_{45}) * \\
&\quad (\hat{a}^\dagger_{4d}\hat{a}^\dagger_{4d}\hat{a}_{5d}\hat{a}_{5d} + \hat{a}^\dagger_{4g}\hat{a}^\dagger_{4g}\hat{a}_{5g}\hat{a}_{5g} + \hat{a}_{4d}\hat{a}_{4d}\hat{a}^\dagger_{5d}\hat{a}^\dagger_{5d} + \hat{a}_{4g}\hat{a}_{4g}\hat{a}^\dagger_{5g}\hat{a}^\dagger_{5g}) \ . \quad (7.34)
\end{aligned}$$

In principle, the transformation defined by Eqs. 7.27–7.30 is all that is necessary to accomplish these goals, but the following relationships are quite useful for algebraic manipulation:

$$v_4 = \frac{1}{2}\left(v_A + v_B - \hat{O}_+\right) \tag{7.35}$$

$$v_5 = \frac{1}{2}\left(v_A + v_B + \hat{O}_+\right) \tag{7.36}$$

$$\ell_4 = \frac{1}{2}\left(\ell_A + \ell_B - \hat{O}_-\right) \tag{7.37}$$

$$\ell_5 = \frac{1}{2}\left(\ell_A + \ell_B + \hat{O}_-\right), \tag{7.38}$$

in which

$$\hat{O}_\pm = \hat{a}^\dagger_{Bd}\hat{a}_{Ad} + \hat{a}^\dagger_{Ad}\hat{a}_{Bd} \pm \hat{a}^\dagger_{Bg}\hat{a}_{Ag} \pm \hat{a}^\dagger_{Ag}\hat{a}_{Bg}. \tag{7.39}$$

Upon transformation, the resultant local mode Hamiltonian has the form

$$\begin{aligned}
\hat{H}^{\text{eff}}_{\mathcal{L}} &= \omega_A\hat{v}_A + \omega_B\hat{v}_B \\
&+ x_{AA}\hat{v}_A\hat{v}_A + x_{AB}\hat{v}_A\hat{v}_B + x_{BB}\hat{v}_B\hat{v}_B \\
&+ g_{AA}\hat{\ell}_A\hat{\ell}_A + g_{AB}\hat{\ell}_A\hat{\ell}_B + g_{BB}\hat{\ell}_B\hat{\ell}_B \\
&+ (\lambda + \lambda_A\hat{v}_A + \lambda_B\hat{v}_B)\hat{O}_+ \\
&+ \lambda_\ell(\ell_A + \ell_B)\hat{O}_- \\
&+ s_{AB}(\hat{a}^\dagger_{Ad}\hat{a}^\dagger_{Ag}\hat{a}_{Bd}\hat{a}_{Bg} + \hat{a}_{Ad}\hat{a}_{Ag}\hat{a}^\dagger_{Bd}\hat{a}^\dagger_{Bg}) \\
&+ r_{AB}(\hat{a}_{Ad}\hat{a}^\dagger_{Ag}\hat{a}^\dagger_{Bd}\hat{a}_{Bg} + \hat{a}^\dagger_{Ad}\hat{a}_{Ag}\hat{a}_{Bd}\hat{a}^\dagger_{Bg}) \\
&+ \frac{1}{4}(r_{AB} + 2g_{AB}) * \\
&\quad (\hat{a}^\dagger_{Ad}\hat{a}^\dagger_{Ad}\hat{a}_{Bd}\hat{a}_{Bd} + \hat{a}^\dagger_{Ag}\hat{a}^\dagger_{Ag}\hat{a}_{Bg}\hat{a}_{Bg} + \hat{a}_{Ad}\hat{a}_{Ad}\hat{a}^\dagger_{Bd}\hat{a}^\dagger_{Bd} + \hat{a}_{Ag}\hat{a}_{Ag}\hat{a}^\dagger_{Bg}\hat{a}^\dagger_{Bg}),
\end{aligned} \tag{7.40}$$

where the local mode parameters are defined in terms of the normal mode parameters, according to

$$\begin{aligned}
\omega_A &= \omega_B = \frac{\omega_4 + \omega_5}{2} \\
&+ \frac{1}{8}[-4g_{45} - r^\circ_{45} + 2(g_{44} + g_{55} + x_{44} - x_{45} + x_{55})]
\end{aligned} \tag{7.41}$$

$$x_{AA} = x_{BB} = \frac{1}{16}[2g_{45} + 3r^{\circ}_{45} + 2s_{45} + 4(x_{44} + x_{45} + x_{55})] \quad (7.42)$$

$$x_{AB} = \frac{1}{4}[-3g_{45} - 2r^{\circ}_{45} - s_{45} + x_{45} + g_{44} + g_{55} + 3(x_{44} + x_{55})] \quad (7.43)$$

$$g_{AA} = g_{BB} = \frac{1}{16}[4(g_{44} + g_{55}) + 6g_{45} - r^{\circ}_{45} - 2s_{45}] \quad (7.44)$$

$$g_{AB} = \frac{1}{4}[x_{44} - x_{45} + x_{55} - g_{45} + 3(g_{44} + g_{55}) + s_{45})] \quad (7.45)$$

$$\lambda = \frac{\omega_5 - \omega_4}{2} \quad (7.46)$$

$$\lambda_A = \lambda_B = \frac{x_{55} - x_{44}}{2} \quad (7.47)$$

$$\lambda_\ell = \frac{g_{55} - g_{44}}{2} \quad (7.48)$$

$$r_{AB} = \frac{1}{2}[x_{44} - x_{45} + x_{55} - g_{44} + g_{45} - g_{55} + r^{\circ}_{45} - s_{45}] \quad (7.49)$$

$$s_{AB} = \frac{1}{2}[x_{44} - x_{45} + x_{55} - g_{44} + g_{45} - g_{55} - r^{\circ}_{45} + s_{45}] \ . \quad (7.50)$$

It should be clear that it is also possible to transform the entire normal mode effective Hamiltonian for acetylene (see for example Ref. [5]), including the stretch modes, to a Hamiltonian that is local in *both* the stretches and bends. One would simply follow the above treatment for the bend modes, and apply a similar transformation (following Baggott [105], for example) to convert from symmetric and anti-symmetric CH stretch to local mode CH stretch coordinates. The CC stretch coordinate can be treated identically in both normal and local mode Hamiltonians. I have carried out this transformation, but do not report the results here because they are quite straightforward (other than the stretch-bend resonance terms) and would be out of place in a chapter devoted to a local mode description of the *bending* system of acetylene.

7.9 Appendix: Explicit Local Bend Hamiltonian

In the preceding sections, it has been emphasized that it is possible to define exact transformations (either analytical or numerical) between local and normal mode descriptions of the acetylene bend degrees of freedom. Thus, although an accurate effective Hamiltonian for the acetylene bends has only been developed up to this point

in the *normal mode* representation (Chapter 6), it is possible to gain insights into the bending dynamics using either the normal or local mode representation, as appropriate. Figures 7-9 and 7-10 demonstrate the complementary insights to be gained by using both representations.

In this Appendix I develop an explicit local mode model for the acetylene bends. That is, the parameters in a local mode Hamiltonian are determined by fitting them to the experimentally determined bending eigenstate energies. The details of the fit methodology are described in some detail in Section 6.2. However, predicting spectroscopic intensities is somewhat more complicated in a local mode than a normal mode basis set. In the normal mode formalism, the bright state is a member of the basis set, and thus the eigenvector matrix that results from diagonalizing a polyad in the normal mode basis can be used trivially to determine the fractional bright state character in each eigenstate. In the local mode formalism, the bright state is not a member of the local mode basis set, and the most straightforward way to calculate intensities is to transform the normal mode bright state into the local mode basis. This can be accomplished by recognizing that the vibrationless level is identical in the normal and local mode representations

$$|0^0, 0^0\rangle_{\mathcal{N}} = |0^0, 0^0\rangle_{\mathcal{L}} \tag{7.51}$$

and then applying shift operators to both sides of this equality to generate the bright state of interest in both representations

$$\begin{aligned} |v_4^0, 0^0\rangle_{\mathcal{N}} &= (\hat{a}_{4d}^\dagger)^{v_4/2}(\hat{a}_{4g}^\dagger)^{v_4/2}|0^0, 0^0\rangle_{\mathcal{N}} && (7.52)\\ &= (\hat{a}_{4d}^\dagger)^{v_4/2}(\hat{a}_{4g}^\dagger)^{v_4/2}|0^0, 0^0\rangle_{\mathcal{L}} && (7.53)\\ &= \frac{1}{2^{v_4/2}}(\hat{a}_{Ad}^\dagger - \hat{a}_{Bd}^\dagger)^{v_4/2}(\hat{a}_{Ag}^\dagger - \hat{a}_{Bg}^\dagger)^{v_4/2}|0^0, 0^0\rangle_{\mathcal{L}} \ . && (7.54) \end{aligned}$$

The local mode fit Hamiltonian is that in Eq. 7.40 augmented by the following

terms, which were found to be necessary in order to achieve an acceptable fit:

$$y_{AAA}\hat{v}_A\hat{v}_A\hat{v}_A + y_{AAB}\hat{v}_A\hat{v}_A\hat{v}_B + y_{ABB}\hat{v}_A\hat{v}_B\hat{v}_B + y_{BBB}\hat{v}_B\hat{v}_B\hat{v}_B + (\lambda_{AA}\hat{v}_A\hat{v}_A + \lambda_{BB}\hat{v}_B\hat{v}_B)\hat{O}_+ \ . \tag{7.55}$$

These parameters are of course subject to the constraints

$$y_{AAA} = y_{BBB} \tag{7.56}$$

$$y_{AAB} = y_{ABB} \tag{7.57}$$

$$\lambda_{AA} = \lambda_{BB} \ . \tag{7.58}$$

Also included in the fit is a parameter, $K_{r/s}$, that causes the strength of the quartic resonance parameters (r_{AB}, s_{AB}) to be dependent on the number of quanta of bend excitation:

$$r_{45} = r_{45}^{\circ} + K_{r/s}(\hat{v}_A + \hat{v}_B) \tag{7.59}$$

$$s_{45} = s_{45}^{\circ} + K_{r/s}(\hat{v}_A + \hat{v}_B) \ . \tag{7.60}$$

The y_{AAA}, y_{AAB}, y_{ABB}, y_{BBB}, λ_{AA}, λ_{BB}, and $K_{r/s}$ terms are among those that result from analytically transforming the sextic normal mode terms y_{444}, y_{445}, y_{455}, y_{555}, r_{445}, and r_{545} to the local mode representation, using the methods of Section 7.8.

An RMS agreement of 1.35 cm^{-1} between the calculated and experimental eigenenergies is achieved with the 14 independent parameters in Table 7.3. The agreement for two specific bright state fractionation patterns is depicted graphically in Fig. 7-12. It is clear that the fitted local mode model achieves the same level of agreement with experiment as the fitted normal mode model described in Chapter 6, but with 2 fewer parameters.

The explicit local mode model developed here can be used to gain insights into acetylene unimolecular dynamics, in a manner similar to the detailed analysis of the normal mode effective Hamiltonian in Chapter 6. Here I provide a single example of this type of analysis—a zero-order energy diagram for the $[22,0]^{g+}$ polyad (Fig. 7-

Table 7.3: Parameters determined from least-squares fit of the local mode pure bending effective Hamiltonian to the data set in Tables 6.1 and 6.2. Numbers in parentheses are 1σ uncertainties. All parameters are in units of cm^{-1}.

$\omega_A = \omega_B$	668.000 (0.023)
$x_{AA} = x_{BB}$	-1.688 (0.011)
x_{AB}	1.762 (0.022)
$g_{AA} = g_{BB}$	5.0307 (0.0079)
g_{AB}	0.144 (0.014)
$y_{AAA} = y_{BBB}$	0.00585 (0.00072)
$y_{AAB} = y_{ABB}$	-0.0270 (0.0010)
λ	-60.536 (0.036)
$\lambda_A = \lambda_B$	3.025 (0.010)
$\lambda_{AA} = \lambda_{BB}$	-0.02447 (0.00045)
λ_ℓ	-1.4200 (0.0078)
r°_{AB}	4.110 (0.017)
s_{AB}	1.519 (0.015)
$K_{r/s}$	-0.01648 (0.00070)

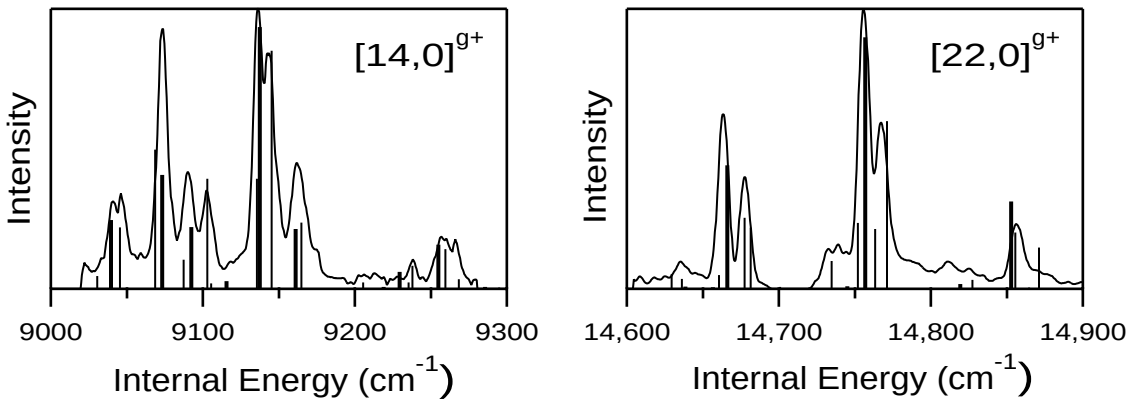

Figure 7-12: Comparison of predictions of the fitted local mode bending effective Hamiltonian (vertical lines) with the experimentally observed fractionated bright states (solid line). The thick vertical lines correspond to ($J = 1$, $\ell = 0$, e parity); the thin vertical lines represent ($J = 2$, $\ell = 2$, f parity).

13) in the local mode basis set (it has been argued above that the local mode basis is a better zero-order representation than the normal mode basis for this polyad). This zero-order diagram is organized in much the same way as those in Fig. 6-6, which were used to rationalize trends in dynamics in the normal mode basis set. Each horizontal line represents the energy of one local mode zero-order state, and the states are grouped into columns according to the number of quanta of excitation in each local bending oscillator. In each column, the states with maximal $|\ell_A| = |\ell_B|$ are at the top; the identities of a few of the zero-order states are marked explicitly on the diagram. It should be noted that the zero-order states depicted have well-defined parity and g/u symmetry. Thus, the labels on the states should be interpreted with caution. For example,

$$|22^0, 0^0\rangle_{\mathcal{L}}^{g+} \Rightarrow \frac{1}{\sqrt{2}}\left[|22^0, 0^0\rangle_{\mathcal{L}} + |0^0, 22^0\rangle_{\mathcal{L}}\right] \tag{7.61}$$

$$|11^{+11}, 11^{-11}\rangle_{\mathcal{L}}^{g+} \Rightarrow \frac{1}{\sqrt{2}}\left[|11^{+11}, 11^{-11}\rangle_{\mathcal{L}} + |11^{-11}, 11^{+11}\rangle_{\mathcal{L}}\right] \tag{7.62}$$

$$\begin{aligned} |12^{+10}, 10^{-10}\rangle_{\mathcal{L}}^{g+} \Rightarrow & \frac{1}{2}[|12^{+10}, 10^{-10}\rangle_{\mathcal{L}} + |12^{-10}, 10^{+10}\rangle_{\mathcal{L}} \\ & + |10^{+10}, 12^{-10}\rangle_{\mathcal{L}} + |10^{-10}, 12^{+10}\rangle_{\mathcal{L}}] \ . \end{aligned} \tag{7.63}$$

Several anharmonic resonances couple these zero-order states, including local-mode versions of Darling-Dennison resonances and vibrational ℓ-resonance, as well as the 1:1 resonance represented by the $\hat{O}_+$ operator (Eq. 7.39). However, for a given zero-order state, usually only one or two of these resonances strongly couple it to other states. For example, consider the $|11^{+9}, 11^{-9}\rangle_{\mathcal{L}}^{g+}$ state. It is coupled to the $|11^{+11}, 11^{-11}\rangle_{\mathcal{L}}^{g+}$ and $|11^{+7}, 11^{-7}\rangle_{\mathcal{L}}^{g+}$ states by the local mode version of vibrational ℓ-resonance. However, these states are widely spaced, and a numerical investigation reveals that the vibrational ℓ-resonance is of little consequence for these states, as well as for all others at the top of the polyad. On the other hand, the $|11^{+9}, 11^{-9}\rangle_{\mathcal{L}}^{g+}$ state is very nearly degenerate with $|13^{+9}, 9^{-9}\rangle_{\mathcal{L}}^{g+}$, to which it is coupled by the local mode version of the Darling-Dennison I resonance. These two states are in fact strongly mixed. The $g+$ symmetry eigenstate at 15306.7 cm^{-1} (see Table 7.2 and the lower left panel of

Fig. 8-8) can be approximated as

$$0.72|11^{+9}, 11^{-9}\rangle_{\mathcal{L}}^{g+} + 0.54|13^{+9}, 9^{-9}\rangle_{\mathcal{L}}^{g+} \ , \tag{7.64}$$

while the eigenstate at 15,240.2 cm^{-1} is approximately

$$0.60|11^{+9}, 11^{-9}\rangle_{\mathcal{L}}^{g+} - 0.78|13^{+9}, 9^{-9}\rangle_{\mathcal{L}}^{g+} \ ; \tag{7.65}$$

in other words, these two eigenstates can be considered to arise largely from a single resonant interaction between the $|13^{+9}, 9^{-9}\rangle_{\mathcal{L}}^{g+}$ and $|11^{+9}, 11^{-9}\rangle_{\mathcal{L}}^{g+}$ zero-order states.[8]

[8]This interaction can also be observed in the correlation diagram in Fig. 7-9. The $|13^{+9}, 9^{-9}\rangle_{\mathcal{L}}^{g+}$ and $|11^{+9}, 11^{-9}\rangle_{\mathcal{L}}^{g+}$ zero-order states are the two nearly degenerate states above 15,200 cm^{-1} on the local mode side of the $[22, 0]^{g+}$ diagram; the repulsion between the two is evident as the resonances are turned on.

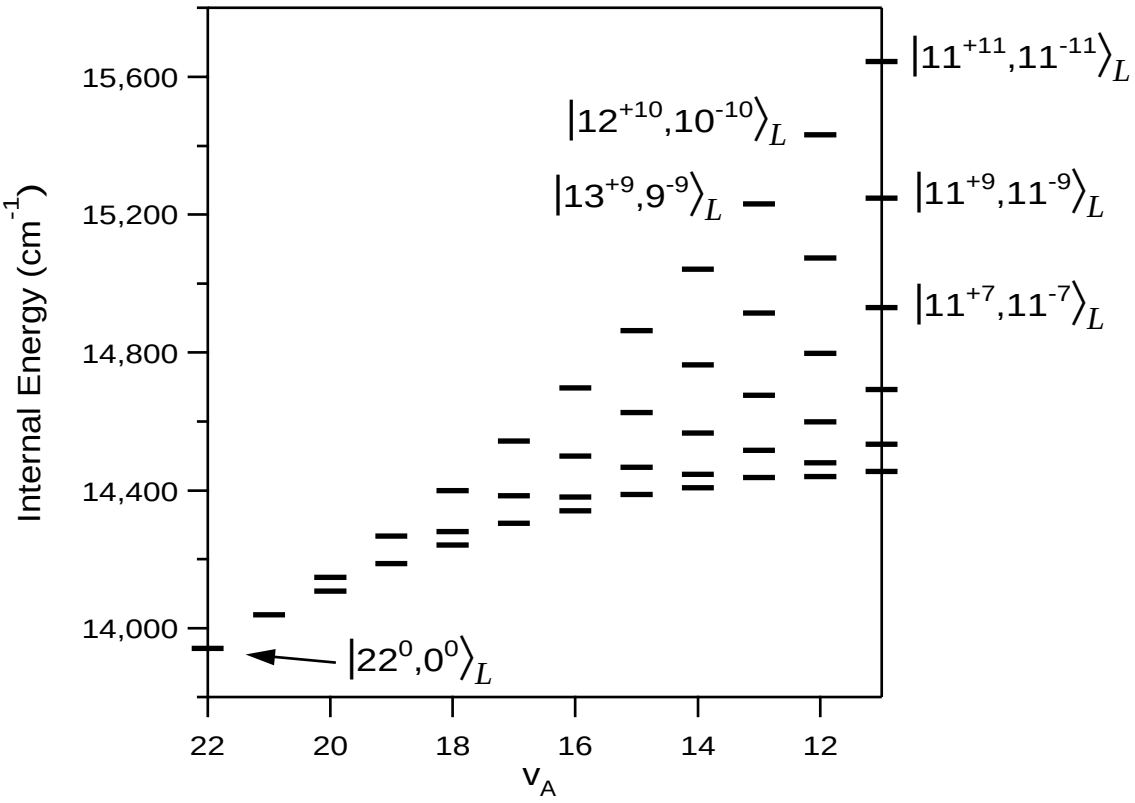

Figure 7-13: Energies of the zero-order states within the $[22,0]^{g+}$ polyad in the local mode basis, plotted as a function of v_A. In each column, the states with maximal $|\ell_A| = |\ell_B|$ are at the top; the identities of a few of the zero-order states are marked explicitly on the diagram.

Chapter 8

Semiclassical Analysis of Bending Vibrational Structure

This study resulted from a collaboration between Christof Jung, Howard Taylor, Bob Field, and myself. This chapter, in a slightly modified form, has been accepted for publication at the Journal of Chemical Physics.

8.1 Introduction

In this chapter, techniques of semiclassical and nonlinear classical mechanics are employed to investigate the bending dynamics of acetylene, with particular emphasis on the dynamics near 15,000 cm^{-1} of internal energy. The semiclassical and classical studies described here are all based upon the effective Hamiltonian model of the acetylene bend degrees of freedom which was defined in Chapter 6. This model is expressed in terms of 16 empirically adjusted parameters and reproduces 84 pure bending vibrational levels of acetylene up to 15,000 cm^{-1} of internal energy with an RMS accuracy of ± 1.4 cm^{-1}.

In this and previous chapters, I have argued that, in the absence of a potential surface with sufficient accuracy, effective Hamiltonians can provide substantial insights into quantum vibrational dynamics. Studies of the time-domain dynamics (Chapter 6) and quantum eigenfunctions (Chapter 7) associated with the acetylene bend effective Hamiltonian have revealed that the quantum bending dynamics of acetylene at high energies ($\sim$15,000 cm^{-1}) is strikingly different from that at low energies, where the eigenstates can be assigned normal mode quantum numbers. In particular, the study of the quantum eigenstates in Chapter 7 revealed that at high energy, many of the eigenfunctions have surprisingly well-defined nodal coordinates, distinct from the normal mode coordinates, which can be interpreted as local bend (one hydrogen bending) and counter-rotation (the two hydrogens undergoing circular motion at opposite ends of the molecule) motions.

Here, techniques of nonlinear classical mechanics are employed to study the same system. Standard semiclassical correspondence rules are used to transform the quantum effective Hamiltonian to a classical one. The structure of phase space of this classical system (i.e., important periodic orbits, fraction of phase space occupied by

classical chaos) is studied in some detail as a function of energy. Particular attention is paid to the high energy regime ($\sim$15,000 cm^{-1}), where the classical mechanics not only confirms the existence of stable local bend and counter-rotation motions but also uncovers several more complicated yet stable bending vibrational motions that had not previously been inferred from the quantum wavefunctions.

I wish to mention briefly at the outset what I consider to be the most salient conclusions of this work. First, the vast majority of the eigenstates of the quantum bending effective Hamiltonian have well-defined nodal coordinates that coincide with the stable periodic orbits of the classical system [144]. Despite the fact that chaos becomes prominent in the classical mechanics at energies as low as $\sim$6000 cm^{-1}, the majority of the eigenstates can be assigned semiclassical quantum numbers (number of quanta of excitation along the various stable periodic orbits), even near 15,000 cm^{-1}. It should be emphasized that the nodal coordinates of eigenfunctions in three or more dimensions are not always obvious by inspecting the eigenfunctions in an arbitrary set of coordinates, but the stable periodic orbits form a set of *natural* coordinates for visualizing the eigenfunctions [144].

The semiclassical assignment of the quantum eigenstates of acetylene is more than a simple cataloging exercise. The ability to associate the quantum eigenfunctions with stable classical motions may lead to new strategies for mode selective chemistry. It is possible, for example, to identify pairs of nearly isoenergetic eigenstates that are associated with qualitatively different vibrational motions; such pairs of eigenstates might then be expected to have exploitably distinct chemical properties, such as rates of reaction in certain bimolecular reactions.

A second, related conclusion is the contrast between the exceptionally complicated appearance of the experimental spectra and the surprisingly simple dynamics (either quantum or classical) that can be inferred from these spectra, when properly analyzed. This contrast has been a recurring theme in Part II of this thesis and is amplified here. In Chapter 5, it was demonstrated that much of the *perceived complexity* of acetylene $S_1 \rightarrow S_0$ dispersed fluorescence spectra can be accounted for by the energetic interleaving of polyad fractionation patterns—groups of peaks that terminate

on eigenstates which are characterized by the same set of polyad quantum numbers. Once separated from each other, many of the polyad fractionation patterns, which encode the quantum dynamics of the molecule, can be observed to be surprisingly simple. In this chapter another layer of complexity is removed, namely the energetic interleaving of eigenstates that belong to the same polyad but are associated with (i.e., have nodal coordinates along) qualitatively distinct periodic orbits.

This chapter will proceed as follows. In Section 8.2, the classical Hamiltonian that is studied in this chapter is derived from the quantum effective Hamiltonian. The approach taken is standard, and the technical details presented may be skipped by a reader who is interested primarily in the physical insights that have been gained into large-amplitude vibrational motion. It should be cautioned, however, that the notation which is used throughout the chapter is defined in this section. Section 8.3 explores the qualitative changes in the classical dynamics of the system as a function of energy, from the primarily normal mode dynamics at low energy, through the onset of chaos at $\sim$6000 cm^{-1}, to the high energy ($\sim$15,000 cm^{-1}) regime, where new stable bending motions coexist with classical chaos. Section 8.4 provides a detailed enumeration of the important periodic orbits near 15,000 cm^{-1}, and in Section 8.5, most of the quantum eigenfunctions near 15,000 cm^{-1} are demonstrated to have nodal coordinates that coincide with these periodic orbits, thus permitting semiclassical assignment of the majority of eigenstates. The remarks in the conclusion, Section 8.6, are directed largely toward a comparison of this work with other classical and semiclassical studies of acetylene and other small polyatomic molecules.

8.2 Classical Hamiltonian

The acetylene quantum bending effective Hamiltonian is discussed extensively in Chapters 6 and 7; Eq. 7.5 in particular expresses the effective Hamiltonian in terms of raising and lowering operators for the two-dimensional harmonic oscillator. Here an analogous classical Hamiltonian is derived using standard semiclassical rules [145]. It is particularly convenient to write the classical Hamiltonian in terms of action (I_j)

and angle (ϕ_j) variables (as opposed to positions and momenta), because the quantum mechanical raising and lowering operators can be replaced by

$$\hat{a}_j \rightarrow \sqrt{I_j}\exp(-i\phi_j) \tag{8.1}$$

$$\hat{a}_j^\dagger \rightarrow \sqrt{I_j}\exp(i\phi_j). \tag{8.2}$$

The acetylene bend effective Hamiltonian has four degrees of freedom, since each bend mode, *trans* (mode 4) and *cis* (mode 5) bend, is doubly degenerate. These four degrees of freedom will continue to be denoted by $4d$, $4g$, $5d$, $5g$. Using these semiclassical correspondence rules, the classical analog of the acetylene bend effective Hamiltonian, expressed in terms of the 16 molecular constants, is

$$\begin{aligned}
H_C &= -E^\circ + \omega_4(I_{4d}+I_{4g}) + \omega_5(I_{5d}+I_{5g}) \\
&+ x_{44}(I_{4d}+I_{4g})^2 + x_{45}(I_{4d}+I_{4g})(I_{5d}+I_{5g}) + x_{55}(I_{5d}+I_{5g})^2 \\
&+ y_{444}(I_{4d}+I_{4g})^3 + y_{445}(I_{4d}+I_{4g})^2(I_{5d}+I_{5g}) \\
&+ y_{455}(I_{4d}+I_{4g})(I_{5d}+I_{5g})^2 + y_{555}(I_{5d}+I_{5g})^3 \\
&+ g_{44}(I_{4d}-I_{4g})^2 + g_{45}(I_{4d}-I_{4g})(I_{5d}-I_{5g}) + g_{55}(I_{5d}-I_{5g})^2 \\
&+ 2s_{45}(I_{4d}I_{4g}I_{5d}I_{5g})^{1/2}\cos(\phi_{4d}+\phi_{4g}-\phi_{5d}-\phi_{5g}) \\
&+ 2[r^\circ_{45} + r_{445}(I_{4d}+I_{4g}-1) + r_{545}(I_{5d}+I_{5g}-1)] * \\
&\quad (I_{4d}I_{4g}I_{5d}I_{5g})^{1/2}\cos(-\phi_{4d}+\phi_{4g}+\phi_{5d}-\phi_{5g}) \\
&+ 1/2[r^\circ_{45} + 2g_{45} + r_{445}(I_{4d}+I_{4g}-1) + r_{545}(I_{5d}+I_{5g}-1)] * \\
&\quad [I_{4d}I_{5d}\cos 2(\phi_{4d}-\phi_{5d}) + I_{4g}I_{5g}\cos 2(\phi_{4g}-\phi_{5g})].
\end{aligned} \tag{8.3}$$

The numerical values of the 16 parameters are given in Table 6.3. Note that the zero point energy associated with the quantum effective Hamiltonian, $E^\circ = 1338.965$ cm^{-1}, has been subtracted to permit easier comparison with the quantum mechanical energy levels, which in the spectroscopic tradition are conventionally referenced to the zero-point energy.

Since two conserved (polyad) quantum numbers (N_b, the total number of quanta

of bend excitation, and ℓ, the total vibrational angular momentum; see Section 6.2) are associated with the quantum effective Hamiltonian, it is expected that two corresponding conserved quantities should be associated with H_C. These conserved quantities are

$$K_a = (I_{4d} + I_{4g} + I_{5d} + I_{5g})/4 \tag{8.4}$$

and

$$K_b = (I_{4d} - I_{4g} + I_{5d} - I_{5g})/4, \tag{8.5}$$

which correspond to the polyad quantum numbers, N_b and ℓ, respectively. Please note that K_a is defined here as a conserved action and should not be confused with the symmetric rotor rotational quantum number. The conservation of these quantities can be verified by computing their Poisson brackets (classical mechanical analog of the commutator) with H_C. Specifically, $4K_a$ is the total excitation of all elementary oscillators, including the zero point excitations. Since in the harmonic limit each of the four oscillators has 1/2 quantum of zero-point excitation, the correspondence between the classically and quantum mechanically conserved total actions can be established as $N_b = 4K_a - 2$. K_b is one-fourth of the total vibrational angular momentum ($\ell = 4K_b$). Note that, when referring to experimental data, I will continue to use the quantum mechanical polyad numbers, N_b and ℓ, as well as the notation of Chapters 6 and 7 for the pure bending polyads, $[N_b, \ell]^{g+}$, where the superscript indicates (when relevant) two other quantum mechanically conserved quantities—g/u symmetry, and parity $(+/-)$.

The existence of the two conserved quantities (K_a and K_b) implies that, although H_C was defined in Eq. 8.3 in terms of four degree of freedom ($4d$, $4g$, $5d$, and $5g$), it can be studied in just two (nonconserved) dimensions; this reduction in dimensionality makes possible a very detailed study of both the classical dynamics and quantum-classical correspondence, as will be seen below. In a technical sense, the dimensionality reduction is accomplished by performing a canonical transformation to rewrite H_C in terms of a new set of action/angle variables that include the conserved quantities K_a and K_b as two of the actions. H_C in this new set of action/angle

variables can be considered a two degree of freedom system, in which the values of the conserved quantities, K_a and K_b, enter as parameters. The angles that are conjugate to K_a and K_b will be designated θ_a and θ_b, respectively. The other two, non-conserved actions are labeled as J_a and J_b, and their conjugate angles are ψ_a and ψ_b.

The transformation from the original set of actions and angles (i.e., $4d$, $4g$, $5d$, $5g$) to this new set of actions and angles, with the conserved quantities made explicit, is defined by the following generating function [146]:

$$\begin{aligned} G(\phi_{4d}, \phi_{4g}, \phi_{5d}, \phi_{5g}, K_a, K_b, J_a, J_b) &= K_a(\phi_{4d} + \phi_{4g} + \phi_{5d} + \phi_{5g}) \\ &+ K_b(\phi_{4d} - \phi_{4g} + \phi_{5d} - \phi_{5g}) \\ &+ J_a(\phi_{4d} + \phi_{4g} - \phi_{5d} - \phi_{5g}) \\ &+ J_b(-\phi_{4d} + \phi_{4g} + \phi_{5d} - \phi_{5g}). \end{aligned} \tag{8.6}$$

The ability to specify a generating function for the transformation guarantees that it is canonical (i.e., that the form of the Hamiltonian equations of motion are invariant upon transformation). The explicit form of the transformation is

$$\begin{aligned} \phi_{4d} &= (\theta_a + \theta_b + \psi_a - \psi_b)/4 \\ \phi_{4g} &= (\theta_a - \theta_b + \psi_a + \psi_b)/4 \\ \phi_{5d} &= (\theta_a + \theta_b - \psi_a + \psi_b)/4 \\ \phi_{5g} &= (\theta_a - \theta_b - \psi_a - \psi_b)/4 \\ I_{4d} &= K_a + K_b + J_a - J_b \\ I_{4g} &= K_a - K_b + J_a + J_b \\ I_{5d} &= K_a + K_b - J_a + J_b \\ I_{5g} &= K_a - K_b - J_a - J_b. \end{aligned} \tag{8.7}$$

It should be noted that a similar canonical transformation has been used in other theoretical studies of acetylene [109, 27]. One minor difference is that here the angles have been reduced by a factor of two, so that the Hamiltonian is periodic in the angles

ψ_a and ψ_b with period 2π, instead of period π.

In these new coordinates the Hamiltonian function acquires the form

$$H_C = H_C^{\rm lin} + H_C^{\rm anh} + H_C^{\rm int} - E^\circ \tag{8.8}$$

$$H_C^{\rm lin} = 2\omega_4(K_a + J_a) + 2\omega_5(K_a - J_a) \tag{8.9}$$

$$\begin{aligned} H_C^{\rm anh} &= 4x_{44}(K_a + J_a)^2 + 4x_{45}(K_a + J_a)(K_a - J_a) + 4x_{55}(K_a - J_a)^2 \\ &+ 8y_{444}(K_a + J_a)^3 + 8y_{445}(K_a + J_a)^2(K_a - J_a) \\ &+ 8y_{455}(K_a + J_a)(K_a - J_a)^2 + 8y_{555}(K_a - J_a)^3 \\ &+ 4g_{44}(K_b - J_b)^2 + 4g_{45}(K_b - J_b)(K_b + J_b) + 4g_{55}(K_b + J_b)^2 \end{aligned} \tag{8.10}$$

$$\begin{aligned} H_C^{\rm int} &= 2s_{45}[(K_a^2 - K_b^2)^2 + (J_a^2 - J_b^2)^2 \\ &\quad - 2(K_a^2 + K_b^2)(J_a^2 + J_b^2) - 8K_aK_bJ_aJ_b]^{1/2}\cos(\psi_a) \\ &+ 2[r_{45}^\circ + r_{445}(2(K_a + J_a) - 1) + r_{545}(2(K_a - J_a) - 1)] * \\ &\quad [(K_a^2 - K_b^2)^2 + (J_a^2 - J_b^2)^2 - 2(K_a^2 + K_b^2)(J_a^2 + J_b^2) - 8K_aK_bJ_aJ_b]^{1/2}\cos(\psi_b) \\ &+ 1/2\{r_{45}^\circ + 2g_{45} + r_{445}[2(K_a + J_a) - 1] + r_{545}[2(K_a - J_a) - 1]\} * \\ &\quad \{[(K_a + K_b)^2 - (J_a - J_b)^2]\cos(\psi_a - \psi_b) \\ &\quad + [(K_a - K_b)^2 - (J_a + J_b)^2]\cos(\psi_a + \psi_b)\} \end{aligned} \tag{8.11}$$

Note that the angles θ_a and θ_b do not appear in H_C. This Hamiltonian defines the system investigated in the remainder of this chapter. Note that, for convenience in later sections, the Hamiltonian H_C has been divided into four parts: the zero-point energy E°, which was defined previously; a linear (harmonic) component, $H_C^{\rm lin}$; an anharmonic component, $H_C^{\rm anh}$, which contains all of the terms that arise from the diagonal anharmonicities in the quantum effective Hamiltonian; and an "interaction" component, $H_C^{\rm int}$, which contains all of the terms that arise from the off-diagonal resonances in the quantum effective Hamiltonian.

8.3 Gross Changes in the Dynamics with Increasing Energy

A discussion of the classical dynamics at very low energy is in some sense gratuitous, since it can be expected (correctly) that the dynamics would be dominated by the normal mode motions—*trans* and *cis* bend. However, in order to take advantage of a dimensionality reduction made possible by the conserved quantities K_a and K_b, the classical Hamiltonian H_C in Eqs. 8.8–8.11 is defined in terms of *abstract* actions and angles (J_a,J_b,ψ_a,ψ_b) that are not related in a simple way to physical motions of the molecule (see Section 8.7). This section investigates how the simple normal mode motions at low energy are represented in the abstract action/angle space in which H_C has been defined. The transition to more complex dynamics as energy increases, including the appearance of large-scale classical chaos, is also discussed. In this section and throughout this chapter, only bending dynamics with zero total angular momentum ($\ell = K_b = 0$) will be considered.

At low energy, the values of all actions (conserved and non-conserved) remain small, and thus the (linear) harmonic (Eq. 8.9) contribution to H_C dominates over the contributions of the (nonlinear) anharmonic (Eq. 8.10) and interaction (Eq. 8.11) terms. Thus, as $E \rightarrow 0$,

$$H_C \approx H_C^{\text{lin}} - E^\circ = 2\omega_4(K_a + J_a) + 2\omega_5(K_a - J_a) - E^\circ. \tag{8.12}$$

Keeping in mind that the dynamics are *parametrically* dependent on the conserved quantities K_a (and K_b), H_C in the low energy limit is dependent upon only one action, J_a, which makes the dynamics particularly simple. First, consider the range of energy that is accessible for a given value of K_a in this limiting case of H_C. [Note that specifying K_a is the classical mechanical equivalent of specifying a particular pure bending polyad; although the quantum mechanical conserved quantity, N_b, can only take integer values, K_a can take any positive value.] Given that $|J_a| \leq K_a$, which is required by the positivity of the elementary actions in Eq. 8.7, H_C^{lin} can vary only

between $4\omega_4 K_a$ and $4\omega_5 K_a$; thus

$$4\omega_4 K_a - E^\circ \leq E \leq 4\omega_5 K_a - E^\circ. \tag{8.13}$$

The lower end of the polyad corresponds to a maximal value of J_a ($J_a \approx K_a$) and it is clear from Eq. 8.7 that all trajectories at the bottom of the polyad must represent *trans* bending motion. Similarly, at the upper end of the polyad the value of J_a is minimal ($J_a \approx -K_a$) and all trajectories represent *cis* bending motion. In between, the dynamics changes gradually from *trans* to *cis* bending motion. These conclusions are of course entirely consistent with the studies of the quantum mechanical effective Hamiltonian in Chapters 6 and 7.

Now consider the dynamics associated with Eq. 8.12 in the abstract action/angle space (J_a,J_b,ψ_a,ψ_b). According to Hamilton's equations

$$\dot{\psi}_a = \frac{\partial H}{\partial J_a} = 2(\omega_4 - \omega_5) \tag{8.14}$$

$$\dot{\psi}_b = \frac{\partial H}{\partial J_b} = 0. \tag{8.15}$$

Keeping in mind that $\omega_5 > \omega_4$, every trajectory must rotate on the configuration torus, at fixed ψ_b, in the negative ψ_a direction with speed $2(\omega_5 - \omega_4)$. Thereby the entire phase space is filled by periodic orbits that rotate, and neighboring periodic orbits are quite similar to each other.

Inclusion of interaction terms in the Hamiltonian destroys most of these periodic orbits and generally distorts greatly those that remain. Even at low energy ($K_a \leq 2$), the anharmonic and interaction terms in H_C do play some role in the classical mechanics, and standard numerical methods [147, 148] can be used to investigate the changes in the dynamics as the non-harmonic terms increase in importance with increasing energy. One key element in this numerical investigation is the use of surfaces of section to gain an overview of the dynamics. The points on a generic surface of section represent the intersection of trajectories with a particular plane that cuts through phase space. Note that the use of surfaces of section in this study

is only possible due to the reduction of the dimensionality of H_C to two dimensions by making the conserved actions explicit. The patterns of points on the surfaces of section provide an excellent overview of the dynamics associated with H_C for each polyad. Tori, or more specifically trajectories running along tori, appear as concentric closed loops. Chaos tends to look like a randomly packed pattern of points. Periodic orbits are fixed points on the surface of section.

Two such surfaces of section are shown in Fig. 8-1. The surface of section on the left was calculated for the [4,0] polyad at 2461 cm^{-1}, but is typical of all of the surfaces of section at low energy. The intersection condition in this case is $\psi_a = 0$, $\dot{\psi}_a > 0$. The surface of section indicates the presence of two periodic orbits, which in fact are the only two stable periodic orbits (of period one) that survive when the anharmonic and interaction terms in H_C are included. These orbits rotate along ψ_a with $\psi_b = 0$ and $\psi_b = \pi$ respectively, both with constant value $J_b = 0$. Both orbits are elliptic (stable) and organize torus bundles (collections of concentric tori) around them in the 3D energy shell of the 4D abstract phase space. The two torus bundles are separated by dividing surfaces called separatrices, which are located at $\psi_b = \pi/2$ and $\psi_b = 3\pi/2$.

Thus, even with the inclusion of the anharmonic and interaction terms, the dynamics at low energy (< 5000 cm^{-1}) is quite simple. Regular (as opposed to chaotic) dynamics dominates and is organized by two torus bundles. Although no explicit calculations have been presented, it is clear that the dynamics corresponding to any arbitrary trajectory is closely related to the *trans* and *cis* bend motions. As energy increases, however, the anharmonic and interaction terms in H_C become increasingly important, leading to qualitatively new types of motion. Three "break points" in K_a can be identified at which fundamental changes in the dynamics occur. These break points are

1. The onset of trajectories that do not rotate in the ψ_a direction. This is actually a dual break point, with nonrotational motion occurring first at the bottom of the polyad, at $K_a = 2.21$, and then, at slightly higher K_a, at the top of the polyad ($K_a = 2.63$).

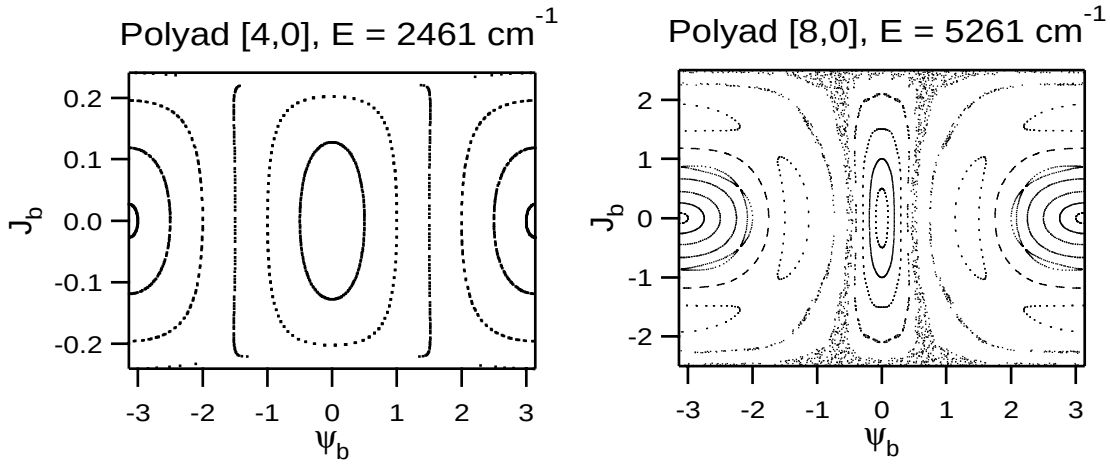

Figure 8-1: Surfaces of section representative of the regular, normal mode motions that dominate at low energy (left panel), and the onset of chaos and qualitatively new types of motion at higher energy (right panel). The intersection condition in both cases is $\psi_a = 0$, $\dot{\psi}_a > 0$. Note in the left panel the presence of two periodic orbits that cross the surface of section at ($J_b = 0$, $\psi_b = 0$) and ($J_b = 0$, $\psi_b = \pm\pi$) and organize torus bundles about them. The two tori are separated by separatrices at $\psi_b = \pm\pi/2$.

2. The onset of "large-scale" classical chaos ($K_a \approx 2.5$).

3. The crossing of the effective frequencies of the *trans* and *cis* bend motions ($K_a \approx 3.86$).

Each of these phenomena, which collectively give rise to the qualitatively new types of motions that dominate the dynamics at high energy, will be discussed briefly.

As K_a increases, the first sign of nonrotating motion (along ψ_a) occurs at the energetic bottom of the polyad at $K_a = 2.21$ ($N_b \approx 7$), and at the energetic top of the polyad at $K_a = 2.63$ ($N_b \approx 8$). At these values of K_a, the interaction terms $H_C^{\rm int}$ have grown sufficiently large that for at least some set of $(J_a, J_b, \psi_a, \psi_b)$, their contribution to $\dot{\psi}_a = \partial H_C/\partial J_a$ overcomes the tendency of $H_C^{\rm lin}$ to make the trajectories rotate in the negative ψ_a direction. The value of $\partial H_C^{\rm int}/\partial J_a$ is clearly largest when $\cos(\psi_a)$ and $\cos(\psi_b)$ are largest in magnitude (see Eq. 8.11), independent of the values of J_a and J_b. This occurs at the configuration space points $(\psi_a, \psi_b) = (0, 0)$ and (π, π). [The terms in $H_C^{\rm int}$ with $\cos(\psi_a \pm \psi_b)$ are much less important given the values of the fitted parameters.] These points are also extrema of H_C with respect to ψ_a and ψ_b; the point

(π, π) maximizes the energy, and the point $(0, 0)$ minimizes it, for arbitrary values of J_a and J_b. Hence localization appears first at $(0, 0)$ and (π, π) on the configuration space torus and expands into finite areas about these points as K_a increases. As a result, except for unphysically large values of K_a, the polyad energy range can be found easily by scanning through the allowed range of values of J_a and J_b separately for $(\psi_a, \psi_b) = (0, 0)$ and (π, π) to find $E_{\min}$ and $E_{\max}$ respectively. For $K_a > 2.21$, $E_{\min}$ occurs at a single point in phase space, which is clearly a fixed point of the dynamics. Similarly, $E_{\max}$ occurs at a single point in phase space for $K_a > 2.63$.

At roughly the same values of K_a for which nonrotating trajectories can first be identified, classical chaos can first be identified in the surfaces of section. Specifically, as can be seen in Fig. 8-1, at an energy of 5261 cm^{-1}, in the middle of the [8,0] polyad ($K_a = 2.5$, $K_b = 0$), chaos has grown to a volume that is recognizable on the scale of other features in the surface of section. In the language of dynamics, "large scale chaos" has appeared. At higher energy, the fraction of phase space occupied by chaos depends in complicated ways on both K_a and the energy within the polyad. Chaos in the $[22, 0]$ polyad will be considered in some detail in Section 8.4. Fig. 8-2 provides a few additional glimpses of the role of chaos at lower energy. The upper left panel is a surface of section for the same polyad as in the right panel of Fig. 8-1, but at slightly higher energy. Clearly, the fraction of phase space occupied by chaos depends sensitively on the energy within the polyad. The remaining panels in Fig. 8-2 depict similar surfaces of section, with the polyad number and the energy constrained by $N_b \approx E/668$ (with E in units of cm^{-1}). This constraint ensures that the energy for each surface of section remains very nearly in the middle of the polyad; note that classically, the polyad number is not required to be an integer. Chaos can be observed to develop rapidly at these energies and dominates the higher energy surfaces of section. It should be kept in mind, however, that at other energies within the same polyad, chaos may play a relatively minor role.

A third break point in K_a at which the classical and quantum dynamics change greatly occurs when the effective frequencies of the *trans* and *cis* bend modes become

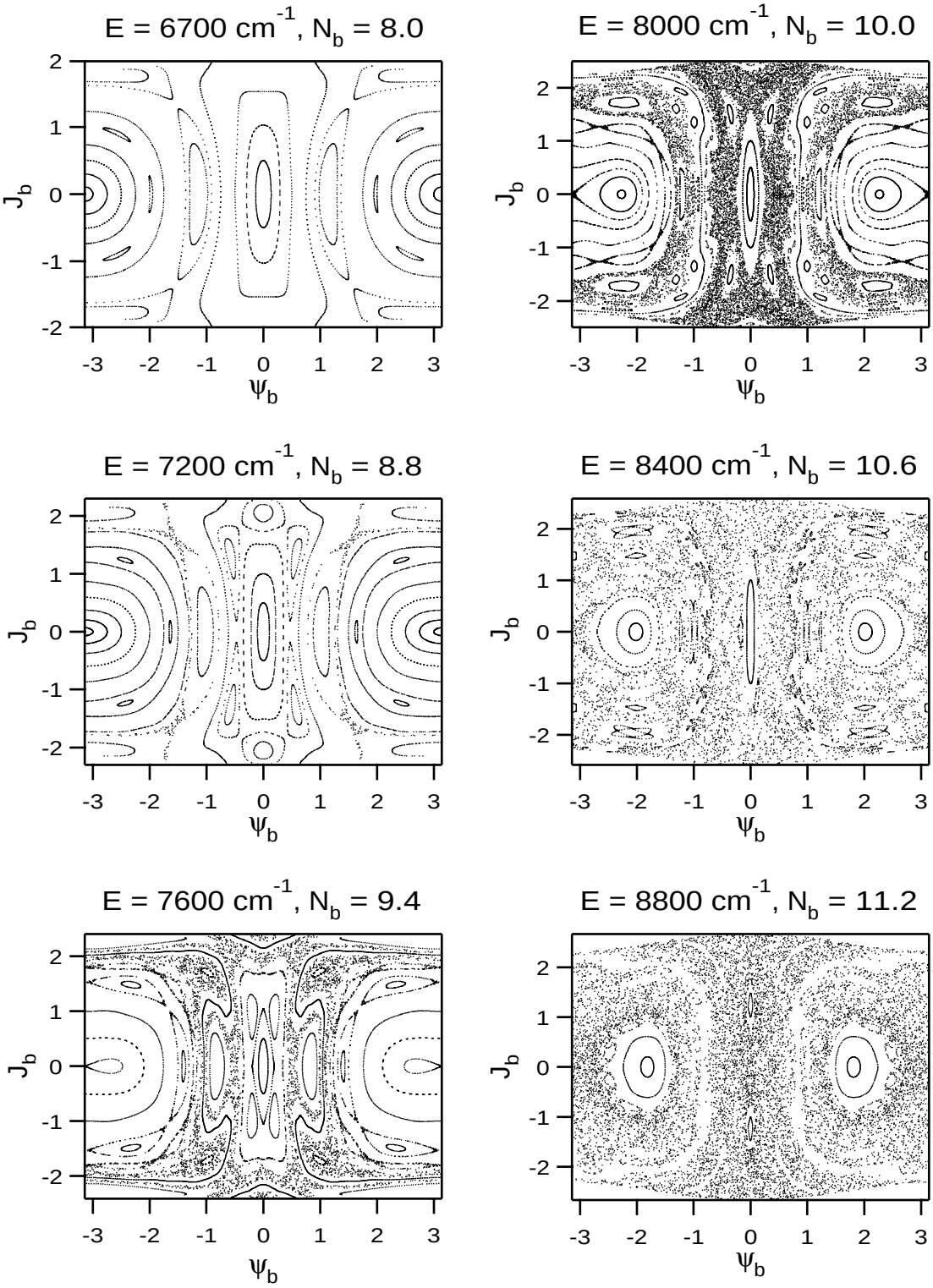

Figure 8-2: Surfaces of section with the polyad number and the energy constrained by $N_b \approx E/668$, with E in units of cm^{-1}, which ensures that the energy for each surface of section remains very nearly in the middle of the polyad; note that classically, the polyad number is not required to be an integer.

equal. The effective frequencies can be defined as

$$\omega_4^{\text{eff}} = \partial H_C^0 / \partial I_{4g} \tag{8.16}$$

and

$$\omega_5^{\text{eff}} = \partial H_C^0 / \partial I_{5g}, \tag{8.17}$$

where $H_C^\circ = H_C^{\text{lin}} + H_C^{\text{anh}}$. In general, degeneracies make any system more vulnerable to perturbations. In this particular case, when the effective frequencies become nearly equal, then the overall motion in the ψ_a direction becomes slower. When the difference between the effective frequencies becomes zero, then the motion becomes structurally unstable, meaning that even small interaction terms can change the dynamics qualitatively. The reason that the effective frequencies become equal at all is that the anharmonicities of the two modes have opposite signs (i.e., $x_{44} > 0$, $x_{55} < 0$). A straightforward but tedious analytical calculation reveals that the resonance condition $\omega_4^{\text{eff}} = \omega_5^{\text{eff}}$ can be achieved for some values of the actions in any polyad as long as $K_a > 3.86$. Above the onset of this resonance, the regions of phase space that contain motions other than the normal mode motions become dominant.

8.4 Classical Dynamics in the [22,0] Polyad

The major concern of this section is a description of each of the important classes of periodic orbits that exist within [22,0] polyad (i.e., $K_a = 6$ and $K_b = 0$), which lies at roughly 15,000 cm^{-1}. Periodic motions of the system, as opposed to arbitrary nonperiodic trajectories, are the focus of this discussion, because the periodic orbits organize phase space; the more stable a periodic orbit, the more strongly (quasi-periodic) trajectories in its vicinity (i.e., on the tori) mimic the periodic orbit motion. In addition, it will be seen in the next section that many of the quantum eigenstates have nodal coordinates which coincide with the stable periodic orbits, and thus can be assigned semiclassical quantum numbers indicating the number of nodes along a particular orbit.

A critical first step in investigating the classical dynamics in the [22,0] polyad (or any other) is the evaluation of accessibility: What regions of configuration space are accessible to the dynamics as a function of energy? A straightforward calculation that is outlined in Section 8.3 demonstrates that the lowest energy that is accessible within the [22,0] polyad is $E_{\min} = 13{,}806$ cm^{-1}, and this energy corresponds to a single point in the configuration space, $(\psi_a, \psi_b) = (0, 0)$. Conversely, the high energy end of the polyad converges to the point $(\psi_a, \psi_b) = (\pi, \pi)$ at $E_{\max} = 15{,}870$ cm^{-1}. The top rows of Figs. 8-3 and 8-4 consist of several "accessibility diagrams" that illustrate the accessibility of configuration space at intermediate energies.

Based upon these diagrams, the energy range of polyad $[22, 0]$ can be divided into four qualitatively distinct regions. At energies sufficiently close to $E_{\min}$ or $E_{\max}$, the dynamics is confined to the neighborhood of the points $(\psi_a, \psi_b) = (0, 0)$ and $(\psi_a, \psi_b) = (\pi, \pi)$ respectively. For the low energy end of the polyad, the motion in configuration space is confined in this way for energies up to $E_a = 14{,}086$ cm^{-1}, at which energy rotation in the ψ_b direction first becomes possible. The energies between $E_{\min}$ and E_a will be referred to as Region I. Region II begins at E_a when the point $(\psi_a, \psi_b) = (0, \pi)$ first becomes accessible. This point can be considered a saddle point of the Hamiltonian; that is, it is an extremal point of the Hamiltonian, in the sense that H_C increases in one direction but decreases in the perpendicular direction, not unlike the saddle point of a mountain. Region II ends at $E_b = 14{,}211$ cm^{-1}, which is the energy at which rotation in the ψ_a direction first becomes possible. In Region III, which ends at $E_c = 14{,}916$ cm^{-1}, rotation in both the ψ_a and ψ_b directions is possible. Finally, Region IV refers to energies between E_c and $E_{\max}$, where the dynamics becomes restricted to the vicinity of $(\psi_a, \psi_b) = (\pi, \pi)$ (that is, no rotation in either the ψ_a or ψ_b direction is possible). Also shown on the accessibility diagrams are projections of each important periodic orbit onto the (ψ_a, ψ_b) plane.

Accompanying each accessibility diagram is a representative surface of section at the same energy. The intersection condition used for the surfaces of section in Regions I, II, and III is $\psi_a = 0$, $\dot{\psi}_a > 0$, while for Region IV the intersection condition is $\psi_a = \pi$, $\dot{\psi}_a > 0$. The periodic orbits at the center of the important torus bundles

are also labeled on the surfaces of section. Together, the surfaces of section and the accessibility diagrams provide an excellent overview of the structure of phase space for this polyad. The dynamics in Regions I and IV, which lie at the energy extremes of the polyad, are the simplest and will be discussed first, followed by the somewhat more complicated intermediate regions, II and III.

The lowest energy region (I) is dominated by regular motion that is organized by the periodic orbits labeled L_1 and L_2, both of which librate (oscillate) about the minimum energy, stable elliptical fixed point $(\psi_a, \psi_b) = (0, 0)$. This librational motion of the periodic orbits in the abstract phase space provides no direct insight into the physical motions of the molecule. However, by applying the procedure of "lifting" that is discussed in Section 8.7, a reasonable representation of the physical molecular motion associated with the periodic orbit is obtained. The two left panels of Fig. 8-5 depicts the result of the lift procedure for periodic orbit L_1 at an energy quite close to $E_{\min}$; each panel represents the motion of one of the hydrogens in a plane perpendicular to the molecular axis. It is clear from this plot that one of the two hydrogens bends strongly from linearity, while the other undergoes only very small deviations (in the same plane as the other hydrogen).

It is interesting to note that the "lifted" motion of the periodic orbit L_2 at the same energy (not shown) is virtually indistinguishable from that of orbit L_1. The only significant difference is that the second hydrogen moves on a very small scale perpendicular to the motion of the first hydrogen. In fact, every motion (periodic or quasi-periodic) in the vicinity of $(\psi_a, \psi_b) = (0, 0)$ as $E \rightarrow E_{\min}$ looks basically like a *L*ocal bend motion (thus the label "L" for the periodic orbits that originate in this region), and lifting the point $(\psi_a, \psi_b) = (0, 0)$ itself, at $E_{\min}$, yields the most "perfect" local bend (i.e., minimum motion of the second hydrogen). The periodic orbits L_1 and L_2 can be conceptualized as normal modes of the deviation from pure local mode behavior. That is, the dynamics is formally equivalent to that of a 2 degree of freedom nonlinear oscillator. As $E \rightarrow E_{\min}$ the dynamics becomes increasingly harmonic, and there must be 2 basic mode motions, which are L_1 and L_2. As energy increases from $E_{\min}$ to E_a (the boundary between Regions I and II), the surfaces of section show

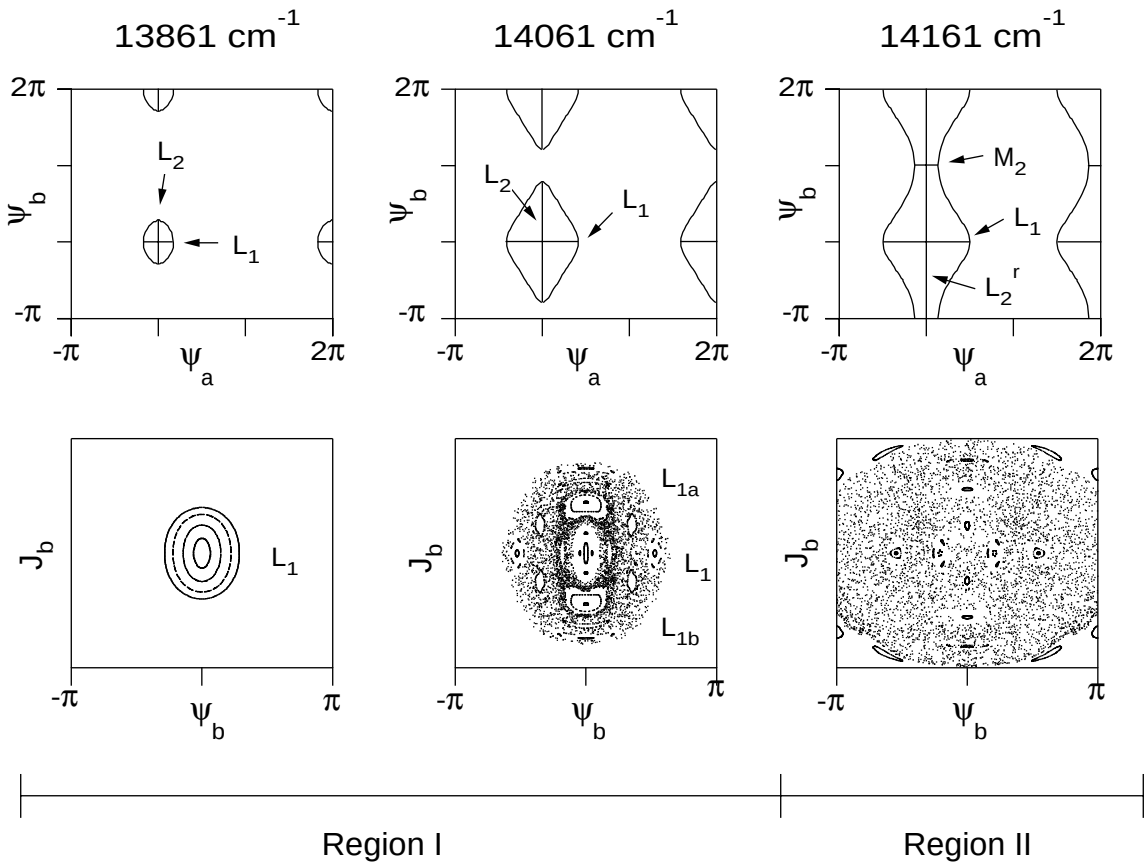

Figure 8-3: Overview of the classical dynamics in the [22,0] polyad. Top row: accessibility diagrams, which represent those regions of the configuration space (ψ_a, ψ_b) that are accessible to the classical dynamics, as well as projections of the important periodic orbits onto the (ψ_a, ψ_b) plane. Bottom row: representative surfaces of section at each energy that provide an overview of the regular and chaotic regions of phase space. The intersection condition is $\psi_a = 0$, $\dot{\psi}_a > 0$.

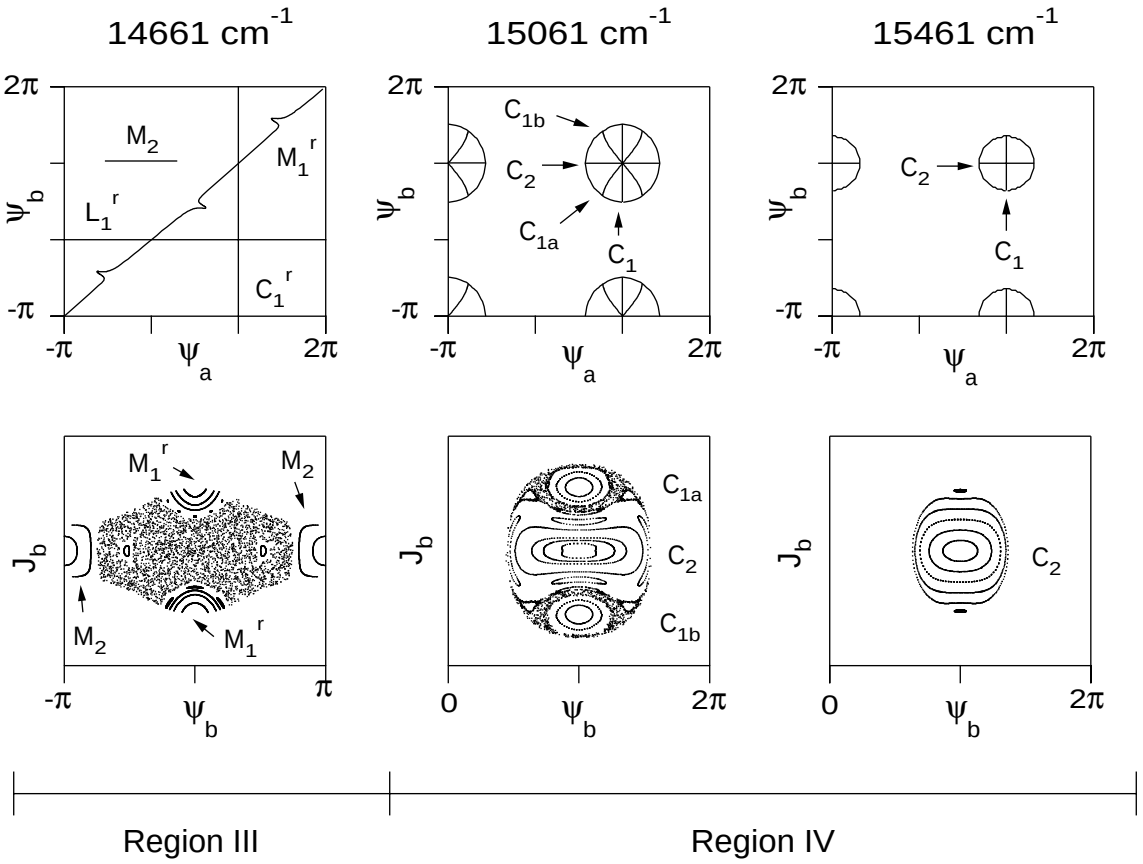

Figure 8-4: Continuation of Fig. 8-3. For the surface of section in Region III, the intersection condition is $\psi_a = 0$, $\dot{\psi}_a > 0$; for the those in Region IV it is $\psi_a = \pi$, $\dot{\psi}_a > 0$.

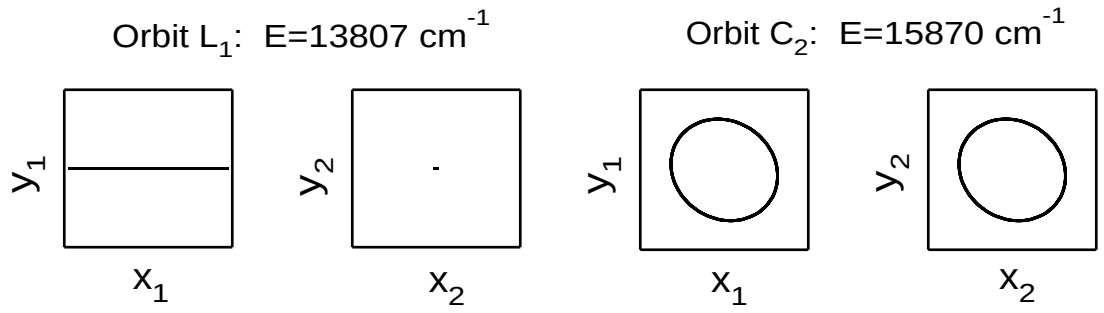

Figure 8-5: Physical motions of the hydrogen atoms that correspond to several of the most important periodic orbits in Regions I and IV of the [22,0] polyad, as determined by the "lifting" procedure described in Section 8.7. The left- and right-hand plots each describe the motion of one hydrogen in a plane perpendicular to the CC axis.

that L_2 bifurcates several times, and chaos becomes significant as $E \rightarrow E_a$ (the chaos grows mainly out of the separatrix lines created by the bifurcations of L_2, and in saddle-node bifurcations that create orbits similar to L_2). The fate of the L_1 and L_2 periodic orbits at energies greater than E_a will be discussed below, when Regions II and III are examined.

Like Region I, Region IV is dominated by regular motion that is organized by two periodic orbits, which are labeled C_1 and C_2 and which librate about the maximum energy, stable elliptic fixed point $(\psi_a, \psi_b) = (\pi, \pi)$. The lifted C_2 periodic orbit motion, at an energy close to $E_{\max}$, is shown in the two right panels of Fig. 8-5. Both hydrogens undergo nearly circular motions on opposite ends of the molecule. Although it is not obvious from this figure, the hydrogens rotate in opposite directions to satisfy the constraint of zero total vibrational angular momentum. Thus, this motion is named "counter-rotation". In close analogy to Region I, every motion (periodic or quasi-periodic) in the vicinity of $(\psi_a, \psi_b) = (\pi, \pi)$ as $E \rightarrow E_{\max}$ looks basically like a *C*ounter-rotation motion (thus the label "*C*" for the periodic orbits that originate in this region), and lifting the point $(\psi_a, \psi_b) = (\pi, \pi)$ itself, at $E_{\max}$, yields the most perfect counter-rotation (most nearly circular motions of both hydrogens). The dynamics in Region IV, as in Region I, is formally equivalent to that of a 2 degree of freedom nonlinear oscillator, and as $E \rightarrow E_{\max}$ it becomes increasingly harmonic, such that the C_1 and C_2 periodic orbits can be considered to be normal

modes of the deviations from pure counter-rotation behavior. As energy decreases from $E_{\max}$ to E_c, periodic orbit C_1 undergoes several bifurcations, producing other periodic orbits that mimic the libration of C_1 but are slightly displaced in phase space (see orbits C_{1a} and C_{1b} in Fig. 8-4). The average of all of these motions spawned from C_1 is quite close to the motion obtained by pretending that C_1 continues unaffected throughout the region. Note also that chaos arises near E_c.[1]

Whereas Regions I and IV are dominated by regularity, and organized by a few simple periodic motions, Regions II and III are dominated by chaos. As can be seen from the surface of section in Fig. 8-3, Region II is almost entirely chaotic, whereas in Region III (Fig. 8-3), two large-scale (i.e., large enough to quantize eigenfunctions) regions of stability coexist with the chaos. As might be expected, the stable periodic orbits in Region III can be considered descendants of the two stable orbits in Region IV, C_1 and C_2. More surprising is that the two important Region III periodic orbits can also be considered to be descendants of the periodic orbits in Region I (i.e., traced back through the highly chaotic Region II). Thus, it is possible to create a "family tree" of periodic orbits (Fig. 8-6) from $E_{\min}$ to $E_{\max}$, which specifically links orbits L_1 with C_1, and orbit L_2 with C_2.[2]

Consider first the L_1/C_1 linkage. Orbit L_1, which commences at $E_{\min}$, is dynamically stable up to ∼14,060 cm^{-1} (within Region I), where it suffers a pitchfork bifurcation in which it splits off two new orbits, L_{1a} and L_{1b}, that are mirror images of each other. When these new orbits branch off, they first run in the ψ_a direction. With increasing energy they begin to tilt towards the diagonal direction (i.e., $\psi_a = \psi_b$). Periodic orbit L_1 itself can be followed through Region II and into Region III, where, at 14471 cm^{-1}, it changes from libration to rotation in the ψ_a direction. Periodic orbits with both orientations of rotation exist, which are labeled L_1^{r+} and L_1^{r-}, but these are

[1]This chaos grows mainly out of the separatrix double loop that is created in the pitchfork bifurcation of C_1. That is, in a pitchfork bifurcation, the fixed point changes from elliptic (stable) to hyperbolic (unstable) and splits off two new elliptic fixed points, with the result that the invariant manifolds form a "figure 8" structure. In the nonintegrable case, this figure 8 is actually a fine strip of chaos.

[2]Note that amusingly (because we could not think of a deeper reason) the most stable orbit at the top of the polyad, C_2, shares one branch of the family tree with the less stable of the two at the bottom, L_2. Likewise, the less stable L_1 connects to the more stable C_1.

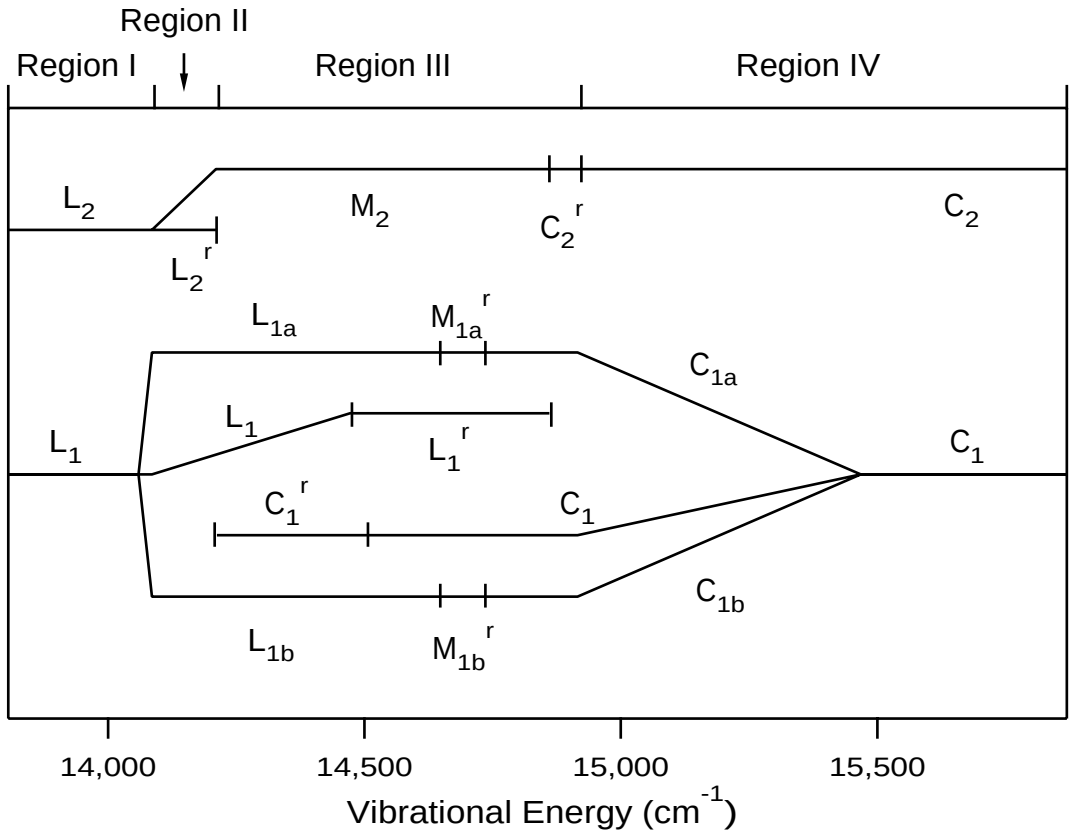

Figure 8-6: Family tree of periodic orbits in the [22,0] polyad. The periodic orbits are grouped into two branches, which specifically link L_1 with C_1 and L_2 with C_2. The vertical positions of the lines on the diagram are arbitrary.

always rather unstable and disappear at energies around 14,861 cm^{-1}. The bifurcated orbits L_{1a} and L_{1b} can also be followed into Region III, up to 14641 cm^{-1}, where they do not terminate but rather change their nature from librational to rotational; the new rotating orbits are labeled M^r_{1a} and M^r_{1b}. ["M" stands simply for *M*iddle and is used to denote those periodic orbits in Region III that link the C and L periodic orbits. The superscript "r" denotes periodic orbits have rotational, as opposed to librational, character.] Note that, in order not to overload the accessibility diagram for Region III in Fig. 8-4, only the projection of orbit M^r_{1a} is included (the M^r_{1b} orbit is related to M^r_{1a} by reflection through the line $\psi_b = 0$ or $\psi_b = \pi$). Continuing to higher energy, the orbits M^r_{1a} and M^r_{1b} can be linked to C_{1a} and C_{1b}, which arise from a pitchfork bifurcation of C_1 within Region IV, at 15,489 cm^{-1}. In close analogy to the $L_{1a/b}$ periodic orbits, when C_{1a} and C_{1b} are created, they run approximately in the ψ_b direction, but with decreasing energy they tilt increasingly towards the diagonal direction. These orbits transform into $M^r_{1a/b}$ as soon as they change from libration about the point (π, π) into rotation through the configuration torus in the diagonal direction.

The motion corresponding to periodic orbit M^r_1 is a compromise between the local bend and counter-rotation motions. As can be seen in the top two panels of Fig. 8-7, orbit M^r_1 involves one of the two hydrogens undergoing a primarily circular motion, reminiscent of the counter-rotation motion, while the motion of the other is reminiscent of a local bend, although the approximate plane of the bend switches its orientation periodically by $\pi/2$. Due to the existence of the K_b constant of the motion, however, both the "rectilinear" and "circular" motions of the hydrogens are distorted in such a way as to conserve zero total internal angular momentum at all times.

The L_2/C_2 linkage is somewhat easier to discuss by moving from high to low energy. Periodic orbit C_2 changes its behavior from libration to rotation in the ψ_a direction at the boundary of Regions IV and III (E_c = 14,916 cm^{-1}). The rotating version of the periodic orbit, C^r_2, remains stable or very slightly unstable down to 14,854 cm^{-1}, where it changes from rotation to libration about the point $(0, \pi)$. The

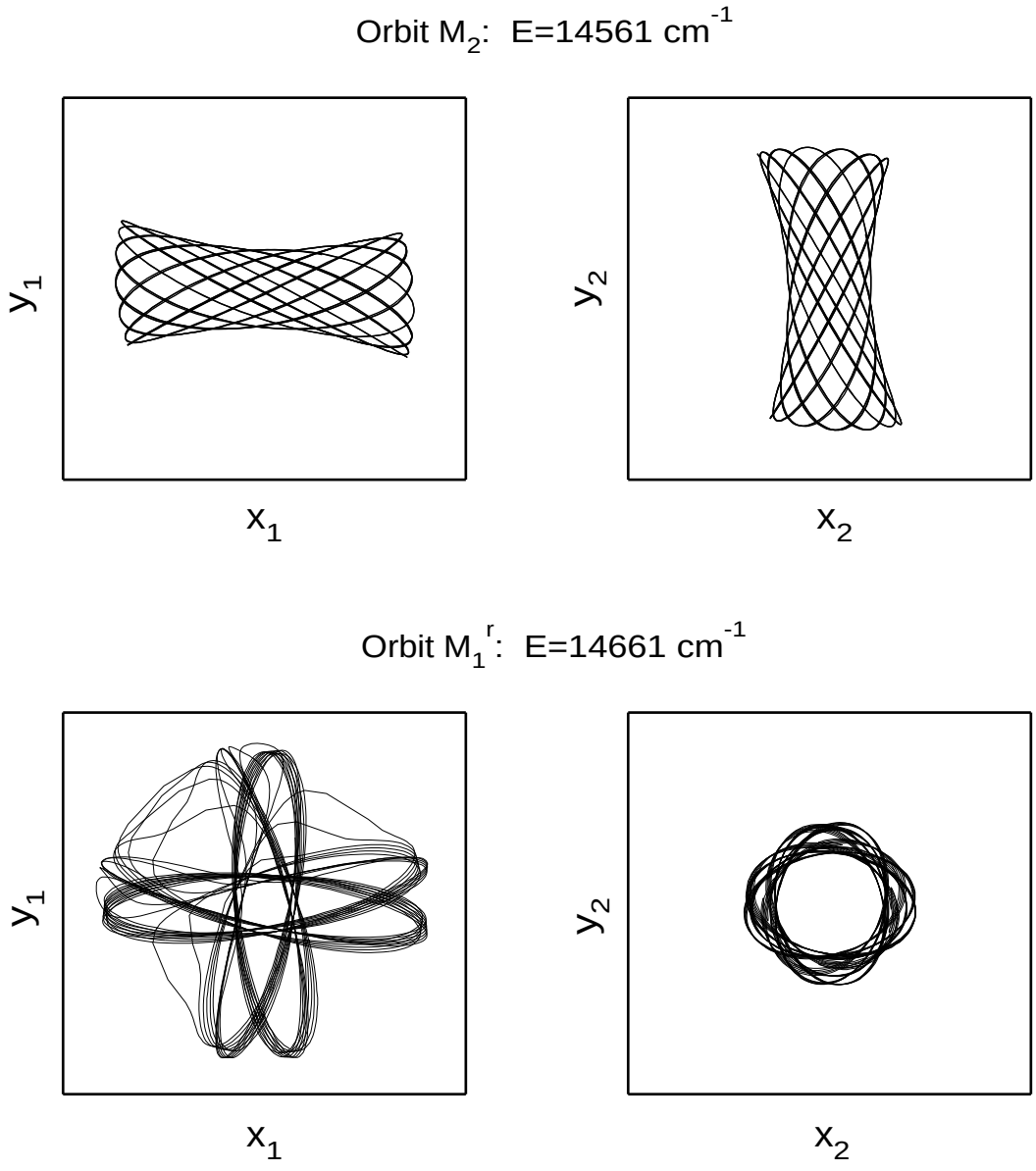

Figure 8-7: Physical motions of the hydrogen atoms that correspond to several of the most important periodic orbits in Regions II and III of the [22,0] polyad, as determined by the "lifting" procedure described in Section 8.7. The left- and right-hand plots each describe the motion of one hydrogen in a plane perpendicular to the CC axis.

new librating version of the orbit, M_2, persists throughout Regions III and II. The M_2 orbit remains stable down to 14,431 cm^{-1} and organizes a sizeable regular region that is embedded in chaos, as seen in the surface of section in Fig. 8-4. Below 14,161 cm^{-1} (i.e., in Region II) orbit M_2 is unstable but remains constrained to the vicinity of $(0, \pi)$; at E_a (the boundary between Regions I and II), it merges in a bifurcation process with periodic orbit L_2, which rotates along $\psi_a = 0$, and which is unstable in Region II.[3]

The L_2/C_2 link can also be seen in the "lifted" periodic orbits. As mentioned previously, as $E \rightarrow E_{\min}$, orbit L_2 corresponds to a large amplitude linear motion of one hydrogen and a small amplitude motion of the other hydrogen in a perpendicular direction. With increasing energy, the amplitude of the motion of the second hydrogen increases, and as $E \rightarrow E_a$, the amplitudes of motion of the two hydrogens become equal. As energy increases above E_a, the motion associated with M_2 increasingly involves a counter-rotational component (see Fig. 8-7). The rotational motion of the hydrogens associated with the orbit M_2 becomes more pronounced as energy increases within Region III (i.e., closer to the energy at which M_2 becomes C_2). Thus, in a satisfying way, the motions corresponding to both orbits M_1^r and M_2 provide bridges between the local bend and counter-rotation motions at the bottom and top of the polyad, respectively.

8.5 Semiclassical Assignments

This section addresses the question of quantum-classical correspondence: To what extent can the quantum eigenfunctions of the acetylene bend system be assigned quantum numbers (or at least be rationalized) in terms of the classical periodic orbits?

In Chapter 7, the quantum eigenfunctions of the acetylene pure bending effective Hamiltonian were examined, and prominent local mode and counter-rotation states were recognized in the $[22, 0]$ polyad. One can, in principle, address the issue of

[3] At the boundary between Regions I and II, $E_a = 14{,}086$ cm^{-1}, the orbit L_2 becomes homoclinic to the orbit M_2. By homoclinic we mean a trajectory that is not itself periodic but that converges forward as well as backward in time to the same periodic orbit.

quantum-classical correspondence by comparing the "lifted" classical periodic orbits with the quantum eigenfunctions. Two examples of this type of comparison are provided in Fig. 8-8. In each of these examples one of the quantum eigenfunctions, in the $(\rho_4, \rho_5, \phi_{45})$ coordinates defined in Chapter 7, is compared with an isoenergetic periodic orbit, which is represented in the same set of coordinates by using the lift procedure (see Section 8.7). The upper panels depict quantum-classical correspondence near the bottom of the [22,0] polyad, where the dynamics are dominated by local bend motions, while the bottom panels depict the counter-rotation motions that dominate the top of the polyad. In both cases, the similarity between the quantum eigenfunctions and classical periodic orbits is striking. Notice especially how the probability in the E = 15,306.7 cm^{-1} quantum eigenfunction tends to accumulate near regions in configuration space where the periodic orbit passes many times.

The examples of quantum-classical correspondence in Fig. 8-8 are particularly simple ones, because each of the periodic orbits depicted evolves at a single value of ϕ_{45}. The corresponding eigenfunctions have their probability distributed along ϕ_{45} in a near-Gaussian distribution, with the maximum of probability occurring at the classical value of ϕ_{45}. However, many of the important periodic orbits do not evolve with constant ϕ_{45}, and thus it becomes more difficult to establish quantum-classical correspondences by comparing projections of the periodic orbits and quantum eigenstates onto the (ρ_4, ρ_5) plane and the ϕ_{45} coordinate. Specialized software can permit comparisons of orbits and eigenfunctions in three-dimensional space, but a more general approach, which is adopted in the remainder of this section, is to generate *semiclassical* eigenfunctions in the same abstract (ψ_a, ψ_b) coordinates that were so useful for understanding the classical dynamics. The semiclassical eigenfunctions and classical periodic orbits can then be compared in a straightforward manner in two dimensions, making possible semiclassical assignments of the majority of the eigenstates within the polyad.

Semiclassical eigenfunctions can be obtained by quantizing the Hamiltonian defined in Eq. 8.8 (Schrödinger quantization can still be used after linear canonical

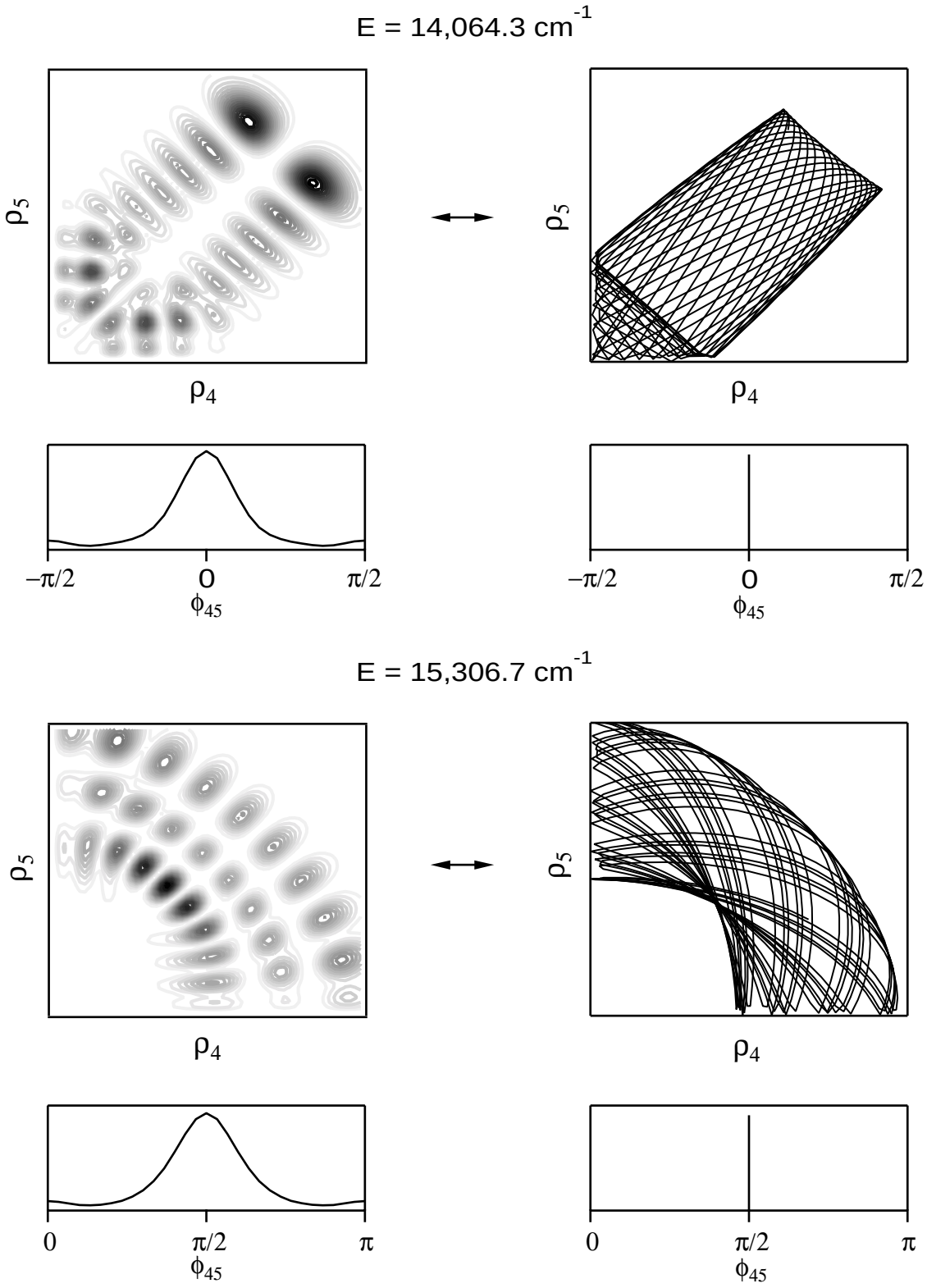

Figure 8-8: Left column: Isoenergetic quantum eigenfunctions (left) and periodic orbits (right) in the $[22,0]^{g+}$ polyad projected onto the (ρ_4, ρ_5) plane and the ϕ_{45} coordinate.

transformations) with the substitution

$$J \rightarrow \frac{\hbar}{i}\frac{\partial}{\partial\psi}. \tag{8.18}$$

The resultant semiclassical Hamiltonian can then be diagonalized in a plane wave basis set (Φ^{SC}) with the classical angles as coordinates,

$$\Phi^{SC} = \prod_{k=a,b} exp(ij_k\psi_k) \tag{8.19}$$

where k is an index over the classical degrees of freedom, and j_k is a semiclassical quantum number. Unfortunately there is no unique way to order the classical actions and angles, and different choices of ordering lead to distinct quantum Hamiltonians. That is, off-diagonal interaction terms such as $J_k\cos(\psi_k)$ and $\cos(\psi_k)J_k$ are equivalent in classical mechanics but distinct in the semiclassical Hamiltonian that results from applying the transformation in Eq. 8.18. This of course is an historic problem and it is noted that all orderings of the actions and angles are equivalent in the limit $\hbar \rightarrow 0$. There are a number of possible strategies for addressing this difficulty in practice; we adopted the same approach as McCoy and Sibert [27], and treat the actions as constants, with values

$$J_k = \frac{j'_k + j''_k}{2}, \tag{8.20}$$

where j'_k and j''_k refer to the quantum numbers of two semiclassical basis functions that are coupled by a given interaction term. The semiclassical eigenenergies that are obtained using this procedure are in excellent agreement with the "exact" quantum eigenvalues; the RMS error in the semiclassical eigenenergies is 1.05 cm^{-1}, and the errors in all cases are less than 2.0 cm^{-1}.

In this study, however, the "exact" quantum Hamiltonian is known, and was in fact the starting point of the study. Thus, a "requantization" of the classical Hamiltonian is in some sense gratuitous. The semiclassical wavefunctions can also be obtained without the requantization step by simply postulating a one-to-one correspondence between the semiclassical and quantum basis sets. That is, the quantum Hamiltonian

is diagonalized in a basis set of two 2D harmonic oscillators (Φ^Q), as in Chapter 7, to obtain the eigenfunctions

$$\Psi_\alpha = \sum_\beta c_{\alpha\beta}\Phi^Q_\beta. \tag{8.21}$$

However, one can choose to represent the eigenfunctions in the semiclassical basis set (Φ^{SC}) defined above

$$\Psi_\alpha = \sum_\beta c_{\alpha\beta}\Phi^{SC}_\beta \tag{8.22}$$

with the quantum numbers related according to

$$j_a = \frac{v_4 - v_5}{4} \tag{8.23}$$

$$j_b = \frac{\ell_4 - \ell_5}{4}, \tag{8.24}$$

as implied by the canonical transformation in Eq. 8.7. It should be emphasized that this approach is no less approximate than the semiclassical quantization approaches discussed above. That is, whereas the usual semiclassical quantization is approximate due to ambiguities in the ordering of the operators (leading to approximate eigenvalues, for example), the approach taken here uses the exact quantum Hamiltonian but establishes an approximate correspondence between the quantum and semiclassical basis sets, which is expected to be exact only in the classical limit. The eigenfunctions that are obtained from the two approaches are quite similar; only in rare cases can differences in the corresponding eigenfunctions be detected by eye. Moreover the minor differences do not affect the analysis of quantum-classical correspondence. All of the eigenfunctions depicted in this section were calculated using the exact quantum Hamiltonian rather than the requantization approach. The eigenstates are labelled as $E_n^{g/u,+/-}$, where the superscript indicates the symmetry and the subscript indicates the rank of the eigenstate within the polyad, starting from the lowest energy state.

Figures 8-9, 8-10, 8-11, 8-12, 8-13, 8-14, and 8-16 depict a few of the semiclassical wavefunctions of various symmetries in the (ψ_a, ψ_b) coordinates. Since the angles ψ are cyclic in 2π, in principle a domain of $[0, 2\pi]$ would be sufficient to represent the wavefunctions. For the purposes of obtaining semiclassical assignments by node

counting, however, it is helpful to plot the wavefunctions over a somewhat larger range of angles. As was discussed in the previous section, most of the stable periodic orbits are centered around $(0,0)$ (at the bottom of the polyad) and (π,π) (at the top). The saddle point at $(0,\pi)$ also plays an important role in the dynamics. To understand the relationship between the eigenfunctions and the classical mechanics, it is particularly useful to plot the eigenfunctions with none of these three important fixed points at the domain boundaries, and thus a domain of $[-\pi, 2\pi]$ is chosen for each angle.

Figure 8-9 plots several eigenfunctions that lie within Region I, including the lowest energy eigenfunctions in the $[22,0]$ polyad with all four possible symmetries. As can be expected from the accessibility diagrams for Region I, these eigenstates are centered about the point $(0,0)$. Notice also that these eigenstates appear in pairs with opposite g/u symmetry but identical parity. In Chapter 7, the existence of these doublets at bottom of the polyad (i.e., for well-defined local bend states) was rationalized qualitatively using the principle of the indistinguishability of identical nuclei in quantum mechanics. Section 8.8 provides a different explanation for this phenomenon, which is based upon understanding the effects of the parity and inversion (i.e., g/u symmetry) operators in the (ψ_a, ψ_b) configuration space, and which is valid throughout the polyad.

The lowest energy eigenfunctions for $[22,0]^{g+}$ and $[22,0]^{u+}$ both look like Gaussians centered about $(0,0)$, while those for $[22,0]^{g-}$ and $[22,0]^{u-}$ display one node in the ψ_b direction. Remembering that L_1 librates over $(0,0)$ in the ψ_a direction, while L_2 runs approximately in the ψ_b direction, the eigenfunctions can be assigned quantum numbers, n_{L_1} and n_{L_2}, that correspond to the number of quanta of excitation along each periodic orbit. Thus, the lowest energy eigenstates in both $[22,0]^{g+}$ and $[22,0]^{u+}$ can be assigned as $(n_{L_1}, n_{L_2}) = (0,0)$, and those for $[22,0]^{g-}$ and $[22,0]^{u-}$ as $(n_{L_1}, n_{L_2}) = (0,1)$. The rest of the eigenstates in Region I can be assigned in a similar way, such as the pair of states at the bottom of Fig. 8-9, which are assigned as $(n_{L_1}, n_{L_2}) = (1,0)$. Table 8.1 lists the assignments for the remaining states in Region I, all of which appear in g/u pairs.

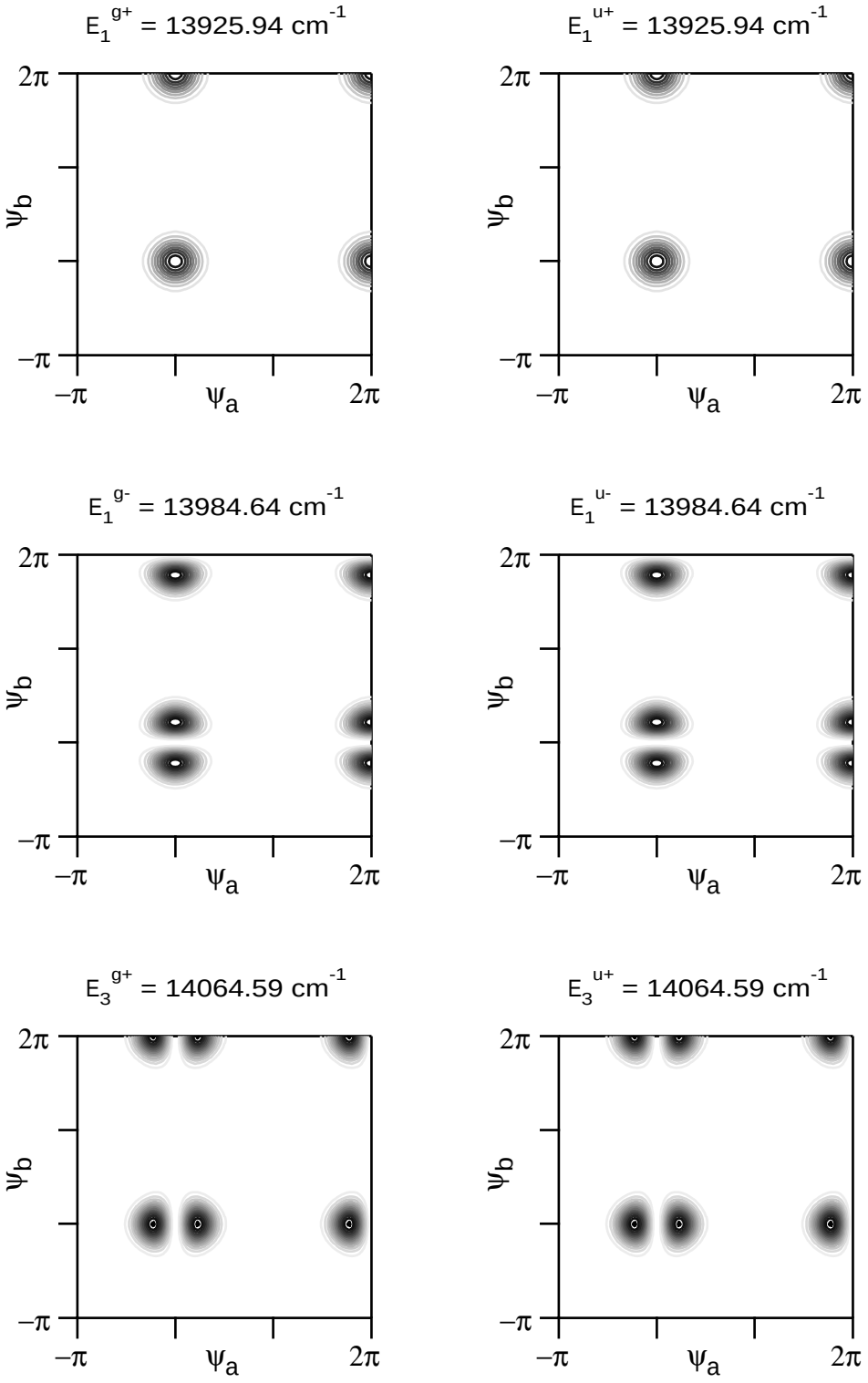

Figure 8-9: Selected semiclassical eigenfunctions (contour plots of probability density) in Region I of polyad [22,0]. The wavefunctions are centered about $(\psi_a, \psi_b) = (0, 0)$ and appear in pairs of opposite g/u symmetry. These states can be assigned as (n_{L_1}, n_{L_2}) = (0,0) (top), (0,1) (middle), and (1,0) (bottom).

Table 8.1: Semiclassical assignments for the eigenstates of $[22, 0]$, of all symmetries, in Regions I and II. All of the eigenstates in these regions can be assigned in terms of local bend motions of the molecule. Specifically, two quantum numbers, (n_{L_1}, n_{L_2}), are assigned that correspond to the number of quanta of excitation along the two periodic orbits, L_1 and L_2, which grow out the stable elliptical fixed point at the bottom of the polyad, $(\psi_a, \psi_b) = (0, 0)$. The eigenstates that organize about these periodic orbits occur as symmetry pairs with opposite g/u symmetry. Region I ends (and Region II begins) at 14086 cm^{-1}. The states for which an assignment is not provided mutually perturb each other and can each be assigned as a roughly 50/50 mixture of (2,0) and (1,2). All energies are in units of cm^{-1} and are referenced to the zero-point energy.

Region	g-symmetry eigenstate	u-symmetry eigenstate	$E^g - E^u$	(n_{L_1}, n_{L_2})
I	$E_1^{g+} = 13926.21$	$E_1^{u+} = 13926.21$	6.4 x 10^{-8}	(0,0)
I	$E_1^{g-} = 13984.89$	$E_1^{u-} = 13984.89$	2.4 x 10^{-8}	(0,1)
I	$E_2^{g+} = 14035.81$	$E_2^{u+} = 14035.81$	-2.8 x 10^{-7}	(0,2)
I	$E_3^{g+} = 14064.59$	$E_3^{u+} = 14064.59$	-3.1 x 10^{-6}	(1,0)
I	$E_2^{g-} = 14080.88$	$E_2^{u-} = 14080.88$	5.3 x 10^{-5}	(0,3)
II	$E_4^{g+} = 14119.99$	$E_4^{u+} = 14119.99$	-2.0 x 10^{-3}	(0,4)
II	$E_3^{g-} = 14136.28$	$E_3^{u-} = 14136.28$	1.6 x 10^{-5}	(1,1)
II	$E_4^{g-} = 14153.51$	$E_4^{u-} = 14153.46$	4.8 x 10^{-2}	(0,5)
II	$E_5^{g+} = 14180.63$	$E_5^{u+} = 14181.30$	-0.67	(0,6)
II	$E_6^{g+} = 14187.85$	$E_6^{u+} = 14187.85$	-2.8 x 10^{-5}	*
II	$E_7^{g+} = 14196.81$	$E_7^{u+} = 14196.83$	-1.4 x 10^{-2}	*
II	$E_5^{g-} = 14204.70$	$E_5^{u-} = 14200.12$	4.58	(0,7)

Table 8.2: Semiclassical assignments for the eigenstates of $[22, 0]$, of all symmetries, in Region IV. All of the eigenstates in this region can be assigned in terms of counter-rotation motions of the molecule. Specifically, two quantum numbers, (n_{C_1}, n_{C_2}), are assigned that correspond to the number of quanta of excitation along the two periodic orbits, C_1 and C_2, which grow out the stable elliptical fixed point at the top of the polyad, $(\psi_a, \psi_b) = (\pi, \pi)$. The eigenstates that organize about these periodic orbits occur as symmetry pairs with opposite g/u symmetry and opposite parity $(+/-)$. All energies are in units of cm^{-1} and are referenced to the zero-point energy.

g-symmetry eigenstate	u-symmetry eigenstate	$E^g - E^u$	(n_{C_1}, n_{C_2})
$E^{g+}_{42} = 15671.61$	$E^{u-}_{36} = 15671.61$	9.3 x 10^{-6}	(0,0)
$E^{g+}_{41} = 15478.39$	$E^{u-}_{35} = 15478.39$	1.1 x 10^{-3}	(0,1)
$E^{g-}_{30} = 15446.01$	$E^{u+}_{36} = 15446.01$	-4.3 x 10^{-5}	(1,0)
$E^{g+}_{40} = 15306.79$	$E^{u-}_{34} = 15306.74$	5.2 x 10^{-2}	(0,2)
$E^{g-}_{29} = 15263.69$	$E^{u+}_{35} = 15263.70$	-4.5 x 10^{-3}	(1,1)
$E^{g+}_{39} = 15240.42$	$E^{u-}_{33} = 15240.42$	1.6 x 10^{-3}	(2,0)
$E^{g+}_{38} = 15157.87$	$E^{u-}_{32} = 15156.61$	1.26	(0,3)
$E^{g-}_{28} = 15106.74$	$E^{u+}_{34} = 15106.90$	-0.16	(1,2)
$E^{g+}_{37} = 15067.83$	$E^{u-}_{31} = 15067.65$	0.18	(2,1)
$E^{g-}_{27} = 15053.61$	$E^{u+}_{33} = 15053.64$	-2.2 x 10^{-2}	(3,0)
$E^{g+}_{36} = 15040.44$	$E^{u-}_{30} = 15026.37$	14.07	(0,4)
$E^{g-}_{26} = 14970.79$	$E^{u+}_{32} = 14974.07$	-3.28	(1,3)
$E^{g+}_{34} = 14928.57$	$E^{u-}_{29} = 14929.54$	-0.97	(2,2)

The eigenstates in Region IV are of course organized about $(\psi_a, \psi_b) = (\pi, \pi)$. The symmetry arguments in Section 8.8 suggest that these states will appear in $g+/u-$ and $g-/u+$ pairs that can be assigned quantum numbers (n_{C_1},n_{C_2}), indicating the number of quanta of excitation along each of the two important periodic orbits in this region. The clearly assigned $(0, 0)$ and $(1, 1)$ eigenstates are depicted in the top and middle rows of Fig. 8-10. Depicted at the bottom of Fig. 8-10 are the last pair of eigenstates that fall within Region IV; they are assigned as $(n_{C_1}, n_{C_2}) = (2, 2)$. This assignment is clearly somewhat approximate, and the distorted appearance of the wavefunction can be considered to reflect the multiple bifurcations that have occurred by this energy along the C_1 coordinate. Table 8.2 lists the assignments for the remaining states in Region IV.

Given that Regions I and IV are dominated by regular motion organized about periodic orbits that evolve from the stable elliptical fixed points at the top and bottom

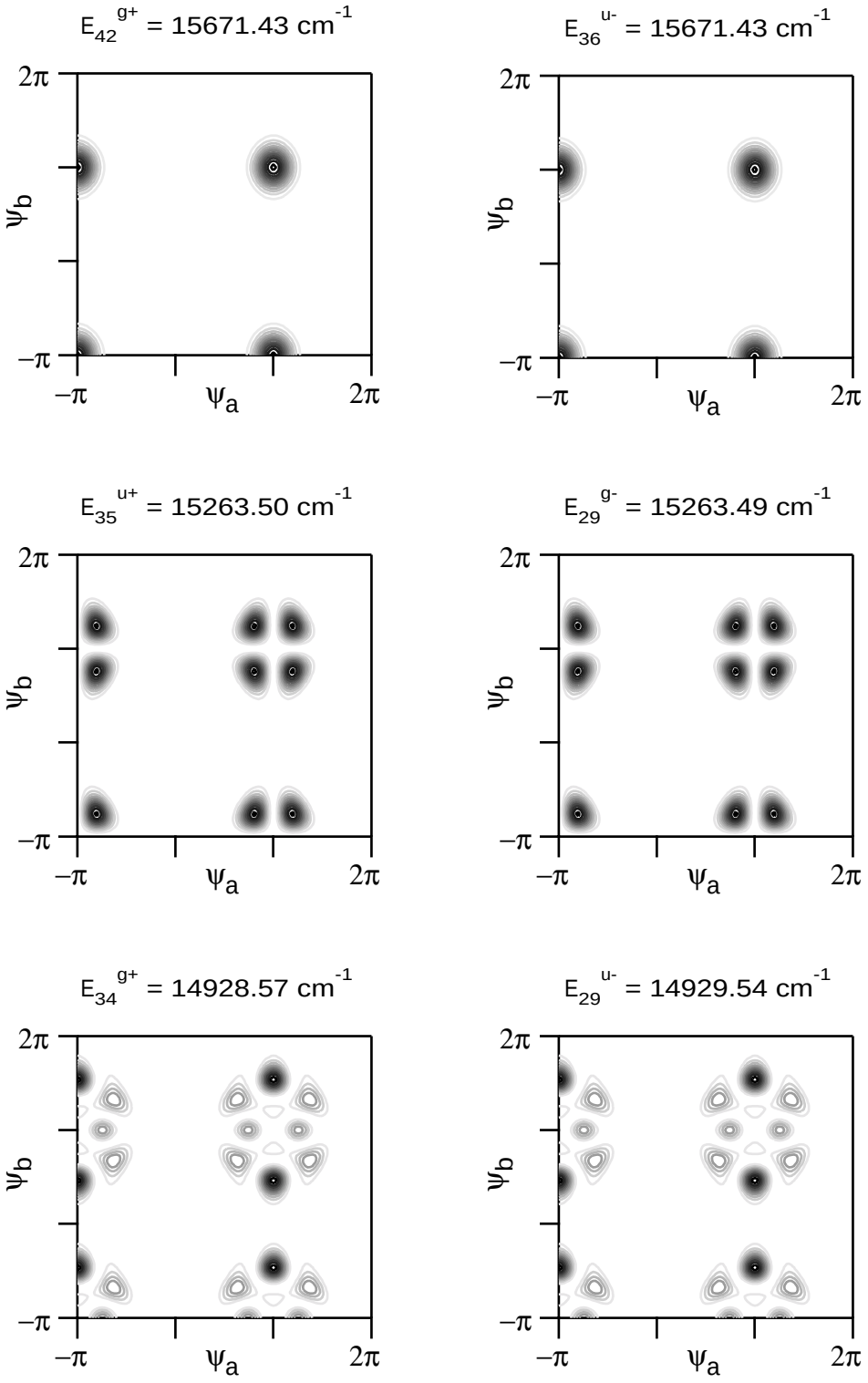

Figure 8-10: Selected semiclassical eigenfunctions in Region IV of polyad [22,0]. The wavefunctions are centered about $(\psi_a, \psi_b) = (\pi, \pi)$ and appear in pairs of opposite g/u symmetry *and* opposite parity. These states can be assigned as $(n_{C_1}, n_{C_2}) = (0,0)$ (top), (1,1) (middle), and (2,2) (bottom).

of the polyad, it is not surprising that the eigenfunctions that lie in these regions can be assigned semiclassical quantum numbers in such a simple manner. The eigenstates in Regions II and III, in which chaos plays a substantial role, can be expected to present greater difficulties for assignment. Interestingly, however, the eigenstates within Region II, which is the most highly chaotic region, present little difficulty for semiclassical assignment. The local bend assignments (n_{L_1},n_{L_2}) from Region I can be continued throughout Region II, as can be seen in Table 8.1. The last three assignments in Table 8.1 are, however, somewhat more approximate. The eigenstate pairs E_6^{g+}/E_6^{u+} and E_7^{g+}/E_7^{u+} cannot be assigned a unique (n_{L_1}, n_{L_2}) quantum number label, but visual inspection of these eigenstates (see Fig. 8-11) makes it clear that each can be assigned as a roughly 50/50 mixture of $(2,0)$ and $(1,2)$.[4]

The last assignment in Table 8.1 is also somewhat approximate, as can be seen in the bottom two panels of Fig. 8-11. The $g-$ and $u-$ symmetry eigenstates in this case appear to be nearly but not exactly identical. In both cases, a total of 7 nodes can be counted along the ψ_b direction from $-\pi$ to π, but the wavefunction is highly distorted from a harmonic oscillator state, such that the majority of the probability is located in the outer lobes of the wavefunction, near $\psi_b = \pm\pi$. This accumulation of probability can of course be rationalized in terms of the classical motions of the molecule; periodic orbit L_2 at these energies rotates along ψ_b, but slows down significantly near the saddle point $(0,\pi)$, leading to the accumulation of probability there. It will be seen below that this phenomenon is related to the role that the saddle point plays in linking local bend with counter-rotation states.

Many of the eigenstates in Region III cannot be assigned as readily as those in the other regions. The major reason for this appears not to be the existence of extensive chaos in this region, since all eigenstates in the highly chaotic Region II could be assigned, at least approximately. This is not the case in Region III, where a number

[4]That is, $(2,0)$ and $(1,2)$ states mutually perturb each other. This effect can be considered a manifestation of anharmonicities in the dynamics in the abstract action/angle space. As $E \rightarrow E_{\min}$, the periodic orbits L_1 and L_2 reduce to the normal modes of the deviation from "ideal" local bend behavior, as represented by the fixed point $(\psi_a, \psi_b) = (0,0)$. As energy increases, however, this orthogonality condition is relaxed, in much the same way that anharmonicities in molecular potential energy surfaces make IVR possible.

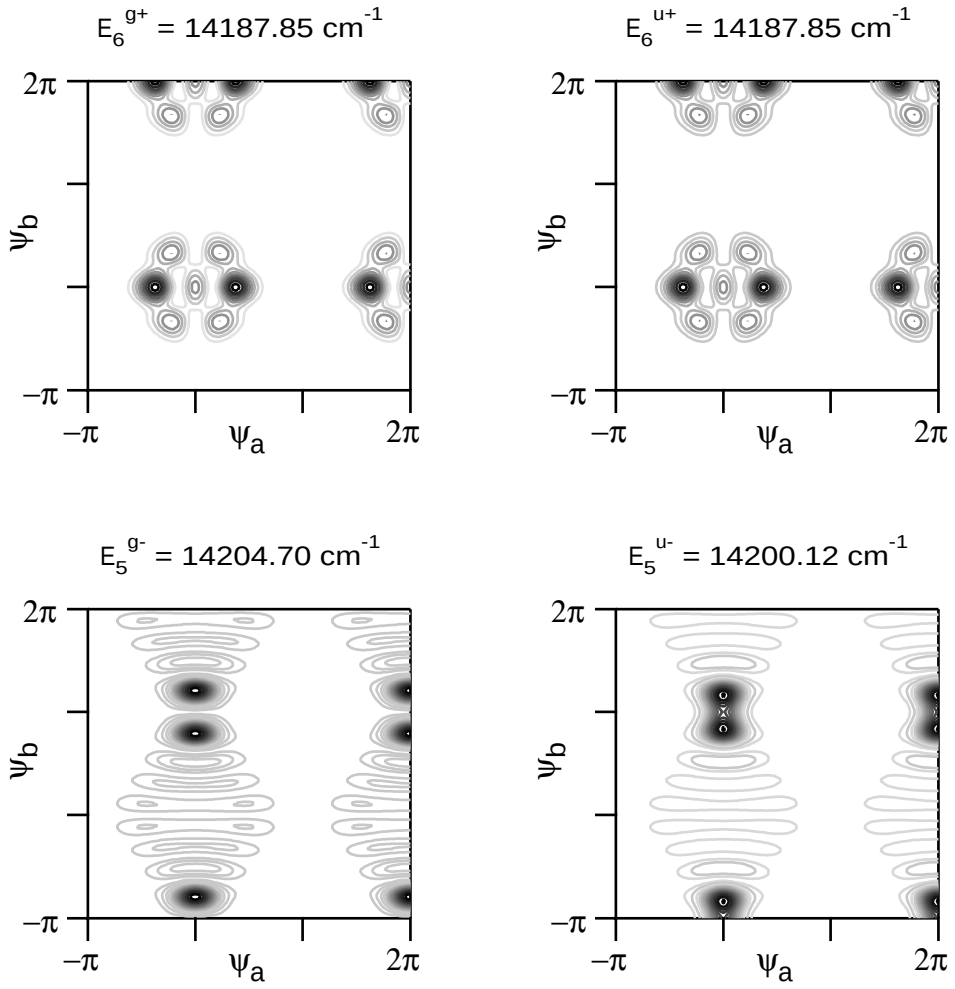

Figure 8-11: Selected semiclassical eigenfunctions in Region II of polyad [22,0]. The wavefunctions remain organized primarily around $(\psi_a, \psi_b) = (0, 0)$ and appear in pairs of opposite g/u symmetry, as they do in Region I. Despite Region II being almost entirely classically chaotic, all of the states in Region II can be assigned, at least approximately, quantum numbers corresponding to excitation along the L_1 and L_2 periodic orbits. The assignments for the two pairs of eigenfunctions shown here are the most approximate ones within Region II. The upper eigenstate pair, E_6^{g+} and E_6^{u+}, is involved in a mutual perturbation with another pair of states, E_7^{g+} and E_7^{u+}, which are not shown. Each of the states involved in the perturbation can be assigned as a roughly 50/50 mixture of $(n_{L_1}, n_{L_2}) = (2,0)$ and $(1,2)$. The bottom pair of eigenstates can clearly be assigned as $(n_{L_1}, n_{L_2}) = (0,7)$, but notice that the probability accumulates largely near $(\psi_a, \psi_b) = (0, \pi)$, which acts as a saddle point of the Hamiltonian.

of eigenstates cannot be clearly assigned in terms of any of the periodic orbits, and the assignments for many of the rest of the eigenstates are approximate. The key to the increased complexity in Region III appears to be the fact that the two most important fixed points, $(\psi_a, \psi_b) = (0, 0)$ and (π, π), do not play any strong role in organizing the dynamics, as they do in Regions I and IV, respectively. As a result the important periodic orbits change their character rapidly in this region, from local bend to counter-rotation character as energy increases, and the quantum eigenstates reflect this complexity.

The saddle point at $(0, \pi)$ does play some role in organizing the dynamics in Region III, as can be seen from the eigenstates in Fig. 8-12. These eigenstates can be assigned quantum numbers representing excitation along M_2, which librates over $(\psi_a, \psi_b) = (0, \pi)$, and transverse to it (i.e., along L_2^r). The symmetry arguments that were applied to the eigenstates in Region IV (i.e., that they should appear in pairs of opposite g/u symmetry and opposite parity) apply here as well, since the states are localized near $\psi_b = \pi$. The first pair of eigenstates in Fig. 8-12 can be assigned as $(n_{M_2}, n_{L_2}) = (3, 0)$, and the second pair as $(2, 1)$. Several other pairs of states can be assigned similarly; the results are in Table 8.3. Note that the energy splittings between the nominal symmetry pairs are much larger here than in Regions I and IV, reflecting the increased complexity that results when all of the (ψ_a, ψ_b) configuration space is accessible.

Two specific links between the local bend periodic orbits at the bottom and the counter-rotation periodic orbits at the top of the polyad were discussed in the preceding section. Each of these links is manifested in the quantum wavefunctions in Region III. Some of the quantum manifestations of the link between L_1 and C_1, mediated by $L_{1a/b}$, M_1^r, and $C_{1a/b}$, are seen in Fig. 8-13. Here, only one of the four possible symmetries of eigenstates $(u-)$ are plotted, for simplicity. Near the bottom of Region III, many eigenstates can be assigned approximately in terms of local bend quantum numbers, such as E_{14}^{u-}, which is localized around $(\psi_a, \psi_b) = (0, 0)$, and is clearly assignable as $(n_{L_1}, n_{L_2}) = (3, 1)$. Eigenstate E_{19}^{u-} still appears to be localized *primarily* around $(\psi_a, \psi_b) = (0, 0)$, and can be assigned approximately as $(n_{L_1}, n_{L_2}) = (4, 1)$,

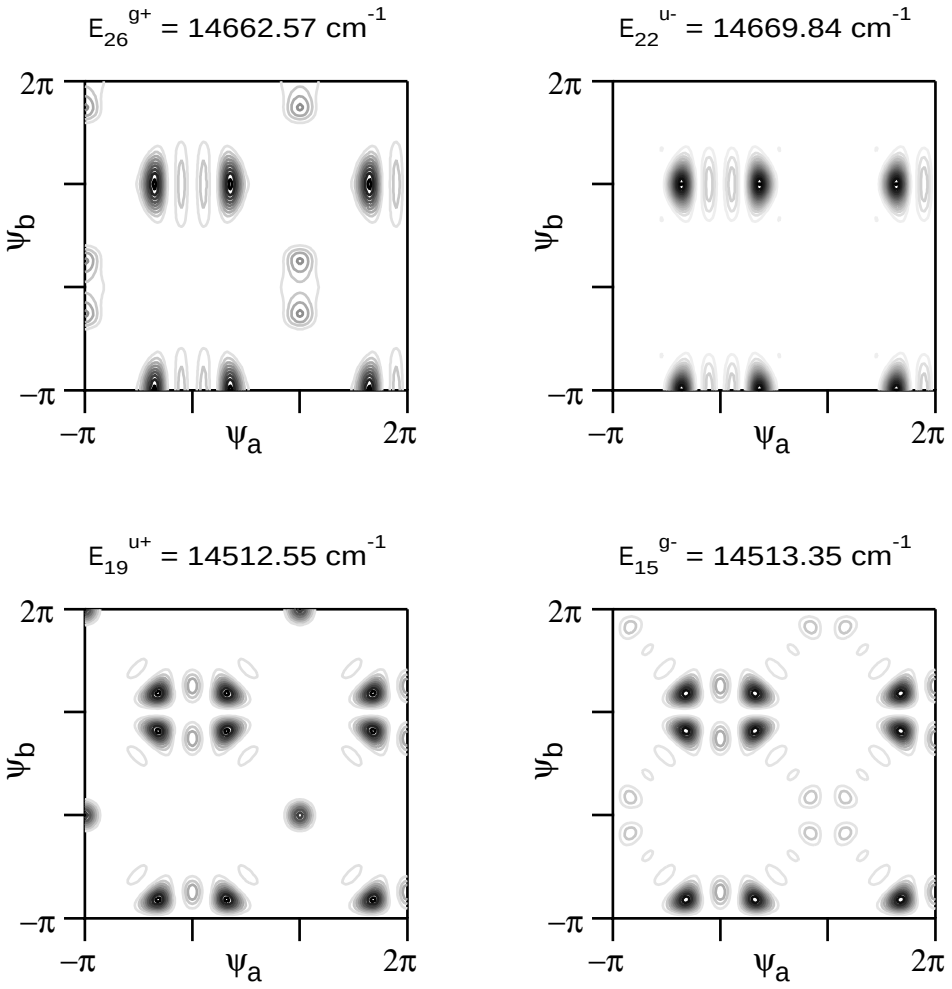

Figure 8-12: Selected semiclassical eigenfunctions in Region III of polyad [22,0] that organize around the point $(\psi_a, \psi_b) = (0, \pi)$. These states can be assigned in terms of the number of quanta of excitation along the M_2 and L_2 periodic orbits, and appear in pairs of opposite g/u symmetry *and* opposite parity. The specific assignments are (n_{M_2}, n_{L_2}) = (3,0) (top), and (2,1) (bottom).

Table 8.3: Semiclassical assignments for those eigenstates in Region III of polyad $[22, 0]$ that organize around the saddle point $(\psi_a, \psi_b) = (0, \pi)$ and can be assigned semiclassical quantum numbers (n_{M_2}, n_{L_2}) referring to the periodic orbits associated with the saddle point. All energies are in units of cm^{-1} and are referenced to the zero-point energy.

g-symmetry eigenstate	u-symmetry eigenstate	$E^g - E^u$	(n_{M_2}, n_{L_2})
$E_8^{g+} = 14213.12$	$E_6^{u-} = 14228.06$	-14.94	(0,0)
$E_7^{g-} = 14249.49$	$E_8^{u+} = 14226.32$	23.17	(0,1)
$E_{12}^{g-} = 14390.26$	$E_{14}^{u+} = 14382.53$	7.73	(1,1)
$E_{15}^{g+} = 14392.83$	$E_{13}^{u-} = 14389.94$	2.89	(1,0)
$E_{16}^{g-} = 14520.13$	$E_{19}^{u+} = 14512.74$	7.39	(2,1)
$E_{21}^{g+} = 14537.03$	$E_{18}^{u-} = 14537.67$	-0.64	(2,0)
$E_{20}^{g-} = 14658.48$	$E_{24}^{u+} = 14621.02$	37.46	(3,1)
$E_{26}^{g+} = 14662.71$	$E_{22}^{u-} = 14669.94$	-7.23	(3,0)
$E_{23}^{g-} = 14776.63$	$E_{26}^{u+} = 14703.95$	72.68	(4,1)
$E_{30}^{g+} = 14755.07$	$E_{25}^{u-} = 14789.21$	-34.14	(4,0)

but a small amount of probability is also localized around $(\psi_a, \psi_b) = (\pi, \pi)$. In E_{24}^{u-} the situation is just the opposite. A small amount of probability is localized around $(\psi_a, \psi_b) = (0, 0)$ [and can be assigned as $(n_{L_1}, n_{L_2}) = (5, 1)$], but the majority organizes around $(\psi_a, \psi_b) = (\pi, \pi)$ and the better assignment for this eigenstate is $(n_{C_1}, n_{C_2}) = (4, 1)$.

The eigenstate E_{27}^{u-} is included for comparison. Its energy places it at the bottom of Region IV, and it is assignable as $(n_{C_1}, n_{C_2}) = (4, 0)$, although there is some distortion in the outer lobes of the wavefunction that can be attributed to the linking of C_1 with L_1 in the following way. At this energy the orbit C_1 has already become unstable in the pitchfork bifurcation, in which the orbits C_{1a} and C_{1b} branch off (see Fig. 8-4). The bifurcated orbits are stable and are more important in directing the dynamics than C_1 itself. Therefore quantum eigenstates associated with these orbits can be expected to have their probability concentrated around the turning points of C_{1a} and C_{1b}, which do not lie exactly along the line $\psi_a = \pi$. Of course, quantum mechanically the probability density must be distributed symmetrically between C_{1a} and C_{1b}. Thus, the outermost lobes of the E_{27}^{u-} wavefunction are split in a double hump, with the humps located approximately at the turning points of the periodic

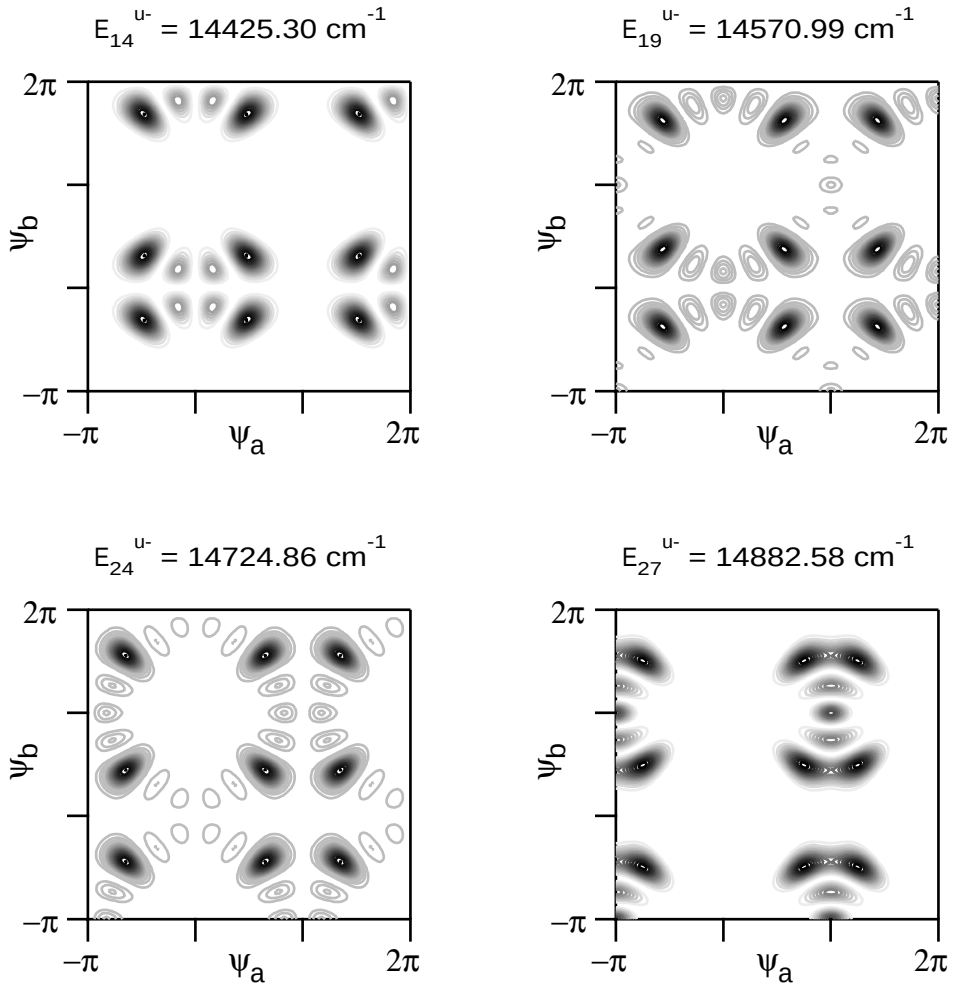

Figure 8-13: Semiclassical eigenfunctions in Region III of polyad [22,0] that illustrate the link between the L_1 and C_1 periodic orbits. Near the bottom of Region III, many eigenstates, such as E_{14}^{u-}, remain organized around $(\psi_a, \psi_b) = (0, 0)$, and can be assigned (n_{L_1}, n_{L_2}) quantum numbers, which in this case are (3,1). The eigenstate E_{19}^{u-} can clearly be assigned as (n_{L_1}, n_{L_2}) = (4,1), but notice the small amount of probability around $(\psi_a, \psi_b) = (\pi, \pi)$. For eigenstate E_{24}^{u-}, the better assignment is (n_{C_1}, n_{C_2}) = (4,1), because it is organized primarily around $(\psi_a, \psi_b) = (\pi, \pi)$. Eigenstate E_{27}^{u-} is shown for reference; although it can be assigned as (n_{C_1}, n_{C_2}) = (4,0), the outer lobes of the wavefunction are clearly distorted due to the C_{1a} and C_{1b} bifurcated orbits.

orbits C_{1a} and C_{1b}.

Similar observations can be made for the wavefunctions E_{19}^{u-} and E_{24}^{u-}. Note that in each case, the probability density is large around the points $\psi_a = \pm\pi/2$, $\psi_b = \pm\pi/2$. These are exactly the points where the orbits M_{1a}^r and M_{1b}^r have high curvature in configuration space (see Fig. 8-7) and where they move with extremely low speed.

The second link between the top and bottom of the polyad is between L_2 and C_2, mediated by the M_2 periodic orbit that organizes within Region III around the saddle point $(\psi_a, \psi_b) = (0, \pi)$. The state E_5^{g+} (Fig. 8-14), in Region II, is organized primarily around $(\psi_a, \psi_b) = (0, 0)$ and can be assigned as $(n_{L_1}, n_{L_2}) = (0, 6)$, although it is clear that the probability is concentrated near the saddle point at $(\psi_a, \psi_b) = (0, \pi)$. With E_8^{g+}, the primary organizing center is clearly $(\psi_a, \psi_b) = (0, \pi)$, and thus this state is assigned as $(n_{M_2}, n_{L_2}) = (0, 0)$. However, a close inspection of this eigenstate also reveals that eight nodes can be counted between $\psi_b = \pi$ and $-\pi$, so that this state could also be assigned approximately as $(n_{L_1}, n_{L_2}) = (0, 8)$. This is the quantum mechanical manifestation of the L_2/M_2 link.

Figure 8-15 provides another viewpoint on the transition from eigenstates being dominated by the $(\psi_a, \psi_b) = (0, 0)$ fixed point to the $(0, \pi)$ saddle point. It plots the energy differences between adjacent members of the $(n_{L_1} = 0, n_{L_2})$ series of states, for both g and u symmetry (n_{L_2}=odd states have $-$ parity, and n_{L_2}=even states have $+$ parity). Up to $n_{L_2} = 6$, the energy differences are very nearly the same for the g and u symmetry series, indicating that the states occur in nearly degenerate g/u pairs. [The energy difference between consecutive members of the sequence is, to a good approximation, the period of the L_2 periodic orbit at an energy half-way between the two states.] By $n_{L_2} = 7$, the two series diverge, indicating that the states are organized primarily about the $(0, \pi)$ saddle point.

The link between M_2 and C_2 can be seen in the eigenfunctions E_{30}^{g+} and E_{35}^{g+}. E_{30}^{g+} is clearly organized around the saddle point $(\psi_a, \psi_b) = (0, \pi)$, and can be assigned as $(n_{M_2}, n_{L_2}) = (4, 0)$, while E_{35}^{g+} is organized around $(\psi_a, \psi_b) = (\pi, \pi)$ and can be assigned as $(n_{C_1}, n_{C_2}) = (0, 5)$. This observation is consistent with the fact that E_{30}^{g+} lies just below, and E_{35}^{g+} lies just above, E_c, the boundary between Regions III and

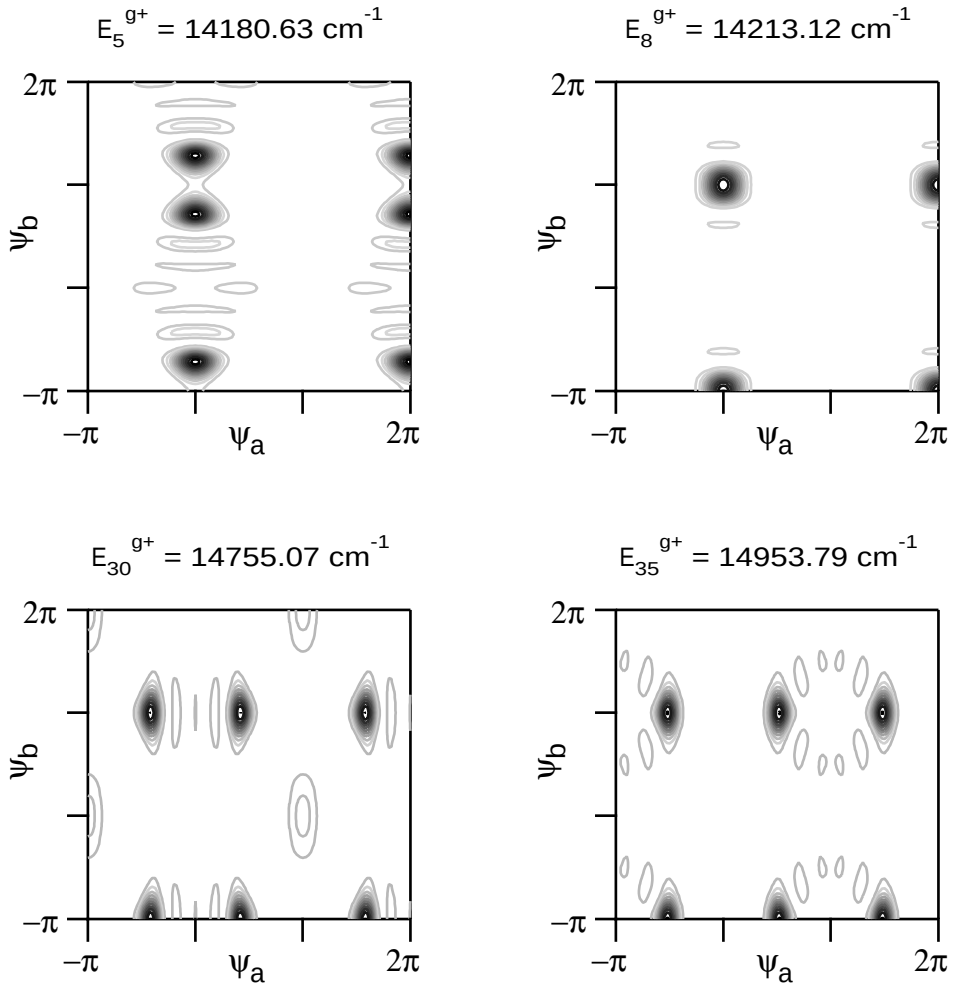

Figure 8-14: Semiclassical eigenfunctions in Region III of polyad [22,0] that illustrate the link between the L_2 and M_2, and M_2 and C_2, periodic orbits. Eigenstate E_5^{g+} can be assigned as (n_{L_1}, n_{L_2}) = (0,6), but its probability density is strongly localized near the $(\psi_a, \psi_b) = (0, \pi)$ saddle point. The eigenstate E_8^{g+}, on the other hand, is clearly localized around $(\psi_a, \psi_b) = (0, \pi)$, and is best assigned as (n_{M_2}, n_{L_2}) = (0,0). The bottom two panels depict the way in which the series of eigenstates with excitation along M_2 link to the series of states with excitation along C_2 (the change occurs at E_c, the boundary between Regions III and IV). Eigenstate E_{30}^{g+}, which lies within Region III, is assigned as (n_{M_2}, n_{L_2}) = (4,0), while eigenstate E_{35}^{g+}, in Region IV, is better assigned as (n_{C_1}, n_{C_2}) = (0,5).

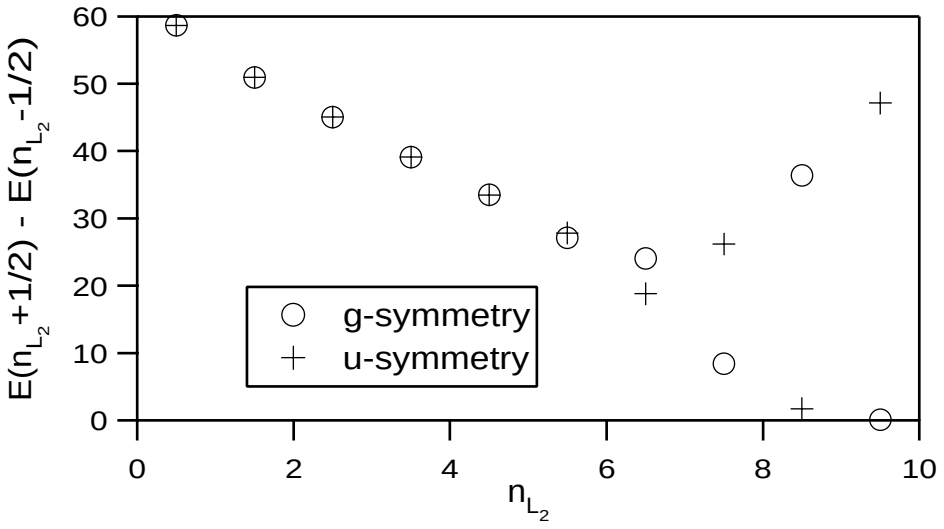

Figure 8-15: Energy differences between adjacent members of the series of states which can be assigned as $(n_{L_1} = 0, n_{L_2})$. This series originates within Region I, where the eigenstates appear in nearly degenerate pairs, with opposite g/u symmetry, which share the same semiclassical assignment. Thus, the energy differences of the g and u symmetry states are very nearly identical. As energy increases, free rotation becomes possible for the L_2 periodic orbit, which runs along ψ_b with $\psi_a = 0$, but the point $(\psi_a, \psi_b) = (0, \pi)$ acts as a saddle point, and the probability of the series of eigenstates localizes near this point (for $n_{L_2} > 6$ in particular). The divergence of the progressions above $n_{L_2} = 6$ indicates that the nominal assignments, as $(n_{L_1} = 0, n_{L_2})$, are only approximate.

IV, where M_2 becomes C_2. However, both eigenstates are organized along $\psi_b = \pi$, and the outer lobes of probability in each case are located at $\psi_b \approx \pi/2$.

As mentioned previously, many of the states within Region III can be assigned only approximately, or, in a few cases, not at all. Several such states are depicted in Fig. 8-16. There exist several eigenstates like E_{10}^{g+} that clearly organize around $(\psi_a, \psi_b) = (0, 0)$, but whose nodes appear to form a ring rather than align parallel to either L_1 or L_2. No periodic orbit is known that forms such a ring structure, but close inspection of this eigenfunction reveals that there is exactly one node in the ψ_a direction, at $\psi_a = 0$, and thus this state can be assigned approximately as $(n_{L_1}, n_{L_2}) = (1, 5)$. A corresponding state near the top of Region III, E_{31}^{g+}, clearly organizes primarily around $(\psi_a, \psi_b) = (\pi, \pi)$, but again appears to form a ring, making assignment difficult. This eigenstate can be assigned approximately as $(n_{C_1}, n_{C_2}) = (2, 3)$, particularly after comparing it with the eigenstates at the bottom of Fig. 8-10, which could be assigned as $(n_{C_1}, n_{C_2}) = (2, 2)$. The ring-shaped nodal structure of states such as E_{10}^{g+} and E_{31}^{g+} appears to be generated by the multiple bifurcations that L_1 and C_1 (respectively) have undergone before they enter Region III. That is, within Region III, L_1 and C_1 are no longer as important as $L_{1a/b}$ and $C_{1a/b}$ in organizing the quantum eigenfunctions, and the bifurcated orbits do not run along $\psi_b = 0$ and $\psi_a = \pi$, respectively, but rather tend to move in a more diagonal direction.

Other eigenstates, such as E_{20}^{g+} and E_{29}^{g+}, do not appear to yield to even approximate assignment. In the case of E_{29}^{g+}, some fraction of the probability appears to organize around $(\psi_a, \psi_b) = (\pi, \pi)$, and this portion of the wavefunction can perhaps be assigned approximately as $(n_{C_1}, n_{C_2}) = (4, 1)$. However, much of the probability density is localized elsewhere, particularly near $\psi_b = 0$. Since there is substantial probability localized near *both* $\psi_b = 0$ and $\psi_b = \pi$, this eigenstate will not appear in a doublet (according to the symmetry arguments of Section 8.8), and thus is probably best considered to be "unassignable". Eigenstate E_{20}^{g+}, on the other hand, has most of its probability localized near $(\psi_a, \psi_b) = (\pi, 0)$. Unlike $(\psi_a, \psi_b) = (0, \pi)$, the point $(\psi_a, \psi_b) = (\pi, 0)$ cannot be considered a saddle point, but the L_1 periodic orbit does slow down substantially near this point, which probably accounts for the accumula-

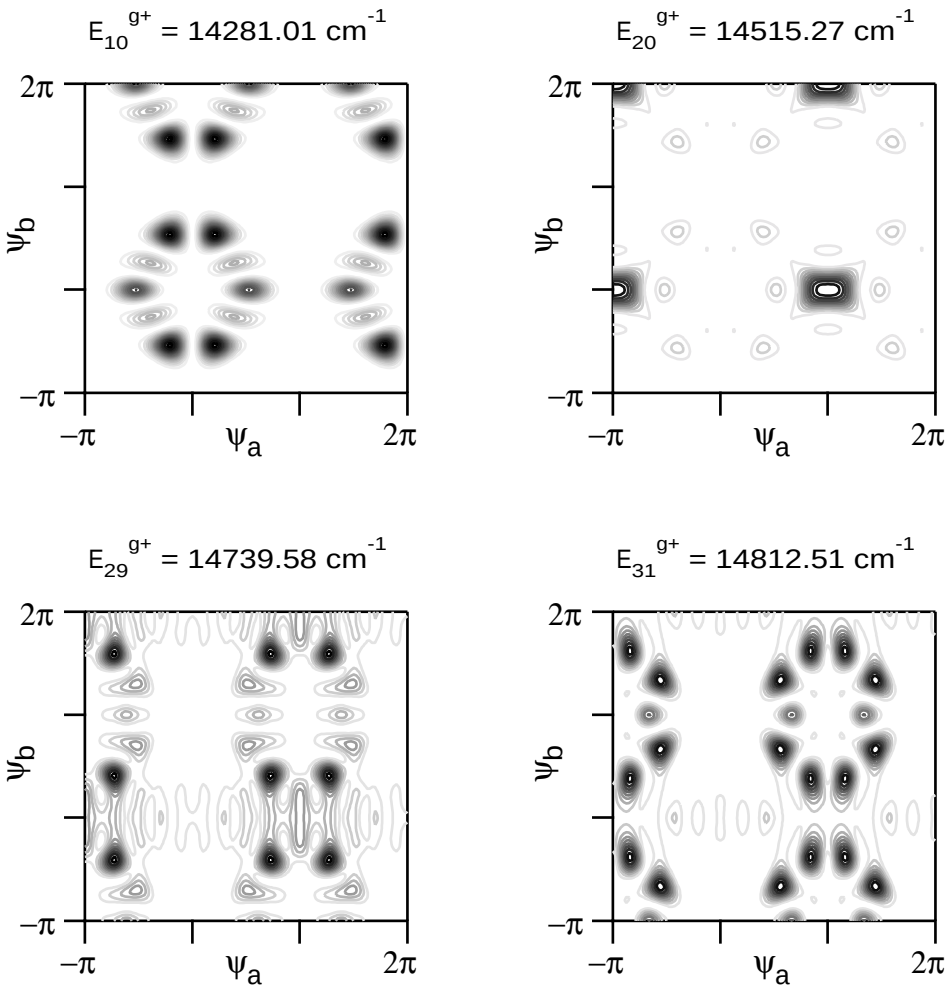

Figure 8-16: Several eigenstates of $g+$ symmetry within Region III that can only be assigned semiclassical quantum numbers approximately, or not at all.

tion of probability there. However, beyond this qualitative explanation, there appears to be no reasonable quantum number assignment for this state.

At this point, it is probably worthwhile to say a few words about how the semiclassical eigenstate assignments made here compare to the quantum mechanical assignments made in Chapter 7. In Chapter 7, a harmonically coupled, anharmonic *local* mode model was derived for the bend modes of acetylene and shown to provide a much better zero-order description of the eigenstates at high energy, as exemplified by polyad [22,0], than the conventional normal mode model. A total of 65 of the 144 states in the polyad could be assigned local mode quantum numbers using the Hose-Taylor criterion [149]. The same set of quantum numbers, $|v_1^{\ell_1}, v_2^{\ell_2}\rangle$, were used to describe states both at the bottom and top of the polyad (for [22,0], a state like $|22^0, 0^0\rangle$ would represent a local bender, and a state like $|11^{-11}, 11^{+11}\rangle$ would represent a counter-rotator). Many eigenstates in the middle of the polyad could not be assigned in this way. In this chapter, although a few states in the middle of the polyad might be considered "intrinsically unassignable", many others have well-defined nodal patterns that are simply not well described in terms of local bend or counter-rotation motions.

To be fair, in this work, no rigorous basis set was defined for making the semiclassical assignments; rather, visual inspection was used to reveal quantum number assignments associated with particular isoenergetic periodic orbits. Three different quantum number assignment schemes were used, depending on which fixed point of the dynamics the eigenstate appeared to organize around, although the assignments at the top and bottom of the polyad can be "linked" based upon the evolution of the periodic orbits. Based upon visual inspection, 122 of the 144 states in the [22,0] polyad can be assigned semiclassical quantum numbers, at least approximately. Each assigned eigenstate is understood to be a quantum mechanical manifestation of a particular type of classical motion. For example, the observed spectral pattern for polyad $[22,0]^{g+}$ consists, to a good approximation, of just 3 peaks (see Chapter 6) that terminate on eigenstates E_{26}^{g+} (see Fig. 8-12), E_{30}^{g+} (see Fig. 8-14) and E_{32}^{g+}. Each of these eigenstates can be assigned in terms of increasing excitation along M_2 (Fig. 8-

7), which, as mentioned above, implies an increasingly counter-rotational component to the classical motion.

8.6 Conclusion

The aim of this concluding section is to place the work reported here into the context of other recent studies of vibrational motion in small polyatomic molecules that employ the techniques of non-linear dynamics. It is not possible to review the literature on semiclassical methods and their application to molecular vibrational motion; the literature is too vast, and there exists an excellent, although by now somewhat outdated, review article by Gomez and Pollak [150], as well as textbooks by Child [151] and Gutzwiller [18], which provide didactic overviews of different aspects of the field. However, several recent studies that have collectively provided inspiration for this work include:

- Classical and semiclassical analyses of the local mode behavior of molecules with multiple hydrogen stretch modes [152, 33];
- Studies of algebraic Hamiltonians with a single resonance, including a series of papers by Kellman [109, 153, 119, 111, 112, 110, 154] and Ezra [155], as well as earlier work of Heller and coworkers [123]; and
- Several studies of triatomic molecules, including water [156, 141] (as represented by the Baggott Hamiltonian [105]) and HCP [26].

Acetylene has been the subject of several studies as well, including the early studies of Holme and Levine [157, 158, 159], and the more recent studies of Farantos [160], Kellman [109, 153], and McCoy and Sibert [27]. The most recent contribution is by van der Pals and Gaspard [134], who studied the periodic orbits associated with an effective Hamiltonian for all degrees of freedom of acetylene, including the bending modes. Their study differs from this one in that quantum-classical correspondence is addressed in the time-domain, using vibrograms, as opposed to the direct comparison of eigenstates with periodic orbits performed here.

One feature of this work that distinguishes it from all of the other classical and semiclassical studies of acetylene listed above is that it is based upon a model that reproduces the observed vibrational levels to very high internal energy (15,000 cm^{-1}). It is worth repeating that no potential surface was used in this work, since no surface was available that could reproduce the observed eigenvalues adequately. As such, an effective Hamiltonian model was fitted to the observed spectra and used to generate a detailed semiclassical analysis of the bend degrees of freedom of acetylene. As has been pointed out in previous work [141], this approach has a number of advantages. Effective Hamiltonians not only tend to be much easier to fit to experimental spectra than potential surfaces, but they can also make explicit the existence of approximately conserved dynamical quantities (polyad numbers) that reduce the dimensionality of the problem.

If a potential surface for acetylene with sufficient accuracy becomes available, then two approaches will be possible. One is to use the potential surface to calculate directly the classical dynamics, as was done in the Prosmiti and Farantos study of acetylene [160]. In the case of acetylene, these calculations are six-dimensional, as opposed to the two dimensional Hamiltonian considered in this chapter that resulted from exploiting the existence of three approximately conserved polyad numbers. Thus, assessing quantum-classical correspondence would be substantially more difficult if one were to calculate the classical dynamics and quantum eigenstates directly from the 6D potential surface.

A second possible approach if a potential surface is available is to use perturbation theory (Gustavson [26] or canonical Van Vleck [24]) to solve the Hamilton-Jacobi equations for the action-angle variables and also to construct to some high order an effective Hamiltonian that can then be analyzed in a spirit similar to what is done here. In such an approach, the lifting procedure, which relates the abstract action/angle space of the classical calculations to the physical coordinates of the molecule, is exact. This strategy appears in the work of Joyeux [26] as well as Sibert and McCoy [24], who also have considered the bending modes of acetylene. The potential surface used by Sibert and McCoy has not been refined sufficiently to reproduce the experimental

eigenvalues up to 15,000 cm^{-1}, but their approach influenced in many ways the work reported here.

Recent work on the simpler system of HCP illustrates both approaches. An early version of the HCP potential surface [116] was used directly for calculating periodic orbits that were instrumental in elucidating unusual spectroscopic observations [161, 162] associated with qualitative changes in the potential energy surface near the barrier to isomerization. Recently, a potential surface has been constructed for HCP that does an excellent job of reproducing the experimental stimulated emission pumping spectra. This potential surface has been used by Joyeux [26] to obtain an effective Hamiltonian using perturbation theory. This effective Hamiltonian has two conserved polyad numbers that reduce the dimensionality of the problem to 1D.

Two major challenges face the application of the methods used here to other systems. First, the approach used here relies on the existence of conserved quantities to reduce the number of degrees of freedom of the Hamiltonian to two or fewer. These approximately conserved, polyad quantum numbers are known to exist in many molecules. However, particularly for molecules larger than acetylene, the number of such polyad numbers may not be sufficient to reduce the dimensionality of the problem substantially. The second problem is that effective Hamiltonian models are not generally applicable to systems with multiple accessible minima, such as isomerizing systems. Acetylene itself is known to be capable of isomerizing to vinylidene somewhat above 15,000 cm^{-1} [4]. Thus, the ability to extrapolate the effective Hamiltonian model of acetylene bending dynamics to higher energies may be limited, although judicious use of such models may permit some insight at energies above a saddle point, because initially only a small fraction of phase space will be occupied by trajectories that access multiple minima. The situation is not unlike the successful use of bound state methods to calculate resonances in the continuum [163].

Finally, the authors of this study wish to stress that the combination of classical, semiclassical, and quantum approaches holds a great advantage over methods limited to any one approach. The periodic orbits give the stable classical motions of the molecule; their projections into configuration space provide a natural set of

coordinates for quantum number assignments (i.e., by node counting) which allow the untangling of interleaved energy level sequences and wave function interferences that occur upon quantization.

Acknowledgments

This research was supported by DOE Grants No. DE-FG0287ER13671 (RWF) and 53-4815-2480 (HST). Howard Taylor acknowledges partial support from the Petroleum Research Fund of the American Chemical Society, and enlightening conversations with E. L. Sibert, A. B. M. McCoy, and M. E. Kellman. My work on this project was supported by the Department of the Army under a National Defense Science and Engineering Graduate Fellowship, and by the Fannie and John Hertz Foundation.

8.7 Appendix: Lifting

This Appendix addresses the question of how to relate trajectories in the abstract action/angle space $(J_a, \psi_a, J_b, \psi_b)$ to physical motions of the molecule. The relationships derived will necessarily be approximate; in the absence of an accurate potential energy surface for the molecule, it is not possible to solve the Hamilton-Jacobi equations for the relation between position and momentum variables ($\bar{p}$,$\bar{x}$) and the actions and angles ($\bar{I}$,$\bar{\phi}$). However, it is possible to determine the relationship between the ($\bar{I}$,$\bar{\phi}$) and ($\bar{p}$,$\bar{x}$) for an approximate, physically plausible model, and assume these actions and angles to be those of H_C.

The natural model to relate the ($\bar{I}$,$\bar{\phi}$) to ($\bar{p}$,$\bar{x}$) is that of two uncoupled, isotropic, two-dimensional harmonic oscillators (i.e., the zeroth order part of the Hamiltonian that was fit to the observed spectra):

$$H^\circ = H_4^\circ + H_5^\circ \tag{8.25}$$

$$H_i^\circ = \frac{p_{x_i}^2}{2} + \frac{p_{y_i}^2}{2} + \frac{\omega_i^2}{2}(x_i^2 + y_i^2) \quad (i = 4, 5) \tag{8.26}$$

in which the indices 4 and 5 refer, as usual, to the *cis* and *trans* bend normal coordinates. A general solution for the motion of this system is

$$x_i(t) = x_{id}(t) + x_{ig}(t) = A_{id}\cos(\omega_i t + \alpha_{id}) + A_{ig}\cos(\omega_i t + \alpha_{ig}) \tag{8.27}$$

$$y_i(t) = y_{id}(t) + y_{ig}(t) = A_{id}\sin(\omega_i t + \alpha_{id}) - A_{ig}\sin(\omega_i t + \alpha_{ig}), \tag{8.28}$$

where the four constants A_{id}, A_{ig}, α_{id}, and α_{ig} are determined by the initial conditions. The action of an oscillator i is given as

$$I_i^\circ = \frac{1}{2\pi}\int_0^{2\pi/\omega_i} dt[\dot{x}_i(t)p_{ix}(t) + \dot{y}_i(t)p_{iy}(t)] \tag{8.29}$$

and thus

$$I_{id}^\circ = \omega_i A_{id}^2 \tag{8.30}$$

$$I_{ig}^\circ = \omega_i A_{ig}^2. \tag{8.31}$$

Since the oscillators do not interact in this model,

$$I_{total}^\circ = I_{4d}^\circ + I_{4g}^\circ + I_{5d}^\circ + I_{5g}^\circ = \omega_i(A_{4d}^2 + A_{4g}^2 + A_{5d}^2 + A_{5g}^2). \tag{8.32}$$

Thus, the total actions in zero order relate to those of the individual oscillators in exactly the same manner as do their abstract analogues in the fully coupled case. This suggests that the A's and angles can be evaluated by equating the I° with I, and $\omega t + \alpha$ with ϕ, all with the same index:

$$x_i = \sqrt{I_{id}/\omega_i}\cos(\phi_{id}) + \sqrt{I_{ig}/\omega_i}\cos(\phi_{ig}) \tag{8.33}$$

$$y_i = \sqrt{I_{id}/\omega_i}\sin(\phi_{id}) - \sqrt{I_{ig}/\omega_i}\sin(\phi_{ig}). \tag{8.34}$$

Invoking the canonical transformation gives the final result

$$\begin{aligned} x_4(t) &= [(K_a + K_b + J_a - J_b)/\omega_4]^{1/2}\cos[(\theta_a + \theta_b + \psi_a - \psi_b)/4] \\ &+ [(K_a - K_b + J_a + J_b)/\omega_4]^{1/2}\cos[(\theta_a - \theta_b + \psi_a + \psi_b)/4] \end{aligned} \tag{8.35}$$

$$
\begin{aligned}
y_4(t) &= [(K_a + K_b + J_a - J_b)/\omega_4]^{1/2} \sin[(\theta_a + \theta_b + \psi_a - \psi_b)/4] \qquad (8.36)\\
&- [(K_a - K_b + J_a + J_b)/\omega_4]^{1/2} \sin[(\theta_a - \theta_b + \psi_a + \psi_b)/4]\\
x_5(t) &= [(K_a + K_b - J_a + J_b)/\omega_5]^{1/2} \cos[(\theta_a + \theta_b - \psi_a + \psi_b)/4] \qquad (8.37)\\
&+ [(K_a - K_b - J_a - J_b)/\omega_5]^{1/2} \cos[(\theta_a - \theta_b - \psi_a - \psi_b)/4]\\
y_5(t) &= [(K_a + K_b - J_a + J_b)/\omega_5]^{1/2} \sin[(\theta_a + \theta_b - \psi_a + \psi_b)/4] \qquad (8.38)\\
&- [(K_a - K_b - J_a - J_b)/\omega_5]^{1/2} \sin[(\theta_a - \theta_b - \psi_a - \psi_b)/4].
\end{aligned}
$$

Finally, for purposes of plotting the orbits, one can transform to rectilinear coordinates that describe the motions of the two individual hydrogens, which are labeled 1 and 2 (a similar transformation was invoked in Chapter 7):

$$
\begin{aligned}
x_1 &= x_4 + x_5 \qquad (8.39)\\
y_1 &= y_4 + y_5 \qquad (8.40)\\
x_2 &= -x_4 + x_5 \qquad (8.41)\\
y_2 &= -y_4 + y_5. \qquad (8.42)
\end{aligned}
$$

These are the coordinates that are plotted in Figs. 8-5 and 8-7.

The prescription for obtaining the bending motions of the molecule in a physical coordinate space is now in principle simple. For a given trajectory or periodic orbit in the abstract space, $J_a(t)$, $J_b(t)$, $\psi_a(t)$, and $\psi_b(t)$ are known, as are $K_a = (N_b+2)/4$ and $K_b = \ell/4$. To use Eqs. 8.35–8.38, one also needs to know $\theta_a(t)$ and $\theta_b(t)$, which can be obtained from solving Hamilton's equations as

$$
\dot{\theta}_{a,b}(t) = \frac{\partial H(\bar{J}(t), \bar{\psi}(t), \bar{K})}{\partial K_{a,b}}. \qquad (8.43)
$$

Several points are worth discussing here. First is the question of the initial conditions to use in solving Eq. 8.43. The θ's do not appear in H_C, and thus all trajectories are independent of these variables. In practice, different choices of the initial conditions correspond to trivial differences in the orientations of the motions (e.g. bending along the x versus y direction). This is because Eqs. 8.35–8.38 show that $\theta_a/4$ represents

a common shift of all oscillator phases, which is equivalent to a translation in time, and $\theta_b/4$ rotates the plane of the (x,y) coordinate system. Neither of these operations affects the relative motions of the hydrogens.

A more subtle point concerning Eq. 8.43 is that, in general, most of the "lift" comes from $\theta_a(t)$, while $\theta_b(t)$ has a small effect that comes in at higher orders. $\theta_a(t)$ is a "fast" variable whose time dependence in the harmonic limit is $2(\omega_4 + \omega_5)t$. To appreciate this, notice that at the fixed points $(\psi_a, \psi_b) = (0,0)$ or (π, π), all derivatives of H_C with respect to $\bar{J}$ and $\bar{\psi}$ must be zero, which in turn requires from Hamilton's equations that $\dot{\overline{J}} = \dot{\overline{\psi}} = 0$. Hence at the extreme points, θ_a is solely responsible for the lifting, and according to Eq. 8.43, only the harmonic part of H_C contributes to the time dependence. As Kellman has pointed out [164], a fixed point in the abstract action/angle space (ψ_a, ψ_b) must lift to a periodic orbit in the physical coordinates of the molecule (i.e., x_4, x_5, y_4, y_5) that lies on a full dimension torus.

The lift of periodic orbits (as opposed to fixed points) in the abstract action/angle space is still dominated by $\theta_a(t)$, but the lifted trajectory will now be quasiperiodic on the torus in the physical coordinate space. Similarly, the lift of quasi-periodic orbits in the abstract action/angle space results in quasi-periodic fluctuations in the trajectory in the (x, y) coordinates that tend to replace the periodic orbit with a braid-like trajectory. Note that the dominance of θ_a in controlling the lift implies that the motion in the abstract action/angle coordinates tracks the deviation from the "ideal" trajectory found at the fixed point. Near the fixed point where the 2D motion is effectively harmonic, the two basic periodic orbits reduce to the normal modes of this deviation.

8.8 Appendix: Symmetry Properties of the Semiclassical Wavefunctions

This Appendix considers how g/u symmetry and parity, which are quantum mechanically conserved, are manifested in the semiclassical eigenfunctions.

Parity is the symmetry with respect to inversion of the space-fixed axes, and is

equivalent, for a symmetric top, to the $\hat{\sigma}_v$ point group operation (see, for example, Ref. [165]). In terms of the rectilinear displacement coordinates defined for each hydrogen in Section 8.7, the effect of the parity operation can be taken to be

$$\hat{\sigma}_v(x_1, y_1, x_2, y_2) \rightarrow (x_1, -y_1, x_2, -y_2). \tag{8.44}$$

These relationships in turn imply that the normal mode displacement coordinates transform as

$$\hat{\sigma}_v(x_4, y_4, x_5, y_5) \rightarrow (x_4, -y_4, x_5, -y_5). \tag{8.45}$$

Inspection of Eqs. 8.35–8.38 reveals that this transformation of the normal mode coordinates can be generated by the following simple transformation among the abstract coordinates:

$$\hat{\sigma}_v(K_b, \theta_b, \psi_b, J_b) \rightarrow (-K_b, -\theta_b, -\psi_b, -J_b). \tag{8.46}$$

This transformation can therefore be considered to represent the effect of the parity operation in the abstract coordinates.

The g/u symmetry refers to inversion through the molecular center of symmetry, denoted by $\hat{\imath}$. In the rectilinear displacement coordinates, the effect of inversion is

$$\hat{\imath}(x_1, y_1, x_2, y_2) \rightarrow (-x_2, -y_2, -x_1, -y_1). \tag{8.47}$$

or

$$\hat{\imath}(x_4, y_4, x_5, y_5) \rightarrow (x_4, y_4, -x_5, -y_5) \tag{8.48}$$

(mode 5, *cis* bend, has Π_u symmetry, while mode 4, *trans* bend, has Π_g symmetry). This symmetry operation, like parity, can be generated by a simple transformation among the abstract coordinates, which in this case is

$$\hat{\imath}(K_b, \theta_b, J_b, \psi_b) \rightarrow (K_b, \theta_b + 2\pi, J_b, \psi_b + 2\pi). \tag{8.49}$$

This transformation might appear to be a trivial one, since θ_b and ψ_b are cyclic in 2π. However, notice that the canonical transformation of Eq. 8.7 is only one-to-one on a

region of angles from 0 to 4π in ψ_a and in ψ_b. In a similar manner, the equations that defined the "lift", Eqs. 8.35–8.38, indicate that motion in the space (x_1, x_2, y_1, y_2) is periodic upon changes of 4π in any or all of the four angles ψ_a, ψ_b, θ_a, θ_b, but is not periodic upon changes of 2π.

In this chapter only polyads with $K_b = 0$ are considered, and for this case H_C is invariant under the both of the symmetry operations in Eqs. 8.46 and 8.49. In addition, the semiclassical wavefunctions should be expected to, at most, change sign under the corresponding transformations in the configuration space:

$$\hat{\sigma}_v(\psi_a, \psi_b) \rightarrow (\psi_a, -\psi_b) \tag{8.50}$$

$$\hat{\imath}(\psi_a, \psi_b) \rightarrow (\psi_a, \psi_b + 2\pi). \tag{8.51}$$

These symmetry properties can be used to explain the appearance of symmetry doublets among the eigenfunctions in polyad [22,0] and other high energy polyads.

Consider first a semiclassical eigenfunction that is localized around $\psi_b = 0$ (i.e., a state that has very nearly zero amplitude near $\psi_b = \pi$). Because the accessible phase space in Region I is restricted to the vicinity of $(\psi_a, \psi_b) = (0, 0)$, all eigenstates in Region I fulfill this condition, but certain states in Regions II and III could be similarly restricted due to dynamical localization. First, the symmetry property in Eq. 8.50 implies that any semiclassical eigenfunctions must be either symmetric or antisymmetric about $\psi_b = 0$; this symmetry reflects the parity of the eigenstate. In the context of states localized around $\psi_b = 0$, those states with even quanta of excitation along L_2 have positive parity, and states with odd quanta have negative parity. The symmetry property of Eq. 8.51 implies that the wavefunction must be symmetric or antisymmetric with respect to a shift of 2π along ψ_b; this operation reflects the g/u symmetry. Thus, if a state has negligible amplitude near $\psi_b = \pi$, then it must appear in a doublet with a state of opposite g/u symmetry (i.e., a state with nearly identical probability distribution, but different signs at $\psi_b = 0, 2\pi, 4\pi, \cdots$). If the state is mostly organized around $\psi_b = 0$, but has non-negligible amplitude in the vicinity of $\psi_b = \pi$, then the doublet pairs will be split slightly, in a manner analogous

to tunneling in a double well minimum.

Similar arguments can be given for states localized about $\psi_b = \pi$, which includes all states within Region IV, as well as those states in Region III that are organized around $(\psi_a, \psi_b) = (0, \pi)$ or (π, π). Note that reflection about the line $\psi_b = \pi$ is equivalent to the application of both symmetry operations, Eqs. 8.50 and 8.51, in succession (in either possible order). As a result, states with an even number of quanta of excitation in the ψ_b direction [i.e., along C_1, for those states organized about $(\psi_a, \psi_b) = (\pi, \pi)$; or along L_2, for those states organized around $(\psi_a, \psi_b) = (0, \pi)$], must have either $g+$ or $u-$ symmetry; those states with an odd number of quanta in the ψ_b direction must be either $g-$ or $u+$. As long as the states in question have little probability near $\psi_b = 0$, then they will appear in doublets of $g+/u-$ or $g-/u+$.

Chapter 9

Anomalously Simple Stretch-Bend IVR

This chapter, other than the Appendix, has been published in the Journal of Chemical Physics as Ref. [166].

9.1 Introduction

Chapters 6, 7, and 8 examined in some detail the *bending* vibrational dynamics of acetylene, particularly at high vibrational energy ($\sim$15,000 cm^{-1}). This chapter explores vibrational energy flow between the bend and stretch degrees of freedom, with particular emphasis on the phenomenon of anomalously slow intramolecular vibrational redistribution (IVR). At high internal energy (>10,000 cm^{-1}) most of the observed bright states (which have nonzero quanta in the CC stretch and *trans* bend modes) display complicated fractionation patterns, corresponding to fast IVR (see Fig. 5-13). However, a series of bright states can be identified, up to at least 15,000 cm^{-1}, that display virtually no fractionation at all (at $\sim$7 cm^{-1} resolution). The bright states that display this anomalously slow IVR share the property that $v_4 \leq 8$, with the rest of the vibrational excitation in the CC stretch mode. Thus, at high internal energy, the rate of IVR is very sensitive to the way in which vibrational excitation is divided among the two Franck-Condon active modes.

This observation is clearly at odds with statistical models of vibrational relaxation, but it should also be noted at the outset that this phenomenon is not well-described by the theoretical constructs of "extreme motion" or "exterior" states [100, 101], which are frequently invoked to explain similar instances of anomalously slow IVR. Exterior states are those zero-order states which have all of their vibrational excitation residing in just one of the modes (or, in the case of larger molecules, in a small number of modes) of the molecule. At a phenomenological level, exterior states are expected to have fractionation patterns that are atypically simple, because they are coupled to fewer other zero-order states, *via* the important anharmonic resonances, than states with vibrational excitation that is distributed more democratically among the modes. More rigorous justifications for this type of anomalously slow IVR have been advanced, in terms of an adiabatic decoupling of the extreme motion (exterior)

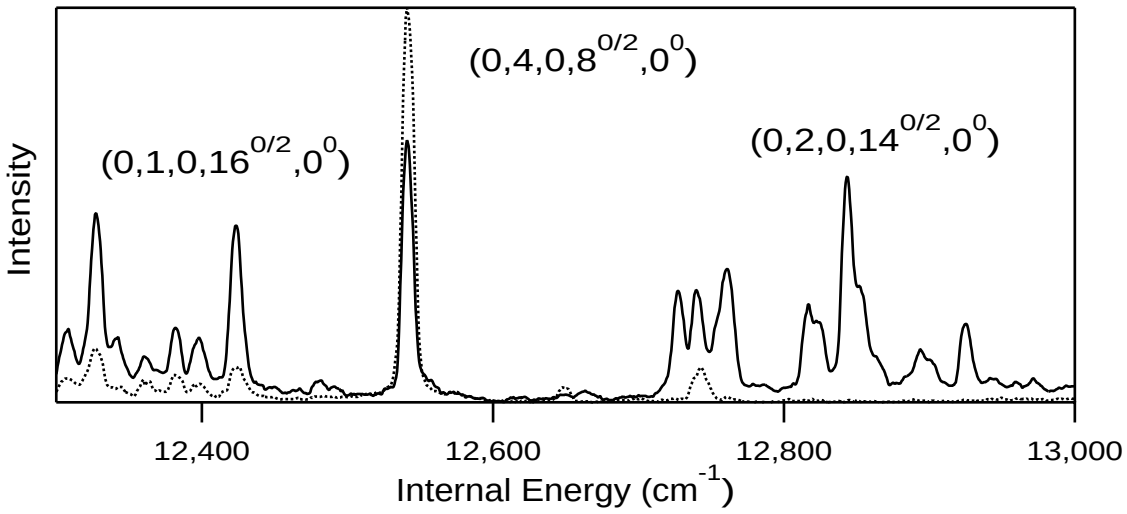

Figure 9-1: Acetylene $S_1 \rightarrow S_0$ dispersed fluorescence spectra recorded using the $Q(1)$ lines of the $V_0^2 K_0^1$ (dotted line) and $2_0^1 V_0^2 K_0^1$ (solid line) absorption bands. Groups of lines in the spectra can be assigned as single fractionated bright states using a pattern recognition approach.

states from other states [100, 101]. However, these formalisms provide little insight into the slow IVR that is reported here, because the bright states which have been identified as anomalous do not have all of their vibrational excitation in one mode; rather, several of these states approach the limit $v_2 \approx v_4$. By contrast, the bright states with all of their vibrational excitation in the *trans* bend mode ($v_2 = 0$) do *not* display anomalously slow IVR (see Chapter 6).

9.2 Vibrational Assignments

Figure 9-1 illustrates the coexistence of minimally and extensively fractionated bright states at high internal energy. The two spectra depicted are dispersed fluorescence (DF) spectra of acetylene $S_1 \rightarrow S_0$ emission, which were recorded using the $Q(1)$ lines of the $V_0^2 K_0^1$ (dotted line) and $2_0^1 V_0^2 K_0^1$ (solid line) absorption bands (V represents the *trans* bending mode, v_3' in the S_1 state and v_4'' in the S_0 state; "2" represents the CC stretch; and K has its conventional meaning as the unsigned body-fixed projection of the total angular momentum). See Chapter 5 for experimental details.

Using the arguments laid out in Section 5.4, the clump of peaks at the low energy end of Fig. 9-1 can be identified as a single fractionated bright state, because the relative intensities of the peaks are nearly identical in both of the spectra. The zero-order bright state that gives rise to this fractionation pattern has been assigned as $(0,1,0,16^{0/2},0^0)$ based upon its approximate zero-order energy[1] [the "0/2" superscript on the v_4 quantum number reflects the fact that both ($J = 1$, $\ell = 0$) and ($J = 2$, $\ell = 2$) rotational lines are observed experimentally]. The relative intensity of the pattern in the two spectra implies that the Franck-Condon factor for this bright state is greater in the $2_0^1V_0^2K_0^1$ spectrum than it is in the $V_0^2K_0^1$ spectrum. Two other bright state fractionation patterns can be identified similarly. Note that the $(0,2,0,14^{0/2},0^0)$ bright state has virtually zero Franck-Condon intensity in the $V_0^2K_0^1$ spectrum. The $(0,4,0,8^{0/2},0^0)$ bright state has appreciable Franck-Condon intensity in both spectra, but it appears to consist of a single peak, despite being located directly between two bright states that each fractionate, in a complicated fashion, over several hundred cm^{-1}. Thus, in this region of internal energy, there coexist three bright states, distinguished only by the way in which vibrational excitation is divided between the Franck-Condon bright modes, with greatly disparate rates of IVR.

In the preceding discussion, the identity of the small peak at 12,742.5 cm^{-1} in the $V_0^2K_0^1$ DF spectrum in Fig. 9-1 was not considered. Clearly, this peak does not belong to the $(0,2,0,14^{0/2},0^0)$ fractionation pattern, since this bright state has nearly zero Franck-Condon intensity in the $V_0^2K_0^1$ spectrum. A more likely hypothesis is that this small peak belongs to the $(0,4,0,8^{0/2},0^0)$ bright state pattern, and its identity has been somewhat obscured by overlap with the $(0,2,0,14^{0/2},0^0)$ fractionation pattern. As described in Chapter 5, the Extended Cross Correlation pattern recognition technique (Chapter 2) allows the individual fractionated bright states to be disentangled from each other by processing all five of the DF spectra in the data set simultaneously, even when the bright states overlap each other strongly. Using this procedure,

[1]The zero-order energy of the bright state can be approximated by the center of gravity of the observed fractionation pattern.

the fractionation patterns of 38 bright states, with up to 15,000 cm^{-1} of internal energy, have been identified. The application of the numerical pattern recognition algorithms to the data in Fig. 9-1 (together with the other three DF spectra, which are not shown) confirms that the peak at 12,742.5 cm^{-1} does, in fact, belong to the $(0, 4, 0, 8^{0/2}, 0^0)$ bright state pattern. In other words, this transition is observable in the spectrum because the vibrational level on which the transition terminates is involved in a (relatively weak) mutual perturbation with the zero-order bright state (the vibrational level at 12,541.2 cm^{-1} is the slightly perturbed bright state). This minor fractionation of the $(0, 4, 0, 8^{0/2}, 0^0)$ bright state implies highly restricted IVR, at least on the ∼1 ps timescale associated with the resolution (∼7 cm^{-1}) of the DF spectra.

It would be difficult to identify unambiguously the perturber of $(0, 4, 0, 8^{0/2}, 0^0)$ based upon just one fractionation pattern. However, between 10,000 and 15,000 cm^{-1} of internal energy, five other anomalously simple fractionation patterns were observed, each of which has been assigned to a bright state with either 6 or 8 quanta of *trans* bend, and the remainder of the excitation in the CC stretch mode.[2] Figure 9-2 displays all of the fractionated bright state patterns of the form $(0, v_2, 0, 6^{0/2}, 0^0)$ or $(0, v_2, 0, 8^{0/2}, 0^0)$ that were extracted from the DF data set up to 15,000 cm^{-1}. The IVR associated with all of the zero-order bright states represented in Fig. 9-2 is minimal. Each of the fractionation patterns consists of one main peak which carries at least 90% of the intensity (the perturbed bright state), and in most cases, at least one smaller peak at higher internal energy ("perturbers" of the bright state). For all of the bright states with $v_2 \leq 4$, the second tallest peak in each fractionation pattern, which contains ∼3-7% percent of the bright state intensity, is marked with an asterisk. Note that the positions of these peaks appear to follow a well-defined trend, gradually growing more distant from the perturbed bright state as v_2 increases.

[2]It should be noted that several fractionated bright states with $v_4 = 4$ were also extracted, but with poor signal-to-noise, because the Franck-Condon factors for those bright states are small for transitions from all of the vibrational levels that were used as intermediates in the S_1 state of acetylene. As a result, all of the extracted fractionation patterns for the bright states $(0, v_2, 0, 4^{0/2}, 0^0)$ are single spectral lines.

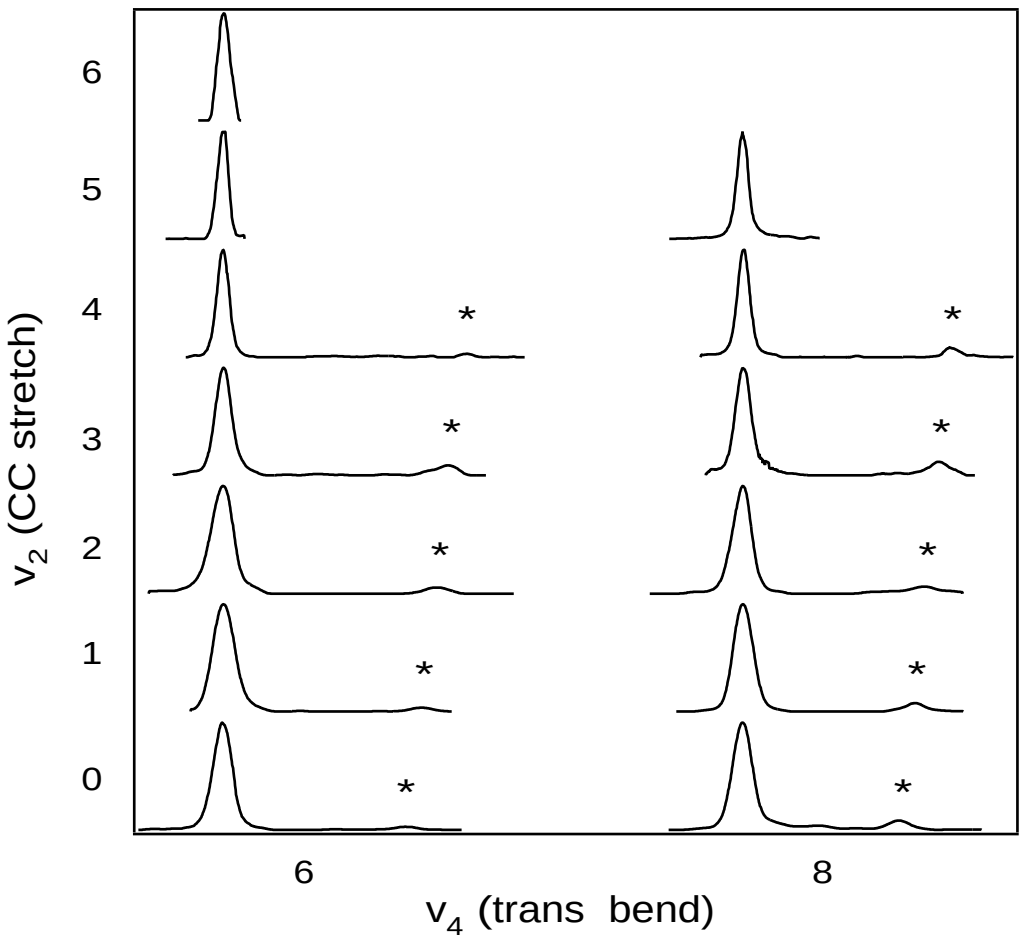

Figure 9-2: Fractionated bright state patterns with $v_4 = 6$ or 8 that were extracted from the DF data set using numerical pattern recognition, up to $E_{\rm vib}$=15,000 cm^{-1}. The patterns for all of the bright states with $v_2 \leq 4$ consist of one main peak and one or more "perturber" peaks. No perturber peaks were identified for the $v_2 > 4$ bright states, likely due to the weaker intensities of these patterns in the DF spectra (small Franck-Condon factors). The centers of the most intense peaks in each pattern are aligned vertically in each column. The second most intense peaks in each of the $v_2 \leq 4$ patterns are marked with asterisks; note the increase in the energy difference between the two most intense peaks as v_2 increases.

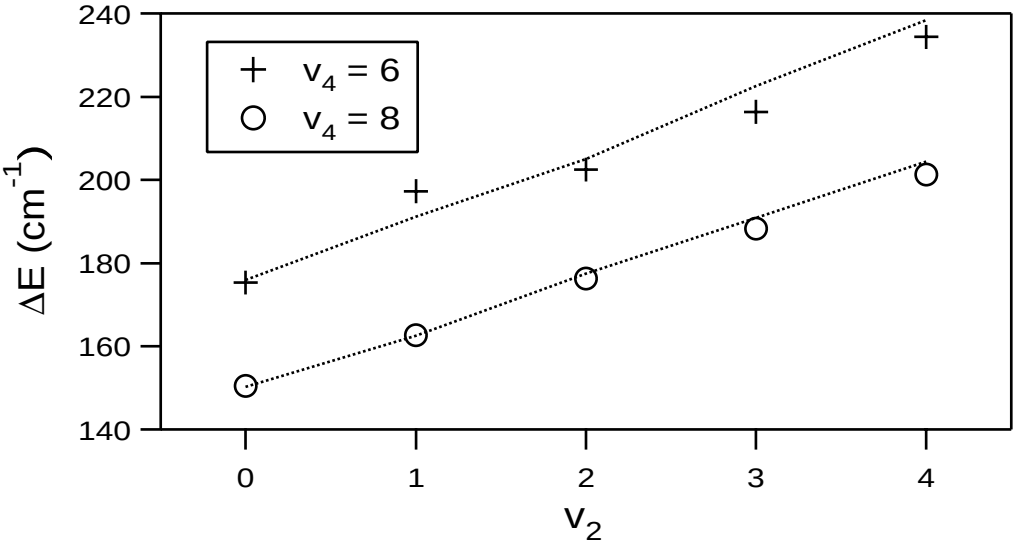

Figure 9-3: Energy differences between the two most intense peaks in the $v_2 \leq 4$ fractionated bright state patterns in Fig. 9-2. The crosses represent the series of bright states with $v_4 = 6$, and the circles, $v_4 = 8$. For both series, the energy difference appears to increase approximately linearly with v_2. The dotted lines represent the predicted energy differences of the refined global effective Hamiltonian.

In fact, as Fig. 9-3 makes clear, the splittings between these pairs of peaks grow very nearly linearly with increasing v_2. Several of the fractionation patterns also show evidence of other perturbers, even weaker ($\sim$1% of the bright state intensity) than the peaks with the asterisk, but the positions of these peaks do not follow any simple trend. No perturber peaks were identified by the numerical pattern recognition algorithms for the bright states with $v_2 > 4$. This does not imply that these bright states are free from perturbation, but rather that any perturbation that exists is too weak to be detected. It should be noted that the bright states with high v_2 tend to have small Franck-Condon factors in the DF spectra, and as such, the necessarily weak perturber peaks, if they exist, approach the noise level in the spectra.

The most remarkable aspect of Fig. 9-2 is that IVR appears not to increase with v_2, the number of quanta of CC stretch. The minimally fractionated bright state in Fig. 9-1, $(0, 4, 0, 8^{0/2}, 0^0)$, has a fractionation pattern which is at least as "simple" as that of $(0, 0, 0, 8^{0/2}, 0^0)$, despite being more than 7,000 cm^{-1} higher in internal energy. The anomalously slow IVR at high internal energy can thus be considered to be a

manifestation of the insensitivity of the rate of IVR to the number of quanta of CC stretch for these series of bright states ($v_4 \leq 8$). The remainder of this chapter is devoted to understanding the IVR that is represented in Fig. 9-2. A starting point for this analysis is the recognition that the fractionation patterns for the two bright states with $v_2 = 0$ have already been adequately modeled. These two bright states belong to polyads in which all of the states involve excitation only in the *trans* and *cis* bending modes, the so-called pure bending polyads. In Chapter 6 it is demonstrated that an effective Hamiltonian which incorporates only 3 quartic anharmonic resonances (Darling-Dennison Bend I and II, vibrational ℓ-resonance) is capable of reproducing all experimentally observed pure bending eigenstates (up to 15,000 cm^{-1}), with $\pm$ 1.4 cm^{-1} accuracy (1σ). This model reveals that the relatively weak "perturber" peaks that are observed for the $(0,0,0,6^{0/2},0^0)$ and $(0,0,0,8^{0/2},0^0)$ bright states gain their intensity through Darling-Dennison bending resonances. More precisely, within the constraints of the effective Hamiltonian model, the redistribution of the vibrational excitation from the bright states to the rest of the polyad must proceed through one of two "gateway" states, which are coupled directly to the bright state. For instance, the gateway states that correspond to the $(0,0,0,6^0,0^0)$ bright state are $(0,0,0,4^0,2^0)$ and $(0,0,0,4^{+2},2^{-2})$, which interact with the bright state through Darling-Dennison Bend I and II resonances respectively. At higher internal energy, the vibrational excitation can flow from the gateway states into the interior of the polyad, creating more complicated IVR, but for $v_4 \leq 10$, the IVR is adequately described in terms of restricted energy flow only among the bright state and the two gateway states.

Within polyads that do involve excitation in the stretching degrees of freedom, a number of additional anharmonic resonances have been demonstrated to exist [5], including a Darling-Dennison stretch resonance (between the two CH stretch modes) and at least four resonances that couple the stretch and bend degrees of freedom. However, only one of these additional resonances can couple a zero-order bright state, $(0,v_2,0,v_4^{0/2},0^0)$, directly with another zero-order state within the polyad. This anharmonic resonance is referred to as (1,244), meaning that it exchanges two quanta of *trans* bend together with one quantum of CC stretch for one quantum of symmetric

CH stretch. Thus, for any ($\ell = 0$) bright state with $v_2 > 0$, there are three possible gateway states:

1. $(0, v_2, 0, (v_4 - 2)^0, 2^0)$, *via* a Darling-Dennison Bend I resonance

2. $(0, v_2, 0, (v_4 - 2)^{+2}, 2^{-2})$, *via* a Darling-Dennison Bend II resonance

3. $(1, v_2 - 1, 0, (v_4 - 2)^0, 0^0)$, *via* a (1,244) resonance.

Because the IVR represented in Fig. 9-2 does not suddenly increase from $v_2 = 0$ to $v_2 = 1$, it appears to be unlikely that the (1,244) resonance plays a significant role in the observed IVR for the bright states with $v_2 \neq 0$. On the contrary, the regularity of the positions and intensities of the peaks marked with asterisks from $v_2 = 0$ to 4 suggests that the rather weak IVR in the $v_2 \neq 0$ bright states is also due primarily, though not necessarily exclusively, to Darling-Dennison bending resonances.

The hypothesis that the perturber peaks gain their intensity through Darling-Dennison bending resonances is also supported by the gradual, nearly linear increase in the separation between the two most intense peaks with increasing v_2 (Fig. 9-3). Although the relevant Darling-Dennison matrix elements do not depend on v_2, the increase in the separation can be explained in terms of a detuning of the zero-order energy of the bright state relative to the Darling-Dennison gateway states. The zero-order energy of the $(0, v_2, 0, v_4^0, 0^0)$ bright states can be expressed, up to x-terms, as

$$E_b = \omega_2 v_2 + \omega_4 v_4 + x_{22} v_2^2 + x_{44} v_4^2 + x_{24} v_2 v_4 \ , \tag{9.1}$$

while the gateway state $(0, v_2, 0, (v_4 - 2)^0, 2^0)$ has

$$\begin{aligned} E_g &= \omega_2 v_2 + \omega_4 (v_4 - 2) + 2\omega_5 + x_{22} v_2^2 + x_{44} (v_4 - 2)^2 \\ &+ 4x_{55} + x_{24} v_2 (v_4 - 2) + 2x_{45} (v_4 - 2) + 2x_{25} v_2 \ . \end{aligned} \tag{9.2}$$

Note that the energy of the other gateway state, $(0, v_2, 0, (v_4 - 2)^{+2}, 2^{-2})$, is identical, except for the following additional terms: $4g_{44} - 4g_{45} + 4g_{55}$. The zero-order energy

difference between the bright state and the Darling-Dennison perturber is therefore

$$\begin{aligned} E_g - E_b &= -2\omega_4 + 2\omega_5 - 4(v_4 - 1)x_{44} + 4x_{55} - 2x_{24}v_2 \\ &+ 2x_{45}(v_4 - 2) + 2x_{25}v_2 + [4(g_{44} - g_{45} + g_{55})], \end{aligned} \tag{9.3}$$

where the term in square brackets is relevant only to the perturber with $\ell_4 = -\ell_5 = 2$. Note that for either of the Darling-Dennison gateway states, only 2 of the terms in this expression depend on v_2, and this simple model predicts, as observed, a linear dependence on v_2 of the zero-order energy difference between the bright state and the gateway states. More precisely, the model predicts a dependence of $2v_2(x_{25} - x_{24})$ for the energy difference. Using previously published values for x_{24} and x_{25} of -12.5 cm^{-1} and -1.83 cm^{-1} [5], the predicted dependence is $21.4v_2$ (cm^{-1}), which is in modest agreement with the approximate slopes of the lines in Fig. 9-3 ($\sim$13 cm^{-1}), considering that the level shifts due to mutual perturbation have been neglected, as well as higher order terms in the Dunham expansion. Nonetheless, a more complete model is clearly needed to obtain quantitative agreement with the observed fractionation patterns. Such a model is presented in the next two sections, which also provides insight into the precise mechanism of the anomalously slow IVR (e.g. which of the two Darling-Dennison gateway states is the primary perturber of the bright state?).

9.3 Effective Hamiltonian Fit

A global H^{eff} for the acetylene S_0 state was first reported by Abbouti Temsamani and Herman, who demonstrated that 122 observed vibrational energy levels, up to 12,000 cm^{-1}, could be reproduced with 0.74 cm^{-1} (1σ) accuracy using a total of 35 parameters, including a Dunham expansion for the diagonal elements and 9 anharmonic resonances (off-diagonal elements) [5]. The bending constants in this model have since been extensively refined (see Chapter 6). In particular, the pure bending effective Hamiltonian reproduces 84 pure bending vibrational levels of acetylene, up to 15,000 cm^{-1}, with 1.4 cm^{-1} (1σ) accuracy, using only 16 parameters. In the con-

text of the anomalously slow IVR discussed here, the global H^{eff} model does, in fact, qualitatively reproduce the minimal fractionation for the bright states in Fig. 9-2. However, the energies of the predicted vibrational levels are in error by up to 30 cm^{-1} at high internal energy. For this reason, the global H^{eff} has been selectively refined against the data in Fig. 9-2 in order to permit the most detailed possible analysis of the anomalous IVR (and also, as will be seen in Chapter 10, to permit identification of similar states above 15,000 cm^{-1}).

Of the 39 parameters in the global H^{eff} model, only a handful can be expected to impact sensitively the observed vibrational energy levels in Fig. 9-2 (using qualitative arguments like the ones presented in the preceding section, or a quantitative sensitivity analysis of the H^{eff}). Further, several of these important parameters belong to the set of "pure bending parameters" that have been extensively refined (Chapter 6), using observed levels with up to 22 quanta of bending excitation. These include the Dunham expansion terms ω_4, ω_5, x_{44}, x_{45}, x_{55}, g_{44}, g_{45}, g_{55}, y_{444}, y_{445}, y_{455}, and y_{555}, as well as the parameters relevant to the bending resonances, r_{45}°, r_{445}, r_{545}, and s_{45}. On the other hand, the global H^{eff} model has not previously been refined using states with high excitation in the CC stretch mode, and thus the ω_2, x_{22}, x_{24}, x_{25}, and y_{244} parameters in the H^{eff} are less well-characterized (no y_{222} or y_{224} terms were included previously, and I did not find it necessary to include them here).

Accordingly, I have chosen to perform a selective refinement of just these 5 parameters in the global H^{eff}. That is, standard least-squares techniques (a modified version of the Numerical Recipes [44] Levenberg-Marquardt algorithm) have been used to minimize the difference between the experimental and predicted eigenvalues by adjusting only the ω_2, x_{22}, x_{24}, x_{25}, and y_{244} terms in the global H^{eff} model. The experimental data that were included in the fit are listed in Table 9.1. These vibrational energy levels include the most intense lines in each of the fractionation patterns in Fig. 9-2, as well as all of the levels marked by an asterisk. Note, however, that the $v_2 = 0$ patterns are excluded, because the energies of these vibrational levels are independent of the 5 fit parameters. The vibrational levels listed in the bottom section of Table 9.1 were observed primarily by absorption spectroscopy and were previously

included in the Abbouti Temsamani and Herman fit [5]. These vibrational levels are included in this fit because they involve excitation primarily in the CC stretch, *trans* bend, and *cis* bend modes, and thus can be expected to aid in determining the 5 parameters in question.

Details of the methodology of the fit can be found in Section 6.2. The parameters that were determined from the fit are listed in Table 9.2, along with their (2σ) uncertainties, as estimated from the covariance matrix. All five of the parameters have been determined to higher precision than in the Abbouti Temsamani and Herman fit, due to the inclusion in this fit of much more highly excited states. The two parameters that changed by the greatest fractional amount relative to the previous fit are x_{25} and y_{244}, which have the new/old values of -1.83/-2.151 and 0.15/0.3021 respectively. The five parameters in Table 9.2, together with the 34 other parameters in the global H^{eff} which were not modified in the fit, reproduce the 31 vibrational levels in Table 9.1 to ± 1.7 cm^{-1} (1σ). The agreement between the model and experimental observations is also depicted in Fig. 9-3. The dotted lines represent the splittings between the two most intense lines in the calculated bright state fractionation patterns. Overall, the refined parameters reproduce the splittings fairly accurately, but the observed splitting for the $(0,1,0,6^{0/2},2^0)$ bright state pattern appears to be an outlier. A portion of the discrepancy between the observed and predicted splitting can be accounted for by measurement error ($\sim$3 cm^{-1}, based on estimates of the calibration error; see Chapter 5), but the remainder of the error may be due to a local perturbation that is omitted from, or poorly modeled by, the H^{eff}. In the absence of an explanation for this discrepancy, however, I chose not to omit these vibrational energy levels from the fit.

9.4 Mechanism of Anomalous IVR

The refined global H^{eff} for the acetylene S_0 state can be used to gain detailed insight into the origin and mechanism of the anomalously slow IVR. To focus the discussion of these insights, the $(0,4,0,8^0,2^0)$ bright state fractionation pattern will be

Table 9.1: Eigenenergies included in the fit. The top portion of the table contains eigenstates that were identified in the DF data set, as detailed in Chapter 5. These levels were not included in previous fits. The bottom portion of the table contains eigenstates that were included in the Abbouti Temsamani and Herman fit, which were observed by primarily by absorption spectroscopy. The $N_{\rm res}$, N_s, and ℓ columns list the polyad quantum numbers (defined in Chapter 5) for the vibrational levels; the g/u labels have their conventional meaning as symmetry with respect to inversion in the body-fixed coordinate system through the molecular center of symmetry. The "Nominal Assignment" column indicates the zero-order state with maximal character in the eigenstate, as determined from the fit model. Note that ℓ_4 and ℓ_5 are not specified for certain levels because the eigenstates correspond to a mixture of $(0, v_2, 0, v_4^0, 2^0)$ and $(0, v_2, 0, v_4^{+2}, 2^{-2})$; see Section 9.4 for details.

$N_{\rm res}$	N_s	ℓ	g/u	Nominal Assignment	$E_{\rm obs}$	$E_{\rm calc}$	Reference
9	1	0/2	g	$(0,1,0,6^{0/2},0^0)$	5676.3	5678.8	[68]
9	1	0/2	g	$(0,1,0,4,2)$	5873.6	5870.0	[68]
11	1	0	g	$(0,1,0,8^0,0^0)$	6960.0	6960.3	[68]
11	1	0	g	$(0,1,0,6,2)$	7122.6	7122.9	[68]
12	2	0/2	g	$(0,2,0,6^{0/2},0^0)$	7570.5	7571.5	[68]
12	2	0/2	g	$(0,2,0,4,2)$	7773.0	7776.6	[68]
14	2	0/2	g	$(0,2,0,8^{0/2},0^0)$	8836.3	8837.6	[68]
14	2	0/2	g	$(0,2,0,6,2)$	9012.6	9015.1	[68]
15	3	0/2	g	$(0,3,0,6^{0/2},0^0)$	9449.4	9448.2	[68]
15	3	0/2	g	$(0,3,0,4,2)$	9665.8	9670.7	[68]
17	3	0/2	g	$(0,3,0,8^{0/2},0^0)$	10698.1	10697.2	[68]
17	3	0/2	g	$(0,3,0,6,2)$	10886.4	10888.1	[68]
18	4	0/2	g	$(0,4,0,6^{0/2},0^0)$	11309.0	11309.0	[68]
18	4	0/2	g	$(0,4,0,4,2)$	11543.4	11547.6	[68]
20	4	0/2	g	$(0,4,0,8^{0/2},0^0)$	12541.2	12540.9	[68]
20	4	0/2	g	$(0,4,0,4,2)$	12742.5	12745.3	[68]
21	5	0/2	g	$(0,5,0,6^{0/2},0^0)$	13154.6	13153.8	[68]
23	5	0/2	g	$(0,5,0,8^{0/2},0^0)$	14368.3	14368.5	[68]
24	6	0/2	g	$(0,6,0,6^{0/2},0^0)$	14983.5	14982.6	[68]
3	1	0	g	$(0,1,0,0^0,0^0)$	1974.3	1975.1	[167]
4	1	1	g	$(0,1,0,1^1,0^0)$	2574.7	2575.3	[87]
4	1	1	u	$(0,1,0,0^0,1^1)$	2703.1	2703.2	[168]
5	1	0	g	$(0,1,0,0^0,2^0)$	3420.4	3419.9	[169]
5	1	2	u	$(0,1,0,0^0,2^2)$	3434.1	3433.8	[169]
5	1	0	u	$(0,1,0,1^1,1^{-1})$	3300.6	3300.7	[170]
5	1	2	u	$(0,1,0,1^1,1^1)$	3307.7	3307.8	[170]
6	1	1	u	$(0,1,0,0^0,3^1)$	4140.1	4139.1	[171]
6	2	0	g	$(0,2,0,0^0,0^0)$	3933.9	3934.2	[172]
8	2	0	u	$(0,2,0,1^1,1^{-1})$	5230.0	5230.2	[168]
11	2	1	g	$(0,2,0,5^1,0^0)$	6945.3	6944.9	[138]
11	3	0	g	$(0,3,0,2^0,0^0)$	7037.0	7036.5	[138]

Table 9.2: Parameters determined from least-squares fit to the data set described in the text. Numbers in parentheses are 2σ uncertainties in the last digit, as determined from the covariance matrix.

ω_2	1983.054 (87)
x_{22}	-7.981 (32)
x_{24}	-12.910 (50)
x_{25}	-2.151 (42)
y_{244}	0.3021 (63)

used as a representative example. Figure 9-4 illustrates the agreement between the observed and calculated fractionation patterns for the $(0,4,0,8^{0/2},0^0)$ bright state. Both the energies and intensities of the two largest peaks in the pattern are reproduced well by the model. The most intense transition in the spectrum terminates on the lowest energy eigenstate within the polyad and contains 95.3% bright state character, which reconfirms that it is reasonable to label it as the nominal, or perturbed, bright state. The zero-order state with the second highest character in this eigenstate is $(0,4,0,6^0,2^0)$, at 3.9%. By contrast, the other possible Darling-Dennison perturber, $(0,4,0,6^{+2},2^{-2})$, contributes <0.1% character to this eigenstate. This observation would appear to indicate that the most intense perturber line, at 12742.5 cm^{-1}, should be assignable (nominally) as $(0,4,0,6^0,2^0)$. This is not quite the case. The eigenstate at 12742.5 cm^{-1} is *not* well represented by either *one* of the Darling-Dennison gateway states, but rather is composed of a mixture of the two: 49.7% character of $(0,4,0,6^0,2^0)$ and 39.6% $(0,4,0,6^{+2},2^{-2})$.

The key to reconciling these observations is that the two Darling-Dennison gateway states mutually perturb each other, quite strongly, *via* vibrational ℓ-resonance. This phenomenon can be understood by applying degenerate perturbation theory to a simplified H^{eff} of 3 interacting states: the bright state, $|B\rangle$, and the two Darling-Dennison perturbers, $|P_0\rangle$ ($\ell_4 = \ell_5 = 0$) and $|P_2\rangle$ ($\ell_4 = -\ell_5 = 2$). The matrix representation of this three-level system is depicted in the left column of Fig. 9-5.

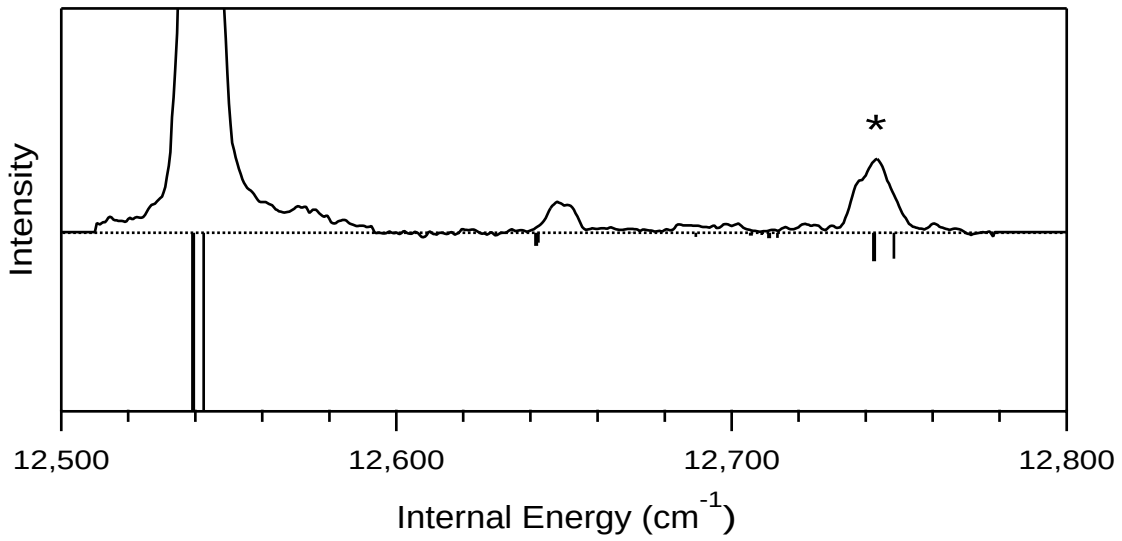

Figure 9-4: Agreement between the predictions of the effective Hamiltonian (vertical lines) and the experimentally identified fractionation pattern for the $(0, 4, 0, 8^{0/2}, 0^0)$ bright state (solid line). The thick and thin vertical lines represent the calculated fractionation patterns for $(0, 4, 0, 8^0, 0^0)$ and $(0, 4, 0, 8^2, 0^0)$, respectively. The transition represented by the large, off-scale peak on the left terminates on the perturbed bright state; it has been cut off in order to emphasize the smaller perturbing lines. (Note that the vertical lines have been scaled such that their maximum is equal to the maximum of the experimental pattern). The peaks at 12649.2 and 12,742.5 cm^{-1} can be identified as Darling-Dennison perturbers of the bright state. The lower intensity Darling-Dennison perturber is itself perturbed by an anharmonic (3,245) resonance.

	$\|B\rangle$	$\|P_0\rangle$	$\|P_2\rangle$
$\|B\rangle$	E_b	x_0	x_2
$\|P_0\rangle$	x_0	$E_p + \Delta/2$	x_ℓ
$\|P_2\rangle$	x_2	x_ℓ	$E_p - \Delta/2$

	$\|B\rangle$	$\|P_+\rangle$	$\|P_-\rangle$
$\|B\rangle$	E_b	$ax_0 + bx_2$	$bx_0 - ax_2$
$\|P_+\rangle$	$ax_0 + bx_2$	$E_p - \alpha$	0
$\|P_-\rangle$	$bx_0 - ax_2$	0	$E_p + \alpha$

Figure 9-5: Left: Matrix representation of the simple three-level model for anomalously simple IVR. Right: The three-level model with the vibrational ℓ-resonance pre-diagonalized.

The diagonal elements of the system (zero-order energies) will be designated as

$$\langle B|H^{\rm eff}|B\rangle = E_b \tag{9.4}$$

$$\langle P_0|H^{\rm eff}|P_0\rangle = E_p + \frac{\Delta}{2} \tag{9.5}$$

$$\langle P_2|H^{\rm eff}|P_2\rangle = E_p - \frac{\Delta}{2}\ , \tag{9.6}$$

where Δ, the zero-order energy difference between the two Darling-Dennison gateway states, is 9.8 cm^{-1} *for all of the relevant polyads*. The values of E_b and E_p, of course, vary from polyad to polyad, but $(E_p - E_b) \gg \Delta$ in all cases ($E_p - E_b > 100$ cm^{-1}). The off-diagonal elements (and their Hermitian conjugates) are

$$\langle B|H^{\rm eff}|P_0\rangle = x_0 \ \text{[Darling-Dennison Bend I]} \tag{9.7}$$

$$\langle B|H^{\rm eff}|P_2\rangle = x_2 \ \text{[Darling-Dennison Bend II]} \tag{9.8}$$

$$\langle P_0|H^{\rm eff}|P_2\rangle = x_\ell \ \text{[vibrational } \ell\text{-resonance]}. \tag{9.9}$$

All three of these matrix elements are independent of v_2, but do depend on v_4. For $v_4 = 6$, $x_0 = -25.7$ cm^{-1}, $x_2 = 8.9$ cm^{-1}, $x_\ell = -29.8$ cm^{-1}; for $v_4 = 8$, $x_0 = -34.3$ cm^{-1}, $x_2 = 12.7$ cm^{-1}, $x_\ell = -41.8$ cm^{-1}. Note that in either case, $x_\ell > \Delta$, which indicates that the P_0/P_2 sub-block of the matrix should be pre-diagonalized before applying nondegenerate second-order perturbation theory.

This prediagonalization is equivalent to defining new basis states according to

$$|P_+\rangle = a|P_0\rangle + b|P_2\rangle \tag{9.10}$$

$$|P_-\rangle = b|P_0\rangle - a|P_2\rangle \ , \tag{9.11}$$

where the normalized a and b coefficients are determined from diagonalizing the P_0/P_2 sub-block:

$$a = \frac{\alpha - \Delta}{\sqrt{4x_\ell^2 + (\alpha - \Delta)^2}} \tag{9.12}$$

$$b = \frac{-2x_\ell}{\sqrt{4x_\ell^2 + (\alpha - \Delta)^2}} \tag{9.13}$$

with $\alpha = \sqrt{\Delta^2 + 4x_\ell^2}$. The matrix representation of the three-level model in this new basis is depicted in the right column of Fig. 9-5, and consists of the following elements:

$$\langle P_+|H^{\text{eff}}|P_+\rangle = E_p - \alpha \tag{9.14}$$

$$\langle P_-|H^{\text{eff}}|P_-\rangle = E_p + \alpha \tag{9.15}$$

$$\langle P_+|H^{\text{eff}}|P_-\rangle = 0 \tag{9.16}$$

$$\langle P_+|H^{\text{eff}}|B\rangle = ax_0 + bx_2 \tag{9.17}$$

$$\langle P_-|H^{\text{eff}}|B\rangle = bx_0 - ax_2 \ . \tag{9.18}$$

By applying second-order perturbation theory to this system, the lowest energy eigenstate, $|1\rangle$, can be approximated as

$$|1\rangle \approx |B\rangle + \left(\frac{ax_0 + bx_2}{E_b - E_p + 0.5\alpha}\right)|P_+\rangle + \left(\frac{bx_0 - ax_2}{E_b - E_p - 0.5\alpha}\right)|P_-\rangle \ . \tag{9.19}$$

Evaluating this expression numerically for the polyad that contains the $(0, 4, 0, 8^0, 0^0)$ bright state yields

$$|1\rangle \approx |B\rangle + 0.108|P_+\rangle + 0.165|P_-\rangle \tag{9.20}$$

$$\approx \quad |B\rangle + 0.195|P_0\rangle - 0.029|P_2\rangle \ . \tag{9.21}$$

That is, this simple 3 level model predicts that the bright state should gain 3.8% character from one Darling-Dennison perturber, $(0, 4, 0, 6^0, 2^0)$, but only 0.08% character from the other, $(0, 4, 0, 6^{+2}, 2^{-2})$. These results are in very close agreement with the predictions of the full global $H^{\rm eff}$ that were discussed above (3.9% and 0.06%, respectively). Thus, despite the large number of parameters in the global $H^{\rm eff}$ and the relatively large total number of states within the polyad (38), the perturbation of the bright state is describable in terms of just three mutually interacting states.

Similarly, the highest energy eigenfunction of the 3-level system can be approximated as

$$|3\rangle \approx |P_-\rangle + \left(\frac{bx_0 - ax_2}{E_p + \alpha - E_b}\right)|B\rangle = 0.747|P_0\rangle - 0.665|P_2\rangle - 0.165|B\rangle \ .$$

In other words, this eigenstate contains 2.7% bright state character, but is otherwise well-described as a mixture of both perturbers, 55.8% $(0, 4, 0, 6^0, 2^0)$ and 44.2% $(0, 4, 0, 6^{+2}, 2^{-2})$. The predicted bright state character agrees closely with that predicted by the global $H^{\rm eff}$ model (2.6%), but the global $H^{\rm eff}$ predicts only 49.7% and 39.6% character for the two Darling-Dennison gateway states (respectively), which is lower, for each, by $\sim$5% than predicted by the 3-level model. The origin of this discrepancy is that the three levels that are included in the simplified $H^{\rm eff}$ together account for only 92.0% of the character of the eigenstate near 12,742.5 cm^{-1}. The remainder of the character of that eigenstate is accounted for largely by states with 4 quanta of *cis* bend, i.e., states in the next tier of the Darling-Dennison ladder. Note, however, that the ratio of the characters of the two gateway states, $|\langle 3|P_2\rangle|^2/|\langle 3|P_0\rangle|^2$, is nearly identical (1.26 in both cases) for both the global and simplified models, implying that the 12,742.5 cm^{-1} eigenstate can be labeled as a perturbed $|P_-\rangle$ state. Thus, the simplified 3-level Hamiltonian, treated at the level of second-order perturbation theory, replicates all of the key behaviors of the global $H^{\rm eff}$ noted previously, namely that the bright state appears to be perturbed by only one of the Darling-

Dennison gateway states, but the second most intense line in the fractionation pattern (marked by an asterisk) corresponds to an eigenstate with significant character of both gateway states.

The simplified model also predicts the existence of a third eigenstate, intermediate in energy between the two just discussed, which is characterized as

$$|2\rangle \approx |P_+\rangle + \left(\frac{ax_0 + bx_2}{E_p - \alpha - E_b}\right)|B\rangle = 0.665|P_0\rangle + 0.747|P_2\rangle - 0.108|B\rangle \ . \qquad (9.22)$$

This eigenstate is predicted to have less intensity than $|3\rangle$ (1.2% bright state character, as opposed to 3.8%), and is predicted to have an energy of

$$E_2 \approx E_p - \frac{\alpha}{2} + \frac{(ax_0 + bx_2)^2}{E_p - E_b - 0.5\alpha} = 12672.0 \ . \qquad (9.23)$$

Here, the predictions of this simple model differ from those of the global $H^{\rm eff}$. As can be seen in Fig. 9-4, the global $H^{\rm eff}$ predicts a line at 12641.8 cm^{-1}, which is in better agreement with the weak transition that is observed in the experimental fractionation pattern at 12,649.2 cm^{-1}. The origin of the discrepancy between the reduced model and the global $H^{\rm eff}$ is that the Darling-Dennison gateway states are themselves perturbed *via* a (3,245) stretch-bend anharmonic resonance. In the example under consideration, the $(0,3,1,5^{+1},1^{-1})$ zero-order state perturbs both the $(0,4,0,6^0,2^0)$ and $(0,4,0,6^{+2},2^{-2})$ gateway states.

The reduced effective Hamiltonian model can be extended to include this stretch-bend resonance. The (3,245) perturber will be represented as as $|P_\varepsilon\rangle$, and

$$\langle P_\varepsilon|H^{\rm eff}|P_0\rangle = \varepsilon_0 \qquad (9.24)$$

$$\langle P_\varepsilon|H^{\rm eff}|P_2\rangle = \varepsilon_2 \ . \qquad (9.25)$$

Transforming to the P_+/P_- basis,

$$\langle P_\varepsilon|H^{\rm eff}|P_+\rangle = a\varepsilon_0 + b\varepsilon_2 \approx -43.54 \qquad (9.26)$$

$$\langle P_\varepsilon|H^{\rm eff}|P_-\rangle = b\varepsilon_0 - a\varepsilon_2 \approx 0.57 \ , \qquad (9.27)$$

where the numerical values refer to the polyad containing the $(0, 4, 0, 8^0, 0^0)$ bright state. Thus, the eigenstate at 12,742.5 cm^{-1}, which is dominated by $|P_-\rangle$, can only be minutely influenced by the (3,245) perturber. On the other hand, the eigenstate near 12,649.2 cm^{-1}, which is dominated by $|P_+\rangle$, *is* influenced by this perturbation. That is, this eigenstate is observed experimentally at lower internal energy than predicted for the $|2\rangle \approx |P_+\rangle$ level by the 3-level model, because the (3,245) perturber lies at higher internal energy. The discrepancy between the observed peak position and that predicted by the global H^{eff} indicates that the (3,245) resonance is inadequately modeled by the global H^{eff}. Either the zero-order energy of the (3,245) perturber or the strength of the resonance predicted by the global H^{eff} is in error, or perhaps both, and a further refinement of the H^{eff} will be necessary to eliminate the discrepancy. The results presented here are insufficient for such a refinement, but the other, more highly fractionated (but not yet fitted) bright states at high internal energy are expected to yield a wealth of information about the acetylene stretch-bend resonances.

The selectivity of the (3,245) resonance with respect to the two (prediagonalized) Darling-Dennison gateway states is not unique to the polyad that contains the $(0, 4, 0, 8^0, 0^0)$ bright state. In fact, the value of the $\langle P_\varepsilon|H|P_-\rangle$ matrix element does not exceed 1.0 cm^{-1} for any of the polyads represented in Fig. 9-2 (this consistent behavior arises from the fact that the ratio ε_2:ε_0 is independent of v_2 and similar in magnitude to the ratio b:a). As a result, the highest energy eigenstate in the reduced model, $|3\rangle$, which is closely approximated as $|P_+\rangle$, will in general display no measurable effects of the (3,245) perturbation, except in unusual circumstances when the zero-order energy of the (3,245) perturber is very close to that of $|P_+\rangle$. Thus, the regularity in the progression of the peaks marked by asterisks in Fig. 9-2 results, in part, from a "shutting off" of the important (3,245) resonance, which otherwise could lead to further fractionation, corresponding to exchange of energy between the stretch and bend degrees of freedom. On the other hand, vibrational levels that correspond to the $|2\rangle$ eigenstate of the 3-level model, when they are observed, are heavily perturbed, and unlike the peaks marked by asterisks, do not form a simple progression.

To summarize, in all of the fractionated bright states that have been studied in this chapter, *two* nearly perfect interference effects have been observed. In each fractionation pattern, the bright state appears to be perturbed by only one state, despite being strongly coupled to two Darling-Dennison perturbers. In addition, one of the two (prediagonalized) Darling-Dennison perturbers is itself strongly perturbed *via* the (3,245) resonance, while the other is almost entirely unaffected. These two interference effects are, of course, intimately related, since each can be described by the simple 4-level model. The key conceptual element of this model is the prediagonalization of the two Darling-Dennison perturbers, which are coupled by vibrational ℓ-resonance. Thus, the double interference effect suggests that a "dressed basis set", in which the vibrational ℓ-resonance is pre-diagonalized and "absorbed" into the basis set, is more appropriate for describing the dynamics in these polyads, and others. In the Appendix to this chapter, I demonstrate that it is possible to define an *analytical* and completely general transformation from the conventional normal mode basis set to a basis set in which the vibrational ℓ-resonance has been effectively eliminated. This transformation provides greater insight into the dual interference effects discussed in this section, and I also discuss how these interference effects profoundly impact the dynamics of zero-order bright states that do *not* display anomalously simple IVR.

9.5 Conclusion

This chapter has examined a surprising trend in the unimolecular dynamics of acetylene. The IVR of a series of bright states with relatively low quanta of *trans* bend (≤ 8) depends only weakly on the number of quanta of CC stretch (up to at least 6 quanta); thus, IVR does not increase with internal energy for this series of bright states, up to at least 15,000 cm^{-1}. As a result, there exist bright states at high internal energy that display minimal fractionation, such that certain observed vibrational levels can be assigned normal mode quantum numbers up to at least 15,000 cm^{-1}; some of these normal mode assignments are labelled in the $2_0^1 V_0^2 K_0^1$ DF spectrum in Fig. 9-6. A simple model of four mutually interacting zero-order states, coupled by

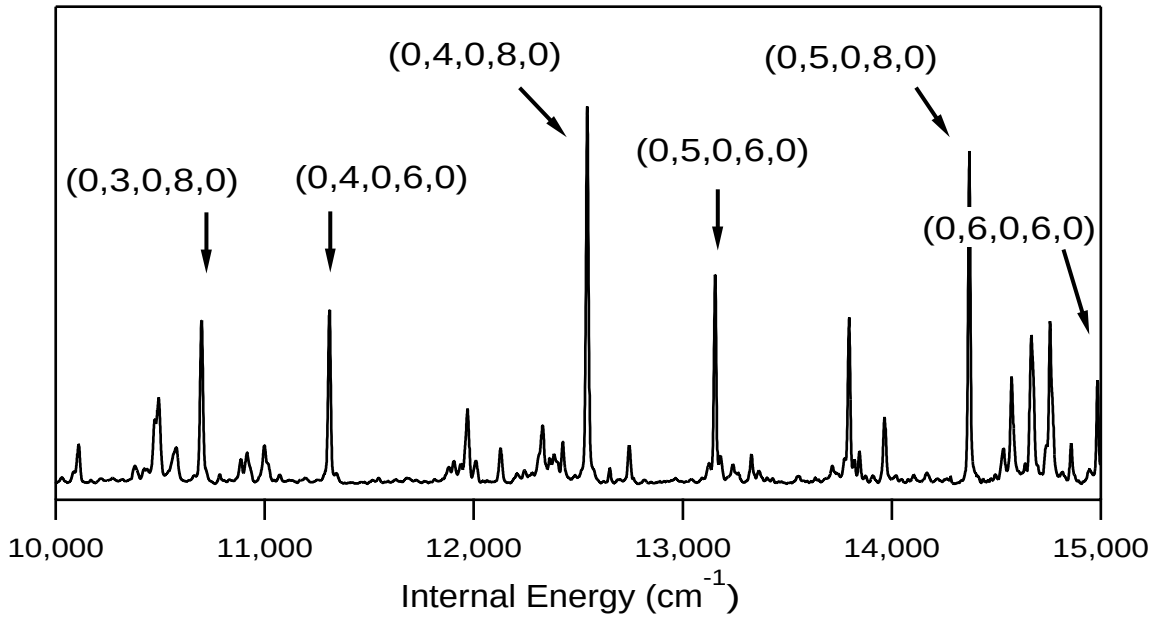

Figure 9-6: The $2_0^1 V_0^2 K_0^1$ DF spectrum, with nominal normal mode quantum number assignments for several observed vibrational levels. The majority of the unlabeled levels cannot be assigned normal mode quantum numbers, even approximately.

Darling-Dennison bending resonances, vibrational ℓ-resonance, and an anharmonic (3,245) resonance, is sufficient to describe the weak IVR. The bright states which display this anomalously simple IVR at high internal energy do so because they remain isolated from the other states within the relevant polyad. That is, the anharmonicities of the molecule conspire to cause the bright state to be located substantially lower in energy than any of the other zero-order states with which it can interact strongly *via* the known anharmonic resonances.

From this perspective, the existence of the minimally fractionated bright states at high internal energy is striking evidence of the approximate conservation of the polyad quantum numbers up to 15,000 cm^{-1}. Although the minimally fractionated zero-order states are well isolated from other states within the *same* polyad, they are nearly degenerate with many zero-order states from *different* polyads; if strong inter-polyad couplings did exist, then at least some of these bright states should display more complicated fractionation patterns than the simple two or three line patterns that were analyzed here.

Based upon the data presented here, one cannot rule out the possibility that the nominal bright states that have been assigned here are fractionated within the resolution ($\sim$7 cm^{-1}) of the DF spectra, which would imply destruction of the polyad quantum numbers on a timescale longer than $\sim$1 ps. However, Prof. David Moss (Boston University) has performed stimulated emission pumping (SEP) experiments in our laboratory that suggest that the polyad quantum numbers are conserved on a significantly longer timescale. Specifically, he observed the nominal $(0, 5, 0, 8^0, 0^0)$ bright state, which displays anomalously slow IVR (see Fig. 9-2 and 5-6), in SEP spectra with $\sim$0.05 cm^{-1} resolution [80]. This resolution corresponds to a timescale of roughly 100 ps, and if the polyad quantum numbers were destroyed on that timescale, one would expect the DF feature corresponding to the nominal $(0, 5, 0, 8^0, 0^0)$ bright state to be fractionated at the SEP resolution. However, no such fractionation was observed, at least at low rotational quantum number (there was evidence of a weak perturbation at $J \approx 9$, but this perturbation has not yet been fully analyzed). This experiment does not rule out the possibility that the polyad numbers become non-conserved on a $\sim$100 ps timescale for other states at high internal energy, but it is striking evidence that extremely stable vibrational motions exist at $\sim$15,000 cm^{-1}.

Acknowledgments

This research was supported by the Department of Energy Grant No. DE-FG0287-ER13671. My work on this chapter was supported by the Department of the Army under a National Defense Science and Engineering Graduate Fellowship.

9.6 Appendix: A New Basis Set for Acetylene

This is the most conceptually difficult section of this thesis. The goal here is to demonstrate that the interference effect involving the (3,245) resonance (described in Section 9.4) also profoundly impacts the dynamics associated with many bright states that do *not* display anomalously simple IVR. In addition, a more detailed theoretical

foundation is provided for this interference effect, and in the process a basis set for acetylene is discovered which has a number of advantages over the traditional normal mode basis set. It should be emphasized from the outset that this treatment raises a number of interesting questions which have yet to be fully answered, and that I hope that algebraic theory [118] will provide deeper insights into the intriguing results presented here.

First, I briefly review the nature of the (3,245) interference effect, as observed in the bright state fractionation patterns that display anomalously simple IVR. These bright states, $(0, v_2, 0, v_4^0, 0^0)$ with $v_4 = 6$ or 8, are minimally perturbed through Darling-Dennison resonances by the states $(0, v_2, 0, (v_4 - 2)^0, 2^0)$ and $(0, v_2, 0, (v_4 - 2)^{+2}, 2^{-2})$, and these Darling-Dennison perturbers are each themselves perturbed, through a (3,245) resonance, by the state $(0, v_2 - 1, 1, (v_4 - 3)^{+1}, 1^{-1})$. The Darling-Dennison perturbers are nearly degenerate and strongly coupled by vibrational ℓ-resonance, and thus "prediagonalizing" these two states in the effective Hamiltonian yields the greatest insights into the dynamics. The (3,245) "interference effect" refers to the observation that one of the two resultant prediagonalized Darling-Dennison perturbers is strongly coupled to the state $(0, v_2 - 1, 1, (v_4 - 3)^{+1}, 1^{-1})$ by the (3,245) resonance, while the other is almost entirely unaffected.

This (3,245) interference effect also profoundly impacts the dynamics of other classes of bright states. As an example, consider the bright state $(0, 3, 0, 14^0, 0^0)$. This bright state does not display anomalously simple IVR (see the IVR map, Fig. 5-13), and the associated dynamics cannot be described in terms of a simple 4-state model as in Section 9.4. The polyad that contains the $(0, 3, 0, 14^0, 0^0)$ bright state (characterized by $N_s = 3$, $N_{\text{res}} = 23$, $\ell = 0$) includes a total of 111 states. Only a few of these states are included in Fig. 9-7, but the states chosen represent the most important IVR pathways. The basis states are represented in Fig. 9-7 by horizontal lines at the appropriate zero-order energy, as determined by the refined effective Hamiltonian model (this chapter and Chapter 6). Two important resonances that couple these zero-order states, vibrational ℓ-resonance and the (3,245) stretch-bend resonance, are represented by arrows, and the numerical values of the specific matrix elements (in

units of cm^{-1}) are labeled in boxes near the relevant arrows. Other resonances, such as (1,244), (1,255), and (14,35) [5], play a more minor role in the short-time dynamics and are not discussed here. Note that the 4-state model, discussed in Section 9.4, represents a subset of the states included in Fig. 9-7; 5 additional states have been included here, in order to understand the more extensive IVR associated with $(0,3,0,14^0,0^0)$.

The zero-order states that are included in Fig. 9-7 are grouped into two "Darling-Dennison stacks"; that is, the states in these stacks are coupled to each other by the Darling-Dennison I and II resonances (the arrows for these resonances are omitted to reduce clutter). The Darling-Dennison stack on the left includes the bright state. As explained in Section 9.4, only three zero-order states are directly coupled to the $(0,3,0,14^0,0^0)$ bright state. One of these, $(1,2,0,12^0,0^0)$, is coupled to the bright state through the (1,244) resonance, and is not considered here because it is relatively unimportant to the dynamics, particularly for the discussion that follows. The other two states are the Darling-Dennison perturbers $(0,3,0,12^0,2^0)$ and $(0,3,0,12^{+2},2^{-2})$; here, the term "perturber" is used loosely, because these states are coupled quite strongly to the bright state, and perturbation theory is inappropriate. The two $(0,3,0,12,2)$ states in turn interact through Darling-Dennison resonances with $(0,3,0,10^0,4^0)$, $(0,3,0,10^{+2},4^{-2})$, and $(0,3,0,10^{+4},4^{-4})$. The Darling-Dennison stack continues upward, with $(0,3,0,8,6)$, $(0,3,0,6,8)$, etc., but for this discussion it is sufficient to truncate the stack. The states in this first Darling-Dennison stack interact through the (3,245) resonance with another Darling-Dennison stack, which is represented on the right side of the diagram and is characterized by $v_1 = 0$, $v_2 = 2$ and $v_3 = 1$.

It is clear from this diagram that states differing only in ℓ_4 and ℓ_5 are nearly degenerate and are very strongly coupled through vibrational ℓ-resonance. Following the approach outlined in Section 9.4, each of these "ℓ-stacks" can be numerically prediagonalized. Having done so, the resultant zero-order states can no longer be labeled using ℓ_4 and ℓ_5; Roman numerals are used instead to mark the rank of the state within an ℓ-stack. The results of this numerical procedure are presented in

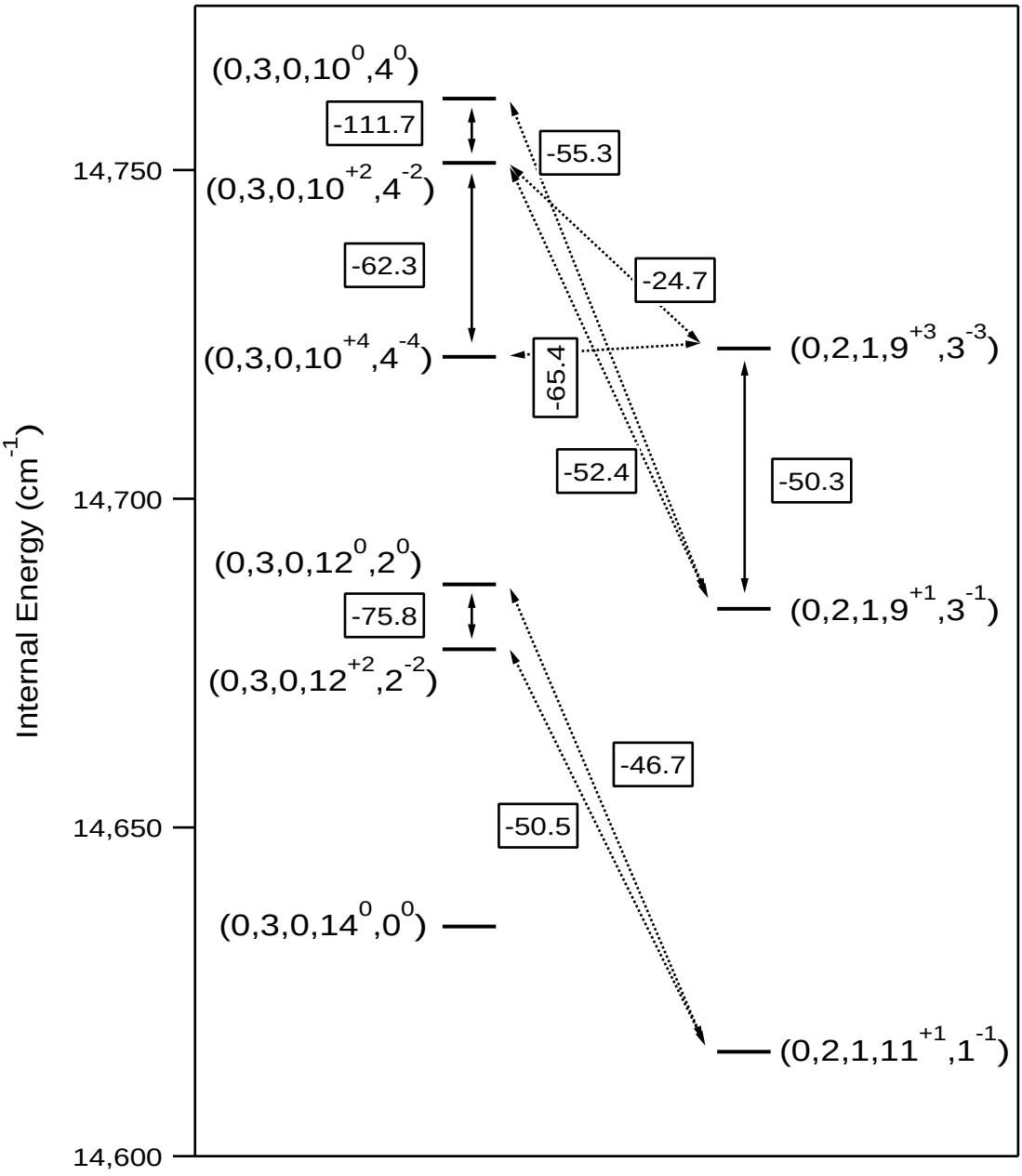

Figure 9-7: Zero-order energy diagram for the polyad ($N_s = 3$, $N_{\rm res} = 23$, $\ell = 0$). Only 9 of the 111 zero-order states in the polyad are included, but these states represent the most important IVR pathways that originate with the $(0, 3, 0, 14^0, 0^0)$ bright state. The arrows mark interactions (anharmonic resonances) between zero-order states, and the numbers in boxes are specific values of interaction matrix elements, in $\rm cm^{-1}$. The solid arrows indicate vibrational ℓ-resonance, and the dotted arrows indicate the (3,245) stretch-bend resonance. Darling-Dennison resonances are omitted, to reduce clutter, but couple states within the two columns.

Fig. 9-8. The prediagonalization, of course, eliminates all vibrational ℓ-resonance interactions from the diagram. However, the prediagonalization also has another effect, which is entirely nontrivial. Many of the (3,245) resonances that couple the two Darling-Dennison stacks become very nearly zero. In fact, only 3 of these matrix elements have numerical values greater than 1.0 cm^{-1}. By contrast, in the original normal mode basis set, there were a total of 6 nonzero (3,245) resonance matrix elements.

This simplification of the (3,245) couplings in the prediagonalized basis set provides insights into acetylene IVR that are not obvious in the normal mode basis set. The interference effect discussed in Section 9.4 is one example, but these insights are not limited to polyads with anomalously simple IVR. The IVR associated with the $(0,3,0,14^0,0^0)$ bright state is also easier to understand in the basis set in which vibrational ℓ-resonance has been prediagonalized. The observed fractionation pattern for the $(0,3,0,14^{0/2},0^0)$ bright state, depicted in the bottom panel of Fig. 9-9, appears to consist primarily of two peaks. The effective Hamiltonian model reproduces the pattern fairly well (middle panel), despite the fact that this bright state was not included in any fits of the model. The top panel of Fig. 9-9 reveals something remarkable. When the (3,245) resonance is excluded from the model, the predicted fractionation pattern *appears* to become more complicated! This is highly counterintuitive, and in fact, appearances are deceptive in this case. The fractionation in the middle panel, as judged by the dilution factor (see Section 6.4), is actually greater than that in the top panel. The fractionation only appears to be simpler in the middle panel because many small peaks (i.e., eigenstates with a few percent or less of bright state character) blend together near the baseline. When the (3,245) resonance is slowly turned on, it becomes clear that the states marked by the asterisks are virtually unchanged (other than shifting somewhat in energy), whereas the peaks marked by # gradually fractionate into a large number of very small peaks.

These observations are entirely consistent with the view of IVR that arises from Fig. 9-8. The most important IVR pathway for the $(0,3,0,14,0)$ bright state is the chain of Darling-Dennison resonances that connect it with $(0,3,0,12,2)$, $(0,3,0,10,4)$,

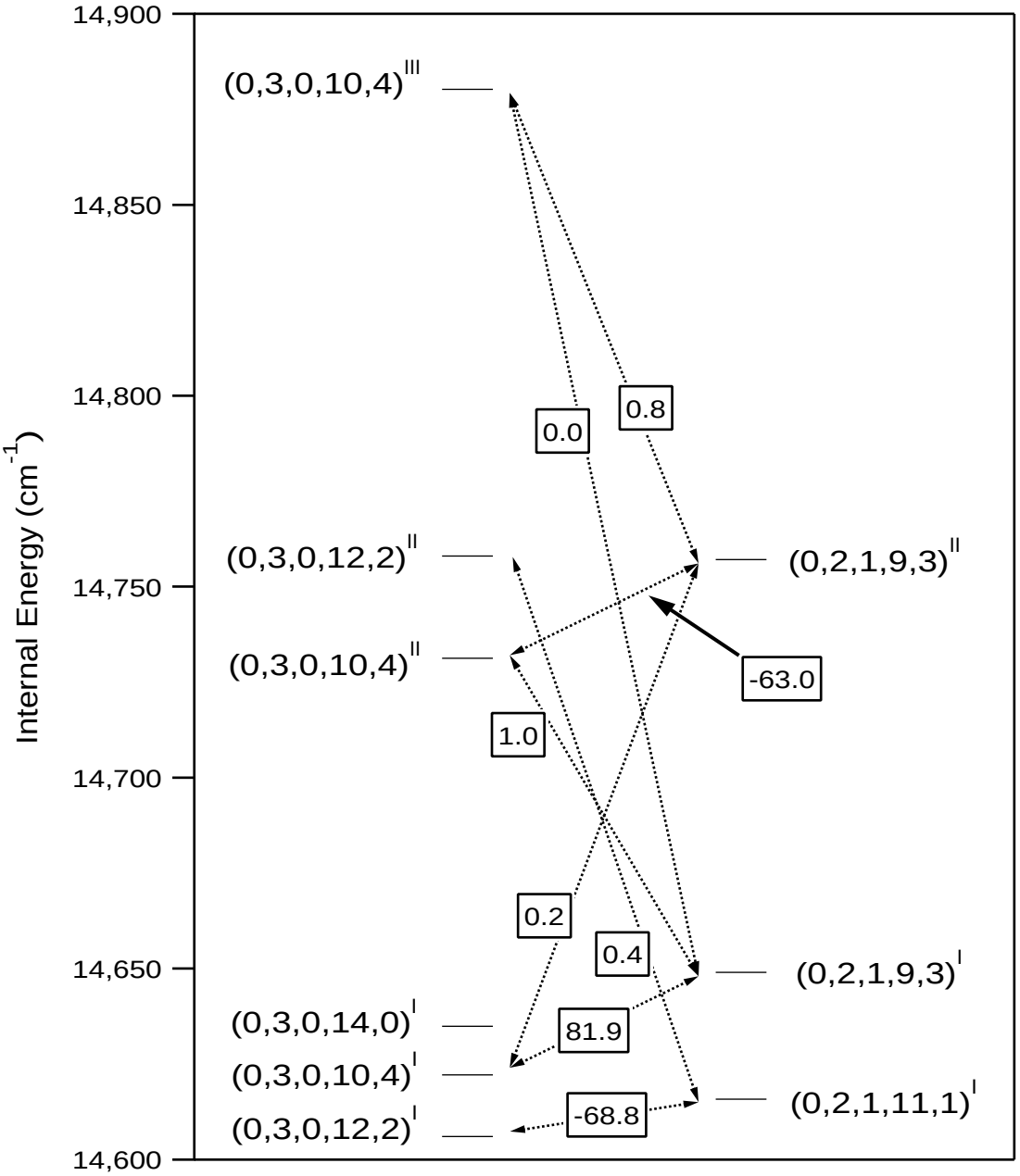

Figure 9-8: Zero-order energy diagram for the polyad ($N_s = 3$, $N_{\rm res} = 23$, $\ell = 0$), after the vibrational ℓ-resonance has been numerically prediagonalized. The ℓ_4 and ℓ_5 quantum numbers are meaningless after this transformation, and the states are labeled with Roman numerals that indicate rank within an ℓ-stack. The prediagonalization not only eliminates the vibrational ℓ-resonance from the diagram, but also modifies the (3,245) resonances such that many of the individual matrix elements become quite small and can be ignored. The states in the Darling-Dennison stack on the left, which contains the bright state, become divided into two sets—those that couple to the adjacent stack through (3,245), and those that do not.

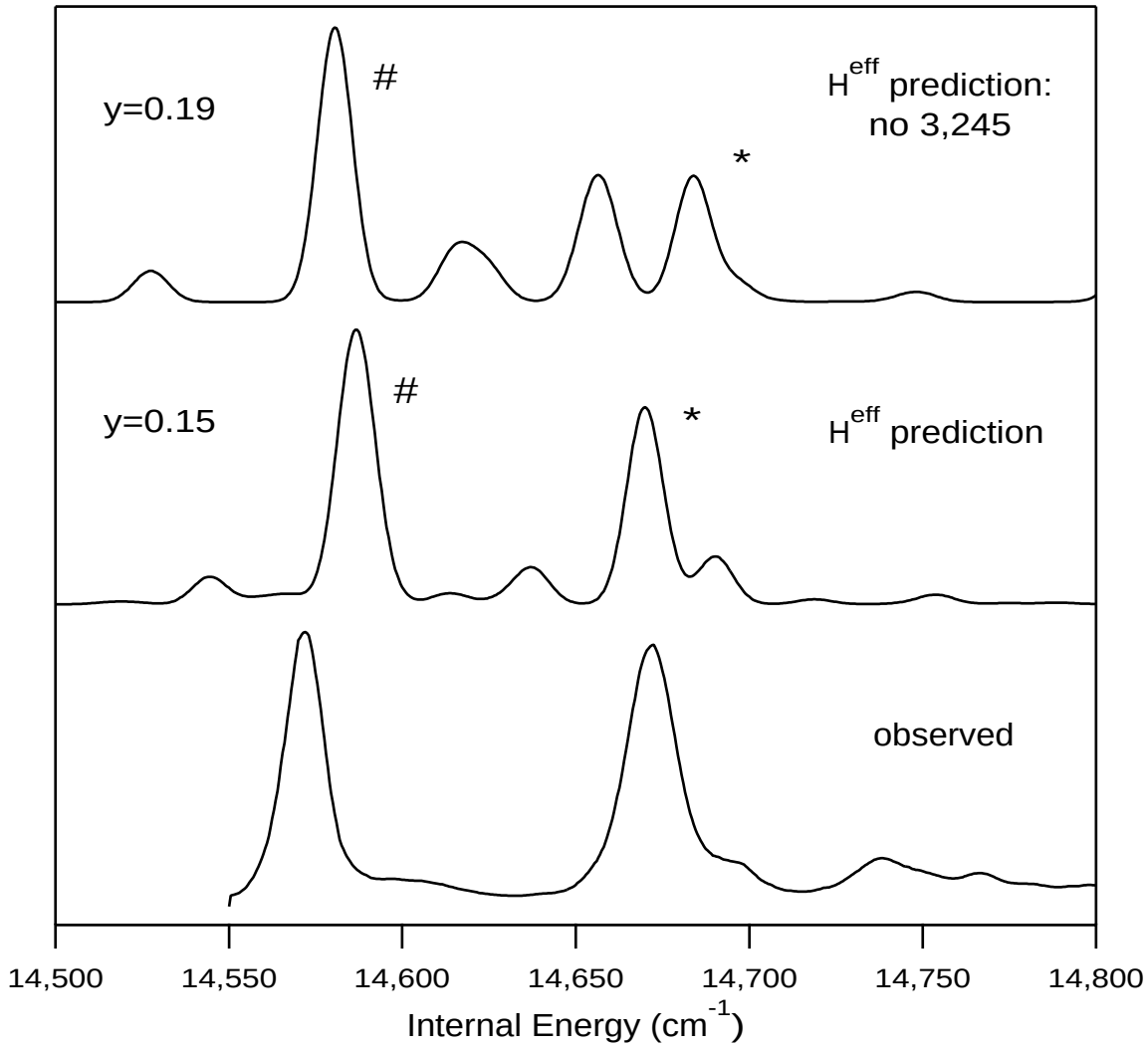

Figure 9-9: Example of the "interference" effect involving the (3,245) resonance in the ($N_s = 3$, $N_{\rm res} = 23$, $\ell = 0$) polyad. Bottom: The observed fractionation pattern for the $(0, 3, 0, 14^{0/2}, 0^0)$ bright state. Middle: The prediction of the $H^{\rm eff}$ model for the $(0, 3, 0, 14^0, 0^0)$ bright state fractionation pattern; the predicted pattern for the $\ell = 2$ bright state is similar. Top: Same as in the middle panel, except with all of the stretch-bend resonances "turned off".

etc. The (prediagonalized) states in this first Darling-Dennison stack belong to two classes: states that are "immune" to the (3,245) resonance, including $(0,3,0,12,2)^{\mathrm{II}}$ and $(0,3,0,10,4)^{\mathrm{III}}$, and states that are strongly affected by it (the remaining states). It can be envisioned that the peaks marked by asterisks are somehow associated with the former group, and the peaks marked by # with the latter group, and in fact this hypothesis can be verified by projecting the eigenstates of the effective Hamiltonian onto the prediagonalized basis set. For example, for the state on the right marked by the asterisk (middle panel), the three largest components of its projection onto the first Darling-Dennison stack consist of

$$|*\rangle \approx 0.46(0,3,0,14,0)^{\mathrm{I}} - 0.28(0,3,0,12,2)^{\mathrm{II}} - 0.39(0,3,0,10,4)^{\mathrm{III}}. \tag{9.28}$$

All three of these states are expected, on the basis of Fig. 9-8, to be minimally influenced by the (3,245) resonance. By contrast, the state near 14,650 cm^{-1} that is marked by a # (top panel) has the following composition (again, three largest components within the primary Darling-Dennison stack):

$$|\#\rangle \approx 0.36(0,3,0,14,0)^{\mathrm{I}} + 0.39(0,3,0,10,4)^{\mathrm{II}} - 0.29(0,3,0,8,6)^{\mathrm{III}}. \tag{9.29}$$

The $(0,3,0,8,6)^{\mathrm{III}}$ state is not depicted in Fig. 9-8 due to space constraints, but it, like $(0,3,0,10,4)^{\mathrm{II}}$, belongs to the class of prediagonalized states that are strongly perturbed through the (3,245) resonance.

Figure 9-10 provides a time domain perspective on the IVR associated with the $(0,3,0,14,0)$ bright state. The survival probability (see Section 6.3) undergoes a fast early-time decay ($\sim$100 fs 1/e time) followed by a series of regular partial recurrences, which reach nearly 50%. This behavior can also be rationalized in terms of Fig. 9-8. As the excitation leaves the bright state and delocalizes into the primary Darling-Dennison stack, some fraction of the excitation (roughly half) is quickly randomized into all of the modes of the molecule, with the (3,245) resonance acting as the facilitator of the fast and irreversible component of the IVR. Much of the remaining excitation becomes "trapped" in those states in the primary Darling-Dennison

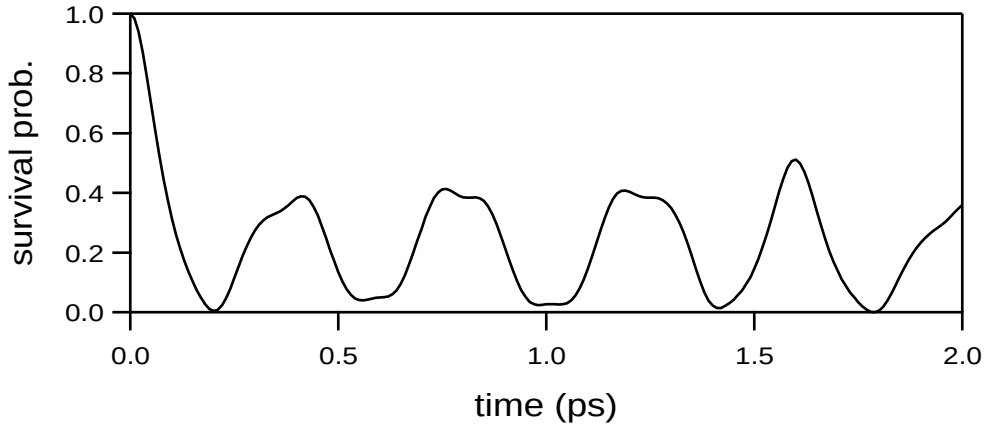

Figure 9-10: Survival probability of the $(0,3,0,14^0,0^0)$ bright state as predicted by the effective Hamiltonian. The fast early-time decay is followed by a regular series of partial recurrences.

stack that are uncoupled from (3,245), accounting for the regular series of partial recurrences.

This is an intriguing type of IVR that is not encountered elsewhere in this thesis, and I wish to make a few speculative remarks regarding its significance. Although it is easiest to discuss the IVR using a state space framework, one can also visualize the IVR associated with $(0,3,0,14,0)$ using a wavepacket picture. Roughly half of the wavepacket would quickly and irreversibly fragment and explore large regions of phase space (to use a semiclassical term), while the other half would remain trapped in a relatively small region of phase space. The portion of the excitation that remains trapped, on a timescale of several picoseconds, will certainly be associated with a stable classical motion of the molecule, while the irreversible component of the IVR would likely be associated with chaotic regions of phase space. This hypothesis can be directly tested using the semiclassical methods of Chapter 8, but the number of dimensions involved poses technical challenges.

At this point, it has been established that the interference effect involving the (3,245) resonance that was discussed in Section 9.4 also has important implications for bright states that do not display anomalously simple IVR, using the case of $(0,3,0,14^0,0^0)$ as an example. In both Section 9.4 and here, it has been emphasized that the interference effects observed are "nearly" perfect, meaning that when

the vibrational ℓ-resonance is prediagonalized, certain (3,245) matrix elements become very nearly, but not precisely zero. I now demonstrate that it is possible to define a new basis set which has two remarkable properties:

1. In this new basis set, the values of (roughly) half of the (3,245) matrix elements become *precisely* zero.

2. The new basis set is related to the normal mode basis set by an *analytical* transformation.

Before defining this new basis set, I note first that the "prediagonalization" of the vibrational ℓ-resonance that is discussed above is equivalent mathematically to performing a unitary transformation on the normal mode basis set, in which the unitary matrix is defined by the eigenvectors of the Hamiltonian

$$\hat{H} = \hat{a}_{4d}\hat{a}^{\dagger}_{4g}\hat{a}^{\dagger}_{5d}\hat{a}_{5g} + \text{c.c.} \; . \tag{9.30}$$

This is the vibrational ℓ-resonance written in terms of raising and lowering operators for the bend modes of acetylene; see Section 7.2 for an explanation of the notation. It has already been established that, by applying the unitary transformation defined by the eigenvectors of this Hamiltonian, certain (3,245) matrix elements become very nearly zero. But is there a unitary transformation that would make certain (3,245) matrix elements become exactly zero? The remarkable answer, which I discovered serendipitously, is that such a unitary transformation does exist, and it is defined by the eigenvectors of the Hamiltonian

$$\hat{H} = \frac{\hat{\ell}_4\hat{\ell}_5}{2} + \hat{a}_{4d}\hat{a}^{\dagger}_{4g}\hat{a}^{\dagger}_{5d}\hat{a}_{5g} + \text{c.c.} \tag{9.31}$$

This is simply the vibrational ℓ-resonance plus a diagonal term, which is usually associated with the constant g_{45}. Here, g_{45} and r_{45}, the constant generally used to describe the strength of the vibrational ℓ-resonance, are constrained according to $g_{45} = r_{45}/2$.

What is even more remarkable (to me at least) is that this unitary transformation can also be generated analytically, and is in fact formally equivalent to the Clebsch-Gordan coefficients for transforming between coupled and uncoupled representations. To see this, I first demonstrate that the Hamiltonian in Eq. 9.31 is equivalent to a Hamiltonian that represents angular momentum coupling. Let us define for the bend degrees of freedom of acetylene a (pseudo)-angular momentum basis set $|j_4, m_4, j_5, m_5\rangle$ which has a one-to-one correspondence with the traditional normal mode basis set $|v_4^{\ell_4}, v_5^{\ell_5}\rangle$ according to

$$j_4 = v_4/2 \tag{9.32}$$

$$j_5 = v_5/2 \tag{9.33}$$

$$m_4 = \ell_4/2 \tag{9.34}$$

$$m_5 = \ell_5/2 \ . \tag{9.35}$$

Now, consider the Hamiltonian

$$\hat{H} = \vec{J}_4 \cdot \vec{J}_5. \tag{9.36}$$

Introducing the usual angular momentum ladder operators, this Hamiltonian is equivalent to

$$\hat{H} = \frac{1}{2}(J_{4+}J_{5-} + J_{4-}J_{5+}) + J_{4z}J_{5z}. \tag{9.37}$$

The $J_{4z}J_{5z}$ term generates diagonal matrix elements

$$\langle j_4, m_4, j_5, m_5|J_{4z}J_{5z}|j_4, m_4, j_5, m_5\rangle = m_4 m_5. \tag{9.38}$$

Transforming to the conventional normal mode basis set,

$$\langle v_4^{\ell_4}, v_5^{\ell_5}|J_{4z}J_{5z}|v_4^{\ell_4}, v_5^{\ell_5}\rangle = \frac{1}{4}\ell_4\ell_5 \ ; \tag{9.39}$$

thus $J_{4z}J_{5z}$ is equivalent to the g_{45} term in the normal mode basis. The $(J_{4+}J_{5-} +$

$J_{4-}J_{5+}$) term generates off-diagonal matrix elements

$$\langle j_4, m_4, j_5, m_5|(J_{4+}J_{5-} + J_{4-}J_{5+})|j_4, (m_4 \pm 1), j_5, (m_5 \mp 1)\rangle = \\ [(j_4 \mp m_4)(j_4 \pm m_4 + 1)(j_5 \pm m_5)(j_5 \mp m_5 + 1)]^{1/2} \tag{9.40}$$

which in the normal mode basis set becomes

$$\langle v_4^{\ell_4}, v_5^{\ell_5}|(J_{4+}J_{5-} + J_{4-}J_{5+})|v_4^{\ell_4}, v_5^{\ell_5}\rangle = \\ \frac{1}{4}\left[(v_4 \mp \ell_4)(v_4 \pm \ell_4 + 1)(v_5 \pm \ell_5)(v_5 \mp \ell_5 + 1)\right]^{1/2}. \tag{9.41}$$

These matrix elements are identical to those for the vibrational ℓ-resonance (see, for example, Ref. [5], or Chapter 7).

Thus, it should be clear that the Hamiltonian in Eq. 9.31 is exactly equivalent to an angular momentum coupling term such as $\vec{J}_4 \cdot \vec{J}_5$; the operators specifically transform as

$$J_z \quad \Leftrightarrow \quad a_d^\dagger a_d - a_g^\dagger a_g = \ell \tag{9.42}$$

$$J_+ \quad \Leftrightarrow \quad a_d^\dagger a_g \tag{9.43}$$

$$J_- \quad \Leftrightarrow \quad a_d a_g^\dagger. \tag{9.44}$$

The angular momentum coupling term $\vec{J}_4 \cdot \vec{J}_5$ is, of course, diagonal in the basis $|j_4, j_5, J, M\rangle$, where J and M are the total angular momentum and its projection. Specifically,

$$\vec{J}_4 \cdot \vec{J}_5 = \frac{1}{2}(J^2 - J_4^2 - J_5^2) \tag{9.45}$$

and

$$\langle j_4, j_5, J, M|\vec{J}_4 \cdot \vec{J}_5|j_4, j_5, J, M\rangle = \frac{1}{2}[J(J+1) - j_4(j_4+1) - j_5(j_5+1)]. \tag{9.46}$$

Recall that $j_4 = v_4/2$ and $j_5 = v_5/2$. The quantum number M is defined by

$$M = m_4 + m_5 = \frac{1}{2}(\ell_4 + \ell_5) = \frac{\ell}{2}, \tag{9.47}$$

and is thus equivalent to the total angular momentum polyad number ℓ (other than a factor of 2), which is conserved by the effective Hamiltonian, but J is a new, nonconserved quantum number, which corresponds roughly to the "rank" within an ℓ-stack that was used in Fig. 9-8.

The transformation between the $|j_4, m_4, j_5, m_5\rangle$ and $|j_4, j_5, J, M\rangle$ basis sets is defined by the Clebsch-Gordan coefficients [173]. Thus, it is possible to define a new bending basis set for acetylene, $|v_4, v_5, J\rangle$, by applying an analytical unitary transformation, using the appropriate Clebsch-Gordan coefficients, to the usual normal mode basis $|v_4^{\ell_4}, v_5^{\ell_5}\rangle$. The $|v_4, v_5, J\rangle$ basis set is nearly identical to the basis set in Fig. 9-8, in which the vibrational ℓ-resonance was prediagonalized, but with two key differences. First, the transformation from $|v_4^{\ell_4}, v_5^{\ell_5}\rangle$ to $|v_4, v_5, J\rangle$ is analytical, while the prediagonalized basis set could only be defined by a numerical unitary transformation. Second, as can be seen in Fig. 9-11, in the $|v_4, v_5, J\rangle$ basis set many of the (3,245) matrix elements are *precisely* zero, whereas in the prediagonalized basis set they were only *nearly* zero. In fact, among the states included in Fig. 9-11, the only strong resonance couplings that remain in the $|v_4, v_5, J\rangle$ basis set are the (modified) Darling-Dennison resonances that couple states within a column, and three (3,245) resonances. This simplification of the resonance couplings makes the $|v_4, v_5, J\rangle$ basis set exceptionally useful for understanding the dynamics associated with the $(0, 3, 0, 14^0, 0^0)$ bright state, and many others.[3]

It should be emphasized that the above discussion of the formal equivalence of vibrational ℓ-resonance with angular momentum coupling is implicit in algebraic theory

[3]In Chapter 7, a local mode basis set is defined for the acetylene bend degrees of freedom. This basis set is demonstrated to be very useful for describing the pure bending dynamics of acetylene above ∼10,000 cm^{-1}. The $|v_4, v_5, J\rangle$ basis set introduced here is useful primarily at lower levels of bend excitation (<16 quanta), and because of the simplification of the (3,245) resonance structure, is particularly useful for polyads with nonzero stretch excitation. The conventional normal mode basis set only provides a good zero-order representation in the limit of very low bend excitation.

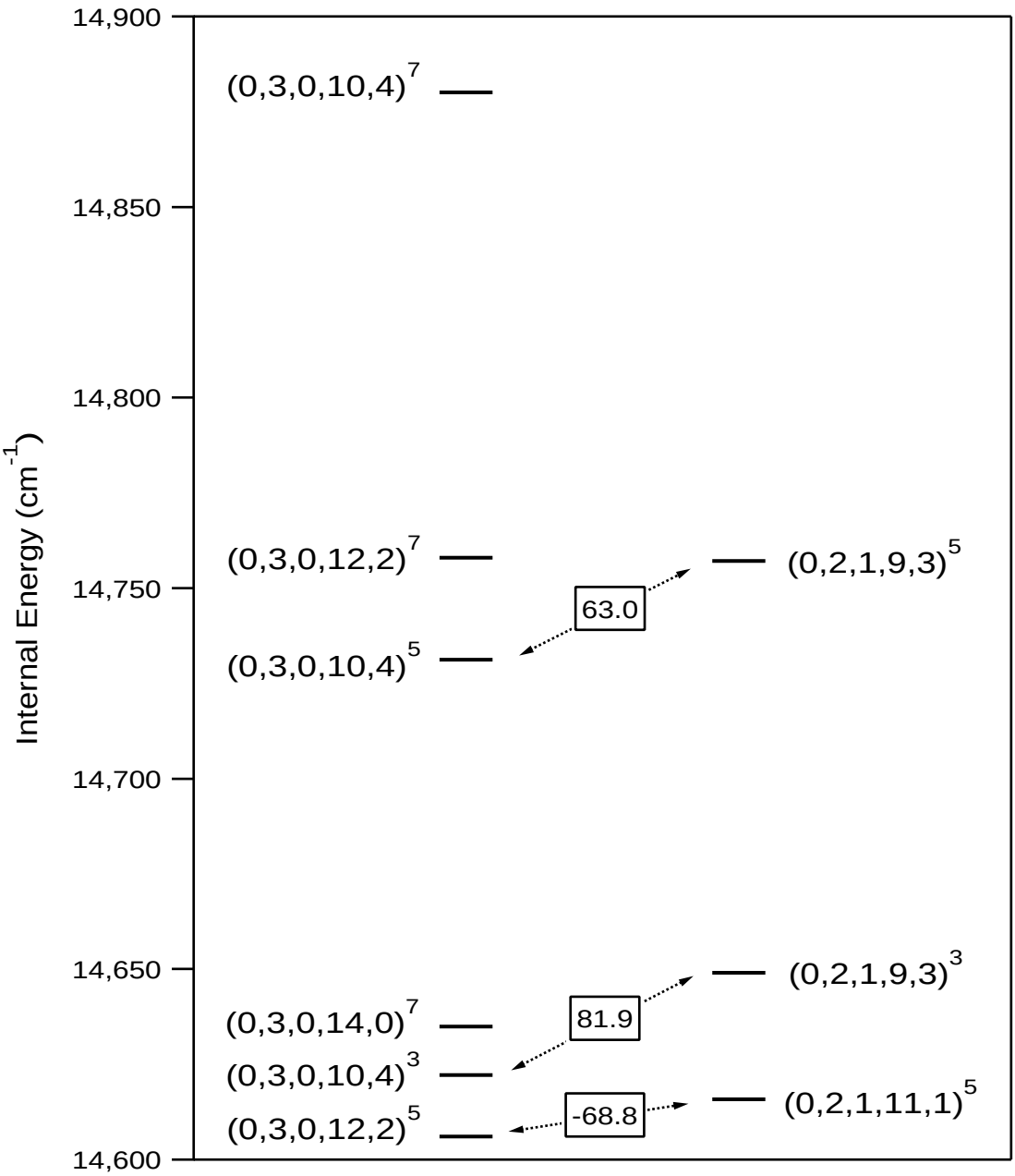

Figure 9-11: Zero-order energy diagram for the polyad ($N_s = 3$, $N_{\rm res} = 23$, $\ell = 0$), in the $(v_1, v_2, v_3, v_4, v_5)^J$ basis set. Only three (3,245) matrix elements are nonzero.

[118] treatments of acetylene and other linear molecules. Specifically, it is equivalent to treating each (bending) two-dimensional oscillator using the $U(3)$ Lie algebra [174]. It is my hope that algebraic theory will provide deeper insight into the intriguing but mysterious simplification of the (3,245) resonance structure in the $|v_4, v_5, J\rangle$ basis.

Chapter 10

Ongoing Work

This chapter summarizes ongoing work on the unimolecular dynamics of acetylene that has not yet been published. In the preceding chapters, a detailed and essentially complete understanding of the short-time ($\sim$1 ps) unimolecular dynamics of acetylene below 15,000 cm^{-1} has been developed. Thus, much of the ongoing work discussed here is concerned with understanding the vibrational dynamics of acetylene above the isomerization barrier. The work in Section 10.4 represents a collaboration with Michelle Silva, who will continue the work on $^{13}C_2H_2$; Richard Duan also contributed substantially to this work.

10.1 Identity of the "Extra Patterns"

In Chapter 5, pattern recognition algorithms based upon the XCC (Chapter 2) were utilized to extract fractionated bright state patterns from the $^{12}C_2H_2$ DF data set. However, this procedure also identified an unexpected series of patterns that could not be accounted for by the expected bright states. In Section 5.6, several experimental studies of these "extra" patterns are described. Although these studies failed to identify the origin of the unexpected patterns, they did confirm that the unexpected patterns do not arise from emission from the single rovibrational levels in the S_1 state that are populated by the laser in the DF studies. Since the unexpected features in the DF spectra could be identified as patterns and extracted, they posed no serious difficulties for the analysis of vibrational dynamics/structure in $^{12}C_2H_2$.

I have recently performed a new series of experiments that has identified of the origin of the extra patterns. In Fig. 10-1 are depicted small sections of a dispersed emission spectrum recorded using the $Q(1)$ rotational line of the $V_0^2K_0^1$ band. The top panel shows the results of a pressure study. The relative intensities of several small peaks in the dispersed emission spectrum were determined to be dependent on pressure. These peaks are marked by arrows and correspond to the unexpected patterns that were identified previously by pattern recognition. The pressure dependence of these features suggests that collisional energy transfer plays a role in their origin. Additional evidence for this hypothesis is presented in the bottom panel of Fig. 10-1.

The amplitude of the extra patterns depends also on the time window (relative to the laser pulse passing through the sample cell) used to record the spectra. The DF spectra in Section 5 were recorded using a 1.5 μs gate, which permitted the entire fluorescence decay of acetylene to be recorded. Here, it is clear that the amplitudes of the unexpected patterns are *relatively* larger at later times. Our ICCD system is not capable of using gate widths much smaller than those depicted here, so other experiments will be needed to obtain precise kinetic information. However, this study is certainly consistent with the hypothesis that the extra patterns arise from some species created through collisions.

To identify the mechanism for the appearance of the unexpected patterns, it is quite helpful to first separate them from the expected patterns, which can be accomplished using the XCC pattern recognition technique. This task has already been largely accomplished in Chapter 5, by extracting the patterns from a data set of five DF spectra recorded using different vibrational bands. A more straightforward approach is illustrated here, in which no attempt is made to identify individual bright state fractionation patterns, but only to extract all of the unexpected features from the spectra. The assumption underlying this approach is that the amplitude of *all* of the extra patterns varies in the same way with pressure. Thus, the XCC can be applied to the 2 spectra in the top panel of Fig. 10-1 (plus an additional spectrum recorded at 1.00 Torr) to identify all of the unexpected features as a single pattern; all of the expected fractionated bright state patterns will of course also be identified as a second pattern.

The results of this application of the XCC/linear inversion technique (see Chapter 2) are depicted in Figs. 10-2 and 10-3. As expected, all of the features in the "main" pattern can be identified as fractionated bright state patterns.[1] The features observed in Fig. 10-3 are intriguing because they tend to appear as doublets with a spacing of $\sim$56 cm^{-1}. This energy happens to be nearly equal to the splitting between the

[1]It is my recommendation that in the future all dispersed fluorescence spectra be recorded at two pressures or with two different time windows (gates). The XCC can then be used to pre-process the spectra and remove any spectral features due to species created through collisions, as has been done in Fig. 10-2.

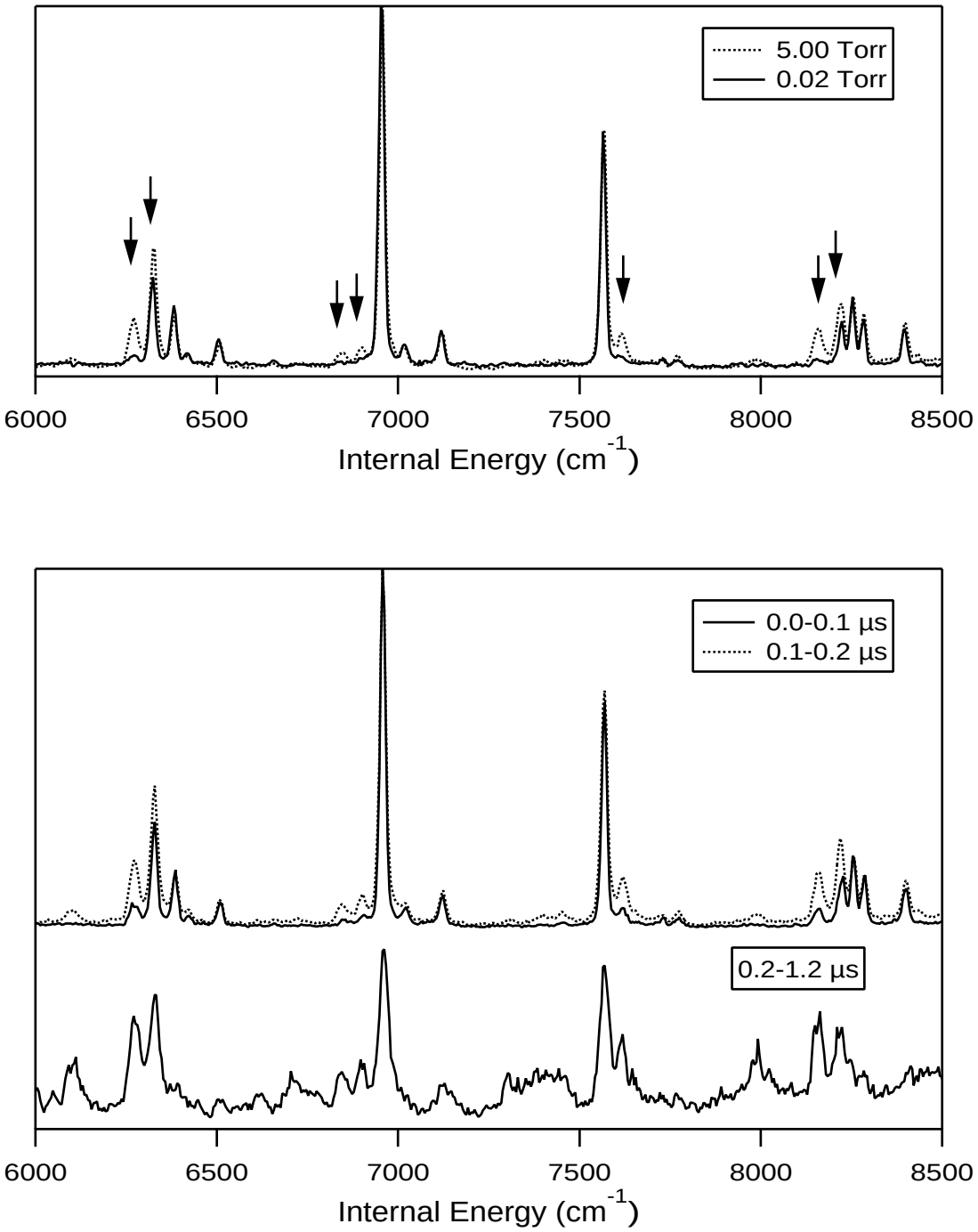

Figure 10-1: Dispersed emission that results from PUMPing the $Q(1)$ rotational line of the $V_0^2 K_0^1$ band, at varying pressure (top) and at varying time windows following the laser pulse (bottom). The two spectra in the top panel, as well as two of the three in the lower panel, are normalized to the intensity of the tallest peak. The arrows point to features whose intensities change as a function of pressure and gate position; these are the extra patterns discussed in Section 5.6.

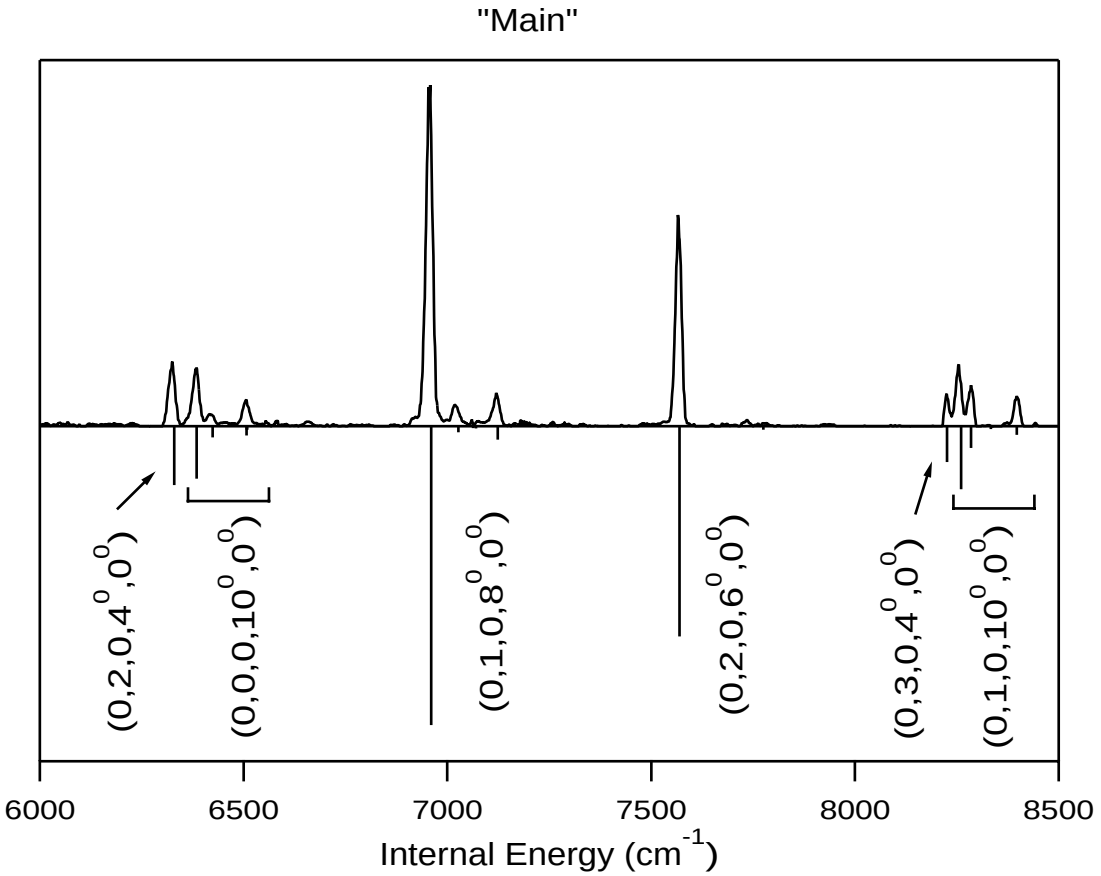

Figure 10-2: The expected bright state fractionation patterns, extracted from the spectra in the top panel of Fig. 10-1 using the XCC pattern recognition technique. The features in this pattern can be accounted for by emission from $K'_a = 1$ intermediate states to $(0, v_2, 0, v_4^{0/2}, 0^0)$ bright states with v_4=even. Only the predicted $\ell_4 = 0$ patterns are depicted; the $\ell_4 = 2$ patterns are nearly identical.

$K'_a = 0$ and 2 subbands of the $2v'_3$ vibrational level in the $^{12}C_2H_2$ S_1 state. No $K'_a = 0$ or 2 levels are populated by the laser; with $\sim$0.05 cm^{-1} resolution, it is possible to populate only the $(J' = 1, K'_a = 1)$ level. However, $K'_a = 0$ and 2 levels could be populated through collisions of $K'_a = 1$ molecules with molecules in the ground electronic state.

This hypothesis for the origin of the unexpected patterns can be tested numerically using the effective Hamiltonian developed in Chapters 6 and 9. The $K'_a - \ell'' = \pm 1$ propensity rule implies that only states with odd ℓ'' will be observed in emission from $K'_a = 0$ or 2 levels. In Chapter 5, the Franck-Condon principle is used to demonstrate

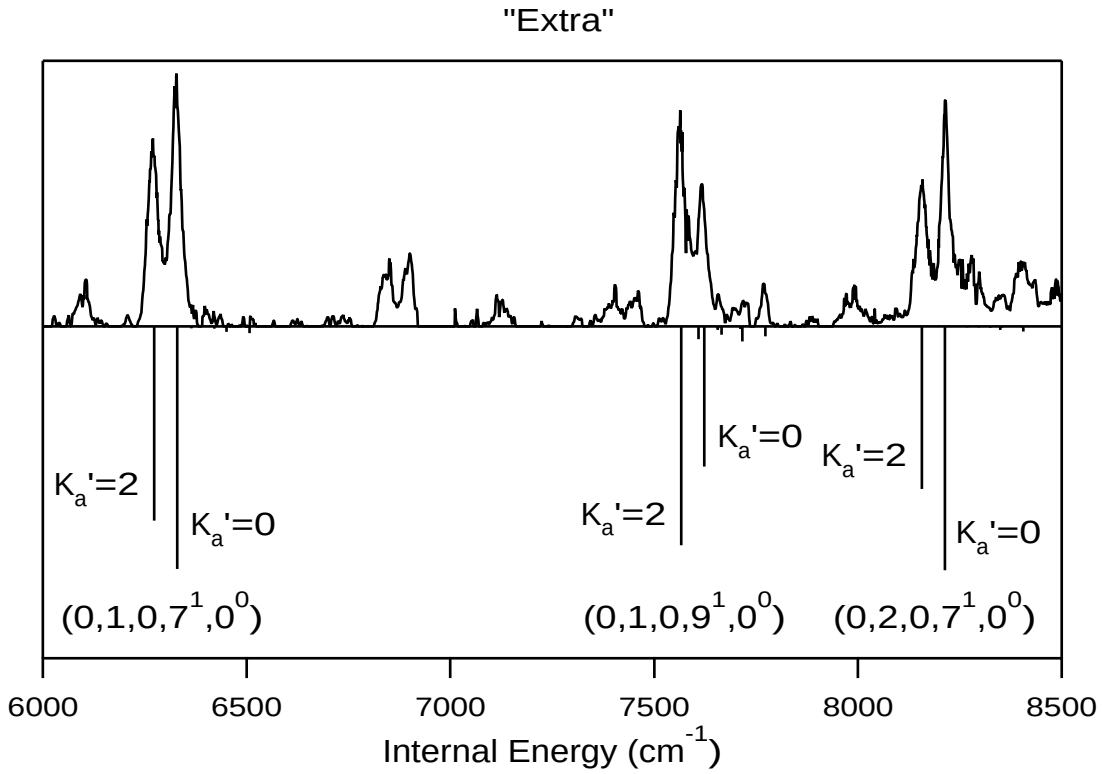

Figure 10-3: The unexpected DF features, extracted as a pattern from the spectra in the top panel of Fig. 10-1 using the XCC pattern recognition technique. The most intense features in this pattern can be accounted for by emission from $K'_a = 0$ or 2 intermediate states to $(0, v_2, 0, v_4^{\ell_4}, 0^0)$ bright states with v_4=odd. Only the predicted $\ell_4 = 1$ patterns are depicted; the $\ell_4 = 3$ patterns are nearly identical.

that only zero-order states of the form $(0, v_2, 0, v_4^{\ell_4}, 0^0)$ are bright in emission from the S_1 state of acetylene. Thus, $\ell_4 = \ell''$, and if ℓ'' is odd, v_4 must be odd also. Both $K'_a = 0$ and $K'_a = 2$ levels can emit to $\ell'' = 1$ levels; $K'_a = 2$ levels can also emit to $\ell'' = 3$ levels, but these levels will tend to be nearly degenerate with the corresponding $\ell'' = 1$ levels, for the same reason that $\ell'' = 0$ and $\ell'' = 2$ levels cluster together (see Section 5.2 and Ref. [69]). The emission from a pair of $K'_a = 0$ and $K'_a = 2$ levels to the same $\ell'' = 1$ state, however, will not be observed at the same frequency in emission due to the difference in term values between $K'_a = 0$ and $K'_a = 2$, which is $4A' \approx 56$ cm^{-1}. The negative-going sticks in Fig. 10-3 represent the predicted positions of the odd v_4 bright state fractionation patterns in the DF spectrum, from both $K'_a = 0$ and $K'_a = 2$ levels (assuming minimal change in J'). It is clear that the K'_a-changing collisions can account for all of the most intense "unexpected" features in the spectrum.

Thus, in most of the acetylene DF spectra that our group had recorded up to this point, we had been unintentionally been performing studies of K-changing intermolecular energy transfer in acetylene, akin to the many performed for formaldehyde (see, for example, Refs. [175, 176]). Our group is now investigating these energy transfer processes deliberately; Richard Duan has initiated experiments to determine a kinetic model for the energy transfer. Acetylene provides an interesting system to study this type of energy transfer, because the odd and even K'_a levels emit to entirely distinct bright states/polyads (even v''_4 bright states from odd K'_a, and odd v''_4 bright states from even K'_a). The relatively large separation between the emission features originating from even and odd K'_a will make the study of collisional energy transfer in this system relatively simple. Another intriguing aspect of the collisional energy transfer is its highly nonlinear dependence on pressure. The two spectra in the top panel of Fig. 10-1 were recorded using pressures differing by a factor of 250, but the amplitude of the features arising from $K'_a = 0$ or 2 varies only by a factor of $\sim$7.

10.2 New Dispersed Fluorescence Methodologies

The methodology that we utilize to record dispersed fluorescence spectra continues to evolve as we strive to obtain the best quality spectra possible (frequency calibration, intensity calibration, signal-to-noise). The spectra that are discussed in Sections 10.3 and 10.4 were recorded and processed using somewhat different techniques than those presented in Chapter 5, and the most significant improvements are discussed here.

The first improvement, primarily as a time-saving measure, is an automated means of removing "cosmic rays" from spectra. Because gamma rays from the sun can be detected by our ICCD detector, every spectrum is always recorded twice; it is unlikely that a gamma ray will strike the same pixels on the detector during two separate accumulations of signal. Under the conditions that are typically used to record spectra, 0–10 spurious peaks are observed in any one spectrum. It is not difficult to remove these spurious peaks from the spectrum manually, by comparing the two spectra recorded under the same conditions and noting discrepancies between the two.

This process is tedious, however, and I have devised an automated algorithm for removing the spurious peaks. Figure 10-4 illustrates the use of this technique with two sample spectra. Plotting a recursion map (see Chapter 2) for the two spectra (bottom left panel) reveals the presence of spurious peaks in the two spectra as "outliers". That is, since the two spectra were recorded under nearly identical conditions, most of the points on the recursion map cluster closely near the line $I_1 = I_2$. Note that the slope of this line is not precisely 1.0 because the laser power varies slightly for each spectrum. In this case, the laser power was slightly higher during the recording of spectrum 1. The presence of a spurious peak in spectrum 1 (such as the one marked by the letter B) is marked on the recursion map by points that lie above the line $I_1 = I_2$; spurious peaks in spectrum 2 (such as "A") give rise to points below that line.

The outliers can be identified numerically and automatically in the following way. The first step is to determine the precise slope of the line of points in the recursion

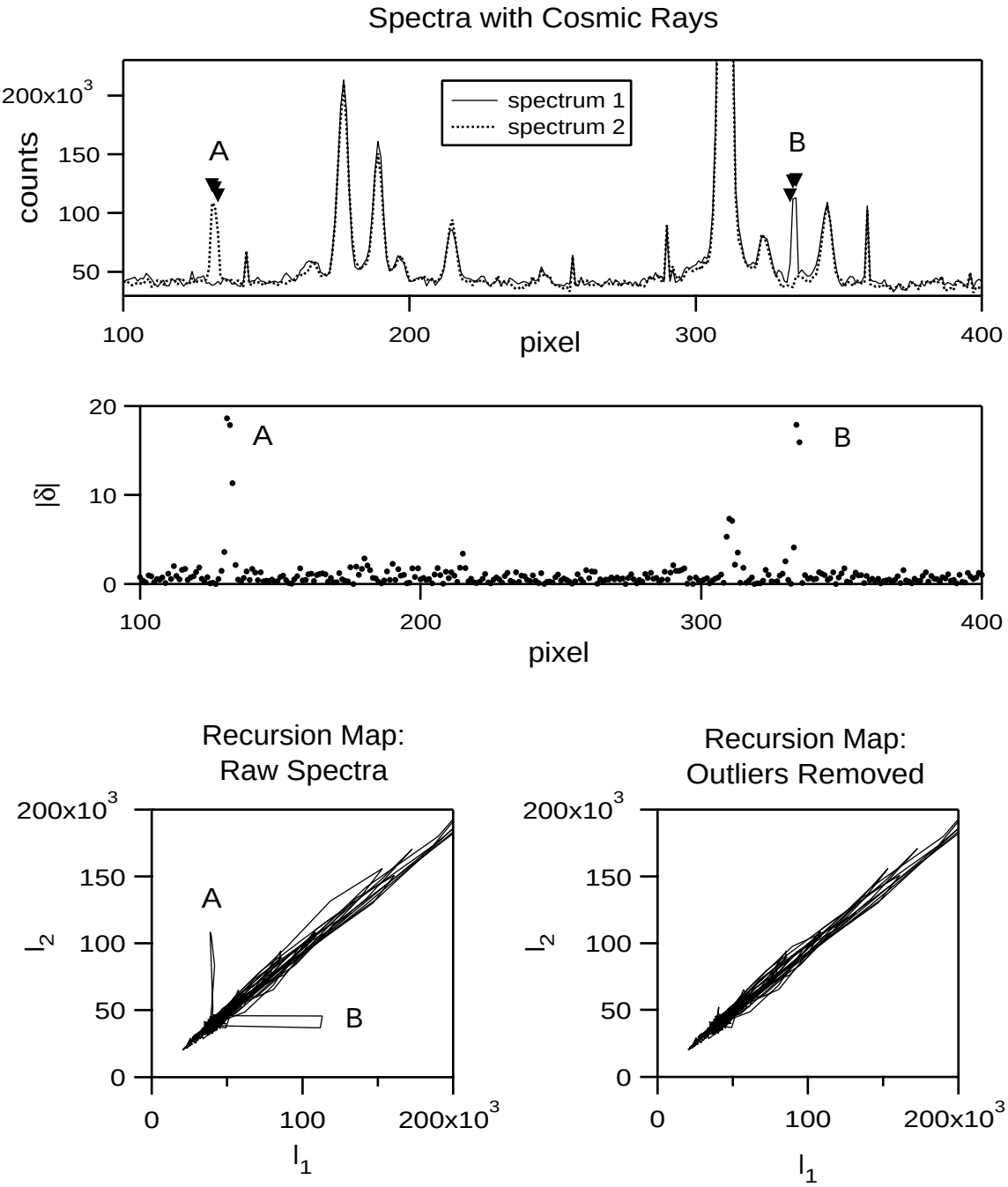

Figure 10-4: Top: Two sample spectra recorded under nearly identical conditions. Spurious peaks due to cosmic rays can be observed in each spectrum. These spurious peaks are particularly obvious in the recursion map representation of the data (lower left). They can be removed by applying a cutoff to $|\delta|$, the absolute weighted deviation from a fit line determined by XCC. The recursion map after removal of the spurious peaks is shown in the lower right panel.

map. Least-squares fitting would not be a good choice, since the presence of outliers due to spurious peaks will skew the fit results. A robust estimator is a better choice, and in fact the XCC (Chapter 2) is ideal. Having determined the best-fit slope (ratio direction) using the XCC, the outliers can then be identified by their distance from the fit line. More specifically, one can choose a cutoff for the absolute value of the weighted residuals $|\delta|$:

$$\delta = \frac{I_{\text{obs}} - I_{\text{calc}}}{\sigma} \tag{10.1}$$

where σ is the estimated measurement error (experimental noise). Here a cutoff of $|\delta| = 5$ was used, which insures that there is an exceptionally small chance of labeling a real peak as "spurious". Having isolated the spurious peaks, it is then trivial to remove them by changing the intensity in the relevant spectrum such that $\delta = 0$ for the affected points.

A second, more significant improvement to the dispersed fluorescence methodology is a doubling of the number of individual spectral segments recorded. At any grating angle of the monochromator, the dispersed fluorescence of the molecule can be recorded over a range of wavelengths which spans several nm (10–20 nm, depending on which monochromator and grating order are used). Previously, we would record the dispersed fluorescence at one grating angle, and then change the angle such that the next segment would overlap minimally with the previous one. This procedure permits the quickest possible recording of a spectrum. However, intensity calibration of the resultant spectra can be somewhat problematic. In order to compare the intensities of the peaks in adjacent segments, one needs to normalize for fluctuations in the laser power. This was accomplished previously by monitoring the integrated fluorescence signal out a side window of the DF cell using a PMT. These measurements required great care in order to be reproducible.

Intensity calibration of the spectra is much simpler if twice as many DF segments are recorded for each spectrum. That is, instead of choosing the grating angles for adjacent segments to create minimal overlap between the wavelength ranges covered, one can choose to overlap the adjacent segments significantly, as with the two segments

depicted in the top panel of Fig. 10-5. Intensity calibration between adjacent segments is then trivial. Once the segments are frequency calibrated, a recursion map can be constructed for those portions of the segments that overlap. The slope of the line in the recursion map reveals the relative intensities of the laser between segments (as well as any other changes that could result in different signal levels). These particular segments were chosen because the signal levels vary significantly between the segments; in general the slope on the recursion map is closer to one. Least-squares fitting can be used to find the proper scaling coefficient for the two spectra, as long as all cosmic rays have already been removed (otherwise XCC would be a better choice). Note that an error estimate can be obtained for the scaling coefficient (i.e., from the covariance matrix of the least-squares fit), which can be propagated to estimate the global error in the intensity calibration.

It is particularly convenient to choose the grating angles such that each segment overlaps with half of each adjacent segment, as in the top panel of Fig. 10-6. In addition to providing excellent intensity calibration, this arrangement permits an increase in signal-to-noise, since the emission at each wavelength is recorded twice and can be averaged. In addition, since each segment is frequency calibrated independently, it is possible to obtain an accurate estimate of the frequency calibration error, and gross errors can be identified and eliminated. Note that in general, one must choose the segments to overlap each other by slightly more than half in order to have a margin of safety. Any "excess" spectrum can be discarded (the "X's" in the top panel of Fig. 10-6).

10.3 Dispersed Fluorescence of $^{12}C_2H_2$ above the Isomerization Barrier

The pattern recognition analysis of the DF data set in Chapter 5 was terminated at 15,000 cm^{-1} of vibrational energy. Although bright state fractionation patterns could be identified above this energy in the data set, both by eye and with numerical pattern recognition algorithms, the extreme congestion at such high internal energy

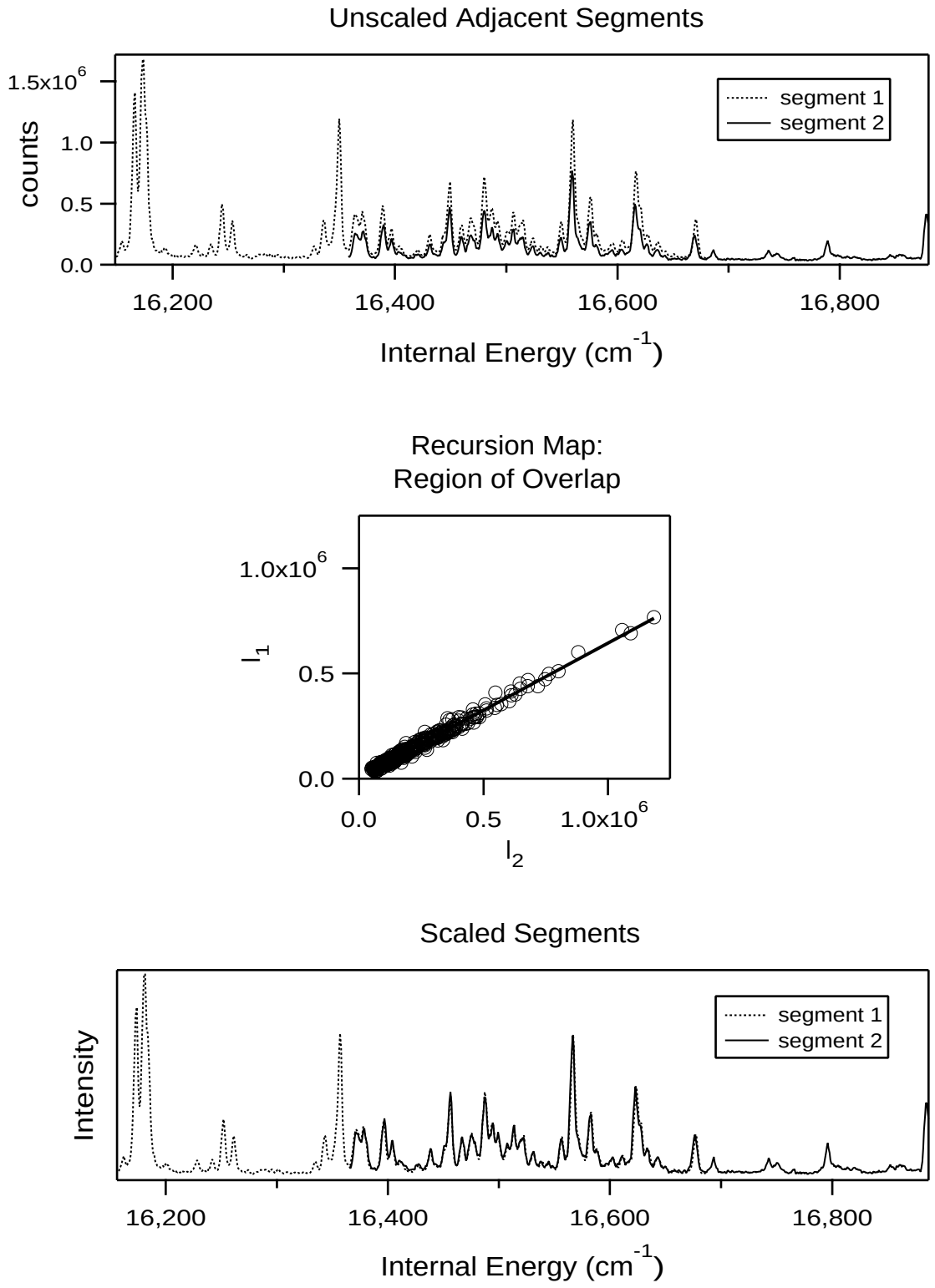

Figure 10-5: Top: Two adjacent DF spectra with substantial overlap. Middle: Recursion map of the overlap region between the two segments. Bottom: The two segments scaled properly, using the slope of the line on the recursion map.

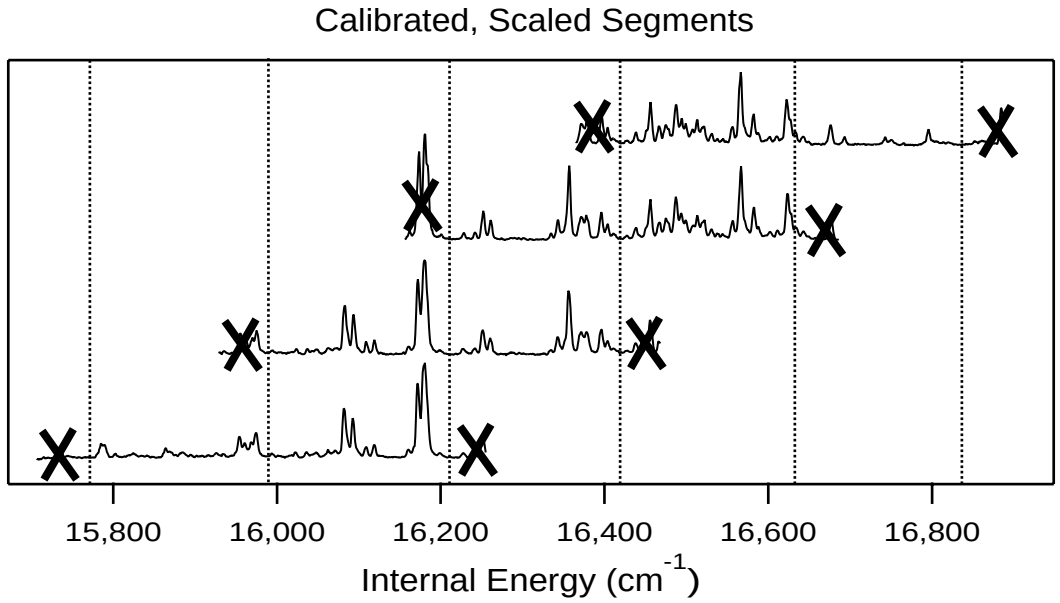

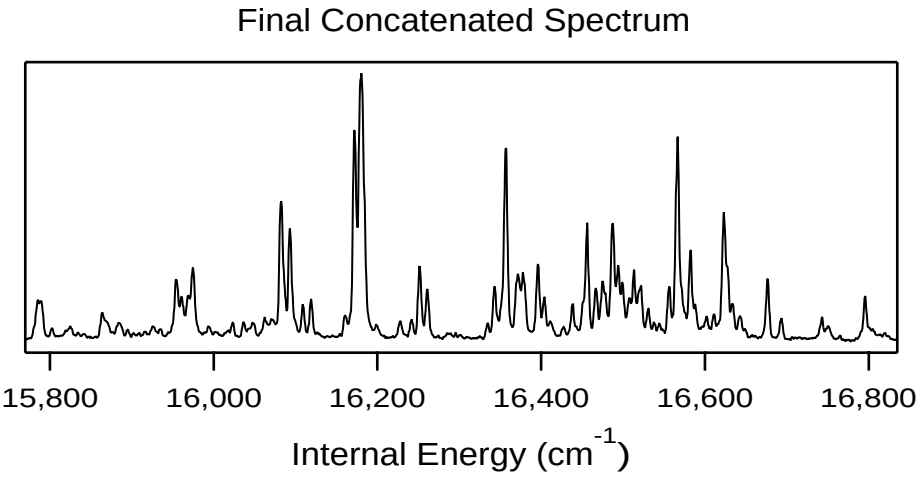

Figure 10-6: Top: Four DF segments with the grating angles chosen such that each segment overlaps with at least one-half of each adjacent segment. The emission at every wavelength is recorded at (at least) two different grating angles and is averaged to create the final concatenated spectrum.

made the analysis difficult. In addition, above $E_{\text{vib}} \approx$ 15,200 cm^{-1}, acetylene is believed to be energetically capable of isomerizing to vinylidene [4], and it is desirable to obtain the best possible quality DF spectra above this energy in order to identify any spectroscopic manifestations of isomerization, which may be subtle. To this end, I have recently recorded the dispersed fluorescence from the $2_0^1V_0^1K_0^1$ and $2_0^1V_0^2K_0^1$ bands of acetylene at 4.0 cm^{-1} resolution using the methodologies in Section 10.2. Other experimental conditions were identical to those described in Chapter 5. The resultant calibrated spectra are depicted in Fig. 10-7; the frequency calibration is good to $\sim$0.5 cm^{-1} (1σ).

The advantage of these higher resolution spectra over the lower resolution spectra that are documented in Chapter 5 is made clear in Fig. 10-8. Depicted here is the $(0,0,0,22^{0/2},0^0)$ bright state fractionation pattern that has been extracted, using XCC, from spectra with resolutions of $\sim$18 cm^{-1}, $\sim$8 cm^{-1}, and $\sim$4 cm^{-1}. The $\sim$4 cm^{-1} resolution spectra reveal details of the fractionation pattern that the lower resolution spectra cannot, with excellent signal-to-noise. Many of the fractionation patterns that are observed at higher internal energy are even more congested.

Dispersed fluorescence spectra with $\sim$4 cm^{-1} resolution have, so far, only been recorded using two absorption bands, $2_0^1V_0^1K_0^1$ and $2_0^1V_0^2K_0^1$. The reason that no more spectra have been recorded is not due to the difficulty of recording these spectra (they are relatively easy to obtain, when the optical alignment of the apparatus is optimal), but is rather due to the success of a new research direction, involving $^{13}C_2H_2$, which is detailed in Section 10.4. As explained below, it is my belief that $^{13}C_2H_2$ is a better choice than $^{12}C_2H_2$ for studies of unimolecular dynamics above the threshold of isomerization, due to the relative simplicity of the observed fractionation patterns. Thus, efforts to record additional high resolution DF spectra of $^{12}C_2H_2$ have been dropped in favor of moving forward rapidly with $^{13}C_2H_2$.

However, it is probably worthwhile to provide a brief summary of the insights that the $\sim$4 cm^{-1} resolution spectra have already provided. In particular, it has been possible to assign polyad quantum numbers to quite a few of the eigenstates above 15,000 cm^{-1}, although a complete analysis using the numerical pattern recognition

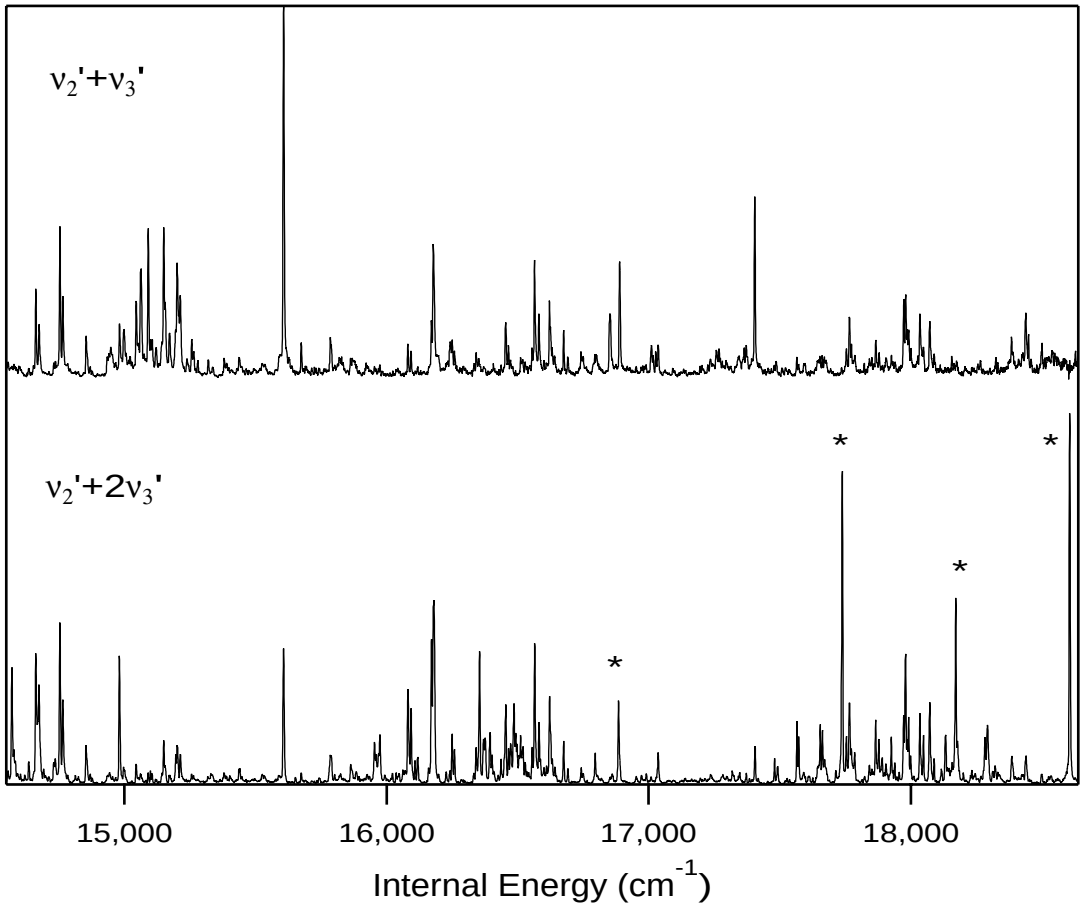

Figure 10-7: High resolution (4.0 cm^{-1}) dispersed fluorescence spectra of acetylene recorded using the $2_0^1V_0^1K_0^1$ and $2_0^1V_0^2K_0^1$ absorption bands. In the $2_0^1V_0^2K_0^1$ spectrum, the peaks marked with asterisks represent low lying ($<$5000 cm^{-1}) vibrational levels observed in third order; the remaining peaks are observed in second order. For the $2_0^1V_0^2K_0^1$ spectrum, a long-pass optical filter was used so that only second order emission was recorded.

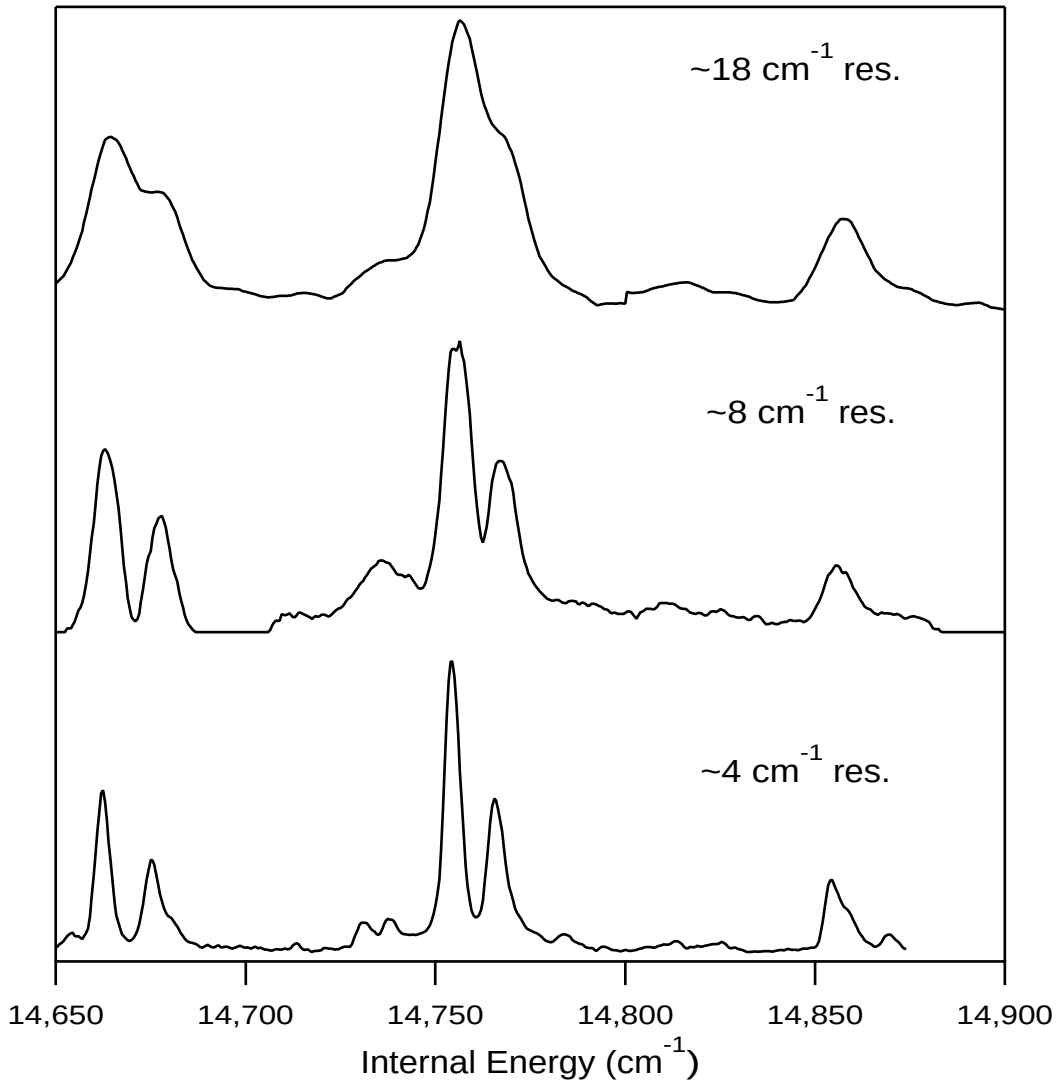

Figure 10-8: The $(0,0,0,22^{0/2},0^0)$ bright state fractionation pattern that has been extracted, using XCC, from DF spectra with resolutions of $\sim$18 cm^{-1}, $\sim$8 cm^{-1}, and $\sim$4 cm^{-1}.

algorithms (XCC with linear inversion) is not possible with just two spectra (there are regions of energy where 3 patterns overlap). In addition, the effective Hamiltonian model that has been developed in Chapters 9 and 6 has been found to extrapolate nicely above 15,000 cm^{-1}; that is, it is able to predict the qualitative fractionation patterns for bright states that were not included in the fit. This is, of course, evidence that the feasibility of isomerization does not result in a *catastrophic* breakdown of the polyad model, at least up to ∼18,000 cm^{-1}; more substantial evidence for this statement is presented in Section 10.4.

First we consider the pure bending polyads above 15,000 cm^{-1}. The highest pure bending fractionated bright state that was identified in Chapter 5 and studied in Chapters 6–8 was $(0,0,0,22^{0/2},0^0)$. In the ∼4 cm^{-1} resolution spectra, the fractionated bright state patterns for $(0,0,0,24^{0/2},0^0)$ and $(0,0,0,26^{0/2},0^0)$ can also be identified and are depicted in Fig. 10-9. Note that the $(0,0,0,26^{0/2},0^0)$ fractionation pattern could not be extracted by linear inversion, because it overlaps strongly (above 17,700 cm^{-1}) with at least two other patterns. However, most of the $(0,0,0,26^{0/2},0^0)$ fractionation pattern can be clearly identified in the $2_0^1V_0^2K_0^1$ spectrum by comparison with the predictions of the H^{eff} model, which does a good job of predicting the key qualitative features of the fractionation patterns.

The other series of fractionated bright states that are particularly easy to identify above 15,000 cm^{-1} are those with a large number of quanta of excitation in the CC stretch mode ($v_2 \geq 5$), i.e., states similar to those considered in Chapter 9 which displayed anomalously slow IVR. Figure 10-10 depicts two such bright states that have been identified in the ∼4 cm^{-1} resolution spectra, $(0,5,0,10^{0/2},0^0)$ and $(0,6,0,10^{0/2},0^0)$. Both bright states are minimally fractionated and are readily identified using the H^{eff} model. The $(0,5,0,12^{0/2},0^0)$ and $(0,6,0,8^{0/2},0^0)$ bright states can be identified in a similar manner.

The assignments that have been made above 15,000 cm^{-1} (using pattern recognition and the H^{eff} model) can be confirmed using Franck-Condon trends. Figure 10-11 displays the experimentally observed Franck-Condon factors for the $(0,v_2,0,10^{0/2},0^0)$ series of bright states. The Franck-Condon factors for the bright states with $v_2'' \leq 4$

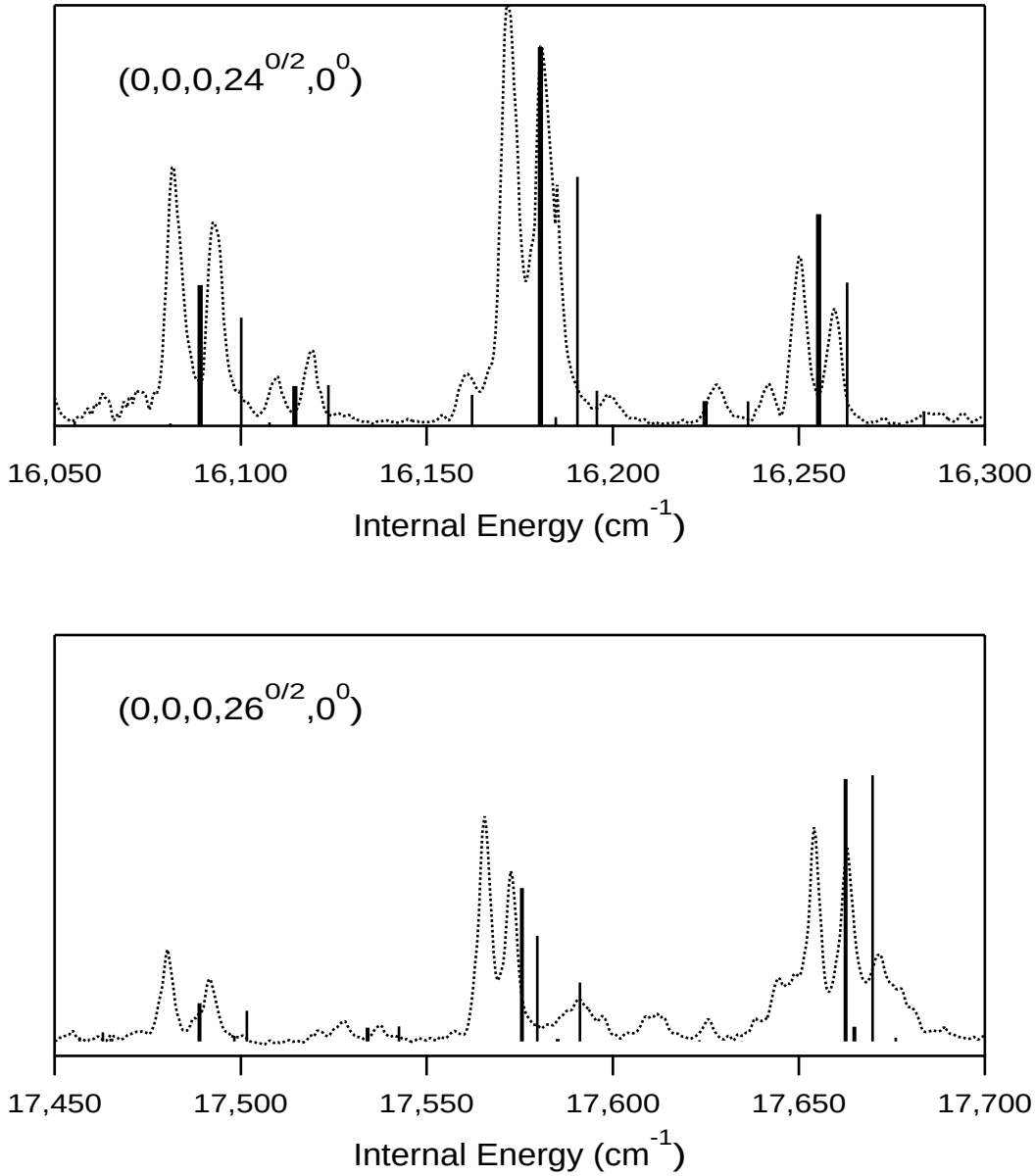

Figure 10-9: Identification of the $(0,0,0,24^{0/2},0^0)$ and $(0,0,0,26^{0/2},0^0)$ bright state fractionation patterns in the $\sim$4 cm^{-1} resolution dispersed fluorescence spectra. Top: The $(0,0,0,24^{0/2},0^0)$ fractionation pattern as extracted by XCC/linear inversion from the two $\sim$4 cm^{-1} resolution DF spectra. Bottom: The $(0,0,0,26^{0/2},0^0)$ fractionation pattern could not be extracted by linear inversion, because it overlaps strongly (above 17,700 cm^{-1}) with at least two other patterns. However, in the section of the $2_0^1V_0^2K_0^1$ spectrum shown here, most of the $(0,0,0,26^{0/2},0^0)$ fractionation pattern can be identified by comparison with the predictions of the $H^{\rm eff}$ model. In both the top and bottom, the thick vertical sticks are the predictions for the $(J=1,\ell=0)$ rotational components, and the thin vertical lines are for the $(J=2,\ell=2)$ components.

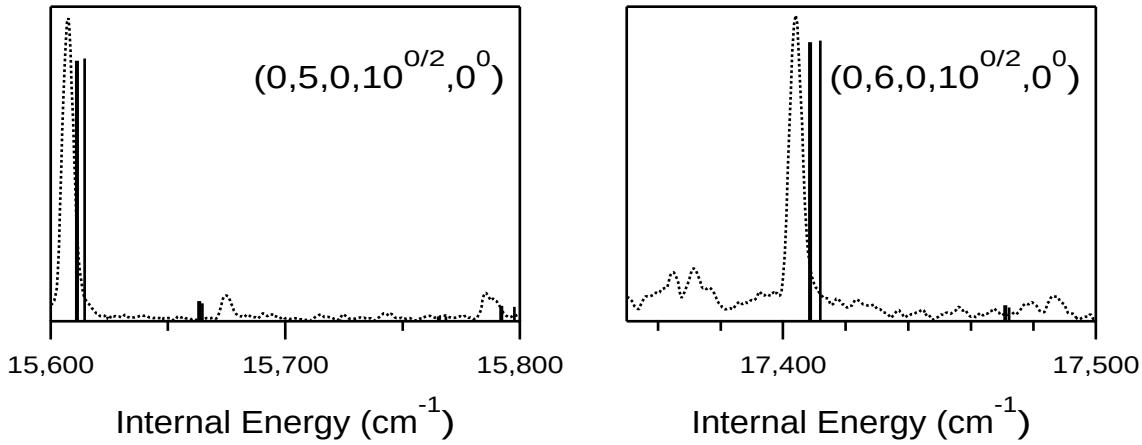

Figure 10-10: Identification of the $(0, 5, 0, 10^{0/2}, 0^0)$ and $(0, 6, 0, 10^{0/2}, 0^0)$ bright state fractionation patterns in the $\sim$4 cm^{-1} resolution dispersed fluorescence spectra. Left: The $(0, 5, 0, 10^{0/2}, 0^0)$ fractionation pattern as extracted by XCC/linear inversion from the two $\sim$4 cm^{-1} resolution DF spectra. Right: The $(0, 6, 0, 10^{0/2}, 0^0)$ bright state, which is minimally fractionated, can be clearly identified in the $2^1_0V^1_0K^1_0$ DF spectrum, by comparison with the predictions of the H^{eff} model. In both panels, the thick vertical sticks are the predictions for the $(J = 1, \ell = 0)$ rotational components, and the thin vertical lines are for the $(J = 2, \ell = 2)$ components.

were obtained by integrating the fractionation patterns that were extracted from the $\sim$18 cm^{-1} spectra using numerical pattern recognition (see Chapter 5). The states with $v''_2 > 4$ are those that are identified in Fig. 10-10. Their Franck-Condon factors were estimated by identifying the corresponding peaks in the $\sim$18 cm^{-1} spectra (the only series that is fully intensity calibrated) and integrating these peaks. Note that in the emission from both the $2^1_0V^1_0K^1_0$ and $2^1_0V^2_0K^1_0$ bands, there is one minimum in the Franck-Condon factors at $v''_2 = 2$, which corresponds to the node along the CC stretch coordinate in the excited state wavefunction. The continuity of the $v''_2 = 5$ and 6 Franck-Condon factors with the trends observed for the bright states below 15,000 cm^{-1} ($v''_2 \leq 4$) lends credibility to the assignment of $(0, 5, 0, 10^{0/2}, 0^0)$ and $(0, 6, 0, 10^{0/2}, 0^0)$ in Fig. 10-10.

Other bright state fractionation patterns have been successfully identified above 15,000 cm^{-1} in the $^{12}C_2H_2$ DF spectra but will not be reported here, because the corresponding analysis for the $^{13}C_2H_2$ DF spectra, considered in Section 10.4, is significantly simpler.

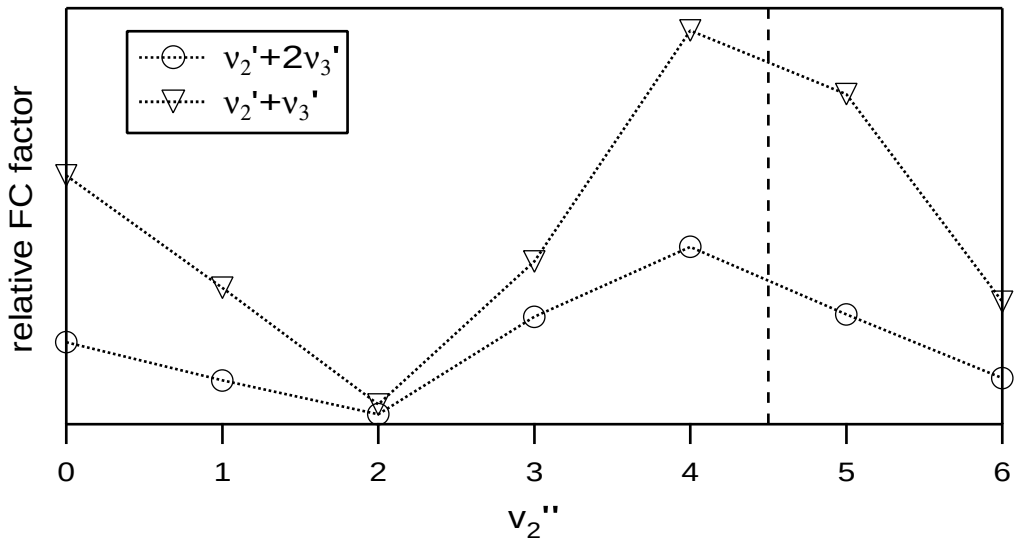

Figure 10-11: The observed relative Franck-Condon factors for the $(0, v_2, 0, 10^{0/2}, 0^0)$ bright states in the $2_0^1 V_0^2 K_0^1$ (circles) and $2_0^1 V_0^1 K_0^1$ (triangles) DF spectra. For progressions of bright states with constant v_4'', the emission from S_1 state vibrational levels with $v_2' = 1$ displays one minimum in the Franck-Condon factors at $v_2'' = 2$, which corresponds to the node in the excited state wavefunction. The bright states with $v_2'' \leq 4$ lie below 15,000 cm^{-1}, while those with $v_2'' > 4$ lie above 15,000 cm^{-1}. The continuity of the Franck-Condon trends helps to confirm the assignments made above 15,000 cm^{-1}.

10.4 Dispersed Fluorescence Studies of $^{13}C_2H_2$

The dispersed emission has been recorded at ∼18 cm^{-1} from the $Q(1)$ lines of four vibrational bands of $^{13}C_2H_2$: $V_0^2K_0^1$, $2_0^1V_0^1K_0^1$, $2_0^1V_0^2K_0^1$, and $V_0^4K_0^1$.[2] $^{13}C_2H_2$ has been studied much less extensively than $^{12}C_2H_2$, and for this reason, none of these bands, other than $V_0^2K_0^1$ [10], had been identified spectroscopically previously, to our knowledge. As a reference for future studies of $^{13}C_2H_2$, we depict in Figs. 10-12, 10-13, and 10-14 a few of the laser induced fluorescence (LIF) spectra that we recorded in order to identify these bands. The vibrational assignments of the bands were made by estimating the isotope shifts for the relevant vibrational levels from $^{12}C_2H_2$ to $^{13}C_2H_2$. In all cases, the bands depicted were located within ∼10 cm^{-1} of the calculated transition frequency; the vibrational assignment of the bands can be confirmed from the Franck-Condon trends observed in the DF spectra. The rotational transitions were assigned by combination-differences.

A number of peaks in the $2_0^1V_0^1K_0^1$ and $2_0^1V_0^2K_0^1$ LIF spectra are unassigned and are assumed to be due to interloping absorption bands (probably hot bands). There is no evidence of these bands being significantly perturbed, either from the LIF spectra or the DF spectra recorded from the $Q(1)$ lines; however, the bands have not extensively analyzed, in terms of fitting them to an effective rotational Hamiltonian. The $V_0^4K_0^1$ band appears to be relatively free from overlap with other bands, but there are a number of striking intensity anomalies, the most notable of which is $Q(4)$, which is at least twice as intense as expected based upon the intensities of the other lines. There also appears to be an intriguing intensity alternation in the R-branch, with the transitions terminating on even-J' being anomalously weak. These intensity anomalies have not been explained. Evidence is presented below that the $4\nu_3'$, $K_a = 1$ vibrational level is perturbed, but the perturber is remote, in the sense that the strength of the perturbation (mixing coefficient) appears to be independent of J. As such, we believe the intensity anomalies to be unrelated to the perturbation. It

[2] As in $^{12}C_2H_2$, the $V_0^3K_0^1$ band is not used because the $3\nu_3'$ vibrational level appears to be strongly perturbed at low J.

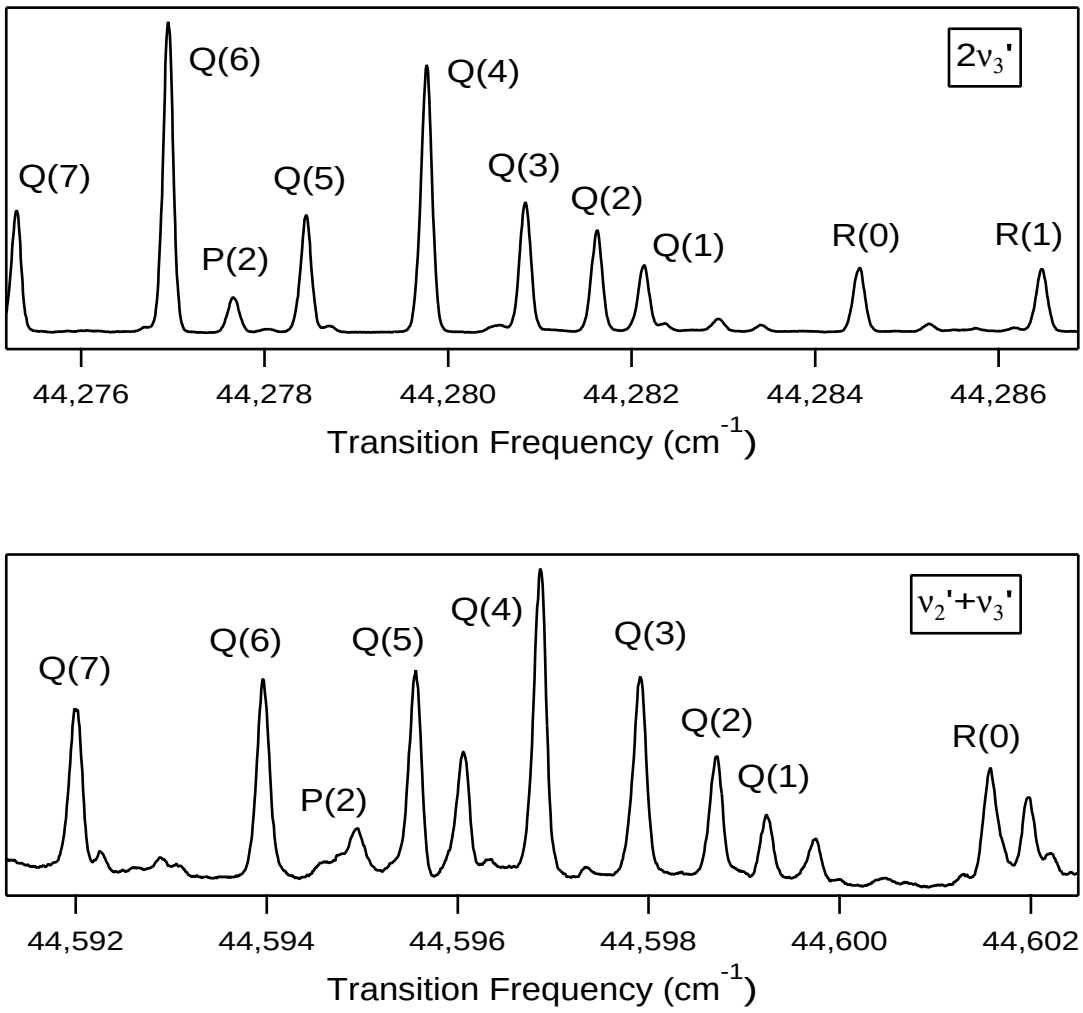

Figure 10-12: LIF spectra of the $V_0^2K_0^1$ and $2_0^1V_0^1K_0^1$ bands of $^{13}C_2H_2$.

should be noted that the $4\nu_3'$ vibrational level lies above the first ground electronic state dissociation limit.

The calibrated dispersed fluorescence spectra that have been recorded for $^{13}C_2H_2$ are displayed in Fig. 10-15. The dispersed fluorescence methodologies described in Section 10.2 were employed. In addition, only 1.0 Torr of acetylene was used to record these spectra, as opposed to 5.0 Torr, which was used to record the spectra described in Chapter 5. Using lower acetylene pressure has a number of advantages. One practical consideration is that, at higher pressures, the windows on the DF cell "burn" much more quickly where the UV laser beam passes through them (presumably due to polyacetylene formation on the windows), necessitating frequent cleaning/replacement of

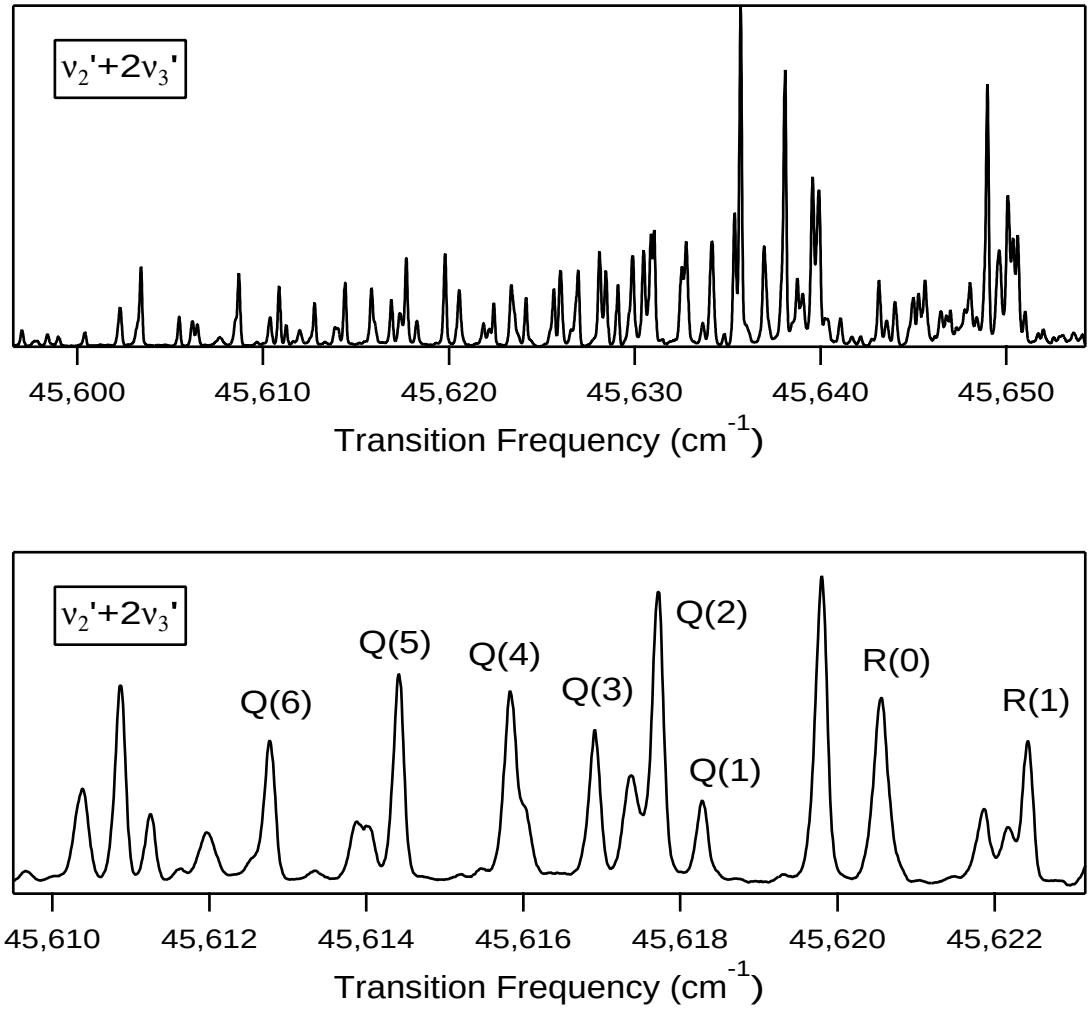

Figure 10-13: LIF spectra of the $2_0^1 V_0^2 K_0^1$ band of $^{13}C_2H_2$, which overlaps significantly with at least one other (as yet unassigned) band.

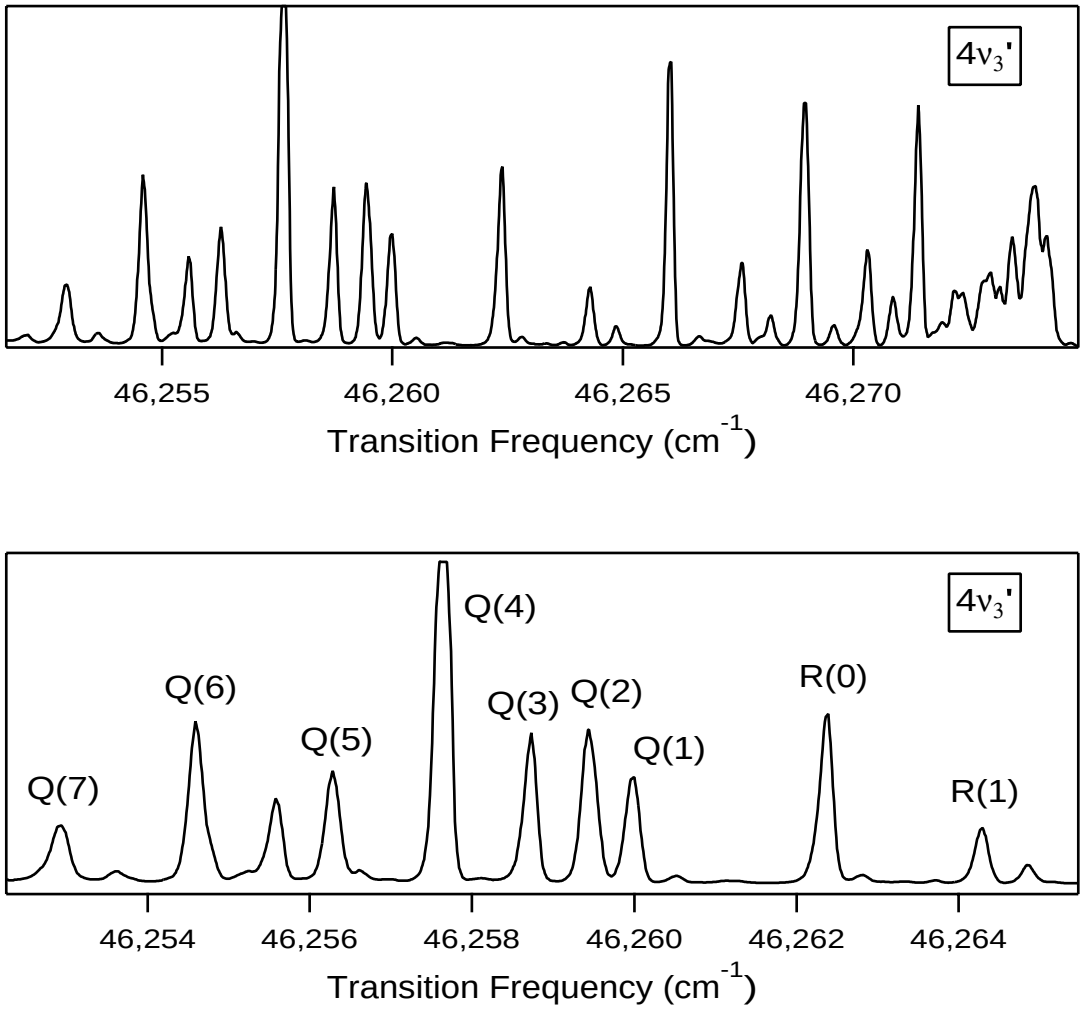

Figure 10-14: LIF spectra of the $V_0^4 K_0^1$ band of $^{13}C_2H_2$, which displays a number of intensity anomalies. The $Q(4)$ line is anomalously strong and the R-branch lines that terminate on even J' are anomalously weak.

the windows. At 1.0 Torr, it was possible to complete an entire spectrum, which entails several hours of total signal integration time (roughly half a million laser shots with energy > 0.5 mJ), without changing the windows. Another advantage of lower acetylene pressure is that the amplitude of the quasi-continuous baseline and the "extra patterns", both of which are believed to be related to collisional energy transfer, are diminished at lower pressure, as discussed in Chapter 5. These unwanted contributions to the DF spectra are also minimized by gating over only the first 200 ns after the laser fires, as opposed to $\sim$1 μs, as was conventionally used for the spectra in Chapter 5. The success of these strategies at diminishing the quasi-continuous baseline is evident in Fig. 10-15; these spectra have *not* been processed using baseline stripping algorithms. The "extra patterns", which are believed to be due to emission from $K'_a = 0$ and 2 levels populated by collisions, are present in the data set, but are much less prominent than in the $^{12}C_2H_2$ data set. Finally, I wish to point out the excellent signal-to-noise that is achieved in these spectra. Fig. 10-16 is a close-up view of the $2^1_0 V^2_0 K^1_0$ DF spectrum at low internal energy. The spectrum is scaled such that the tallest peak has intensity 1.0, and the noise level is less than 0.001.

Dispersed fluorescence spectra recorded using corresponding absorption bands in $^{13}C_2H_2$ and $^{12}C_2H_2$ are not expected to be grossly different; after all, the only difference between the two molecules is that the mass of the carbons varies by 8%. Figure 10-17 appears to validate this conclusion. The DF spectra at $\sim$18 cm^{-1} resolution, recorded using the $2^1_0 V^2_0 K^1_0$ band, are compared for $^{12}C_2H_2$ and $^{13}C_2H_2$ at relatively low internal energy. It is possible to make correspondences between the peaks in each of the spectra. Specifically, for every intense peak in the $^{12}C_2H_2$ spectrum, there is a corresponding intense peak, at somewhat lower internal energy, in the $^{13}C_2H_2$ spectrum. The energy shifts between the two spectra are expected to be due largely to the difference in the CC stretch frequency (ω_2) between the two molecules, which should be $\sim$4%. Eigenstates with greater CC stretch excitation would then exhibit greater shifts.

All of these predictions can be verified numerically at low energy, where the $(0, v_2, 0, v_4, 0)$ bright states are minimally fractionated. However, the difference is car-

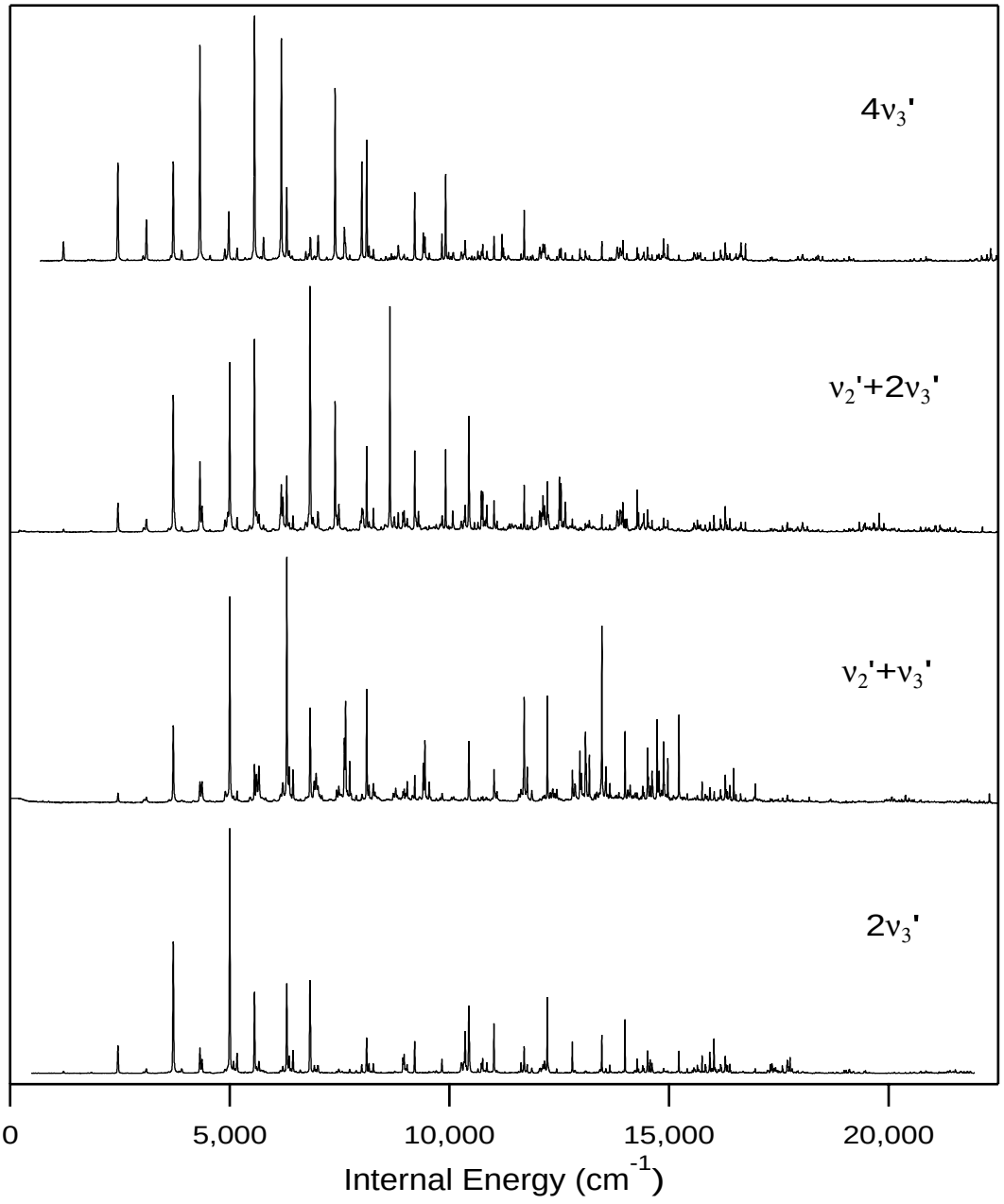

Figure 10-15: Dispersed fluorescence spectra recorded at $\sim$18 cm^{-1} resolution *via* the $Q(1)$ lines of four vibrational bands of $^{13}C_2H_2$: $V_0^2K_0^1$, $2_0^1V_0^1K_0^1$, $2_0^1V_0^2K_0^1$, and $V_0^4K_0^1$.

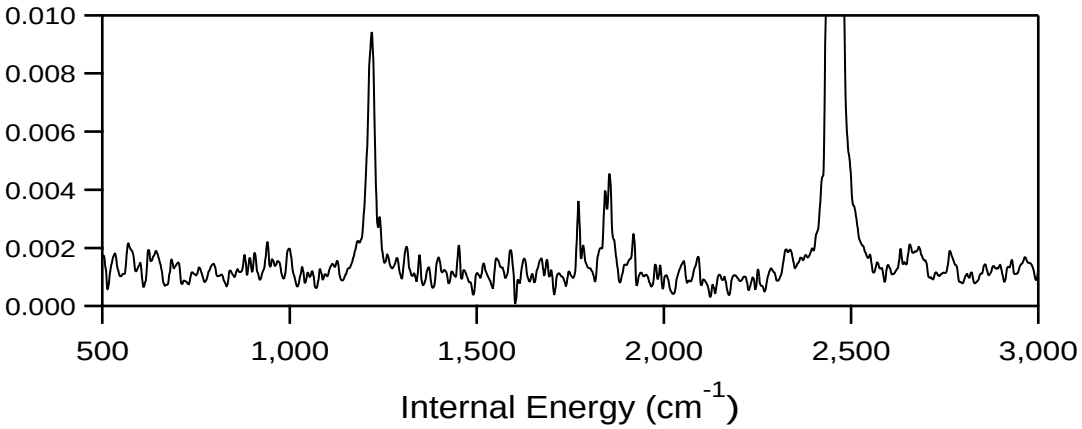

Figure 10-16: Closer view of the $2_0^1 V_0^2 K_0^1$ DF spectrum in Fig. 10-15 at low internal energy. The spectrum is scaled such that the tallest peak has intensity 1.0, and the noise level is less than 0.001.

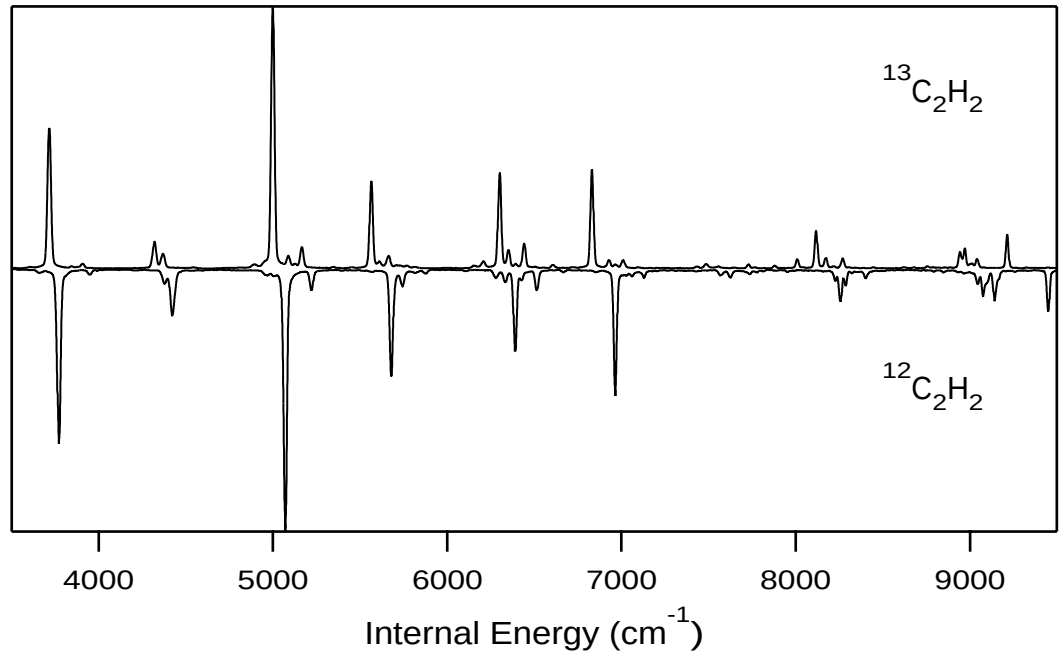

Figure 10-17: Dispersed fluorescence spectra recorded via the $2_0^1 V_0^2 K_0^1$ bands of $^{12}C_2H_2$ (bottom, inverted) and $^{13}C_2H_2$ (top).

bon masses also IVR—the redistribution of energy from the zero-order bright states into other states of the molecule. This issue can, of course, be addressed by processing the $^{13}C_2H_2$ spectra using the same numerical pattern recognition algorithms (XCC plus linear inversion) that provided us with so much insight into the vibrational dynamics of $^{12}C_2H_2$. The $V_0^4K_0^1$ band DF spectrum has been excluded from this analysis, because there is strong evidence (discussed at the end of this section) that the $4\nu_3'$ vibrational level is perturbed.

Figure 10-18 is the IVR map that has been constructed for $^{13}C_2H_2$ (the corresponding plot for $^{12}C_2H_2$ is Fig. 5-13). This IVR map includes all of the fractionated bright state patterns that have been extracted from the DF data set using numerical pattern recognition up to 18,000 cm^{-1}. "Holes" appear in the IVR map because not every fractionated bright state pattern could be extracted from the spectra, for one of two reasons. First, certain bright states have low Franck-Condon factors in all three of the DF spectra analyzed. An example is $(0, 2, 0, 18, 0)$. Intermediate vibrational levels with $v_2' = 1$ have nearly zero emission to zero-order bright states with $v_2'' = 2$ (i.e., the node in the excited state wavefunction creates a minimum in the Franck-Condon progressions). Thus, the $(0, 2, 0, 18, 0)$ bright state does not appear in the DF spectra recorded using the $2_0^1V_0^1K_0^1$ or $2_0^1V_0^2K_0^1$ bands. In addition, intermediate vibrational levels with $v_3' = 2$ have nearly zero emission to zero-order bright states with $v_4'' = 12$ or 18. Thus, the $(0, 2, 0, 18, 0)$ bright state also does not appear in the DF spectrum recorded using the $V_0^2K_0^1$ absorption band. We intend to record the origin band DF spectrum for $^{13}C_2H_2$ to alleviate this problem (since the zero-point vibrational level has no nodes, all bright states should appear).

The second reason for the "holes" in the IVR map is that the numerical pattern recognition algorithms were unable to identify and extract all of the fractionated bright states that are observed in the spectra. This occurs when two patterns that overlap in the spectra happen to have nearly identical ratio directions (relative amplitudes in each of the spectra). As discussed in some detail in Chapter 2, even if the XCC succeeds in identifying such pairs of fractionated bright states as separate patterns, the noise amplification associated with the linear inversion process will be

nearly infinite. The recording of the origin band DF spectrum for $^{13}C_2H_2$ is expected to alleviate this problem as well; it is less likely that two overlapping patterns will have the same ratio directions in four spectra than in just three.

Even with these holes, the IVR map still provides an enormous quantity of information about vibrational energy redistribution in $^{13}C_2H_2$. Among the most intriguing aspects of this IVR map is its simplicity relative to the IVR map for $^{12}C_2H_2$. Figure 10-19 provides a close-up view of a few of the bright state fractionation patterns (v_2'' = 0 or 1; v_4'' = 10–14) for both $^{12}C_2H_2$ and $^{13}C_2H_2$. For $^{13}C_2H_2$, the fractionation patterns for the bright states with the same v_4'' but different v_2'' are extremely similar, almost uncannily so. For $^{12}C_2H_2$, on the other hand, the fractionation patterns for the bright states with $v_2'' = 1$ appear to be significantly more complicated than those for the corresponding $v_2'' = 0$ bright states. The simplicity of the (vertical) trends in the $^{13}C_2H_2$ IVR map is not limited to $v_2'' = 0$ and 1. Fig. 10-20 depicts two of the columns of the $^{13}C_2H_2$ IVR map, $v_4'' = 8$ and $v_4'' = 14$. In both columns, the fractionation decreases in a regular, consistent manner with increasing v_2'' (see Section 9.4 for a qualitative explanation of this trend), and it is possible to identify simple trends in the fractionation patterns.

The relative simplicity of the $^{13}C_2H_2$ IVR map, particularly with respect to increasing v_2'', appears to be due to the relative unimportance of the (3,245) stretch-bend resonance in $^{13}C_2H_2$. The $v_2'' = 0$ bright states belong to the pure bending polyads that are discussed in Chapters 6, 7, and 8. All of the states in these polyads are characterized by zero stretch excitation, and thus resonances that exchange bend and stretch excitation play no role. These stretch-bend resonances can, however, impact the observed IVR (fractionation patterns) for bright states with $v_2'' > 0$. If this is the case, as it appears to be for $^{12}C_2H_2$ (Fig. 10-19), then the bright state fractionation increases significantly from $v_2'' = 0$ to $v_2'' = 1$. Previous studies of the $(0, v_2, 0, v_4, 0)$ bright state fractionation patterns have emphasized the particular importance of the (3,245) resonance (see Ref. [177], as well as Chapter 9), which strongly influences the vibrational dynamics in $^{12}C_2H_2$ because the energy difference $\omega_3 - (\omega_2 + \omega_4 + \omega_5) \approx 2$ cm^{-1}. In $^{13}C_2H_2$, on the other hand, $\omega_3 - (\omega_2 + \omega_4 + \omega_5) > 50$ cm^{-1} (using previously

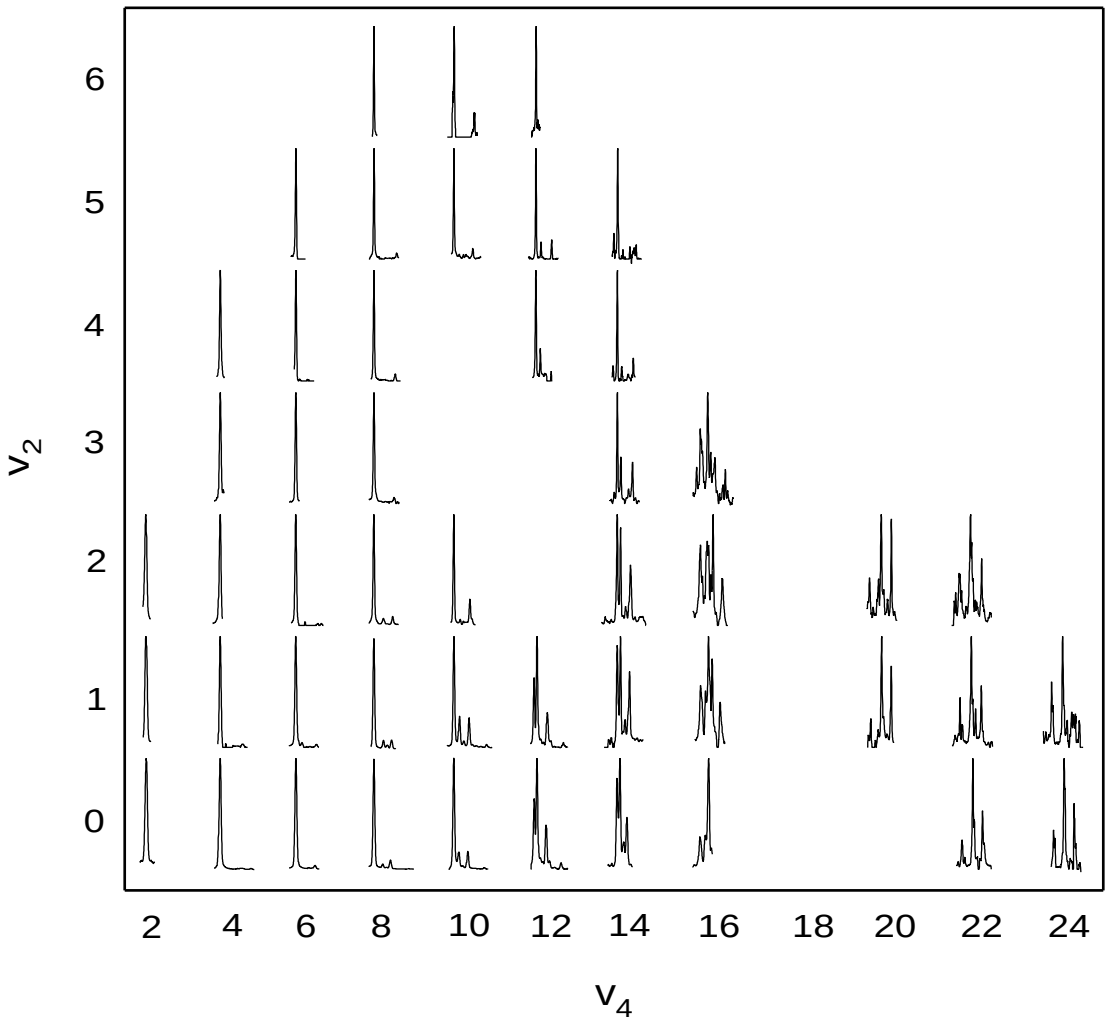

Figure 10-18: IVR map for $^{13}C_2H_2$. The fractionated bright state patterns are arranged according to the number of quanta of the two Franck-Condon active modes: CC stretch (v_2) and *trans* bend (v_4).

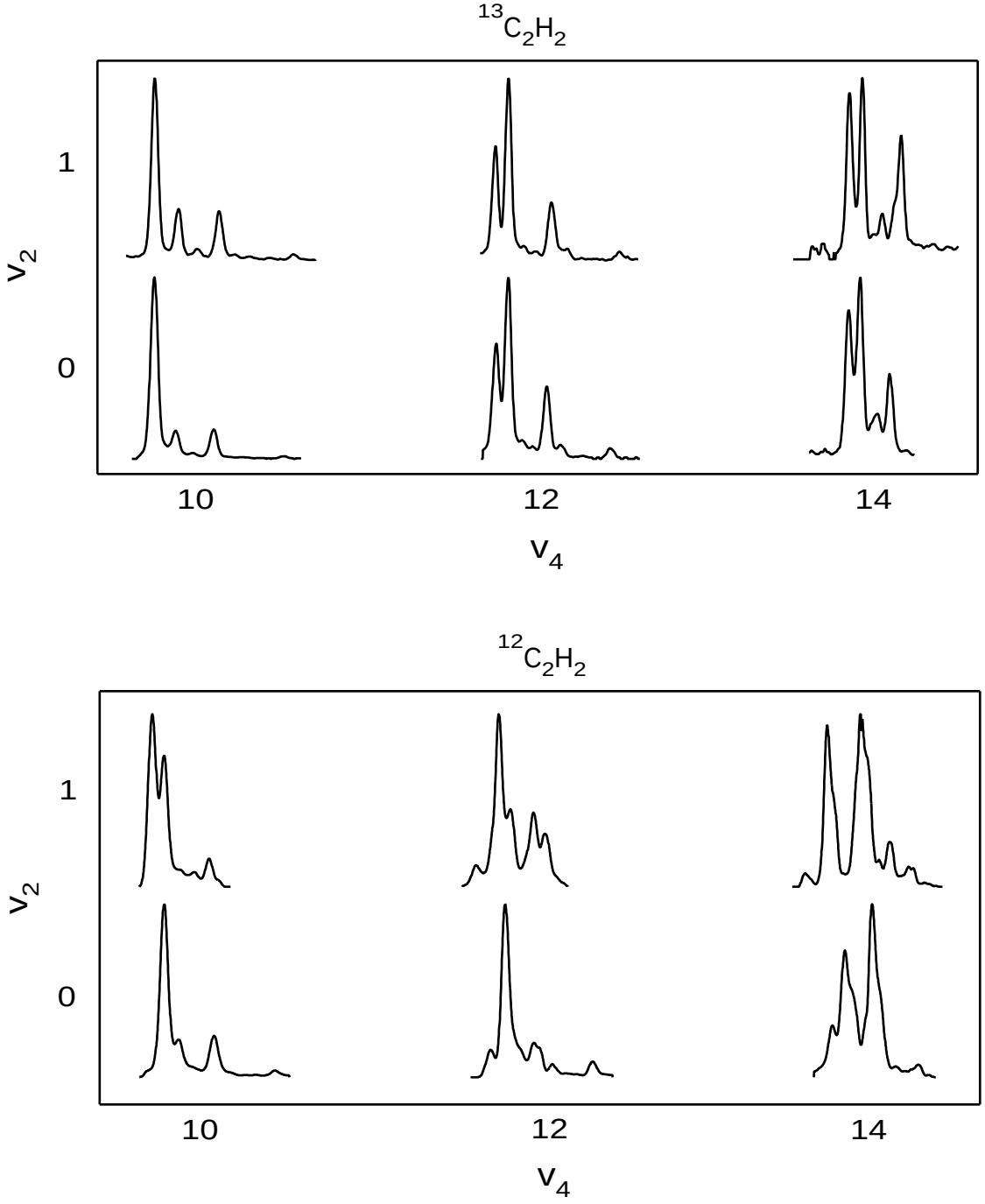

Figure 10-19: Comparison of portions of the IVR maps for $^{12}C_2H_2$ and $^{13}C_2H_2$. In $^{12}C_2H_2$, the fractionation patterns with $v_2'' = 1$ are substantially more complex than the $v_2'' = 0$ fractionation patterns with the same v_4''. In $^{13}C_2H_2$, the fractionation patterns appear to be essentially independent of v_2''.

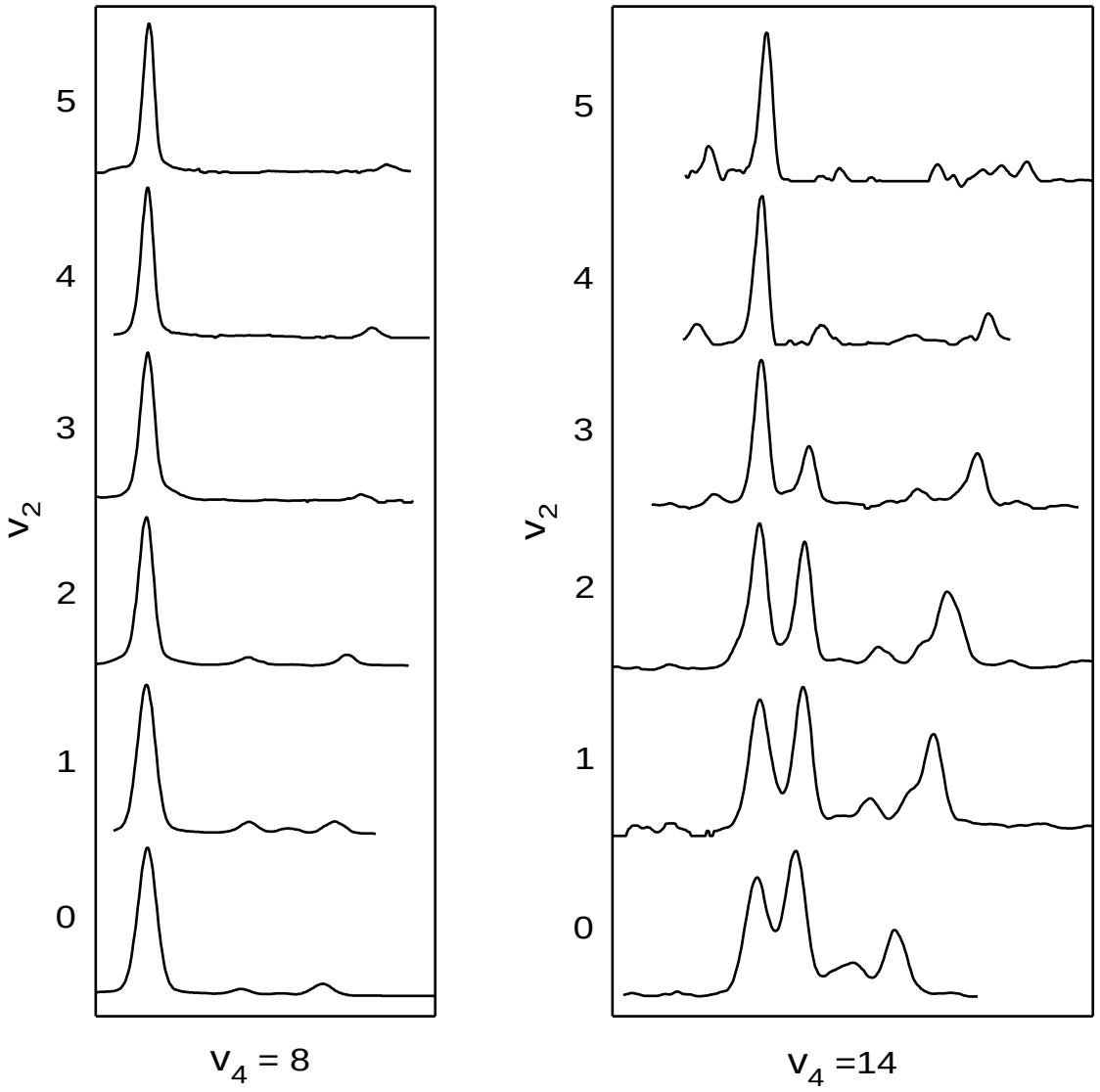

Figure 10-20: Close-up view of two of the columns of the $^{13}C_2H_2$ IVR map. For both $v_4'' = 8$ and $v_4'' = 14$, IVR decreases with increasing quanta of CC stretch.

published constants plus our own preliminary fits), and thus the (3,245) resonance can be expected to play a much less significant role in the dynamics. The striking regularity of the progressions of $^{13}C_2H_2$ bright state fractionation patterns with differing v_2'' (Fig. 10-19) suggests that stretch-bend resonances in general play little role in the observed IVR. We are currently developing both normal and local mode effective Hamiltonian models for $^{13}C_2H_2$ in order to study the IVR in greater detail.

Another remarkable aspect of the $^{13}C_2H_2$ IVR map is that it contains twelve bright state fractionation patterns that lie above 16,000 cm^{-1}, and thus above the energy at which acetylene-vinylidene isomerization is expected to be energetically feasible [4]. These fractionation patterns were no more easy or difficult to extract from the spectra than those below 16,000 cm^{-1} and do not demonstrate any significant increase in complexity. On the contrary, these fractionation patterns appear to simply continue the trends in IVR observed at lower internal energy. For example, the $v_2'' = 4$ and 5, $v_4'' = 14$ fractionation patterns in Fig. 10-20 both lie above 16,000 cm^{-1}. Figure 10-21 provides another example. Of the fractionation patterns depicted here, only the $v_4'' =$ 22 and 24 pure bending bright states ($v_2'' = 0$) lie below 16,000 cm^{-1}. The remaining patterns reproduce the same qualitative pattern, which consists primarily of just 3 lines and is associated with the local mode limit for the bend degrees of freedom (see Chapters 6, 7, and 8). Although these results should be considered preliminary, the regularity of the bright state fractionation patterns above 16,000 cm^{-1} certainly suggests that vinylidene plays little role in the <1 ps dynamics that is sampled by our spectra, up to at least 18,000 cm^{-1}. However, careful numerical modelling of these results may reveal systematic changes above 16,000 cm^{-1}, and higher resolution DF and SEP spectra may reveal that vinylidene influences the IVR on a longer timescale.

The $V_0^4K_0^1$ band DF spectrum was excluded from the above analysis of the $^{13}C_2H_2$ DF data set due to a suspected perturbation of the $4v_3'$, $K_a' = 1$ vibrational band. Figure 10-22 provides evidence for this suspected perturbation. In each panel, the $V_0^4K_0^1$ band DF spectrum is compared with the pure bending bright state fractionation patterns extracted from the $V_0^2K_0^1$, $2_0^1V_0^1K_0^1$, and $2_0^1V_0^2K_0^1$ band DF spectra. Each of these panels provides evidence of two classes of bright states in the emission from the

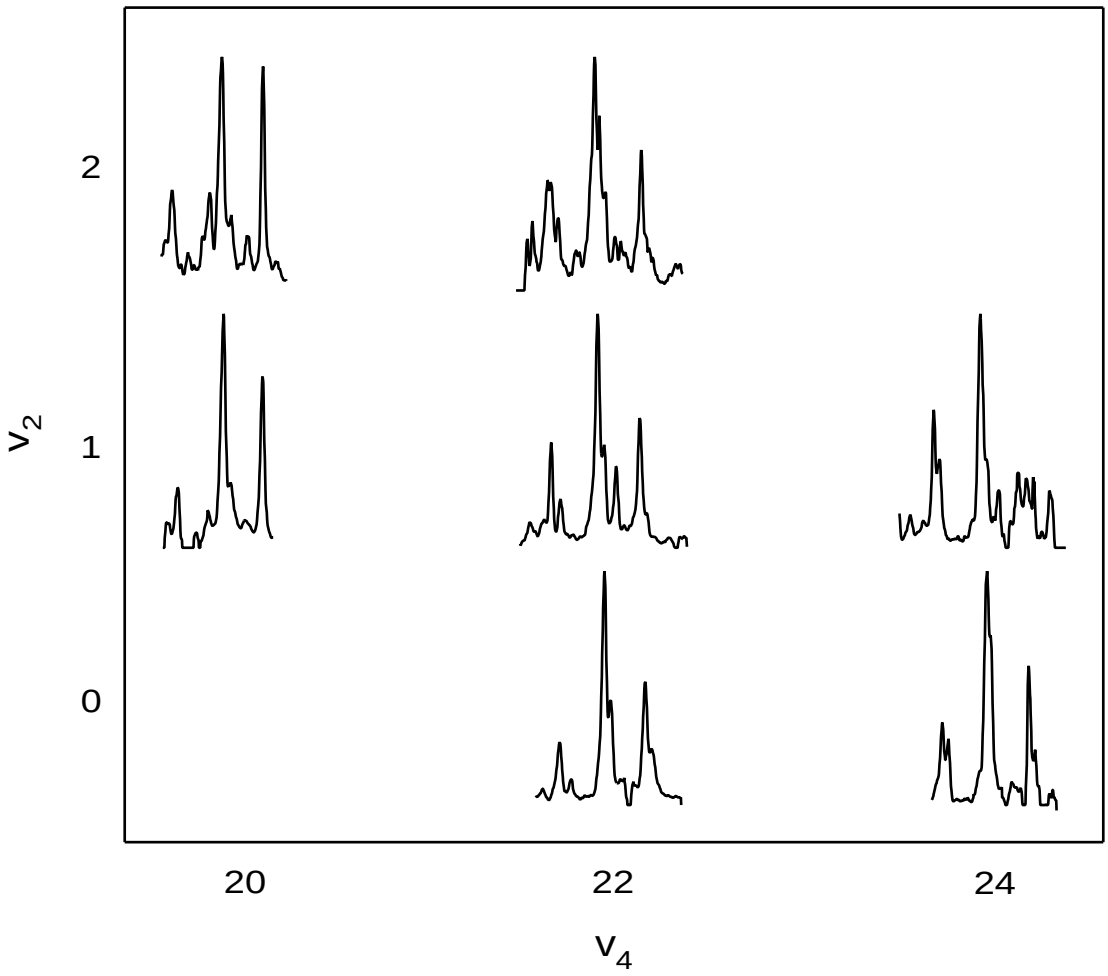

Figure 10-21: Close-up view of the $v_4'' \geq 20$ bright state fractionation patterns that have been identified in the $^{13}C_2H_2$ DF data set.

$4v_3'$, $K_a' = 1$ vibrational band. The usual bright states, $(0, v_2, 0, v_4, 0)$, are of course present, but there is also strong evidence that states of the type $(0, v_2, 0, v_4 - 2, 2)$ have their own intrinsic intensity as well.

Consider the top left panel of Fig. 10-22 first. The dotted line is the $(0, 0, 0, 6^{0/2}, 0^0)$ bright state fractionation pattern extracted from the $V_0^2K_0^1$, $2_0^1V_0^1K_0^1$, and $2_0^1V_0^2K_0^1$ DF spectra. The solid line is the scaled $V_0^4K_0^1$ band DF spectrum. The peak at $\sim$3720 cm^{-1} is the perturbed bright state and can be assigned the nominal normal mode quantum numbers $(0, 0, 0, 6, 0)$. The peak at $\sim$3910 cm^{-1} can be assigned as the Darling-Dennison perturber of the bright state, $(0, 0, 0, 4, 2)$ (see Chapter 9 for more detail). In the extracted fractionation pattern, the relatively weak intensity of this peak arises solely from resonant interaction with the bright state. However, the intensity of this peak in the $V_0^4K_0^1$ band DF spectrum is significantly larger (relative to the perturbed bright state). A likely explanation is that in the $V_0^4K_0^1$ DF spectrum, the $(0, 0, 0, 4, 2)$ state has its own intrinsic intensity, as opposed to only borrowing intensity from the bright state.

This hypothesis is bolstered by the top right panel of Fig. 10-22. In this case, the dotted line is the extracted bright state fractionation pattern for $(0, 0, 0, 8^{0/2}, 0^0)$. The peak at $\sim$5010 cm^{-1} is the perturbed bright state, and at least two weak perturbers can be observed at $\sim$5090 cm^{-1} and $\sim$5170 cm^{-1}. The $(0, 0, 0, 8, 0)$ bright state, however, has nearly zero Franck-Condon intensity from the $4v_3'$, $K_a' = 1$ vibrational level (the four "nodes" in the *trans*-bend, v_4'', Franck-Condon progression occur at 8, 14, 18 and 24 quanta); the peak at $\sim$4975 cm^{-1} in this spectrum arises from a different bright state, $(0, 2, 0, 2, 0)$. Despite the perturbed $(0, 0, 0, 8, 0)$ bright state having little intensity in the $V_0^4K_0^1$ DF spectrum, the perturbers of the bright state $[(0, 0, 0, 6^0, 2^0)$ and $(0, 0, 0, 6^{+2}, 2^{-2})]$x do have appreciable intensity. The discrepancies in the fractionation patterns in the lower two panels can also be qualitatively explained in terms of interference effects between $(0, v_2, 0, v_4, 0)$ and $(0, v_2, 0, v_4 - 2, 2)$ bright states.

Zero-order states of the type $(0, v_2, 0, v_4 - 2, 2)$ are usually not bright in our dispersed fluorescence spectra because the *cis*-bend mode is Franck-Condon inactive.

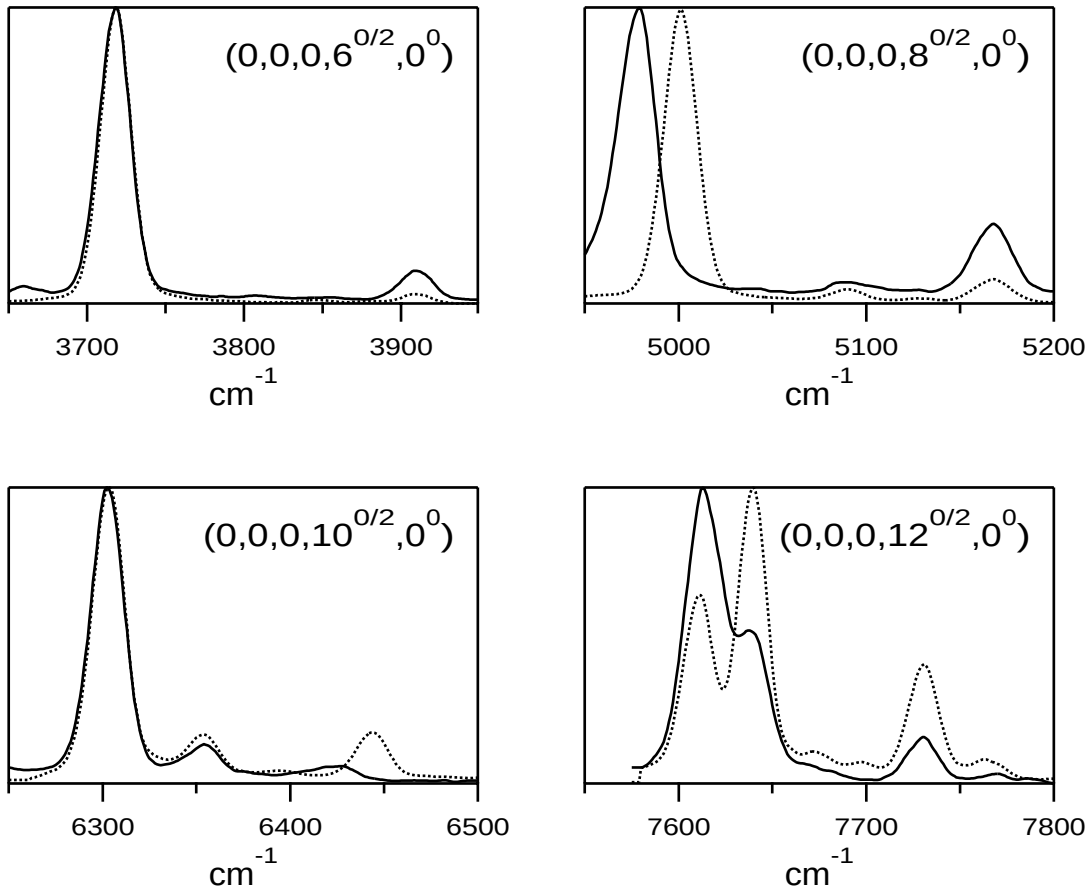

Figure 10-22: Comparisons of the $V_0^4K_0^1$ band DF spectrum (solid line) with several pure bending bright state fractionation patterns extracted from the $V_0^2K_0^1$, $2_0^1V_0^1K_0^1$, and $2_0^1V_0^2K_0^1$ band DF spectra (dotted line). The fractionation patterns observed in the $V_0^4K_0^1$ band DF spectrum indicate the presence of two classes of bright states, $(0, v_2, 0, v_4, 0)$ and $(0, v_2, 0, v_4 - 2, 2)$. Bright states with $v_5'' = 2$ could only have intrinsic intensity if the $4v_3'$, $K_a' = 1$ vibrational level is perturbed.

The only way that such states can have their own intrinsic brightness in emission is if the excited state wavefunction has some *cis*-bending character. The $4v_3'$, $K_a' = 1$ vibrational level, of course, nominally involves excitation only in the *trans* bend mode, but it could acquire *cis* bend character through a perturbation with a state involving excitation in the v_4' (*cis* bend) or v_6' (torsion) modes, both of which correlate to the v_5'' ground state *cis* bend mode. Anharmonic perturbations of this general type have been postulated to be responsible for the extensive perturbation of the $3v_3'$, $K_a = 1$ band in $^{12}C_2H_2$ [178, 179].

The results presented here are insufficient to unambiguously identify the perturber of the $4v_3'$, $K_a' = 1$ vibrational level. However, Fig. 10-23 provides strong evidence that the perturber is remote and that the perturbation is rotationally homogeneous. Specifically, Fig. 10-23 depicts the dispersed fluorescence recorded from the $Q(1)$, $Q(2)$, $Q(3)$, $Q(4)$, $R(0)$, $R(1)$, $R(2)$, and $R(3)$ lines of $V_0^4K_0^1$ over the same energy region as the lower right panel of Fig. 10-22. The observed fractionation pattern in this region of the $V_0^4K_0^1$ DF has been attributed to interference effects between $(0,0,0,12,0)$ and $(0,0,0,10,2)$ bright states, and the exact appearance of the spectrum should be quite sensitive to the relative intensities of the two bright states. That is, if the mixing fraction between the $4v_3'$, $K_a' = 1$ vibrational level and its perturber were to change with J', then the observed pattern of lines in the DF spectra recorded from different J' should change as well. However, Fig. 10-23 makes it clear that the changes in the observed patterns are minor, which implies that the perturber of the $4v_3'$, $K_a' = 1$ vibrational level is likely remote and likely interacts through an anharmonic mechanism.

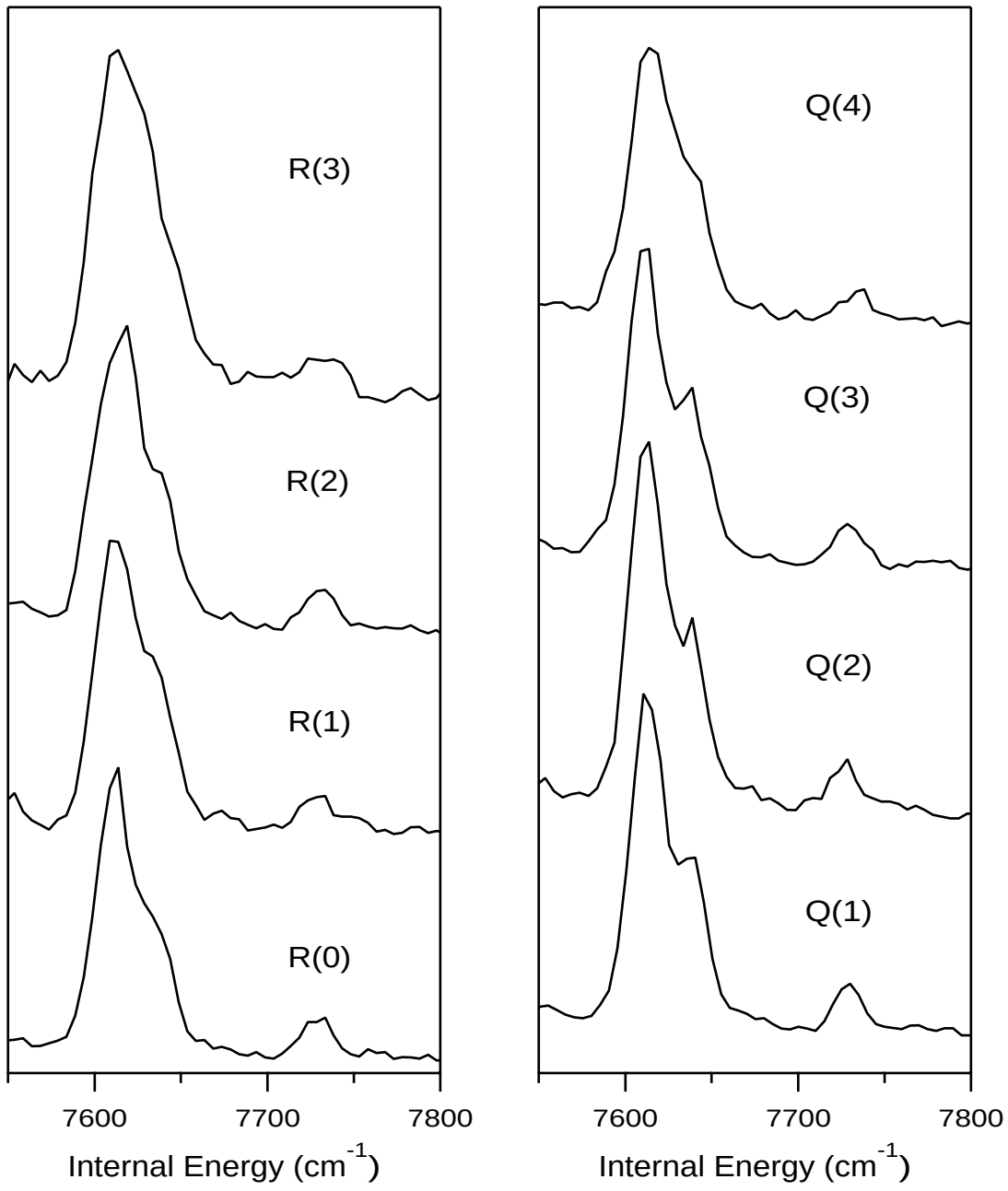

Figure 10-23: Dispersed fluorescence recorded from the $Q(1)$, $Q(2)$, $Q(3)$, $Q(4)$, $R(0)$, $R(1)$, $R(2)$, and $R(3)$ lines of $V_0^4 K_0^1$ over the same energy region as the lower right panel of Fig. 10-22.

Bibliography

[1] A. F. Ruckstuhl, W. A. Stahel, and K. Dressler, J. Mol. Spec. **160**, 434 (1993).

[2] W. A. Stahel, A. F. Ruckstuhl, P. Senn, and K. Dressler, Journal of the American Statistical Association **89**, 788 (1994).

[3] A. F. Ruckstuhl and K. Dressler, J. Mol. Spec. **168**, 185 (1994).

[4] J. F. Stanton and J. Gauss, J. Chem. Phys. **110**, 1831 (1999).

[5] M. Abbouti Temsamani and M. Herman, J. Chem. Phys. **102**, 6371 (1995).

[6] M. I. El Idrissi, J. Liévin, A. Campargue, and M. Herman, J. Chem. Phys. **110**, 2074 (1999).

[7] D. H. Mordaunt and M. N. R. Ashfold, J. Chem. Phys. **101**, 2630 (1994).

[8] J. P. O'Brien, Ph.D. thesis, Massachusetts Institute of Technology, 1997.

[9] S. A. B. Solina, Ph.D. thesis, Massachusetts Institute of Technology, 1996.

[10] D. M. Jonas, Ph.D. thesis, Massachusetts Institute of Technology, 1992.

[11] Y. Chen, Ph.D. thesis, Massachusetts Institute of Technology, 1988.

[12] E. H. Abramson, Ph.D. thesis, Massachusetts Institute of Technology, 1985.

[13] C. Kittrell, in *Molecular Dynamics and Spectroscopy by Stimulated Emission Pumping*, edited by H.-L. Dai and R. W. Field (World Scientific, Singapore, 1995), p. 109.

[14] L. E. Fried and G. S. Ezra, J. Chem. Phys. **86**, 6270 (1987).

[15] M. E. Kellman, J. Chem. Phys. **93**, 6630 (1990).

[16] M. E. Kellman and G. Chen, J. Chem. Phys. **95**, 8671 (1991).

[17] C. Jaffe and M. E. Kellman, J. Chem. Phys. **92**, 7196 (1990).

[18] M. C. Gutzwiller, *Chaos in Classical and Quantum Mechanics* (Springer-Verlag, New York, 1990).

[19] R. W. Field, S. L. Coy, and S. A. B. Solina, Progress of Theoretical Physics **116**, 143 (1994).

[20] M. J. Bramley, S. Carter, N. C. Handy, and I. M. Mills, J. Mol. Spec. **301**, 301 (1993).

[21] J. A. Bentley, R. E. Wyatt, M. Menou, and C. Leforestier, J. Chem. Phys. **97**, 4255 (1992).

[22] L. Liu and J. T. Muckerman, J. Chem. Phys. **107**, 3402 (1997).

[23] L. Halonen, M. S. Child, and S. Carter, Mol. Phys. **47**, 1097 (1982).

[24] A. B. McCoy and E. L. Sibert III, J. Chem. Phys. **105**, 459 (1996).

[25] J. M. L. Martin, T. J. Lee, and P. R. Taylor, J. Chem. Phys. **108**, 676 (1998).

[26] M. Joyeux, J. Chem. Phys. **109**, 2111 (1998).

[27] E. L. Sibert III and A. B. McCoy, J. Chem. Phys. **105**, 469 (1996).

[28] M. Joyeux, S. Yu. Grebenshchikov, and R. Schinke, J. Chem. Phys. **109**, 8342 (1998).

[29] R. Mecke, Z. Physik **81**, 313 (1933).

[30] M. S. Child and R. T. Lawton, Faraday Discuss. **71**, 273 (1981).

[31] B. R. Henry and W. Siebrand, J. Chem. Phys. **49**, 5369 (1968).

[32] K. K. Lehmann, J. Chem. Phys. **79**, 1098 (1983).

[33] M. E. Kellman, J. Chem. Phys. **83**, 3843 (1985).

[34] M. M. Gallo, T. P. Hamilton, and H. F. Schaefer III, J. Am. Chem. Soc. **112**, 8714 (1990).

[35] J. Levin, H. Feldman, A. Baer, D. Ben-Hamu, O. Heber, D. Zajifman, and Z. Vager, Phys. Rev. Lett. **81**, 3347 (1999).

[36] K. M. Ervin, J. Ho, and W. C. Lineberger, J. Chem. Phys. **91**, 5974 (1989).

[37] T. Carrington, Jr., L. M. Hubbard, H. F. Schaefer III, and W. H. Miller, J. Chem. Phys. **80**, 4347 (1984).

[38] P. Avouris, W. M. Gelbart, and M. A. El-Sayed, Chemical Reviews **77**, 793 (1977).

[39] J. H. Keifer, P. S. Mudipalli, A. F. Wagner, and L. Harding, J. Chem. Phys. **105**, 8075 (1996).

[40] R. Schork and H. Köppel, Theor. Chem. Acc. **100**, 204 (1998).

[41] M. P. Jacobson, S. L. Coy, and R. W. Field, J. Chem. Phys. **107**, 8349 (1997).

[42] S. L. Coy, M. P. Jacobson, and R. W. Field, J. Chem. Phys. **107**, 8357 (1997).

[43] I. Dabrowski, D. W. Tokaryk, and J. K. G. Watson, J. Mol. Spec. **189**, 95 (1998).

[44] W. H. Press, S. A. Teukolsky, W. T. Vetterling, and B. P. Flannery, *Numerical Recipes in FORTRAN, Second Edition* (Cambridge University Press, Cambridge, UK, 1992).

[45] S. L. Coy, D. Chasman, and R. W. Field, in *Molecular Dynamics and Spectroscopy by Stimulated Emission Pumping*, edited by H.-L. Dai and R. W. Field (World Scientific, Singapore, 1995), p. 891.

[46] R. Hernandez, K. K. Lehmann, and W. Lafferty, unpublished data.

[47] S. L. Coy and K. K. Lehmann, Spectrochim. Acta **45A**, 47 (1989).

[48] K. K. Lehmann and S. L. Coy, J. Chem. Soc., Faraday Trans. 2 **84**, 1389 (1988).

[49] M. Meloun, M. Houalla, A. Proctor, and J. N. Fiedor, *PC-Aided Statistical Data Analysis*, Vol. 1 of *Chemometrics for Analytical Chemistry* (Ellis Horwood, New York, 1992).

[50] D. M. Hercules, M. Houalla, A. Proctor, and J. N. Fiedor, Anal. Chim. Acta **283**, 42 (1993).

[51] J. N. Fiedor, A. Proctor, M. Houalla, and D. M. Hercules, Surf. Interface Anal. **20**, 1 (1993).

[52] L. J. Frasinski, K. Codling, and P. A. Hatherly, Science **246**, 1029 (1989).

[53] D. E. Larch, SPIE **2758**, 2 (1996).

[54] J. Zupan and J. Gasteiger, Anal. Chim. Acta **248**, 1 (1991).

[55] J. Szczepanski, C. Chapo, and M. Vala, Chem. Phys. Lett. **205**, 434 (1993).

[56] G. Strang and T. Nguyen, *Wavelets and Filter Banks* (Wellesley-Cambridge, Wellesley, MA, 1996).

[57] I. Borg and P. Groenen, *Modern Multidimensional Scaling* (Springer, New York, 1997).

[58] M. J. Davis, J. Chem. Phys. **98**, 2614 (1993).

[59] I. A. Cowe, J. W. McNicol, and D. C. Cuthbertson, Anal. Proc. **27**, 61 (1990).

[60] A. J. Berger, T.-W. Koo, I. Itzkan, and M. S. Feld, Analytical Chemistry **70**, 623 (1998).

[61] B. L. Upschulte, B. D. Green, W. A. M. Blumberg, and S. J. Lipson, J. Phys. Chem. **98**, 2328 (1994).

[62] K. W. Holtzclaw, B. L. Upschulte, G. E. Caledonia, J. F. Cronin, B. D. Green, S. J. Lipson, W. A. M. Blumberg, and J. A. Dodd, J. Geophys. Res. **102**, 4521 (1997).

[63] J. A. Dodd, S. J. Lipson, J. R. Lowell, P. S. Armstrong, W. A. M. Blumberg, R. M. Nadile, S. M. Adler-Golden, W. J. Marinelli, K. W. Holtzclaw, and B. D. Green, J. Geophys. Res. **99**, 3559 (1994).

[64] P. S. Armstrong, S. J. Lipson, J. A. Dodd, J. R. Lowell, W. A. M. Blumberg, and R. M. Nadile, Geophys. Res. Lett. **21**, 2425 (1994).

[65] J. A. Dodd, J. R. Winick, W. A. M. Blumberg, S. J. Lipson, P. S. Armstrong, and J. R. Lowell, Geophysical Research Letters **20**, 2683 (1993).

[66] H. Dothe, F. von Esse, and R. D. Sharma, J. Geophys. Res. **101**, 19715 (1996).

[67] D. L. Vititoe, S. J. Lipson, C. L. Allred, R. B. Lockwood, W. A. M. Blumberg, P. S. Armstrong, M. P. Jacobson, S. L. Coy, and R. W. Field, Eos, Trans. Amer. Geophys. Union **78**, F526 (1997).

[68] J. P. O'Brien, M. P. Jacobson, J. J. Sokol, S. L. Coy, and R. W. Field, J. Chem. Phys. **108**, 7100 (1998).

[69] S. A. B. Solina, J. P. O'Brien, R. W. Field, and W. F. Polik, J. Phys. Chem. **100**, 7797 (1996).

[70] M. Abbouti Temsamani, M. Herman, S. A. B. Solina, J. P. O'Brien, and R. W. Field, J. Chem. Phys. **105**, 11357 (1996).

[71] M. Abbouti Temsamani and M. Herman, J. Chem. Phys. **105**, 1355 (1996).

[72] Y. Osamura, H. F. Schaefer III, S. K. Gray, and W. H. Miller, J. Am. Chem. Soc. **103**, 1904 (1981).

[73] R. J. Bouwens, J. A. Hammerschmidt, T. A. Stegink, M. M. Grzeskowiak, P. M. Yorba, and W. F. Polik, J. Chem. Phys. **104**, 460 (1996).

[74] M. Drabbels, J. Heinze, and W. L. Meerts, J. Chem. Phys. **100**, 165 (1994).

[75] N. Ochi and S. Tsuchiya, Chem. Phys. **152**, 319 (1991).

[76] P. Dupré, R. Jost, M. Lombardi, P. G. Green, E. Abramson, and R. W. Field, Chem. Phys. **152**, 293 (1991).

[77] D. M. Jonas, S. A. B. Solina, R. J. Silbey, and R. W. Field, J. Chem. Phys. **97**, 2813 (1992).

[78] J. K. G. Watson, M. Herman, J. C. van Craen, and R. Colin, J. Mol. Spec. **95**, 101 (1982).

[79] J. T. Hougen and J. K. G. Watson, Can. J. Phys. **43**, 298 (1965).

[80] D. B. Moss, M. P. Jacobson, R. Z. Duan, J. P. O'Brien, and R. W. Field, J. Mol. Spec. in preparation (1999).

[81] J. K. G. Watson, to be published.

[82] S. Oss, private communication.

[83] A. Frank, private communication.

[84] M. P. Jacobson, J. P. O'Brien, R. J. Silbey, and R. W. Field, J. Chem. Phys. **109**, 121 (1998).

[85] S. A. B. Solina, J. P. O'Brien, R. W. Field, and W. F. Polik, Ber. Bunsen-Ges. **99**, 555 (1995).

[86] R. W. Field, J. P. O'Brien, M. P. Jacobson, S. A. B. Solina, W. F. Polik, and H. Ishikawa, Advances in Chemical Physics **101**, 463 (1997).

[87] J. Plíva, J. Mol. Spec. **44**, 165 (1982).

[88] R. J. Bell and P. Dean, Discuss. Faraday Soc. **50**, 55 (1970).

[89] G. M. Stewart and J. D. McDonald, J. Chem. Phys. **78**, 3907 (1983).

[90] D. S. Perry, J. Chem. Phys. **98**, 6665 (1993).

[91] D. M. Leitner and P. G. Wolynes, Chem. Phys. Lett. **258**, 18 (1996).

[92] D. M. Leitner and P. G. Wolynes, J. Phys. Chem. **101**, 541 (1997).

[93] D. M. Leitner and P. G. Wolynes, J. Chem. Phys. **105**, 11226 (1996).

[94] K. S. J. Nordholm and S. A. Rice, J. Chem. Phys. **61**, 203 (1974).

[95] E. J. Heller, Phys. Rev. A **35**, 1360 (1987).

[96] E. J. Heller, J. Chem. Phys. **72**, 1337 (1980).

[97] L. Kaplan and E. J. Heller, Physica D **121**, 1 (1998).

[98] G. Hose, A. Yogev, and R. M. J. Benmair, Chem. Phys. **102**, 365 (1986).

[99] Y. S. Choi and C. B. Moore, J. Chem. Phys. **94**, 5414 (1991).

[100] G. Hose and H. S. Taylor, Chem. Phys. **84**, 375 (1984).

[101] P. Brumer and M. Shapiro, Adv. Chem. Phys. **70**, 365 (1998).

[102] J. E. Gambogi, J. H. Timmermans, K. K. Lehmann, and G. Scoles, J. Chem. Phys. **99**, 9314 (1993).

[103] C. Cohen-Tannoudji, B. Diu, and F. Laloë, *Quantum Mechanics* (John Wiley and Sons, New York, 1977), Vol. 1, pp. 727–741.

[104] M. P. Jacobson, R. J. Silbey, and R. W. Field, J. Chem. Phys. **110**, 845 (1999).

[105] J. E. Baggott, Mol. Phys. **65**, 739 (1988).

[106] H. Ishikawa, C. Nagao, N. Mikami, and R. W. Field, J. Chem. Phys. **109**, 492 (1998).

[107] R. Marquardt and M. Quack, J. Chem. Phys. **95**, 4854 (1991).

[108] R. Marquardt, M. Quack, J. Stohner, and E. Sutcliffe, J. Chem. Soc., Faraday Trans. 2 **82**, 1173 (1986).

[109] J. P. Rose and M. E. Kellman, J. Chem. Phys. **105**, 10743 (1996).

[110] L. Xiao and M. E. Kellman, J. Chem. Phys. **90**, 6086 (1989).

[111] L. Xiao and M. E. Kellman, J. Chem. Phys. **93**, 5805 (1990).

[112] M. E. Kellman and L. Xiao, J. Chem. Phys. **93**, 5821 (1990).

[113] M. Joyeux, J. Mol. Spec. **175**, 262 (1996).

[114] J. Main, C. Jung, and H. S. Taylor, J. Chem. Phys. **107**, 6577 (1997).

[115] H.-M. Keller, M. Stumpf, T. Schröder, C. Stöck, F. Temps, R. Schinke, H.-J. Werner, C. Bauer, and P. Romus, J. Chem. Phys. **106**, 5359 (1997).

[116] C. Beck, H.-M. Keller, S. Yu. Grebenshchikov, R. Schinke, S. Farantos, K. Yamashita, and K. Morokuma, J. Chem. Phys. **107**, 9818 (1997).

[117] T. Sako and K. Yamanouchi, Chem. Phys. Lett. **264**, 403 (1997).

[118] F. Iachello and R. D. Levine, *Algebraic Theory of Molecules* (Oxford University Press, New York, 1995).

[119] M. E. Kellman, Annu. Rev. Phys. Chem. **46**, 395 (1995).

[120] F. Perez Bernal, R. Bijker, A. Frank, R. Lemus, and J. M. Arias, Chem. Phys. Lett. **258**, 301 (1996).

[121] J. Manz and H. H. R. Schor, Chem. Phys. Lett. **107**, 542 (1984).

[122] S. K. Gray and M. S. Child, Mol. Phys. **53**, 961 (1984).

[123] E. J. Heller, E. B. Stechel, and M. J. Davis, J. Chem. Phys. **73**, 4720 (1980).

[124] M. E. Kellman, J. Chem. Phys. **76**, 4528 (1982).

[125] I. M. Mills and A. G. Robiette, Mol. Phys. **56**, 743 (1985).

[126] I. M. Mills and F. J. Mompean, Chem. Phys. Lett. **124**, 425 (1986).

[127] K. K. Lehmann, J. Chem. Phys. **84**, 6524 (1986).

[128] R. G. Della Valle, Mol. Phys. **63**, 611 (1988).

[129] R. T. Lawton and M. S. Child, Mol. Phys. **40**, 773 (1980).

[130] W. Siebrand and D. F. Williams, J. Chem. Phys. **49**, 1860 (1968).

[131] M. S. Child and L. Halonen, Advances in Chemical Physics **57**, 1 (1984).

[132] Y. Chen, D. M. Jonas, J. L. Kinsey, and R. W. Field, J. Chem. Phys. **91**, 3976 (1989).

[133] E. L. Sibert III and R. C. Mayrhofer, J. Chem. Phys. **99**, 937 (1993).

[134] P. van Ede van der Pals and P. Gaspard, J. Chem. Phys. **110**, 5619 (1999).

[135] E. L. Sibert III, W. P. Reinhardt, and J. T. Hynes, J. Chem. Phys. **77**, 3583 (1982).

[136] E. L. Sibert III, J. T. Hynes, and W. P. Reinhardt, J. Chem. Phys. **77**, 3595 (1982).

[137] G. M. Schmid, S. Coy, R. W. Field, and R. J. Silbey, Chem. Phys. Lett. **219**, 331 (1994).

[138] D. M. Jonas, S. A. B. Solina, B. Rajaram, R. J. Silbey, R. W. Field, K. Yamanouchi, and S. Tsuchiya, J. Chem. Phys. **99**, 7350 (1993).

[139] G. Hose and H. S. Taylor, J. Chem. Phys. **76**, 5356 (1982).

[140] K. K. Lehmann, J. Chem. Phys. **96**, 8117 (1992).

[141] J. P. Rose and M. E. Kellman, J. Chem. Phys. **105**, 7348 (1996).

[142] J. F. Stanton, C.-M. Huang, and P. G. Szalay, J. Chem. Phys. **101**, 356 (1994).

[143] S. Tsuchiya, private communication.

[144] H. S. Taylor and J. Zakrzewski, Phys. Rev. A **38**, 3732 (1988).

[145] W. Heisenberg, Z. Phyz. **33**, 879 (1925).

[146] H. Goldstein, *Classical Mechanics*, 2nd ed. (Addison Wesley, Reading, Massachusetts, 1980).

[147] S. C. Farantos, Theochem. **341**, 91 (1995).

[148] E. Reithmeir, *Periodic Solutions of Nonlinear Dynamic Systems*, *Lecture Notes in Mathematics* (Springer, New York, 1991).

[149] G. Hose and H. S. Taylor, Phys. Rev. Lett. **51**, 947 (1983).

[150] J. M. Gomez Llorente and E. Pollak, Annu. Rev. Phys. Chem **43**, 91 (1992).

[151] M. S. Child, *Semiclassical Mechanics with Molecular Applications* (Clarendon Press, Oxford, 1991).

[152] E. L. Sibert III, W. P. Reinhardt, and J. T. Hynes, J. Chem. Phys. **77**, 3583 (1982).

[153] J. P. Rose and M. E. Kellman, J. Chem. Phys. **103**, 7255 (1995).

[154] M. E. Kellman and E. D. Lynch, J. Chem. Phys. **85**, 7216 (1986).

[155] G. S. Ezra, J. Chem. Phys. **104**, 26 (1996).

[156] S. Keshavamurthy and G. S. Ezra, J. Chem. Phys. **107**, 156 (1997).

[157] T. A. Holme and R. D. Levine, J. Chem. Phys. **89**, 3380 (1988).

[158] T. A. Holme and R. D. Levine, Chem. Phys. Lett. **150**, 393 (1988).

[159] T. A. Holme and R. D. Levine, Chem. Phys. **131**, 169 (1989).

[160] R. Prosmiti and S. C. Farantos, J. Chem. Phys. **103**, 3299 (1995).

[161] H. Ishikawa and Y.-T. Chen and Y. Ohshima and J. Wang, and R. W. Field, J. Chem. Phys. **105**, 7383 (1996).

[162] H. Ishikawa, C. Nagao, N. Mikami, and R. W. Field, J. Chem. Phys. **106**, 2980 (1997).

[163] A. Hazi and H. S. Taylor, Phys. Rev. A **1**, 1109 (1970).

[164] Z.-M. Liu and M. E. Kellman, J. Chem. Phys. **107**, 1 (1997).

[165] T. Oka, J. Mol. Spec. **48**, 503 (1973).

[166] M. P. Jacobson, J. P. O'Brien, and R. W. Field, J. Chem. Phys. **109**, 3831 (1998).

[167] Y. Kabbadj, M. Herman, G. Di Lonardo, L. Fusina, and J. W. Johns, J. Mol. Spec. **150**, 535 (1991).

[168] B. C. Smith and J. S. Winn, J. Chem. Phys. **89**, 4638 (1988).

[169] A.-M. Tolonen and S. Alanko, Mol. Phys. **75**, 1155 (1992).

[170] J. Vander Auwera, D. Hurtmans, M. Carleer, and M. Herman, J. Mol. Spec. **157**, 337 (1993).

[171] R. D'Cunha, Y. A. Sarma, G. Guelachvili, R. Farrenq, Q. Kou, V. Malathy Devi, D. C. Benner, and K. Nahari Rao, J. Mol. Spec. **148**, 213 (1991).

[172] H. Finsterholzl, H. W. Schrotter, and G. Strey, J. Raman Spectrosc. **11**, 375 (1981).

[173] R. N. Zare, *Angular Momentum* (Wiley, New York, 1988).

[174] F. Iachello and S. Oss, J. Chem. Phys. **104**, 6956 (1996).

[175] A. K. Chen and W. F. Polik, J. Phys. Chem. **100**, 10027 (1996).

[176] P. W. Fairchild and E. K. C. Lee, J. Phys. Chem. **84**, 3346 (1980).

[177] K. Yamanouchi, N. Ikeda, S. Tsuchiya, D. M. Jonas, J. K. Lundberg, G. W. Adamson, and R. W. Field, J. Chem. Phys. **95**, 6330 (1991).

[178] G. J. Scherer, Y. Chen, R. L. Redington, J. L. Kinsey, and R. W. Field, J. Chem. Phys. **85**, 6315 (1986).

[179] A. L. Utz, J. D. Tobiason, E. Carrasquillo M., L. J. Sanders, and F. F. Crim, J. Chem. Phys. **98**, 2742 (1993).